

AWARD NUMBER: W81XWH-09-1-0405

TITLE: Understanding Collagen Organization in Breast Tumors to Predict and Prevent Metastasis

PRINCIPAL INVESTIGATOR: Edward Brown

CONTRACTING ORGANIZATION: University of Rochester Medical Center  
Rochester, NY 14642

REPORT DATE: November 2015

TYPE OF REPORT: Final

PREPARED FOR: U.S. Army Medical Research and Materiel Command  
Fort Detrick, Maryland 21702-5012

DISTRIBUTION STATEMENT: Approved for Public Release;  
Distribution Unlimited

The views, opinions and/or findings contained in this report are those of the author(s) and should not be construed as an official Department of the Army position, policy or decision unless so designated by other documentation.

# REPORT DOCUMENTATION PAGE

*Form Approved*  
OMB No. 0704-0188

Public reporting burden for this collection of information is estimated to average 1 hour per response, including the time for reviewing instructions, searching existing data sources, gathering and maintaining the data needed, and completing and reviewing this collection of information. Send comments regarding this burden estimate or any other aspect of this collection of information, including suggestions for reducing this burden to Department of Defense, Washington Headquarters Services, Directorate for Information Operations and Reports (0704-0188), 1215 Jefferson Davis Highway, Suite 1204, Arlington, VA 22202-4302. Respondents should be aware that notwithstanding any other provision of law, no person shall be subject to any penalty for failing to comply with a collection of information if it does not display a currently valid OMB control number. **PLEASE DO NOT RETURN YOUR FORM TO THE ABOVE ADDRESS.**

<b>1. REPORT DATE</b> November 2015		<b>2. REPORT TYPE</b> Final		<b>3. DATES COVERED</b> 1Sep2009 - 31Aug2015	
<b>4. TITLE AND SUBTITLE</b>  Understanding Collagen Organization in Breast Tumors to Predict and Prevent Metastasis				<b>5a. CONTRACT NUMBER</b>	
				<b>5b. GRANT NUMBER</b> W81XWH-09-1-0405	
				<b>5c. PROGRAM ELEMENT NUMBER</b>	
<b>6. AUTHOR(S)</b> Edward Brown  E-Mail:Edward_brown@urmc.rochester.edu				<b>5d. PROJECT NUMBER</b>	
				<b>5e. TASK NUMBER</b>	
				<b>5f. WORK UNIT NUMBER</b>	
<b>7. PERFORMING ORGANIZATION NAME(S) AND ADDRESS(ES)</b>  University of Rochester Medical Center Department of Biomedical Engineering 601 Elmwood Avenue Box 639 Rochester, NY 14642				<b>8. PERFORMING ORGANIZATION REPORT NUMBER</b>	
<b>9. SPONSORING / MONITORING AGENCY NAME(S) AND ADDRESS(ES)</b>  U.S. Army Medical Research and Materiel Command Fort Detrick, Maryland 21702-5012				<b>10. SPONSOR/MONITOR'S ACRONYM(S)</b>	
				<b>11. SPONSOR/MONITOR'S REPORT NUMBER(S)</b>	
<b>12. DISTRIBUTION / AVAILABILITY STATEMENT</b>  Approved for Public Release; Distribution Unlimited					
<b>13. SUPPLEMENTARY NOTES</b>					
<b>14. ABSTRACT</b> The ordering of collagen fibers within a tumor has significant influence on tumor metastasis: in murine breast tumor models, tumor cells move towards blood vessels along fibers that are visible via second harmonic generation (SHG), and SHG is exquisitely sensitive to molecular ordering. Tumor cells that are moving along SHG-producing (i.e. ordered) collagen fibers move significantly faster than those cells that are moving independently of SHG-producing fibers, and the extent of SHG-associated tumor cell motility is correlated with metastatic ability of the tumor model. Furthermore, the tumor-host interface of murine breast tumor models is characterized by radially oriented SHG-producing fibers associated with tumor cells invading the surrounding tissue. Consequently we believe that the process of establishing ordered fibers offers an exciting, and currently unexploited, therapeutic target. To take advantage of this, we must first learn the cellular players and molecular signals by which collagen ordering is induced. Therefore, in this application we propose to determine the key cells and signals which influence the ordering of collagen in breast tumors, determine if this ordering is predictive of metastasis, and develop new optical tools to study this ordering.					
<b>15. SUBJECT TERMS</b> Microscopy, metastasis					
<b>16. SECURITY CLASSIFICATION OF:</b> U			<b>17. LIMITATION OF ABSTRACT</b>  Unclassified	<b>18. NUMBER OF PAGES</b>  221	<b>19a. NAME OF RESPONSIBLE PERSON</b> USAMRMC
<b>a. REPORT</b>  Unclassified	<b>b. ABSTRACT</b>  Unclassified	<b>c. THIS PAGE</b>  Unclassified			<b>19b. TELEPHONE NUMBER</b> (include area code)

## Table of Contents

	<u>Page</u>
<b>1. Introduction.....</b>	<b>1</b>
<b>2. Keywords.....</b>	<b>1</b>
<b>3. Overall Project Summary.....</b>	<b>2</b>
<b>4. Key Research Accomplishments.....</b>	<b>8</b>
<b>5. Conclusion.....</b>	<b>8</b>
<b>6. Publications, Abstracts, and Presentations.....</b>	<b>9</b>
<b>7. Inventions, Patents and Licenses.....</b>	<b>12</b>
<b>8. Reportable Outcomes.....</b>	<b>12</b>
<b>9. Other Achievements.....</b>	<b>12</b>
<b>10. References.....</b>	<b>13</b>
<b>11. Appendices.....</b>	<b>218</b>

## **Introduction.**

The extent and nature of the ordering of collagen fibers within a tumor has significant influence on the process of tumor metastasis: in murine breast tumor models, tumor cells move towards blood vessels along fibers that are visible via second harmonic generation (SHG), and SHG is exquisitely sensitive to molecular ordering. Tumor cells that are moving along SHG-producing (i.e. ordered) collagen fibers move significantly faster than those cells that are moving independently of SHG-producing fibers, and the extent of SHG-associated tumor cell motility is correlated with metastatic ability of the tumor model. Furthermore, the tumor-host interface of murine breast tumor models is characterized by radially oriented SHG-producing fibers associated with tumor cells invading the surrounding tissue. Lastly, we have shown that treatment of tumors with the hormone relaxin, known to alter metastatic ability, alters the collagen ordering as detectable by SHG.

As locomotion along ordered (SHG-producing) fibers plays a pivotal role in the metastatic process, we believe that the process of establishing ordered fibers offers an exciting, and currently unexploited, therapeutic target. To take advantage of this, we must first learn the cellular players and molecular signals by which collagen ordering is induced. Therefore, in this application we propose to *determine the key cells and signals which influence the ordering of collagen in breast tumors*. We will do this by disrupting candidate cells and signals in mouse models of breast cancer using SHG-based measures of collagen ordering, and metastasis, as readouts. Additionally, we will *determine if SHG measures of collagen ordering in breast tumors are clinically useful predictors of metastatic outcome in breast cancer patient biopsies*.

This work will have great impact for several reasons. It will provide important insight into the molecular and cellular mechanisms by which the collagen in breast tumors is ordered, and how this ordering affects metastatic ability. In future work we can then exploit these findings by developing and evaluating clinically useful therapeutic techniques that will target, for the first time, the ordering of tumor collagen and hence attempt to inhibit metastatic ability, improving patient survival. This project will also explore whether collagen ordering in the tumor, as quantified by SHG, is a clinically viable predictor of metastatic outcome in patient biopsies. A measure of metastatic ability is extremely exciting, because there is currently an identified, pressing need for patient stratification based upon metastatic risk, in order to minimize 'over treatment' of patients who only require local therapy after resection, not systemic chemotherapy. This would improve patients' quality of life. Hence, this project has promise to be clinically relevant through two separate paths.

**Keywords:** Collagen, Metastasis, Second Harmonic Generation, Nonlinear Microscopy

## **Overall Project Summary:**

The Statement of Work for this grant proposal was as described below. In summary, we were interested in exploring the cellular and signaling mechanisms underlying collagen ordering in breast tumors, understanding the impact this ordering has on metastasis, and determining if optical signatures (affected by this ordering) could be used to predict metastatic outcome in the clinical setting:

*Specific Aim 1. Determine the role of macrophages in governing collagen ordering in tumors, and their mechanism of action. (Months 1-30)*

1a) Modulate the presence of macrophages, then evaluate the effects on collagen ordering in tumors, and the effects on metastatic burden. (Months 1-12) Uses liposome treatment. ~50 mice. Verifies involvement of macrophages' in collagen ordering in tumors, the exact nature of their particular impact on collagen ordering, and the impact on metastasis.

1b) Manipulate the expression of candidate genes in macrophages, and evaluate the effects on collagen ordering in tumors, and the effects on metastatic burden (Months 13-30) Uses bone marrow transfer after irradiation. Source animals are one of 7 knockouts, for 7 candidate genes. ~50x7= 350 mice. Produces identity of key signaling molecules involved in collagen ordering in tumors, the exact nature of their particular impact on collagen ordering, and the impact on metastasis.

*Specific Aim 2. Determine the role of Th1, Th2, and Tregs in governing collagen ordering in tumors, and their mechanism of action. (Months 31-60)*

2a) Modulate the presence of each cell type, then evaluate the effects on collagen ordering in tumors, and the effects on metastatic burden.(Months 31-42) Uses cell transfer after antibody treatment. ~3x50=150 mice. Produces identity of key cells involved in collagen ordering in tumors, the exact nature of their particular impact on collagen ordering, and the impact on metastasis.

2b) Manipulate the expression of candidate genes in those cell types found significant in 2a, and evaluate the effects on collagen ordering in tumors, and the effects on metastatic burden (Months 43-60) Uses cell transfer after antibody treatment. Source animals are one of 7 knockouts, for 7 candidate genes. ~3x50x7=1050 mice. Produces identity of key signaling molecules involved in collagen ordering in tumors, the exact nature of their particular impact on collagen ordering, and the impact on metastasis.

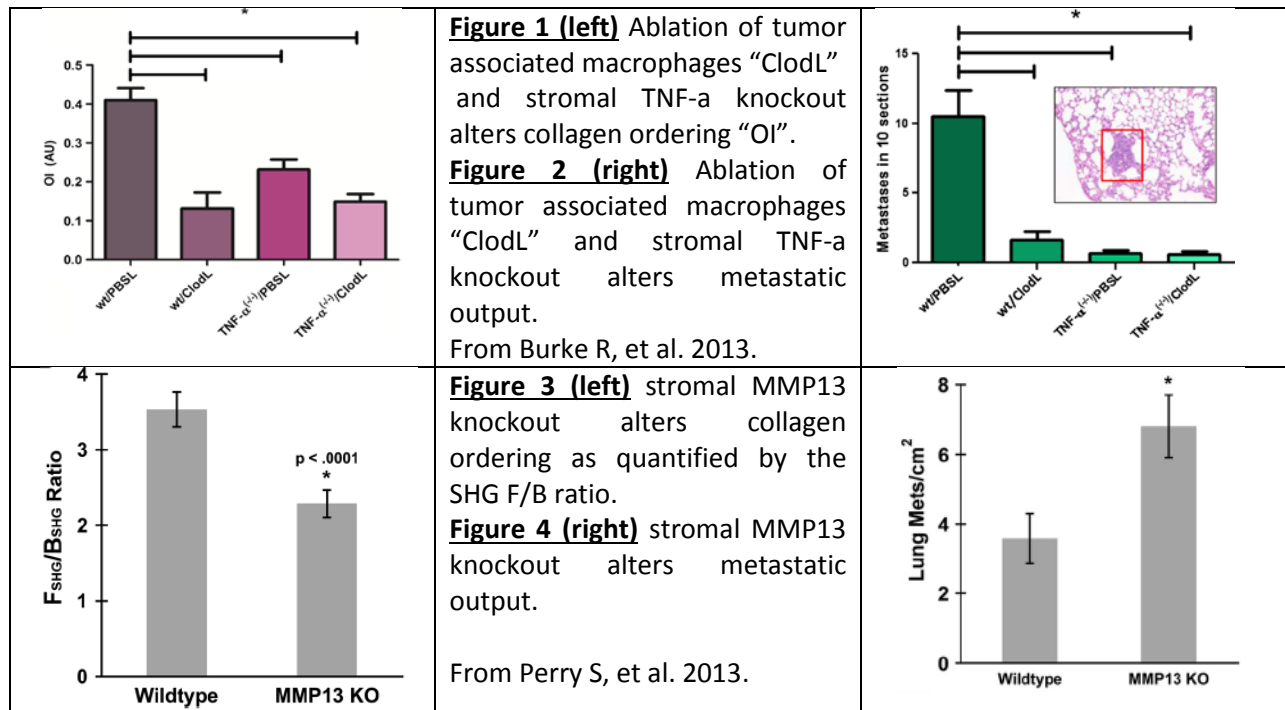
*Specific Aim 3. Determine if collagen ordering is a clinically useful predictor of metastatic ability in human tissue samples (Months 1-60).*

1a) In archival specimens from breast tumors we will evaluate the predictive relationships between collagen ordering and metastatic outcome (Months 1-60). Uses pathology samples of 4 breast tumor types to determine if SHG can predict metastatic outcome. ~4x50=200 samples. Produces an assessment of SHG's predictive ability.

In this summary I will first discuss progress on Specific Aims 1 and 3, as our results closely mirrored our expectations for those Aims. Last, I will describe progress on Specific Aim 2, in which the science led us to make great progress in a direction different from (but related to) our expectations in 2009.

Specific Aim 1. Determine the role of macrophages in governing collagen ordering in tumors, and their mechanism of action.

We have explored stromal effects of macrophages in the E0771 murine mammary adenocarcinoma grown in the mammary fat pad. In (Burke R, et al. 2013) we describe how ablation of stromal TNF- $\alpha$  as well as tumor associated macrophages altered collagen microstructure as quantified with SHG (Figure 5 in Burke R, et al. 2013, Figure 1 here), and altered metastatic outcome (Figure 6 in Burke R, et al. 2013, Figure 2 here). Looking downstream, in (Perry S, et al. 2013) we found that ablation of stromal matrix metalloproteinase 13 (MMP-13) altered collagen microstructure as measured by SHG (Figure 6 in Perry S, et al. 2013, Figure 3 here), and altered metastatic outcome (Figure 7 in Perry S, et al. 2013, Figure 4 here).



Specific Aim 3. Determine if collagen ordering is a clinically useful predictor of metastatic ability in human tissue samples.

Based upon our progress in instrumentation and technique development (described under Specific Aim 2, below), we shifted our analysis from the “Order Index” used in the works described above (backscattered SHG divided by anti-collagen immunolabeling), to the SHG scattering directionality, i.e. the amount of SHG scattered in the forward direction (of laser propagation) divided by the amount scattered in the backwards direction, the F/B ratio. In (Burke K, et al. 2013) we

demonstrated that the SHG F/B ratio predicted lymphatic metastatic burden at the time of clinical presentation in patent breast cancer samples, and also revealed several intriguing relationships between stromal collagen ordering and tumor type, stage, and grade (Figures 2,3 and 4 in Burke K, et al. 2013: Data not shown here). These relationships between F/B and stage, grade, etc., were specifically between F/B and the stage/grade of the primary tumor *at the time the patient presented themselves to the clinic*. Based upon the clear relationship between breast tumor F/B and N stage (lymphatic metastasis) at that time of presentation, as shown in Burke K, et al. 2013, we wondered if F/B could be used in patients who did NOT have evident metastasis at time of presentation. In other words could it predict the appearance of *future* metastasis? We determined that it can, as is published in **Burke K, et al. 2015a**. In ER+ invasive ductal carcinoma (IDC) F/B is a significant predictor of duration of metastasis-free survival, based upon ten year followup data (K-M Log Rank  $p < 0.05$ ) (Figure 2 in Burke K, et al. 2015a, Figure 5 here). It is not predictive in ER- IDC patients nor in the cohort of all IDC patients (ER+ and ER-) (Data not shown). The relationship is not limited to breast cancer, as F/B is also a significant predictor of patient survival in Stage 1 colon adenocarcinoma patients (K-M Log Rank  $p < 0.05$ ) (Figure 4 in Burke K, et al. 2015a, Figure 5 here), but not predictive in stage 2 or higher patients, nor is it predictive in lung adenocarcinoma patients (Figure 4 in Burke K, et al. 2015a, Data not shown here). These two results are significant because, in the two patient cohorts in which F/B is predictive, significant clinical decisions must be made: the primary tumor is removed in these patients but who gets, or does not get, adjuvant chemotherapy must be decided. In these patient cohorts there is a significant problem of “overtreatment” where patients often receive treatment who otherwise would not have metastasized. We believe that our data shows that SHG F/B is a rapid optical method to help further classify these patients and reduce overtreatment. We have filed a provisional patent on this work (**Provisional Patent Application 61/977,618**), which has been licensed by a local company.

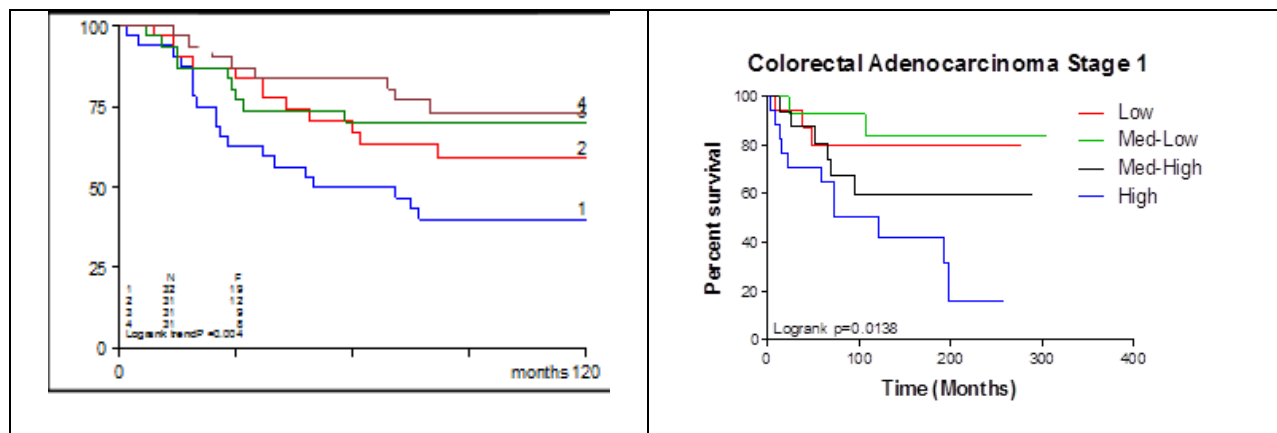


**Figure 5. A. (left)** Kaplan-Meier analysis reveals that SHG F/B is a significant indicator of metastasis free survival in Invasive Ductal Carcinoma (IDC) that has not metastasized to the sentinel lymph nodes (N0) upon presentation at the clinic. 221 patients were divided into four equally sized groups based upon the F/B of their primary tumor. B. **(Right)** K-M analysis of 69 patients reveals that F/B is also a significant indicator of overall survival in Stage 1 Colon Adenocarcinoma. From Burke K et al. 2015a.

In the above observation from clinical samples, an SHG measure of microstructure predicted metastatic outcome. However, the underlying mechanism of the microstructure/metastasis relationship was unclear: This relationship may be entirely due to collagen microstructure’s ability to alter cell

motility. Alternatively, it may be entirely due to the influence of an upstream actor within the tumor which influences collagen microstructure and tumor cell motility separately. Or it might be a combination of these mechanisms. Therefore we explored the relationship between collagen microstructure (as quantified with SHG) and tumor cell motility in a relatively “clean” collagen gel system, in which confounding upstream actors are not present, published as **Burke K et al. 2015b**. We developed optically thin collagen gels with different F/Bs and found that tumor cell motility was altered by the gel F/B ratio (Figure 6 in Burke K et al. 2015b, Figure 6 here). This suggests that the observed relationships between SHG measures of collagen microstructure and metastatic outcome are due, at least in part, to an influence of microstructure on cell motility.

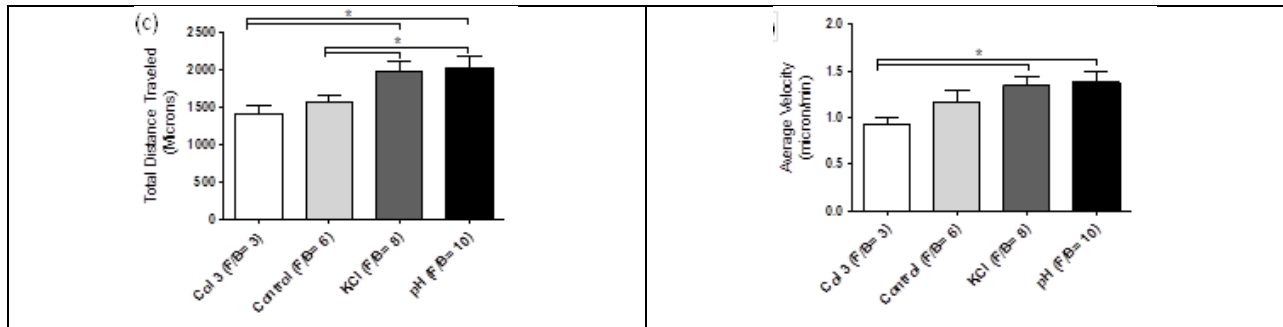


**Figure 6.** The average distance traveled by 4T1 tumor cells (**a, left**) was affected by gel F/B (ANOVA  $p < 0.05$ ). Post hoc analysis revealed the distance traveled in the two highest F/B gel categories was significantly higher than in the two lowest category. The average velocity of 4T1 tumor cells (**b, right**) was affected by gel F/B (ANOVA  $p < 0.05$ ). Post hoc analysis revealed that the average velocity in the two highest F/B gel categories was significantly higher than in the lowest category. From Burke K, 2015b.

Specific Aim 2. Determine the role of Th1, Th2, and Tregs in governing collagen ordering in tumors, and their mechanism of action. (Months 31-60)

We have found that ablating T-cells altered SHG-based measures of collagen microstructure in the primary tumor (N=7, 9,  $p < 0.05$ ) and increased the number of lung metastasis although the increase was not statistically significant (N=7,9,  $p = 0.08$ ) (Figure 7).

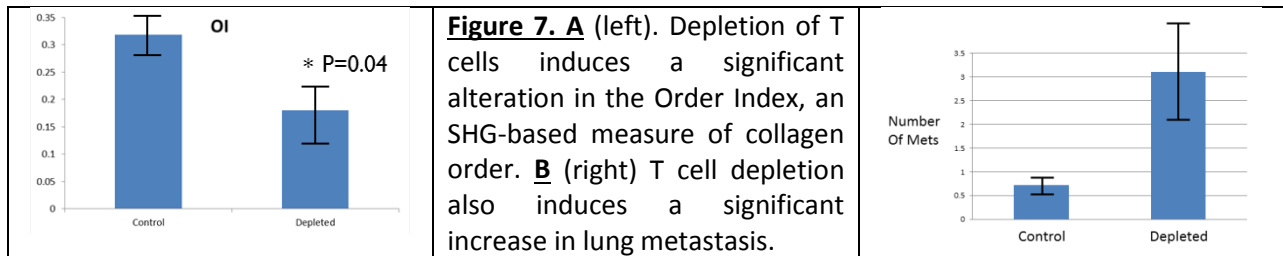
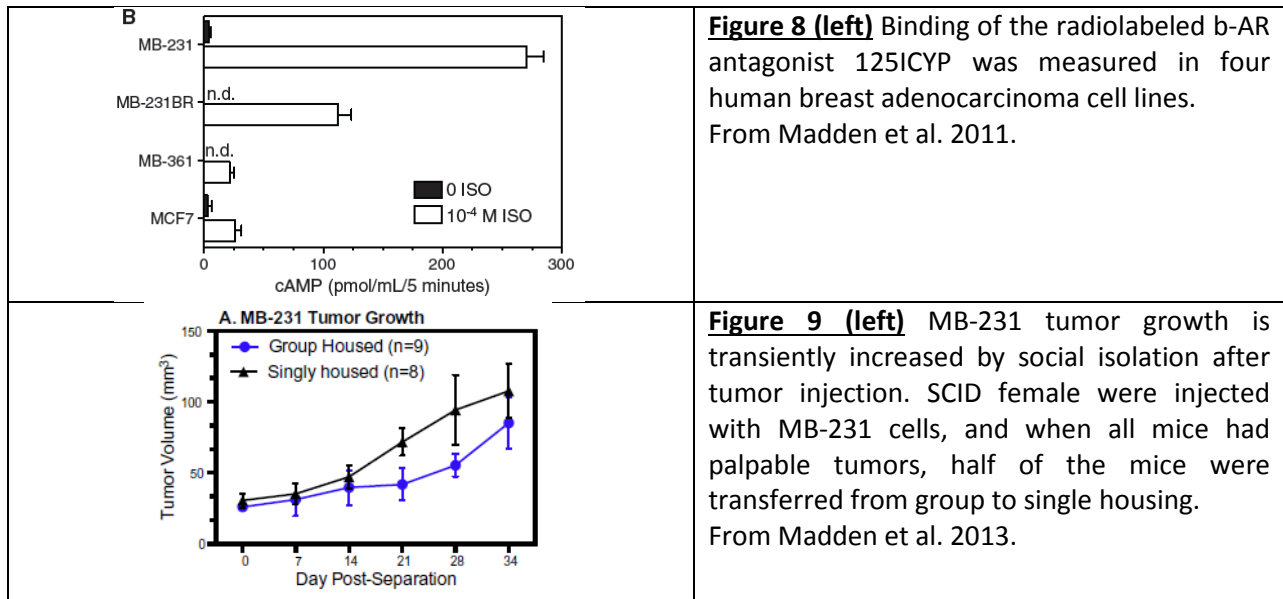


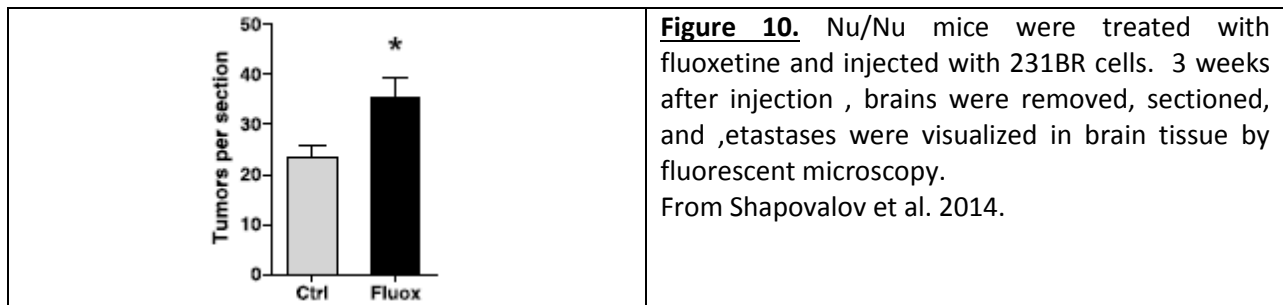
**Figure 7. A** (left). Depletion of T cells induces a significant alteration in the Order Index, an SHG-based measure of collagen order. **B** (right) T cell depletion also induces a significant increase in lung metastasis.

Due to the known effects of emotional stress on the immune system, in parallel work we explored the impact of emotional stress on breast tumor growth. This led to a series of exciting results which became a focus of this Aim. First, in **Madden K, et al. 2011** we found that the relevant molecular machinery,  $\beta$ -adrenergic receptor expression and function, is highly heterogeneous in different breast tumor cell lines (Figure 1 in Madden K, et al. 2011, Figure 8 here). In **Madden K, et al. 2013** we found

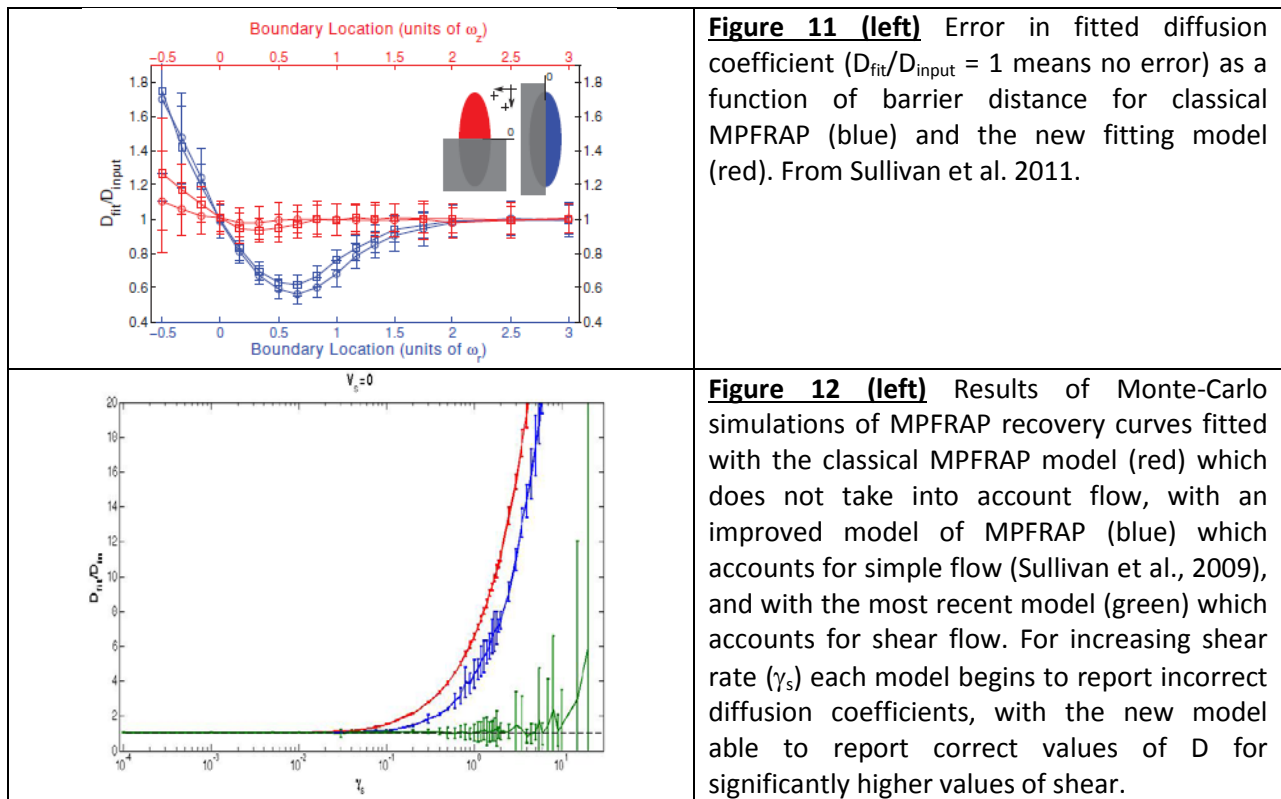
that social isolation was a functional model of emotional stress in mice and impacted tumor progression in breast tumor cell lines grown in the mammary fat pad (Figure 2 in Madden K, et al. 2013, Figure 9 here). We then found that pharmacological activation of the adrenergic receptor (AR) pathway altered tumor progression *in vivo* even in the absence of functional  $\beta$ -adrenergic receptors in the tumor cells themselves. Our aforementioned discovery that tumor associated macrophages influence SHG readouts of collagen ordering and metastatic output, and possibly operate via TNF- $\alpha$ , provided an unexpected candidate mechanism for this effect, and in **Szpunar M, et al. 2013** we found that AR stimulation does indeed alter collagen ordering as quantified by SHG (Figure 5 in Szpunar M, et al. 2013, Data not shown here).



This intersection of neuroscience and cancer, via the influence of the stromal compartment, has been extended by work revealing that administration of antidepressants affects the number of metastasis to the brain in a mouse model of brain metastatic breast cancer (**Shapovalov, et al. 2014**) although apparently through modulation of blood brain barrier permeability and not through the extracellular matrix of the brain parenchyma as we originally expected (Figure 1 in Shapovalov et al. 2014, Figure 10 here).



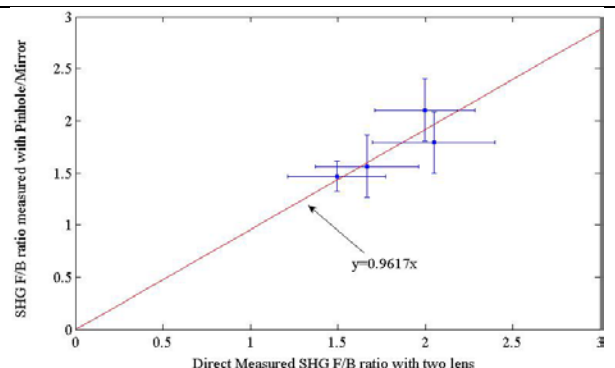
A cornerstone of our program to study the role of the extracellular matrix in tumor metastasis is to develop the optical techniques required for that study. Multiphoton Fluorescence Recovery After Photobleaching (MPFRAP) is a method to measure the diffusion coefficient of fluorescent tracer molecules with 3D resolution deep inside optically scattering tissue. The diffusion coefficient and size of a tracer molecule is an accurate reporter on the hindrance properties and pore sizes of the surrounding ECM. To apply this technique to the complex *in vivo* environment, with cell walls and other barriers to diffusion, in **Sullivan et al., 2011** we developed and demonstrated the theoretical framework necessary to perform MPFRAP in the presence of nearby barriers to diffusion of different geometries (Figure 3 in Sullivan et al., 2011, Figure 11 here). One must also take into account the presence of shear flow profiles, and we have developed the theoretical model to fit MPFRAP curves in the presence of shear flow, and tested that model in simulations and *in vitro* (Figure 4).



We have also developed two novel methods that can measure the scattering directionality of second harmonic generation (the SHG “F/B ratio”) in thick intact tissue, with a single image scan. This will be necessary for us to pursue our goal of quantifying matrix changes dynamically, in intact tumor models. The first method determines F/B by generating a series of backscattered images using a series of different sized confocal pinholes and was developed under a previous Era of Hope Scholar Award (Han et al., 2010). The second method takes an image pair using a “pinhole mirror” placed in the confocal plane. Backwards-propagating SHG passes through the pinhole and reaches one detector, while forward-propagating SHG diffuses down into the tissue, some returns to the object plane via multiple scattering, reflects off of the mirror, and reaches a second detector. With suitable calibration F/B can be

deduced (Figure 13). A provisional patent has been filed on this technique (**Provisional Patent Application 61/330,619**).

**Figure 13.** The new pinhole mirror method can measure SHG F/B in intact thick tissues. F/B was determined with the new method, then the samples were excised, thinly sliced, and F/B was also determined with classic two-detector direct measurement from thin samples. A slope of one indicates agreement between the two methods.



Finally, due to the work funded by this grant, the laboratory has developed significant expertise in the extracellular matrix, and optical methods for its study, and disseminated that expertise in a series of collaborative works (**Chen et al. 2013, Arendt et al. 2013, Huang et al. 2015, Kottmann et al. 2015**) and one invited review article (**Perry et al. 2012**).

#### **Key Research Accomplishments:**

- 1) Using second harmonic generation scattering directionality (F/B), which reports on collagen microstructure, we determined that tumor associated macrophages, stromal TNA-a, and stromal MMP-13 play a role in defining collagen microstructure and metastatic outcome.
- 2) In *in vitro* experiments we determined that collagen microstructure, as measured by F/B, directly influences tumor cell motility.
- 3) We discovered that F/B is significantly different in patient biopsy samples of different invasiveness and lymph node involvement. This led to the discovery that F/B is a significant predictor of metastasis free survival in ten-year follow up data in IDC N0 patients and stage 1 colon adenocarcinoma patients. These are two patient populations who suffer from “overtreatment” and for whom additional predictors of metastatic outcome are needed.
- 4) We expanded the applicability of the MP-FRAP technique to regions close to barriers to diffusion, and to regions with shear flow, and developed two novel techniques to measure SHG F/B in intact scattering tissue.

#### **Conclusion**

In conclusion we feel that we have successfully addressed the specific aims of the original proposal and made a significant contribution to the prevention of breast cancer mortality.

## Publications, Abstracts, and Presentations:

### Peer Reviewed Publications:

- Sullivan K, **Brown E.** (2011) Diffusion and multi-photon fluorescence recovery after photobleaching in bounded systems. *Physical Review E.* 83(5): 051916 PMC3413246
- Madden K, Szpunar M, **Brown E.** (2011)  $\beta$ -adrenergic receptors regulate VEGF and IL-6 production by divergent pathways in high  $\beta$ -AR-expressing breast cancer cell lines. *Breast Cancer Research and Treatment.* 130(3): 747-758 PMC3126869
- Madden K, Szpunar M, **Brown E.** (2013) Early Impact of Social Isolation and Breast Tumor Progression in Mice. *Brain Behavior and Immunity.* 30 S135-S141. PMC3431437
- Burke K, Tang P, **Brown E.** (2013) SHG Reveals Matrix Alterations During Breast Tumor Progression. *J Biomed Optics.* 18(3) 031106. PMC3595714
- Arendt O, Schwaller B, **Brown E,** Eilers J, Schmidt H. (2013) Restricted diffusion of calretinin in cerebellar granule cell dendrites implies  $\text{Ca}^{2+}$  dependent interactions via its EF-hand 5 domain. *Journal of Physiology.* 591:3887-3899. PMC3764635
- Burke R, Madden K, Perry S, Zettel M, **Brown E.** (2013) Tumor-associated macrophages and stromal TNF- $\alpha$  regulate collagen structure in breast tumor models as visualized by second harmonic generation. *Journal of Biomedical Optics.* 18(8):860003. PMC3731198
- Perry S, Schueckler J, Burke K, Arcuri G, **Brown E.** (2013) Stromal Matrix Metalloprotease-13 knockout alters collagen I structure at the mammary tumor-host interface and increases lung metastasis. *BMC Cancer.* 13:411. PMC3766650
- Szpunar M, Burke K, Dawes R, **Brown E,** Madden, K. (2013) The Antidepressant Desipramine and alpha2-Adrenergic Receptor Activation Promote Breast Tumor Progression in Association with Altered Collagen Structure. *Cancer Prevention Research.* 6(12):1262-72. PMC3862035
- Chen T, Hilton M, **Brown E,** Zuscik M, Awad H. (2013) Engineering superficial zone features in tissue engineered cartilage. *Biotechnology and Bioengineering.* 110: 1476-1486. PMC3694346
- Shapovalov Y, Zettel M, Kelly E, Sipe G, Dickerson I, Majewska A\*, and **Brown E\***. (2014) Fluoxetine Modulates Breast Cancer Metastasis to the Brain. *BMC Cancer.* 14:598
- Burke K, Dawes R, Cheema M, Van Hove A, Benoit D, Perry S, and **Brown E.** (2015) Second-harmonic generation scattering directionality predicts tumor cell motility in collagen gels. *Journal of Biomedical Optics* 20(5):051024.

Huang C, Ness VP, Yang C, Chen H, Luo J, **Brown EB**, Zhang X. (2015) Spatiotemporal Analyses of Osteogenesis and Angiogenesis via Intravital Imaging in Cranial Bone Defect Repair. *Journal of Bone and Mineral Research*. 30(7):1217-30.

Kottmann R, Sharp J, Owens K, Phipps R, Sime P, **Brown E**, Perry S. (2015) SHG Microscopy Reveals Altered Collagen Microstructure in Usual Interstitial Pneumonia vs Healthy Lung. *Respiratory Research*. 16:61

Burke K, Smid M, Dawes R, Timmermans M, Salzman P, van Deurzen C, Beer D, Foekens J, and **Brown E**. (2015) Using Second Harmonic Generation to Predict Patient Outcome in Solid Tumors. *BMC Cancer*. 15(1): 929

#### **Invited Articles:**

Perry S, Burke R, **Brown E**. (2012) Two Photon and Second Harmonic Microscopy in Clinical and Translational Cancer Research. *Invited Review Annals of Biomedical Engineering*. 40(2) 277-291. PMC3342697

#### **Abstracts (2011 and onwards):**

Lapeira-Soto J, Madden K, **Brown E**. Multiphoton Microscopy Reveals Flawed Pro-Angiogenic Signaling in Breast Tumor Endothelial Cells. Biomedical Engineering Society Annual Meeting. 2011.

Madden K, Szpunar M, Bouta E, **Brown E**. Detection of sympathetic tyrosine hydroxylase-positive (TH+) nerve fibers in orthotopic mammary tumors by multiphoton laser scanning microscopy (MPLSM). Psychoneuroimmunology Research Society Annual Meeting. PNI Mechanisms of Disease: From Pathophysiology to Prevention and Treatment. 2011.

Madden K, Szpunar M, Byun D, Liverpool K, **Brown E**. Detection of Sympathetic Innervation and Norepinephrine in Orthotopic and Spontaneously Occurring Animal Models of Breast Cancer. AACR Special Conference on Tumor Microenvironmental Complexity: Emerging Roles in Cancer Therapy. 2011.

Szpunar M, Madden K, Liverpool K, **Brown E**. Sympathetic nervous system innervation and function in breast cancer models. AACR Special Conference on Tumor Microenvironmental Complexity. 2011.

Shapovalov Y, Sipe G, Zettel M, **Brown E**, Majewska A. Fluoxetine Enhances the Development of Breast Tumor Metastasis in the Brain. AACR Special Conference on Tumor Microenvironmental Complexity. 2011.

Szpunar M, Madden K, Liverpool K, **Brown E**. Sympathetic nervous system innervation and function in a beta-adrenergic receptor negative breast cancer model. Psychoneuroimmunology Research Society. 2011

Szpunar M, Madden K, Liverpool K, **Brown E**. Sympathetic nervous system innervation and function in breast cancer models. DoD Breast Cancer Research Program Era of Hope Conference. 2011. *Student Poster contest finalist.*

Madden K, Szpunar M, Liverpool K, **Brown E**. Sympathetic Nerves in Breast Cancer: Function and In Vivo Imaging in an Orthotopic Animal Model. DoD Breast Cancer Research Program Era of Hope Conference. 2011.

Burke R, Perry S, Madden K, **Brown E**. Understanding Collagen Ordering to Predict and Prevent Metastasis. DoD Breast Cancer Research Program Era of Hope Conference. 2011.

Han X, Lapeira-Soto J, Sullivan K, Szpunar M, Madden K, **Brown E**. Angiogenic Signaling in Living Breast Tumor Models. DoD Breast Cancer Research Program Era of Hope Conference. 2011.

Majewska A, Shapovalov Y, Zettel M, Sipe G, **Brown E**. Brain Plasticity and Its Effects on Breast Tumor Metastasis to the Brain. DoD Breast Cancer Research Program Era of Hope Conference. 2011.

Majewska A, Shapovalov Y, Zettel M, Cash S, **Brown E**. The Influence of Neuronal Activity on Breast Tumor Metastasis to the Brain. DoD BCRP Era of Hope Conference. 2011.

Lapeira-Soto J, Madden K, **Brown E**. Abnormal VEGF-induced Ca<sup>2+</sup> Signalling in Purified Tumor Endothelial Cells. Biomedical Engineering Society Annual Meeting. 2012

Lapeira-Soto J, Perry S, O'Connell P, Brown E, and **Brown E**. Expanding the applicability of multi-photon fluorescence recovery after photobleaching by incorporating shear stress in a laminar flow model. Presentation, Biomedical Engineering Society Annual Meeting. 2012

Szpunar M, Madden K, Burke K, Byun D, Liverpool K, **Brown E**. Evidence for Sympathetic Nervous System Modulation of Mammary Tumor Pathogenesis via Tumor Collagen. Psychoneuroimmunology Research Society Annual Meeting. 2012.

Burke K. and **Brown E**. Using SHG to Study Breast Cancer Tumor Progression. The Engineering in Medicine and Biology Conference. 2012.

Burke K. and **Brown E**. Using SHG to Study Breast Cancer Tumor Progression. American Association of Cancer Research. 2013.

Dawes R, Burke K, Stastka P, Madden K, **Brown E**. The neurotransmitter norepinephrine and  $\beta$ 2-AR activation of MB-231 breast cancer cells alters fibrillar collagen structure. American Association of Cancer Research: Advances in Breast Cancer Research. 2013

Bouta E, Wood R, **Brown E**, Rahimi H, Ritchlin C, Schwarz E. Pressure and Viscosity Measurements in Afferent Lymphatics to Elucidate the Mechanisms of Arthritic Flare. Vascular Biology and Microcirculation Society Meeting, 2013.

Shapovalov Y, Amico-Ruvio S, Spielman S, Lamantia C, **Brown E**, Majewska A. " Analysis of glial activation in a murine model of brain metastatic breast cancer". American Association of Cancer Research: Advances in Breast Cancer Research. 2013

**Patents, Patent Applications:**

Han XX, **Brown E** (2010) Epidetection method and apparatus for measuring the ratio of forward-propagating to back-propagating second harmonic signal. US Patent 8,812,085 B2

**Brown E**, Perry W, Burke K, Kottman R, Sime P, Sharp J. (2014) Method and apparatus to diagnose metastatic and progressive potential of cancer, fibrosis, and other diseases. Provisional Patent Application 61/977,618

**Reportable Outcomes:** N/A

**Other Achievements:**

Promotion to Associate Professor with tenure, May 2011. Secured transition from Medical Center appointment to Main Campus (9 month) appointment, 2013. Appointment as Scientific Director, University of Rochester Multiphoton Microscopy Core Facility, July 2011. Appointment to Integration Panel, Department of Defense Ovarian Cancer Research Program, 2013. 3 graduate students have secured individual training grants while working on these projects (2 DoD BCRP, 1 NIH). 6 graduate students who have contributed to these results have earned their Ph.D. degrees.

**Tumor-associated macrophages and stromal TNF- $\alpha$  regulate collagen structure in a breast tumor model as visualized by second harmonic generation**

Ryan M. Burke  
Kelley S. Madden  
Seth W. Perry  
Martha L. Zettel  
Edward B. Brown, III

# Tumor-associated macrophages and stromal TNF- $\alpha$ regulate collagen structure in a breast tumor model as visualized by second harmonic generation

Ryan M. Burke,<sup>a</sup> Kelley S. Madden,<sup>b</sup> Seth W. Perry,<sup>b</sup> Martha L. Zettel,<sup>a</sup> and Edward B. Brown III<sup>b</sup>

<sup>a</sup>University of Rochester, Aab Cardiovascular Research Institute, 601 Elmwood Avenue Box CVRI, Rochester, New York 14642

<sup>b</sup>University of Rochester, Department of Biomedical Engineering, Goergen Hall, River Campus Box 270168, Rochester, New York 14627

**Abstract.** Collagen fibers can be imaged with second harmonic generation (SHG) and are associated with efficient tumor cell locomotion. Preferential locomotion along these fibers correlates with a more aggressively metastatic phenotype, and changes in SHG emission properties accompany changes in metastatic outcome. We therefore attempted to elucidate the cellular and molecular machinery that influences SHG in order to understand how the microstructure of tumor collagen fibers is regulated. By quantifying SHG and immunofluorescence (IF) from tumors grown in mice with and without stromal tumor necrosis factor (TNF)- $\alpha$  and in the presence or absence of tumor-associated macrophages (TAMs), we determined that depletion of TAMs alters tumor collagen fibrillar microstructure as quantified by SHG and IF. Furthermore, we determined that abrogation of TNF- $\alpha$  expression by tumor stromal cells also alters fibrillar microstructure and that subsequent depletion of TAMs has no further effect. In each case, metastatic burden correlated with optical readouts of collagen microstructure. Our results implicate TAMs and stromal TNF- $\alpha$  as regulators of breast tumor collagen microstructure and suggest that this regulation plays a role in tumor metastasis. Furthermore, these results indicate that quantification of SHG represents a useful strategy for evaluating the cells and molecular pathways responsible for manipulating fibrillar collagen in breast tumor models. © The Authors. Published by SPIE under a Creative Commons Attribution 3.0 Unported License. Distribution or reproduction of this work in whole or in part requires full attribution of the original publication, including its DOI. [DOI: [10.1117/1.JBO.18.8.086003](https://doi.org/10.1117/1.JBO.18.8.086003)]

Keywords: second harmonic generation; cancer; extracellular matrix; collagen; metastasis; multiphoton microscopy.

Paper 130206RR received Apr. 30, 2013; revised manuscript received Jun. 25, 2013; accepted for publication Jul. 2, 2013; published online Aug. 2, 2013.

## 1 Introduction

Fibrillar collagen is an extracellular matrix protein providing significant structural support to tumors and is characterized in part by its strong signal when imaged with a light-scattering process called second harmonic generation, or SHG. Collagen fibers that produce significant detectable SHG have been noted in breast tumor models as pathways of improved tumor cell locomotion.<sup>1,2</sup> This efficient, biased movement along SHG-producing fibers contrasts strongly with the random walk exhibited by cells moving independently of the fibers and also positively correlates with increased metastatic behavior.<sup>3,4</sup> This prometastatic role is enhanced by a tendency of SHG-producing fibers to orient themselves radially within tumors, extending through the tumor-host interface.<sup>3</sup> The areas where these fibers cross the interface are associated with tumor cells intravasating into healthy tissue, one step in metastasis to distant organs.<sup>3</sup> In human breast cancer samples, the presence of oriented SHG-producing fibers is an independent prognostic factor for disease-free survival, independent of grade, size, and receptor status.<sup>5</sup> In addition to these morphological properties of SHG-producing collagen fibers (direction, tortuosity, etc.), the SHG emission properties of the fibers themselves are of interest, as SHG scattering directionality has been shown to change in the transition from healthy ovarian tissue to ovarian cancer<sup>6</sup> and to evolve in concert with metastatic outcome in breast

cancer patient samples.<sup>7</sup> Finally, in addition to being used to study metastasis, SHG has been used to study drug transport, where therapeutic alteration of the tumor collagenous matrix led to an alteration in molecular transport within a tumor model.<sup>8</sup> These connections between SHG properties and metastasis/transport suggest that the next logical step is to understand the molecular machinery by which tumors control their collagenous matrix assembly and hence define their SHG properties. Consequently, in this work, we begin dissecting the cells and molecular signals responsible for manipulating tumor collagen fiber properties to which SHG is sensitive. This may, in turn, lead to novel therapeutic targets to manipulate the tumor matrix and hence alters metastatic output and/or drug delivery.

SHG is defined as the nonabsorptive combination of two excitation photons into one emission photon of exactly half the wavelength and twice the energy of the individual incoming photons.<sup>9–11</sup> SHG is a coherent phenomenon (the scatterers produce emission waves exhibiting a constant phase relationship), and as such depends on the ordering of the individual scatterers.<sup>12</sup> In the tumor, SHG is produced primarily by fibrillar collagen<sup>8</sup> and the scatterers are the individual collagen triple helices. These helices are bundled together end-to-end and side-by-side into fibrils, which are in turn bundled into generally regularly spaced arrays producing the collagen fiber. As a result of the coherent nature of SHG emission, the SHG epidetected from a given fiber is influenced by the amount of collagen triple helices in the focal volume as well as the diameter of the fibrils, their spacing, and the degree of order versus disorder in their packing.<sup>11–15</sup> In this work, we will define a change in collagen “microstructure” as a change in these last three parameters (fibril

Address all correspondence to: Edward B. Brown III, University of Rochester, Department of Biomedical Engineering, Goergen Hall, River Campus Box 270168, Rochester, New York 14627. Tel: (585) 273-5918; Fax: (585) 276-2254; E-mail: [edward\\_brown@umc.rochester.edu](mailto:edward_brown@umc.rochester.edu)

diameter, spacing, and packing order). To help distinguish changes in fiber microstructure from simple alterations in local fibril density, we will compare SHG emission signal to signal from collagen I immunofluorescence (IF) in the manner of Diop-Frimpong et al.<sup>16</sup> and Ingman et al.<sup>17</sup> We chose to quantify collagen content with collagen I IF because collagen I is the primary fibrillar collagen that generates SHG *in vivo*, and while other fibrillar collagens such as III and V can contribute to SHG emission,<sup>18,19</sup> *in vivo* they exist in molar ratios to collagen I of significantly less than one.<sup>20,21</sup> The SHG signal from a given focal point in a multiphoton laser-scanning microscope is sensitive to collagen fiber microstructure (as defined above) as well as fiber content, whereas IF yields information as to the total number of accessible epitopes present in the focal volume and is therefore sensitive to fiber content. We will therefore define the ratio of SHG to collagen I IF as an “ordering index,” or OI. Changes in the OI can then be interpreted as changes primarily in collagen fiber microstructure, distinct from changes in total collagen fiber content which will tend to cancel out in the numerator and denominator. The OI can be determined readily on a pixel-by-pixel basis using simultaneous image capture in two color channels or can be averaged over entire image fields.

To use this SHG-based tool to determine if a given candidate cell type or signal plays a role in defining tumor collagen microstructure, we must now identify some candidate cell types and/or signals to test. Breast tumors are not only composed solely of tumor cells but also host cell types including hematopoietic and stromal cells of which up to approximately 50% may be macrophages.<sup>22,23</sup> Leukocyte infiltration in the breast tumor, originally thought to simply indicate an antitumor response, has been recognized as far more complicated. Clinical data indicate that high densities of leukocyte infiltration, particularly tumor-associated macrophage (TAM) invasion, correlate with poor clinical prognosis and increased instance of metastatic disease.<sup>24,25</sup> TAMs are uniquely suited to tumorigenic promotion—they produce a wide variety of growth factors, cytokines, matrix-altering enzymes, and chemokines that coordinate to assist in matrix remodeling and angiogenesis.<sup>22</sup> Hence, we have identified the TAM as a promising candidate for a cell that manipulates collagen microstructure.

The identification of the TAM as a candidate cell that may manipulate collagen microstructure in breast tumor models is supported by one key recent study, in which mice deficient in colony-stimulating factor 1 (a protein essential to macrophage proliferation, survival, and chemotactic recruitment) showed marked alterations in terminal end bud formation in the mammary duct.<sup>17</sup> The abortive development of the end bud was noted as well as a steep decrease in the SHG around the mammary duct. Curiously enough, the total amount of collagen present as detected by IF was unaffected. This represents a decrease in OI accompanying the loss of macrophages in the breast bud area and identifies macrophages as a cell type capable of affecting OI in at least one model system. A previous study showed that upon treatment with the hormone relaxin, soft tissue sarcomas respond by altering collagen I structure with SHG intensity as a readout.<sup>8</sup> Relaxin binds specifically to macrophage glucocorticoid receptors, which results in alterations in macrophage cytokine expression, including negative modulation of TNF- $\alpha$  expression by macrophages *in vitro*.<sup>26,27</sup> Hence, we have identified TAMs as candidate cells, and TNF- $\alpha$  signaling as a candidate signaling molecule to manipulate the OI.

Interestingly, TNF- $\alpha$  is also shown to be essential to primary growth and metastatic progression in Lewis lung carcinoma.<sup>28</sup>

We, therefore, hypothesize that TAMs can affect collagen fiber microstructure in tumors, as measured by the OI, and that this is accomplished through TAM expression of TNF- $\alpha$ . To test this hypothesis, we grew mammary fat pad (MFP) tumors using a breast tumor cell line (E0771, a mammary adenocarcinoma derived from C57Bl/6 mice) in wild-type mice and mice genetically incapable of expressing TNF- $\alpha$ . Additionally, in both types of mice, TAMs were depleted by periodic injections of clodronate-containing liposomes (ClodL).<sup>29</sup> OI and metastatic burden were evaluated, and we show for the first time that the expression of TNF- $\alpha$  by the host stromal cells of the tumor affects collagen microstructure (as measured by OI), that TAMs affect collagen microstructure in tumors, and that the influence of TAMs and stromal TNF- $\alpha$  expression is not additive. We also show that these effects on collagen microstructure each correlate with a significant decrease in metastatic events. Consequently, these results may provide a platform for therapies that manipulate collagen microstructure and thereby impact the metastatic output of the tumor. This work further serves to demonstrate the utility of SHG as an additional tool to reveal cells and signals which play a role in defining tumor collagen properties.

## 2 Materials and Methods

### 2.1 Cells and Reagents

A murine medullary mammary adenocarcinoma syngeneic with C57Bl/6 mice (E0771, Roswell Park Cancer Institute, Buffalo, NY) was maintained in RPMI 1640 medium (Gibco/Invitrogen, Carlsbad, CA) supplemented with 10% gamma-irradiated fetal calf serum (HyClone/Thermo-Fisher, Waltham, MA) and Primocin (InvivoGen, San Diego, CA). Cells were passaged no more than five times before being replaced from frozen stocks. After harvesting with 25% trypsin/ethylenediaminetetraacetic acid (EDTA), cells were centrifuged and resuspended in sterile phosphate buffered saline (PBS) and kept on ice until implantation into a mammary fat pad. T47D and MCF-7 human breast cancer cell lines [American Type Culture Collection (ATCC), Manassas, VA] were also cultured in RPMI 1640 medium for use in *in vitro* proliferation assays. RAW264.7 transformed murine macrophages (ATCC) were used as a positive control for TNF- $\alpha$  production and were cultured in Dulbecco's modified Eagle's medium (DMEM) supplemented with 4.5 g/L glucose, 10% fetal calf serum (FCS), and Primocin. To activate RAW264.7 cells, lipopolysaccharide (LPS, *Escherichia coli* serotype 026:B6, Sigma-Aldrich, St. Louis, MO) was added to media at 100 ng/mL for 24 h prior to assaying for TNF- $\alpha$ . All lines were tested for mycoplasma contamination bi-monthly using MycoFluor detection kit (Invitrogen, Carlsbad, CA) and only certified mycoplasma-free cultures were used for implantation.

### 2.2 Purification of Tumor CD11b+ Cells by Magnetic Separation

E0771 tumors grown in mammary fat pads were finely minced, washed with RPMI 1640 and then shaken in medium supplemented with 0.5 mg/mL of collagenase type D (Sigma-Aldrich, St. Louis, MO) at 37°C for 180 min. The cell dispersion was passed through metal mesh (100- $\mu$ m pore size) and washed

three times in RPMI 1640, then resuspended in MACS buffer (Miltenyi Biotec, Auburn, CA) containing 2% EDTA and 5% bovine serum albumin (BSA) in PBS. To harvest CD11b<sup>+</sup> cells, the single-cell suspension was incubated with anti-CD11b antibody conjugated to magnetic beads (Miltenyi Biotec, Auburn, CA). The cell suspension was then applied to a type LS positive selection column with MidiMACS (Miltenyi Biotec) according to manufacturer instructions. Selected cells were cultured to ~70% confluence in DMEM supplemented with 10% FCS and Primocin.

### 2.3 Animals and Husbandry

C57Bl/6 female mice (Jackson Laboratories, Bar Harbor, ME) were used between 15 and 19 weeks of age. Mice were housed in two-way static (nonventilated) conditions in groups of five, and were allowed *ad libitum* access to standard food and water. To determine the effects of global deletion of TNF- $\alpha$ , female B6.129S-Tnf<sup>tm1Gkl</sup>/J (Jackson Labs) mice were used between 15 and 19 weeks of age and housed as above. C57Bl/6 animals represent a valid control genotype for this knockout. All animal work was done in accordance with University Committee for Animal Resources regulations.

### 2.4 Tumor Implantation and Liposome Administration

Animals were anesthetized with a ketamine/xylazine mixture (90/9 mg/kg body weight) delivered intraperitoneally (i.p.). The ventral surface of the animal was depilated and  $1 \times 10^5$  E0771 cells were implanted in the right inguinal mammary fat pad using a 27-gauge needle. Four hours following this procedure, mice were administered either PBS- or clodronate-containing liposomes (Encapsula NanoSciences, Nashville, TN, 5 mg/mL stock solution) i.p. at 0.4 mL/20 g body weight on day 0.<sup>29</sup> After the first injection, liposomes were injected every third day at 0.2 mL/20 g body weight. The long and short axes of each tumor were measured on days 3, 9, 15, 21, and 27 with digital calipers. Tumor volume was calculated using the formula for a prolate spheroid [ $V = (4/3)\pi N^2 L$ ] and standardized to volume at day 3 (multiplicity). On day 27 post-implantation, animals were sacrificed by sodium pentobarbital overdose and subsequent cervical dislocation. Half the tumor was frozen in dry ice for sectioning and immunohistochemistry. The other half was placed in cell culture media and prepared for flow cytometric analysis. Lungs were placed in 10% neutral-buffered formalin for hematoxylin and eosin (H&E) staining.

### 2.5 Flow Cytometry

To prepare a single cell suspension, tumors were finely minced, washed with RPMI 1640, and strained through a 70- $\mu$ m mesh filter to remove debris. After centrifuging two times, the cells were counted by cytometer with trypan blue exclusion. Viable cells ( $2 \times 10^6$ ) were incubated at 4°C for 15 min in ACK buffer to lyse red blood cells, centrifuged, and resuspended in flow wash buffer consisting of 1% BSA and 25% sodium azide in sterile PBS. Cells were incubated for 30 min with 25- $\mu$ L anti-mouse CD16/CD32 antibody at 1:50 dilution (BD Pharmingen, Franklin Lakes, NJ) to block  $F_c\gamma$  receptors and then were resuspended in 100  $\mu$ L buffer containing either: (1) buffer only (autofluorescence); (2) 1:50 peridinin chlorophyll-conjugated rat IgG<sub>2a</sub> [BD Pharmingen (isotype control)], or (3) fluorescein isothiocyanate (FITC)-conjugated rat (IgG<sub>2a</sub>)

anti-mouse F4/80 (Abcam, Cambridge, MA). Cells were incubated in the dark for 30 min at 4°C. Cells were then centrifuged in flow wash buffer twice and resuspended in 4% paraformaldehyde. Samples were stored in the dark at 4°C until cytometric analysis using a FACSAria flow cytometer (BD Biosciences, Franklin Lakes, NJ) equipped with FlowDiVa software.

### 2.6 TNF- $\alpha$ Determination

A Quantikine enzyme-linked immunosorbent assay (ELISA) kit specific for mouse TNF- $\alpha$  (R&D Systems, Minneapolis) with a sensitivity of 5.1 pg/mL was employed to measure TNF- $\alpha$  in cell culture supernatants and tumor lysates. To prepare cell culture supernatants, cells were grown to 70% confluence in a T-75 tissue culture flask and then media was removed and replaced with reduced serum media for 48 h. This media was removed, centrifuged, and immediately assayed for TNF- $\alpha$ . Tumor lysates were prepared by homogenization of excised tumor tissue in RIPA buffer containing sodium deoxycholate and HALT protease/phosphatase inhibitor (Pierce Protein Research, Rockford, IL). Lysates were centrifuged at 18,000  $\times$  g for 10 min and supernatants were removed for assay. Total protein concentration in tumor lysates was determined with a bicinchoninic acid assay (Pierce Protein Research, Rockford, IL) per manufacturer specifications. For the ELISA, absorption was measured at 450 nm using a multiwell plate reader (Synergy HT, BioTek Instruments Inc, Winooski, VT). Curve fitting and sample concentration calculations were conducted with Gen5 software (Biotek). Results are presented as TNF- $\alpha$  concentration standardized to sample protein concentration.

### 2.7 Proliferation Assays

*In vitro* proliferation was determined with the use of a fluorescent CyQuant Cell Proliferation Assay (Molecular Probes/Invitrogen, Carlsbad, CA) following manufacturer's instructions. To detect DNA fluorescence, a plate reader (BioTek) exciting bound dye at 480 nm and detecting at 520 nm was used. This assay effectively measures viable cell number, and we have determined that fluorescent intensity correlates directly with actual cell number (data not shown).

### 2.8 Immunohistochemistry

Snap-frozen tumor halves were sectioned at 7  $\mu$ m on a cryostat (Reichert-Jung, Depew, NY) at -21°C and static-mounted on positively charged slides (VWR, Radnor, Pennsylvania). Each slide contained at least four sections from each experimental group to minimize possible staining artifacts between samples. Sections were fixed in a 3:1 mixture of acetone/methanol for 20 min at -20°C. Slides were rehydrated twice in sterile PBS for 5 min and then placed in peroxidase blocking solution (5% BSA, 2% Triton X-100) for 1 h, followed by two 5 min PBS washes. Sections were incubated at room temperature for 2 h in a humidified chamber with PBS containing 5% BSA and combinations of the following antibodies: (1) rabbit anti-mouse collagen I (Abcam, Cambridge, MA), 1:200 dilution; (2) FITC-conjugated rat IgG<sub>2a</sub> anti-mouse CD31 (BD Pharmingen, Franklin Lakes, NJ), 1:500 dilution; or (3) FITC-conjugated rat IgG<sub>2a</sub> anti-mouse F4/80, 1:50 dilution. To detect rabbit anti-mouse collagen I, sections were then washed 2  $\times$  5 min and incubated for 2 h at room temperature in AlexaFluor 594-conjugated goat anti-rabbit IgG (Invitrogen, Carlsbad,

CA), 1:500 dilution. Optimal antibody dilutions were predetermined. Slides were then washed and coverslipped in Prolong Gold AntiFade without DAPI (Invitrogen, Carlsbad, CA) and allowed to dry 24 h before imaging.

## 2.9 Evaluation of Metastatic Burden

Automated H&E staining (Dako, Carpinteria, CA) was performed on 3  $\mu\text{m}$  rotary microtome sections of paraffin-embedded lungs. H&E-stained lung sections were obtained at 50  $\mu\text{m}$  intervals through both lobes of the lung and evaluated by a blinded observer using brightfield microscopy (Olympus BX-51, Center Valley, PA). Malignant cells lose their differentiation and undergo increased proliferation, frequently exhibiting enlarged and variable sized nuclei as well as evidence of accelerated mitosis. Consequently, accepted criteria for recognizing metastatic foci in H&E-stained sections include a high ratio of hematoxylin relative to eosin, surrounding abnormalities in lung structure, abnormal shape/size of nuclei and/or presence of abnormal mitotic spindles, and differences in cell shape and size.<sup>30</sup> We used these criteria to identify lung metastases, with results presented as the number of metastases in 10 sections per animal.

## 2.10 Imaging and Image Analysis

Slides were imaged by a blinded observer using a custom-built two-photon microscope (Olympus). Two-photon (2P) excitation was achieved by a MaiTai Ti:sapphire laser providing 100 fs pulses at 80 MHz and 810 nm. Beam scanning and image acquisition were performed with a Fluoview FV300 scanning system interfaced with a BX61WI upright microscope (Olympus, Center Valley, PA). The focusing objective was a XLUMPLFL20xW water immersion lens (20 $\times$ , 0.95 N.A., Olympus). The objective focused the 810 nm excitation beam on the sample and at the same time collected both backscattered SHG signal and the two-photon excited IF from the antibody of interest. The backscattered SHG and IF signals were separated from the excitation beam by a short pass dichroic mirror (670 DCSX, Chroma, Rockingham, VT), with the SHG and IF emissions then separated into two channels with a long pass dichroic mirror (475 DCSX, Chroma, Rockingham, VT). SHG was collected with a bandpass filter centered at 405 nm (HQ405/30m-2P, Chroma) and detected by a photomultiplier tube (PMT) (HC125-02 Hamamatsu Corporation, Hamamatsu, Japan). The IF signal was collected with a bandpass filter centered at 635 nm (HQ635/30m-2P, Chroma). For capturing this red IF channel, a red-sensitive PMT was used (Hamamatsu HC125-01), and the emission signal was additionally filtered (Chroma E700SP-2P) to block any stray near-infrared infrared (IR) laser light. Resulting images are 680  $\mu\text{m}$  across. Laser power was monitored and kept constant throughout the experiment and across experimental repetitions, as were PMT voltage, gain, and offset. Ten tissue slices were chosen by a blinded observer, spaced throughout each tumor half (the other half is used to verify macrophage depletion) and five fields of view were generated from each slice. The five imaged fields of view formed an "x" pattern; one in the tumor center, then four adjacent diagonal fields of view (i.e., one to the upper left of the first central image, with the corners of the images not quite touching, one to the upper right of the first central image, etc.). Hence, 50 image pairs were analyzed as described below to produce a single average SHG/IF value for each tumor.

Image analysis was performed as follows. In IMAGE J (Rasband, W. S., IMAGE J, U. S. National Institutes of Health, Bethesda, Maryland, USA, <http://imagej.nih.gov/ij/>, 1997–2011), the background in each channel (SHG and IF) was defined by the average pixel counts of an image with no excitation laser and subtracted from the raw SHG and IF images, respectively. A single common threshold was then chosen by a blinded observer which passed the most collagen pixels while rejecting the most background pixels (typically individual pixels not clearly laying in a fibrillar pattern). The common threshold was then applied to all SHG images, setting collagen fiber pixels to 1 and any remaining dim background pixels to zero, producing an "SHG mask." The same thresholding procedure was followed with IF images, producing an "IF mask." The SHG image was multiplied by the SHG mask, producing the "masked SHG image," and the IF image was multiplied by the IF mask to produce the "masked IF image." The average pixel count of the masked SHG image, divided by the average pixel count of the SHG mask, is then the average pixel count of those pixels above threshold, i.e., within collagen fibers, likewise with the masked IF image. The average SHG pixel count, average IF pixel count, and their ratio, of those pixels within collagen fibers, are then reported as the images' SHG, IF, and OI, respectively. Note that due to fluctuations in pixel counts, there are occasional pixels which are above threshold in the SHG image but below threshold (and hence set to zero) in the IF image. Consequently, the SHG/IF ratio is infinity for those pixels. This makes it problematic to calculate an average SHG/IF for the imaged region by first producing an SHG/IF ratio image and then calculating the average pixel count of that image. We avoid this problem by first separately calculating the average SHG and IF pixel counts of the whole imaged region and then dividing these two (nonzero) numbers to produce the SHG/IF for the whole imaged region.

## 2.11 Statistical Analysis

Statistical analysis was performed using Prism 5 software (GraphPad, La Jolla, CA). Student's (unpaired) *t*-tests were employed to make pairwise comparisons where appropriate. To analyze the effects of macrophage depletion and TNF- $\alpha$  knockout, two-way analysis of variance (ANOVA) was used. Significant main effects or interactions were analyzed with Bonferroni posttests to adjust for multiple comparisons. Tumor growth curves were assessed by two-way ANOVA with repeated measures, followed by multiple group comparisons using Bonferroni *posthoc* analysis. Probability values (*p*) less than or equal to 0.05 were considered significant differences between groups. When *N* is reported for animal experiments in the figures or text, it represents the number of animals studied.

## 3 Results

### 3.1 E0771 does not Produce TNF- $\alpha$ nor Proliferate in Response to TNF- $\alpha$ In Vitro or In Vivo

Pilot experiments were conducted to determine: (1) if E0771 cells produce TNF- $\alpha$  and (2) if E0771 responds to TNF- $\alpha$ . E0771 cells cultured with 10% FCS to 75% confluence did not produce measurable TNF- $\alpha$  [ $<5.1$  pg/mL, Fig. 1(a)]. By comparison, RAW 264.7 macrophages were also tested at 75% confluence in both normal and LPS-activated conditions

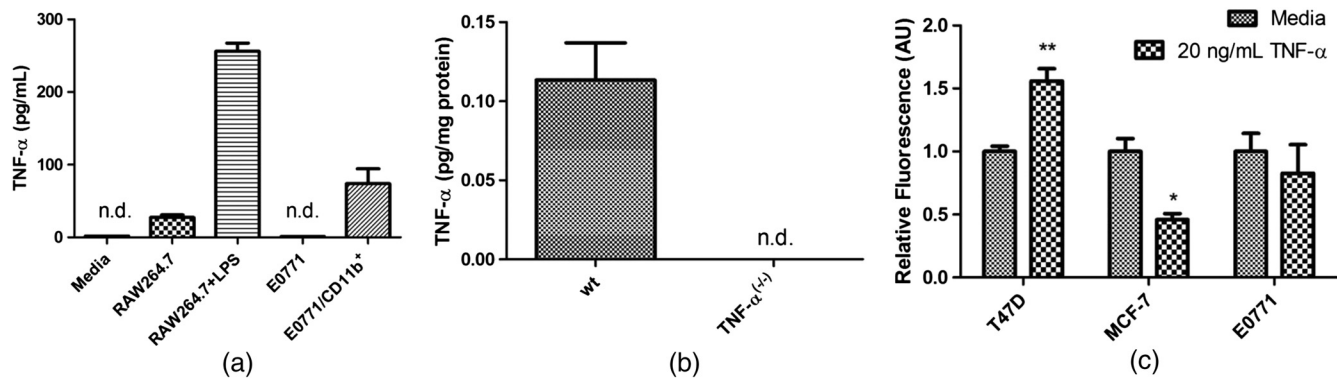


**Fig. 1** E0771 breast cancer cells do not produce nor respond to TNF- $\alpha$ . (a): *In vitro* TNF- $\alpha$  production: Supernatants from E0771 tumor cells showed no detectable TNF- $\alpha$  *in vitro* (E0771 bar). Supernatants from CD11b+ TAMs isolated from E0771 tumors, in contrast, did produce detectable TNF- $\alpha$  (E0771/CD11b+ bar). To confirm sensitivity of the assay, RAW264.7-transformed murine macrophages produced detectable TNF- $\alpha$  both when unstimulated (RAW264.7 bar) and upon activation with 100 ng/mL LPS for 24 h (RAW264.7+LPS bar). TNF- $\alpha$  ELISA sensitivity was 5.1 pg/mL,  $n = 8$  samples for all but E0771/CD11b+, where  $n = 5$ . Both the media alone control (media bar) and E0771 supernatants (E0771 bar) registered below sensitivity (not detectable). (b): *In vivo* TNF- $\alpha$  production: also by this same ELISA assay, TNF- $\alpha$  was detectable in E0771 tumors grown in C57Bl/6 mice (wt bar) but not in mice lacking TNF- $\alpha$  [TNF- $\alpha$ <sup>(-/-)</sup> bar]. (c): Proliferation responses to TNF- $\alpha$ : three breast tumor cell lines (T47D, MCF-7, and E0771) were treated with media control or 20 ng/mL TNF- $\alpha$ . Pairwise comparisons indicate that T47D proliferation was significantly elevated by 20 ng/mL TNF- $\alpha$  at 48 h ( $p < 0.01$ ), MCF-7 proliferation was significantly decreased ( $p < 0.05$ ), whereas only E0771 proliferation was unchanged in response to TNF- $\alpha$ . Proliferation was assessed by fluorescent intensity of CyQuant DNA-binding dye standardized to that of cells in untreated media,  $n = 10$  per group.

and produced significant levels of TNF- $\alpha$  with or without activation by LPS [Fig. 1(a)]. To confirm that TAMs from E0771 tumors produce TNF- $\alpha$ , macrophages were isolated from E0771 tumors using magnetic antibody separation targeted to CD11b.<sup>31</sup> These TAMs also produced TNF- $\alpha$  at detectable levels in culture [Fig. 1(a)]. Furthermore, E0771 tumors were grown in both wild-type and TNF- $\alpha$ <sup>(-/-)</sup> animals. TNF- $\alpha$  was readily detectable in wild-type-derived E0771 tumor lysates at 1:1, 1:10, and 1:25 dilutions, but not in those grown in TNF- $\alpha$ <sup>(-/-)</sup> mice, where levels were again undetectable [ $<5.1$  pg/mL, Fig. 1(b)]. Taken together, these results suggest that the E0771 cell line is not a source of TNF- $\alpha$  production *in vitro* or *in vivo* and that E0771-associated macrophages, as expected, are a primary source of this signal *in vivo*.

The proliferative response of E0771 to TNF- $\alpha$  was determined using a fluorescent DNA-binding dye kit (CyQuant). In another model of breast cancer (T47D), TNF- $\alpha$  was shown to directly promote mitogenic signaling by binding to TNFR1 and activating p42/p44 MAPK, JNK, PI3-K/Akt pathways, and NF- $\kappa$ B transcriptional activation.<sup>32</sup> Furthermore, in that model, application of TNF- $\alpha$  supported tumor growth. Conversely, TNF- $\alpha$  induced apoptosis in MCF-7 breast cancer cells *in vitro*.<sup>33</sup> To determine the response of E0771 cells to TNF- $\alpha$ , we incubated cells for 48 h in either media or media containing 20 ng/mL TNF- $\alpha$  [Fig. 1(c)]. TNF- $\alpha$  did not significantly alter proliferation of E0771, in direct contrast to the human breast tumor cell line T47D, which showed a marked increase in proliferation in response to 20 ng/mL TNF- $\alpha$ , as reported.<sup>32</sup> Furthermore, MCF-7 cells exposed to this level of TNF- $\alpha$  exhibited significant reduction in proliferation, also as expected.<sup>33</sup> Therefore, TNF- $\alpha$  does not significantly stimulate E0771 proliferation nor significantly inhibit its growth.

### 3.2 ClodL Selectively Impairs Macrophage Viability *In Vitro* and Depletes TAMs *In Vivo*

ClodL are commonly used to selectively deplete macrophages in tumors.<sup>29</sup> Macrophages that phagocytose ClodL are destroyed by release of clodronate into the cytoplasm following

degradation of the liposome shell and subsequent formation of a lethal metabolite.<sup>34</sup> To determine if TAM susceptibility to ClodL is specific, we tested the viability of E0771 cells, fibroblasts (HFF-1, transformed human foreskin fibroblasts), and RAW264.7, a transformed murine macrophage cell line in the presence of PBS-containing liposomes (PBSL) or ClodL. ClodL did not alter viability of E0771 or HFF-1 cells relative to PBSL-treated controls. By contrast, RAW264.7 viability was significantly reduced by ClodL [Fig. 2(a)]. Depletion of TAMs *in vivo* was quantified by flow cytometric analysis of F4/80, a marker for mature macrophages.<sup>35</sup> ClodL treatment in E0771-bearing mice dramatically reduced the percentage of F4/80-positive cells in E0771 tumors in both wild-type and TNF- $\alpha$ <sup>(-/-)</sup> mice [Fig. 2(b)]. Together, these results demonstrate that ClodL treatment is selective for TAMs in E0771 tumors. Figure 2(b) also demonstrates that the percentage of E0771-associated F4/80-positive macrophages is not statistically different between wild-type and TNF- $\alpha$ <sup>(-/-)</sup> mice ( $p = 0.35$ ).

### 3.3 Effects of TAM Depletion and TNF- $\alpha$ Knockout on Intensity of SHG-Producing Fibers

To determine if TAM depletion or TNF- $\alpha$  knockout affects the intensity of SHG-producing fibers in the E0771 tumor, tumors were grown orthotopically in either wild-type or TNF- $\alpha$ <sup>(-/-)</sup> mice treated with liposomes containing clodronate to deplete TAMs. Control mice were treated with liposomes containing PBS. SHG imaging of excised E0771 tumors reveals a typical fibrillar structure (Fig. 3). Figure 4(a) shows that either TAM depletion or TNF- $\alpha$  knockout reduced the intensity of SHG-producing fibers in E0771 tumors. By two-way ANOVA, a strong main effect of TAM depletion ( $p < 0.0001$ ) and a strong interaction between TAM depletion and TNF- $\alpha$  knockout ( $p < 0.0004$ ) was revealed. By Bonferroni's posttest for multiple comparisons, the intensity of SHG-producing fibers in wild-type/PBSL mice was significantly elevated relative to all other groups ( $p < 0.05$ ). Intensity of SHG-producing fibers in tumors from TNF- $\alpha$ <sup>(-/-)</sup>/PBSL mice was also greater than that in

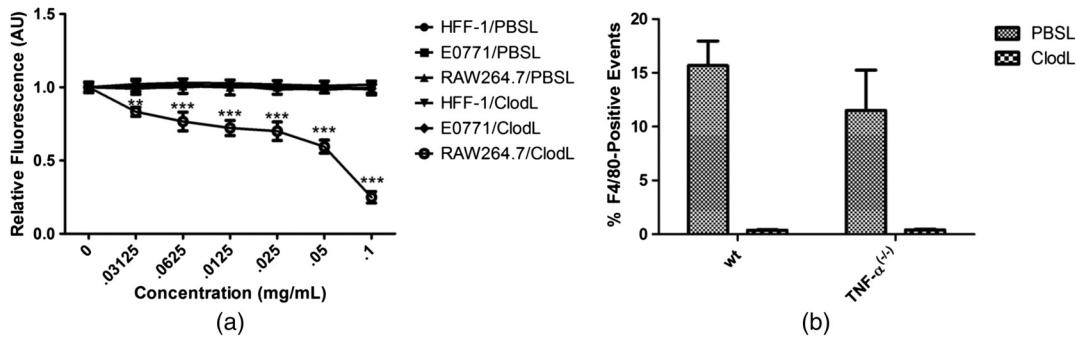


**Fig. 2** ClodL selectively reduces macrophage viability *in vitro* and *in vivo*. (a) Graded dose–response treatments with Clodronate (0 to 0.1 mg/mL) or PBS control liposomes demonstrated that at all Clodronate concentrations tested, only macrophage RAW264.7 cells, but not nonmacrophage E0771 breast tumor cells or HFF-1 fibroblasts, were sensitive to Clodronate depletion ( $n = 8$  each data point,  $p < 0.05$  for RAW264.7 PBSL versus ClodL at all doses). For each cell type, fluorescent intensities were standardized to the PBS control liposome group (no ClodL), to account for differences in proliferative rate inherent to cell type. Liposomes containing PBS (vehicle) only also did not affect proliferation of RAW264.7 macrophages at any liposome concentration (RAW264.7/PBSL trace). (b) Flow cytometric analysis indicated that endogenous F4/80<sup>+</sup> TAMs were depleted by *in vivo* Clodronate treatment in both wild-type (wt) and TNF- $\alpha$ <sup>(-/-)</sup> mice [ $n = 21$  wt/PBSL;  $n = 16$  wt/ClodL;  $n = 15$  TNF- $\alpha$ <sup>(-/-)</sup>/PBSL;  $n = 15$  TNF- $\alpha$ <sup>(-/-)</sup>/ClodL]. Moreover, these data also indicate that under baseline (PBSL, i.e., no depletion) conditions, F4/80<sup>+</sup> macrophage populations were not significantly different in wt versus TNF- $\alpha$ <sup>(-/-)</sup> animals.

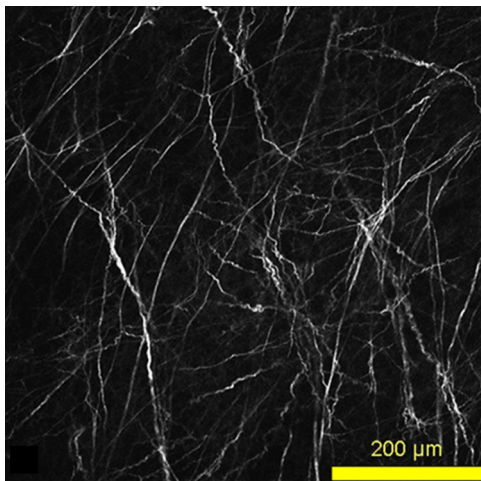


**Fig. 3** SHG image of E0771 murine mammary adenocarcinoma excised from the mammary fat pad of a C57Bl/6 mouse. The tumor sample was excised, sectioned, and fixed. With 810-nm excitation, typical collagen fibrils are imaged via SHG at 405-nm emission.

tumors from wild-type/ClodL mice ( $p < 0.05$ ) but not relative to TNF- $\alpha$ <sup>(-/-)</sup>/ClodL mice ( $p = 0.31$ ). Intensity of SHG-producing fibers did not differ between the two ClodL-treated groups. These results demonstrate that TAM depletion or attenuation of stromal TNF- $\alpha$  reduces intensity of SHG-producing fibers in the E0771 tumor. Furthermore, in the absence of TAMs, the inability to produce TNF- $\alpha$  did not produce a greater effect than either treatment alone. This suggests that nonmacrophage sources of TNF- $\alpha$  do not significantly influence SHG intensity.

### 3.4 Effects of TAM Depletion and TNF- $\alpha$ Knockout on Collagen Fiber IF Intensity

SHG is dependent upon collagen content as well as fiber microstructure. Therefore, in order to produce a more direct measure of fiber microstructure, we normalize the SHG intensity to the total amount of collagen present. As collagen type I is the primary fibrillar collagen *in vivo*,<sup>20,21</sup> we quantify collagen fibril content using fluorescently labeled anticollagen type I antibodies.<sup>16,17</sup> TAM depletion and stromal TNF- $\alpha$  knockout both alter

detected collagen I fiber IF in the E0771 tumor [Fig. 4(b)]. By two-way ANOVA, we see a strong main effect of both TAM depletion and TNF- $\alpha$  knockout (both  $p < 0.0001$ ) and a significant degree of interaction ( $p = 0.04$ ) was detected. By multiple comparison analysis, anticollagen type I IF was significantly lower in wild-type/PBSL mice compared to the three other groups ( $p < 0.05$ ). Furthermore, although IF signal in tumors grown in wild-type/ClodL mice is statistically equivalent to that of both TNF- $\alpha$  knockout groups ( $p > 0.05$ ), tumors grown in TNF- $\alpha$ <sup>(-/-)</sup>/PBSL mice exhibit less IF than do tumors grown in TNF- $\alpha$ <sup>(-/-)</sup>/ClodL mice ( $p < 0.05$ ). We therefore conclude that tumor growth in the presence of TAM depletion results in a significant increase in anticollagen type I IF in E0771 tumors. Growth during attenuation of stromal TNF- $\alpha$  accomplishes this to the same extent. Furthermore, in the absence of TAMs, depletion of stromal TNF- $\alpha$  has no further effect on IF. However, in the absence of stromal TNF- $\alpha$ , depletion of TAMs further increases IF. The combined abrogation of TAMs and TNF- $\alpha$  did not produce a greater increase in IF signal intensity than TAM depletion alone.

### 3.5 Effects of TAM Depletion and TNF- $\alpha$ Knockout on OI

Division of the SHG signal by the IF signal produces the order index (OI), which is primarily sensitive to changes in fibrillar microstructure, such as fibril diameter, spacing, and order versus disorder in fibrillar packing.<sup>11–15</sup> In Fig. 5, OI was reduced by TAM depletion with ClodL or stromal knockout of TNF- $\alpha$ , with a main effect of  $p < 0.0001$  and  $p = 0.013$ , respectively, with a significant interaction ( $p = 0.0027$ ). Bonferroni *post-hoc* analysis shows that wild-type/PBSL mice have significantly elevated OI relative to the three remaining groups ( $p < 0.05$ ). However, none of the three remaining groups exhibit significant differences between their mean OI values ( $p > 0.05$ ). We therefore conclude that tumor growth in the presence of TAM depletion results in a significant decrease in OI in E0771 tumors, as does growth during attenuation of stromal TNF- $\alpha$ , to the same extent. Furthermore, combined abrogation of TAMs and TNF- $\alpha$  did not produce a greater decrease in OI than either depletion alone.

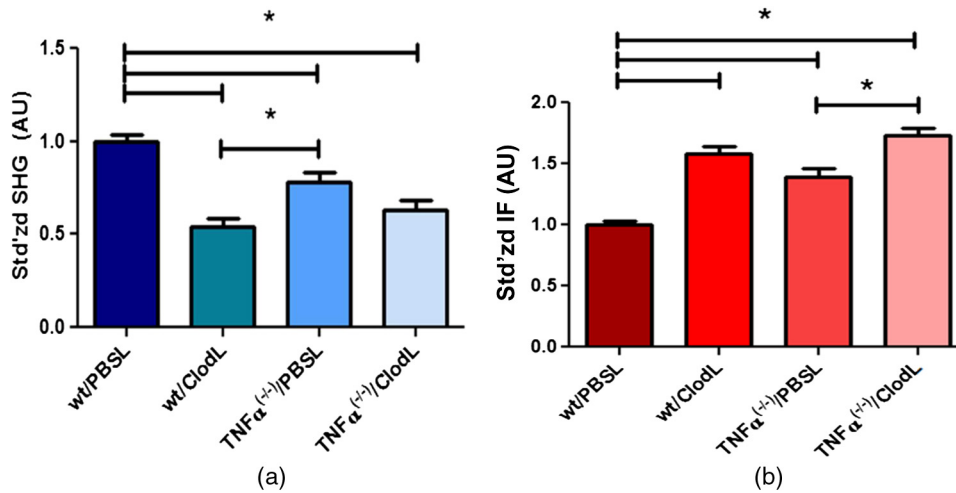


**Fig. 4** Effects of macrophage depletion and TNF- $\alpha$  knockout on SHG and IF signals in the E0771 tumor. (a) SHG-producing fibers in E0771 tumors in wild-type/PBSL mice were significantly brighter compared to all other groups ( $p < 0.05$  for all comparisons). In addition, SHG-producing fibers in E0771 tumors in wild-type/ClodL mice were significantly dimmer compared to TNF- $\alpha$ <sup>(-/-)</sup>/PBSL tumors ( $p < 0.05$ ). No other group was found significantly different from another ( $p > 0.05$ ).  $n = 21$  wt/PBSL,  $16$  wt/ClodL,  $n = 15$  TNF- $\alpha$ <sup>(-/-)</sup>/PBSL, and  $n = 15$  TNF- $\alpha$ <sup>(-/-)</sup>/ClodL. (b) Collagen I immunofluorescence (IF) was significantly lower in E0771 tumors in wild-type/PBSL mice compared to all other groups ( $p < 0.05$  for all comparisons). In addition, collagen I IF in E0771 tumors in TNF- $\alpha$ <sup>(-/-)</sup>/PBSL mice was significantly lower than in E0771 tumors in TNF- $\alpha$ <sup>(-/-)</sup>/ClodL mice. No other group was found significantly different from another ( $p > 0.05$ ).

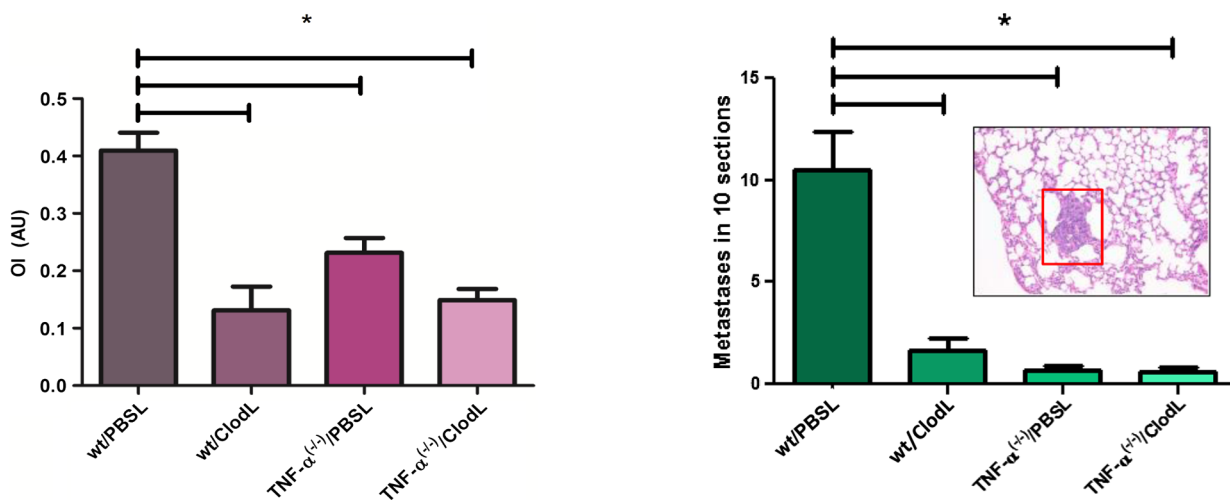


**Fig. 5** Effects of macrophage depletion and TNF- $\alpha$  knockout on OI. E0771 tumors grown in wild-type/PBSL mice had a significantly higher order index (OI, defined as SHG intensity/IF intensity) relative to all other treatment groups ( $p < 0.05$ ). No other group was found significantly different from another ( $p > 0.05$ ).

**Fig. 6** Lung metastatic burden decreases sharply with both macrophage depletion and TNF- $\alpha$  knockout. E0771 tumors grown in wild-type/PBSL mice generated significantly higher numbers of lung metastases, compared to E0771 tumors in TAM depleted and TNF- $\alpha$  knockout mice ( $p < 0.05$ ). Metastatic output was assessed across 10 sections of lung per group. No other group was found significantly different from another ( $p > 0.05$ ).  $n = 21$  wt/PBSL,  $n = 16$  wt/ClodL,  $n = 15$  TNF- $\alpha$ <sup>(-/-)</sup>/PBSL, and  $n = 15$  TNF- $\alpha$ <sup>(-/-)</sup>/ClodL.

### 3.6 Metastatic Burden Correlates Negatively with Both TAM Presence and TNF- $\alpha$ Expression

To evaluate the possibility of a relationship between modulations in OI and modulations in metastatic burden, lungs were resected, sectioned, and stained with H&E and then imaged to determine the extent of metastasis (Fig. 6). E0771 readily metastasizes to the lung from the primary site,<sup>36</sup> and two-way ANOVA shows a strong main effect of both TAM depletion and abrogation of TNF- $\alpha$  on metastatic burden ( $p = 0.0006$  and  $p < 0.0001$ , respectively). The degree of interaction is again significant ( $p = 0.0007$ ). Bonferroni *posthoc* analysis shows that while wild-type/PBSL mice exhibit significantly ( $p < 0.05$ ) higher metastatic burden than any of the other

groups, the other three groups do not show distinguishably different metastatic burdens ( $p > 0.05$ ). We conclude that both TAM depletion and TNF- $\alpha$  knockout result in significant decreases in metastatic events and that these decreases correlate well with OI values in the E0771 tumor.

### 3.7 ClodL and TNF- $\alpha$ Knockout Reduce E0771 Tumor Growth In Vivo

To determine if TAM depletion or TNF- $\alpha$  knockout affect tumor growth, E0771 was implanted in PBSL- or ClodL-treated wild-type or TNF- $\alpha$ <sup>(-/-)</sup> mice and tumor volume was measured over

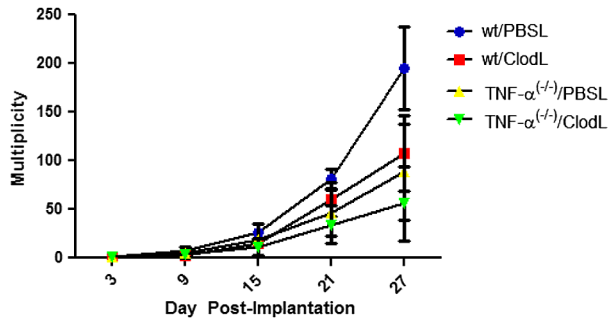


**Fig. 7** E0771 tumor volume multiplicity decreases with TAM depletion or TNF- $\alpha$  knockout, but the effects are not synergistic. After 27 days, E0771 tumors grown in wild-type mice on PBSL therapy ( $n = 21$ ) were larger than those grown in wild-type mice on ClodL therapy ( $n = 16$ ), as well as those grown in TNF- $\alpha$  knockout mice exposed to either PBSL or ClodL ( $p < 0.05$ ,  $n = 15$  for both). No other group was found significantly different from another at 27 days, and no significant differences in tumor volume multiplicity were found at earlier timepoints ( $p > 0.05$ ). Tumor growth was assessed by normalizing measurements to tumor size at day 3 (i.e., tumor volume multiplicity) to minimize the possibility that slightly different numbers of cells may have been injected despite constant injection volumes and cell densities.

the course of 27 days. The data presented in Fig. 7 were normalized at each time point relative to the volume at day 3 post-tumor inoculation. By repeated measure of two-way ANOVA, a treatment by time interaction was revealed ( $p < 0.0005$ ). Wild-type/PBSL mice bore significantly larger tumors at day 27 ( $p < 0.05$ , Bonferroni posttest) compared to any other group. Tumor growth did not differ among the other three groups.

#### 4 Discussion

In this study, our goal was to demonstrate the use of SHG as a tool to help detect cells and signals involved in establishing tumor collagen microstructure. We did this by elucidating a novel mechanistic role for TAMs and stromal TNF- $\alpha$  in the evolution of collagen microstructure in a murine model of breast cancer. In doing so, we made use of the E0771 murine mammary adenocarcinoma, a metastatic cell line syngeneic with the C57Bl/6 mouse. The choice of this cell line was predicated on the availability of the knockout strain B6.129S-Tnf<sup>tm1Gkl</sup>/J, which is incapable of expressing TNF- $\alpha$ . We first established that the E0771 tumor model does not produce TNF- $\alpha$ , is non-responsive to TNF- $\alpha$ , and that it also does not have an intrinsic cellular response to liposome-encapsulated clodronate therapies. Next, we established that these therapies are able to alter the microstructure of collagen I fibers (as measured by the OI) and metastatic burden.

Taken together, our OI data suggest that in the E0771 model of metastatic breast cancer, TAMs influence collagen microstructure (Fig. 5, columns 1 and 2 are different) and that stromal TNF- $\alpha$  influences collagen microstructure (Fig. 5, columns 1 and 3 are different). This suggests three main models: (A) TAMs and TNF- $\alpha$  influence OI independently, (B) stromal TNF- $\alpha$  influences OI via its action on TAMs, and (C) TAMs influence OI via expression of TNF- $\alpha$ . Model A is unlikely because in the absence of TAMs, modulation of stromal TNF- $\alpha$  has no further effect on OI (Fig. 5, columns 2 and 4 are the same) and in the absence of stromal TNF- $\alpha$  modulation of TAMs has no further effect on OI (Fig. 5, columns 3 and 4 are the same). However, models B and C are consistent with our

observations and can be further refined. If stromal TNF- $\alpha$  influences OI via action on TAMs (model B), our data further suggest that stromal TNF- $\alpha$  acts primarily via TAMs. This is because in the absence of TAMs, modulation of stromal TNF- $\alpha$  has no further effect on OI (Fig. 5, columns 2 and 4 are the same). Furthermore, in that model, our data also suggest that no other molecule plays a significant role in stimulating TAMs to influence OI. This is because in the absence of stromal TNF- $\alpha$  modulation of TAMs has no further effect on OI (Fig. 5, columns 3 and 4 are the same). Lastly, if TAMs influence OI via their expression of TNF- $\alpha$  (model C), our data suggest that TAMs influence collagen structure primarily through their TNF- $\alpha$  expression and not via other mechanisms. This is because in the absence of stromal TNF- $\alpha$ , modulation of TAMs has no further effect on OI (Fig. 5, columns 3 and 4 are the same). Furthermore, in that model, our data also suggest that there are no other significant host cell types utilizing TNF- $\alpha$  to influence collagen microstructure. This is because in the absence of TAMs modulation of stromal TNF- $\alpha$  has no further effect on OI (Fig. 5, columns 2 and 4 are the same).

While we used OI to detect a role for TAMs and stromal TNF- $\alpha$  in manipulating collagen microstructure, the information that OI provides about the actual changes in matrix microstructure caused by modulating TAMs or stromal TNF- $\alpha$  is limited. Consequently, results must be interpreted carefully. This is primarily due to the fact that epideTECTED SHG signal depends on several different physical parameters (e.g., fibril diameter, spacing, packing order), and changing any of these parameters alone or in combination will likely result in a change in OI. Furthermore, the relationship between epideTECTED SHG (and hence OI) and a specific fiber physical parameters can be complex, with one illustrative case being the dependence of epideTECTED SHG on the diameter of fibrils within a collagen fiber. An increase in fibril diameter could result in either increased or decreased epideTECTED SHG signal due to the predicted sinusoidal dependence of emitted SHG directionality on fibril diameter.<sup>13</sup> Hence, it is the presence of a modulation of OI, regardless of sign, due to modulation of a cell/signal which indicates that the cell/signal in question influences collagen microstructure. However, the sign of the OI change (i.e., increasing or decreasing) does not tell us how the relevant parameters (e.g., diameter, spacing, packing order) are changing, or what combination of them are changing.

In addition to our primary observations detecting a role for TAMs and stromal TNF- $\alpha$  in modulating OI, there are two secondary observations: TAM presence was able to modulate IF in the absence of stromal TNF- $\alpha$  [Fig. 4(b), columns 3 and 4 are different] and TAM depletion produced a greater SHG reduction than attenuation of stromal TNF- $\alpha$  [Fig. 4(a), columns 2 and 3 are different). In model B (stromal TNF- $\alpha$  operates via TAMs), these two observations imply that there may be other less significant mechanisms, in parallel with stromal TNF- $\alpha$ , which induce TAMs to affect tumor collagen. In model C (TAMs operate via TNF- $\alpha$ ), these two observations imply that there may be other less significant mechanisms by which TAMs affect tumor collagen in addition to their expression of TNF- $\alpha$ . However, the observation that attenuation of TAM presence produced a greater SHG reduction than the attenuation of stromal TNF- $\alpha$  is based upon quantitative comparison of the results of two very different experimental manipulations (TAM depletion versus TNF- $\alpha$  knockout) and may simply be a result of different efficiencies in the two methods.

When macrophage recruitment is specifically disabled in developing mouse mammary tissue, the microstructure of collagen fibers but not their total amount, as measured by SHG and IF, is altered with negative consequence to normal maturation.<sup>17</sup> Interestingly, in contrast to our observations, this same study noted a similar decrease in SHG but without any elevation in IF. This may be due to myriad differences between normal and diseased mammary fat pad, in particular, the well-documented ability of cancer cells to produce stimuli inducing fibroblasts to transition to a more active myofibroblast phenotype, with one consequence being elevated levels of collagen production.<sup>37</sup> Additionally, this may simply be due to differences in antibody–epitope binding between two different model systems.

Our observations that TAMs and stromal TNF- $\alpha$  play a role in altering tumor collagen microstructure are consistent with established roles for both in modulating tumor stroma. Autocrine TNF- $\alpha$  signaling has been noted as necessary to induce high levels of expression of monocyte matrix metalloproteinase (MMP)-9, a gelatinase that is active on basement membrane, via the transcription factor Egr-1.<sup>38–41</sup> TNF- $\alpha$  has also been shown to sharply increase MMP-14 levels in concert with CCL4, a C-C chemokine, in a monocytic human cell line.<sup>42</sup> MMP-14 is able to subsequently activate MMP-2, another gelatinase capable of degrading basement membrane. However, note that the nonfibrillar collagens in basement membrane do not generate significant SHG and were not studied here. Importantly, both direct application of TNF- $\alpha$  and indirect production of it through LPS stimulation of macrophages have been shown to upregulate MMP-1a, -1b, -3, and -13 in rat synovia, and these MMPs can directly affect the fibrillar collagen responsible for SHG signal.<sup>43</sup> On a genetic level, TNF- $\alpha$  is able to induce COX-2 promoter activation via upregulation of p300 binding and p50 acetylation in human foreskin fibroblasts, which is an important step in inflammation, angiogenesis, and tumor promotion.<sup>44–46</sup>

Our demonstration of a novel role for TAMs and TNF- $\alpha$  in manipulating collagen microstructure in the tumor extracellular matrix naturally leads us to ask: what are the possible consequences of this manipulation? As discussed above, there is evidence in the literature that collagen microstructure, as quantified with SHG, influences tumor metastasis.<sup>1–5,7</sup> Consistent with this, our data demonstrate that alterations in collagen microstructure as quantified by the OI correlated with alterations in metastatic output (Figs. 5 and 6). In each case, wild-type mice treated with PBSL had significantly greater OI and metastatic output than all other treatment groups, and all other treatment groups were not statistically significantly different from each other.

The link between TAMs, stromal TNF- $\alpha$ , and metastatic output in this tumor model is consistent with observations that myeloid cells and their TNF- $\alpha$  expression are necessary for the formation of Lewis lung carcinoma metastasis.<sup>28</sup> However, while our observations establish an interesting link between TAMs, stromal TNF- $\alpha$ , and metastatic output in this tumor model, it does not prove that the metastatic effects are transduced via collagen fiber microstructure itself. There may be other effects of TAMs and stromal TNF- $\alpha$  expression that assist in the induction of alterations in metastatic output. For example, our data also demonstrate that tumor growth is correlated with OI (albeit only at the last time point studied), and in turn with metastatic burden (Figs. 5–7). Hence, TAMs and

stromal TNF- $\alpha$  may instead influence tumor growth via alterations in collagen matrix microstructure (note that TNF- $\alpha$  does not directly affect E0771 proliferation *in vitro*), and the altered metastatic output may be a result of the different tumor burden or all three effects (OI, tumor growth, and metastatic output) may share a common cause but operate via independent mechanisms.

In the future, it may be productive to explore how collagen microstructure in different subregions of the tumor (lobular, ductal, perilobular, periductal, distant, etc.) is influenced by these manipulations. While the orthotopic cell injection model used here does not typically preserve the ductal and lobular structure that can be found in and around examples of the human disease, the MMTV mouse model of breast cancer does.<sup>47</sup> By crossbreeding MMTV mice with different transgenic strains, one could explore how collagen microstructure in different breast tumor subregions is regulated. However, using a different measure of collagen microstructure (the SHG forward-scattering to backwards-scattering ratio), we found that in samples of human breast cancer, there is no significant difference in collagen microstructure between different breast tumor subregions.<sup>7</sup>

## 5 Conclusions

In summary, this study serves to demonstrate the ability of SHG to help identify key cells and signals that play a role in establishing tumor collagen microstructure. We show that TAMs as well as stromal TNF- $\alpha$  expression are responsible for significant alterations in the microstructure of collagen fibers within a metastatic breast tumor model (as indicated by the OI). We further demonstrate that this effect is implemented either via TAM expression of TNF- $\alpha$  or stromal TNF- $\alpha$  action on TAMs and that parallel pathways via other cell types or other cytokines are considerably less significant. Lastly, we show that the effects of TAMs and stromal TNF- $\alpha$  on tumor collagen microstructure are correlated with effects on metastatic output, consistent with previous literature connecting SHG and metastatic output.

Discovering a key role for tumor-associated macrophages and stromal TNF- $\alpha$  in influencing the microstructural properties of tumor collagen, as measured by SHG, is interesting because of the previously observed effects of these SHG-producing fibers on metastasis of the primary breast tumor, as well as the previously observed relationship between SHG signal and drug transport in tumors.<sup>1–5,7,8</sup> These findings suggest that manipulation of SHG measures of collagen microstructure may, in turn, manipulate the transport of drugs through tumor tissue as well as manipulate metastatic output of tumors.

## Acknowledgments

The authors wish to acknowledge Tracy Bubel and Khawar-Jamma M. Liverpool for their indispensable technical assistance, Diana Scott for assistance with H&E automation, Michele Au for assistance with flow cytometry, and Dr. Peter Salzman for his assistance with statistical analysis. This work was funded by Department of Defense Breast Cancer Research Program (BCRP) Era of Hope Scholar Research Award W81XWH-09-1-0405 and NIH Director's New Innovator Award 1DP2OD006501 (to EBB), BCRP Idea Award W81XWH-10-01-0087 and NIH R21CA152777-01 (to KSM), and NIH R21DA030256 (to SWP).

## References

- W. Wang et al., "Single cell behavior in metastatic primary mammary tumors correlated with gene expression patterns revealed by molecular profiling," *Cancer Res.* **62**(21), 6278–6288 (2002).
- M. Sidani et al., "Probing the microenvironment of mammary tumors using multiphoton microscopy," *J. Mammary Gland Biol. Neoplasia* **11**(2), 151–163 (2006).
- P. P. Provenzano et al., "Collagen reorganization at the tumor-stromal interface facilitates local invasion," *BMC Med.* **4**(1), 38 (2006).
- J. B. Wyckoff et al., "Direct visualization of macrophage-assisted tumor cell intravasation in mammary tumors," *Cancer Res.* **67**(6), 2649–2656 (2007).
- M. W. Conklin et al., "Aligned collagen is a prognostic signature for survival in human breast carcinoma," *Am. J. Pathol.* **178**(3), 1221–1232 (2011).
- O. Nadiarnykh et al., "Alterations of the extracellular matrix in ovarian cancer studied by Second Harmonic Generation imaging microscopy," *BMC Cancer* **10**, 94 (2010).
- K. Burke, P. Tang, and E. Brown, "Second harmonic generation reveals matrix alterations during breast tumor progression," *J. Biomed. Opt.* **18**(3), 31106 (2013).
- E. Brown et al., "Dynamic imaging of collagen and its modulation in tumors in vivo using second-harmonic generation," *Nat. Med.* **9**(6), 796–800 (2003).
- W. R. Zipfel et al., "Live tissue intrinsic emission microscopy using multiphoton-excited native fluorescence and second harmonic generation," *Proc. Natl. Acad. Sci. U.S.A.* **100**(12), 7075–7080 (2003).
- C. B. Raub et al., "Noninvasive assessment of collagen gel microstructure and mechanics using multiphoton microscopy," *Biophys. J.* **92**(6), 2212–2222 (2007).
- X. Han et al., "Second harmonic properties of tumor collagen: determining the structural relationship between reactive stroma and healthy stroma," *Opt. Express* **16**(3), 1846–1859 (2008).
- L. Moreaux et al., "Coherent scattering in multi-harmonic light microscopy," *Biophys. J.* **80**(3), 1568–1574 (2001).
- R. M. Williams, W. R. Zipfel, and W. W. Webb, "Interpreting second-harmonic generation images of collagen I fibrils," *Biophys. J.* **88**(2), 1377–1386 (2005).
- R. Lacombe, O. Nadiarnykh, and P. J. Campagnola, "Quantitative second harmonic generation imaging of the diseased state osteogenesis imperfecta: experiment and simulation," *Biophys. J.* **94**(11), 4504–4514 (2008).
- R. Lacombe et al., "Phase matching considerations in second harmonic generation from tissues: effects on emission directionality, conversion efficiency and observed morphology," *Opt. Commun.* **281**(7), 1823–1832 (2008).
- B. Diop-Frimpong et al., "Losartan inhibits collagen I synthesis and improves the distribution and efficacy of nanotherapeutics in tumors," *Proc. Natl. Acad. Sci. U.S.A.* **108**(7), 2909–2914 (2011).
- W. V. Ingman et al., "Macrophages promote collagen fibrillogenesis around terminal end buds of the developing mammary gland," *Dev. Dyn.* **235**(12), 3222–3229 (2006).
- V. Ajeti et al., "Structural changes in mixed Col I/Col V collagen gels probed by SHG microscopy: implications for probing stromal alterations in human breast cancer," *Biomed. Opt. Express* **2**(8), 2307–2316 (2011).
- A. K. Miri et al., "Nonlinear laser scanning microscopy of human vocal folds," *Laryngoscope* **122**(2), 356–363 (2012).
- I. P. Minafra et al., "Quantitative determination of collagen types present in the ductal infiltrating carcinoma of human mammary gland," *Cell Biol. Int. Rep.* **9**(3), 291–296 (1985).
- S. H. Barsky et al., "Increased content of Type V Collagen in desmoplasia of human breast carcinoma," *Am. J. Pathol.* **108**(3), 276–283 (1982).
- J. W. Pollard, "Tumour-educated macrophages promote tumour progression and metastasis," *Nat. Rev. Cancer* **4**(1), 71–78 (2004).
- N. C. Direkze et al., "Bone marrow contribution to tumor-associated myofibroblasts and fibroblasts," *Cancer Res.* **64**(23), 8492–8495 (2004).
- J. J. Chen et al., "Tumor-associated macrophages: the double-edged sword in cancer progression," *J. Clin. Oncol.* **23**(5), 953–964 (2005).
- L. Bingle, N. J. Brown, and C. E. Lewis, "The role of tumour-associated macrophages in tumour progression: implications for new anticancer therapies," *J. Pathol.* **196**(3), 254–265 (2002).
- T. Dschietzig et al., "The pregnancy hormone relaxin binds to and activates the human glucocorticoid receptor," *Ann. N. Y. Acad. Sci.* **1041**, 256–271 (2005).
- D. A. Parsell et al., "Relaxin binds to and elicits a response from cells of the human monocytic cell line, THP-1," *J. Biol. Chem.* **271**(44), 27936–27941 (1996).
- S. Kim et al., "Carcinoma-produced factors activate myeloid cells through TLR2 to stimulate metastasis," *Nature* **457**(7225), 102–106 (2009).
- S. M. Zeisberger et al., "Clodronate-liposome-mediated depletion of tumour-associated macrophages: a new and highly effective antiangiogenic therapy approach," *Br. J. Cancer* **95**(3), 272–281 (2006).
- M. D. Barber, J. St J. Thomas, and J. Dixon, *Breast Cancer: An Atlas of Investigation and Management*, p. 118, Clinical Publishing, Ashland, OH (2008).
- A. Zumsteg et al., "Myeloid cells contribute to tumor lymphangiogenesis," *PLoS One* **4**(9), e7067 (2009).
- M. A. Rivas et al., "TNF alpha acting on TNFR1 promotes breast cancer growth via p42/P44 MAPK, JNK, Akt and NF-kappa B-dependent pathways," *Exp. Cell Res.* **314**(3), 509–529 (2008).
- M. E. Burow et al., "Differences in susceptibility to tumor necrosis factor alpha-induced apoptosis among MCF-7 breast cancer cell variants," *Cancer Res.* **58**(21), 4940–4946 (1998).
- J. C. Frith et al., "The molecular mechanism of action of the antiresorptive and antiinflammatory drug clodronate: evidence for the formation in vivo of a metabolite that inhibits bone resorption and causes osteoclast and macrophage apoptosis," *Arthritis Rheum.* **44**(9), 2201–2210 (2001).
- K. Nonaka et al., "Skewing the Th cell phenotype toward Th1 alters the maturation of tumor-infiltrating mononuclear phagocytes," *J. Leukocytes Biol.* **84**(3), 679–688 (2008).
- A. Ewens, E. Mihich, and M. J. Ehrke, "Distant metastasis from subcutaneously grown E0771 medullary breast adenocarcinoma," *Anticancer Res.* **25**(6B), 3905–3915 (2005).
- R. Kalluri and M. Zeisberg, "Fibroblasts in cancer," *Nat. Rev. Cancer* **6**(5), 392–401 (2006).
- S. C. Robinson, K. A. Scott, and F. R. Balkwill, "Chemokine stimulation of monocyte matrix metalloproteinase-9 requires endogenous TNF-alpha," *Eur. J. Immunol.* **32**(2), 404–412 (2002).
- M. G. Ismail et al., "Autocrine regulation of matrix metalloproteinase-9 gene expression and secretion by tumor necrosis factor-alpha (TNF-alpha) in NB4 leukemic cells: specific involvement of TNF receptor type 1," *Leukemia* **12**(7), 1136–1143 (1998).
- T. M. Leber and F. R. Balkwill, "Regulation of monocyte MMP-9 production by TNF-alpha and a tumour-derived soluble factor (MMPSF)," *Br. J. Cancer* **78**(6), 724–732 (1998).
- S. Y. Shin et al., "Transcription factor Egr-1 is essential for maximal matrix metalloproteinase-9 transcription by tumor necrosis factor alpha," *Mol. Cancer Res.* **8**(4), 507–519 (2010).
- V. J. Richardson, "Divergent and synergistic regulation of matrix metalloprotease production by cytokines in combination with C-C chemokines," *Int. J. Immunopathol. Pharmacol.* **23**(3), 715–726 (2010).
- A. Hyc et al., "Influence of LPS, TNF, TGF-ss1 and IL-4 on the expression of MMPs, TIMPs and selected cytokines in rat synovial membranes incubated in vitro," *Int. J. Mol. Med.* **27**(1), 127–137 (2011).
- W. G. Deng, Y. Zhu, and K. K. Wu, "Up-regulation of p300 binding and p50 acetylation in tumor necrosis factor-alpha-induced cyclooxygenase-2 promoter activation," *J. Biol. Chem.* **278**(7), 4770–4777 (2003).
- J. R. Vane et al., "Inducible isoforms of cyclooxygenase and nitric-oxide synthase in inflammation," *Proc. Natl. Acad. Sci. U.S.A.* **91**(6), 2046–2050 (1994).
- M. Tsujii and R. N. DuBois, "Alterations in cellular adhesion and apoptosis in epithelial cells overexpressing prostaglandin endoperoxide synthase 2," *Cell* **83**(3), 493–501 (1995).
- E. Y. Lin et al., "Progression to malignancy in the polyoma middle T oncoprotein mouse breast cancer model provides a reliable model for human diseases," *Am. J. Pathol.* **163**(5), 2113–2126 (2003).

RESEARCH ARTICLE

Open Access

# Stromal matrix metalloprotease-13 knockout alters Collagen I structure at the tumor-host interface and increases lung metastasis of C57BL/6 syngeneic E0771 mammary tumor cells

Seth W Perry\*, Jill M Schueckler, Kathleen Burke, Giuseppe L Arcuri and Edward B Brown

## Abstract

**Background:** Matrix metalloproteases and collagen are key participants in breast cancer, but their precise roles in cancer etiology and progression remain unclear. MMP13 helps regulate collagen structure and has been ascribed largely harmful roles in cancer, but some studies demonstrate that MMP13 may also protect against tumor pathology. Other studies indicate that collagen's organizational patterns at the breast tumor-host interface influence metastatic potential. Therefore we investigated how MMP13 modulates collagen I, a principal collagen subtype in breast tissue, and affects tumor pathology and metastasis in a mouse model of breast cancer.

**Methods:** Tumors were implanted into murine mammary tissues, and their growth analyzed in Wildtype and MMP13 KO mice. Following extraction, tumors were analyzed for collagen I levels and collagen I macro- and micro-structural properties at the tumor-host boundary using immunocytochemistry and two-photon and second harmonic generation microscopy. Lungs were analyzed for metastases counts, to correlate collagen I changes with a clinically significant functional parameter. Statistical analyses were performed by t-test, analysis of variance, or Wilcoxon-Mann-Whitney tests as appropriate.

**Results:** We found that genetic ablation of host stromal MMP13 led to: 1. Increased mammary tumor collagen I content, 2. Marked changes in collagen I spatial organization, and 3. Altered collagen I microstructure at the tumor-host boundary, as well as 4. Increased metastasis from the primary mammary tumor to lungs.

**Conclusions:** These results implicate host MMP13 as a key regulator of collagen I structure and metastasis in mammary tumors, thus making it an attractive potential therapeutic target by which we might alter metastatic potential, one of the chief determinants of clinical outcome in breast cancer. In addition to identifying stromal MMP13 as an important regulator of the tumor microenvironment and metastasis, these results also suggest that stromal MMP13 may protect against breast cancer pathology under some conditions, a finding with important implications for development of chemotherapies directed against matrix metalloproteases.

**Keywords:** Two-photon, Microscopy, Cancer, Second harmonic generation, Collagen, SHG, Tumor, MMP, Matrix metalloprotease, MMP-13, Intravital, Imaging, In vivo, Multiphoton, Intrinsic, Fluorophore

\* Correspondence: Seth\_Perry@urmc.rochester.edu  
Department of Biomedical Engineering, University of Rochester School of  
Medicine and Dentistry, 601 Elmwood Avenue, Rochester, NY 14642, USA

## Background

The structure and function of tumor extracellular matrix (ECM) play critical roles in cancer initiation and outcome [1,2]. More specifically, organization or reorganization of collagen, a key structural component of the ECM, has been shown to be an important factor in tumor genesis, progression, and/or metastasis [3-9]. Tumor cells have been shown to migrate preferentially along aligned collagen fibers [10,11], and others have reported particular “tumor associated collagen signatures” (TACS) – i.e. patterns of collagen alignment around the tumor boundary – that may be associated with breast cancer tumor invasion into host stroma [5] and patient survival [12]. However specific functional mechanisms or molecular mediators that lead to such collagen reorganizations, with consequent effects on tumor progression and metastasis, remain largely undefined and would represent attractive novel therapeutic targets for breast cancer.

Some likely mediators of collagen structure at the tumor-host interface are matrix metalloproteases (MMPs). MMPs are key regulators of the ECM and collagen remodeling [13,14], and are also frequently implicated in cancer [15]. MMP-13 (collagenase-3) was originally isolated from human breast cancer tissue [16], and has been shown to be an important contributor to breast (and other) cancer pathology [15,17,18]. As a collagenase with fairly broad substrate specificity, MMP-13 is capable of cleaving several collagen subtypes including fibrillar collagens I, II, and III [15]. These fibrillar collagens are detectable by second harmonic generation (SHG) microscopy, an optical imaging approach that is increasingly being used to provide diagnostic insights into cancer biology [9], and which has been used extensively in TACS analysis [5,12,19]. Collagen I is the most abundant fibrillar collagen in mammals [20], is a substrate for MMP-13 [15], and is typically increased in breast tumor- versus normal mammary gland-associated stroma [21,22]. Finally, *Coll1a1* transgenic mice with degradation resistant collagen I have been used for TACS analysis of increased collagen deposition in a mammary tumor model [19]. Therefore, in this study we sought to determine whether direct *in vivo* genetic manipulation of host MMP-13 alters collagen I organization at the mammary tumor-host boundary (i.e. TACS), with demonstrable effects on tumor metastasis.

## Methods

### Cells and reagents

Murine medullary mammary adenocarcinoma (E0771) cells syngeneic with C57BL/6 mice (Roswell Park Cancer Institute, Buffalo, NY) were grown in RPMI 1640 medium (Gibco/Invitrogen, Carlsbad, CA) supplemented with 10% gamma-irradiated defined fetal bovine serum

(HyClone/Thermo-Fisher, Waltham, MA) and 100 ug/ml Primocin antibiotic (InvivoGen, San Diego, CA). For mammary tumor implantation experiments, cells were harvested in 0.25% trypsin/EDTA, centrifuged, re-suspended in sterile PBS, and kept on ice until implantation into a mammary fat pad.

### Tumor implantation

Congenetic female C57BL/6 wildtype (WT) or MMP-13 knockout (MMP13 KO) mice [23] were used for E0771 tumor implantation experiments at 15–19 weeks of age. Animals were anesthetized with ketamine/xylazine (90/9 mg/kg) delivered intraperitoneally (i.p.). The animals' ventral surfaces were depilated, followed by implantation of  $1 \times 10^5$  E0771 mammary tumor cells into the right inguinal mammary fat pads using a 27-gauge needle. Caliper-measured tumor sizes were recorded on days 12, 19, and 28 of the experiments. On Day 28 post-implantation, animals were sacrificed by i.p. sodium pentobarbital injection and subsequent cervical dislocation. The E0771 mammary tumors were excised, and immediately snap-frozen on dry ice for subsequent cryo-sectioning and immunohistochemistry. Lungs were excised, fixed in 10% neutral-buffered formalin, then paraffin embedded, sectioned, and hematoxylin-eosin (H&E) stained for analysis of lung metastases. Procedures were performed in accordance with the University Committee on Animal Resources (UCAR).

### Immunohistochemistry

Snap-frozen tumors were cryo-sectioned ( $-21^{\circ}\text{C}$ ) at 20  $\mu\text{m}$ , then static-mounted on positively charged slides. For immunohistochemistry (IHC), sections were cold-fixed ( $-20^{\circ}\text{C}$ ) for 20 minutes in 3:1 acetone/methanol, rehydrated  $2 \times 5$  minutes in sterile PBS, then blocked for one hour (5% BSA, .2% Triton-X 100 in PBS). Primary antibody for Collagen I (Abcam #21286, Cambridge, MA) was then applied for 2 hours at room temperature in a humidified chamber, diluted 1:200 in 0.5% BSA, .2% Triton-X 100 in PBS, followed by  $2 \times 5$  minutes PBS wash, then two hours of Alexa Fluor 594-conjugated goat anti-rabbit IgG (1:500 in the same diluent as the primary; Invitrogen, Carlsbad, CA). Optimal antibody dilutions and incubation times were pre-determined empirically. Following staining for Collagen I protein, tumor sections were washed and mounted in ProLong Gold Antifade reagent (without DAPI; Invitrogen, Carlsbad, CA), then allowed to dry for 24 hours before imaging. Similar procedures were used for IHC against MMP-13 (Millipore #ab8120, Billerica, MA).

### Imaging and image analysis

Slides were imaged by a blinded observer using a custom-built multi-photon microscope. A Mai Tai Titanium:sapphire laser (Newport/Spectra Physics, Santa

Clara, CA) provided two-photon (2P) excitation (100 fs pulses at 80 MHz and 810 nm) for simultaneously epidetecting backwards-directed SHG ( $B_{\text{SHG}}$ ) and immunofluorescence (IF) signals from Collagen I fibers in the excised mammary tumors. Beam scanning and image acquisition were performed with a custom-modified Fluoview FV300 confocal scanner interfaced with a BX61WI upright microscope (Olympus, Center Valley, PA), with an Olympus XLUMPLFL20xW water immersion lens (20 $\times$ , 0.95 N.A.). Backscattered SHG (HQ405/30m-2P emission filter, Chroma, Rockingham, VT; HC125-02 PMT, Hamamatsu Corporation, Hamamatsu, Japan) and 2P-excited Collagen I IF (Chroma HQ635/30 m-2P emission filter; HC125-01 Hamamatsu PMT) signals were separated from the 810 nm excitation beam by a short pass dichroic mirror (Chroma 670 DCSX), and simultaneously captured in two distinct channels (using a 475 DCSX Chroma long pass dichroic, and the emission filters and PMTs above) on every scan. Resulting two-channel ( $B_{\text{SHG}}$  and IF) images are 680 microns across. Laser power was monitored and kept constant throughout each experiment and across experimental repetitions, as were PMT voltage, gain, and offset.

Because MMP13 was knocked out from the host animal, for the results described herein we analyzed images representing random tumor-host interface regions, i.e. random “outer edge” regions of tumors. Images from these areas were obtained as z-stacks (1  $\mu\text{m}$  step size) taken over the entire 20  $\mu\text{m}$  thickness of the tissue section. For each channel ( $B_{\text{SHG}}$  and collagen I IF), maximum projection images were taken from each stack, then image analysis was performed with ImageJ as follows. For each slide (usually 2–3 tumor sections/slide) and for each channel, background was defined by the average pixel counts of a laser-excited image taken from an area of the slide with no tissue, and subtracted from the raw  $B_{\text{SHG}}$  and IF images. These background corrected images were used for image analysis in ImageJ. For assessment of collagen I protein levels, mean pixel intensity of collagen I IF was measured over the tumor periphery FOVs. For coherency analysis, the coherency parameter (see below, and [24–26]) was calculated on these same collagen I IF images using the ImageJ plugin OrientationJ (open source, written by Daniel Sage, Biomedical Image Group, EPFL, Switzerland; <http://bigwww.epfl.ch/demo/orientation/>). This coherency parameter was quantified on a pixel-by-pixel basis, then averaged over all pixels in an image to produce a single coherency value for each image, which could then be averaged across all images in each experimental group. For normalized SHG calculations (i.e.  $B_{\text{SHG}}$  normalized to collagen I IF), the  $B_{\text{SHG}}$  and collagen I IF images were thresholded to select for collagen I-positive features and to reduce artifactual effects from non-specific

background in either channel, applying the same thresholding standard to images from all experimental groups. The  $B_{\text{SHG}}$  channel was then “masked” to the thresholded collagen I IF channel, so that only SHG pixels that *were also positive for collagen I immunofluorescence* were analyzed. Dividing the mean  $B_{\text{SHG}}$  pixel intensity from these masked  $B_{\text{SHG}}$  images, by the mean IF pixel intensity from the corresponding Collagen I IF images from the same FOV, produces a ratiometric value which represents  $B_{\text{SHG}}$  normalized to Collagen I protein levels on a pixel-by-pixel basis over the exact same XYZ pixel space, for each tumor periphery image. This method of analysis allows us to analyze only the  $B_{\text{SHG}}$  signal that is primarily restricted to collagen I, and provides a “normalized”  $B_{\text{SHG}}$  value for collagen I. Since SHG is sensitive to both collagen microstructural properties and collagen abundance [9,27], this “normalized”  $B_{\text{SHG}}$  parameter allows us to primarily assess changes in collagen I microstructural properties with reduced sensitivity to changes in collagen I expression levels, and similar strategies have been employed by others previously [28,29]. To calculate the forward SHG ( $F_{\text{SHG}}$ ) to  $B_{\text{SHG}}$  ratio ( $F_{\text{SHG}}/B_{\text{SHG}}$ ), both  $F_{\text{SHG}}$  and  $B_{\text{SHG}}$  were captured simultaneously above ( $B_{\text{SHG}}$ ) and below ( $F_{\text{SHG}}$ ) the slide specimen in two channels using the microscope setup previously described [30].  $F_{\text{SHG}}$  and  $B_{\text{SHG}}$  images were simultaneously collected as stacks of 11 images spaced 3  $\mu\text{m}$  apart, within a 660  $\mu\text{m}$  field of view. Four images were taken from each tumor sample around the tumor boundary at the tumor-host interface, with 2 tumor samples analyzed per animal from the same cohorts of WT and MMP13 KO animals. Image analysis was conducted with ImageJ. Each stack was maximum intensity projected, serving as an “autofocus” for the effectively single layer of collagen. Projected images were background subtracted using a maximum intensity projection of a matching 11 image scan taken with a closed shutter, then background subtracted  $F_{\text{SHG}}$  and  $B_{\text{SHG}}$  images were divided to create an  $F_{\text{SHG}}/B_{\text{SHG}}$  ratio image. For each image a common threshold was applied to all images to distinguish collagen pixels from background pixels and to select for fibers likely to be collagen I, and subthreshold background (i.e. non collagen fiber) pixels were excluded from analysis by binary masking. The average pixel value these non-background collagen fiber pixels was calculated from all  $F_{\text{SHG}}/B_{\text{SHG}}$  ratio images in the same cohort of MMP13 KO and WT animals, and expressed as mean  $F_{\text{SHG}}/B_{\text{SHG}} \pm \text{SEM}$ .

#### Evaluation of lung metastases

For evaluation of lung metastases, lungs were excised from tumor bearing experimental animals as described above, fixed in 10% neutral-buffered formalin, then paraffin embedded. Five-micron rotary microtome sections

were taken through both lobes of the lung, mounted on positively charged slides, then H&E stained. H&E-stained lung sections were evaluated for lung metastases by a trained blinded observer using brightfield microscopy (Olympus BX-51, Center Valley, PA). Metastatic infiltrating tumor cells were identified by several criteria including: high ratio of hematoxylin relative to eosin, surrounding abnormalities in lung structure, abnormal shape/size of nuclei and/or presence of abnormal mitotic spindles, and differences in cell shape and size, with  $\geq 1$  infiltrating tumor cells counted as a metastatic event. Results are presented as mean number of lung metastases/cm<sup>2</sup>  $\pm$  SEM for each treatment group.

### Statistical analysis

Statistical analysis was performed using Kaleidagraph (Synergy Software, Reading, PA) or Prism 5 (GraphPad Software, La Jolla, CA) software. Student's t-tests (unpaired), ANOVA with protected Fisher LSD post-tests for planned comparisons, or Wilcoxon-Mann-Whitney tests were used for statistical analyses as appropriate. p-values  $\leq .05$  were considered significant.

## Results

### Stromal MMP13 knockout increases mammary tumor Collagen I content, but decreases Collagen I ordering, at the tumor-host interface

Murine medullary breast adenocarcinoma (E0771) tumor cells were implanted into mouse mammary fat pads for 28 days. Consistent with other reports [31], MMP13 KO did not alter mammary tumor size in our E0771 mammary tumor model (Figure 1). MMP-13 expression was decreased in tumors from the MMP13 KO mice versus WT (Additional file 1: Figure S1A) and moreover, in the WT but not MMP13 KO mice, MMP13+ cell bodies were found around the tumor periphery which suggested the presence of peritumor (and possibly infiltrating) MMP13+ stromal cells in WT but not MMP13 KO mice (compare Additional file 1: Figures S1B and S1C, respectively). Also at the tumor periphery, Collagen I protein levels were significantly increased in MMP13 KO versus wildtype animals as quantified by immunofluorescence staining (Figure 2), suggesting that depletion of this collagen degrading enzyme from host cells increases tumor Collagen I content. However, despite this increase in Collagen I content at the tumor boundaries in the MMP13 KO mice, overall collagen *ordering* at tumor boundaries was decreased (i.e. more random) in these MMP13 KO mice versus WT controls. Figure 3 highlights the decreased ordering in MMP13 KO mice, with WT mice demonstrating many robust Collagen I fibers more frequently oriented parallel to the tumor boundary, closely resembling a TACS-2 arrangement as previously described [5,12,19] (Figure 3A). Compared to these WT

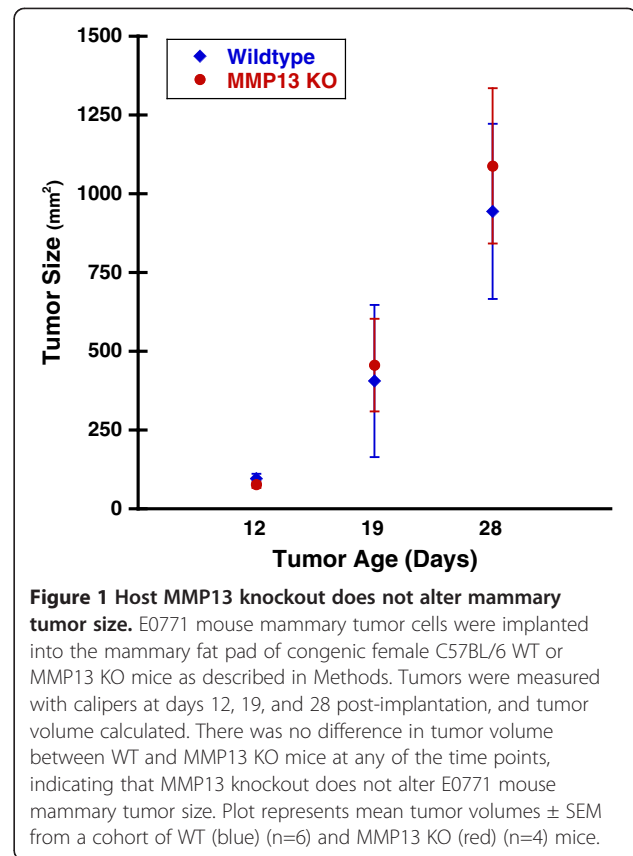


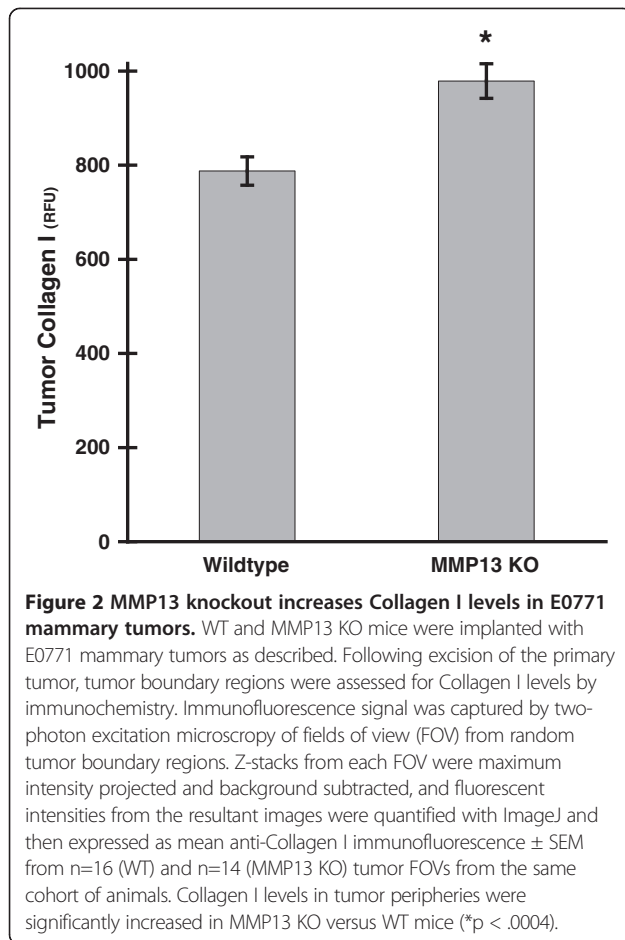
**Figure 1 Host MMP13 knockout does not alter mammary tumor size.** E0771 mouse mammary tumor cells were implanted into the mammary fat pad of congenic female C57BL/6 WT or MMP13 KO mice as described in Methods. Tumors were measured with calipers at days 12, 19, and 28 post-implantation, and tumor volume calculated. There was no difference in tumor volume between WT and MMP13 KO mice at any of the time points, indicating that MMP13 knockout does not alter E0771 mouse mammary tumor size. Plot represents mean tumor volumes  $\pm$  SEM from a cohort of WT (blue) (n=6) and MMP13 KO (red) (n=4) mice.

mice, MMP13 KO mice in contrast, although they had *greater* overall collagen I content (Figure 1), displayed fewer robust linear collagen I fibers, and a more randomly oriented collagen I distribution closely resembling a TACS-1 arrangement (Figure 3B). In adjacent sections of the same WT tumor as shown in Figure 3A, antibody labeling for MMP13 around the tumor periphery appeared to be closely localized with the robust TACS-2 patterned Collagen I fibers oriented parallel to the tumor boundary (Additional file 2: Figure S2), thus further implicating MMP-13 as likely to be a key orchestrator of these observed TACS changes in Collagen I organization.

To quantify these differences in local orientations of collagen I fibers, we performed tensor analysis of local image structure to calculate the coherency parameter (C), which is the ratio of the difference and sum of the largest ( $\lambda_{\max}$ ) and smallest ( $\lambda_{\min}$ ) tensor eigenvalues (averaged for all pixels over the image FOV), as follows:

$$C = (\lambda_{\max} - \lambda_{\min}) / (\lambda_{\max} + \lambda_{\min}) \quad (1)$$

With the upper bound  $C = 1$  indicating highly oriented structures, and the lower bound  $C = 0$  indicating high isotropy [24-26]. This analysis clearly indicated that Collagen I in mammary tumor peripheries of WT mice was more highly oriented (i.e. more ordered; C closer to 1),

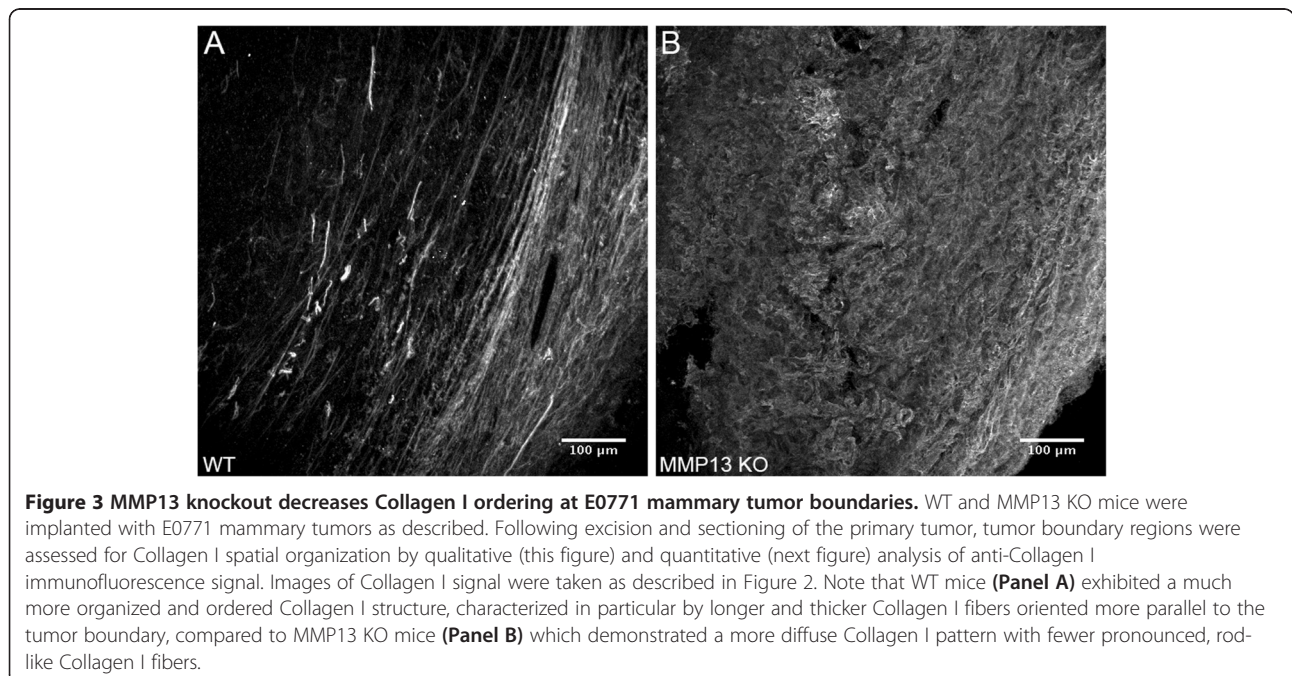


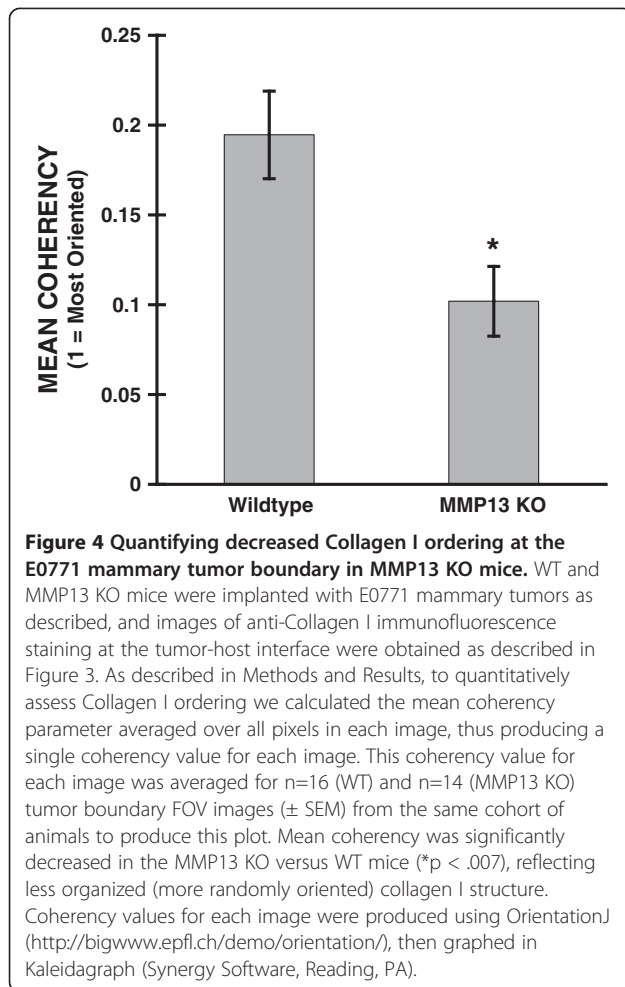
than in the mammary tumor peripheries of MMP13 KO mice (less ordered, C closer to 0) (Figure 4). Figure 5 shows a pseudo-colored map of these coherency values using the same images as in Figure 3 (more visible bright red areas = higher coherency).

Together these results suggest that depletion of host (stromal) MMP13 – a key collagen degrading enzyme – increased total collagen I content, but reduced collagen I organization, in the periphery of E0771 mammary tumors grown in MMP13 KO versus WT mice.

#### Stromal MMP13 knockout alters Collagen I microstructure at the tumor-host interface

SHG results when two photons (e.g. as provided by the near-IR titanium sapphire laser in a multiphoton microscope), interacting simultaneously with a non-centrosymmetric target such as collagen fibers, combine to produce a new photon with exactly twice the energy and half the wavelength of the interacting photons [9,32-36]. As a coherent phenomenon, SHG is intrinsically sensitive to spacing and regularity of scatterers, and hence can be utilized to detect changes in several aspects of collagen *microstructure* including regularity of the arrangement of collagen fibrils within larger collagen fibers; interfibril spacing; and fibril diameter, tilt angle, or pitch angle [4,7,9,27,34,37-41]. Collagen I is a particularly strong SHG emitter *in vivo* [7], is a substrate for MMP13 [15], is increased in breast cancer stroma [21,22], and is an important contributor to TACS [19]. Figures 2, 3, 4 and 5 assessed collagen I *macrostructural* properties (i.e. gross fiber orientations and arrangement)

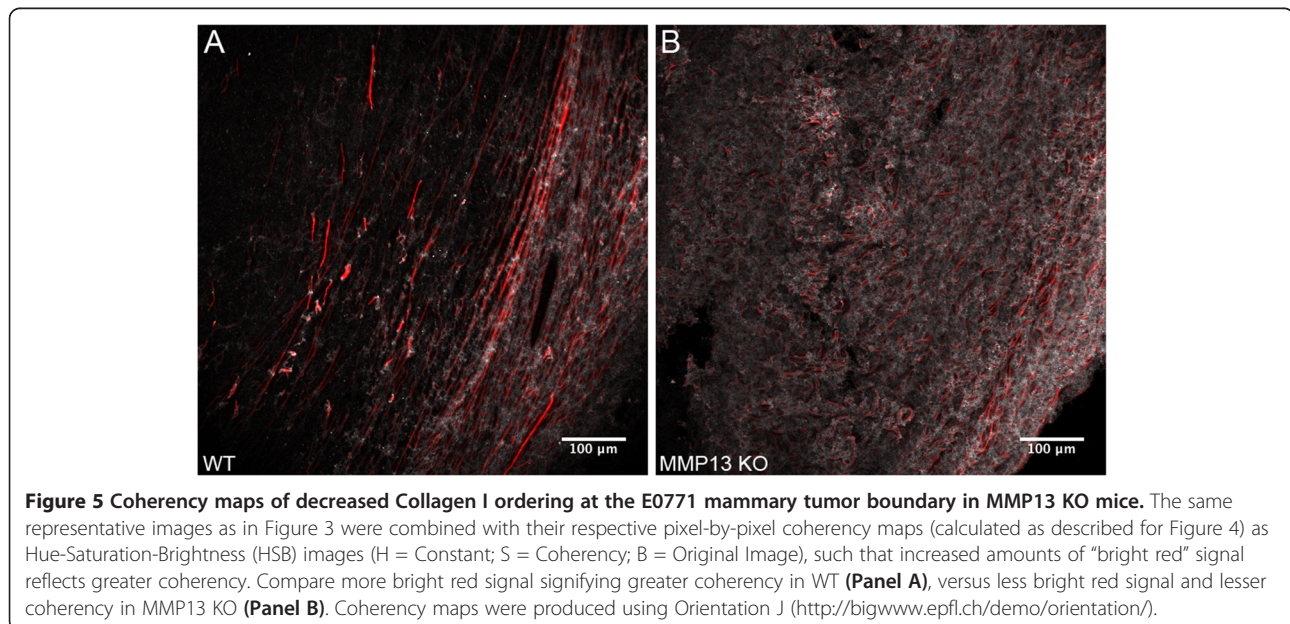




at the tumor-host interface, and to further these findings, we now wished to analyze collagen I *microstructural* properties at the tumor-host interface as assessed by SHG. For these reasons, we restricted our SHG analysis to the intensity of SHG signals emanating primarily from collagen I fibers, specifically using the “normalized  $B_{SHG}$ ” as described in Methods to provide an SHG measure of collagen I *microstructural* properties independent of changes in collagen I protein levels, as well as to gain particular insight into changes in the effective diameter or packing arrangement/density of fibrils within the SHG focal volume [4,27,30,34,42].

Figures 3, 4 and 5 demonstrated that while tumors in both WT and MMP13 KO mice contained both “diffuse” and “large fiber” patterns of collagen I, there was proportionately more “diffuse” collagen I with apparently thinner fiber structure or bundling on average in MMP13 KO tumors, versus proportionately more “large fiber” collagen I in WT tumors (often ordered parallel to the tumor boundary resembling a TACS-2 signature, e.g. Figure 3A). Therefore we hypothesized that knockout of MMP13 collagenase activity could cause differences in collagen I *micro-structural* properties – e.g. regularity or density of collagen fibrils within larger collagen fibers; fibril spacing; and fibril diameter, tilt angle, or pitch angle [4,7,9,27,34,37-41] – which might in turn account for the different collagen I *macrostructural* phenotypes observed in MMP13 KO versus WT mice.

As described here and in Methods, we measured collagen I-normalized  $B_{SHG}$  in the same WT and MMP13 KO animals and tumor-host interface regions as depicted in Figures 1, 2, 3, 4 and 5. We found that normalized  $B_{SHG}$  was significantly higher in the E0771



tumor peripheries of MMP13 KO versus WT mice (Figure 6A), suggesting different collagen I microstructure between these two groups [28,29]. To validate and complement these findings, we also measured the  $F_{\text{SHG}}/B_{\text{SHG}}$  ratio in these same groups and tumor-host interface regions. SHG is emitted both forwards (away from the incoming laser) and backwards (back towards the incoming laser, i.e. epi-directed) from the SHG-generating scatterers in the focal volume, and the  $F_{\text{SHG}}/B_{\text{SHG}}$  ratio is an additional SHG parameter that is primarily sensitive to the spatial extent of SHG-generating scatterers along the optical axis, i.e. the effective diameter or packing arrangement/density of collagen fibrils within the SHG focal volume [4,27,30,34,42]. We found this  $F_{\text{SHG}}/B_{\text{SHG}}$  ratio was significantly decreased in the E0771 tumor peripheries of MMP13 KO versus WT mice (Figure 6B). Together these two pieces of data suggest collagen I microstructure is altered in MMP13 KO versus WT mice, which may in turn relate to the observed changes in collagen I macrostructure (e.g. differences in average fiber density, apparent thickness, and organization) seen in Figures 3, 4 and 5.

Together these results suggest that stromal host MMP13 depletion alters both collagen I macrostructural (i.e. fiber arrangement, ordering, and orientation; Figures 2, 3, 4 and 5), and molecular (fibril) microstructural properties (as quantified by collagen I normalized  $B_{\text{SHG}}$  and  $F_{\text{SHG}}/B_{\text{SHG}}$ ; Figure 6) at the tumor periphery. Since WT tumor peripheries showed significantly more robust “rod

like” collagen I fibers (often in a more TACS-2-like orientation), compared to the higher proportion of “diffuse” fibers in MMP13 KO animals (often in a more TACS-1-like orientation) (Figure 3), these results further suggest the possibility that MMP13 KO changes collagen I microstructure in ways that 1. Could alter collagen’s ability to form and orient larger, more rod-like fibers, and/or 2. May shift the relative balance between “diffuse” and “rod-like” collagen I phenotypes.

#### Stromal MMP13 knockout increases mammary tumor metastasis to lung

Collagen is a key component of the extracellular matrix (ECM) which regulates cell behavior and motility [1,8,10,43], metastasizing breast tumor cells in particular have shown a propensity to “escape” the tumor by traveling along collagen fibers [5], and particular collagen patterns or “TACS” at the breast tumor periphery are associated with poor survival [12]. Therefore the observed collagen I macro- and micro-structural changes at the tumor-host interface might be expected to affect tumor metastasis.

For these reasons, and because breast tumor metastasis to lung is associated with poor prognosis [44], we wished to determine whether the changes in collagen I macro- and micro-structural properties demonstrated above could be associated with changes in this clinically significant parameter. Indeed, we found that along with their differing collagen I macro- and micro-structural

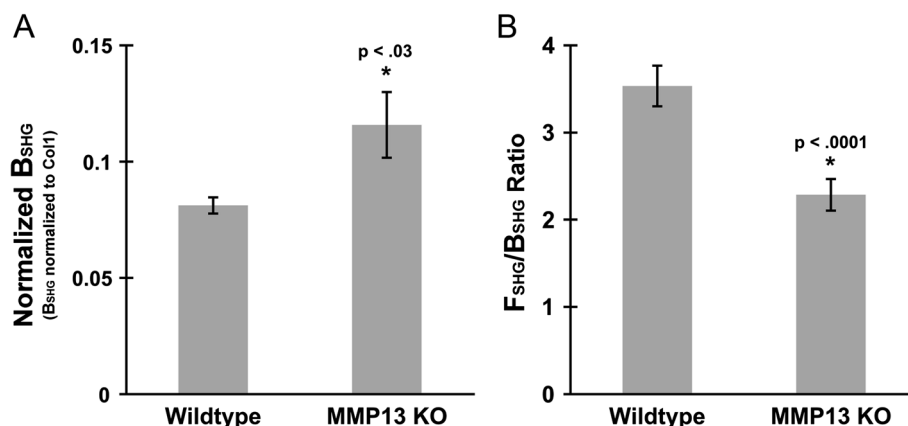


**Figure 6 MMP13 knockout alters Collagen I microstructure at the tumor-host interface.** WT and MMP13 KO mice were implanted with E0771 mammary tumors. **(A)** Following excision of the primary tumor, tumor boundary regions were labeled with anti-collagen I. Collagen I immunofluorescence and  $B_{\text{SHG}}$  signal were captured simultaneously in separate epidetection channels by two-photon excitation microscopy of fields of view (FOV) from random tumor boundary regions. Z-stacks from each FOV were maximum intensity projected and background subtracted, SHG and collagen I immunofluorescence signals masked to the same pixel areas, then from these masked images “normalized  $B_{\text{SHG}}$ ” (i.e.  $B_{\text{SHG}}$  normalized to collagen I levels) was calculated as mean  $B_{\text{SHG}}$  pixel value/mean collagen I immunofluorescence pixel value  $\pm$  SEM for all images over the same XYZ pixels. This ratiometric normalized collagen I SHG value was calculated for 16 (WT) and 14 (MMP13 KO) tumor FOVs from the same cohort of animals, and was higher in MMP13 KO versus WT tumor boundaries ( $p < .03$ ). **(B)** From the same cohort of animals, we also calculated  $F_{\text{SHG}}/B_{\text{SHG}}$  values, which provides insight into microstructural collagen changes, specifically the sub-resolution diameter and/or packing density/arrangement of collagen fibrils.  $F_{\text{SHG}}/B_{\text{SHG}}$  was significantly decreased in tumor boundary regions of MMP13 KO versus WT mice ( $p < .01$ ).

properties (Figures 2, 3, 4, 5 and 6), our MMP13 KO animals also had roughly double the number lung metastases compared to WT animals (Figure 7). This difference in metastasis was not due simply to differences in tumor burden between the WT and MMP13 KO animals, as tumor burden was unchanged (Figure 1).

## Discussion

The ECM, and collagen in particular, are increasingly believed to play important roles in cancer etiogenesis, progression, and outcome [1-9]. Several previous reports have demonstrated that tumor cells may preferentially travel along collagen fibers [10,11], which may represent an important pathway by which invading cells metastasize [5,11]. Accordingly, collagen fibers oriented perpendicularly to the tumor boundary in what has been termed a “TACS-3” configuration, have been associated with increased invasiveness into host stroma [5] and with decreased patient survival [9,12]. In contrast, TACS-2 collagen configuration- i.e. straight “taut” fibers often parallel to the tumor boundary-was associated with regions of decreased tumor invasiveness [5].

MMPs have been implicated in many cancers including breast cancer, most likely due to their ability to modulate this collagen- and ECM-rich extracellular environment [45]. While a majority of studies have found pro-tumorigenic roles for most MMPs, a growing body of literature suggests that some or even many MMPs may have anti-cancer effects as well [46,47]. Protective effects of MMPs against tumor pathology may in part account for the relative failure of MMP inhibitors as effective chemotherapeutics [46,48,49], and this concept is further supported by evidence that endogenous tissue inhibitors of matrix metalloproteinases (TIMPs) can themselves be cancer-promoters [50-53]. MMP13 in

particular has widely been found to promote cancer pathology, but a few emerging reports including this one find an apparently protective role for MMP13 in cancer and other diseases under some conditions [54,55]. Moreover, there remains limited understanding of exactly how MMP-13 interactions with collagen impact tumor pathology – for example, what structural changes result from these interactions, and how do these changes promote or protect against tumor pathology? In the studies described here, we have provided further insights into these important questions.

Herein we extended this previous work by demonstrating that *in vivo* genetic ablation of host MMP-13 in a mouse tumor model leads to altered collagen I macro- and micro-structure at the tumor-host interface, and increases mammary tumor metastasis to the lungs, a clinically significant functional outcome measure. This represents a direct experimental manipulation of the TACS stage of the tumor and therefore implicates stromal MMP13 as one driver of TACS evolution in breast tumors. These results are important because they help clarify the role of host MMP13 in tumor collagen dynamics, breast cancer pathogenesis, and metastasis. They are also important because this is one of few studies that have found a potentially protective effect for host MMP13 in the context of cancer pathology, and it is important to understand these intricacies of MMP13's roles in cancer biology – i.e. when, where, and how it may have protective versus deleterious functions in cancer – in order to develop effective, targeted MMP-based therapies that do more good than harm.

Due to the fact that tumor cells migrate preferentially along aligned collagen fibers [10,11], our findings of decreased metastasis (Figure 7) associated with collagen I TACS-2 patterning (i.e. fibers parallel to the tumor

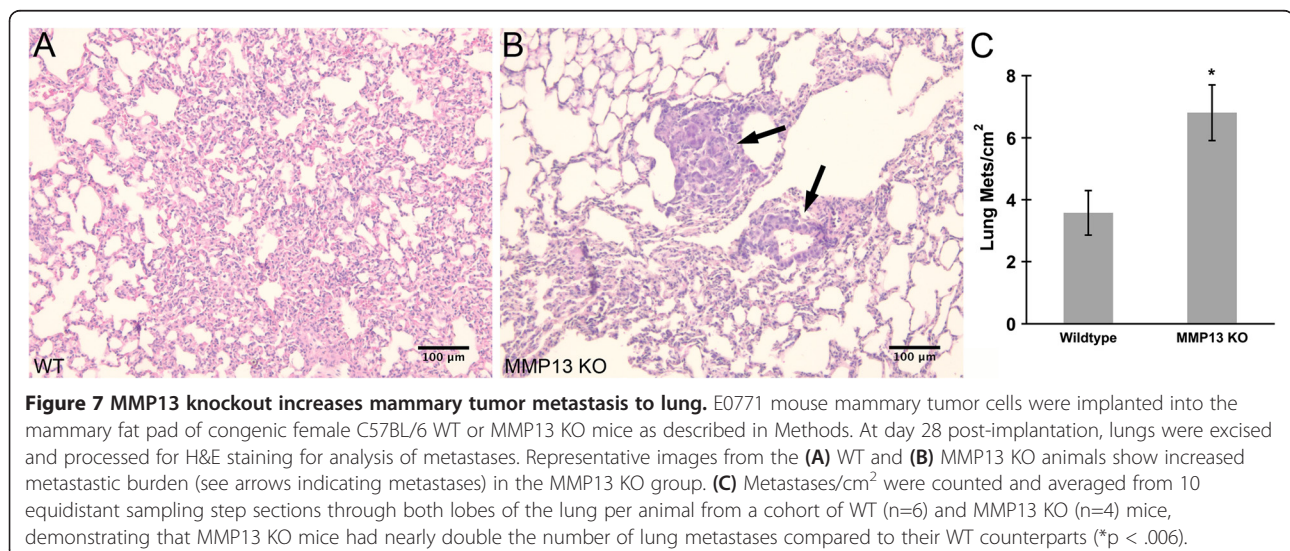


**Figure 7 MMP13 knockout increases mammary tumor metastasis to lung.** E0771 mouse mammary tumor cells were implanted into the mammary fat pad of congenic female C57BL/6 WT or MMP13 KO mice as described in Methods. At day 28 post-implantation, lungs were excised and processed for H&E staining for analysis of metastases. Representative images from the (A) WT and (B) MMP13 KO animals show increased metastatic burden (see arrows indicating metastases) in the MMP13 KO group. (C) Metastases/cm<sup>2</sup> were counted and averaged from 10 equidistant sampling step sections through both lobes of the lung per animal from a cohort of WT (n=6) and MMP13 KO (n=4) mice, demonstrating that MMP13 KO mice had nearly double the number of lung metastases compared to their WT counterparts (\*p < .006).

boundary: Figure 3A) in WT mice, taken with earlier studies demonstrating decreased tumor invasiveness also in TACS-2 areas [5], together support the *hypothesis that alignment of collagen fibers parallel to the tumor boundary may effectively serve as a literal “barrier” or “diversion” to metastasizing tumor cells.* Continuing this argument, it is easily seen how the contrasting TACS-3 pattern found in the literature, i.e. collagen fibers oriented perpendicular to the tumor boundary, may allow metastasizing cells to travel outward along these collagen “tracks” to more readily invade the host [5,10]. While we did not find significant TACS-3 patterning in our model system, our data suggest that the TACS-1 patterning (i.e. increased, more diffuse collagen deposition) resulting from knockout of stromal MMP13 *may also* result in increased metastasis if present in late-stage tumors, we posit because it is far less “barrier like” than TACS-2 patterning (e.g. compare Figures 3A and 3B, respectively), thus allowing for relatively easier escape of metastasizing tumor cells, possibly due to less diversion of those cells onto paths parallel to the tumor boundary.

In these previous reports, TACS-1 patterns were not investigated in detail for metastases effects, because in their model the TACS-1 collagen pattern tended to occur early in tumor formation before significant metastases occurred [5]. TACS-1 is characterized by dense, more diffuse collagen areas [5], consistent with the increased collagen I seen in the TACS-1 MMP13 KO group (Figure 2), which likely results from the absence of this key collagen I-degrading collagenase. Moreover, while E0771 tumor cells appear to have some level of MMP13 expression (Additional file 1: Figure S1 and unpublished data), as is common in mammary tumor cells [56-58], we believe most significant for our findings are the more strongly MMP13+ peritumor cell bodies seen in MMP13 expressing WT animals, but not in the MMP13 KO mice (compare Additional file 1: Figures S1B and S1C respectively, and unpublished data). These MMP13+ cell bodies found around the tumor periphery in WT but not MMP13 KO mice suggest the presence of peritumor (and possibly infiltrating) MMP13+ stromal cells which may contribute to the altered TACS patterns and metastases observed in WT versus MMP13 KO mice. These results, together with our finding that MMP13+ staining appears localized with the “barrier-like” Collagen I fibers around the tumor periphery in the TACS-2 (WT) condition (Additional file 2: Figure S2), all suggest that MMP13 in particular may be a principal contributor to TACS phenotype. The fact that MMP13 KO results in TACS-1 collagen patterning similar to what others have seen in “early stage” tumors in their mammary tumor models [5] suggests that the lack of MMP13 prevents the tumor stroma from progressing to a “late stage” structure. This is supported by the literature

observation that MMP13 can be a critical mediator of “early stage” tumor events [59].

In addition to these *macrostructural* collagen I changes, which we posit may impact tumor cells’ invasive potential, we also found changes in collagen I *microstructure* as measured by SHG. As described above and previously, SHG is sensitive to changes in collagen *microstructure* including regularity of collagen fibrils within larger collagen fibers; fibril compaction; and fibril diameter, tilt angle, or pitch angle [4,7,9,27,34,37-41], and therefore SHG signal normalized to collagen I levels can provide a quantitative measure of collagen I *microstructure* which is less dependent on changes in collagen I protein levels. Furthermore, typically as the diameter of collagen fibrils or small fibers (i.e. small bundles of fibrils) increases, their SHG becomes more forward-directed, and thus the  $F_{SHG}/B_{SHG}$  ratio also increases [42]. Therefore our findings of lower collagen I  $B_{SHG}$  (Figure 6A), and higher  $F_{SHG}/B_{SHG}$  (Figure 6B), in WT versus MMP KO mice is seemingly consistent with our observations of generally more large rod-like collagen I fibers in WT mice, versus apparently thinner and more diffuse collagen I fibers on average in MMP13 KO mice (Figures 3, 4 and 5). These findings also introduce the possibility that changes in collagen I *microstructure* (as measured by SHG) may alter collagen I’s ability to form larger rod-like fibers, thus altering the relative proportions of “diffuse” versus “large fiber” collagen I (and TACS patterning) in WT versus MMP13 KO mice (Figures 3, 4 and 5).

In further support of our work here, another report using mouse mammary tumor virus polyoma middle T (MMTV-PyMT) mice crossed with MMP13 KO mice, noted proportionately more “thin collagen fibers” (relative to total collagen) in tumors from MMP13 KO compared to WT mice as assessed by picrosirius red staining under linearly polarized light [31], although in this study additional macro- or micro-structural collagen changes, and collagen I in particular, were not investigated. Our data here suggest further that collagen I may be a principal contributor to these MMP13-regulated changes in collagen architecture and organization, at least in some mammary tumor models.

This hypothesis that changes in collagen I *microstructural* properties (measurable by SHG) may in turn contribute to observable changes in collagen I *macrostructure* requires further investigation in future studies beyond the scope of this report, but we can propose at least several ways by which this might occur. Regulation of collagen I fibril formation, fiber length and thickness, and organization is exceedingly complex and may involve numerous cellular and biochemical interactions with collagen I, just a few of which include protease activity by many MMPs, proteoglycan interactions, and/or

interactions of collagen I with other fibrillar or fibrillar-associated collagen subtypes or other ECM molecules [20,60,61]. Notably, there are several mechanisms by which MMP-13 in particular could induce collagen I microstructural changes, which further manifest themselves as macrostructural changes in collagen I fiber diameter. First, MMP-13 cleaves the collagen I amino terminal non-helical telopeptide end [62], which in turn promotes lateral fiber growth whereas leaving this site intact decreases lateral growth and is associated with initial formation of thin fibrils [63,64] – thus providing robust support for our results that WT mice (i.e. with normal MMP-13 cleavage of this site) show thicker fibers, whereas MMP13-KO mice (lacking MMP-13 cleavage of this site) have proportionately more thin (diffuse) fibers. Moreover, MMP-13 has been shown to degrade decorin [65], a proteoglycan known to be a key regulator of collagen I fiber diameter [66]. Further supporting our results, less decorin (i.e. more MMP-13) has typically been associated with thicker collagen I fibers [67,68], as we saw in the WT mice. Finally, MMP-13 can degrade collagen III which may result in altered fiber-diameter regulating interactions between collagen I and collagen III [69], or between collagen I and amino-terminal propeptide of type III procollagen which is thought to interact with Collagen I to regulate fiber diameter [70,71].

## Conclusions

In this work we have directly shifted a mouse model of breast cancer from one TACS state to another by knock-out of stromal MMP13, implicating stromal MMP13 as one driver of TACS state. This also altered the metastatic output in a manner consistent with the TACS literature, although the relationship between TACS and metastatic output is not necessarily causal based upon our data. This suggests that pharmacological manipulation of MMP13 activity is an attractive avenue of exploration in order to manipulate TACS state and hence attempt to alter metastatic output. In total, these novel findings that MMP13 may have beneficial roles in cancer biology by significantly altering collagen I dynamics and metastatic potential, help to further clarify MMP13's potentially protective roles in tumor pathology and thus facilitate future design of more specifically targeted and effective MMP-based therapies that minimize risks to the patient.

## Additional files

**Additional file 1: Figure S1.** Decreased MMP13 expression in MMP13 KO tumors. WT and MMP13 KO mice were implanted with E0771 mammary tumors as described. (A) Following excision of the primary tumor, MMP13 gene expression was assessed by quantitative PCR (qPCR) and normalized to 1, showing decreased MMP13 expression in MMP13

KO versus WT tumors ( $p < .03$ ) in the same cohort of WT ( $n=6$ ) and MMP13 KO ( $n=4$ ) mice. In addition, following immunofluorescence labeling for MMP13, the tumors from the (B) WT mice had peritumor MMP13+ cell bodies which were not apparent in the tumors from the (C) MMP13 KO mice. To assure details are visible for illustrative purposes, the original grayscale MMP13 immunofluorescence is shown with "Green" LUT applied in ImageJ, with levels (screen stretch) linear and set the same for both images.

**Additional file 2: Figure S2.** MMP13 at the tumor periphery is patterned like Collagen I in TACS-2. MMP13 immunofluorescence of adjacent sections of the same WT tumor as depicted in Figures 3A and 5A illustrates that MMP13 protein expression appears to align with the TACS-2 patterned Collagen I fibers depicted in Figures 3A and 5A, which are robust and oriented in a "barrier like" fashion around the tumor periphery, as is the MMP13 labeling shown here. Fiber banding patterns are visible amidst the MMP13 fluorescence labeling in this image. For illustrative purposes, the original grayscale MMP13 immunofluorescence is shown with a spectral lookup table ("Fire" LUT in ImageJ) applied and linear screen stretch (levels) set to assure details are visible for qualitative presentation.

## Competing interests

The authors declare that they have no competing interests.

## Authors' contributions

SWP conceived and designed studies, acquired and analyzed data, and wrote the manuscript. JMS, KB, and GLA acquired and analyzed data. EBB conceived and designed studies and wrote the manuscript. All authors read and approved the final manuscript.

## Acknowledgements

The authors thank the reviewers for their helpful suggestions on this manuscript. We thank Dr. Ryan M. Burke and Clark Burris for technical assistance. We thank Dr. Kelley S. Madden for helpful discussions and Dr. Stephen M. Krane for providing the MMP13 knockout mice. This work was supported by Department of Defense Breast Cancer Research Program (DoD BCRP) Era of Hope Scholar Research Award W81XWH-09-1-0405 (to EBB), National Institutes of Health (NIH) Director's New Innovator Award 1DP2 OD006501-01 (to EBB), and NIH Exploratory Developmental Research Grant Award R21DA030256 (to SWP). This paper is subject to the NIH Public Access Policy.

Received: 22 April 2013 Accepted: 28 August 2013

Published: 5 September 2013

## References

1. Lu P, Weaver VM, Werb Z: **The extracellular matrix: a dynamic niche in cancer progression.** *J Cell Biol* 2012, **196**(4):395–406.
2. Spano D, Zollo M: **Tumor microenvironment: a main actor in the metastasis process.** *Clin Exp Metastasis* 2012, **29**(4):381–395.
3. Wolf K, Alexander S, Schacht V, Coussens LM, von Andrian UH, van Rheenen J, Deryugina E, Friedl P: **Collagen-based cell migration models in vitro and in vivo.** *Semin Cell Dev Biol* 2009, **20**(8):931–941.
4. Han X, Burke RM, Zettel ML, Tang P, Brown EB: **Second harmonic properties of tumor collagen: determining the structural relationship between reactive stroma and healthy stroma.** *Opt Express* 2008, **16**(3):1846–1859.
5. Provenzano PP, Eliceiri KW, Campbell JM, Inman DR, White JG, Keely PJ: **Collagen reorganization at the tumor-stromal interface facilitates local invasion.** *BMC Med* 2006, **4**(1):38.
6. Hompland T, Erikson A, Lindgren M, Lindmo T, de Lange Davies C: **Second-harmonic generation in collagen as a potential cancer diagnostic parameter.** *J Biomed Opt* 2008, **13**(5):054050.
7. Brown E, McKee T, DiTomaso E, Pluen A, Seed B, Boucher Y, Jain RK: **Dynamic imaging of collagen and its modulation in tumors in vivo using second-harmonic generation.** *Nat Med* 2003, **9**(6):796–800.
8. Schedin P, Keely PJ: **Mammary gland ECM remodeling, stiffness, and mechanosignaling in normal development and tumor progression.** *Cold Spring Harb Perspect Biol* 2011, **3**(1):a003228.

9. Perry SW, Burke RM, Brown EB: **Two-photon and second harmonic microscopy in clinical and translational cancer research.** *Ann Biomed Eng* 2012, **40**(2):277–291.
10. Provenzano PP, Inman DR, Eliceiri KW, Trier SM, Keely PJ: **Contact guidance mediated three-dimensional cell migration is regulated by Rho/ROCK-dependent matrix reorganization.** *Biophys J* 2008, **95**(11):5374–5384.
11. Wang W, Wyckoff JB, Goswami S, Wang Y, Sidani M, Segall JE, Condeelis JS: **Coordinated regulation of pathways for enhanced cell motility and chemotaxis is conserved in rat and mouse mammary tumors.** *Cancer Res* 2007, **67**(8):3505–3511.
12. Conklin MW, Eickhoff JC, Ricking KM, Pehlke CA, Eliceiri KW, Provenzano PP, Friedl A, Keely PJ: **Aligned collagen is a prognostic signature for survival in human breast carcinoma.** *Am J Pathol* 2011, **178**(3):1221–1232.
13. Binder C, Hagemann T, Husein B, Schulz M, Einspanier A: **Relaxin enhances in-vitro invasiveness of breast cancer cell lines by up-regulation of matrix metalloproteinases.** *Mol Hum Reprod* 2002, **8**(9):789–796.
14. Binder C, Simon A, Binder L, Hagemann T, Schulz M, Emons G, Trumper L, Einspanier A: **Elevated concentrations of serum relaxin are associated with metastatic disease in breast cancer patients.** *Breast Cancer Res Treat* 2004, **87**(2):157–166.
15. Ala-aho R, Kahari VM: **Collagenases in cancer.** *Biochimie* 2005, **87**(3–4):273–286.
16. Freije JM, Diez-Iltza I, Balbin M, Sanchez LM, Blasco R, Tolivia J, Lopez-Otin C: **Molecular cloning and expression of collagenase-3, a novel human matrix metalloproteinase produced by breast carcinomas.** *J Biol Chem* 1994, **269**(24):16766–16773.
17. Balbin M, Pendas AM, Uria JA, Jimenez MG, Freije JP, Lopez-Otin C: **Expression and regulation of collagenase-3 (MMP-13) in human malignant tumors.** *APMIS* 1999, **107**(1):45–53.
18. Zhang B, Cao X, Liu Y, Cao W, Zhang F, Zhang S, Li H, Ning L, Fu L, Niu Y, et al: **Tumor-derived matrix metalloproteinase-13 (MMP-13) correlates with poor prognoses of invasive breast cancer.** *BMC Cancer* 2008, **8**:83.
19. Provenzano PP, Inman DR, Eliceiri KW, Knittel JG, Yan L, Rueden CT, White JG, Keely PJ: **Collagen density promotes mammary tumor initiation and progression.** *BMC Med* 2008, **6**:11.
20. Gelse K, Poschl E, Aigner T: **Collagens—structure, function, and biosynthesis.** *Adv Drug Deliv Rev* 2003, **55**(12):1531–1546.
21. Rudnick JA, Kuperwasser C: **Stromal biomarkers in breast cancer development and progression.** *Clin Exp Metastasis* 2012, **29**(7):633–672.
22. Dvorak HF: **Tumors: wounds that do not heal. Similarities between tumor stroma generation and wound healing.** *N Engl J Med* 1986, **315**(26):1650–1659.
23. Inada M, Wang Y, Byrne MH, Rahman MU, Miyaura C, Lopez-Otin C, Krane SM: **Critical roles for collagenase-3 (Mmp13) in development of growth plate cartilage and in endochondral ossification.** *Proc Natl Acad Sci USA* 2004, **101**(49):17192–17197.
24. Rezakhanlou R, Agianniotis A, Schrauwen JT, Griffa A, Sage D, Bouten CV, van de Vosse FN, Unser M, Stergiopoulos N: **Experimental investigation of collagen waviness and orientation in the arterial adventitia using confocal laser scanning microscopy.** *Biomech Model Mechanobiol* 2012, **11**(3–4):461–473.
25. Bigun J, Bigun T, Nilsson K: **Recognition by symmetry derivatives and the generalized structure tensor.** *IEEE Trans Pattern Anal Mach Intell* 2004, **26**(12):1590–1605.
26. Haußecker H, Jähne B: **A Tensor Approach for Local Structure Analysis in Multi-Dimensional Images.** In *Proceedings 3D Image Analysis and Synthesis '96 Proceedings in Artificial Intelligence*. Edited by Girod B, Niemann H, Seidel H-P. Erlangen, Germany, Sankt Augustin: Infix (now Aka/IOS Press); 1996:171–178.
27. Perry SW, Han X, Brown EB: **Second Harmonic Generation in Tumors: Scattering and Polarization.** In *Second Harmonic Generation Imaging. Volume In Press*. Edited by Pavone FS, Campagnola PJ. London, UK: Taylor and Francis; 2012.
28. Diop-Frimpong B, Chauhan VP, Krane S, Boucher Y, Jain RK: **Losartan inhibits collagen I synthesis and improves the distribution and efficacy of nanotherapeutics in tumors.** *Proc Natl Acad Sci USA* 2011, **108**(7):2909–2914.
29. Ingman WW, Wyckoff J, Gouon-Evans V, Condeelis J, Pollard JW: **Macrophages promote collagen fibrillogenesis around terminal end buds of the developing mammary gland.** *Dev Dyn* 2006, **235**(12):3222–3229.
30. Burke K, Tang P, Brown E: **Second harmonic generation reveals matrix alterations during breast tumor progression.** *J Biomed Opt* 2013, **18**(3):31106.
31. Nielsen BS, Egeblad M, Rank F, Askautrud HA, Pennington CJ, Pedersen TX, Christensen IJ, Edwards DR, Werb Z, Lund LR: **Matrix metalloproteinase 13 is induced in fibroblasts in polyomavirus middle T antigen-driven mammary carcinoma without influencing tumor progression.** *PLoS ONE* 2008, **3**(8):e2959.
32. Mohler W, Millard AC, Campagnola PJ: **Second harmonic generation imaging of endogenous structural proteins.** *Methods* 2003, **29**(1):97–109.
33. Campagnola PJ, Loew LM: **Second-harmonic imaging microscopy for visualizing biomolecular arrays in cells, tissues and organisms.** *Nat Biotechnol* 2003, **21**(11):1356–1360.
34. Mertz J, Moreaux L: **Second harmonic generation by focused excitation of inhomogeneously distributed scatterers.** *Opt Commun* 2001, **196**(1–6):325–330.
35. Pantazis P, Maloney J, Wu D, Fraser SE: **Second harmonic generating (SHG) nanoprobes for in vivo imaging.** *Proc Natl Acad Sci USA* 2010, **107**(33):14535–14540.
36. Reeve JE, Anderson HL, Clays K: **Dyes for biological second harmonic generation imaging.** *Phys Chem Chem Phys* 2010, **12**(41):13484–13498.
37. Brown EB, Campbell RB, Tsuzuki Y, Xu L, Carmeliet P, Fukumura D, Jain RK: **In vivo measurement of gene expression, angiogenesis and physiological function in tumors using multiphoton laser scanning microscopy.** *Nat Med* 2001, **7**(7):864–868.
38. Odin C, Guilbert T, Alkilani A, Boryska OP, Fleury V, Le Grand Y: **Collagen and myosin characterization by orientation field second harmonic microscopy.** *Opt Express* 2008, **16**(20):16151–16165.
39. Plotnikov SV, Millard AC, Campagnola PJ, Mohler WA: **Characterization of the myosin-based source for second-harmonic generation from muscle sarcomeres.** *Biophys J* 2006, **90**(2):693–703.
40. Su PJ, Chen WL, Chen YF, Dong CY: **Determination of collagen nanostructure from second-order susceptibility tensor analysis.** *Biophys J* 2011, **100**(8):2053–2062.
41. Tiaho F, Recher G, Rouede D: **Estimation of helical angles of myosin and collagen by second harmonic generation imaging microscopy.** *Opt Express* 2007, **15**(19):12286–12295.
42. Lacombe R, Nadiarykh O, Townsend SS, Campagnola PJ: **Phase Matching considerations in Second Harmonic Generation from tissues: Effects on emission directionality, conversion efficiency and observed morphology.** *Opt Commun* 2008, **281**(7):1823–1832.
43. Ghajar CM, Bissell MJ: **Extracellular matrix control of mammary gland morphogenesis and tumorigenesis: insights from imaging.** *Histochem Cell Biol* 2008, **130**(6):1105–1118.
44. Welter S, Jacobs J, Krbek T, Totsch M, Stamatis G: **Pulmonary metastases of breast cancer. When is resection indicated.** *Eur J Cardiothorac Surg* 2008, **34**(6):1228–1234.
45. Westermarck J, Kahari VM: **Regulation of matrix metalloproteinase expression in tumor invasion.** *Faseb J* 1999, **13**(8):781–792.
46. Martin MD, Matrisian LM: **The other side of MMPs: protective roles in tumor progression.** *Cancer Metastasis Rev* 2007, **26**(3–4):717–724.
47. Noel A, Gutierrez-Fernandez A, Sounni NE, Behrendt N, Maquoi E, Lund IK, Cal S, Hoyer-Hansen G, Lopez-Otin C: **New and paradoxical roles of matrix metalloproteinases in the tumor microenvironment.** *Frontiers in pharmacology* 2012, **3**:140.
48. Zucker S, Cao J: **Selective matrix metalloproteinase (MMP) inhibitors in cancer therapy: ready for prime time?** *Cancer biology & therapy* 2009, **8**(24):2371–2373.
49. Overall CM, Kleinfeld O: **Tumour microenvironment - opinion: validating matrix metalloproteinases as drug targets and anti-targets for cancer therapy.** *Nat Rev Cancer* 2006, **6**(3):227–239.
50. Bourboulia D, Stetler-Stevenson WG: **Matrix metalloproteinases (MMPs) and tissue inhibitors of metalloproteinases (TIMPs): Positive and negative regulators in tumor cell adhesion.** *Semin Cancer Biol* 2010, **20**(3):161–168.
51. Groblewska M, Siewko M, Mroczko B, Szmitkowski M: **The role of matrix metalloproteinases (MMPs) and their inhibitors (TIMPs) in the development of esophageal cancer.** *Folia Histochem Cytobiol* 2012, **50**(1):12–19.
52. Jiang Y, Goldberg ID, Shi YE: **Complex roles of tissue inhibitors of metalloproteinases in cancer.** *Oncogene* 2002, **21**(14):2245–2252.
53. Hojilla CV, Mohammed FF, Khokha R: **Matrix metalloproteinases and their tissue inhibitors direct cell fate during cancer development.** *Br J Cancer* 2003, **89**(10):1817–1821.
54. Fukuda H, Mochizuki S, Abe H, Okano HJ, Hara-Miyachi C, Okano H, Yamaguchi N, Nakayama M, D'Armiento J, Okada Y: **Host-derived MMP-13 exhibits a protective role in lung metastasis of melanoma cells by local endostatin production.** *Br J Cancer* 2011, **105**(10):1615–1624.
55. Tarin C, Gomez M, Calvo E, Lopez JA, Zaragoza C: **Endothelial nitric oxide deficiency reduces MMP-13-mediated cleavage of ICAM-1 in vascular**

- endothelium: a role in atherosclerosis. *Arterioscler Thromb Vasc Biol* 2009, **29**(1):27–32.
56. Chang HJ, Yang MJ, Yang YH, Hou MF, Hsueh EJ, Lin SR: **MMP13 is potentially a new tumor marker for breast cancer diagnosis.** *Oncol Rep* 2009, **22**(5):1119–1127.
  57. Heppner KJ, Matrisian LM, Jensen RA, Rodgers WH: **Expression of most matrix metalloproteinase family members in breast cancer represents a tumor-induced host response.** *Am J Pathol* 1996, **149**(1):273–282.
  58. Uria JA, Stahle-Backdahl M, Seiki M, Fueyo A, Lopez-Otin C: **Regulation of collagenase-3 expression in human breast carcinomas is mediated by stromal-epithelial cell interactions.** *Cancer Res* 1997, **57**(21):4882–4888.
  59. Pendas AM, Uria JA, Jimenez MG, Balbin M, Freije JP, Lopez-Otin C: **An overview of collagenase-3 expression in malignant tumors and analysis of its potential value as a target in antitumor therapies.** *Clin Chim Acta* 2000, **291**(2):137–155.
  60. Saeidi N: *On the control of collagen fibril organization and morphology. Mechanical Engineering Dissertations Paper 7.* [http://iris.lib.nyu.edu/cgi/viewcontent.cgi?article=1006&context=mech\\_eng\\_diss](http://iris.lib.nyu.edu/cgi/viewcontent.cgi?article=1006&context=mech_eng_diss) 2009.
  61. Bode M: *Characterization of Type I and Type III collagens in human tissues.* heis Dissertation, Oulu University Library. <http://herkules.oulu.fi/isbn9514255534/isbn9514255534.pdf> 2000.
  62. Krane SM, Byrne MH, Lemaitre V, Henriot P, Jeffrey JJ, Witter JP, Liu X, Wu H, Jaenisch R, Eeckhout Y: **Different collagenase gene products have different roles in degradation of type I collagen.** *J Biol Chem* 1996, **271**(45):28509–28515.
  63. Silver FH, Freeman JW, Seehra GP: **Collagen self-assembly and the development of tendon mechanical properties.** *J Biomech* 2003, **36**(10):1529–1553.
  64. Comper WD, Veis A: **Characterization of nuclei in in vitro collagen fibril formation.** *Biopolymers* 1977, **16**(10):2133–2142.
  65. Monfort J, Tardif G, Reboul P, Mineau F, Roughley P, Pelletier JP, Martel-Pelletier J: **Degradation of small leucine-rich repeat proteoglycans by matrix metalloproteinase-13: identification of a new biglycan cleavage site.** *Arthritis Res Ther* 2006, **8**(1):R26.
  66. Vogel KG, Paulsson M, Heinegard D: **Specific inhibition of type I and type II collagen fibrillogenesis by the small proteoglycan of tendon.** *Biochem J* 1984, **223**(3):587–597.
  67. Hakkinen L, Strassburger S, Kahari VM, Scott PG, Eichstetter I, Lozzo RV, Larjava H: **A role for decorin in the structural organization of periodontal ligament.** *Lab Invest* 2000, **80**(12):1869–1880.
  68. Zhang G, Ezura Y, Chervoneva I, Robinson PS, Beason DP, Carine ET, Soslowsky LJ, Lozzo RV, Birk DE: **Decorin regulates assembly of collagen fibrils and acquisition of biomechanical properties during tendon development.** *J Cell Biochem* 2006, **98**(6):1436–1449.
  69. Cameron GJ, Alberts IL, Laing JH, Wess TJ: **Structure of type I and type III heterotypic collagen fibrils: an X-ray diffraction study.** *J Struct Biol* 2002, **137**(1–2):15–22.
  70. Fleischmajer R, Perlish JS, Burgeson RE, Shaikh-Bahai F, Timpl R: **Type I and type III collagen interactions during fibrillogenesis.** *Ann N Y Acad Sci* 1990, **580**:161–175.
  71. Romanic AM, Adachi E, Kadler KE, Hojima Y, Prockop DJ: **Copolymerization of pNcollagen III and collagen I. pNcollagen III decreases the rate of incorporation of collagen I into fibrils, the amount of collagen I incorporated, and the diameter of the fibrils formed.** *J Biol Chem* 1991, **266**(19):12703–12709.

doi:10.1186/1471-2407-13-411

**Cite this article as:** Perry et al.: Stromal matrix metalloproteinase-13 knockout alters Collagen I structure at the tumor-host interface and increases lung metastasis of C57BL/6 syngeneic E0771 mammary tumor cells. *BMC Cancer* 2013 **13**:411.

**Submit your next manuscript to BioMed Central and take full advantage of:**

- Convenient online submission
- Thorough peer review
- No space constraints or color figure charges
- Immediate publication on acceptance
- Inclusion in PubMed, CAS, Scopus and Google Scholar
- Research which is freely available for redistribution

Submit your manuscript at  
[www.biomedcentral.com/submit](http://www.biomedcentral.com/submit)



# Journal of Biomedical Optics

SPIEDigitalLibrary.org/jbo

## **Second harmonic generation reveals matrix alterations during breast tumor progression**

Kathleen Burke  
Ping Tang  
Edward Brown



# Second harmonic generation reveals matrix alterations during breast tumor progression

Kathleen Burke,<sup>a</sup> Ping Tang,<sup>b</sup> and Edward Brown<sup>a</sup>

<sup>a</sup>University of Rochester, Department of Biomedical Engineering, Goergen Hall Box 270168, Rochester, New York 14627

<sup>b</sup>University of Rochester Medical Center, School of Medicine and Dentistry, Department of Pathology and Laboratory Medicine, 601 Elmwood Avenue, Box 626, Rochester, New York 14627

**Abstract.** Alteration of the extracellular matrix in tumor stroma influences efficiency of cell locomotion away from the primary tumor into surrounding tissues and vasculature, thereby affecting metastatic potential. We study matrix changes in breast cancer through the use of second harmonic generation (SHG) of collagen in order to improve the current understanding of breast tumor stromal development. Specifically, we utilize a quantitative analysis of the ratio of forward to backward propagating SHG signal (F/B ratio) to monitor collagen throughout ductal and lobular carcinoma development. After detection of a significant decrease in the F/B ratio of invasive but not *in situ* ductal carcinoma compared with healthy tissue, the collagen F/B ratio is investigated to determine the evolution of fibrillar collagen changes throughout tumor progression. Results are compared with the progression of lobular carcinoma, whose F/B signature also underwent significant evolution during progression, albeit in a different manner, which offers insight into varying methods of tissue penetration and collagen manipulation between the carcinomas. This research provides insights into trends of stromal reorganization throughout breast tumor development. © The Authors.

Published by SPIE under a Creative Commons Attribution 3.0 Unported License. Distribution or reproduction of this work in whole or in part requires full attribution of the original publication, including its DOI. [DOI: [10.1117/1.JBO.18.3.031106](https://doi.org/10.1117/1.JBO.18.3.031106)]

Keywords: second harmonic generation; forward to backward ratio; breast cancer; tumor stage; tumor grade.

Paper 12374SS received Jun. 14, 2012; revised manuscript received Oct. 22, 2012; accepted for publication Oct. 30, 2012; published online Nov. 22, 2012.

## 1 Introduction

There are two primary forms of invasive breast carcinomas, ductal and lobular, named after the breast structure from which they originate. The replication of tumor cells within these structures without interacting with the surrounding tissue is called carcinoma *in situ*, where ductal carcinoma *in situ* (DCIS) makes up 25 to 30% of all diagnosed breast cancer.<sup>1</sup> Seventy-five to 80% of invasive breast carcinomas are categorized as invasive ductal carcinoma (IDC),<sup>2</sup> which is the progression of a primary tumor from within the breast duct to an invasion of surrounding tissue by penetrating through the basement membrane of the duct. Invasive lobular carcinoma (ILC) is the invasive growth of cancer cells that originate in the lobules and penetrate the surrounding breast tissue. Lobular carcinoma *in situ* (LCIS) is characterized as abnormal proliferation of acinar cells in terminal ductal lobular units that are commonly undetectable by mammograms but, if detected (usually in biopsies taken for other reasons), can serve as a marker for increased risk of future invasive carcinomas (ILC or IDC) in either breast.<sup>3</sup> With the increased capabilities of early detection and treatment of cancer, mortality rates due to the primary tumor have decreased, and currently 90% of cancer mortality is a result of metastatic events.<sup>4</sup> It is therefore becoming increasingly important to uncover prognostic markers that can help us understand the metastatic potential of a primary tumor to aid in determining the optimal course of patient treatment, as well as for assisting in the creation of new methods of treatment. Previous research

points to tumor size,<sup>5,6</sup> lymph-node status,<sup>6</sup> histologic grade,<sup>7</sup> urokinase plasminogen activator (uPA) protein levels,<sup>8,9</sup> as well as other genetic and physiological factors of the tumor to predict levels of metastasis.<sup>10</sup> Changes in these factors are accompanied by changes in the extracellular matrix (ECM) in the tumor stroma<sup>10–12</sup> that result from the release of signals and proteases from surrounding stromal cells such as cancer associated fibroblasts<sup>13</sup> and macrophages.<sup>14</sup> A major focus of ECM modification is alterations in collagen, including degradation of collagen IV, XV, & XVIII in the basement membrane surrounding the tumor,<sup>15</sup> and remodeling of collagen I throughout the connective tissue.<sup>13,16,17</sup> Modified fibrillar collagen in the connective tissue allows for a more efficient dispersal of tumor cells into the surrounding tissue and vasculature to spread to a secondary location.<sup>16,17</sup>

Second harmonic generation (SHG) is a scattering phenomenon in which two incoming photons of the same wavelength are scattered by a noncentrosymmetric structure into one photon of exactly half the wavelength. The resultant emission is coherent, hence the directionality, intensity, and polarization of the outgoing light are sensitive to various properties of the scatterers, including scatterer order and spacing and angle, as well as overall spatial extent of the scatterer distribution along the laser axis.<sup>18–20</sup> Collagen, primarily type I collagen, is capable of producing an SHG signal that can be detected in biological samples and used as a technique for monitoring the changes in ECM structure throughout tumor development. This technique results in high-resolution two-photon images without the need for fluorescent staining and without photobleaching and can be applied to the surface of a primary tumor, excised tissue, or a sectioned sample to provide insight into matrix properties.

Address all correspondence to: Edward Brown, University of Rochester, Department of Biomedical Engineering, Goergen Hall Box 270168, Rochester, New York 14627. Tel: 001-585-273-5918; E-mail: [Edward\\_Brown@URMC.Rochester.edu](mailto:Edward_Brown@URMC.Rochester.edu)

The progression of breast tumors is diagnosed along a two-axis classification scheme, based upon the ability to visually differentiate the tumor cells from healthy cells, as well as the stage of the growth and metastatic properties of the tumor (see Sec. 2.2). Fenhalls et al. used Northern analysis of tumor samples to show that tumor staging is accompanied by changes in the level of collagen mRNA.<sup>21</sup> Following this study, many groups have incorporated two-photon techniques to analyze collagen SHG signals in an attempt to differentiate healthy and tumor tissue. Morphological collagen changes, such as the shape of fibrillar collagen<sup>22</sup> or its orientation with regards to the border of the primary tumor,<sup>23</sup> have been investigated in order to differentiate between healthy and malignant tumors as well as to predict survival rates associated with primary tumor samples. Further studies have incorporated third harmonic generation signals<sup>24</sup> or intrinsic fluorescence analysis<sup>25,26</sup> to increase the morphological information provided by a tumor sample and to standardize quantitative SHG measurements using the ratio of SHG/two-photon excited fluorescence (TPEF). In a mouse model of epithelial carcinoma SHG and TPEF of intrinsic signals was used to track the progression of tumors throughout different pathological phases.<sup>27</sup> Zhuo et al. showed that backward propagating SHG of freshly removed ectocervical samples could be used to differentiate between healthy tissue, cervical intraepithelial neoplasia (pre-cancer), and cancer, showing the potential of SHG techniques to not only differentiate between healthy and tumor tissue intra-operatively but to provide insight into the progression of the tumor.<sup>28</sup>

The ratio of the forward to backward propagating SHG signal (F/B ratio) is sensitive to the spatial extent of the scatterers along the optical axis (in collagen, the effective fibril diameter) as well as order versus disorder in fibril packing.<sup>18–20</sup> In this study we will use the phrase collagen “microstructural properties” to indicate those properties of an individual collagen fiber, which influence SHG F/B from that fiber, as distinct from collagen “morphology,” which will indicate macroscopic properties such as fiber orientation, tortuosity, and overall density of fibers. It has been shown previously that the F/B ratio can be used to differentiate between healthy and tumor ovarian cancer,<sup>29</sup> which is particularly interesting because F/B analysis is intrinsically ratiometric and hence is less susceptible to variations in excitation intensity and is also less susceptible to user-to-user variability of morphology-based analysis techniques. We are interested in exploring the application of F/B imaging to breast tumor samples to learn about the evolution of fibrillar collagen microstructural properties during tumor progression.

## 2 Methods

### 2.1 Breast Cancer Tissue Samples

The samples used throughout this study are primarily tissue microarray (TMA) slides, which are composed of 0.6- to 1.0-mm-diameter samples from cylindrical cores of paraffin embedded tissue specimens sectioned into 5- $\mu$ m thick slices. One advantage of these samples is that due to their thickness the effect of subsequent scattering or absorption of SHG light is negligible [the absorption coefficient is  $\mu_a \sim 20 \text{ cm}^{-1}$ , while the reduced scattering coefficient is  $\mu'_s \sim 10 \text{ cm}^{-1}$ .<sup>30,31</sup> Each 5- $\mu$ m thick,  $\sim 1.0$ -mm-diameter specimen corresponds with a different patient/tumor and is mounted on a slide, with several tens of samples on each slide. The tumor specimens

are staged by a certified pathologist, and every tenth section of the TMA block is used to create an H&E stained slide, which is analyzed by the pathologist to ensure that each sample is within the tumor and demonstrates properties of the diagnosis. Hence in the direction perpendicular to the plane of the sample, each tissue section is at least 50  $\mu$ m from the tumor surface. In the plane of the sample, sections are chosen that are entirely within the tumor and do not contain significant healthy tissue, based upon inspection of the adjacent H&E stained slides. However, the distance from the outer edge of the core to the tumor surface is not known. Consequently any significant variation of tumor SHG properties with distance from the tumor edge may increase the variance in our measurements.

The breast cancer tissue microarray samples used throughout this study came from two sources. Samples of healthy breast tissue, as well as various grades and stages of IDC and ILC, were purchased from Biomax (Rockville Maryland, slides BR1921, BR20830, BR805, BR961, and BR954). Pure DCIS and IDC tissue microarray slides were received from Dr. Ping Tang and created in the Department of Pathology and Laboratory Medicine at the University of Rochester Medical Center.

In addition to the tissue microarray samples, several LCIS and ILC samples were generated from paraffin embedded tissue blocks, cut to 5  $\mu$ m thickness. In these samples we utilized an adjacent H&E stained slide to identify the region of tumor, then generated a single SHG field of view from the center of tumor in the unstained slide. Table 1 summarizes which samples were used to create each data set.

### 2.2 Sample Grading and Staging

Invasive breast tumors are graded on a three-state classification system dependent upon tubule formation, nuclear polymorphism, and mitotic count, where Grade 1 has the most differentiated tissue with the best prognosis and Grade 3 is the least differentiated with the worst prognosis. The TNM staging system is a method of tumor classification determined by the size of the primary tumor ( $T$ ), regional lymph node involvement ( $N$ ), and presence of distant metastases ( $M$ ). Staging of the primary tumor ( $T$ ) as well as the metastatic events in the lymph node ( $N$ ) incorporates multiple degrees of staging as opposed to metastatic staging ( $M$ ), which is a binary system determined simply by the presence or absence of a distant metastases. The primary tumor staging is split into categories based on tumor diameters of between 1 to 20 mm ( $T1$ ), between 20 to 50 mm ( $T2$ ), and greater than 50 mm ( $T3$ ). Tumors that have penetrated the chest wall or skin, independent of the size of the tumor are staged as  $T4$  tumors. The lymph node (LN) staging scale begins at  $N0$  indicating there are no metastatic events present in the LN that are greater than 0.2 mm or 200 cells. The two middle stages,  $N1$  and  $N2$ , describe increasing involvement in the axillary LNs, or metastasis to the internal mammary LNs without spread to the axillary LNs. Specifically,  $N1$  tumors have either micrometastases, one to three axillary LN metastases, or sentinel LN metastases detected through biopsy.  $N2$  tumors are characterized by four to nine axillary LN metastases, or clinically detected sentinel LN metastases.  $N3$  stage is the most far reaching metastatic LN events, including either greater than 10 axillary events with at least one event greater than 2 mm, infraclavicular LN metastases, or clinically detected internal mammary and axillary LN metastases.<sup>32</sup> Note that grading information was not available for ILC samples, which are uniformly low grade, nor was  $M$

**Table 1** Table of the tissue microarray slides that were used, along with how many samples from each slide were used to create each set of results. The number given (i.e., "BR1921") is the part number of the Biomax microarray slide, while "URMC" refers to the full sections or tissue microarray (TMA) slide manufactured by the University of Rochester Department of Pathology. Note that samples are "double counted" in that a sample that is IDC T1 and N0 would count in both the IDC T1 column as well as the IDC N0 column.

	Healthy	DCIS	IDC T				IDC N				IDC M		Grade			LCIS	ILC T				ILC N					
			T1	T2	T3	T4	N0	N1	N2	N3	M1	M0	1	2	3		T1	T2	T3	T4	N0	N1	N2	N3		
1921	30		7	55	7	6	30	34	8		75	4	57	12		5	49	5	4	42	19	4				
20830			5	25	6	5	12	13	13	4	42	4	31	3												
954	7			17	10		9	5	8	5	9	19														
805															1	4	12	1		8	5	5	1			
URMC TMA		20																								
URMC Full section																8										3

stage information available because distant metastases for this tumor type, if they occur, usually appear many years after initial diagnosis and hence are not known during preparation of the TMA. All samples were classified based upon the aforementioned grading and staging scheme by a certified pathologist, and all parties were blinded to the classification of the samples during image acquisition and analysis.

### 2.3 Imaging

The excitation light is a Spectra Physics MaiTai Ti:Sapphire laser at 810 nm, with 100 fs pulses at 80 MHz. It is directed to the sample through an Olympus BX61WI upright microscope, with beam scanning and image acquisition controlled by an Olympus Fluoview FV300 scanning system. Before entering the scan box, the laser passes through a Berek compensator (Model 5540, New Focus) adjusted such that the excitation light reaching the objective lens is circularly polarized (verified as <2% variation in transmitted power versus angle of an analyzer set after the dichroic and before the objective lens). An Olympus UMPLFL20XW water-immersion lens (20 $\times$ , 0.5 NA) is used to focus excitation light and capture backward propagating SHG signal. After passing through the objective, the signal is separated from the excitation beam using a 670-nm short-pass dichroic mirror, filtered using a 405-nm filter (HQ405/30m-2P, Chroma, Rockingham, Vermont), and collected by a photomultiplier tube (Hamamatsu HC125-02). In the forward direction an Olympus 0.9 NA optical condenser was used to collect the signal, reflected by a 475-nm long-pass dichroic mirror (475 DCSX, Chroma, Rockingham, Vermont) in order to remove excess excitation light, filtered by a 405-nm filter (HQ405/30m-2P, Chroma, Rockingham, VT) and captured by photomultiplier tube (Hamamatsu HC125-02).

### 2.4 F/B Analysis

Forward and backward images were simultaneously collected as a stack of 11 images spaced 3  $\mu$ m apart, with a 660- $\mu$ m field of view from unstained samples of IDC, DCIS, ILC, LCIS, and healthy breast tissue. One stack was made from the geometric center of each TMA sample. For the non-TMA samples, the image field in an unstained section was chosen based upon imaging of an adjacent H&E stained section to identify the

center of the visible tumor structure. Image analysis was conducted in with ImageJ Software.<sup>33</sup> Each stack was maximum intensity projected, serving as an "autofocus" for the effectively single layer of collagen that exists in these 5- $\mu$ m sections and producing a single-image pair for each sample. Projected images were background subtracted using a maximum intensity projection of an 11 image scan taken with a closed shutter. Day to day variations in optical alignments were accounted for by imaging one tissue sample (not included in the data pool) each day as a standard SHG sample and determining a normalization factor for each detector pathway that rendered the signal from that standard sample constant over time. For each image, a common threshold was applied to all images taken in that imaging session and chosen by a blinded observer to distinguish collagen pixels from background pixels. The threshold of the backward-collected image was then used to create a mask, in which all of the pixels above threshold were set to 1, and all of the pixels below the threshold were zero. That mask was then used to exclude background (i.e., non-fiber) pixels from consideration and the average pixel value of fiber (i.e., non-background) pixels was calculated from an F/B ratio image. Due to the small sample thickness (5  $\mu$ m), we assume that the measured F/B ratio is due solely to the original ratio of forward-emitted and backward-emitted SHG and is not significantly affected by subsequent backscattering of either component.<sup>30,31</sup> Note that unless otherwise specified (see Sec. 2.5) all quantification of SHG F/B is performed in unstained specimens.

### 2.5 Analysis of Spatial Heterogeneity of F/B

H&E stained sections of DCIS, LCIS, and healthy breast were imaged with a CCD camera (Olympus, SP-350) through the microscope eyepiece and an SHG F/B image of the same approximate field of view was generated as described above. Based upon the tissue H&E staining patterns imaged by the CCD camera, in the SHG images regions of interest within 50  $\mu$ m of ductal or lobular structures were outlined with ImageJ, producing at the same time regions of interest *greater* than 50  $\mu$ m from ductal or lobular structures. The average F/B ratio within those regions of interest (per-ductal, peri-lobular, or distant from either feature) was then calculated as described in the previous section.

## 2.6 Effects of H&E Staining on SHG F/B

In DCIS, LCIS, and healthy breast samples, pairs of adjacent 5- $\mu\text{m}$  sections were cut and mounted on glass slides, and one of the pair was H&E stained. SHG F/B of each adjacent section were analyzed as described in F/B Analysis above and compared to determine the effects of H&E staining on SHG F/B. In addition to quantifying the effects of staining on SHG F/B averaged over the entire 600- $\mu\text{m}$  field of view, peri-ductal regions, peri-lobular regions, or regions distant from either feature were independently analyzed as described in Analysis of Spatial Heterogeneity of F/B above.

## 2.7 Statistics

Statistical analysis was performed using Prism 5 software (GraphPad, La Jolla, California). Statistically significant data was defined as a  $p$ -value less than 0.05. Comparisons of two groups were analyzed using unpaired student's  $t$ -tests. If the  $F$ -test for this data returned a value  $<0.05$ , a Mann-Whitney non-parametric  $t$ -test was used. For grouped analysis a one-way ANOVA was used with a Newman-Keuls multiple comparison post-hoc test to determine the difference between groups. If the Barrett's test for equal variance results in a  $p$ -value less than 0.05, a non-parametric Kruskal-Wallis test with a Dunn's post-hoc test was performed.

## 3 Results

Figure 1 shows images of backscattered SHG signal and F/B ratio as compared with tissue organization apparent in H&E

staining, taken from the same section of healthy and tumor samples. These example SHG images demonstrate some typical collagen morphological changes that occur through the progression of ductal and lobular carcinoma, including changes in density, length, and organization of fibrillar collagen as seen in, for example, the "healthy" SHG image, which has an appearance of many wavy fibers matted together, versus the "IDC" image where the collagen appears to form sparser, longer, and straighter fibers.

Changes in SHG F/B ratio were first analyzed in the progression from healthy tissue to DCIS to IDC, as shown in Fig. 2(a). The DCIS samples did not differ significantly from the healthy samples, but both the healthy and the DCIS samples had a significantly higher F/B ratio than the IDC samples. While IDC samples are typically homogenous fields of invasive cells within tumor matrix, DCIS and healthy tissue exhibit a heterogeneous structure with obvious clusters of ductal and lobular structures separated by regions of relatively cell free matrix (Fig. 1). This leaves open the possibility that SHG F/B in DCIS is indeed changing, but that these changes are confined to the immediate vicinity of ductal structures and are missed in our wide-area ( $660 \times 660 \mu\text{m}$ ) averaging. In H&E stained samples, we found no statistically significant difference between F/B in periductal regions (within 50  $\mu\text{m}$  of ductal structures) versus perilobular regions or versus regions distant from ducts or lobes (greater than 50  $\mu\text{m}$  from ductal or lobular structures) in DCIS or in healthy tissue ( $n = 5$  patients each,  $p > 0.05$ , data not shown). To determine if this use of H&E staining affects SHG F/B, we evaluated F/B in adjacent tissue sections (one stained, one

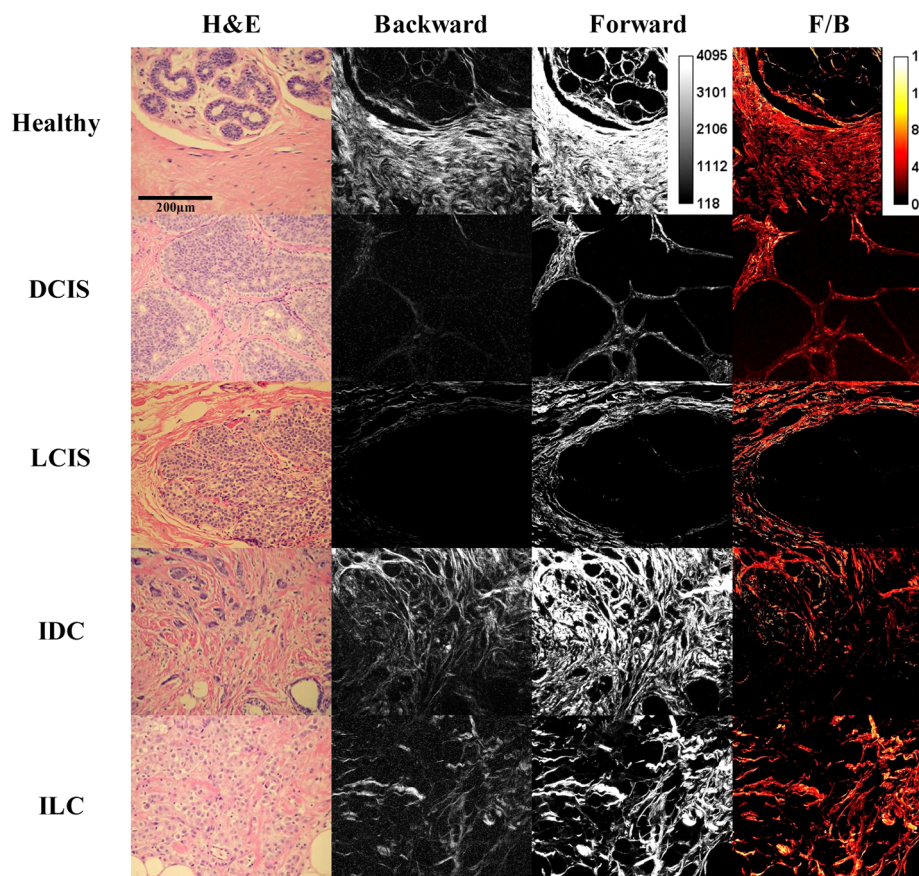


**Fig. 1** Sample images of five types of tissue analyzed in this study, from top to bottom: healthy tissue, DCIS, LCIS, IDC, and ILC. The left column shows H&E staining, the middle columns show backward- and forward-scattered SHG, and the right column shows the F/B ratio image.

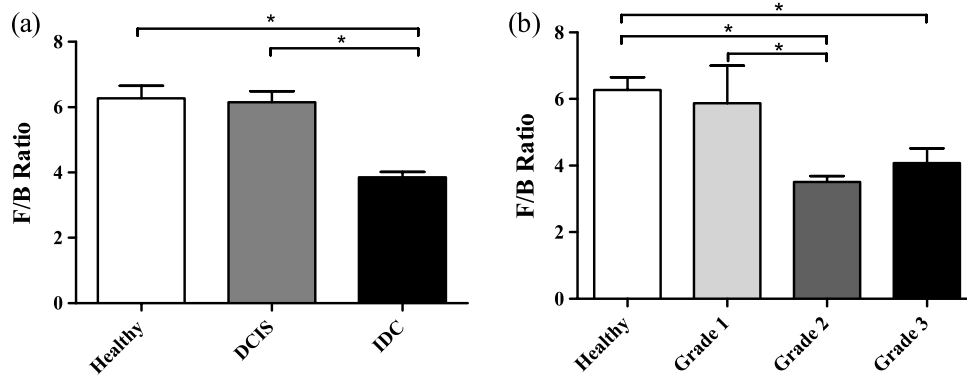


**Fig. 2** IDC F/B ratio throughout (a) ductal carcinoma progression and (b) increasing grade, or decreasing tumor cell differentiation. (a) These results show no difference between DCIS ( $n = 20$ ) and healthy tissue ( $n = 37$ ), but there was a significant difference between IDC ( $n = 147$ ) and the two other tissue types. (b) As the IDC tumor progresses into higher grades the F/B ratio differs significantly from healthy tissue. Specifically, there is no difference between healthy and Grade 1 IDC ( $n = 8$ ), but both of these are significantly higher than Grade 2 IDC ( $n = 88$ ). Grade 3 ( $n = 15$ ) is significantly lower than healthy tissue. Error bars represent standard error and \* signifies a significant difference between the pair indicated by brackets.

unstained) and found no statistically significant difference in F/B caused by staining in periductal regions, perilobular regions, nor regions distant from ducts or lobes, in either DCIS or in healthy tissue ( $N = 5$  patients each,  $p > 0.05$ , data not shown).

The fact that SHG F/B in IDC was statistically significantly different from healthy tissue led to the question of whether all IDC tumors are immediately differentiable from healthy tissue or if there is an evolution of the fibrillar collagen microstructural properties that become significantly different at a specific grade or stage. Looking first at tumor grade, which signifies how different the tumor cells appear in comparison to healthy cells, it was apparent that Grade 1 tumors were not significantly different from healthy tissue [Fig. 2(b)]. As this tumor type progressed to Grade 2, it developed a significantly lower F/B ratio which remained at approximately this level for Grade 3 tumors as well.

Invasive tumor staging is determined by the TMN system, which is dependent on three different properties of the tumor, including its size (T), extent of LN metastatic events (N), and metastasis to sites other than LNs (M) (as described in Sec. 2.2). The F/B ratio was measured as a function of these three categories to determine the change of collagen microstructural properties throughout different stages of IDC tumor development. The F/B ratio was significantly lower in all stages of T-progression than in healthy tissue, but there were no differences or noticeable trends throughout the groups [Fig. 3(a)].

One of the more interesting questions regarding the use of SHG analysis to study breast cancer progression is how the microstructural properties of fibrillar collagen in the primary tumor (as indicated by SHG F/B) relate to the potential of the tumor to metastasize. Figure 3(b) shows that the binary M-status did not have a significant effect on the F/B ratio of IDC tumors. However, this M-status is coarse, in that it divides tumors into only two categories, those with and without known metastases to distant organs other than the lymph nodes. It is possible to further test the relationship between SHG F/B and metastatic potential of a tumor by looking at N-stage progression, which increases through four classification stages dependent upon the severity of LN involvement in metastatic events (as described in Sec. 2.2). This gives a more detailed description than M-status, because metastatic events in the

LN are more commonly detected than in other secondary sites, and the scale of progression is more finely detailed than the simple binary grading of the M-status. Figure 3(c) shows that between healthy tissue and IDC tumors that are not metastatic to the LNs (N0) or minimally metastatic breast tumors (N1, N2), there is a significant decrease in the F/B ratio of SHG<sup>+</sup> pixels relative to healthy tissue. However, in the N3 stage F/B is not different from healthy tissue. We then pooled the N0, N1, and N2 data and compared this pooled set to the N3 data. This allows us to compare SHG F/B for highly metastatic IDC tumors, which have either greater than 10 axillary events with at least one event greater than 2 mm, infraclavicular LN metastases, or clinically detected internal mammary and axillary LN metastases (i.e., N3), versus those less metastatic IDC tumors, which do not have any of those properties (i.e., N0, N1, or N2). This reveals a statistically significant difference between the two groups [Fig. 3(d)].

In order to gain further understanding of breast cancer progression, the same analysis was run on lobular carcinoma samples, to understand how SHG F/B evolves after initiation of the tumor in a different location. ILC showed a significant decrease in F/B ratio compared with healthy tissue, but was not significantly different from the ratio of IDC [Fig. 4(a)]. In contrast to the behavior of F/B in ductal carcinoma, LCIS showed a significant decrease in F/B ratio relative to healthy breast, with no significant difference between LCIS and ILC [Fig. 4(b)]. In a similar fashion to IDC and DCIS discussed above, ILC samples are typically homogenous fields of invasive cells within tumor matrix, while LCIS and healthy tissue exhibit a heterogeneous structure with obvious clusters of ductal and lobular structures separated by regions of relatively cell free matrix (Fig. 1). This leaves open the possibility that SHG F/B in LCIS is indeed changing, but that these changes are confined to the immediate vicinity of lobular structures and are missed in our wide-area ( $660 \times 660 \mu\text{m}$ ) averaging. In H&E stained samples, we found no statistically significant difference between F/B in perilobular regions (within  $50 \mu\text{m}$  of lobular structures) versus periductal regions or versus regions distant from ducts or lobes (greater than  $50 \mu\text{m}$  from ductal or lobular structures) in LCIS or in healthy tissue ( $n = 5$  patients each,  $p > 0.05$ , data not shown). To determine if this use of H&E staining affects SHG F/B we evaluated F/B in adjacent tissue sections (one stained, one unstained) and found no statistically significant difference in F/B

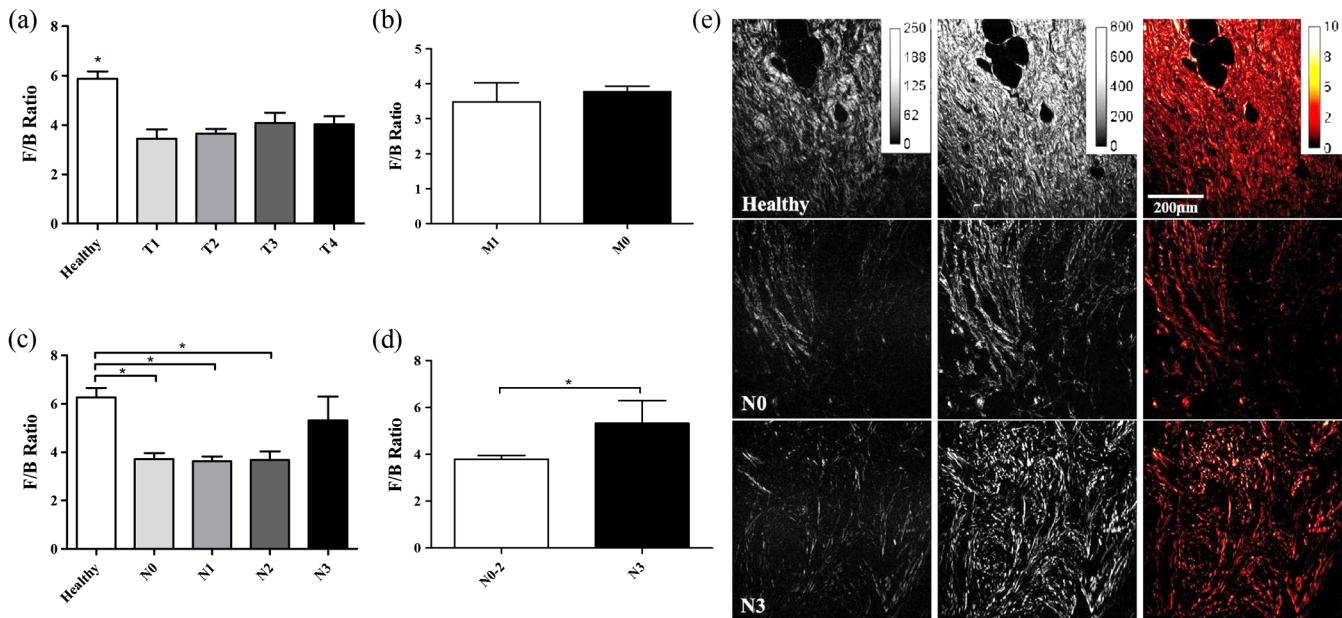


**Fig. 3** IDC F/B ratio as a function of (a) *T*-stage, (b) *M*-status, and (c) and (d) *N*-stage. (a) Healthy tissue ( $n = 37$ ) was significantly higher than all *T* stages (sample sizes of *T*1-*T*4 were  $n = 12$ ,  $n = 97$ ,  $n = 24$ , and  $n = 11$ , respectively). (b) The average F/B ratio of *M*1 tumors ( $n = 9$ ) was not significantly different than the *M*0 tumors ( $n = 51$ ), *N*1 ( $n = 52$ ), and *N*2 ( $n = 29$ ), but was not significantly different than *N*3 ( $n = 9$ ). (c) The F/B of healthy tissue was significantly greater than that of *N*0 ( $n = 51$ ), *N*1 ( $n = 52$ ), and *N*2 ( $n = 29$ ), but was not significantly different than *N*3 ( $n = 9$ ). (d) F/B of *N*3 tumors, which have 10 or greater lymph-node metastatic events, is significantly greater than tumors with less lymph-node involvement, i.e., *N*0 to *N*2 tumors. (e) From left to right are the backward-scattered SHG image, forward-scattered SHG image, and the F/B ratio image for healthy tissue (top), *N*0 IDC (middle), and *N*3 IDC (bottom). Error bars represent standard error and \* signifies a significant difference between the pair indicated by brackets. An \* directly on a single bar, without a bracket, represents a significant difference from all other groups being compared.

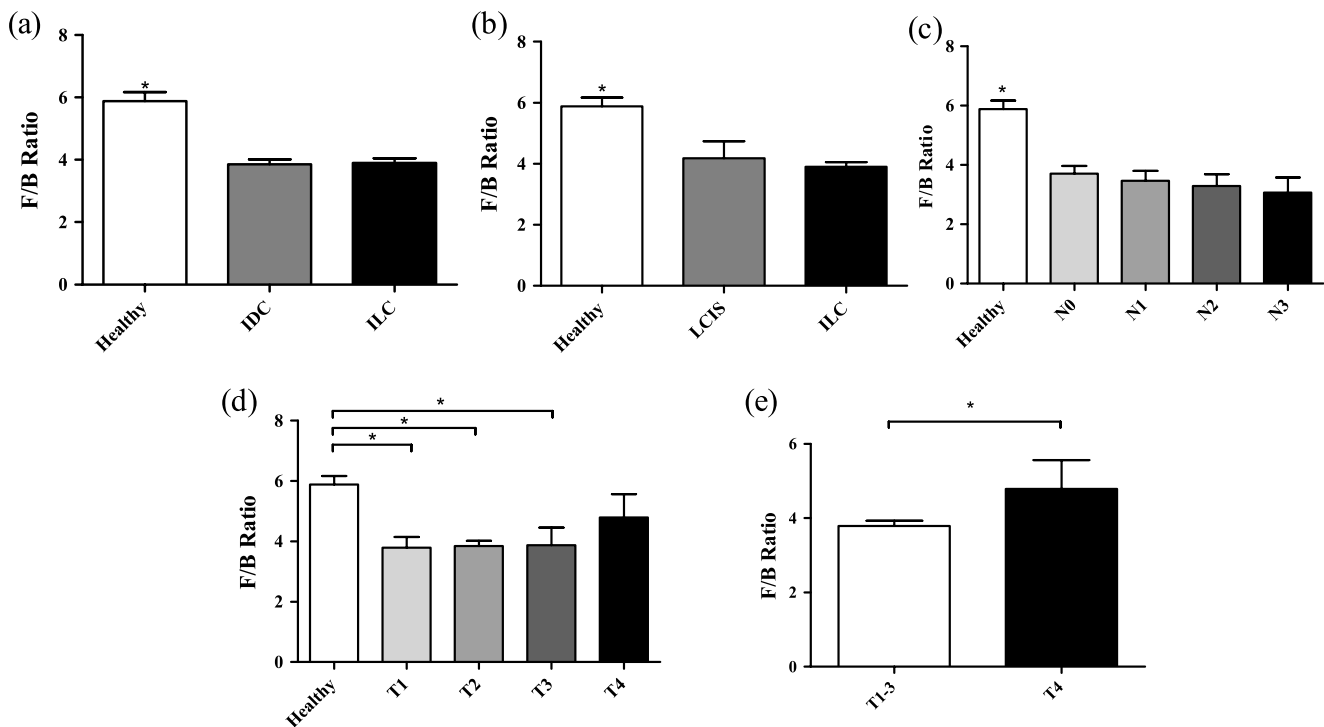


**Fig. 4** F/B ratio of (a) ILC, (b) LCIS, (c) ILC *N*-stage, and (d) and (e) ILC *T*-stage. (a) F/B ratio of ILC ( $n = 153$ ) is not significantly different than IDC ( $n = 145$ ), but are both significantly lower than healthy breast tissue ( $n = 37$ ). (b) LCIS ( $n = 8$ ) and ILC are both significantly lower than healthy breast tissue. (c) All *N*-stage ILC tumors are significantly lower than healthy tissue ( $n = 49$ ,  $n = 29$ ,  $n = 11$ , and  $n = 4$ , for *N*0 to *N*3, respectively). (d) *T*1 ( $n = 29$ ), *T*2 ( $n = 96$ ), and *T*3 ( $n = 12$ ) ILC tumors all had significantly lower F/B ratios than healthy tissue, but *T*4 ( $n = 10$ ) tumors were not significantly different than healthy tissue. (e) *T*4 ILC tumors were significantly higher than pooled *T*1-3 ILC tumors. Error bars represent standard error, and \* signifies a significant difference between the pair indicated by brackets. An \* directly on a single bar, without a bracket, represents a significant difference from all other groups being compared.

caused by staining in perilobular regions, periductal regions, nor regions distant from ducts or lobes, in either LCIS or in healthy tissue ( $n = 5$  patients each,  $p > 0.05$ , data not shown).

$N$ -status analysis of ILC samples showed that there was a significant decrease in the F/B ratio for all  $N$  groups relative to healthy tissue, with no significant difference between any of the stages studied [Fig. 4(c)], similar to the trend of IDC for groups  $N0$ - $N2$  but unlike the behavior of IDC  $N3$  tumors. Analysis of the effects of  $T$ -status on the fibrillar collagen showed that the F/B ratio decreased significantly between healthy tissue and  $T1$ ,  $T2$ , and  $T3$ , stages while  $T4$  is no longer differentiable from healthy tissue [Fig. 4(d)].  $T4$  is characterized by the interaction of *any* size tumors with either the chest wall or the skin, hence we pooled the other  $T$  stages of tumor (producing a group of any sized tumor that does not interact with the chest wall nor the skin) and compare the pooled group to the  $T4$  tumors, demonstrating a significant difference in the F/B ratio [Fig. 4(e)] between these two groups.

## 4 Discussion

We analyzed SHG F/B images throughout breast tumor progression in order to understand how this optical signature, which is influenced by fibrillar collagen microstructural properties, evolved alongside the tumor size, cell morphology, and metastatic changes that determine the grade and stage of the tumor. This provided several insights into the biology of ductal and lobular carcinoma.

### 4.1 Biology of Ductal Carcinoma

The changes in SHG F/B in Fig. 2(a) demonstrate that there is no significant alteration in fibrillar collagen microstructural properties between healthy breast tissue and DCIS, but that there is an alteration in them as the tumor progresses from an *in situ* to an invasive carcinoma. This is consistent with the fact that the majority of SHG<sup>+</sup> collagen fibers in healthy tissue are surrounding the ducts, so as the tumor cells exclusively fill in the ducts in DCIS, the surrounding collagen microstructural properties remain relatively unaffected. It is only when the tumor cells begin to invade the breast tissue outside of the duct that they induce changes in microstructural properties of the surrounding fibrillar collagen, as observed in the statistically significant difference between SHG F/B of IDC and healthy breast tissue [Fig. 2(a)].

Taking a closer look at this phenomenon, we examined whether invasion through the basement membrane into the surrounding tissue (i.e., the transition from DCIS to IDC) causes an immediate change in the F/B ratio by comparing SHG F/B to the grade of the IDC tumor [Fig. 2(b)]. Our results showed that in Grade 1 IDC the F/B ratio is still not significantly different from the DCIS tissue nor the healthy tissue, but as IDC progresses to a Grade 2 or 3 tumor, the SHG F/B ratio becomes significantly different. This suggests that the overall fibrillar collagen microstructural properties as determined by the F/B ratio are constantly evolving away from the healthy state as the IDC tumor cells become less differentiated.

Regarding the changes in primary tumor F/B seen throughout IDC tumor staging, there is interestingly no difference between the IDC samples that are at different primary tumor sizes ( $T$  stage), although they are all different than the healthy tissue cohort. Presumably, the transition from healthy to tumor SHG F/B occurs when tumors are small enough to not be included in our cohorts of tumor samples, which means that it occurs when

the tumor diameter is less than 1 mm. Once tumors are greater than 1 mm and hence large enough to be included in the  $T1$ - $T4$  grading scheme, the size of the primary tumor does not influence collagen microstructural properties as quantified by SHG F/B. Combined with the fact that F/B of Grade 1 IDC does *not* differ significantly from healthy tissue, this suggests that during early tumor growth and progression, there is a complex interplay between tumor size and grade, whereby small high-grade tumors may produce a more significantly altered matrix than larger low-grade ones.

As tissues progress from healthy to  $N0$  IDC (IDC with no LN involvement), the SHG F/B ratio statistically significantly decreases, and remains low as tumors progress to  $N1$  (small metastatic events or  $\leq 3$  axillary events) and  $N2$  (4–9 axillary events or clinically detected internal mammary LN metastases). Interestingly, as tumors progress to  $N3$  stage ( $>10$  events, further reaching LN metastases, or metastases to both internal mammary and axillary LN) SHG F/B becomes indistinguishable from healthy F/B [Fig. 3(c)] and is markedly different from the pooled group of other IDC tumors [Fig. 3(d)]. This evolution of SHG F/B suggests two intriguing possibilities. The first is based upon the view that  $N$ -stage progression is a chronological progression, with a single IDC advancing from having no LN metastases, through the subsequent  $N$  stages, and ending as an IDC with distant LN metastases. From that perspective, this data demonstrates that during tumor progression fibrillar collagen microstructural properties evolve in ways that affect SHG F/B and raises the possibility that this evolution may influence efficient travel of metastatic tumor cells to distant LNs. After the initial evolution of collagen microstructural properties from normal to abnormal as the tissue progresses from healthy to an  $N0$  tumor, there is a subsequent “normalization” back to the microstructural properties of healthy fibrillar collagen (as quantified by F/B) that may facilitate distant metastasis and lead to the  $N3$  highly metastatic case. Alternatively, these matrix changes may not represent an evolution of individual tumors in time, but suggest instead that those tumors that do not undergo an initial decrease in SHG F/B as the tissue first progresses from healthy to cancerous and maintains a high F/B, may be more likely to produce extensive distant metastases. Although the F/B ratio reveals that there is a similarity in the collagen microstructural properties between the  $N3$  tumor and healthy tissue, inspection of SHG images of healthy and  $N3$  samples reveal that these similarities do not extend to the overall morphology of the fibers, as these are noticeably different between the two tissue states as shown in Fig. 4(d).

In traditional  $M$  staging, IDC tumors are divided into  $M0$  (no known metastases to distant non-lymph-node organs) and  $M1$  (any number of metastases to distant non-lymph-node organs). For IDC tumors, there is no relationship between SHG F/B and  $M$  status group [Fig. 3(b)]. This suggests either that there is no relationship between fibrillar collagen microstructural properties and the ability of the IDC to metastasize to different (non-LN) organs, or that the act of pooling all numbers of metastases to any non-LN organs into the single category of “ $M1$ ” has hidden any subtle differences such as those that were evident in IDC when classified according to the more finely divided  $N$  stage classification scheme.

### 4.2 Biology of Lobular Carcinoma

Like IDC, ILC causes a change in the fibrillar collagen microstructural properties in breast tissue, as indicated by a decrease

in the F/B ratio relative to healthy tissue [Fig. 4(a)]. However, LCIS F/B is significantly different from healthy tissue F/B whereas DCIS is not [Fig. 4(b)]. This difference in matrix alterations is consistent with the significant difference in behavior of the two diseases. Unlike DCIS, which is categorized as cancer and if left untreated is likely to progress to IDC,<sup>34</sup> LCIS is described as a development of abnormal cells, which is not believed to progress to ILC (although it does correlate with increased likelihood of the patient developing ILC or IDC later in life).<sup>3</sup>

In contrast to IDC, the stage of LN involvement [Fig. 4(c)] has no effect on the F/B ratio of ILC, and all *N* stages are statistically different from healthy tissue. The stable F/B ratio throughout increasing LN involvement could result from the ILC's characteristic lack of a strong inflammatory response after penetrating the basement membrane,<sup>35</sup> a response that would otherwise aid in the remodeling of the stromal collagen through recruitment of fibroblasts and macrophages.<sup>13,14</sup> In ILC there is a change in SHG F/B with tumor *T* stage, specifically a loss of F/B difference relative to healthy tissue that occurs in the *T4* stage of tumor progression [Fig. 4(c) and 4(d)], which is when the tumor interacts with tissues surrounding the breast, such as chest and skin. The marked difference between behavior of IDC and ILC at this stage contrasts with the close quantitative similarity of F/B values between the tumor types at earlier *T* stages [compare Figs. 3(a) and 4(d)]. This suggests that the mechanisms by which ILC and IDC recruit stromal cells to produce the collagenous matrix is subtly different, a difference that only becomes evident once the source of stromal cells shifts from breast tissue to the chest wall and/or the skin.

## 5 Conclusion

This study has shown a series of changes in collagen microstructural properties, as evaluated with SHG F/B, that occur throughout ductal and lobular carcinoma progression, including those that accompany growth, metastasis and changes in tissue morphology. SHG F/B has revealed a surprisingly complex evolution of the matrix with grade and *T*, *N*, and *M* stage with perhaps the most interesting result being the fact that IDC tumors with the most "normal" F/B values have the largest number of distant LN metastases. This offers the possibility that either developing breast tumors undergo a "normalization" of collagen microstructural properties (but not macroscopic morphology) that correlates with enhanced distant metastases, or that those tissues that retain their healthy collagen microstructural properties upon transition to IDC are most likely to produce significant numbers of distant metastases.

## Acknowledgments

This work was funded by Department of Defense Breast Cancer Research Program (BCRP) Era of Hope Scholar Research Award W81XWH-09-1-0405 and NIH Director's New Innovator Award 1DP2OD006501. The authors would like to thank Drs. Seth Perry, Kelley Madden, and Ania Majewska for helpful discussions.

## References

1. S. Bianchi and V. Vezzosi, "Microinvasive carcinoma of the breast," *Pathol. Oncol. Res.* **14**(2), 105–111 (2008).
2. G. D. Leonard and S. M. Swain, "Ductal carcinoma *in situ*, complexities and challenges," *J. Natl. Canc. Inst.* **96**(12), 906–920 (2004).
3. R. V. Hutter et al., "Clinical and pathologic correlation with mammographic findings in lobular carcinoma *in situ*," *Cancer* **23**(4), 826–839 (1969).
4. E. R. Fisher et al., "The pathology of invasive breast cancer. A syllabus derived from findings of the National Surgical Adjuvant Breast Project (protocol no. 4)," *Cancer* **36**(1), 1–85 (1975).
5. S. Koscielny et al., "Breast cancer: relationship between the size of the primary tumour and the probability of metastatic dissemination," *Br. J. Canc.* **49**(6), 709–715 (1984).
6. C. L. Carter, C. Allen, and D. E. Henson, "Relation of tumor size, lymph node status, and survival in 24,740 breast cancer cases," *Cancer* **63**(1), 181–187 (1989).
7. C. W. Elston and I. O. Ellis, "Pathological prognostic factors in breast cancer. I. The value of histological grade in breast cancer: experience from a large study with long-term follow-up," *Histopathology* **41**(3A), 154–161 (2002).
8. M. P. Look et al., "Pooled analysis of prognostic impact of urokinase-type plasminogen activator and its inhibitor PAI-1 in 8377 breast cancer patients," *J. Natl. Canc. Inst.* **94**(2), 116–128 (2002).
9. J. A. Foekens et al., "The urokinase system of plasminogen activation and prognosis in 2780 breast cancer patients," *Canc. Res.* **60**(3), 636–643 (2000).
10. B. Weigelt, J. L. Peterse, and L. J. van't Veer, "Breast cancer metastasis: markers and models," *Nat. Rev. Canc.* **5**, 591–602 (2005).
11. M. Sund and R. Kalluri, "Tumor stroma derived biomarkers in cancer," *Canc. Metast. Rev.* **28**(1–2), 177–183 (2009).
12. G. P. Gupta and J. Massagué, "Cancer metastasis: building a framework," *Cell* **127**(4), 679–695 (2006).
13. R. Kalluri and M. Zeisberg, "Fibroblasts in cancer," *Nat. Rev. Canc.* **6**(5), 392–401 (2006).
14. J. W. Pollard, "Macrophages define the invasive microenvironment in breast cancer," *J. Leukoc. Biol.* **84**(3), 623–630 (2008).
15. R. Kalluri, "Basement membranes: structure, assembly and role in tumour angiogenesis," *Nat. Rev. Canc.* **3**(6), 422–433 (2003).
16. P. P. Provenzano et al., "Collagen reorganization at the tumor-stromal interface facilitates local invasion," *BMC Med.* **4**(1), 38–53 (2006).
17. J. Condeelis and J. E. Segall, "Intravital imaging of cell movement in tumours," *Nat. Rev. Canc.* **3**(12), 921–930 (2003).
18. R. Lacombe et al., "Phase matching considerations in second harmonic generation from tissues: effects on emission directionality, conversion efficiency and observed morphology," *Optic. Comm.* **281**(7), 1823–1832 (2008).
19. J. Mertz and L. Moreaux, "Second-harmonic generation by focused excitation of inhomogeneously distributed scatterers," *Optic. Comm.* **196**(1–6), 325–330 (2001).
20. X. Han et al., "Second harmonic properties of tumor collagen: determining the structural relationship between reactive stroma and healthy stroma," *Optic. Express* **16**(3), 1846–1859 (2008).
21. G. Fenhalls et al., "Breast tumour cell-induced down-regulation of type I collagen mRNA in fibroblasts," *Br. J. Canc.* **81**(7), 1142–1149 (1999).
22. G. Falzon, S. Pearson, and R. Murison, "Analysis of collagen fibre shape changes in breast cancer," *Phys. Med. Biol.* **53**(23), 6641–6652 (2008).
23. M. W. Conklin et al., "Aligned collagen is a prognostic signature for survival in human breast carcinoma," *Am. J. Pathol.* **178**(3), 1221–1232 (2011).
24. S. P. Tai et al., "Optical biopsy of fixed human skin with backward-collected optical harmonics signals," *Optic. Express* **13**(20), 8231–8242 (2005).
25. R. M. Williams et al., "Strategies for high-resolution imaging of epithelial ovarian cancer by laparoscopic nonlinear microscopy," *Trans. Oncol.* **3**(3), 181–194 (2010).
26. N. D. Kirkpatrick, M. A. Brewer, and U. Utzinger, "Endogenous optical biomarkers of ovarian cancer evaluated with multiphoton microscopy," *Canc. Epidemiol. Biomark. Prev.* **16**(10), 2048–2057 (2007).
27. W. Zheng et al., "Diagnostic value of nonlinear optical signals from collagen matrix in the detection of epithelial precancer," *Optic. Lett.* **36**(18), 3620–3622 (2011).
28. S. Zhuo et al., "Quantitatively linking collagen alteration and epithelial tumor progression by second harmonic generation microscopy," *Appl. Phys. Lett.* **96**(21), 213704 (2010).

29. O. Nadiarnykh et al., "Alterations of the extracellular matrix in ovarian cancer studied by second harmonic generation imaging microscopy," *BMC Canc.* **10**(1), 94–107 (2010).
30. H. L. Fu et al., "A low-cost, portable, and quantitative spectral imaging system for application to biological tissues," *Optics Express* **18**(12), 12630–12645 (2010).
31. O. Nadiarnykh et al., "Second harmonic generation imaging microscopy studies of osteogenesis imperfecta," *J. Bio. Optic.* **12**(5), 051805 (2007).
32. S. B. Edge, D. R. Byrd, and C. C. Compton, *AJCC Cancer Staging Manual*, 7th ed., Springer, Chicago, IL (2009).
33. C. A. Schneider, W. S. Rasband, and K. W. Eliceiri, "NIH image to ImageJ: 25 years of image analysis," *Nat. Methods* **9**, 671–675 (2012).
34. E. S. Hwang et al., "Patterns of chromosomal alterations in breast ductal carcinoma *in situ*," *Clin. Canc. Res.* **10**(15), 5160–5167 (2004).
35. N. Wasif et al., "Invasive lobular vs. ductal breast cancer: a stage-matched comparison of outcomes," *Ann. Surg. Oncol.* **17**(7), 1862–1869 (2010).

RESEARCH ARTICLE

Open Access



# Using second harmonic generation to predict patient outcome in solid tumors

K. Burke<sup>1</sup>, M. Smid<sup>2</sup>, R. P. Dawes<sup>3</sup>, M. A. Timmermans<sup>2</sup>, P. Salzman<sup>4</sup>, C. H. M. van Deurzen<sup>5</sup>, David G. Beer<sup>6</sup>, J. A. Foekens<sup>2</sup> and E. Brown<sup>1,7\*</sup>

## Abstract

**Background:** Over-treatment of estrogen receptor positive (ER+), lymph node-negative (LNN) breast cancer patients with chemotherapy is a pressing clinical problem that can be addressed by improving techniques to predict tumor metastatic potential. Here we demonstrate that analysis of second harmonic generation (SHG) emission direction in primary tumor biopsies can provide prognostic information about the metastatic outcome of ER+, LNN breast cancer, as well as stage 1 colorectal adenocarcinoma.

**Methods:** SHG is an optical signal produced by fibrillar collagen. The ratio of the forward-to-backward emitted SHG signals (F/B) is sensitive to changes in structure of individual collagen fibers. F/B from excised primary tumor tissue was measured in a retrospective study of LNN breast cancer patients who had received no adjuvant systemic therapy and related to metastasis-free survival (MFS) and overall survival (OS) rates. In addition, F/B was studied for its association with the length of progression-free survival (PFS) in a subgroup of ER+ patients who received tamoxifen as first-line treatment for recurrent disease, and for its relation with OS in stage I colorectal and stage 1 lung adenocarcinoma patients.

**Results:** In 125 ER+, but not in 96 ER-negative (ER-), LNN breast cancer patients an increased F/B was significantly associated with a favorable MFS and OS (log rank trend for MFS:  $p = 0.004$  and for OS:  $p = 0.03$ ). On the other hand, an increased F/B was associated with shorter PFS in 60 ER+ recurrent breast cancer patients treated with tamoxifen (log rank trend  $p = 0.02$ ). In stage I colorectal adenocarcinoma, an increased F/B was significantly related to poor OS (log rank trend  $p = 0.03$ ), however this relationship was not statistically significant in stage I lung adenocarcinoma.

**Conclusion:** Within ER+, LNN breast cancer specimens the F/B can stratify patients based upon their potential for tumor aggressiveness. This offers a “matrix-focused” method to predict metastatic outcome that is complementary to genomic “cell-focused” methods. In combination, this and other methods may contribute to improved metastatic prediction, and hence may help to reduce patient over-treatment.

**Keywords:** Cancer, Collagen, Second harmonic generation, F/B ratio, Prognosis

## Background

Breast cancer is the leading cause of cancer related mortality in women [1], predominantly due to metastasis [2]. After surgical resection of the primary tumor, the clinician must choose adjuvant therapy based upon the metastatic potential. Due to their aggressive biological behavior, ER-negative (ER-) tumors are treated with chemotherapy in

the majority of patients. However, in ER+ patients whose cancer has not yet spread to the lymph nodes (LNN), the choice between hormonal therapy alone, or in combination with chemotherapy, is more uncertain. Following current standard of care, it is estimated that 40 % of these patients will be “over-treated”, receiving chemotherapy even though they would *not* go on to develop metastatic disease, causing many to endure the emotional distress and severe side effects accompanying chemotherapy [3]. As such, there is a pressing clinical need to accurately predict which ER+, LNN patients have a lower metastatic potential and thus can be spared from over-treatment.

\* Correspondence: Edward\_Brown@URMC.Rochester.edu

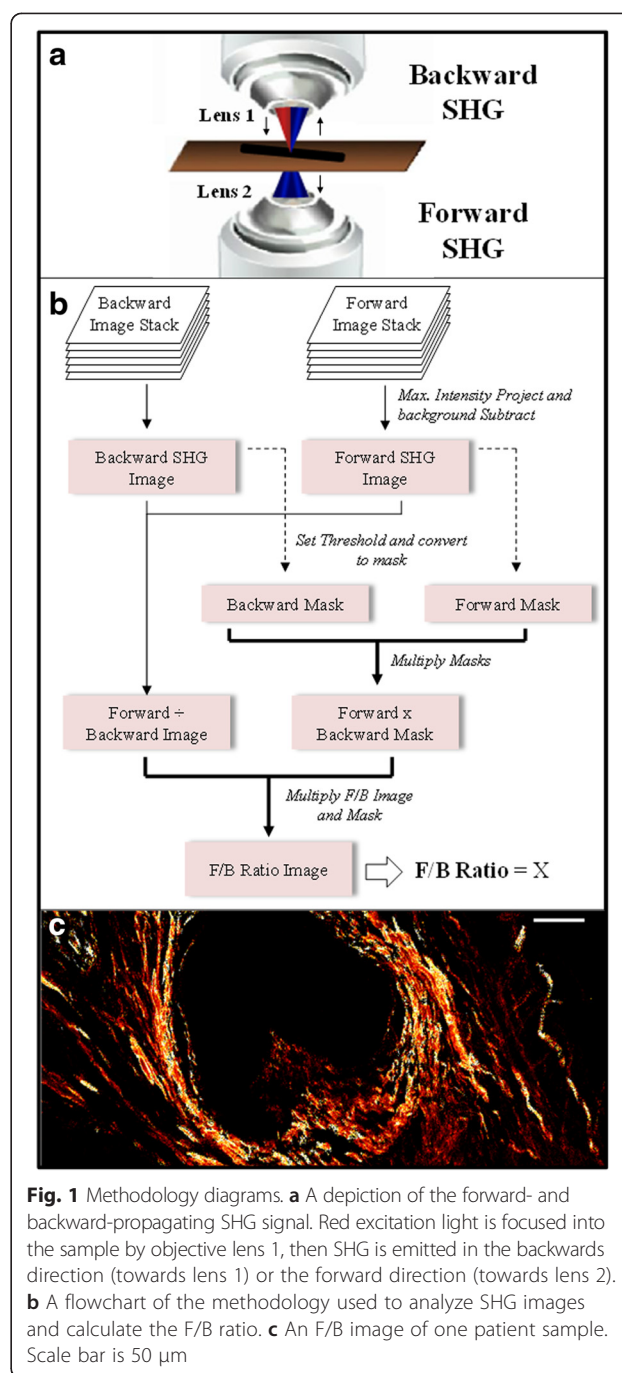
<sup>1</sup>Department of Biomedical Engineering, University of Rochester, 207 Robert B. Goergen Hall, Box 270168, Rochester, NY 14627, USA

<sup>7</sup>Department of Neurobiology and Anatomy, University of Rochester, 601 Elmwood Ave, Rochester, NY 14642, USA

Full list of author information is available at the end of the article

Metastatic potential and treatment response can be predicted to varying degrees of accuracy using traditional histopathology, gene expression measurements [4–8], immunohistochemistry of gene related protein products [9, 10], mass-spectrometry based protein levels [11], image analysis of cell-stromal interactions within the tumor [12], and various other techniques. These techniques provide insights into neoplastic cell function, however, implicit in Steven Paget’s “Seed and Soil” hypothesis is the idea that metastasis involves interactions between tumor cells and their microenvironment [13]. Therefore, we have explored the possibility that the tumor extracellular matrix, specifically the structure of individual collagen fibers as quantified with second harmonic generation microscopy, may provide additional information on tumor metastatic ability.

SHG is an intrinsic optical signal in which two incoming photons scatter off of material, producing one emission photon of half the incoming wavelength (Fig. 1). In tumors, SHG is generated by fibrillar collagen and is sensitive to the microscopic structure of the scattering material. Hence SHG emission directionality is sensitive to the diameter of the fibrils that are bundled into collagen fibers, as well as their spacing within the fiber, and the disorder in their packing [14–16]. The ratio of the forward-emitted to backward-emitted SHG (where “forward” is the direction of the incident excitation laser) is known as the F/B ratio and is sensitive to these structural properties of collagen fibers (Fig. 1) [14–16]. Note that these structural properties are intrinsic properties of individual fibers, as opposed to the overall orientation distribution, and its anisotropy, of ensembles of fibers [17]. We have shown that the average F/B of patient biopsy samples can differentiate healthy and breast tumor tissue, and changes with tumor grade and stage [18]. Since SHG is an intrinsic optical signature, measurements of F/B can be performed on typical pathology slides without additional contrast reagents. Furthermore, determination of the average F/B in a sample involves only a straightforward, automated application of pixel intensity analysis that does not require a trained observer. Therefore F/B analysis is an attractive candidate to apply to the prediction of tumor aggressiveness. Here we show that F/B can predict MFS in ER+, LNN breast cancer patients. Similar automated analysis can be performed on the larger scale spatial anisotropy of the orientation of the multiple collagen fibers in these SHG images by performing FFT image analysis [17], therefore for comparison we evaluated the predictive ability of that method as well and found no significant predictive relationship. Based upon its predictive ability in ER+ LNN patients we next investigated F/B in breast cancer patients treated with tamoxifen in a recurrent setting, and found that F/B is also associated with shorter PFS. We further show that the F/B was related to OS in stage I colorectal adenocarcinoma, pointing to the possibility that collagen structure,



as reported on by the F/B, and tumor metastatic capacity are linked in both tumor types.

## Methods

### Patient samples

Three-hundred and 44 human breast tumor samples were used from a collection at the Erasmus Medical Center (Rotterdam, Netherlands), which were primarily from one breast cancer genetic expression study [5] and later supplemented by 58 additional ER- samples [19]. These fresh-

frozen tissues were initially processed for microarray analysis, and were at a later stage processed for inclusion on a tissue-microarray (TMA) in cases where formalin-fixed paraffin embedded tissues were available as well. Initial sample acquisition was performed in the context of routine measurement of ER and PgR by biochemical assays. The studies on secondary use of archived tissues was approved in writing by the Medical Ethics Committee of the Erasmus Medical Center Rotterdam, The Netherlands (MEC 02.953) and was performed in accordance to the Code of Conduct (The Code for Proper Secondary Use of Human Tissue) of the Federation of Medical Scientific Societies in The Netherlands (<http://www.federa.org/codes-conduct>). Such secondary use did not require informed consent. All patients were LNN and had not been treated with neoadjuvant nor adjuvant therapy. This allowed for the study of the natural course of the disease and pure tumor aggressiveness, without potentially being confounded by systemic therapy. Some patients received radiation therapy, which has been shown not to affect distant metastases [20], our main focus of this study. The median patient age was 52 years. Follow-up data was recorded every 3 months for 2 years, every 6 months for years 3–5, and every 12 months afterwards. All samples were collected in triplicate as 5  $\mu\text{m}$  thick, 0.5 mm diameter core tissue samples and mounted as TMA slides, in which the uniform tumor presence was verified by hematoxylin and eosin (H&E) staining. Note that the presence of H&E staining does not affect the reported F/B (15), but that the effects of possible variation in time between excision from patient and fixation, as well as the effects of possible variation in time of fixation, are not known and those times are not recorded for the data sets studied here. Patients were tested for ER and progesterone receptor (PgR) status using immunohistochemistry, where the cutoff for receptor positivity was 10 % positive tumor cells. Bloom and Richardson grade and HER2 status data were assessed as described [21] and were available as well for the tissues included in the TMA. In total, 221 TMA-cases were eligible for analysis of F/B ratio, of which 125 were ER+ and 96 were ER-.

Stage I colorectal adenocarcinoma samples were purchased from Yale Tissue Pathology Services (YTMA-8, New Haven Connecticut). Samples were processed as a TMA with one 5  $\mu\text{m}$  thick, 0.5 mm diameter sample per patient, unstained, from within the primary tumor. Samples were collected from 1970–1982 with up to 31 years of follow-up data, resulting in a total of 69 stage I primary colorectal tumors. Lung adenocarcinoma samples were acquired at the University of Michigan, providing a total of 55 stage I lung adenocarcinoma cases [22]. Written subject consent and approval of the Institutional Review Board of the University of Michigan Medical School were obtained to collect specimens from patients undergoing

resection for cancer at the University of Michigan Medical Center (Ann Arbor MI) from 1994–2000. All patients underwent the same treatment, surgical resection with intra-thoracic nodal sampling. The lung adenocarcinoma samples were provided as a 5  $\mu\text{m}$  thick section through the full diameter of the tissue. Analysis of H&E stained samples by a trained clinical pathologist was used to ensure images were taken within the tumor proper.

### Imaging

A Spectra Physics MaiTai Ti:Sapphire laser (circularly polarized, 810 nm, 100 fs pulses at 80 MHz) was directed through an Olympus Fluoview FV300 scanner. This was focused through an Olympus UMPLFL20XW water-immersion lens (20 $\times$ , 0.95 NA), which subsequently captured backward propagating SHG signal. This SHG signal was separated from the excitation beam using a 670 nm dichroic mirror, filtered using a 405 nm filter (HQ405/30 m-2P, Chroma, Rockingham, Vermont), and collected by a photomultiplier tube (Hamamatsu HC125-02). The forward scattered SHG was collected through an Olympus 0.9 NA condenser, reflected by a 565 nm dichroic mirror (565 DCSX, Chroma, Rockingham, Vermont) to remove excitation light, filtered by a 405 nm filter (HQ405/30 m-2P, Chroma, Rockingham, VT) and captured by photomultiplier tube (Hamamatsu HC125-02). During acquisition of the daily calibration sample, a dilute fluorescein isothiocyanate (FITC) solution, a 535/40 filter (535/40 m-2P, Chroma, Rockingham, VT) replaced the 405 nm filters. Forward- and backward-scattered SHG images were simultaneously collected as a stack of 11 images spaced 3  $\mu\text{m}$  apart, with a 660  $\mu\text{m}$  field of view. Imaging conducted on TMA slides of H&E stained, 0.5 mm diameter breast cancer and colon cancer samples permitted one image stack at the center of each sample. For the larger (approximately 3 cm wide) lung cancer samples, 3 locations were chosen randomly in each sample and the 3 resultant F/B values (see below) were averaged.

### F/B image analysis

Image analysis was conducted with ImageJ [23]. Tissue sections were 5  $\mu\text{m}$  thick, comparable to the axial resolution of the SHG images, hence there was effectively a single layer of collagen in each sample, “auto-focused” with a maximum intensity projection of both the forward and backward image stacks. This produced a single image pair (forward scattered SHG “F”, and backwards scattered SHG “B”) for each imaged location. A maximum intensity projection of an 11 image scan taken with a closed microscope shutter was used to determine the background noise of the imaging system, which was then subtracted from each image. A common threshold (40 out of a maximum possible pixel count of 4095 a.u.)

was initially determined by a blinded observer viewing ~30 image pairs and choosing the threshold that best distinguished pixels within fibers from those in the background. This single threshold was applied to each image to identify pixels within fibers by creating a pair of masks (one for F, one for B), in which all of the pixels above threshold were set to 1, and all of the pixels below threshold were set to zero. These masks were multiplied to create one “forward x backward mask” whose pixels were equal to 1 only when they were equal to 1 in both the forward and backward masks. The background subtracted F and B images were divided to produce an F/B image of the sample, which was multiplied by the “forward x backward mask”, and the average value of all nonzero pixels yielded the sample’s average F/B (Fig. 1).

Day-to-day variations in optical alignments were normalized by imaging a standard solution of FITC daily and applying a normalization factor for each detector pathway that rendered the signal from the standard FITC sample constant over time.

#### FFT image analysis

FFT analysis was performed as previously described [17]. Specifically, the fast Fourier transform of each “F” image was generated via Matlab (MathWorks, Natick, MA). The FFT image was then binarized to include only the pixels with a value greater than 20. A linear regression was applied to the points using R Software (R Foundation, Vienna, AUS) and the  $R^2$  value was reported as a measure of the anisotropy of the overall orientation of the ensemble of collagen fibers in the image.

#### Statistics

STATA, release 13 (StataCorp, Texas, USA) and Prism 5 software (GraphPad, La Jolla, CA) was used for statistical analysis. MFS was defined as the date of confirmation of a distant metastasis after symptoms reported by the patient, detection of clinical signs, or at regular follow-up. OS was defined as time until death, any cause, while patients who died without evidence of disease were censored at their last follow-up time.

PFS was defined as the time from start of tamoxifen treatment until a second line of treatment was needed, or until death. The relationship between the natural log of F/B (ln F/B) and survival rate was assessed using the Kaplan-Meier method and evaluated using the log-rank test for trend. Multivariate Cox proportional hazard analysis was applied to evaluate the prognostic value of the natural log of F/B, age, menopausal status, tumor size, tumor grade, ER, PgR and HER2 status. Differences were considered statistically significant when the 2-sided  $p$ -value was below 0.05.

## Results

### F/B and its relationship with patient and tumor characteristics

The median ln F/B of and interquartile range in all tumors was 2.228 (0.416) (Table 1). There was no significant association between ln F/B and age or menopausal status of the patient. There were also no significant correlations with tumor size, tumor grade, and HER2 status. In contrast, compared with steroid hormone-positive tumors, ln F/B was higher in ER- ( $p < 0.001$ ) and PgR-negative tumors ( $p = 0.003$ ), respectively (Table 1).

### F/B and metastasis-free survival in breast cancer patients

Univariate analysis of the primary tumor ln F/B showed no statistically significant relationship between ln F/B and the length of MFS (Hazard Ratio, HR = 0.706; 95 %

**Table 1** ln F/B and its association with breast cancer patient and tumor characteristics

Characteristics	No. patients (%)	Median levels (interquartile range)	$p$
All patients	221 (100 %)	2.228 (0.416)	
Age (years)			0.773 <sup>a</sup>
≤ 40	33 (14.9 %)	2.160 (0.566)	
41–55	94 (42.5 %)	2.215 (0.410)	
56–70	70 (31.7 %)	2.291 (0.456)	
> 70	24 (10.9 %)	2.198 (0.327)	
Menopausal status			0.497 <sup>b</sup>
Premenopausal	113 (51.1 %)	2.200 (0.447)	
Postmenopausal	108 (48.9 %)	2.250 (0.379)	
Tumor size			0.188 <sup>a</sup>
pT1 (≤2 cm)	109 (49.3 %)	2.239 (0.356)	
pT2 (2–5 cm)	105 (47.5 %)	2.237 (0.505)	
pT3/pT4 (>5 cm)	7 (3.2 %)	1.830 (0.614)	
Tumor grade <sup>c</sup>			0.700 <sup>a</sup>
I	37 (16.7 %)	2.207 (0.288)	
II	77 (34.8 %)	2.233 (0.366)	
III	101 (45.7 %)	2.264 (0.491)	
ER status			<0.001 <sup>b</sup>
Positive	125 (56.6 %)	2.168 (0.407)	
Negative	96 (43.4 %)	2.311 (0.452)	
PgR status			0.003 <sup>b</sup>
Positive	104 (47.1 %)	2.159 (0.392)	
Negative	117 (52.9 %)	2.302 (0.425)	
HER2 status			0.121 <sup>b</sup>
Positive	26 (11.8 %)	2.299 (0.399)	
Negative	195 (88.2 %)	2.215 (0.432)	

<sup>a</sup>Kruskal-Wallis test

<sup>b</sup>Two-sample Wilcoxon rank-sum (Mann-Whitney) test

<sup>c</sup>Scarff-Bloom-Richardson grade (6 missing values)

confidence interval, CI 0.351–1.422;  $p = 0.330$ ) within the combined (ER+ and ER-) sample set. Because mechanisms of breast tumor progression varies based on ER status, and because ER+ and ER- tumors are biologically very different tumors [24, 25], we then analyzed the prognostic value of ln F/B in ER subgroups separately. Within the ER+ subgroup, in Cox regression analysis using ln F/B as a continuous variable there was a statistically significant relationship between the primary tumor ln F/B and MFS (HR = 0.23; 95 % CI 0.08–0.65;  $p = 0.005$ ) (Table 2), but within the ER- population the relationship was not statistically significant (HR = 2.72; 95 % CI 0.8104–9.173;  $p = 0.105$ ). The ER+, LNN patient samples were then divided into four equal quarters consisting of a high ln F/B (above 2.354: Q4), a low ln F/B (below 1.954: Q1), and 2 mid-range categories (range 1.954–2.168: Q2, and 2.168–2.354: Q3), and plotted in a Kaplan Meier curve (Fig. 2a). Patients with tumors with low F/B (Q1) showed the worst MFS, while those with high F/B (Q4) showed the best MFS. The 2-mid range categories (Q2 and Q3) showed an intermediate MFS (logrank trend  $p = 0.004$ ). In Cox multivariate regression analysis for MFS in ER+ patients, corrected for the traditional prognostic factors age, menopausal status of the patient, tumor size, tumor grade, PgR and HER2 status, an increasing ln F/B was significantly associated with longer MFS (HR = 0.16; 95 % CI 0.05–0.55;  $p = 0.004$ ) (Table 2).

### F/B and overall survival in breast cancer patients

Next we tested whether ln F/B of the primary tumor was also significantly related to OS in the ER+, LNN group of patients. Univariate Cox regression analysis showed that the primary tumor ln F/B was borderline statistically significantly related to OS (HR = 0.34; 95 % CI 0.11–1.03;  $p = 0.057$ ). A logrank test for trend analysis of Kaplan Meier curves with ln F/B divided into Q1–Q4 shows a significant relationship between increasing ln F/B of the primary tumor and longer OS (Fig. 2b,  $p = 0.03$ ). A multivariate Cox analysis of this data showed that ln F/B, when corrected for traditional prognostic factors, was borderline significantly related to OS (HR = 0.28; 95 % CI 0.07–1.10;  $p = 0.068$ ) (Table 3).

### Anisotropy and metastasis-free survival, as well as overall survival, in breast cancer patients

For comparison purposes we also evaluated whether the anisotropy of the orientation of the ensemble of collagen fibers in each image was predictive of metastasis free survival as well as overall survival. Univariate analysis of the primary tumor ln R value showed no statistically significant relationship between ln R and the length of MFS within the combined (ER+ and ER-) sample set (HR = 0.347; CI 0.077–1.557;  $p = 0.167$ ), nor within the ER+ subpopulation (HR = 0.129; CI 0.015–1.074;  $p = 0.058$ ), nor within the ER- subpopulation (HR = 0.945; CI 0.112–8.004;

**Table 2** Cox univariate and multivariate regression analysis for MFS in 125 ER+ patients

Variable	Univariate analysis			Multivariate analysis <sup>a</sup>		
	HR	95 % CI	$p$	HR	95 % CI	$p$
Age						
41–55 vs 40 years	0.59	0.27–1.32	0.203	0.80	0.35–1.84	0.599
56–70 vs 40 years	0.56	0.25–1.26	0.159	0.41	0.13–1.34	0.140
> 70 vs 40 years	0.46	0.15–1.36	0.159	0.32	0.08–1.27	0.105
Menopausal status						
Post-vs premenopausal	0.98	0.55–1.73	0.938	2.46	0.89–6.84	0.083
Tumor size						
2–5 vs $\leq 2$ cm	1.76	0.98–3.14	0.056	0.85	0.43–1.70	0.650
> 5 vs <2 cm	1.51	0.36–6.38	0.579	0.50	0.10–2.42	0.386
Tumor grade						
II vs I	3.15	1.30–7.61	0.011	2.76	1.10–6.92	0.030
III vs I	4.38	1.68–11.45	0.003	3.38	1.15–9.93	0.027
PgR status						
Positive vs negative	0.71	0.38–1.35	0.297	0.61	0.30–1.24	0.170
HER2 status						
Positive vs negative	4.06	1.71–9.65	0.002	3.67	1.10–6.92	0.009
Log of F/B ratio	0.23	0.08–0.65	0.005	0.16	0.05–0.55	0.004

<sup>a</sup>The multivariate model included 123 patients due to 2 missing values for tumor grade

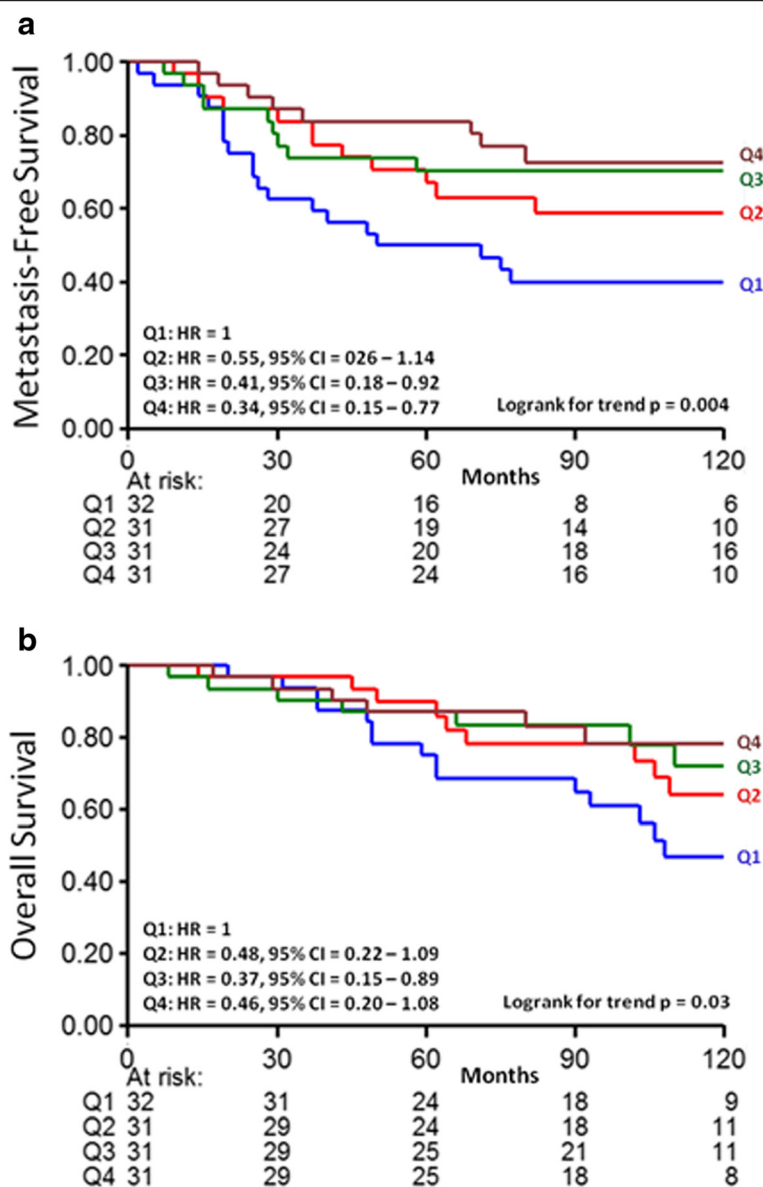


**Fig. 2** Metastasis-free (a) and overall survival (b) as a function of F/B in ER+, LNN breast cancer. The patients are divided in four equal quarters (Q1-Q4) based on their F/B tumor level. Patients at risk at various time points are indicated

$p=0.959$ ). Likewise univariate analysis showed no significant relationship between ln R and length of OS within the combined sample set (HR = 0.567; CI 0.133–2.42;  $p = 0.443$ ), nor within the ER+ subpopulation (HR = 0.213; CI 0.025–1.789;  $p = 0.154$ ), nor within the ER- subpopulation (HR = 0.137; CI 0.203–9.18 l;  $p = 0.749$ ).

**Tamoxifen treatment**

The previous studies were conducted in untreated patients in order to analyze the relationship between F/B of the primary tumor and tumor aggressiveness and pure prognosis. A subset of these patients did metastasize to

a distant site and were then treated with tamoxifen as first-line monotherapy. Therefore we evaluated this subset of ER+ breast cancer patients to determine whether the F/B of the primary tumor was also significantly related to PFS after start of therapy for recurrent disease. The hazard ratio of the primary tumor ln F/B was 3.39 (95 % CI 1.22–9.37;  $p = 0.019$ ) and the logrank test for trend analysis of Kaplan Meier curves in equal quarters showed a significant relationship ( $p = 0.02$ ) between primary tumor ln F/B and PFS (Fig. 3). Interestingly, the trend in PFS (i.e. lower primary tumor F/B was associated with slower disease progression) was found to be the opposite of that observed in

**Table 3** Cox univariate and multivariate regression analysis for OS in 125 ER+ patients

Variable	Univariate analysis			Multivariate analysis <sup>a</sup>		
	HR	95 % CI	p	HR	95 % CI	p
Age						
41–55 vs 40 years	0.49	0.21–1.17	0.108	0.61	0.25–1.52	0.289
56–70 vs 40 years	0.57	0.24–1.35	0.204	0.29	0.09–0.95	0.041
> 70 vs 40 years	0.33	0.09–1.26	0.105	0.20	0.04–0.95	0.043
Menopausal status						
Post- vs premenopausal	1.14	0.61–2.11	0.686	2.90	0.99–8.49	0.052
Tumor size						
2–5 vs ≤2 cm	1.25	0.66–2.37	0.494	0.56	0.26–1.20	0.137
> 5 vs ≤2 cm	1.66	0.39–7.11	0.492	0.75	0.15–3.72	0.720
Tumor grade						
II vs I	2.53	1.02–6.24	0.044	2.16	0.84–5.55	0.111
III vs I	5.02	1.89–13.36	0.001	4.88	1.64–14.56	0.004
PgR status						
Positive vs negative	0.51	0.26–1.01	0.055	0.48	0.23–1.01	0.054
HER2 status						
Positive vs negative	3.15	1.11–8.96	0.031	3.80	1.18–12.20	0.025
Log of F/B ratio	0.34	0.11–1.03	0.005	0.29	0.07–1.10	0.068

<sup>a</sup>The multivariate model included 123 patients due to 2 missing values for tumor grade

MFS and OS in the untreated ER+ patients (i.e. lower primary tumor F/B was associated with shorter MFS and OS times).

**Overall survival as a function of F/B in other solid tumor types**

Based on the significant relationships revealed in the breast cancer samples, we investigated colorectal and lung adenocarcinoma, other solid tumor types in which tumor

cell/matrix interactions may significantly affect metastasis. Similar to ER+, LNN breast cancer patients, stage I colorectal and lung adenocarcinoma are subsets of patients where there is a clinical need to assist the physician in deciding the appropriate level of treatment for the patient. In stage I colorectal adenocarcinoma there was a significant relationship between the F/B of the primary tumor and patient OS (Fig. 4a). Notably, the observed trend (i.e. a lower F/B was associated with longer OS) was the opposite of the trend observed in the untreated ER+, LNN breast cancer samples, suggesting a different mechanistic relationship between metastasis and collagen fiber microstructure. In contrast, stage I lung adenocarcinoma showed no significant relationship between the F/B of the primary tumor and OS (Fig. 4b). This suggests that not all solid tumors undergoing metastasis elicit identical collagen restructuring or utilize identical mechanisms relating metastatic ability and collagen microstructure.

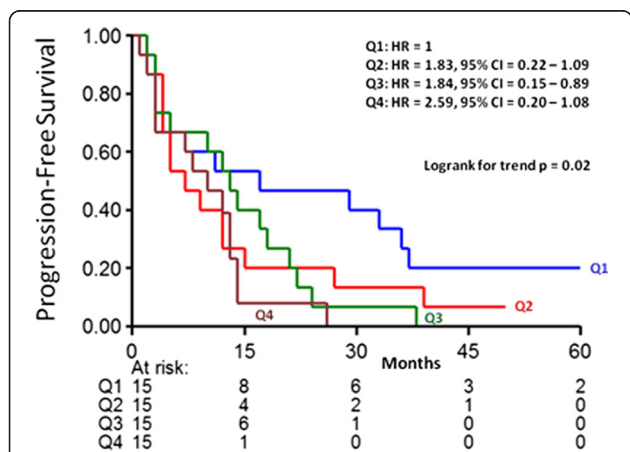


**Fig. 3** Progression-free survival as a function of F/B in ER+ recurrent breast cancer patients treated with tamoxifen. The patients are divided in four equal quarters (Q1-Q4) based on their F/B tumor level. Patients at risk at various time points are indicated

**Discussion**

Currently the ER+, LNN breast cancer population suffers from over-treatment as many patients receive chemotherapy even though metastatic disease never would have arisen. As such, there is a pressing need to improve clinicians’ ability to predict which tumors are likely to metastasize in this population. Current methods to predict metastasis are “cell focused”, using quantification of gene and protein expression levels, or cellular

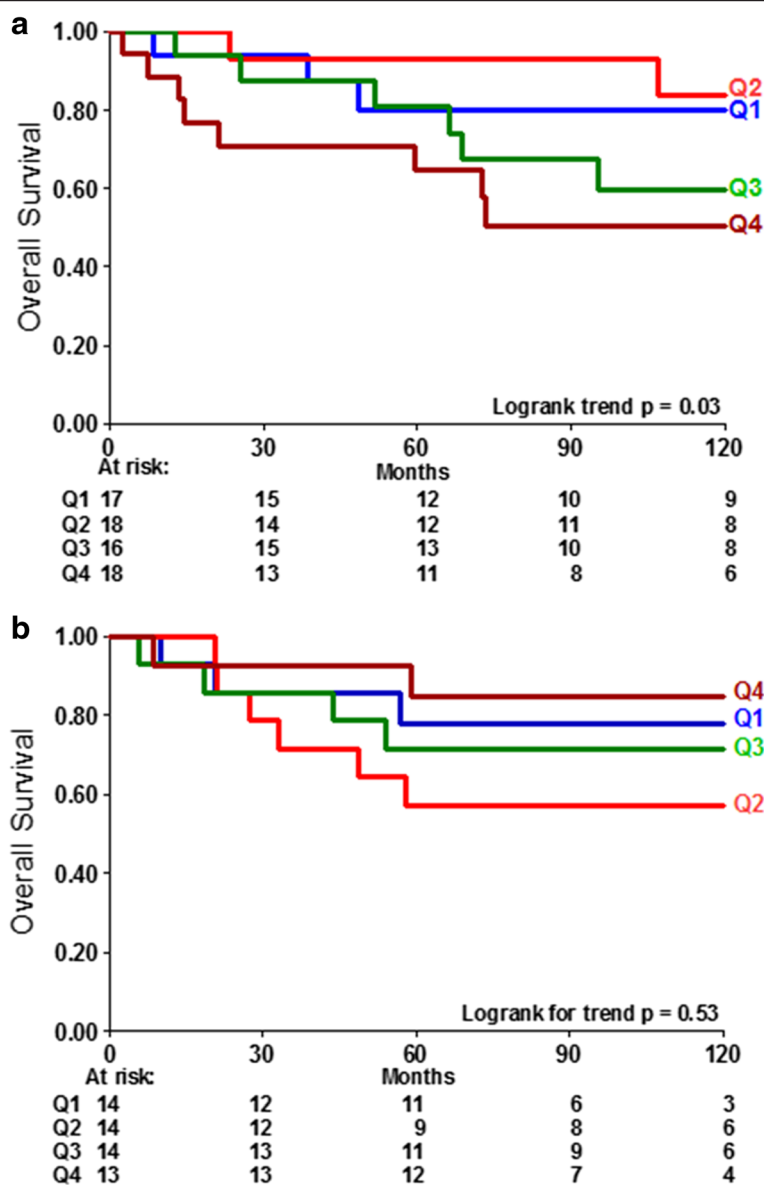


**Fig. 4** Overall survival of additional solid tumors as a function of F/B ratio. Overall survival in stage I colorectal adenocarcinoma (a) is significantly related to F/B of the primary tumor ( $p = 0.03$ ). F/B of Stage I lung adenocarcinoma (b) is not significantly related to OS ( $p = 0.53$ ). The blue line is Group 1 has the lowest F/B and the brown line is Group 4 has the highest F/B ratio. Patients at risk at various time points are indicated

morphology and cell-cell interactions [7–9, 11]. However, the process of metastasis is a complex interplay between tumor cells and their microenvironment, including the extracellular matrix [26, 27]. Therefore we explored the prognostic ability of a “matrix focused” measurement, the SHG F/B of the primary tumor.

Studies demonstrating that SHG imaging can differentiate healthy and tumor tissue in ovarian [28], basal cell [29], and pulmonary cancers [30], have established that SHG is an intrinsic signal which reports on clinically relevant properties of the tumor extracellular matrix. We recently applied this methodology in breast

cancer, demonstrating that the simple intensity-based SHG F/B is significantly different amongst different breast tumor types [18] hence we explored its ability to predict metastatic outcome. For comparison we also explored the ability of simple FFT analysis of fiber anisotropy. While the two methods report upon different structural properties (F/B is affected by fibril diameter, spacing, and disorder within a fiber [14–16], while anisotropy reports on the overall orientation of ensembles of fibers in an image [17]) both are easily automatable analyses. In the current work, we demonstrate that F/B analysis of the primary tumor is a prognostic indicator

in the ER+, LNN population. Unlike the ER- or ER+ node-positive patients, in whom adjuvant chemotherapy is universally applied, the choice of whether or not to prescribe adjuvant chemotherapy (e.g. doxorubicin, fluorouracil, etc.) in addition to tamoxifen for ER+, LNN patients is not easily apparent. Hence this is a population with a significant over-treatment problem requiring improved prognostic indicators. Our results suggest that SHG F/B from the primary tumor specimen may offer insight into eventual metastatic outcome of the patient and thus may help reduce over-treatment. Currently, predicting the time to metastasis in this population is primarily facilitated by histopathology and by genetic screens. These genetic screens quantify gene expression in cells within the tumor, including both the tumor and stromal cells. The SHG-based method demonstrated here may be highly complementary to those genetic screens, as it derives its information from the structure of the extracellular matrix in the primary tumor, rather than from the tumor cells themselves. SHG imaging has been used previously to predict breast cancer survival times, however these studies focused on analysis of morphological information from collagen images, requiring trained pathologists to score the orientation of collagen fibers in images [31]. Furthermore, the majority of that sample population was lymph node positive, while our study focuses on the LNN population, in which the key decision on adjuvant chemotherapy must be made and for whom the risk of over-treatment is high.

Based on the important role that tamoxifen plays as a treatment in almost all ER+ breast cancer patients, after identifying the significant relationship between F/B and patient outcome in untreated patients, we were interested in exploring the prognostic capability of F/B to determine the effects of tamoxifen on patients with recurrent tumors. Our results revealed that F/B as measured on the primary tumor was prognostic of PFS after patients who developed a metastasis at a distant site were treated with tamoxifen. Interestingly, the actual relationship between F/B and outcome displayed a trend that was opposite to that in the MFS and OS findings from untreated ER+ patients: In tamoxifen treated recurrent ER+ patients a high F/B was associated with a faster rate of progression, whereas in untreated ER+ patients a high F/B was associated with improved MFS and OS. Tamoxifen is an ER antagonist, indicating this contrast between tamoxifen treated ER+ tumors and untreated ER+ tumors could be due to the roles of ER in tumor progression. To explain this pattern of relationships between recurrence and F/B in ER+ tamoxifen treated tumors, as opposed to untreated ER+ tumors, we therefore hypothesize that differences in primary tumor collagen microstructure may indicate differences in the mechanism

by which tumor cells spread, which has the effect of altering susceptibility to later treatment. In an ER+ primary tumor with a low F/B, cells spread into vasculature and to secondary locations, and upon tamoxifen administration these secondary tumors are effectively treated. In an ER+ primary tumor with a high F/B ratio, tumor cells metastasize via different mechanisms which decrease the tumor cell sensitivity to tamoxifen treatment.

The results demonstrating another significant relationship between F/B of the primary tumor and OS, in stage I colorectal adenocarcinoma, indicate that the mechanisms relating metastasis to collagen microstructure may be similar between breast cancer and other solid tumors. Analyzing collagen structure in colorectal adenocarcinomas may thus aid in predicting the OS rates in patients, consequently helping to tailor the choice of chemotherapy in that tumor type as well, with low-risk patients receiving no treatment and high-risk patients being considered for neoadjuvant chemotherapy (fluorouracil, etc.). The fact that the primary tumor F/B was not predictive of metastasis in stage I lung adenocarcinoma provides support for the idea that multiple mechanisms of tumor metastasis may exist, involving differential interplay between tumor cells and matrix microstructure. These alternative mechanisms could be the result of different levels of fibrous tissue in the tissues of origin, (e.g. collagen density is high in breast and colon but not in lung tissue). In the future it may therefore be beneficial to investigate the relationship between primary tumor F/B and metastatic outcome in other solid tumors that are typically characterized as more fibrous, such as pancreatic cancer.

## Conclusions

In summary, we have identified the F/B, a simple and easily automated, intensity-based measurement as an independent prognostic indicator of metastatic outcome in ER+ LNN breast cancer patients. Furthermore, escaped tumor cells with a low F/B at the primary site show a better responsiveness to tamoxifen treatment of the recurrence, indicating a possible mechanism by which collagen structure at the primary site affects sensitivity to treatment. The primary tumor F/B is also prognostic in stage I colon adenocarcinoma, suggesting this assay may be useful in multiple types of solid tumors. By imaging the tumor “soil” this method provides information complementary to that offered by current cell-focused techniques, and therefore in combination with those methods may improve prediction of recurrence and hence reduce over-treatment.

## Abbreviations

ER+: Estrogen receptor positive; ER-: Estrogen receptor negative; F/B: Ratio of the forward-to-backward emitted SHG signals; FITC: Fluorescein isothiocyanate; H&E: Hematoxylin and eosin; HR: Hazard ratio; LNN: Lymph node-negative;

MFS: Metastasis-free survival; OS: Overall survival; PFS: Progression-free survival; PgR: Progesterone receptor; SHG: Second harmonic generation; TMA: Tissue-microarray.

#### Competing interests

KB and EB are inventors on a provisional patent related to the methods used in the manuscript. All other authors declare that they have no competing interests.

#### Authors' contributions

All authors have made substantial intellectual contributions to this study. KB, MS, JF, and EB have been involved in the design of the study and drafting the manuscript. RD, MT, PS, CvD and DB revised the manuscript for important intellectual content. KB and RD performed image acquisition. MS and PS performed the statistical analysis. MT and CvD performed histological scoring of tumors. DB and FJ have provided the clinical samples and follow-up information for breast cancer and lung adenocarcinoma. All authors have read and approved the final manuscript.

#### Acknowledgements

The project described was supported by Award Number F31CA183351 from the National Cancer Institute to KB, as well as an NIH Director's New Innovator Award 1DP2OD006501-01 and DoD BCRP Era of Hope Scholar Research Award W81XWH-09-1-0405 to EB.

#### Author details

<sup>1</sup>Department of Biomedical Engineering, University of Rochester, 207 Robert B. Goergen Hall, Box 270168, Rochester, NY 14627, USA. <sup>2</sup>Department of Medical Oncology, Erasmus MC Cancer Institute, Erasmus University Medical Center, Rotterdam, Netherlands. <sup>3</sup>Neuroscience Graduate Program, University of Rochester, 601 Elmwood Ave, Rochester, NY 14642, USA. <sup>4</sup>Department of Biostatistics and Computational Biology, University of Rochester, 601 Elmwood Ave, Rochester, NY 14642, USA. <sup>5</sup>Department of Pathology, Erasmus Medical Center, Rotterdam, The Netherlands. <sup>6</sup>Departments of Surgery and Radiation Oncology, University of Michigan, Ann Arbor, MI 48109, USA. <sup>7</sup>Department of Neurobiology and Anatomy, University of Rochester, 601 Elmwood Ave, Rochester, NY 14642, USA.

Received: 13 May 2015 Accepted: 5 November 2015

Published online: 24 November 2015

#### References

- American Cancer Society. *Cancer Facts & Figures 2012*. Atlanta: American Cancer Society; 2012.
- Fisher ER, Gregorio RM, Fisher B, Redmond C, Vellios F, Sommers SC. The pathology of invasive breast cancer. A syllabus derived from findings of the National Surgical Adjuvant Breast Project (protocol no. 4). *Cancer*. 1975;36(1):1-85.
- Weigelt B, Peterse JL, van't Veer LJ. Breast cancer metastasis: markers and models. *Nat Rev Cancer*. 2005;5(8):591-602.
- Paik S, Shak S, Tang G, Kim C, Baker J, Cronin M, et al. A multigene assay to predict recurrence of tamoxifen-treated, node-negative breast cancer. *N Engl J Med*. 2004;351(27):2817-26.
- Wang Y, Klijn JG, Zhang Y, Sieuwerts AM, Look MP, Yang F, et al. Gene-expression profiles to predict distant metastasis of lymph-node-negative primary breast cancer. *Lancet*. 2005;365(9460):671-9.
- van 't Veer LJ, Dai H, van de Vijver MJ, He YD, Hart AA, Mao M, et al. Gene expression profiling predicts clinical outcome of breast cancer. *Nature*. 2002;415(6871):530-6.
- Parker JS, Mullins M, Cheang MC, Leung S, Voduc D, Vickery T, et al. Supervised risk predictor of breast cancer based on intrinsic subtypes. *J Clin Oncol*. 2009;27(8):1160-7. doi:10.1186/s12885-015-1911-8. *Oncology* 2009, 27(8):1160-1167.
- Filipits M, Rudas M, Jakesz R, Dubsy P, Fitzal F, Singer CF, et al. A new molecular predictor of distant recurrence in ER-positive, HER2-negative breast cancer adds independent information to conventional clinical risk factors. *Clin Cancer Res*. 2011;17(18):6012-20.
- Ring BZ, Seitz RS, Beck R, Shasteen WJ, Tarr SM, Cheang MC, et al. Novel prognostic immunohistochemical biomarker panel for estrogen receptor-positive breast cancer. *J Clin Oncol*. 2006;24(19):3039-47.
- Philippart U, Roussos ET, Oser M, Yamaguchi H, Kim HD, Giampieri S, et al. A Mena invasion isoform potentiates EGF-induced carcinoma cell invasion and metastasis. *Dev Cell*. 2008;15(6):813-28.
- Liu NQ, Stingl C, Look MP, Smid M, Braakman RB, De Marchi T, et al. Comparative proteome analysis revealing an 11-protein signature for aggressive triple-negative breast cancer. *J Natl Cancer Inst*. 2014;106(2):djt376.
- Robinson BD, Sica GL, Liu YF, Rohan TE, Gertler FB, Condeelis JS, et al. Tumor microenvironment of metastasis in human breast carcinoma: a potential prognostic marker linked to hematogenous dissemination. *Clin Cancer Res*. 2009;15(7):2433-41.
- Paget S. The distribution of secondary growths in cancer of the breast. *Lancet*. 1889;133(3421):571-3.
- Han X, Burke RM, Zettel ML, Tang P, Brown EB. Second harmonic properties of tumor collagen: determining the structural relationship between reactive stroma and healthy stroma. *Opt Express*. 2008;16(3):1846-59.
- Lacomb R, Nadiarykh O, Townsend SS, Campagnola PJ. Phase matching considerations in second harmonic generation from tissues: effects on emission directionality, conversion efficiency and observed morphology. *Opt Commun*. 2008;281(7):1823-32.
- Williams RM, Zipfel WR, Webb WW. Interpreting second-harmonic generation images of collagen I fibrils. *Biophys J*. 2005;88(2):1377-86.
- Rao RA, Mehta MR, Toussaint Jr KC. Fourier transform-second-harmonic generation imaging of biological tissues. *Opt Express*. 2009;17(17):14534-42.
- Perry SW, Schueckler JM, Burke K, Arcuri GL, Brown EB. Stromal matrix metalloproteinase-13 knockout alters Collagen I structure at the tumor-host interface and increases lung metastasis of C57BL/6 syngeneic E0771 mammary tumor cells. *BMC Cancer*. 2013;13:411.
- Yu JX, Sieuwerts AM, Zhang Y, Martens JW, Smid M, Klijn JG, et al. Pathway analysis of gene signatures predicting metastasis of node-negative primary breast cancer. *BMC Cancer*. 2007;7:182.
- Effects of Radiotherapy and Surgery in Early Breast Cancer. An overview of the randomized trials. *N Engl J Med*. 1995;333(22):1444-56.
- Liu NQ, De Marchi T, Timmermans AM, Beekhof R, Trapman-Jansen AM, Foekens R, et al. Ferritin heavy chain in triple negative breast cancer: a favorable prognostic marker that relates to a cluster of differentiation 8 positive (CD8+) effector T-cell response. *Mol Cell Proteomics*. 2014;13(7):1814-27.
- Beer DG, Kardia SLR, Huang C-C, Giordano TJ, Levin AM, Misek DE, et al. Gene-expression profiles predict survival of patients with lung adenocarcinoma. *Nat Med*. 2002;8(8):816-24.
- Schneider CA, Rasband WS, Eliceiri KW. NIH Image to ImageJ: 25 years of image analysis. *Nat Methods*. 2012;9(7):671-5.
- Gruvberger S, Ringner M, Chen Y, Panavally S, Saal LH, Borg A, et al. Estrogen receptor status in breast cancer is associated with remarkably distinct gene expression patterns. *Cancer Res*. 2001;61(16):5979-84.
- Anderson WF, Chu KC, Chatterjee N, Brawley O, Brinton LA. Tumor variants by hormone receptor expression in white patients with node-negative breast cancer from the surveillance, epidemiology, and end results database. *J Clin Oncol*. 2001;19(1):18-27.
- Helleman J, Jansen MP, Ruigrok-Ritstier K, van Staveren IL, Look MP, -Meijer-van Gelder ME, et al. Association of an extracellular matrix gene cluster with breast cancer prognosis and endocrine therapy response. *Clin Cancer Res*. 2008;14(17):5555-64.
- Joyce JA, Pollard JW. Microenvironmental regulation of metastasis. *Nat Rev Cancer*. 2009;9(4):239-52.
- Nadiarykh O, LaComb RB, Brewer MA, Campagnola PJ. Alterations of the extracellular matrix in ovarian cancer studied by Second Harmonic Generation imaging microscopy. *BMC Cancer*. 2010;10:94.
- Lin SJ, Jee SH, Kuo CJ, Wu RJ, Lin WC, Chen JS, et al. Discrimination of basal cell carcinoma from normal dermal stroma by quantitative multiphoton imaging. *Opt Lett*. 2006;31(18):2756-8.
- Wang CC, Li FC, Wu RJ, Hovhannisyants VA, Lin WC, Lin SJ, et al. Differentiation of normal and cancerous lung tissues by multiphoton imaging. *J Biomed Opt*. 2009;14(4):044034.
- Conklin MW, Eickhoff JC, Riching KM, Pehlke CA, Eliceiri KW, Provenzano PP, et al. Aligned collagen is a prognostic signature for survival in human breast carcinoma. *Am J Pathol*. 2011;178(3):1221-32.

# Journal of Biomedical Optics

SPIEDigitalLibrary.org/jbo

## **Second-harmonic generation scattering directionality predicts tumor cell motility in collagen gels**

Kathleen A. Burke  
Ryan P. Dawes  
Mehar K. Cheema  
Amy Van Hove  
Danielle S. W. Benoit  
Seth W. Perry  
Edward Brown



# Second-harmonic generation scattering directionality predicts tumor cell motility in collagen gels

Kathleen A. Burke,<sup>a</sup> Ryan P. Dawes,<sup>b</sup> Mehar K. Cheema,<sup>c</sup> Amy Van Hove,<sup>a</sup> Danielle S. W. Benoit,<sup>a,d,e,f</sup> Seth W. Perry,<sup>a</sup> and Edward Brown<sup>a,b,\*</sup>

<sup>a</sup>University of Rochester, Department of Biomedical Engineering, 207 Robert B. Goergen Hall, P.O. Box 270168, Rochester, New York 14627, United States

<sup>b</sup>University of Rochester, Department of Neurobiology and Anatomy, 601 Elmwood Avenue, Rochester, New York 14642, United States

<sup>c</sup>State University of New York at Stony Brook, Department of Biomedical Engineering, Stony Brook, New York 11790, United States

<sup>d</sup>University of Rochester, Department of Biomedical Genetics, 601 Elmwood Avenue, Rochester, New York 14642, United States

<sup>e</sup>University of Rochester, Department of Chemical Engineering, 206 Gavett Hall, Rochester, New York 14627, United States

<sup>f</sup>University of Rochester Medical Center, Center for Musculoskeletal Research, 601 Elmwood Avenue, Rochester, New York 14642, United States

**Abstract.** Second-harmonic generation (SHG) allows for the analysis of tumor collagen structural changes throughout metastatic progression. SHG directionality, measured through the ratio of the forward-propagating to backward-propagating signal (F/B ratio), is affected by collagen fibril diameter, spacing, and disorder of fibril packing within a fiber. As tumors progress, these parameters evolve, producing concurrent changes in F/B. It has been recently shown that the F/B of highly metastatic invasive ductal carcinoma (IDC) breast tumors is significantly different from less metastatic tumors. This suggests a possible relationship between the microstructure of collagen, as measured by the F/B, and the ability of tumor cells to locomote through that collagen. Utilizing *in vitro* collagen gels of different F/B ratios, we explored the relationship between collagen microstructure and motility of tumor cells in a “clean” environment, free of the myriad cells, and signals found in *in vivo*. We found a significant relationship between F/B and the total distance traveled by the tumor cell, as well as both the average and maximum velocities of the cells. Consequently, one possible mechanism underlying the observed relationship between tumor F/B and metastatic output in IDC patient samples is a direct influence of collagen structure on tumor cell motility. © The Authors. Published by SPIE under a Creative Commons Attribution 3.0 Unported License. Distribution or reproduction of this work in whole or in part requires full attribution of the original publication, including its DOI. [DOI: [10.1117/1.JBO.20.5.051024](https://doi.org/10.1117/1.JBO.20.5.051024)]

Keywords: second-harmonic generation; multiphoton microscopy; F/B ratio; collagen; metastasis.

Paper 140642SSPR received Oct. 2, 2014; accepted for publication Dec. 9, 2014; published online Jan. 27, 2015.

## 1 Introduction

Breast cancer is the most frequently diagnosed form of invasive carcinoma and the second leading cause of cancer-induced mortality in the female population.<sup>1</sup> 90% of cancer mortalities are the result of metastasis of the tumor to a secondary location.<sup>2</sup> The tumor stroma, consisting of nontumor cells and the extracellular matrix (ECM), has been known to play a vital role in metastatic efficiency.<sup>3</sup> Collagen, a key component of the ECM, produces an intrinsic optical signal caused by the scattering phenomenon second-harmonic generation (SHG), which allows us to monitor changes in the tumor ECM throughout tumor progression. SHG occurs when two incoming photons scatter off of a noncentrosymmetric structure to produce one emission photon at twice the energy and half the wavelength of the individual incoming photons. SHG emission is coherent, therefore, the directionality of the signal, often quantified through the ratio of the forward-propagating to backward-propagating signal (the F/B ratio), is affected by the properties of a collagen fiber such as fibril diameter, spacing, and order versus disorder in fibril packing within a fiber.<sup>4–6</sup> Collectively, we will herein describe these properties as the collagen fiber “microstructure.”<sup>7</sup> Multiphoton imaging of fluorescence and SHG signals has shown that tumor cells move more efficiently along

SHG producing fibers than those moving independently of collagen fibers.<sup>8,9</sup> SHG imaging has previously been used to show that in human invasive ductal carcinoma (IDC) breast cancer there is a relationship between tumor collagen microstructure (as indicated by F/B) and the ability of the tumor to metastasize to the lymph nodes.<sup>10</sup> Specifically, primary IDC tumors with a higher F/B ratio significantly produce more metastases in the tumors’ draining lymph nodes upon clinical presentation.

The observed relationship between F/B ratio and local metastasis in IDC is interesting for several reasons. New methods to predict metastatic ability of tumors are highly desirable to reduce the problem of “overtreatment” whereby patients receive adjuvant chemotherapy after removal of the primary tumor even though they were not, in fact, destined to get a distant metastasis.<sup>11</sup> Furthermore, exploration of novel pathways governing the metastatic process may reveal new targets for therapeutics to inhibit metastasis. However, the underlying mechanism of the observed relationship between the F/B and IDC metastatic output is currently unclear. This relationship may be entirely due to an ability of collagen microstructure (which determines F/B) to alter tumor cell motility. Alternatively, it may be entirely due to the influence of an upstream actor within the tumor which influences collagen microstructure and tumor cell motility separately. Or it might be a combination of these mechanisms. The goal of this study is to understand the relationship between F/B and tumor cell motility in a relatively “clean” *in vitro* collagen gel system, in which confounding upstream actors are not present.

\*Address all correspondence to: Edward Brown, E-mail: [Edward.Brown@URMC.Rochester.edu](mailto:Edward.Brown@URMC.Rochester.edu)

Collagen gels create *in vitro* environments to study tumor cell motility where, unlike the *in vivo* situation, the presence of extrinsic signals can be closely controlled. In addition to the simplified environmental cues, the alteration of known factors of fibrillogenesis allows for the controlled manipulation of collagen fiber microstructure,<sup>12–14</sup> allowing one to manipulate F/B and hence to explore the relationship between F/B ratio and tumor cell motility. In this work, we change the F/B ratio of collagen gels by three different methods: via alterations in pH, ionic strength [KCl], and collagen I/collagen III ratio. Changing fibrillogenesis using any one of these methods significantly and reproducibly alters the F/B ratio of collagen fibers, allowing us to study how the motility of cells responds to differences in microstructure. Altering F/B using multiple methods helps us to ensure that any consistently observed changes in motility are in response to changes in physical properties of the gel, such as its microstructure, and not due to an alteration of cellular function through an unanticipated direct signaling effect of the fibrillogenesis method (e.g., an alteration in cellular myosin expression in response to changes in the gel's collagen III component). Collagen gel-based techniques have been used in the field of SHG to show that tumor cells more readily travel along aligned collagen fibers,<sup>15</sup> but little has been discovered so far about the relation of fiber microstructure (as indicated by F/B ratio) to tumor mobility. This research will exploit the “clean” environment of collagen gels to provide important insight into the possible mechanisms underlying the relationship between F/B ratio and lymph node metastasis in IDC patients, with the twin goals of improving anti-metastatic treatment and reducing overtreatment.

## 2 Methods

### 2.1 Multiphoton Image Setup and Acquisition

*The following microscopy apparatus was used for the assessment of SHG F/B:*

Multiphoton laser scanning microscopy (MPLSM) was conducted using a Ti:Sapphire excitation laser controlled through a BX61WI upright microscope (Olympus, Shinjuku, Tokyo), with beam scanning and image acquisition controlled by an Olympus Fluoview FV300 scanning system. For all imaging, the excitation light was circularly polarized with 100 fs pulses at 80 MHz, where circular polarization at the sample was achieved by passing the excitation light through a Berek compensator (Model 5540, New Focus, Irvine, CA) before entering the scan box. The light was focused through an Olympus UMPLFL20XW water immersion lens (20 $\times$ , 0.95 N.A.), which was also used to collect the backward propagating SHG and fluorescent signal. Backscattered signals were separated from the excitation beam using a 670 nm short-pass dichroic mirror. The backscattered collagen SHG signal was generated with an excitation wavelength of 810 nm, and the emission was filtered by a 405 nm band-pass filter (HQ405/30m-2P, Chroma, Rockingham, VT). The backward-scattered fluorescence signal, used to image tdTomato-labelled tumor cells, was excited using 740 nm light and the emission signal was filtered using a 580 nm band-pass (HQ580/180m-2P, Chroma) and a 700 nm short-pass filter (E700SP-2P, Chroma). Only SHG was captured in the forward-scattered direction, using an Olympus 0.9 N.A. optical condenser, reflected by a 565 nm long-pass dichroic mirror (565 DCSX, Chroma), and filtered by a 405 nm band-pass

filter (HQ405/30m-2P, Chroma). All signals were captured by Hamamatsu HC125-02 photomultiplier tubes.

### 2.2 *In Vivo* Model of Collagen Microstructural Changes

*In order to study the relationship between collagen gel F/B ratio and tumor cell motility, we first identified a tumor cell line that recapitulated in vivo the relationship between F/B and metastatic output observed in patients:*

Step 1: Mouse preparation. 40 female BALB/cByJ mice (Jackson Laboratories, Bar Harbor, ME) were anesthetized using ketamine/xylazine (90/9 mg/kg body weight). A cohort of 30 mice received an injection of  $5 \times 10^5$  tdTomato-labelled 4T1 mouse mammary carcinoma cells in the right inguinal mammary fat pad; the remaining mice were injected with saline. Step 2: Tissue collection. Following 14 days of tumor development and metastasis, the animals were sacrificed using intraperitoneal injection of sodium pentobarbital and subsequent cervical dislocation. Tumors and the draining inguinal lymph node were dissected free of the surrounding tissue and immediately snap-frozen in dry ice. These experiments were performed in accordance with University Committee for Animal Resources regulations. Both tissues were sectioned into 20- $\mu$ m slices using a cryostat (Reichert-Jung, Depew, NY), mounted onto positively charged slides (VWR) and stored at  $-20^\circ\text{C}$  until imaged. Step 3: Imaging of tumor sections. Before the start of each imaging session, a standard fluorescein isothiocyanate (FITC) sample was imaged as a calibration sample using 810 nm excitation and 535 nm emission filters (HQ535/40m-2P, Chroma) for both detection systems. Free FITC emits isotropically, but the measured F/B ratio was different from 1.0 each day due to slight variations in the system alignment. Therefore, a calibration factor was determined from the observed F/B ratio of FITC, which was applied to all SHG F/B ratios for that day. In each tumor section, one region was imaged from the center of the tumor, and then four additional regions were imaged by moving the field of view (FOV) in one of four directions from the center (i.e., up, down, left, and right) until the closest visible tumor edge was  $\sim 300 \mu\text{m}$  distant. At each imaged region, both the forward and backward-scattered SHG were acquired in a series of 11 image pairs spaced 3  $\mu\text{m}$  apart to create a 30- $\mu\text{m}$  thick z-stack.

Step 4: Image Analysis: All image analyses was performed with ImageJ software.<sup>16</sup> A maximum intensity projection of each of the two stacks (F and B) reduced the image stacks to a single image pair for each region. On thin (20  $\mu\text{m}$ ) tissue sections, these 11 image stacks serve as an autofocus for the thin collagen layer. Each image was background subtracted using the average background value for the corresponding PMT determined by generating an F and B image pair with the laser shutter closed. Next, two masks of both the forward and backward-scattered SHG signals were created in which collagen pixels were set to 1 and background pixels were set to 0 by applying a threshold to each of the two images. The same threshold was applied to all images. This single threshold was chosen by a blinded observer to highlight collagen and to reject background by first surveying a random sampling of images. An example forward-scattered SHG image and the corresponding threshold are shown in Fig. 1(a). After trying different thresholds ranging over  $\pm 10$  a.u., we found that the F/B ratio of the sample does not significantly differ as a result of different thresholds [Fig. 1(b), ANOVA  $p = 0.31$ ]. The two masks were multiplied together to create one mask that represents pixels with SHG emission above

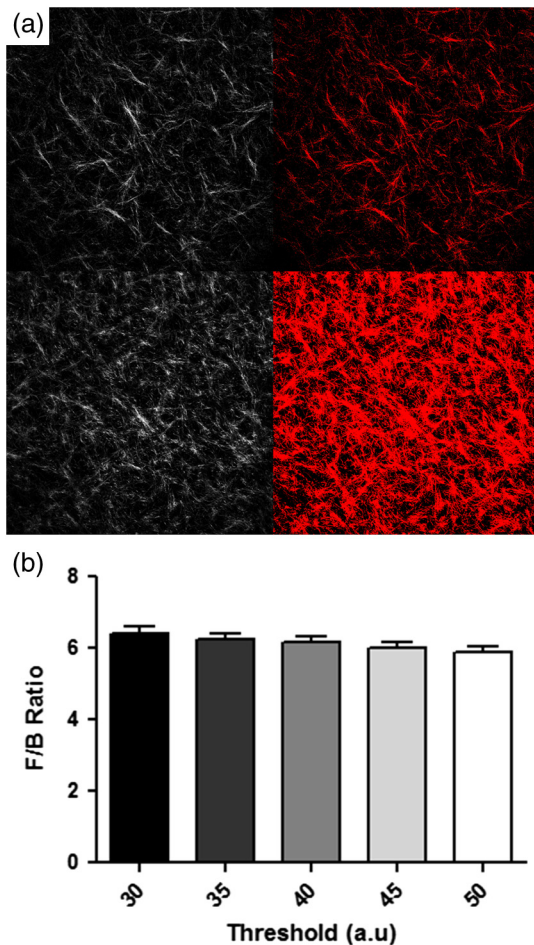


**Fig. 1** A threshold is applied to second-harmonic generation (SHG) images in order to highlight the collagen regions. (a) Example backward-scattered (top) and forward-scattered (bottom) SHG image and corresponding thresholded images. (b) Comparison of F/B ratios at different chosen thresholds demonstrates that a 20 a.u. range causes no significant differences in F/B ratio (ANOVA,  $p = 0.31$ ).

the threshold in both the forward and backward directions for that imaged region. A single F/B ratio image for that region was calculated from the F and B image pair. This F/B image was multiplied by the mask in order to set the value of all non-fiber pixels equal to zero, thereby excluding background (i.e., nonfiber) pixels from consideration. The average pixel value of fiber (i.e., nonbackground) pixels for that region was then calculated for each masked F/B ratio image. The five values of F/B for each tumor section were then averaged to determine the average F/B for that section. Note that, as in previous studies,<sup>10</sup> tissue samples were mounted on full thickness glass slides under coverslips, not between two coverslips. While this does not affect the comparisons between identically mounted samples as performed here, the measured F/B of these tissue sections is an underestimate of the true F/B ratio due to the presence of optical aberrations produced by the underlying glass slide.

**Step 5: Quantify metastases.** To quantify metastasis to the corresponding inguinal lymph nodes, clusters of tdTomato fluorescent cells were counted by a blinded observer on the MPLSM from one section taken from 400  $\mu\text{m}$  within each lymph node. **Step 6: Analysis and statistics.** All tumors were divided into three groups based on the number of associated metastasis, the “Low” metastasis group had less than four metastases

and the “High” group had greater than six metastases. The F/B ratios of the primary tumors were compared between the three groups. Statistical differences were tested using a one-way ANOVA, followed by a Newman–Keuls comparison of all groups. A  $p$ -value of  $p < 0.05$  was significantly considered.

### 2.3 tdTomato Transfected 4T1 Cell Culture

Once the 4T1 cell line was chosen, it was cultured and eventually seeded on collagen gels:

The tdTomato transfected 4T1 mouse mammary adenocarcinoma cell line (Caliper Life Sciences, Hopkinton, MA) was frozen after three initial passages. After being thawed, each aliquot was used for less than 3 months then replaced from frozen stock. Cells were maintained in RPMI (Gibco, Invitrogen Inc., Carlsbad, CA) containing penicillin/streptomycin and 10% fetal calf serum. All cells were added to the surface of the gels in this media.

### 2.4 Preparation of Control Collagen Gels

**Step 1: Dish Preparation.** Mattek petri dishes (Ashland, MA) with 14-mm diameter coverslip-bottomed wells were coated with 1% BSA and incubated for 30 min at 37°C and 5% CO<sub>2</sub>. Within a sterile hood, the BSA solution was removed and the petri dishes were allowed to dry while preparing the collagen gel solution. **Step 2: Making the gel.** Gels were made of human type I collagen solution at a concentration of 3 mg/mL, obtained from advanced biomatrix (San Diego, CA). With temperatures maintained at 4°C to minimize collagen polymerization, 810  $\mu\text{l}$  of collagen solution was combined with 108  $\mu\text{l}$  of RPMI media and 50  $\mu\text{l}$  of distilled H<sub>2</sub>O. Solutions were gently pipetted to avoid bubble formation in the solution. The pH of the total gel solution was increased between 7.5 and 7.7, using 2.5 M NaOH. 100  $\mu\text{l}$  of solution was aliquoted into each of a maximum of six petri dishes. **Step 3: Incubation and imaging.** The gels were incubated for 2 h at 37°C. After this period, the gels were covered in phosphate-buffered saline (PBS) in order to avoid dehydration and a subsequent decrease in overall gel volume. Before imaging the PBS was removed from the top of the gel, media containing the appropriate number of cells was added, the gel was cover slipped, and then imaging proceeded immediately.

### 2.5 Determining the Effect of Cell Seeding on F/B

In preliminary experiments, we applied large numbers of cells to the gels and incubated them for 3 days to explore the effects that the cells themselves can have on gel F/B:

**Step 1: Cell/Gel preparation.** To analyze the effect of cells on the local F/B in a gel, two sets of gels were created: gels with 4T1 cells added to the surface, and identically prepared gels with PBS added to the surface. To seed a gel, 30,000 cells/mL were added to the top of gels in 200  $\mu\text{L}$  of RPMI media and incubated for 3 days, with additional media provided as necessary to prevent drying. Gels without cells were covered in 200  $\mu\text{L}$  of PBS and incubated for 3 days, with addition of PBS if needed to prevent drying. **Step 2: Imaging.** After removal of gels from the incubator, excess media or PBS was carefully discarded, and the gels were immediately cover slipped and imaged. To quantify the effect of the presence of cells on the local F/B ratio, F/B was determined at one location per gel, chosen to have a high tumor cell density if the gel contained cells, and chosen from the

center of the gel if the gel did not have cells. The images were taken as 660- $\mu\text{m}$  FOV stacks of 11 images spaced 3  $\mu\text{m}$  apart, in order to capture the region of fibers affected by the collagen reorganization. Step 3: Image analysis. These images were maximum intensity projected to produce a single F and B image pair, and then the F/B ratio for the imaged region was determined as described above. Step 4: Comparison: The average F/B ratios of these images were compared between the two gel conditions. Statistical difference was detected using a two-tailed Student's *t*-test, *p*-value <0.05.

## 2.6 Determining the F/B Ratio of a Collagen Gel

*Next, lower concentrations of cells were applied to gels, and imaged within 3 h to minimize gel remodeling by the cells. Polymerization conditions of the gels were manipulated to vary F/B ratio, and F/B ratio of the gels was determined and evaluated as a function of imaging depth. Finally, the motility of cells within gels of varying F/B ratio was assessed:*

Step 1: Calibration. Calibration using a standard FITC sample, and determination of background, were performed as described above. Step 2: Imaging through the gel. For F/B ratio analysis of gels, two stacks of simultaneously collected forward and backward images were taken at the geometric center of each gel, consisting of image pairs taken at 10  $\mu\text{m}$  steps through the depth of the gel. Images were 660  $\mu\text{m}$  across. Step 3: Image analysis. The F/B of each imaged depth was determined as described above. Step 4: Analysis as a function of depth. In order to determine how the measured F/B ratio varied as a function of imaging depth, the F/B ratio was plotted as a function of depth within the gel, in 10% increments by depth. This provides 10 values of F/B ratio for each gel, while allowing for slight differences in the overall depth of the gels (ranging from 450 to 550  $\mu\text{m}$ ). A linear fit was applied to each plot to ensure that the slopes of the lines were not significantly different than zero, therefore, ensuring that the measured F/B was not affected by depth into the gel. Step 5: Producing one F/B value. A single value of the average F/B to represent the entire gel was then calculated by taking the average of the F/B ratios taken at each of the 10% depth increments. This value was used in all subsequent comparisons of different gels. All gel comparisons are conducted using a one-way ANOVA, followed by a Newman-Keuls comparison to determine the statistical significance between groups, where *p* < 0.05 was considered statistically significant. Statistical analysis was performed using Prism 5 software (GraphPad, La Jolla, CA).

## 2.7 F/B Ratio Manipulation

The F/B ratio of the gels was altered by manipulating one of three factors within the gel protocol during the previous "Step 2: Making the Gel". The pH was altered by using increasing amounts of NaOH in the final gel solution to bring the total pH to 8.5 to 8.7 or 9.5 to 9.7, measured with a Mettler Toledo Micro Pro pH meter (Columbus, OH). The ionic strength was changed by incorporating potassium chloride (KCl) into the 50  $\mu\text{l}$  dH<sub>2</sub>O added to the collagen gel solution at either 100 mM or 200 mM concentrations. The type of collagen forming the matrix was changed by adding increasing amounts of collagen type III by weight, varying from control gels made of 100% collagen type I to experimental conditions of 90% type 1: 10% type III, or 80% type I: 20% type III.

## 2.8 Analysis of Tumor Cell Motility

Step 1: Make gel and add cells. Control gels and F/B ratio manipulated gels were made as previously stated. To dilute out any remaining differences in pH, KCl, or collagen I/collagen III from the polymerization mixture, gels were incubated in 5 mL of PBS for at least 30 min or until each gel was ready to be imaged (maximum of 12 h). Further preparation and imaging was performed one gel at a time. Immediately before imaging, the incubating PBS was removed and  $1 \times 10^4$  tumor cells resuspended in RPMI media were added to the surface of a single collagen gel in a 200  $\mu\text{L}$  droplet. After allowing the cells to settle onto the gel, the excess media were removed in order to minimize motion during the imaging period. Step 2: Image cells. Live cell images were taken on a Nikon Eclipse Ti, using a Nikon MRH20101 air lens (10x, 0.3 N.A.). Cells were incubated on the microscope stage throughout imaging using a live cell microscope incubator (Pathology Devices, Westminster, MD), at 37°C, 5% CO<sub>2</sub>, and 85% relative humidity. One brightfield image was taken every 2 min for 3 h, and saved as a tiff file.

Step 3: Image Analysis. Using the ImageJ<sup>16</sup> "Template Matching" plugin, stacks were aligned through each time point based upon the SHG channel to minimize slight motion artifacts. For each gel, 10 cells (or the maximum number of cells visible) were tracked using the "Manual Tracking" plugin, which tabulates the XY location of each cell at each time point. From these values, the total distance traveled (sum of the distances traveled between each time point), the average velocity (the average of the distance traveled between each time point, divided by the time interval) and the maximum velocity each cell reached over the time course (the largest distance traveled between any two consecutive time points, divided by the time interval) was calculated for each cell and values were averaged across all cells to represent the values of that gel. Note that this is a two-dimensional analysis of tumor cell motility because over the timescales imaged the tumor cells do not penetrate significantly into the gel and their *xy* motility is significantly greater than their *z* motility. Allowing the cells sufficient time to significantly penetrate into the gel increases the chances that the cells will alter the F/B of the gel, as discussed above. Step 4: Statistical analysis. Significant differences between the various conditions were determined by comparing the average for each gel using a one-way ANOVA, followed by Newman-Keuls post-hoc comparison of all groups, where *p* < 0.05 was considered statistically significant. Additionally, distance and velocity changes were graphed as a function of the average F/B ratio of the gels and the relationship between the two factors was tested using a Pearson's correlation analysis.

## 3 Results

### 3.1 Animal Model

It has previously been shown that the average F/B ratio of the primary tumor of patients with IDC varies with the extent of lymph node involvement (i.e., the "N stage") upon clinical presentation.<sup>10</sup> The primary motivation of this study is to understand the relationship between F/B ratio and tumor cell motility in a relatively "clean" *in vitro* collagen cell system, in which confounding upstream effectors are not present. In order to accomplish this, we must first identify a tumor cell line that recapitulates the observed relationship between F/B and lymph node metastasis. This was accomplished by injecting

tdTomato-labeled 4T1 murine mammary adenocarcinoma cells into the mammary fat pad of BALB/c mice. After 2 weeks of growth, tumors were removed along with the draining of the inguinal lymph node [Figure 2(a)], and the F/B ratio of the primary tumor as well as the number of metastases in the lymph node were assessed as described above, to model previous analyses of human samples. As seen in Fig. 2(b), healthy mammary fat pad tissue has a high F/B ratio, which was significantly decreased in a tumor that has a low or medium number of metastasis to the LN. The F/B ratio was not significantly different from healthy mammary fat pad tissue in tumors that had a high number of lymph node metastases. These results exactly match the pattern in human patients with IDC, as shown previously, wherein weakly and moderately metastatic tumors (N0, N1, and N2) exhibited a significantly lower F/B than healthy breast tissue, while highly metastatic tumors (N3) did not.<sup>10</sup> This suggests that the 4T1 murine mammary adenocarcinoma is a useful model for understanding the relationship between SHG F/B and metastatic output.

### 3.2 Creation of Consistent and Optically Thin Collagen Gels

To evaluate the effect of gel F/B on tumor cell motility, we must next verify that we can produce optically thin gels with consistent F/B ratios. Figure 3(a) shows that the average F/B ratios of control gels were consistent between three different sessions of synthesis and imaging on three different days, demonstrating that the gel formation protocol produces collagen fibers of consistent microstructure. Figure 3(b) shows the average F/B ratio of standard control gels as a function of percent depth into the gel, with the total depths ranging from 450 to 550  $\mu\text{m}$ . These lines were characterized by a slope of zero within the 95% confidence interval, signifying that the measured F/B ratio was not significantly affected by depth, and demonstrating that this method creates optically thin gels, in which the SHG signal was not significantly affected by the thickness of the gel.

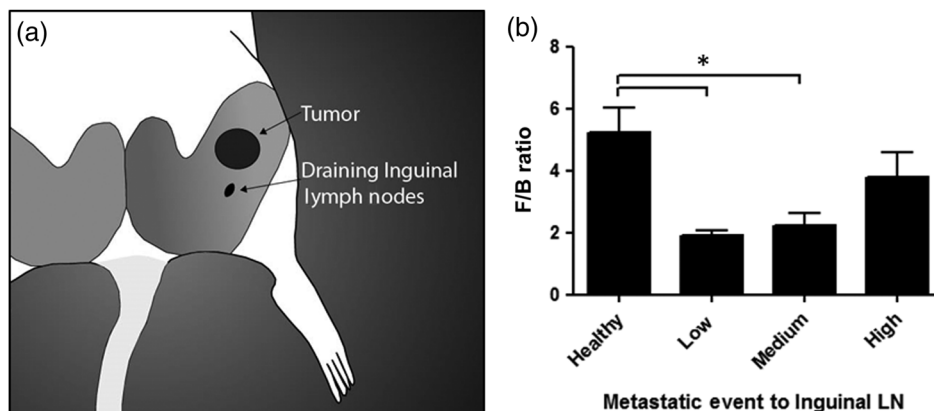


**Fig. 2** The relationship between metastasis to LN and SHG F/B in the 4T1 murine mammary adenocarcinoma model matches human data. (a) Diagram of the mouse torso revealing the location of the mammary fat pad where tumor cells were injected and the draining inguinal lymph node. (b) F/B ratio as a function of tumor metastasis to the lymph nodes. The samples are split into four groups: Healthy mammary fat pad (F/B ratio:  $5.22 \pm 0.79$ ,  $n = 10$ ), Low (1 to 3 mets, F/B ratio:  $1.90 \pm 0.17$ ,  $n = 9$ ) Medium (4 to 6 m, F/B ratio:  $2.24 \pm 0.39$ ,  $n = 10$ ), and High (7 to 12 m, F/B ratio:  $3.78 \pm 0.80$ ,  $n = 11$ ). \* represents difference of  $p < 0.05$ . Results expressed as mean  $\pm$  SEM.

### 3.3 Manipulation of the Average F/B ratio

Gels of significantly different F/B ratios were created by changing properties of the collagen gel during fibrillogenesis, including the ionic strength (concentration of KCl), the pH, and the collagen composition (ratio of type I: type III). Figure 4 shows the significant changes in the average F/B ratio of gels resulting from each of the different manipulations, with a significant decrease in F/B ratio as a function of increasing collagen type III and a significant increase in F/B ratio as a function of increasing pH during fibrillogenesis. The relationship between F/B and ionic strength during fibrillogenesis was biphasic, with a peak F/B at 100 mM KCl. The F/B ratio as a function of depth into the gel was a straight line with a slope of 0 within the 95% confidence interval for all gels in all of these conditions (data not shown). Using three methods of changing the F/B ratio allowed us to test how these changes in the collagen microstructure affected the ability of the tumor cells to move along the fibers, while minimizing the chance that this was due to a direct effect of the fibrillogenesis manipulation itself on cell motility, rather than via physical properties of the resulting fibers.

### 3.4 Cell Manipulation of Collagen Organization

The overall motivation for this project was to determine the effects of collagen fiber F/B ratio on the motility rates of tumor cells. However, it has previously been shown that adding tumor cells to collagen gels induces reorganization of the overall collagen fiber morphology.<sup>9</sup> This suggests that tumor cells may also alter the F/B ratio of collagen gels. We found that by adding a large number of cells ( $3 \times 10^5$  cells/mL of media) and allowing a significant amount of time (3 days), the tumor cells were able to induce a significant increase in the F/B ratio of fibers immediately surrounding cell clusters. Figure 5(a) confirms that in regions of high cellular density, the tumor cells alter the local fiber morphology, with fibers in between and surrounding the two clusters of cells becoming straightened and protruding perpendicularly. The regions adjacent to cellular clusters were also characterized by a higher F/B ratio [Figure 5(b)]. This was significant for the design of subsequent

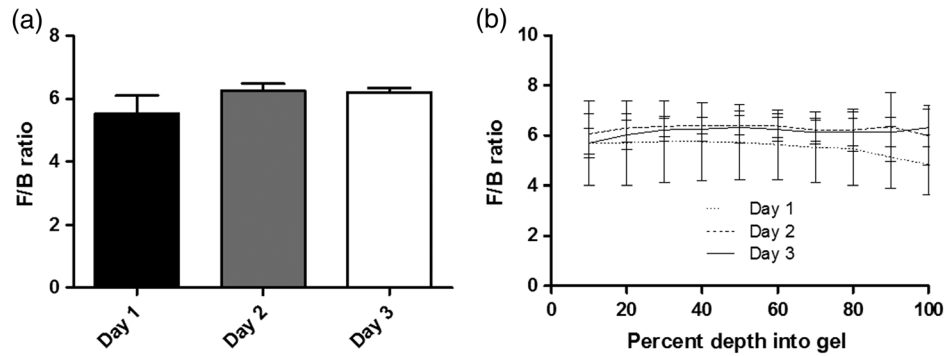


**Fig. 3** Control gels revealing consistent collagen gel structure between (a) different synthesis sessions ( $F/B = 5.52 \pm 0.59$ ,  $6.27 \pm 0.21$ , and  $6.15 \pm 0.14$ ) and (b) throughout the depth of the gel. For all plots control  $n = 6$ . Results expressed as mean  $\pm$  SEM.

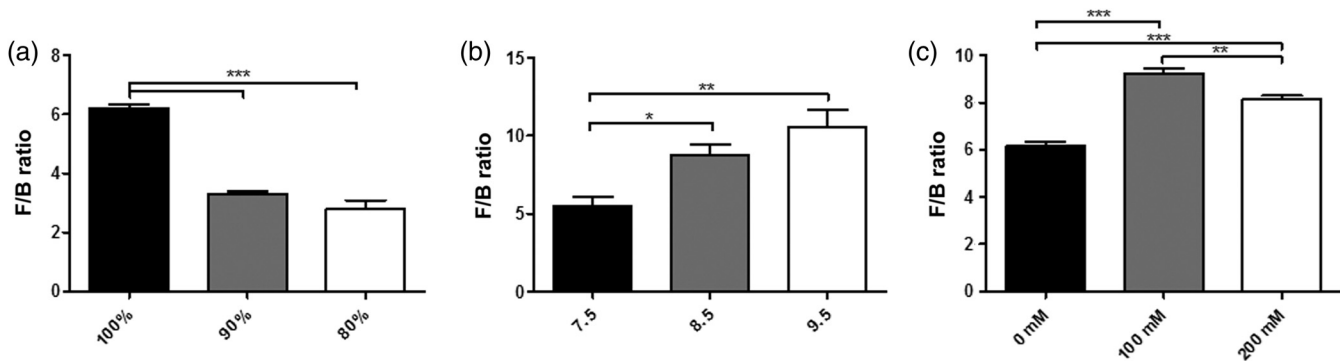


**Fig. 4** Methods for significantly changing the F/B ratio. There were significant changes in the average F/B ratio of gels as a function of changes in (a) percent of the collagen in solution that is collagen type I, relative to type III ( $n = 6,6,6$ ), (b) pH of the gel solution ( $n = 6,6,6$ ) and (c) KCl concentration ( $n = 6,5,5$ ). Results expressed as mean  $\pm$  SEM. \* represents difference of  $p < 0.05$ , \*\* represents difference of  $p < 0.01$ , and \*\*\* represents difference of  $p < 0.001$ .

experiments because in order to determine the effect of gel F/B on cell motility, we must prevent the cells themselves from significantly altering the F/B of the gel. For this reason, in the experiments performed subsequently, the cells were added to the surface of the gels in lower concentrations (1000 versus 6,000 cells/gel) and then promptly imaged (3 h versus 3 days), to minimize significant collagen restructuring by the cells.

### 3.5 Cell Motility

Using the methods described above, gels of different average F/B ratio were used to determine how fibers of different microstructure affect the motility of 4T1 mouse mammary tumor cells. Based upon our previous results, we generated gels with four different F/B values using four different methods: gels generated under control conditions had an F/B of  $6.20 \pm 0.14$ , gels generated with a collagen I/collagen III ratio of 80% had an F/B of  $2.81 \pm 0.29$ , gels generated with 200 mM KCL had an F/B of  $8.13 \pm 0.16$ , while gels generated in a pH of 9.5 had an F/B of  $10.60 \pm 1.08$ . Note that these alterations are present within the polymerization media during gel fibrillogenesis: during the subsequent seeding and locomotion of tumor cells, which is performed well after the gels are polymerized, the components of the media are the same in all cases. As shown in Figs. 6(a) and 6(b), tumor cells were tracked for 3 h

during which the total distance traveled, average velocity, and maximum velocity were measured. There was a significant main effect of the F/B category on total distance traveled (ANOVA  $p < 0.05$ ), and post-hoc analysis revealed that the total distance traveled by cells on gels of the two highest F/B categories was significantly greater than the total distance traveled by cells on gels of the two lowest F/B categories [ $p < 0.05$ , Fig. 6(c)]. The mechanism by which these tumor cells covered more distance may be related to how efficiently the tumor cells pull themselves along the fiber, which would be revealed through differences in cell velocity. Quantification of the average velocity of cells on gels with different F/B ratios revealed a significant main effect of F/B on average velocity [ $p < 0.05$ , Fig. 6(d)] while post-hoc analysis revealed that the average velocity of cells on the two highest F/B category gels was significantly higher than the average velocity of cells on the lowest F/B ratio condition. There was also a trend toward increased maximum velocity with increasing F/B ratio [ANOVA  $p = 0.06$ , Fig. 6(e)]. To quantify the degree to which cell motility and gel F/B ratio are related, a Pearson's correlation analysis and a linear regression were conducted. In these analyses, the F/B groups were formed by collapsing the F/B ratios across treatment conditions to form four distinct F/B ratio groupings, which were compared to the motility data shown in Figs. 5(c) to 5(e). The Pearson analysis revealed a significant positive relationship between F/B ratio and average velocity as well as maximum

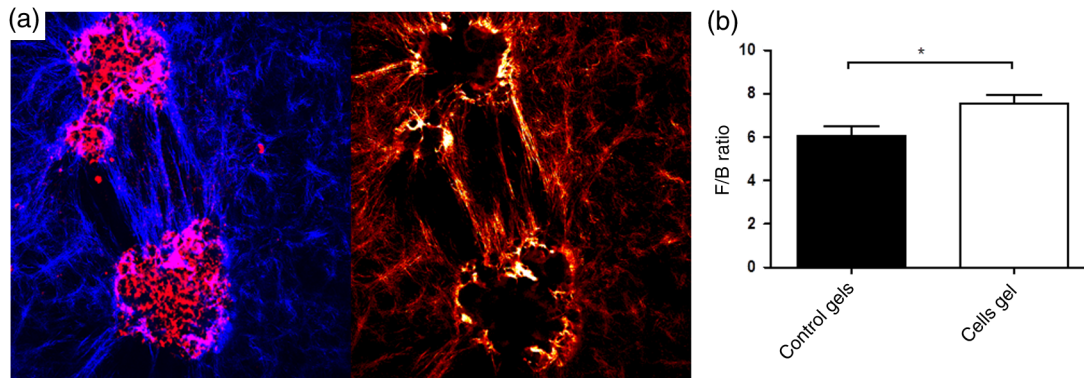


**Fig. 5** Collagen restructuring from mouse mammary adenocarcinoma cells. (a) Over 3 days tumor cell (left, red) clusters result in morphological changes in collagen (left, blue) organization in areas surrounding tumor cells, leading to aligned fibers. This also causes changes in the collagen microstructure demonstrated in a heat map of the F/B ratio in the same area (right). (b) Tumor cell clusters can alter local fiber microstructure, depicted by increases in F/B ratio of those fibers (Control  $n = 10$ , Cell gel  $n = 11$ ). Results expressed as mean  $\pm$  SEM. \*represents  $p < 0.05$ .

velocity (Figs. 5(g) and 5(h)  $p < 0.05$  for both) and a nearly significant relationship between F/B ratio and total distance travelled [Fig. 5(f);  $p = 0.06$ ]. A subsequent regression analysis reveals that these data are closely modeled by a linear fit with a positive slope for the average and maximum velocity ( $R^2 = 0.94$  and  $0.97$ , correspondingly). This suggests that these three motility parameters are highly correlated with, and are linearly related to, the F/B ratio.

#### 4 Discussion

In patients with IDC, primary tumors with high values of F/B produce more metastases to the draining lymph nodes upon clinical presentation than tumors with low values of F/B.<sup>10</sup> Gaining a further understanding of the relationship between F/B ratio and metastasis is difficult in the complex *in vivo* environment. On one extreme, the enhanced metastasis effect may be solely due to a direct influence of collagen microstructure (which dictates F/B) on tumor cell motility, while in the other extreme, both F/B and tumor cell motility may be influenced by some unknown upstream players, but not causally related. To further probe the relationship between F/B and metastasis, it is useful to move to the relatively “clean” *in vitro* environment, where tumor cells can interact with collagen gels free of confounding upstream factors.

To probe the *in vitro* relationship between F/B ratio and motility, one must first choose an appropriate cell line. We demonstrate here that the 4T1 murine mammary adenocarcinoma, a common model of triple negative invasive breast cancer, exhibits the same *in vivo* relationship between F/B of the primary tumor and metastasis to draining lymph nodes as seen in human patients, and hence provides an ideal tumor cell line with which to perform these *in vitro* studies. Next, one must find ways to generate collagen gels with different F/B values for the cells to interact with. These results show that we have established methods of creating collagen gels that have reproducible fiber microstructure, and hence a reproducible F/B ratio. These gels are also optically thin; hence, the emitted SHG signal is not significantly affected by subsequent optical scattering within the gel, allowing us to measure the F/B of the gel without concern for the effects of imaging depth. We next determined that varying three characteristics of the gel polymerization protocol: ionic strength, pH, and collagen I/collagen III ratio, allowed us to

generate highly reproducible differences in the F/B ratio of the fibers within the gels. By varying these three characteristics, we can produce gels with F/B values ranging over threefold.

Using these cells and gels, we discovered a significant relationship between the collagen gel microstructure (revealed by significant increases in F/B ratio) and the total distance traveled by cells moving through the gels, with a higher F/B resulting in a greater distance traveled. One mechanism by which cells travel this greater distance is by an alteration in the average velocity that the cells move through the gel, as evidenced by the significant relationship between average velocity and F/B ratio. Quantitatively, our results further indicate a linear relationship between total distance traveled and F/B, between average velocity and F/B, and between maximum velocity and F/B. The fact that the changes in F/B ratio were accomplished by three different alterations in the gel polymerization process, and that these alterations were diluted out by a subsequent wash step before cells were applied, help to ensure that the observed differences in motility were due to differences in the physical properties of the resulting gels and not due to a direct effect of polymerization media on subsequent cell motility.

These observations qualitatively match our previous results in human breast tumor samples, where IDC tumors with higher F/B ratio had produced more metastases to the draining lymph nodes than tumors with lower F/B ratio upon clinical presentation.<sup>10</sup> In collagen gels, tumor cells moving through gels with higher F/B travel a greater average distance. Together, these collagen gel experiments suggest that *in vitro* collagen microstructure, as indicated by the F/B ratio, can influence tumor cell motility, and that the observed relationship between metastasis in IDC patients and their primary tumor F/B is due to, at least in part, an effect of tumor collagen microstructure on tumor cell motility. However, the detailed mechanism by which collagen microstructure affects tumor cell motility is not yet clear. Collagen fibril diameter, spacing, and packing disorder within the larger fiber all are known to affect F/B of a given fiber.<sup>4-6</sup> It is possible that changes in these microstructural properties that alter F/B ratio in turn affect the ability of tumor cells to “grip” collagen fibers in such a way as to alter the motility of the cell along the fiber. Alternatively, changes in these microstructural properties that alter F/B may affect the ability of tumor cells to degrade and tunnel through obstructive fibers,

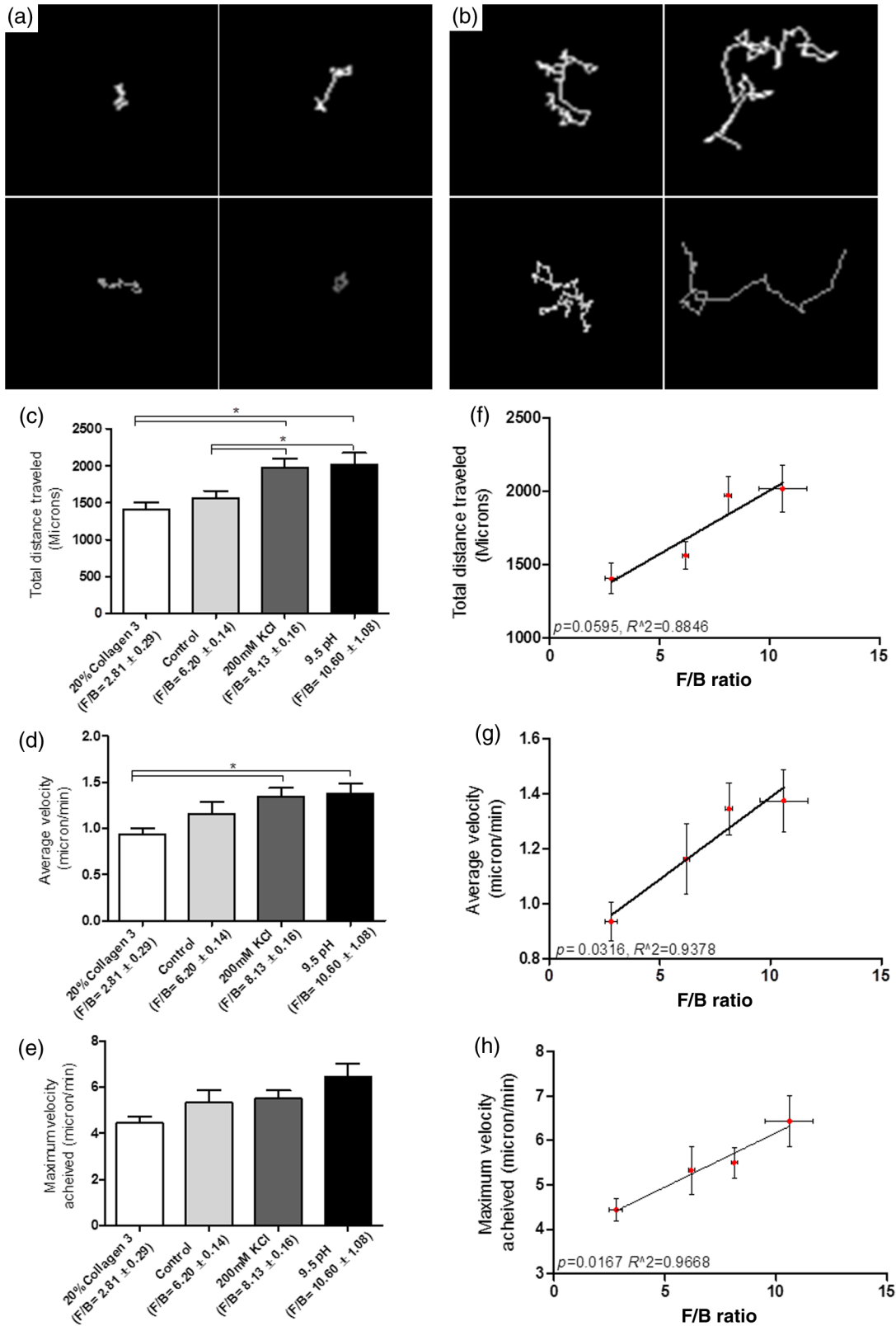


**Fig. 6** Effect of synthesis method and F/B ratio on tumor cell motility in collagen gels. Representative tracks of tumor cells over time on low F/B ratio (a) and high F/B ratio (b) gels, qualitatively revealing differences in tumor cell motility. (c) Total distance traveled versus F/B category; ANOVA  $p < 0.01$ . (d) Average velocity versus F/B category, ANOVA  $p < 0.05$ . (e) Maximum velocity versus F/B category; ANOVA  $p = 0.06$ . (f–g) Correlation analyses: (f) Total distance traveled versus F/B value. ( $p = 0.06$ ;  $R^2 = 0.88$ ). (g) Average velocity versus F/B value ( $p < 0.05$  and  $R^2 = 0.94$ ). (h) Maximum velocity versus F/B value ( $p < 0.05$  and  $R^2 = 0.97$ ). Results expressed as mean  $\pm$  SEM. For all plots control  $n = 6$ , for all other conditions  $n = 5$ . \*represents  $p < 0.05$  based on Newman–Keuls post-hoc test.

or may be related to the overall extent of obstructions present. Additionally, alterations in these microstructural properties that alter F/B may affect the overall stiffness of the collagen, leading to stiffness-sensitive alterations in tumor cell locomotion.<sup>17</sup> Or a combination of these effects may contribute to the relationship between F/B and motility.

In preliminary studies, we determined that at high seeding densities and over long time periods, the 4T1 cell line used here can alter the F/B of the local collagen matrix. This led us to restrict these experiments to lower seeding densities and significantly shorter time periods in order to minimize this effect, and allowed us to evaluate the effect of gel F/B on tumor cells, not the effect of tumor cells on gel F/B. However, this novel observation that tumor cells locally affect collagen F/B ratio *in vitro* offers additional insight. First, the reorganization of the direction and shape of the fibers correlates with a change in collagen microstructure that can be detected through changes in the F/B ratio. This finding suggests that the processes by which morphology and microstructure are modified by tumor cells are linked. Furthermore, we have previously shown that altering the availability of stromal MMP-13 altered F/B and metastatic output.<sup>18</sup> The fact that tumor cells themselves can affect F/B (as shown here), and that alteration of enzymes present in the stroma can alter F/B (as shown previously), suggests that both tumor and stromal cells play key roles in defining the matrix microstructure that dictates F/B.

## 5 Summary

In summary, these results suggest that the relationship between F/B and metastatic output observed in patient IDC samples can be explained at least in part by a direct influence of collagen microstructure on tumor cell motility. Further exploration of the underlying mechanisms of this relationship may lead to anti-metastatic drugs that reduce clinical metastasis by altering tumor collagen microstructure. Furthermore, these results also suggest that in the future, quantitative measurements of the state of collagen microstructure, i.e., F/B, may be useful to predict the metastatic capability of a primary tumor, and subsequently the overall survival of individual patients. The development of improved methods of predicting metastatic outcome would help to reduce the problem of overtreatment, where patients are treated with adjuvant chemotherapy who would otherwise not have suffered a metastasis.<sup>11</sup> Finally, these results reveal that the tumor cells themselves directly modify the collagen microstructure, altering the local F/B ratio, in addition to the previously known role that stromal cells play in this remodeling.

## Acknowledgments

Funding for this research was provided by the NIH [Director's New Innovator Award: DP2 OD006501 (EB), R01AR064200 (DB)], the Department of Defense [Era of Hope Scholar Research Award: W81XWH-09-1-0405 (EB)], the National Science Foundation [DMR1206219 (DB)], and New York State Stem Cell Science [NYSTEM, N11G-035 (DB)]. Kathleen Burke was supported by National Institutes of Health under

Award No. F31CA183351 and Award No. T32AI007285; Ryan P. Dawes was supported by the NIH Training Grant in Neuroscience Award No. 5T32NS007489-13; and Amy Van Hove was supported by a Howard Hughes Medical Institute Med-into-Grad fellowship. Seth W. Perry was supported by NIH Exploratory Developmental Research Grant Award No. R21DA030256.

## References

1. American Cancer Society, *Cancer Facts & Figures 2012*, American Cancer Society, Atlanta (2012).
2. E. R. Fisher et al., "The pathology of invasive breast cancer. A syllabus derived from findings of the national surgical adjuvant breast project (protocol no. 4)," *Cancer* **36**(1), 1–85 (1975).
3. R. R. Langley and I. J. Fidler, "The seed and soil hypothesis revisited—The role of tumor-stroma interactions in metastasis to different organs," *Int. J. Cancer* **128**(11), 2527–2535 (2011).
4. X. Han et al., "Second harmonic properties of tumor collagen: determining the structural relationship between reactive stroma and healthy stroma," *Opt. Express* **16**(3), 1846–1859 (2008).
5. R. Lacombe et al., "Phase matching considerations in second harmonic generation from tissues: effects on emission directionality, conversion efficiency and observed morphology," *Opt. Commun.* **281**(7), 1823–1832 (2008).
6. R. M. Williams, W. R. Zipfel, and W. W. Webb, "Interpreting second-harmonic generation images of collagen I fibrils," *Biophys. J.* **88**(2), 1377–1386 (2005).
7. R. M. Burke et al., "Tumor-associated macrophages and stromal TNF- $\alpha$  regulate collagen structure in a breast tumor model as visualized by second harmonic generation," *J. Biomed. Opt.* **18** (8), 086003 (2013).
8. J. Condeelis and J. E. Segall, "Intravital imaging of cell movement in tumours," *Nat. Rev. Cancer* **3**(12), 921–930 (2003).
9. P. P. Provenzano et al., "Collagen reorganization at the tumor-stromal interface facilitates local invasion," *BMC Med.* **4**(1), 38 (2006).
10. K. Burke, P. Tang, and E. Brown, "Second harmonic generation reveals matrix alterations during breast tumor progression," *J. Biomed. Opt.* **18**(3), 31106 (2013).
11. B. Weigelt, J. L. Peterse, and L. J. van't Veer, "Breast cancer metastasis: markers and models," *Nature Reviews. Cancer* **5**(8), 591–602 (2005).
12. V. Ajeti et al., "Structural changes in mixed Col I/Col V collagen gels probed by SHG microscopy: implications for probing stromal alterations in human breast cancer," *Biomed. Opt. Express* **2**(8), 2307–2316 (2011).
13. C. B. Raub et al., "Noninvasive assessment of collagen gel microstructure and mechanics using multiphoton microscopy," *Biophys. J.* **92**(6), 2212–2222 (2007).
14. B. A. Roeder, K. Kokini, and S. L. Voytik-Harbin, "Fibril microstructure affects strain transmission within collagen extracellular matrices," *J. Biomech. Eng.* **131**(3), 031004 (2009).
15. P. P. Provenzano et al., "Contact guidance mediated three-dimensional cell migration is regulated by Rho/ROCK-dependent matrix reorganization," *Biophys. J.* **95**(11), 5374–5384 (2008).
16. C. A. Schneider, W. S. Rasband, and K. W. Eliceiri, "NIH Image to ImageJ: 25 years of image analysis," *Nat. Methods* **9**(7), 671–675 (2012).
17. C.-M. Lo et al., "Cell movement is guided by the rigidity of the substrate," *Biophys. J.* **79**(1), 144–152 (2000).
18. S. W. Perry et al., "Stromal matrix metalloprotease-13 knockout alters Collagen I structure at the tumor-host interface and increases lung metastasis of C57BL/6 syngeneic E0771 mammary tumor cells," *BMC Cancer* **13**(411) (2013).

Biographies of the authors are not available.

*$\beta$ -Adrenergic receptors ( $\beta$ -AR) regulate VEGF and IL-6 production by divergent pathways in high  $\beta$ -AR-expressing breast cancer cell lines*

**Kelley S. Madden, Mercedes J. Szpunar & Edward B. Brown**

**Breast Cancer Research and Treatment**

ISSN 0167-6806

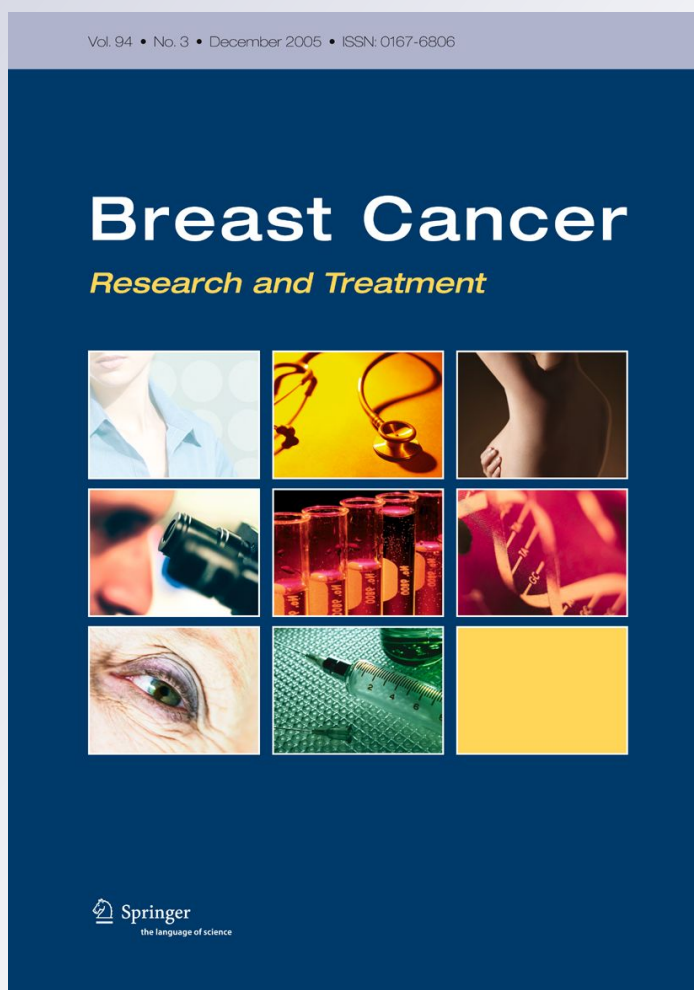
Volume 130

Number 3

Breast Cancer Res Treat (2011)

130:747-758

DOI 10.1007/s10549-011-1348-y



**Your article is protected by copyright and all rights are held exclusively by Springer Science+Business Media, LLC.. This e-offprint is for personal use only and shall not be self-archived in electronic repositories. If you wish to self-archive your work, please use the accepted author's version for posting to your own website or your institution's repository. You may further deposit the accepted author's version on a funder's repository at a funder's request, provided it is not made publicly available until 12 months after publication.**

## $\beta$ -Adrenergic receptors ( $\beta$ -AR) regulate VEGF and IL-6 production by divergent pathways in high $\beta$ -AR-expressing breast cancer cell lines

Kelley S. Madden · Mercedes J. Szpunar · Edward B. Brown

Received: 17 November 2010 / Accepted: 4 January 2011 / Published online: 14 January 2011  
© Springer Science+Business Media, LLC. 2011

**Abstract** Activation of  $\beta$ -adrenergic receptors ( $\beta$ -AR) drives proangiogenic factor production in several types of cancers. To examine  $\beta$ -AR regulation of breast cancer pathogenesis,  $\beta$ -AR density, signaling capacity, and functional responses to  $\beta$ -AR stimulation were studied in four human breast adenocarcinoma cell lines.  $\beta$ -AR density ranged from very low in MCF7 and MB-361 to very high in MB-231 and in a brain-seeking variant of MB-231, MB-231BR. Consistent with  $\beta$ -AR density,  $\beta$ -AR activation elevated cAMP in MCF7 and MB-361 much less than in MB-231 and MB-231BR. Functionally,  $\beta$ -AR stimulation did not markedly alter vascular endothelial growth factor (VEGF) production by MCF7 or MB-361. In the two high  $\beta$ -AR-expressing cell lines MB-231 and MB-231BR,  $\beta$ -AR-induced cAMP and VEGF production differed considerably, despite similar  $\beta$ -AR density. The  $\beta_2$ -AR-selective agonist terbutaline and the endogenous neurotransmitter norepinephrine decreased VEGF production by MB-231, but increased VEGF production by MB-231BR. Moreover,  $\beta_2$ -AR activation increased IL-6 production by both MB-231 and MB-231BR. These functional alterations were driven by elevated cAMP, as direct activation of

adenylate cyclase by forskolin elicited similar alterations in VEGF and IL-6 production. The protein kinase A antagonist KT5720 prevented  $\beta$ -AR-induced alterations in MB-231 and MB-231BR VEGF production, but not IL-6 production. **Conclusions**  $\beta$ -AR expression and signaling is heterogeneous in human breast cancer cell lines. In cells with high  $\beta$ -AR density,  $\beta$ -AR stimulation regulates VEGF production through the classical  $\beta$ -AR-cAMP-PKA pathway, but this pathway can elicit directionally opposite outcomes. Furthermore, in the same cells,  $\beta$ -AR activate a cAMP-dependent, PKA-independent pathway to increase IL-6 production. The complexity of breast cancer cell  $\beta$ -AR expression and functional responses must be taken into account when considering  $\beta$ -AR as a therapeutic target for breast cancer treatment.

**Keywords** Breast cancer ·  $\beta$ -Adrenergic receptors · VEGF · IL-6 · Norepinephrine · cAMP

### Abbreviations

$\beta$ -AR	Beta-adrenergic receptor(s)
cAMP	3',5'-Cyclic adenosine monophosphate
HBSS	Hank's balanced salt solution
BSA	Bovine serum albumin
FCS	Fetal calf serum
IBMX	Isobutylmethylxanthine
ICI	ICI 118,551 hydrochloride
<sup>125</sup> ICYP	<sup>125</sup> I-cyanopindolol
IL-6	Interleukin 6
ISO	Isoproterenol
NE	Norepinephrine
PKA	Protein kinase A
TERB	Terbutaline
VEGF	Vascular endothelial growth factor
ANOVA	Analysis of variance

K. S. Madden (✉) · E. B. Brown  
Department of Biomedical Engineering, University of Rochester  
Medical Center, Goergen Hall, RC Box 270168,  
Rochester, NY 14627, USA  
e-mail: Kelley\_Madden@urmc.rochester.edu

E. B. Brown  
e-mail: Edward\_Brown@urmc.rochester.edu

M. J. Szpunar  
Department of Pathology, University of Rochester Medical  
Center, 601 Elmwood Ave., Rochester, NY 14642, USA  
e-mail: Mercedes\_Szpunar@urmc.rochester.edu

## Introduction

Sympathetic nervous system activation and release of the neurotransmitters norepinephrine (NE) and epinephrine (EPI) can promote solid tumor growth and metastases by activating  $\beta$ -adrenergic receptors ( $\beta$ -AR) expressed by tumor cells or host stromal cells [1–5].  $\beta$ -AR are  $G_s$ -protein coupled receptors that activate adenylate cyclase to elevate intracellular 3',5'-cyclic adenosine monophosphate (cAMP) and activate protein kinase A (PKA), leading to down-stream alterations in gene expression that regulate a variety of cellular functions. More recently,  $\beta$ -AR-activated effector molecules have been identified that diverge from the classical cAMP-PKA pathway [6–8].

Direct stimulation of  $\beta$ -AR expressed by tumor cells may play an important role in tumor pathogenesis. For example, exposure to a chronic stressor promoted in vivo angiogenesis and production of vascular endothelial growth factor (VEGF), a key proangiogenic protein. This effect was eliminated by silencing ovarian tumor cell  $\beta$ -AR expression, implicating tumor cell  $\beta$ -AR expression and signaling as an important facilitator of stress-induced tumor angiogenesis in vivo [1]. In vitro studies using tumor cell lines suggest that NE can promote tumor progression by a  $\beta$ -AR-driven proangiogenic pathway, featuring increased production of VEGF, interleukin-6 (IL-6), and matrix metalloproteinases. This pathway has been demonstrated in multiple tumor types and in normal cells [4, 9–13]. The direct impact of  $\beta$ -AR stimulation of breast tumor cells has not been well characterized, despite the potential for  $\beta$ -AR facilitation of angiogenic and metastatic pathways.

Here, we characterize  $\beta$ -AR expression and signaling capacity in a panel of human breast cancer cell lines and determine the impact of  $\beta$ -AR signaling on production of two proteins that drive tumor angiogenesis, VEGF and IL-6. The results suggest that heterogeneity in  $\beta$ -AR expression and function in breast cancer cells needs to be taken into account when considering  $\beta$ -blockade as a therapeutic strategy to inhibit tumor growth and/or angiogenesis in breast cancer.

## Materials and methods

### Cell lines

Human breast adenocarcinoma cell lines MDA-MB-231 (MB-231), MDA-MB-361 (MB-361), and MCF7 were purchased from American Tissue Type Collection (Manassas, VA). MDA-MB-231BR (MB-231BR), a brain-seeking variant of MB-231, was obtained from Dr. T. Yoneda

(University of Texas Health Science Center, San Antonio, TX) [14]. All cell lines were employed experimentally within 3 months of acquiring and/or thawing and were regularly tested for the absence of mycoplasma contamination. All cell lines were grown in Dulbecco's Modified Essential Medium (DMEM) containing 4.5 g/l glucose, L-glutamine, penicillin/streptomycin and 10% fetal calf serum (FCS). All cells were grown in T75 tissue culture flasks (Corning Inc., Corning, NY) to no greater than 70–80% confluence.

### Reagents

(–)Isoproterenol hydrochloride (ISO), terbutaline hemisulfate (TERB), isobutylmethylxanthine (IBMX), forskolin, and KT 5720 were purchased from Sigma-Aldrich, St. Louis, MO. [ $^{125}$ I]-cyanopindolol ( $^{125}$ ICYP) was purchased from NEN Radiochemicals (Perkin Elmer Life and Analytical Sciences, Waltham, MA). All media, Hank's Balanced Salt Solution (HBSS), and components were purchased from Gibco, Invitrogen Inc., Carlsbad, CA.

### $\beta$ -AR radioligand binding assay

The specific binding of  $^{125}$ ICYP to whole cells was used to quantify  $\beta$ -AR expression [15]. Tumor cells ( $1 \times 10^6$ ) resuspended in HBSS were incubated with varying concentrations of  $^{125}$ ICYP with or without the unlabeled  $\beta$ -AR-antagonist CGP-12177 (1  $\mu$ M) in duplicate tubes. Incubations were carried out for 60 min in a shaking water bath at 37°C, sufficient time for equilibrium binding to occur. Following incubation, 3 ml of ice-cold hypotonic phosphate buffer (3.8 mM  $KH_2O_4$ , 16.2 mM  $Na_2HPO_4$ , and 4 mM  $MgSO_4$ ) was added to each tube for 10 min. The reaction mixtures were filtered under reduced pressure through Whatman glass fiber filters using an automatic harvester (Brandel Corp., Gaithersburg, MD). Filters were rinsed with 16 ml of ice-cold Tris-EGTA buffer to remove unbound radioligand, and radioactivity was determined in a LKB Clinigamma gamma counter. Specific binding is defined as the difference between binding of the radioligand at each concentration in the absence and in the presence of 1  $\mu$ M CGP-12177 and was calculated for each ligand concentration using the specific activity of the radioligand. Specific  $^{125}$ ICYP (M) bound versus the amount of ligand added was plotted, and the maximal number of binding sites ( $B_{max}$ ) and receptor affinity ( $K_d$ ) was determined using non-linear regression analysis (GraphPad Prism software, San Diego, CA). The maximal number of binding sites per cell is calculated from the  $B_{max}$  based on simple stoichiometric assumptions (one molecule binds to one receptor site).

### cAMP assay

Tumor cells ( $1 \times 10^6$ ) were incubated for 20 min at 37°C in a shaking water bath in HBSS containing 0.1% bovine serum albumin (BSA) and 100  $\mu$ M isobutylmethylxanthine (IBMX), a phosphodiesterase inhibitor (HBSS/BSA/IBMX buffer). ISO, forskolin, or buffer alone was added to each tube, and the cells were incubated for 5–60 min at 37°C (final volume = 1 ml). To stop the reaction, 2 ml ice-cold HBSS/BSA/IBMX buffer was added to each tube. The cells were centrifuged two times for 10 min at 200 $\times$ g and then resuspended in 1 $\times$  Cell Lysis Buffer, provided in the cAMP ELISA kit. After subjecting the cells to freezing at –20°C, followed by boiling for 10 min in a 95°C heat block and repeating the sequence, the cells were centrifuged at 600 $\times$ g at 4°C for 10 min to remove cellular debris. Supernatants were collected and stored at –80°C until analysis of cAMP content using the cAMP Parameter ELISA kit from R&D Systems (Minneapolis, MN) following the manufacturer's instructions. Absorption was measured at 450 nm using a multiwell plate reader (Synergy HT, Biotek Instruments Inc, Winooski, VT). Curve fitting and sample concentration calculations were conducted with Gen5 software (Biotek).

### VEGF and IL-6 production in vitro

Tumor cells were resuspended in Advanced DMEM containing 1% FCS, penicillin/streptomycin, and L-glutamax (Invitrogen). Cells were plated in duplicate at  $5 \times 10^4$  cells per well in 24-well flat bottom tissue culture plates (Falcon, Becton-Dickinson, Franklin Lakes, NJ). At this concentration, tumor cells reached confluence by 96 h in culture. Cells were cultured at 37°C in a 5% CO<sub>2</sub> humidified atmosphere and were allowed to adhere for 3 h before addition of adrenergic agonists or antagonists. The  $\beta_2$ -selective blocker ICI 118,551 or the PKA inhibitor KT 5720 was added 30 min prior to  $\beta$ -AR agonists. VEGF or IL-6 concentration in cell-free supernatants was measured using human-specific VEGF or IL-6 Quantikine kits (R&D Systems) according to the manufacturer's instructions. Absorption was measured at 450 nm using a multiwell plate reader. Curve fitting and sample concentration calculations were conducted with Gen5 software.

### Cellular proliferation in vitro

Tumor cells were resuspended in Advanced DMEM containing 1% FCS, penicillin/streptomycin, and L-glutamax (Invitrogen) and plated at  $1\text{--}2 \times 10^4$  cells per well in 96-well flat bottom tissue culture plates (Falcon, Becton-Dickinson) in triplicate, and allowed to adhere for 3 h at 37°C in a 5% CO<sub>2</sub> humidified atmosphere before addition

of adrenergic agonists or antagonists. For blocking experiments, antagonists were added 30 min prior to addition of agonists. Proliferation was measured using a fluorescent DNA binding dye (CyQuant NF Proliferation Assay kit, Invitrogen) according to manufacturer's instructions. Fluorescent intensity was measured at excitation 490 nm and emission 520 nm using a multiwell plate reader equipped with the appropriate filters. Background fluorescence (in the absence of cells) was subtracted automatically from each well.

### Statistical analysis

Statistically significant differences between groups were determined by analysis of variance (ANOVA) using GraphPad Prism software. Initially, two-way ANOVAs were conducted with experimental repetition and drug treatment as a variable. If experimental repetitions were not significantly different, the raw values or values normalized to medium alone were combined for further ANOVA. When experimental repetitions were significantly different from each other, individual experimental repetitions were analyzed separately with concentrations obtained from individual experimental repetitions. In experiments with time in culture as a factor, highly significant ( $P < 0.0001$ ) effects of time in culture were observed. The results reported were analyzed at each time point by one-way ANOVA. When a significant main effect of drug treatment was identified ( $P < 0.05$ ), Newman-Keuls post hoc test to compare between groups with  $P < 0.05$  considered significant.

## Results

$\beta$ -AR expression and signaling capacity varies between breast adenocarcinoma cell lines

$\beta$ -AR expression was measured in four human breast adenocarcinoma cell lines. MB-231 represents the metastatic, aggressive “triple-negative” phenotype and lacks expression of estrogen receptor-alpha (ER- $\alpha$ ) and other hormone receptors [16]. MB-231BR, a variant of MB-231, metastasizes exclusively to the mouse brain [14]. MCF7 is less aggressive and is non-metastatic in mice. MB-361 was isolated from a human brain metastasis [16]. Standard radioligand binding was used to quantify  $\beta$ -AR cell surface density. Specific binding of the  $\beta$ -AR antagonist <sup>125</sup>I-CYP in each cell line is shown in Fig. 1a. The number of binding sites, calculated as described in “Materials and methods” section, ranged from approximately 150–300 sites per cell in MB-361 and MCF7 to ~11,000 to 14,000 sites per cell in MB-231 and MB-231BR (Table 1). High-affinity

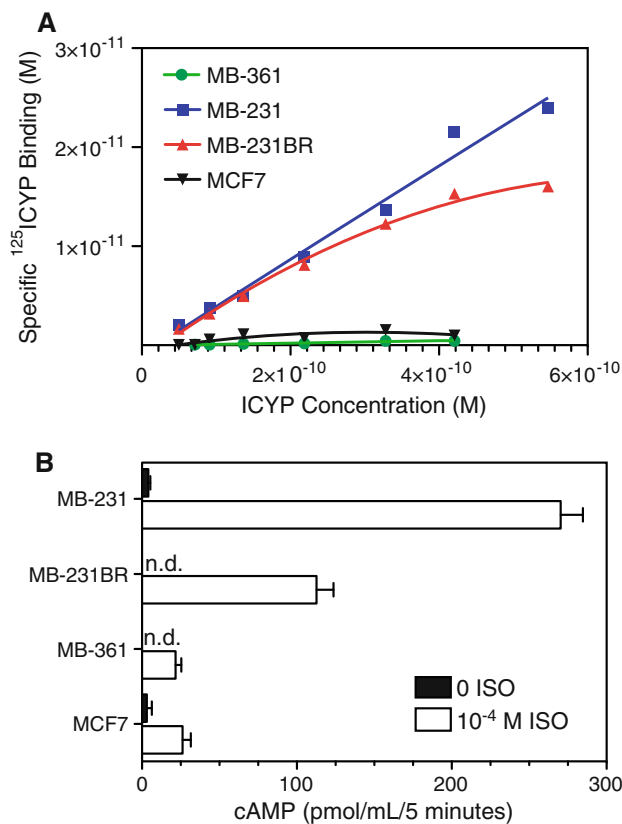


**Fig. 1** Heterogeneity of  $\beta$ -AR expression in breast cancer cell lines. **a** Binding of the radiolabeled  $\beta$ -AR antagonist  $^{125}\text{I}$ CYP was measured in four human breast adenocarcinoma cell lines. Specific binding at each ligand concentration was calculated by subtracting radioligand binding in the presence of unlabeled antagonist CGP-12177 from total ICYP binding. The concentration of  $^{125}\text{I}$ CYP specifically bound for each cell line as described in “Materials and methods” section. Results are representative of 1–3 experimental repetitions. **b** cAMP accumulation in response to  $\beta$ -AR stimulation. cAMP production was measured after stimulating  $1 \times 10^6$  cells with HBSS buffer alone or  $10^{-4}$  M ISO for 5 min. All reactions took place in the presence of  $100 \mu\text{M}$  IBMX. Intracellular cAMP concentration was measured by ELISA. Results shown are mean  $\pm$  SEM of 2–4 experimental repetitions. *n.d.* not detectable; level of detection = 1 pmol/ml

binding of ICYP ( $K_d$ ) was observed, ranging from  $1 \times 10^{-11}$  to  $9 \times 10^{-11}$  M in all cell lines (Table 1).

Next, we determined if  $\beta$ -AR density reflected signaling capacity as measured by  $\beta$ -AR-induced intracellular

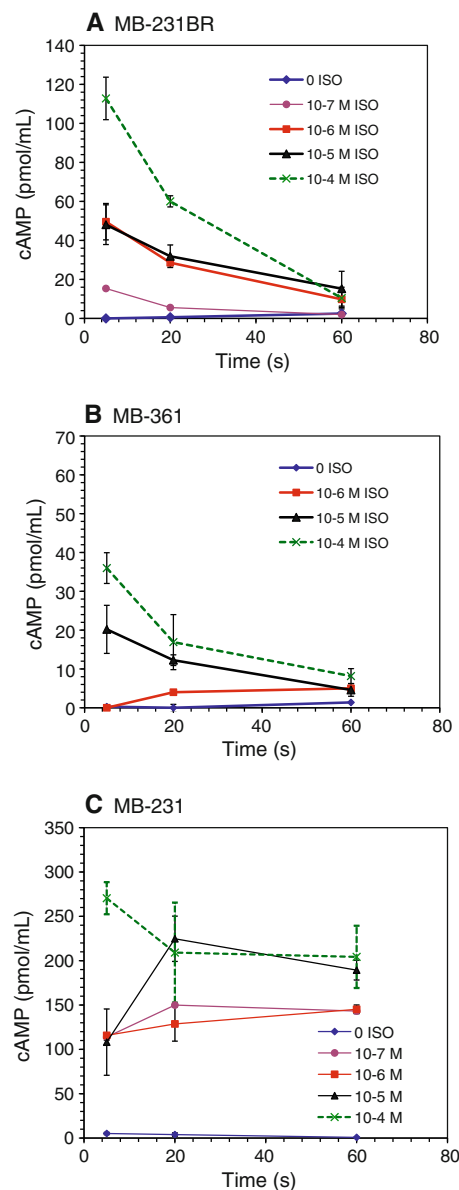


**Fig. 2** Kinetics of cAMP production with  $\beta$ -AR activation. Varying concentrations of ISO was added to **a** MB-231BR, **b** MB-361, or **c** MB-231. Intracellular cAMP production was measured after stimulating  $1 \times 10^6$  cells for 5, 20, or 60 min in the presence of  $100 \mu\text{M}$  IBMX. cAMP concentration was determined by ELISA. Results shown are mean  $\pm$  SEM of 2–5 experimental repetitions

**Table 1** Human breast cancer cell lines:  $\beta$ -AR binding sites and affinity

Cell line	Metastatic? <sup>a</sup>	Species	$B_{\text{max}}$ (M) (SEM)	Sites per cell (SEM)	$K_d$ (M)
MB-231	Yes	Human	$7.2 \times 10^{-11}$ (2.9)	13798 (4858)	$9.4 \times 10^{-11}$ (4.9)
MB-231BR	Yes	Human	$6.1 \times 10^{-11}$ (1.8)	11027 (3991)	$7.8 \times 10^{-11}$ (3.0)
MCF7	No	Human	$0.14 \times 10^{-11}$ (0.003)	297 (13)	$1.1 \times 10^{-11}$ (0.16)
MB-361	Yes	Human	$0.089 \times 10^{-11}$	160	$3.9 \times 10^{-11}$

<sup>a</sup> Metastatic in mice

cAMP. The reaction was conducted in the presence of the phosphodiesterase inhibitor IBMX to prevent hydrolysis of cAMP and to minimize the possibility that potential variation in phosphodiesterase activity contributed to differences in  $\beta$ -AR-induced intracellular cAMP. cAMP accumulation was measured after 5 min incubation with  $10^{-4}$  M isoproterenol (ISO), a non-selective  $\beta$ -AR agonist (Fig. 1b). MB-231 and MB-231BR produced much more cAMP relative to the moderate responses by MB-361 and MCF7, as predicted by  $\beta$ -AR expression. Moreover, the magnitude of the cAMP response was approximately 2.5-fold higher in MB-231 compared to MB-231BR, despite the fact that MB-231 and MB-231BR expressed equivalent numbers of  $\beta$ -AR per cell. Non-stimulated, basal cAMP levels were near the level of detection of the ELISA (1 pmol/ml) in MB-231BR and MB-361, but were somewhat elevated (5 pmol/ml) in MB-231 and MCF7 (Fig. 1b).

To determine if the differences in the  $\beta$ -AR-induced cAMP response between MB-231 and MB-231BR reflected altered kinetics, intracellular cAMP was measured in MB-231 and MB-231BR with varying concentrations of ISO at 5, 20, and 60 min. The cAMP response of the low

$\beta$ -AR-expressing cell line MB-361 was included for comparison. In MB-231BR, a rapid rise and decline in intracellular cAMP was observed at all ISO concentrations ( $\geq 0.1$   $\mu$ M) tested within the 60-min time period (Fig. 2a). Similarly, in MB-361, in response to high concentrations of ISO, cAMP rose rapidly and declined to near baseline by 60 min (Fig. 2b). In marked contrast, in MB-231,  $\beta$ -AR-induced cAMP remained elevated throughout the 60-min time period at all ISO concentrations tested (Fig. 2c). The functional implications of these differences in  $\beta$ -AR signaling capacity were next investigated in vitro.

### $\beta$ -AR stimulation and VEGF production

Several reports have demonstrated that  $\beta$ -AR activation of a variety of tumor cells in vitro increased VEGF [4, 10, 13]. Therefore, we predicted that  $\beta$ -AR stimulation would increase constitutive VEGF production by the breast cancer cell lines, and the magnitude of the response would reflect the magnitude of the  $\beta$ -AR-induced cAMP response. The  $\beta_2$ -AR-selective agonist terbutaline (TERB) ( $\geq 0.1$   $\mu$ M) (Fig. 3a) and ISO (data not shown) increased VEGF

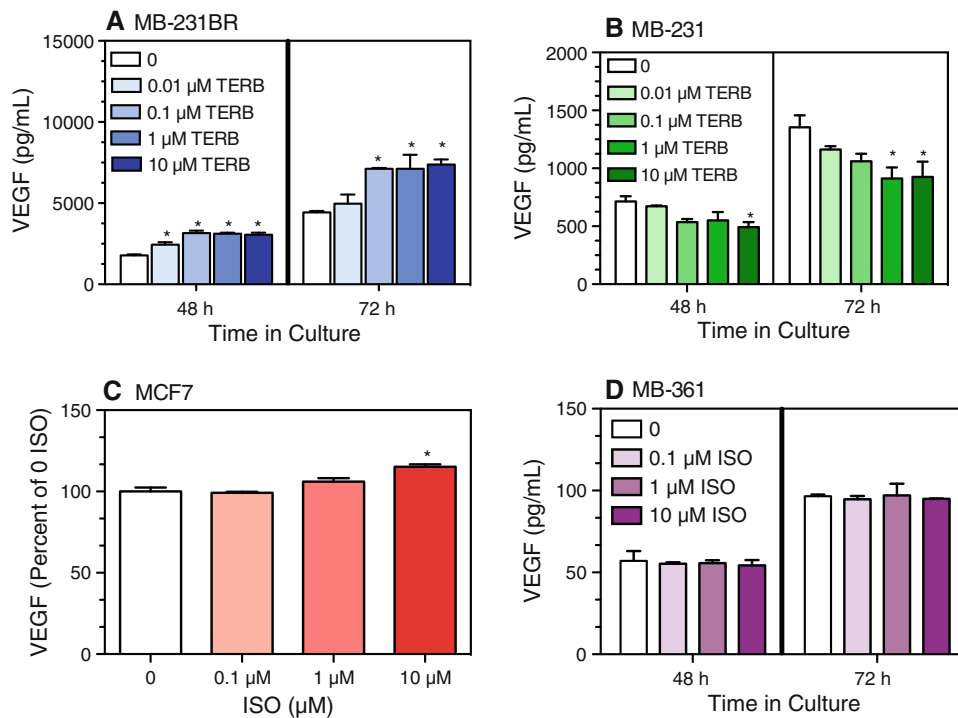


**Fig. 3**  $\beta$ -AR activation and VEGF production by breast cancer cell lines in vitro. The non-selective  $\beta$ -AR agonist ISO or the  $\beta_2$ -AR-agonist TERB were added at varying concentrations to **a** MB-231BR, **b** MB-231, **c** MCF7, and **d** MB-361. Cell-free supernatants were harvested at the indicated time points, and VEGF concentration was determined by ELISA. For **c** MCF7, results shown are at 72 h in culture. Results shown are mean  $\pm$  SEM from 2 to 4 experimental repetitions per cell line. **a, b** One-way ANOVA: main effects of

TERB,  $P < 0.05$  at each time point; **c** for MCF7, VEGF values differed between two experimental repetitions, therefore results from two experimental repetitions were normalized relative to 0 ISO. Baseline VEGF for the two MCF7 experiments at 72 h was 412 and 316 pg/ml. Main effect of drug treatment,  $P = 0.01$ . **d** For MB-361, no main effect of drug treatment. Asterisks indicate statistically significant versus 0 ISO at the respective time point in culture by Newman-Keuls post hoc analysis ( $P < 0.05$ )

production by MB-231BR at 48 and 72 h in culture. In contrast,  $\beta$ -AR stimulation with  $\geq 0.1 \mu\text{M}$  TERB (Fig. 3b) and ISO (data not shown) inhibited VEGF production by MB-231. The highest concentration of ISO tested ( $10 \mu\text{M}$ ) slightly increased production of VEGF by MCF7 (Fig. 3c) and did not alter VEGF production by MB-361 (Fig. 3d).

NE, an endogenous AR ligand, has mixed affinity for both  $\beta$ -AR and  $\alpha$ -AR. NE increased VEGF production by MB-231BR at 48 and 72 h in culture (Fig. 4a). The NE-induced effect in MB-231BR was completely blocked by the  $\beta_2$ -selective blocker ICI 118,551 (ICI) (Fig. 4b). In contrast, NE inhibited VEGF production by MB-231 (Fig. 4c), and the NE-induced inhibition was completely blocked by an equimolar concentration of ICI (Fig. 4d). The effectiveness of low concentrations of the  $\beta_2$ -AR selective agonist TERB and the ability of the  $\beta_2$ -AR selective blocker to block NE-induced effects indicate that  $\beta_2$ -AR activation elicits opposite effects on VEGF production by MB-231 and MB-231BR.

### $\beta$ -AR-induced IL-6 production

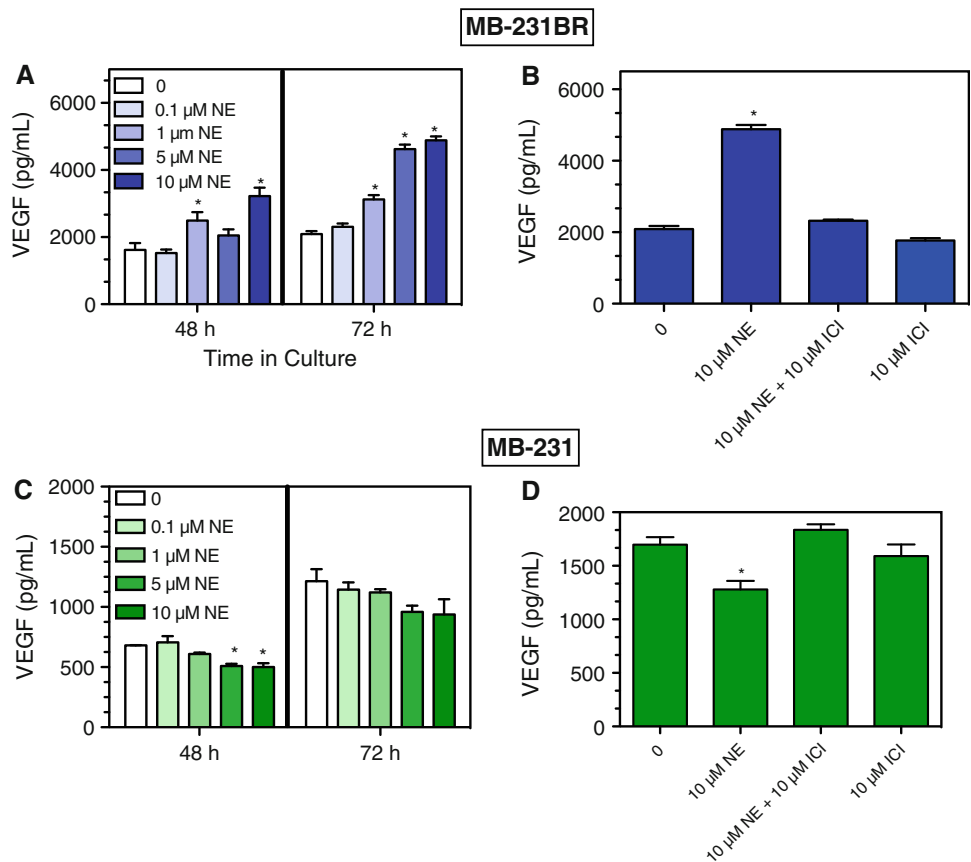
To further investigate this divergent response, we next determined whether other tumor-produced cytokines are similarly altered by  $\beta$ -AR stimulation. IL-6 is a

multifunctional, proinflammatory cytokine that has been implicated in tumor progression and metastasis [17, 18]. Under our low serum culture conditions, constitutive production of IL-6 is detectable in MB-231 and MB-231BR, but not by MCF7 or MB-361 (data not shown).  $\beta_2$ -AR activation with TERB increased IL-6 production in MB-231BR (Fig. 5a) and MB-231 (Fig. 5d) at 48 and 72 h in culture. Moreover, the magnitude of the TERB response was greater in MB-231 compared to MB-231BR (at 72 h,  $10 \mu\text{M}$  TERB compared to 0 drug,  $\sim 5\times$  versus  $\sim 3\times$ , respectively). NE also increased IL-6 in both MB-231 BR and MB-231, but at higher concentrations compared to TERB (Fig. 5b, e). ICI completely prevented the response to NE in MB-231BR (Fig. 5c) and in MB-231 (Fig. 5f). These results indicate that  $\beta_2$ -AR activation increases IL-6 production by MB-231 and MB-231BR.

### $\beta$ -AR stimulation and Cellular Proliferation

To determine if the  $\beta$ -AR-induced alterations in VEGF and IL-6 production are a function of altered cell number, we measured proliferation using a fluorescent DNA binding dye. ISO did not alter proliferation at any time point. Figure 6 shows the normalized results at 72 h in culture by MB-231BR (Fig. 6a) or MB-231 (Fig. 6b).

**Fig. 4** NE-induced alterations in VEGF production are blocked by a  $\beta_2$ -AR-specific antagonist. NE was added at varying concentrations to MB-231BR (a, b) and MB-231 (c, d). VEGF concentration was determined in cell-free supernatants at 48 h (a, c) or 72 h (a–d) in culture. The  $\beta_2$ -AR blocker ICI was added 30 min prior to NE. Results shown are representative of 2–3 experimental repetitions. **a–d** By one-way ANOVA, main effects of NE at each time point,  $P < 0.05$ . In **a** and **c**, asterisks indicate statistical significance versus 0 ISO at the respective time point by Newman–Keuls ( $P < 0.05$ ). In **b** and **d**, asterisks indicate group which is statistically different versus all other groups by Newman–Keuls analysis ( $P < 0.05$ ). No other group differences were detected



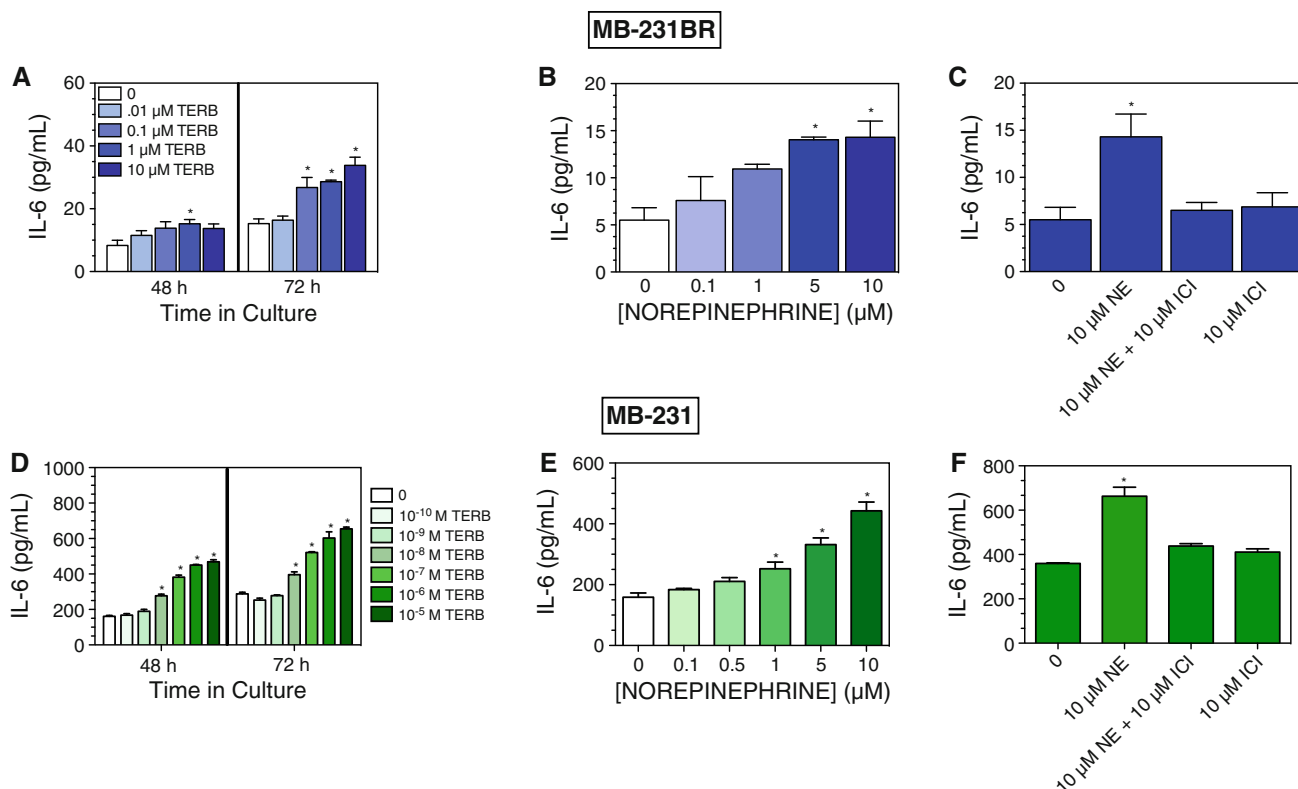


**Fig. 5**  $\beta$ -AR stimulation increases IL-6 production by MB-231BR and MB-231. TERB (a, d) or NE (b, e) were added at varying concentrations to (a–c) MB-231BR or MB-231 (d–f). The  $\beta_2$ -AR blocker ICI was added 30 min prior to NE. Cell-free supernatants were harvested 48 h (a, d) or 72 h (a–f) later. IL-6 concentration was determined by ELISA. Results shown are representative of 2–3 experimental repetitions. In a–f, by one-way ANOVA, significant

main effects of drug treatment were detected ( $P < 0.05$ ). In (a, b, d, e), asterisks indicate significantly different versus 0 ISO at the respective time point in culture by Newman–Keuls ( $P < 0.05$ ). In c and f, asterisk indicates group which is significantly different versus all other groups by Newman–Keuls ( $P < 0.05$ ). No other group differences were detected

Regulation of VEGF and IL-6 production by the adenylyate cyclase-cAMP-PKA pathway

We next tested the role of effectors involved in the classical  $\beta$ -AR-adenylyate cyclase-cAMP pathway in the  $\beta$ -AR-mediated VEGF and IL-6 responses. Forskolin directly activates adenylyate cyclase to elevate cAMP independently of  $\beta$ -AR. In MB-231BR, forskolin (0.1 and 1  $\mu$ M) increased VEGF production, but at 10  $\mu$ M, forskolin-induced VEGF production was attenuated at 48 h and eliminated at 72 h in culture (Fig. 7a). In MB-231, VEGF production was reduced at 48 h (data not shown) and at 72 h (Fig. 7c). In contrast, IL-6 production was increased by forskolin at 48 h (data not shown) and at 72 h in culture in both MB-231BR (Fig. 7b) and MB-231 (Fig. 7d). These forskolin-induced alterations in VEGF and IL-6 production are similar qualitatively to those elicited by  $\beta$ -AR stimulation in both cell lines.

To determine if cAMP activation of PKA plays a role in the  $\beta$ -AR-induced responses in MB-231 and MB-231BR, PKA activity was inhibited by KT 5720, a blocker with

high specificity for PKA. KT 5720 (1  $\mu$ M) completely blocked TERB-induced alterations in VEGF production by MB-231BR (Fig. 8a) and by MB-231 (Fig. 8b). We noted that PKA blockade in the absence of  $\beta$ -AR stimulation slightly inhibited constitutive VEGF production by MB-231BR (Fig. 8a). These results demonstrate a role for  $\beta$ -AR-induced PKA activation in MB-231 and MB-231BR VEGF production.

In terms of IL-6 production, KT 5720 did not alter the  $\beta$ -AR-induced increase in IL-6 production by MB-231BR in response to low or high concentrations of TERB (Fig. 9a, b). In MB-231, KT 5720 ( $\leq 5$   $\mu$ M) alone increased IL-6 production (Fig. 9c), suggesting that constitutively activated PKA in MB-231 inhibits IL-6 production. In the presence of TERB, increasing concentrations of KT 5720 did not block the response to 0.1 or 1  $\mu$ M TERB, but instead augmented the TERB-induced increase in IL-6 production by MB-231 (Fig. 9c), the magnitude being similar to the KT 5720-induced enhancement in the absence of TERB. These results suggest that the  $\beta$ -AR-induced increase in IL-6 production is not dependent

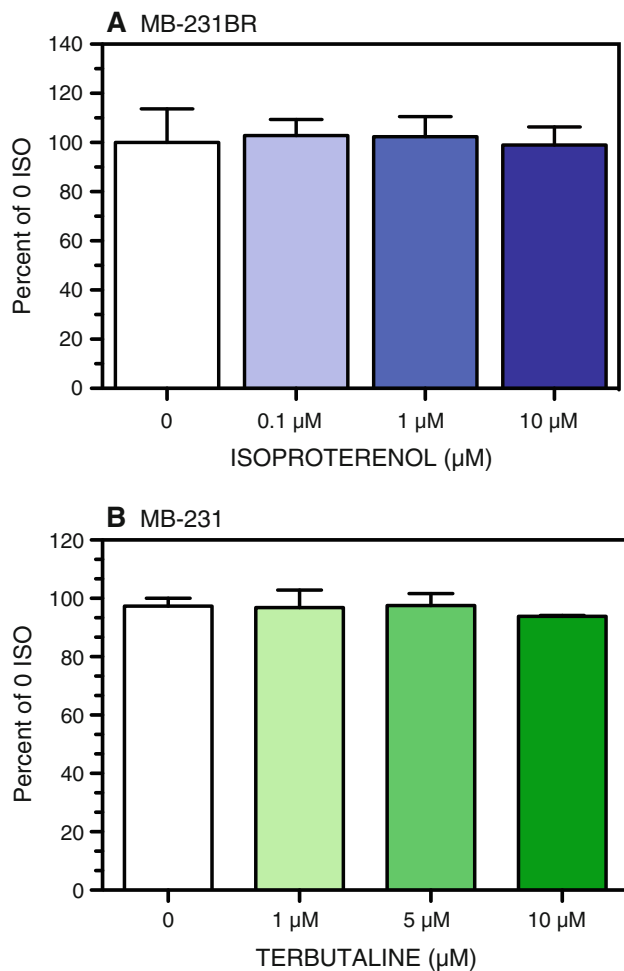


**Fig. 6**  $\beta$ -AR activation does not alter MB-231BR and MB-231 proliferation in vitro. Proliferation of **a** MB-231BR and **b** MB-231 was measured at 72 h in culture with and without the non-selective  $\beta$ -AR agonist ISO or the  $\beta_2$ -AR selective agonist TERB. Results from individual experimental repetitions were normalized to percent of 0 ISO/TERB and averaged across 2–5 experimental repetitions. One-way ANOVA revealed no significant main effects of drug treatment

on PKA activation. Furthermore, it appears that constitutive PKA activation in MB-231 dampens IL-6 production. Together, these results demonstrate that  $\beta$ -AR-induced alterations in constitutive production of VEGF, but not IL-6, are dependent on PKA activation.

## Discussion

Despite the evidence that  $\beta$ -AR expressed by breast, ovarian, and other tumor cell types can modulate tumor growth and metastasis, few reports have evaluated the connection between tumor cell  $\beta$ -AR expression, signaling capacity, and functional capacity in breast cancer. In two human breast adenocarcinoma cell lines (MCF7 and MB-361) with low  $\beta$ -AR expression and signaling capacity,

$\beta$ -AR stimulation elicited little or no change in production of VEGF, a key driver of tumor angiogenesis. In MB-231, a model of aggressive breast cancer, we confirmed high  $\beta$ -AR density [19] and also demonstrated that MB-231BR, a variant of MB-231, retained high  $\beta$ -AR expression. However, the  $\beta$ -AR-induced cAMP response by MB-231 was greater and prolonged compared to MB-231BR. Functionally,  $\beta$ -AR stimulation elicited directionally opposite changes in VEGF production in MB-231 and MB-231BR, while production of IL-6 was increased by  $\beta$ -AR stimulation in both breast cancer cell lines. Elevating cAMP independently of  $\beta$ -AR elicited alterations in VEGF and IL-6 production that mimic the respective responses to  $\beta$ -AR, indicating that cAMP is a key mediator of the functional responses produced by  $\beta$ -AR stimulation. Finally, in MB-231 and MB-231BR, PKA activation was necessary for  $\beta$ -AR-induced alterations in VEGF, but not IL-6 production, indicating that  $\beta$ -AR in MB-231 and MB-231BR regulates VEGF and IL-6 production through divergent pathways with cAMP as a central mediator. These results imply that the impact of direct tumor cell  $\beta$ -AR stimulation, or its antagonism, will vary considerably from individual to individual, depending on tumor cell  $\beta$ -AR density and signaling capacity.

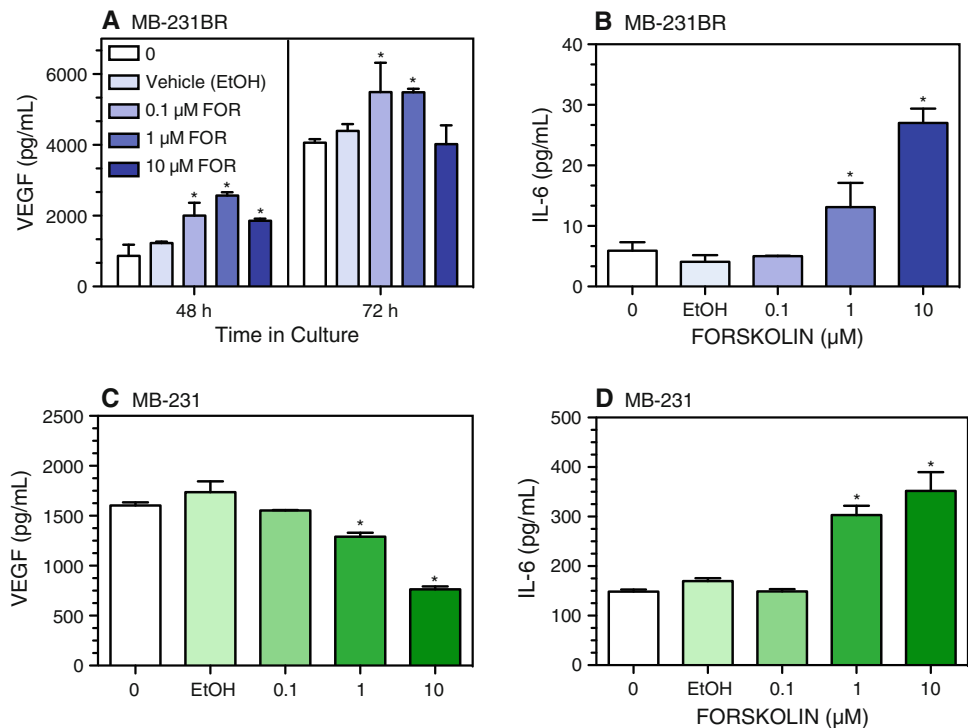
### Heterogeneity of $\beta$ -AR signaling capacity

In all four human breast cancer cell lines, the peak  $\beta$ -AR-induced cAMP response generally reflected  $\beta$ -AR density, demonstrating coupling between  $\beta$ -AR, Gs, and adenylyl cyclase. Furthermore, MB-231BR and MB-361 displayed typical  $\beta$ -AR desensitization, with a rapid peak and decline in cAMP production upon exposure to ISO. In MB-231, however, the magnitude and prolonged duration of  $\beta$ -AR-induced cAMP is evidence of impaired  $\beta$ -AR feedback mechanisms. We measured cAMP induction in the presence of the phosphodiesterase inhibitor IBMX, eliminating the possibility that differences in phosphodiesterase expression may contribute to differences in cAMP response kinetics. Preliminary evidence from our laboratory points to impaired ligand-induced  $\beta$ -AR desensitization in MB-231 (data not shown). The prolonged cAMP response in MB-231 compared to MB-231BR has profound functional significance, as discussed below.

$\beta$ -AR-induced alterations in VEGF production are dependent on  $\beta$ -AR density, cAMP, and PKA activation

In the four breast cancer cell lines, high  $\beta$ -AR density predicted  $\beta$ -AR-induced alterations, but not directionality, in VEGF production. In the high  $\beta$ -AR-expressing cell lines, MB-231 and MB-231BR, we demonstrated that the opposing effects of  $\beta$ -AR activation were mediated by the

**Fig. 7** Forskolin-induced alterations in VEGF and IL-6 production. MB-231BR (a, b) and MB-231 (c, d) were incubated with varying concentrations of forskolin, the EtOH vehicle for 10  $\mu$ M forskolin, or medium only for 48 h (a) or 72 h (a–d). VEGF or IL-6 concentration in cell-free supernatants was measured by ELISA. Results are representative of two experimental repetitions per cell line. In (a–d), one-way ANOVA at each time point revealed main effects of drug treatment,  $P < 0.0001$ . Asterisks indicate different versus 0 drug at the respective time point by Newman–Keuls post hoc analysis ( $P < 0.05$ )



same adrenergic receptor subtype, the  $\beta_2$ -AR. One possible explanation for the differences in the  $\beta$ -AR-induced VEGF responses is divergence from the classical adenylate cyclase-cAMP-PKA pathway as has been described in other cells [6–8]. However, the  $\beta$ -AR-induced alterations in VEGF were mimicked by cAMP elevation and required PKA, implying that effectors downstream of PKA lead to the differential  $\beta$ -AR regulation of VEGF in MB-231 and MB-231BR.

Our working hypothesis is that PKA can phosphorylate multiple substrates with the capacity to either facilitate or inhibit VEGF production in breast cancer cells. The forskolin response in MB-231BR provides evidence for cAMP-mediated fine-tuning of VEGF production, with attenuation of forskolin-induced VEGF production at high-forskolin concentrations (Fig. 7a). Note, however, that such an inhibitory mechanism does not appear to be active with high concentrations of TERB in MB-231BR, perhaps due to the ability of MB-231BR to rapidly down regulate  $\beta$ -AR-induced cAMP production (Fig. 2a). We speculate that the cAMP inhibitory pathway in MB-231 predominates due to the inability to down regulate  $\beta$ -AR-induced cAMP production. Elucidation of the molecular pathways involved in fine-tuning VEGF synthesis by breast tumor cells specifically identification of PKA substrates responsible for regulating VEGF in MB-231 and MB-231BR may yield new therapeutic targets to inhibit tumor cell VEGF production and subsequent tumor angiogenesis. This is particularly important for aggressive breast cancer phenotypes, such as

the “triple negative” phenotype that MB-231 models, for which effective therapies are limited.

It is interesting to speculate that the capacity for  $\beta$ -AR stimulation to elevate VEGF production by MB-231BR may have contributed to the selection pressure that produced this brain-seeking variant of MB-231. However, MB-361, isolated from a human brain metastasis, exhibits very low  $\beta$ -AR expression, a correspondingly low cAMP response to  $\beta$ -AR stimulation, and no change in VEGF production with  $\beta$ -AR stimulation. Therefore, it is apparent that  $\beta$ -AR-induced VEGF production observed in MB-231BR is not a general feature of breast adenocarcinomas isolated from the brain. However, since both MB-231 and MB-231BR express high levels of  $\beta$ -AR and are metastatic in mice, activation of high-density  $\beta$ -AR expressed by breast cancer cells may represent a mechanism to promote metastasis to secondary sites in breast cancer.

$\beta$ -AR-induced IL-6 production in MB-231 and MB-231BR is dependent on cAMP, but independent of PKA activation

IL-6 has been shown to participate in the epithelial–mesenchymal transition in human breast cancer cells and is associated with advanced breast tumor stage and poor prognosis [17, 18, 20, 21].  $\beta$ -AR-induced IL-6 production has been observed in a variety of normal cell types [8, 22] and tumor cell types [10, 23, 24], even in the absence of a pro-inflammatory stimulus [6]. IL-6 production by MB-361

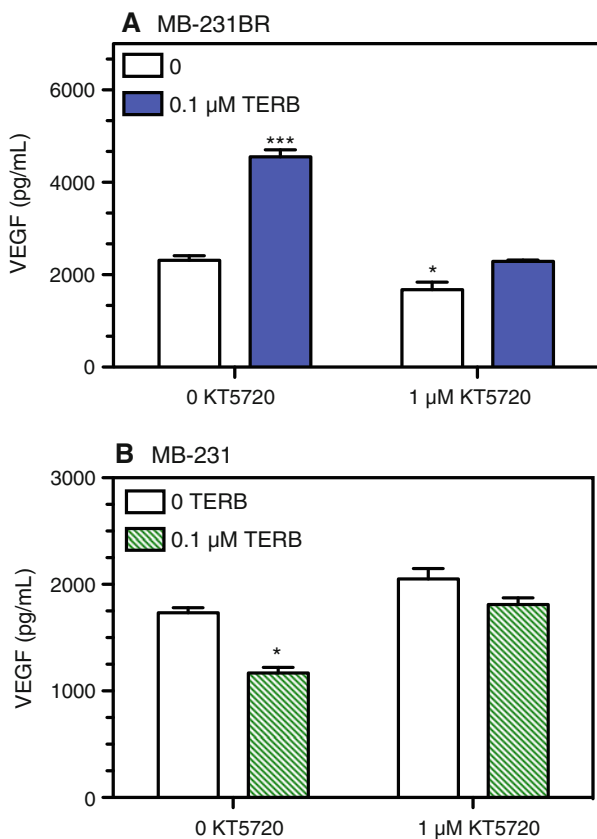


**Fig. 8** PKA inhibition prevents TERB-induced alterations in VEGF production by MB-231BR and MB-231. **a** MB-231BR and **b** MB-231 were stimulated with 0.1 μM TERB. KT 5720 (1 μM) was added 30 min prior to addition of TERB. Supernatants were harvested 72 h after initiation of culture. Results are representative of at least two experimental repetitions. In **a** and **b**, significant main effects of drug treatment were analyzed by Newman–Keuls post hoc analysis. In **a**, \*\*\* indicates different versus all other groups,  $P < 0.001$ ; \* indicates group which is significantly different versus 0 KT 5720, 0 TERB group. In **b**, \* indicates group which is significantly different from all other groups, with no other group differences detected

and MCF7 was undetectable under our culture conditions, and  $\beta$ -AR stimulation did not induce IL-6 production in these cell lines (data not shown). MB-231 and MB-231BR produce detectable IL-6. Its production in both cell lines is elevated by  $\beta_2$ -AR stimulation, and the effect is mimicked by a non- $\beta$ AR-induced elevation of cAMP, similar to VEGF. However, unlike VEGF, PKA inhibition did not significantly block  $\beta$ -AR-induced IL-6 production, indicative of a largely PKA-independent response to  $\beta$ -AR stimulation. The cAMP pathway driving IL-6 production also appears to lack an inhibitory component in response to high-cAMP concentrations, unlike VEGF [for example, compare the forskolin-induced IL-6 response to VEGF in MB-231BR (Fig. 7a vs. b)]. These results are indicative of a divergence in the  $\beta$ -AR-induced pathway immediately downstream of cAMP.

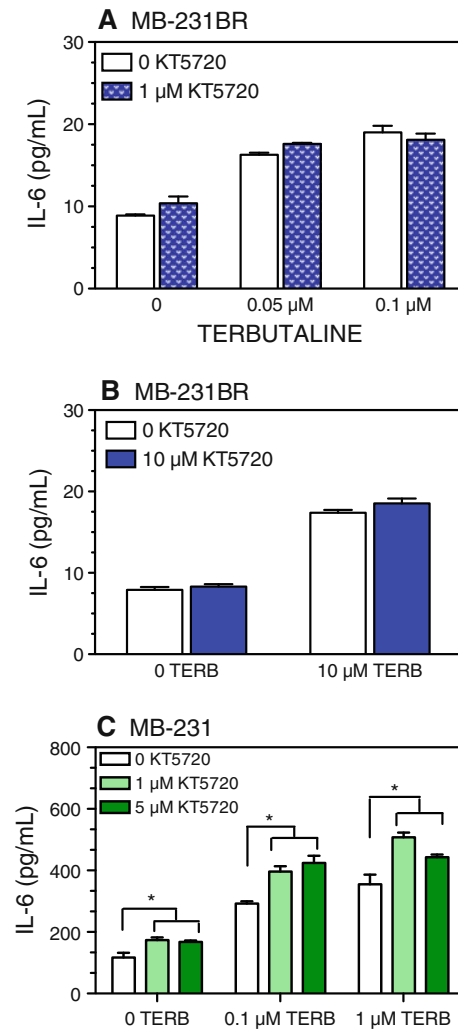


**Fig. 9** PKA inhibition does not block TERB-induced IL-6 production by MB-231BR and MB-231. MB-231BR (**a**, **b**) and MB-231 (**c**) were stimulated with varying concentrations of TERB and/or KT 5720. KT 5720 was added 30 min prior to addition of TERB. Supernatants were harvested 72 h after initiation of culture. Results are representative of at least two experimental repetitions for each experimental condition. By two-way ANOVA, in **a** and **b**, a main effect of TERB ( $P < 0.001$ ) was detected with no significant effects of KT 5720 or interaction between TERB and KT 5720. In **c**, main effects of TERB ( $P < 0.001$ ) and KT 5720 ( $P < 0.001$ ), and a significant TERB by KT 5720 interaction ( $P = 0.0063$ ) were detected. Asterisks indicates significantly different versus the corresponding 0 KT 5720 group by Newman–Keuls post hoc analysis ( $P < 0.05$ )

We also noted that in the absence of  $\beta$ -AR stimulation, PKA inhibition increased IL-6 production in MB-231, but not in MB-231BR (Fig. 9), suggesting that constitutive PKA activation in MB-231 may inhibit IL-6 production. A low level of constitutive PKA activation is consistent with the elevated basal cAMP detected in MB-231 (Fig. 1b). Understanding the intracellular pathway underlying the IL-6 response to  $\beta$ -AR stimulation is critical to blocking

production of this proinflammatory cytokine to inhibit tumor development.

Increased  $\beta$ -AR VEGF and IL-6 production is not associated with increased cellular proliferation

$\beta$ -AR activation did not alter MB-231 or MB-231BR proliferation in vitro. Other investigators have shown reduced MB-231 proliferation with exposure to  $\beta$ -AR agonists in vitro [19, 25]. In our hands, MB-231 proliferation was inhibited 10–15% at the highest concentration of ISO tested (10  $\mu$ M), but this effect was not blocked by  $\beta$ -AR antagonists (data not shown). Carie and Sebt, utilizing an atypical  $\beta$ -AR agonist (ARA-211) reported reduced MB-231 proliferation in the presence of ARA-211, and this effect was blocked by a  $\beta$ -blocker [25]. Interestingly, ARA-211 administration in vivo strongly inhibited tumor growth, and even induced tumor regression, but the  $\beta$ -AR agonist ISO was much less effective. Functional differences between agonists may indicate that signal strength or spatial/temporal aspects of the cAMP response may also contribute to functional heterogeneity to  $\beta$ -AR stimulation in breast cancer cells.

Our inability to demonstrate increased  $\beta$ -AR-induced VEGF production in vitro by MB-231 was unexpected. Thaker et al. showed that chronic stress exposure increased VEGF production in vivo in MB-231 tumors through a  $\beta$ -AR-mediated mechanism [1], but a direct effect of tumor cell  $\beta$ -AR stimulation in vivo was not tested with MB-231, leaving open the possible involvement of VEGF-expressing stromal cells (such as macrophages) in the stress response. In the context of primary breast tumors,  $\beta$ -AR-expressing cells of the tumor stroma may also contribute to  $\beta$ -AR-induced alterations in tumor pathogenesis and most likely involve multiple mechanisms, including altered angiogenesis and/or immunosuppression in vivo [3]. If breast tumor cells express no or low  $\beta$ -AR, as shown here with MCF7 and MB-361,  $\beta$ -AR-mediated alterations in tumor pathogenesis may still be expected. Our in vitro results demonstrate the potential for direct  $\beta$ -AR stimulation of high  $\beta$ -AR-expressing tumor cells altering proangiogenic factor production in vivo. Our goals are to determine the role of  $\beta$ -AR stimulation in breast tumor pathogenesis in vivo and to determine the relative contribution of the variety of  $\beta$ -AR-expressing cells to  $\beta$ -AR stimulation in primary breast tumors.

## Conclusions

The existence of a  $\beta$ -AR-driven proangiogenic pathway in tumor cells suggests that pharmacological  $\beta$ -AR blockade, commonly used in the treatment of cardiovascular disease,

may effectively block undesirable effects of stress exposure and subsequent release of NE. In order to pursue  $\beta$ -AR blockade as a therapeutic option, it is important to understand the ubiquity of  $\beta$ -AR expression, signaling, and function in breast tumors. We have demonstrated heterogeneity in  $\beta$ -AR expression and signaling capacity, and only in the high  $\beta$ -AR-expressing cell lines did the endogenous neurotransmitter NE markedly alter VEGF and IL-6 production. Furthermore, in high  $\beta$ -AR expressing cell lines, differences in  $\beta$ -AR signaling capacity can lead to disparate functional effects, especially with regard to VEGF production. These results suggest that blocking  $\beta$ -AR on tumor cells may reduce stress-induced production of proangiogenic factors, but caution must be used in employing  $\beta$ -AR blockers. For instances, depending on  $\beta$ -AR density and signaling capacity, NE release may *inhibit* tumor cell VEGF production, and therefore  $\beta$ -AR blockade may *increase* VEGF production. Future studies will explore the response of a variety of breast cancer types to  $\beta$ -AR stimulation in vivo so that more accurate predictions can be made regarding responsiveness of breast tumors to  $\beta$ -AR stimulation and the potential impact of  $\beta$ -AR blockade.

**Acknowledgments** This work was supported by Department of Defense IDEA Award (W81XWH-10-01-008), National Institutes of Health (1 R21 CA152777-01), and by the Breast Cancer Coalition of Rochester to KSM, Department of Defense Era of Hope Scholar Research Award (W81XWH-09-1-0405), National Institutes of Health Director's New Innovator Award (1 DP2 OD006501-01), and Pew Scholar in the Biomedical Sciences Award to EBB, and Department of Defense Predoctoral Training Award (W81XWH-10-1-0058) to MJS. MJS is a trainee in the Medical Scientist Training Program funded by NIH T32 GM07356. The content is solely the responsibility of the authors and does not necessarily represent the official views of the National Institute of General Medical Sciences or National Institutes of Health. We thank Kathryn Fitzgerald, Khawarl Liverpool, and Michael Storonsky for their excellent technical assistance.

## References

1. Thaker PH, Han LY, Kamat AA, Arevalo JM, Takahashi R, Lu C, Jennings NB, Armaiz-Pena G, Bankson JA, Ravoori M, Merritt WM, Lin YG, Mangala LS, Kim TJ, Coleman RL, Landen CN, Li Y, Felix E, Sanguino AM, Newman RA, Lloyd M, Gershenson DM, Kundra V, Lopez-Berestein G, Lutgendorf SK, Cole SW, Sood AK (2006) Chronic stress promotes tumor growth and angiogenesis in a mouse model of ovarian carcinoma. *Nat Med* 12(8):939–944
2. Raju B, Haug SR, Ibrahim SO, Heyeraas KJ (2007) Sympathectomy decreases size and invasiveness of tongue cancer in rats. *Neuroscience* 149(3):715–725
3. Sloan EK, Priceman SJ, Cox BF, Yu S, Pimentel MA, Tangkanangkul V, Arevalo JM, Morizono K, Karanikolas BD, Wu L, Sood AK, Cole SW (2010) The sympathetic nervous system induces a metastatic switch in primary breast cancer. *Cancer Res* 70(18):7042–7052. doi:10.1158/0008-5472.CAN-10-0522

4. Yang EV, Sood AK, Chen M, Li Y, Eubank TD, Marsh CB, Jewell S, Flavahan NA, Morrison C, Yeh PE, Lemeshow S, Glaser R (2006) Norepinephrine up-regulates the expression of vascular endothelial growth factor, matrix metalloproteinase (MMP)-2, and MMP-9 in nasopharyngeal carcinoma tumor cells. *Cancer Res* 66(21):10357–10364
5. Shakhar G, Ben-Eliyahu S (1998) In vivo  $\beta$ -adrenergic stimulation suppresses natural killer activity and compromises resistance to tumor metastasis in rats. *J Immunol* 160:3251–3258
6. Tan KS, Nackley AG, Satterfield K, Maixner W, Diatchenko L, Flood PM (2007) Beta2 adrenergic receptor activation stimulates pro-inflammatory cytokine production in macrophages via PKA- and NF-kappaB-independent mechanisms. *Cell Signal* 19(2): 251–260. doi:10.1016/j.cellsig.2006.06.007
7. Pullar CE, Isseroff RR (2006) The beta 2-adrenergic receptor activates pro-migratory and pro-proliferative pathways in dermal fibroblasts via divergent mechanisms. *J Cell Sci* 119(Pt 3):592–602
8. Yin F, Wang YY, Du JH, Li C, Lu ZZ, Han C, Zhang YY (2006) Noncanonical cAMP pathway and p38 MAPK mediate beta2-adrenergic receptor-induced IL-6 production in neonatal mouse cardiac fibroblasts. *J Mol Cell Cardiol* 40(3):384–393. doi: 10.1016/j.yjmcc.2005.12.005
9. Weil J, Benndorf R, Fredersdorf S, Griese DP, Eschenhagen T (2003) Norepinephrine upregulates vascular endothelial growth factor in rat cardiac myocytes by a paracrine mechanism. *Angiogenesis* 6(4):303–309
10. Yang EV, Kim SJ, Donovan EL, Chen M, Gross AC, Webster Marketon JJ, Barsky SH, Glaser R (2009) Norepinephrine upregulates VEGF, IL-8, and IL-6 expression in human melanoma tumor cell lines: implications for stress-related enhancement of tumor progression. *Brain Behav Immun* 23(2):267–275
11. Fredriksson JM, Lindquist JM, Bronnikov GE, Nedergaard J (2000) Norepinephrine induces vascular endothelial growth factor gene expression in brown adipocytes through a beta-adrenoreceptor/cAMP/protein kinase A pathway involving Src but independently of Erk1/2. *J Biol Chem* 275(18):13802–13811
12. Banfi C, Cavalca V, Veglia F, Brioschi M, Barcella S, Mussoni L, Boccotti L, Tremoli E, Biglioli P, Agostoni P (2005) Neurohormonal activation is associated with increased levels of plasma matrix metalloproteinase-2 in human heart failure. *Eur Heart J* 26(5):481–488
13. Lutgendorf SK, Cole S, Costanzo E, Bradley S, Coffin J, Jabbari S, Rainwater K, Ritchie JM, Yang M, Sood AK (2003) Stress-related mediators stimulate vascular endothelial growth factor secretion by two ovarian cancer cell lines. *Clin Cancer Res* 9(12):4514–4521
14. Yoneda T, Williams PJ, Hiraga T, Niewolna M, Nishimura R (2001) A bone-seeking clone exhibits different biological properties from the MDA-MB-231 parental human breast cancer cells and a brain-seeking clone in vivo and in vitro. *J Bone Miner Res* 16(8):1486–1495
15. Engel G, Hoyer D, Berthold R, Wagner H (1981) ( $\pm$ )[125Iodo]cyanopindolol, a new ligand for  $\beta$ -adrenoceptors: identification and quantification of subclasses of  $\beta$ -adrenoceptors in guinea pig. *Naun Schmiedebergs Arch Pharmacol* 317:277–285
16. Neve RM, Chin K, Fridlyand J, Yeh J, Baehner FL, Fevr T, Clark L, Bayani N, Coppe JP, Tong F, Speed T, Spellman PT, DeVries S, Lapuk A, Wang NJ, Kuo WL, Stilwell JL, Pinkel D, Albertson DG, Waldman FM, McCormick F, Dickson RB, Johnson MD, Lippman M, Ethier S, Gazdar A, Gray JW (2006) A collection of breast cancer cell lines for the study of functionally distinct cancer subtypes. *Cancer Cell* 10(6):515–527. doi:10.1016/j.ccr.2006.10.008
17. Sansone P, Storci G, Tavoroli S, Guarnieri T, Giovannini C, Taffurelli M, Ceccarelli C, Santini D, Paterini P, Marcu KB, Chieco P, Bonafe M (2007) IL-6 triggers malignant features in mammospheres from human ductal breast carcinoma and normal mammary gland. *J Clin Invest* 117(12):3988–4002. doi:10.1172/JCI32533
18. Hong DS, Angelo LS, Kurzrock R (2007) Interleukin-6 and its receptor in cancer: implications for Translational Therapeutics. *Cancer* 110(9):1911–1928. doi:10.1002/ncr.22999
19. Slotkin TA, Zhang J, Dancel R, Garcia SJ, Willis C, Seidler FJ (2000) Beta-adrenoceptor signaling and its control of cell replication in MDA-MB-231 human breast cancer cells. *Breast Cancer Res Treat* 60(2):153–166
20. Salgado R, Junius S, Benoy I, Van Dam P, Vermeulen P, Van Marck E, Huget P, Dirix LY (2003) Circulating interleukin-6 predicts survival in patients with metastatic breast cancer. *Int J Cancer* 103(5):642–646. doi:10.1002/ijc.10833
21. Sullivan NJ, Sasser AK, Axel AE, Vesuna F, Raman V, Ramirez N, Oberyszyn TM, Hall BM (2009) Interleukin-6 induces an epithelial-mesenchymal transition phenotype in human breast cancer cells. *Oncogene* 28(33):2940–2947. doi:10.1038/onc.2009.180
22. Rohrbach S, Engelhardt S, Lohse MJ, Werdan K, Holtz J, Muller-Werdan U (2007) Activation of AP-1 contributes to the beta-adrenoceptor-mediated myocardial induction of interleukin-6. *Mol Med* 13(11–12):605–614. doi:10.2119/2007-00071.Rohrbach
23. Nilsson MB, Armaiz-Pena G, Takahashi R, Lin YG, Trevino J, Li Y, Jennings N, Arevalo J, Lutgendorf SK, Gallick GE, Sanguino AM, Lopez-Berestein G, Cole SW, Sood AK (2007) Stress hormones regulate interleukin-6 expression by human ovarian carcinoma cells through a Src-dependent mechanism. *J Biol Chem* 282(41):29919–29926. doi:10.1074/jbc.M611539200
24. Nilsson MB, Langley RR, Fidler IJ (2005) Interleukin-6, secreted by human ovarian carcinoma cells, is a potent proangiogenic cytokine. *Cancer Res* 65(23):10794–10800. doi:10.1158/0008-5472.CAN-05-0623
25. Carie AE, Sebt SM (2007) A chemical biology approach identifies a beta-2 adrenergic receptor agonist that causes human tumor regression by blocking the Raf-1/Mek-1/Erk1/2 pathway. *Oncogene* 26(26):3777–3788. doi:10.1038/sj.onc.1210172



## Early impact of social isolation and breast tumor progression in mice

Kelley S. Madden<sup>a,\*</sup>, Mercedes J. Szpunar<sup>b</sup>, Edward B. Brown<sup>a</sup>

<sup>a</sup> Department of Biomedical Engineering, University of Rochester School of Medicine and Dentistry, Rochester, NY, USA

<sup>b</sup> Department of Pathology, University of Rochester School of Medicine and Dentistry, Rochester, NY, USA

### ARTICLE INFO

#### Article history:

Available online 17 May 2012

#### Keywords:

Social isolation  
Psychosocial stressor  
Breast cancer  
Norepinephrine  
Macrophages  
SCID mice

### ABSTRACT

Evidence from cancer patients and animal models of cancer indicates that exposure to psychosocial stress can promote tumor growth and metastasis, but the pathways underlying stress-induced cancer pathogenesis are not fully understood. Social isolation has been shown to promote tumor progression. We examined the impact of social isolation on breast cancer pathogenesis in adult female severe combined immunodeficiency (SCID) mice using the human breast cancer cell line, MDA-MB-231, a high  $\beta$ -adrenergic receptor (AR) expressing line. When group-adapted mice were transferred into single housing (social isolation) one week prior to MB-231 tumor cell injection into a mammary fat pad (orthotopic), no alterations in tumor growth or metastasis were detected compared to group-housed mice. When social isolation was delayed until tumors were palpable, tumor growth was transiently increased in singly-housed mice. To determine if sympathetic nervous system activation was associated with increased tumor growth, spleen and tumor norepinephrine (NE) was measured after social isolation, in conjunction with tumor-promoting macrophage populations. Three days after transfer to single housing, spleen weight was transiently increased in tumor-bearing and non-tumor-bearing mice in conjunction with reduced splenic NE concentration and elevated CD11b + Gr-1+ macrophages. At day 10 after social isolation, no changes in spleen CD11b+ populations or NE were detected in singly-housed mice. In the tumors, social isolation increased CD11b + Gr-1+, CD11b + Gr-1-, and F4/80+ macrophage populations, with no change in tumor NE. The results indicate that a psychological stressor, social isolation, elicits dynamic but transient effects on macrophage populations that may facilitate tumor growth. The transiency of the changes in peripheral NE suggest that homeostatic mechanisms may mitigate the impact of social isolation over time. Studies are underway to define the neuroendocrine mechanisms underlying the tumor-promoting effects of social isolation, and to determine the contributions of increased tumor macrophages to tumor pathogenesis.

© 2012 Elsevier Inc. All rights reserved.

### 1. Introduction

The emotional stress experienced by cancer patients can be associated with increased tumor progression (Antoni et al., 2006), but the biological pathways involved in stress-induced tumor progression are only beginning to be understood. In animal models of cancer, exposure to stressors potentiates tumor growth and metastasis in a variety of tumors (Hermes et al., 2009; Saul et al., 2005; Shakhbar and Ben-Eliyahu, 1998; Sloan et al., 2010; Thaker et al., 2006; Williams et al., 2009) suggesting that therapies targeting stress biochemical pathways may be effective in reducing tumor progression. Here we examine the impact of social isolation of adult mice, an ethologically relevant

stressor, on breast tumor growth. Social isolation in rodents elicits anxiety and other fearful behaviors (Hermes et al., 2009; Williams et al., 2009). Furthermore, chronic social isolation as experienced by humans has been linked to cancer (Reynolds and Kaplan, 1990), and is a risk factor for cancer mortality and other diseases (Hawkey and Cacioppo, 2003).

The sympathetic nervous system (SNS) is a major stressor pathway characterized by release of the catecholamines norepinephrine (NE) and epinephrine (EPI) from sympathetic noradrenergic nerves and from the adrenal medulla. Several lines of evidence point to a role for the SNS in modulating tumor progression. Regional ablation of sympathetic nerves depleted NE and reduced tumor growth (Raju et al., 2007). Stress-induced increase in tumor growth and/or metastasis can be prevented by pre-treatment with a  $\beta$ -AR blocker prior to stressor exposure or mimicked using  $\beta$ -AR agonists *in vivo* (Shakhbar and Ben-Eliyahu, 1998; Sloan et al., 2010; Thaker et al., 2006). Furthermore, using an ovarian cancer model, Thaker and colleagues showed that  $\beta$ -AR expression by the tumor cells was necessary for stressor-induced tumor growth (Thaker et al., 2006). It is interesting to note the variety of targets in stress- and

*Abbreviations:* IL-6, Interleukin 6; SNS, sympathetic nervous system; NE, norepinephrine; EPI, epinephrine;  $\beta$ -AR, beta-adrenergic receptors; VEGF, vascular endothelial growth factor.

\* Corresponding author. Address: Department of Biomedical Engineering, University of Rochester School of Medicine and Dentistry, RC Box 270168, Goergen Hall, Rochester, NY 14627, USA. Tel.: +1 585 273 5724; fax: +1 585 276 2254.

E-mail address: [Kelley\\_Madden@urmc.rochester.edu](mailto:Kelley_Madden@urmc.rochester.edu) (K.S. Madden).

or SNS-induced potentiation of tumor progression including cells of the immune system (for example, macrophages and natural killer cells) (Shakhar and Ben-Eliyahu, 1998; Sloan et al., 2010), angiogenesis (Thaker et al., 2006), and direct stimulation or inhibition of tumor proliferation (Slotkin et al., 2000). In addition to understanding the stress-induced neuroendocrine mediators/receptors that modulate tumor pathogenesis, it is also important to identify the target cells in order to predict the outcome of stress exposure and to develop therapies with minimal side effects.

The MDA-MB-231 cell line is a human mammary tumor adenocarcinoma representative of the more aggressive triple negative human breast cancer. MB-231 cells express high levels of  $\beta$ -AR, as detected by standard radioligand binding assay, but other breast cancer cell lines displayed a low level of  $\beta$ -AR expression and minimal responsiveness to NE *in vitro* (Madden et al., 2011). By contrast, NE stimulation of MB-231 cells inhibits VEGF production, and dramatically increases IL-6 production *in vitro*. With the view that MB-231 serves as a model of breast cancers expressing high levels of  $\beta$ -AR, we have begun testing the impact of stressor exposure on MB-231 tumor growth, using social isolation as an established model of a psychological stressor that can promote tumor progression, including spontaneous mammary tumor progression (Hermes et al., 2009; Thaker et al., 2006; Williams et al., 2009).

We report here that social isolation transiently increased tumor growth only when social isolation was initiated when tumors were palpable. These changes were associated with alterations in tumor macrophage populations early after social isolation and not associated with elevated tumor or peripheral NE concentration. The results demonstrate the complexity of the response of breast tumors to stressor exposure that needs to be better characterized before targeting stress hormones in the therapeutic treatment of breast cancer.

## 2. Materials and methods

### 2.1. Mice

Female severe combined immunodeficiency (SCID) (NOD.CB17-Prkdc<sup>scid</sup>/J) mice were purchased from The Jackson Laboratory, Bar Harbor, ME between 6 and 8 weeks of age, and were housed 5 per cage with food and water ad lib on a 12:12 light:dark cycle. SCID mice were provided acid water ad lib upon arrival. The mice were housed using microisolator technology to effect a biological barrier at the level of the individual cage. Upon initiation of the experiments, the antibiotic sulfamethoxazole and trimethoprim (Hi-Tech Pharmacol. Co., Amityville, NY) was included in the drinking water throughout the duration of the experiment. The antibiotic treatment was necessary in order to prevent the occasional pneumonia that developed in these immunodeficient mice. All experimental protocols were approved by the University of Rochester University Committee on Animal Resources.

### 2.2. Cell lines

MB-231 tumor cells (American Tissue Type Collection; Manassas, VA) were maintained in Dulbecco's Modified Essential Medium (DMEM) containing 4.5 g/L glucose, L-glutamine, penicillin/streptomycin and 10% fetal calf serum (FCS) (all from Gibco, Invitrogen Inc., Carlsbad, CA). MB-231 cells were employed experimentally within 3 months of acquiring and/or thawing, and were regularly tested for the absence of mycoplasma contamination.

### 2.3. Social isolation

SCID mice were allowed to adapt to group housing (5 per cage) for at least two weeks before being housed singly. Both group- and single-housed mice were housed in cages measuring 7.5"  $\times$  11"  $\times$  5".

### 2.4. Tumor implantation and measures

MB-231 ( $2\text{--}4 \times 10^6$  cells) was injected into a single mammary fat pad of NOD/SCID female mice in mice anesthetized with 90 mg/kg ketamine and 9 mg/kg xylazine. Mice were palpated weekly until tumors were detected. The shortest and longest diameters of each tumor were measured with calipers. Tumor volumes was calculated using the equation:  $0.5 \times \text{length} \times \text{width}^2$ .

### 2.5. Flow cytometry

Single suspensions from spleen or tumors were prepared by pressing tissue through a metal mesh into ice-cold PBS containing 10% fetal calf serum. Red blood cells were lysed using ammonium lysis buffer. After washing, the cells were counted and resuspended in phosphate buffered saline containing 1% bovine serum albumin and 0.25% sodium azide (flow wash). Macrophages were stained using three-color immunofluorescence. Cells ( $1.5 \times 10^6$ ) were incubated in 25  $\mu$ l FcBlock (anti-CD16, diluted 1:50; BD Biosciences,bdbiosciences.com) for 15 min at 4 °C. Rat anti-F4/80 (clone BM8; FITC-conjugated; Abcam Inc.; abcam.com), rat anti-CD11b (clone M1/70; Alexafluor 647-conjugated, BD Biosciences) and rat anti-Gr-1 (anti-Ly-6G and Ly-6C; clone RB6-8C5; PE-conjugated; BD Biosciences) were diluted 1:50 in flow wash. Antibodies (100  $\mu$ l) were incubated 30 min at 4 °C. Cells incubated in flow wash only served as autofluorescent controls. Cells were washed two times in flow wash, fixed in 0.5 ml PBS containing 1% paraformaldehyde, and stored in the dark at 4 °C for no longer than 2 weeks before analysis. Fluorescence was analyzed in the University of Rochester Flow Cytometry Core on a BD LSR II 18-Color flow cytometer. Forward scatter and side scatter gating was used to eliminate non-lymphoid cells from the analysis. Analysis gates were set based on the autofluorescent controls.

### 2.6. Cytokine and norepinephrine determination

For cytokines, tumor homogenates at a concentration of 4% w/v were prepared in RIPA buffer containing protease inhibitors (HALT Protease Inhibitor Cocktail, ThermoScientific; ThermoFisher.com). To measure NE, tumors were homogenized at a concentration of 1% w/v in 1 N HCl. Protein in homogenates was measured colorimetrically using a Pierce BCA Protein Assay kit (ThermoScientific). NE and tumor cytokines in the homogenates were measured by ELISA according to the manufacturer's instructions. A NE ELISA kit was purchased from Rocky Mountain Diagnostics. Mouse- and human-specific VEGF and IL-6 Quantikine kits (R and D Systems, Minneapolis, MN) are highly species specific with little or no cross-reactivity detected with the corresponding analyte from other species. As reported by the manufacturer and confirmed in our laboratory, the only (minimal) cross-reactivity detected is 0.2% cross-reactivity of human VEGF in the mouse VEGF ELISA. Serial dilutions of the tumor homogenates were tested to determine the optimal homogenate dilution for each analyte. Absorption was measured at 450 nm using a multiwell plate reader (Synergy HT, Biotek Instruments Inc., Winooski, VT). Curve fitting and sample concentration calculations were conducted with Gen5 software (Biotek). Results were normalized based on protein concentration or tissue wet weight.

### 2.7. Statistical analysis

Statistically significant differences between groups were determined using GraphPad Prism software. For all analyses,  $p < 0.05$  is considered statistically significant. When comparing two groups, *F*-test for equality of variance was used to determine if the variance differed significantly. If variance between the two groups was

equal, Student's *t*-test was used. For non-equal variance, non-parametric Mann–Whitney was used as indicated. To compare more than two groups, a significant main effect by one-way ANOVA was followed by post hoc Newman–Keuls analysis. Tumor volume over time was analyzed using a two-way repeated measures ANOVA, and significant main effects or interactions were analyzed using Bonferroni's post hoc analysis.

### 3. Results

#### 3.1. Social isolation prior to MB-231 tumor cell injection

We have investigated the impact of stressor exposure in the form of social isolation on orthotopic growth of the human breast tumor cell line, MB-231, in SCID female mice. Mice were separated into single housing one week prior to MB-231 tumor cell injection ( $2 \times 10^6$  cells) into the mammary fat pad. Fig. 1 represents results from three experimental repetitions in which tumor growth was measured over time. In these experimental repetitions, tumor NE, human and mouse VEGF and IL-6 were not consistently altered at the time of sacrifice (day 83 post-MB-231 injection in Fig. 1; data not shown). No difference in lung metastases (the only site of metastasis from the primary MB-231 tumor) was observed between the two groups (data not shown). We postulated that the inability to produce replicable changes in tumor growth was due to the fact that MB-231 is a slow growing tumor *in vivo*, allowing mice to adapt to social isolation. If true, we predicted that social isolation would have a greater impact if transfer to single housing took place closer to the exponential phase of tumor growth.

#### 3.2. Social isolation after MB-231 injection

To test this possibility, SCID mice were injected orthotopically with MB-231 ( $4 \times 10^6$  cells) and tumor growth was monitored over time. One-half of the mice were singly housed when tumors were palpable in all mice (in this experiment, day 14 post-tumor injection; average tumor volume =  $\sim 25$  mm<sup>3</sup>). The other mice remained in their home cages, and tumor growth in all mice was measured over time. MB-231 tumor growth was greater in singly-housed compared to group-housed mice when tumor volume was analyzed through day 28 post-separation (Fig. 2A; repeated measures ANOVA, main effect of housing,  $p < 0.03$  with no interaction by time,  $p = 0.5$ ). By day 34 post-separation, the effect of social isolation had dissipated somewhat. When this time point was included in the analysis, the main effect was no longer significant

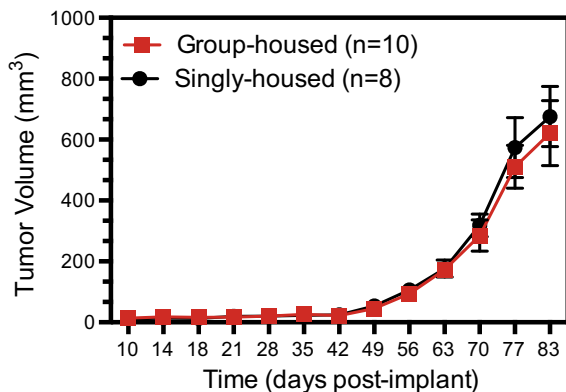


**Fig. 1.** MB-231 tumor growth is not altered by social isolation prior to tumor cell injection. SCID female mice were singly housed seven days prior to orthotopic injection of MB-231 cells. Tumor diameter was measured with calipers on the days indicated. Tumor volume is expressed as mean  $\pm$  SEM,  $n = 8$ –10 mice per group.

( $p = 0.07$ ) with no interaction by day post-separation ( $p = 0.6$ ). Mice were sacrificed at this time point (day 34 post-separation). Tumor weight did not differ between groups (data not shown). Interestingly, a trend towards reduced tumor NE in the singly-housed group was noted (Fig. 2B, Mann–Whitney,  $p = 0.1$ ). Tumor human VEGF concentration did not differ between groups (data not shown), but a trend towards increased human IL-6 was noted in tumors from singly-housed mice (Fig. 2C; Mann–Whitney,  $p = 0.1$ ). Mouse IL-6 did not differ between groups (data not shown). No difference in lung metastases was observed between the two groups (data not shown). These results demonstrate that social isolation facilitated tumor progression, but the duration of the effect on tumor growth was limited.

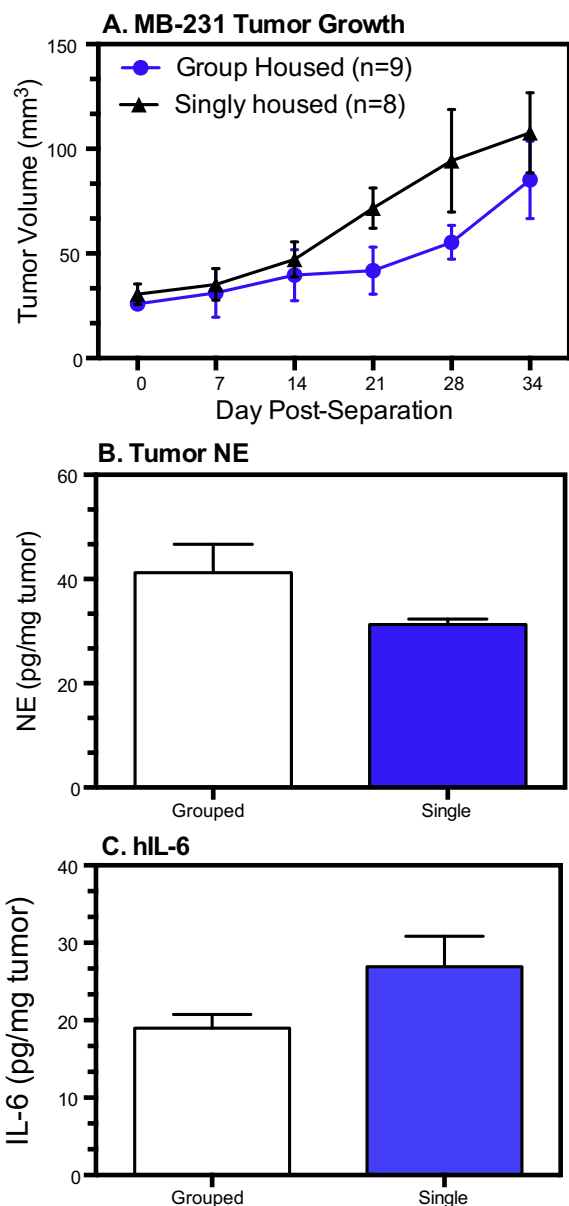


**Fig. 2.** MB-231 tumor growth is transiently increased by social isolation after tumor injection. SCID female were injected with MB-231 cells, and when all mice had palpable tumors, half of the mice were transferred from group to single housing. (A) Tumor volume over time. NE (B) and human IL-6 (C) were measured by ELISA in tumors harvested at day 34 post separation. Results are expressed as mean  $\pm$  SEM,  $n = 8$ –9 mice per group. See text for statistical analysis of tumor growth. For tumor NE and human IL-6, no significant effects based on the non-parametric Mann–Whitney test,  $p = 0.1$ .

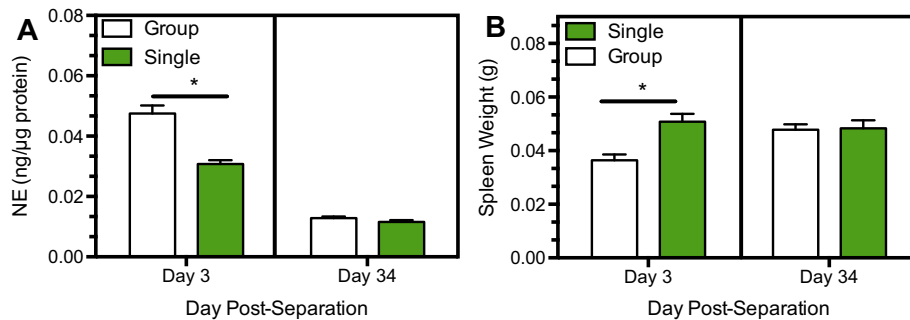


**Fig. 3.** Social isolation reciprocally alters spleen NE (A) and spleen weight (B) early after social isolation. A subset of mice described in Fig. 2 was sacrificed at day 3 post-separation. Results are expressed as mean  $\pm$  SEM,  $n = 5$  mice per group. Asterisk indicates different versus group-housed at the corresponding time point by Newman–Keuls post hoc analysis.

In this same experiment, a subset of mice was sacrificed day 3 after social isolation to determine if sympathetic activation occurred early after social isolation. At this time point, the tumors ( $\leq 10$  mg in weight) were too small to measure NE; therefore the spleen was used as a highly-innervated surrogate organ to compare NE concentration after social isolation. Day 3 post-separation, splenic NE concentration was significantly reduced in the singly-housed mice (Fig. 3A; ANOVA, housing  $\times$  day interaction,  $p < 0.001$ ). The decrease in NE concentration was associated with increased spleen weight (Fig. 3B; ANOVA, housing  $\times$  day interaction,  $p = 0.02$ ), suggesting that the increase in spleen mass reduced NE concentration in the singly housed mice. By day 34 post separation, neither NE concentration nor spleen weight was altered in singly-housed compared to group-housed mice, but compared to day 3, splenic NE concentration was significantly reduced in both groups in conjunction with increased spleen mass (ANOVA, main effect of day,  $p < 0.001$ ).

### 3.3. Effects of social isolation on increased spleen mass are not dependent on tumor

In the next experiment, to determine if the early effect of social isolation on spleen mass was dependent on the presence of growing tumors, non-tumor bearing SCID female mice were socially isolated. In addition, flow cytometry was used to determine if

macrophage populations were altered after social isolation, as reported for other social stressors (Engler et al., 2004). Social isolation increased spleen weight at this time point in association with decreased spleen NE concentration (Fig. 4A and B), similar to the effects at d3 in tumor-bearing mice. The percentage of splenic macrophages expressing F4/80+ and CD11b+Gr-1-cells was not significantly altered (Fig. 4C and E), but the percentage of CD11b+ macrophages that co-express Gr-1+ were significantly increased in socially isolated mice. These cells are myeloid derived suppressor cells that have potent immunosuppressive capabilities (Gabrilovich and Nagaraj, 2009). These results demonstrate that the early effect of social isolation in the spleen is independent of tumor growth, and that specific splenic macrophage populations are sensitive to neurohormonal changes elicited by social isolation. Since these macrophage populations are important regulators of tumor progression, we tested if macrophage populations are altered in spleens and tumors of socially isolated mice.

### 3.4. Social isolation alters spleen and tumor macrophage populations

The next experiment examined alterations in spleen and tumor NE concentration and macrophage populations 10 days after social isolation in mice bearing tumors. Social isolation was initiated when average tumor volume was  $\sim 50$  mm<sup>3</sup>. Social isolation did not alter spleen or tumor weight or NE concentration 10 days after

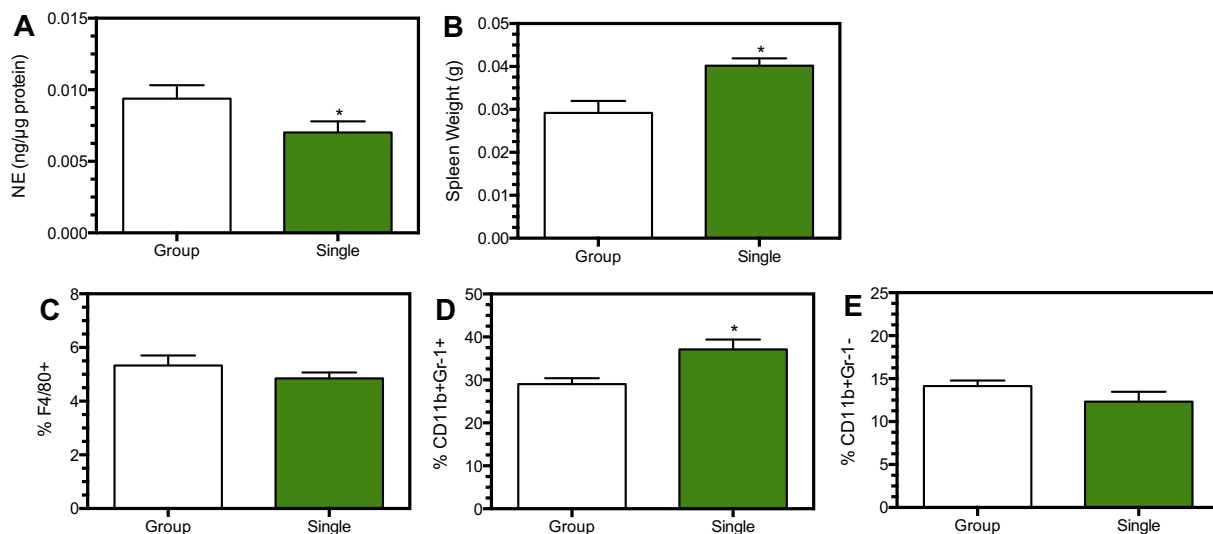


**Fig. 4.** Early effects of social isolation on spleen NE and spleen weight is independent of tumor growth. Three days after transfer to single housing, SCID female mice were sacrificed and spleen NE (A), weight (B), and macrophage populations (C–E) were determined. Asterisk indicates significant difference by Student's *t*-test,  $p < 0.05$ . Results are expressed as mean  $\pm$  SEM,  $n = 5$  mice per group.

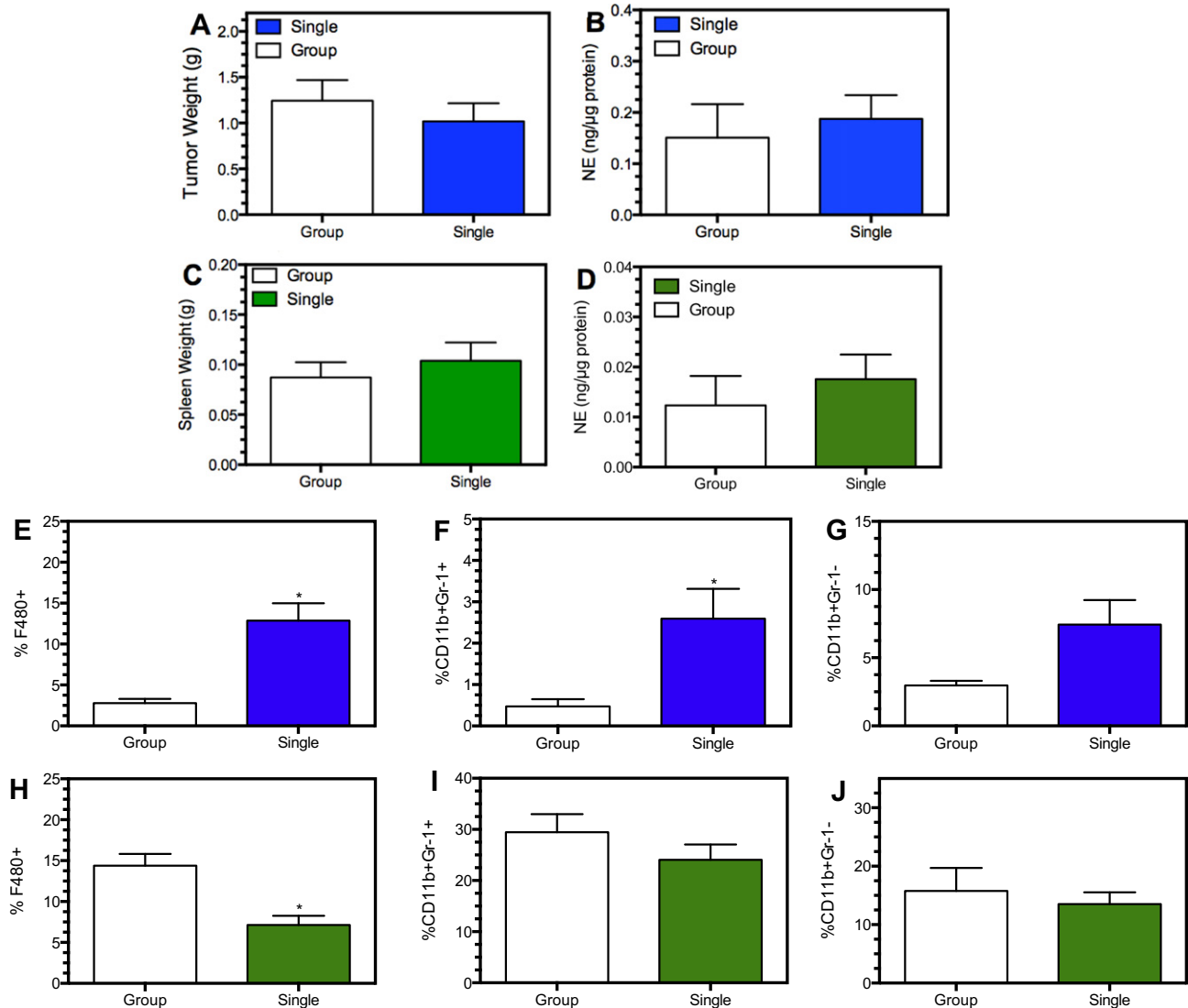


**Fig. 5.** Social isolation alters tumor and spleen macrophage populations. SCID female mice were injected with MB-231 in the mammary fat pad. When tumors were palpable, one-half the mice were transferred from group-housing to single housing. After 10 days, mice were sacrificed and tumor (A and B) and spleen (C and D) weight and NE concentration were determined, and macrophage populations were analyzed by flow cytometry in tumors (E–G) and spleens (H–J). Asterisk indicates significance based on the non-parametric Mann–Whitney test (A and B) or by student's *t*-test (D),  $p < 0.05$ . In (C),  $p = 0.067$ . The results are expressed as mean  $\pm$  SEM of 9–10 mice per group.

social isolation (Fig. 5A–D). However, macrophage populations were increased in tumors from socially isolated mice with significant increases in the percentage of F4/80+ (Fig. 5E) and CD11b + Gr-1+ populations (Fig. 5F) and a trend toward an increase in the CD11b + Gr-1- population (Fig. 5G). In the spleen, the percentage of F480+ macrophages was reduced (Fig. 5H) with no significant changes in either CD11b+ population (Fig. 5I and J). These results demonstrate distinct changes in tumor and spleen macrophage populations with social isolation.

#### 4. Discussion

Social isolation is a well-characterized social stressor that has several advantages to more standard laboratory-type stressors. It is a milder form of stress compared to other forms of stressor exposure. For example, in our hands singly-housed mice do not lose weight (data not shown) nor display elevated tissue NE concentration, in contrast to the weight loss (Sloan et al., 2010) and increased tissue NE concentration (Thaker et al., 2006) reported with daily restraint stress. Yet animals exposed to social isolation

mimic behavioral anxiety and increased vigilance associated with social isolation observed in humans (Hermes et al., 2009; Williams et al., 2009). Here, we demonstrated that social isolation transiently increased MB-231 tumor growth, but only when social isolation was initiated when tumor growth was near exponential phase. No consistent effects of tumor growth or metastasis were observed when social isolation occurred prior to MB-231 injection, suggesting a temporal dependence in the context of a mild stressor. Indeed, early and transient changes in spleen NE concentration and macrophage populations, independent of whether or not the animals were tumor-bearing, were observed. Furthermore, increases in tumor macrophage populations took place before any indications of altered tumor growth. The changes in macrophage populations in the tumors were not associated with altered tumor NE. These results suggest that social isolation can have an impact on tumor progression, but the impact is transient and may not be associated with dramatic changes in tumor growth and metastasis.

The changes in macrophage populations in tumor and spleen indicate that social isolation facilitates leukocyte recruitment – a process described with another social stressor, social disruption

(Engler et al., 2004). Repeated social disruption increased spleen weight in concert with loss of CD11b+ myeloid cells from the bone marrow and an increase in CD11b+ cells in the spleen. Furthermore, the increase in spleen weight elicited by social disruption was mediated through  $\beta$ -AR stimulation, as it was prevented by propranolol pretreatment to block  $\beta$ -AR (Wohleb et al., 2011). The increase in the CD11b+Gr-1+ population in spleen from non-tumor bearing, singly-housed mice shown here (Fig. 4), suggests that this process also occurs with social isolation. A similar stress-induced increase in tumor macrophages has been described by Sloan and colleagues, who demonstrated elevated F4/80+ tumor macrophages and a trend toward increased myeloid derived suppressor cells with restraint stress; this effect was blocked by propranolol treatment (Sloan et al., 2010). Restraint stress did not facilitate primary tumor growth, but increased tumor angiogenesis and dramatically elevated metastasis (Sloan et al., 2010). In our hands, tumor associated macrophage populations expressing F4/80 and CD11b were increased with social isolation. The spleen is an important source of tumor associated macrophages and tumor associated neutrophils (Cortez-Retamozo et al., 2012). The social isolation-induced decrease in the splenic F4/80+ population in conjunction with an increase in this population in tumors suggests that the spleen may contribute to the increased F4/80+ tumor associated macrophages in socially isolated mice. It is likely that both the spleen and bone marrow may be targets of stress hormones that promote the migration of these macrophage populations into the tumor. Both tumor associated macrophages and myeloid derived suppressor cell populations are associated with tumor progression (Gabrilovich and Nagaraj, 2009), but we have yet to establish that the increased tumor macrophages lead to the increased tumor growth in the singly-housed mice.

Social isolation has been characterized as a stressor based on behavior (it elicits anxiety behaviors in female mice) (Palanza et al., 2001), but is less well characterized in terms of hypothalamic pituitary axis or sympathetic nervous system activation. Long-term social isolation increased development of spontaneous mammary tumors and metastasis, but these rats were socially isolated from puberty (Hermes et al., 2009), making it difficult to directly compare to the social isolation procedure here, which was begun when the mice had reached adulthood. Nonetheless, social isolation led to reduced baseline levels of plasma corticosterone at the nadir of the diurnal rhythm in social isolated rats, but an elevated and prolonged corticosterone response to a stressor (Hermes et al., 2009; Williams et al., 2009). Similarly, a 21-day period of single housing did not alter baseline plasma catecholamines, but upon exposure to an acute stressor, plasma catecholamines in socially isolated rats were significantly elevated versus group-housed (Dronjak et al., 2004). Therefore, the social isolation model will be particularly useful for examining the impact of an acute stressor in animals exposed to long-term social isolation. The results presented here suggest that social isolation alone may elicit alterations that have a transient impact. Future plans include using social isolation to understand the biological consequences of multiple stressors on tumor pathogenesis, a more likely scenario in the context of a diagnosis of breast cancer.

The effects of social isolation were not associated with increased NE concentrations in spleen or in tumor, as might be expected if social isolation activated the SNS. However, there are a few caveats in interpreting tissue NE measures. First, NE concentration in the spleen appeared to fluctuate with changes in spleen mass. One way to interpret this finding is that sympathetic nerve fibers within the spleen do not respond rapidly to a rapid expansion in tissue volume, such as the increase in spleen weight with social isolation or even in a growing tumor. We can detect sympathetic nerve fibers in MB-231 tumors independent of tumor size, however the impact of the expanding tumor architecture on NE

concentration has not been systematically examined. Furthermore, measuring only tissue NE may not be an appropriate measure of SNS activation, especially under conditions of a relatively mild stressor such as social isolation where homeostatic mechanisms serve to maintain a constant tissue NE baseline (Eisenhofer et al., 2004). Therefore, we have begun to assess normetanephrine, a product of NE metabolism by catechol-O-methyltransferase, as a potential additional measure of sympathetic activation and released NE. These experiments will help define the role of SNS activation and  $\beta$ -AR stimulation in the context of social isolation.

The results presented here demonstrate an early, but transient effect of a psychological stressor, social isolation, in both tumor-bearing and normal female SCID mice. The results imply that exposures to relatively mild stressors may promote tumor progression, depending on the timing relative to tumor growth, but also suggest the possibility that homeostatic mechanisms can mitigate the impact of social isolation. This is a potential area of investigation in terms of identifying pathways that help minimize the impact of chronic stress experienced in breast cancer patients. It is critical to understand how mild stressors interact to develop into a more severe stressor and to develop therapies that work in concert with standard breast cancer therapies to inhibit tumor progression.

### Grant support

This work was supported by Department of Defense IDEA Award (W81XWH-10-01-008) and National Institutes of Health (1 R21 CA152777-01) to KSM, Department of Defense Era of Hope Scholar Research Award (W81XWH-09-1-0405), National Institutes of Health Director's New Innovator Award (1 DP2 OD006501-01), and Pew Scholar in the Biomedical Sciences Award to EBB, and Department of Defense Predoctoral Training Award (W81XWH-10-1-0058) and predoctoral grant TL1 RR024135 from the National Center for Research Resources, a component of the NIH, and the NIH Roadmap for Medical Research to MJS. MJS is a trainee in the Medical Scientist Training Program funded by NIH T32 GM07356. The content is solely the responsibility of the authors and does not necessarily represent the official views of the National Institute of General Medical Sciences or NIH.

### Conflict of Interest

The authors of this manuscript have nothing to declare.

### Acknowledgments

We thank Khawar Liverpool, Dan Byun, Tracy Bubel, Giuseppe Arcuri, and Taylor Wolfgang for their excellent technical assistance.

### References

- Antoni, M.H., Lutgendorf, S.K., Cole, S.W., Dhabhar, F.S., Sephton, S.E., McDonald, P.G., Stefaneck, M., Sood, A.K., 2006. The influence of bio-behavioural factors on tumour biology: pathways and mechanisms. *Nat. Rev. Cancer* 6, 240–248.
- Cortez-Retamozo, V., Etzrodt, M., Newton, A., Rauch, P.J., Chudnovskiy, A., Berger, C., Ryan, R.J., Iwamoto, Y., Marinelli, B., Gorbатов, R., Forghani, R., Novobrantseva, T.I., Kotelianskiy, V., Figueiredo, J.L., Chen, J.W., Anderson, D.G., Nahrendorf, M., Swirski, F.K., Weissleder, R., Pittet, M.J., 2012. Origins of tumor-associated macrophages and neutrophils. *Proc. Natl. Acad. Sci. USA*.
- Dronjak, S., Gavrilovic, L., Filipovic, D., Radojic, M.B., 2004. Immobilization and cold stress affect sympatho-adrenomedullary system and pituitary-adrenocortical axis of rats exposed to long-term isolation and crowding. *Physiol. Behav.* 81, 409–415.
- Eisenhofer, G., Kopin, I.J., Goldstein, D.S., 2004. Catecholamine metabolism: a contemporary view with implications for physiology and medicine. *Pharmacol. Rev.* 56, 331–349.
- Engler, H., Bailey, M.T., Engler, A., Sheridan, J.F., 2004. Effects of repeated social stress on leukocyte distribution in bone marrow, peripheral blood and spleen. *J. Neuroimmunol.* 148, 106–115.

- Gabrilovich, D.I., Nagaraj, S., 2009. Myeloid-derived suppressor cells as regulators of the immune system. *Nat. Rev. Immunol.* 9, 162–174.
- Hawkley, L.C., Cacioppo, J.T., 2003. Loneliness and pathways to disease. *Brain Behav. Immun.* 17 (Suppl. 1), S98–S105.
- Hermes, G.L., Delgado, B., Tretiakova, M., Cavigelli, S.A., Krausz, T., Conzen, S.D., McClintock, M.K., 2009. Social isolation dysregulates endocrine and behavioral stress while increasing malignant burden of spontaneous mammary tumors. *Proc. Natl. Acad. Sci. USA* 106, 22393–22398.
- Madden, K.S., Szpunar, M.J., Brown, E.B., 2011. Beta-Adrenergic receptors (beta-AR) regulate VEGF and IL-6 production by divergent pathways in high beta-AR-expressing breast cancer cell lines. *Breast Cancer Res. Treat.* 130, 747–758.
- Palanza, P., Gioiosa, L., Parmigiani, S., 2001. Social stress in mice: gender differences and effects of estrous cycle and social dominance. *Physiol. Behav.* 73, 411–420.
- Raju, B., Haug, S.R., Ibrahim, S.O., Heyeraas, K.J., 2007. Sympathectomy decreases size and invasiveness of tongue cancer in rats. *Neuroscience* 149, 715–725.
- Reynolds, P., Kaplan, G.A., 1990. Social connections and risk for cancer: prospective evidence from the Alameda County Study. *Behav. Med.* 16, 101–110.
- Saul, A.N., Oberyzyzn, T.M., Daugherty, C., Kusewitt, D., Jones, S., Jewell, S., Malarkey, W.B., Lehman, A., Lemeshow, S., Dhabhar, F.S., 2005. Chronic stress and susceptibility to skin cancer. *J. Natl. Cancer Inst.* 97, 1760–1767.
- Shakhar, G., Ben-Eliyahu, S., 1998. In vivo b-adrenergic stimulation suppresses natural killer activity and compromises resistance to tumor metastasis in rats. *J. Immunol.* 160, 3251–3258.
- Sloan, E.K., Priceman, S.J., Cox, B.F., Yu, S., Pimentel, M.A., Tangkanangnukul, V., Arevalo, J.M., Morizono, K., Karanikolas, B.D., Wu, L., Sood, A.K., Cole, S.W., 2010. The sympathetic nervous system induces a metastatic switch in primary breast cancer. *Cancer Res.* 70, 7042–7052.
- Slotkin, T.A., Zhang, J., Dancel, R., Garcia, S.J., Willis, C., Seidler, F.J., 2000. Beta-adrenoceptor signaling and its control of cell replication in MDA-MB-231 human breast cancer cells. *Breast Cancer Res. Treat.* 60, 153–166.
- Thaker, P.H., Han, L.Y., Kamat, A.A., Arevalo, J.M., Takahashi, R., Lu, C., Jennings, N.B., Armaiz-Pena, G., Bankson, J.A., Ravoori, M., Merritt, W.M., Lin, Y.G., Mangala, L.S., Kim, T.J., Coleman, R.L., Landen, C.N., Li, Y., Felix, E., Sanguino, A.M., Newman, R.A., Lloyd, M., Gershenson, D.M., Kundra, V., Lopez-Berestein, G., Lutgendorf, S.K., Cole, S.W., Sood, A.K., 2006. Chronic stress promotes tumor growth and angiogenesis in a mouse model of ovarian carcinoma. *Nat. Med.* 12, 939–944.
- Williams, J.B., Pang, D., Delgado, B., Kocherginsky, M., Tretiakova, M., Krausz, T., Pan, D., He, J., McClintock, M.K., Conzen, S.D., 2009. A model of gene-environment interaction reveals altered mammary gland gene expression and increased tumor growth following social isolation. *Cancer Prev. Res.* 2, 850–861.
- Wohleb, E.S., Hanke, M.L., Corona, A.W., Powell, N.D., Stiner, L.M., Bailey, M.T., Nelson, R.J., Godbout, J.P., Sheridan, J.F., 2011. Beta-adrenergic receptor antagonism prevents anxiety-like behavior and microglial reactivity induced by repeated social defeat. *J. Neurosci.* 31, 6277–6288.

# Cancer Prevention Research



## The Antidepressant Desipramine and $\alpha_2$ -Adrenergic Receptor Activation Promote Breast Tumor Progression in Association with Altered Collagen Structure

Mercedes J. Szpunar, Kathleen A. Burke, Ryan P. Dawes, et al.

*Cancer Prev Res* 2013;6:1262-1272.

**Updated version** Access the most recent version of this article at:  
<http://cancerpreventionresearch.aacrjournals.org/content/6/12/1262>

**Cited Articles** This article cites by 45 articles, 9 of which you can access for free at:  
<http://cancerpreventionresearch.aacrjournals.org/content/6/12/1262.full.html#ref-list-1>

**E-mail alerts** [Sign up to receive free email-alerts](#) related to this article or journal.

**Reprints and Subscriptions** To order reprints of this article or to subscribe to the journal, contact the AACR Publications Department at [pubs@aacr.org](mailto:pubs@aacr.org).

**Permissions** To request permission to re-use all or part of this article, contact the AACR Publications Department at [permissions@aacr.org](mailto:permissions@aacr.org).

## The Antidepressant Desipramine and $\alpha_2$ -Adrenergic Receptor Activation Promote Breast Tumor Progression in Association with Altered Collagen Structure

Mercedes J. Szpunar<sup>1</sup>, Kathleen A. Burke<sup>2</sup>, Ryan P. Dawes<sup>3</sup>, Edward B. Brown<sup>2</sup>, and Kelley S. Madden<sup>2</sup>

### Abstract

Emotional stress activates the sympathetic nervous system (SNS) and release of the neurotransmitter norepinephrine to promote breast tumor pathogenesis. We demonstrate here that the metastatic mammary adenocarcinoma cell line 4T1 does not express functional adrenergic receptors (AR), the receptors activated by norepinephrine, yet stimulation of adrenergic receptor *in vivo* altered 4T1 tumor progression *in vivo*. Chronic treatment with the antidepressant desipramine (DMI) to inhibit norepinephrine reuptake increased 4T1 tumor growth but not metastasis. Treatment with a highly selective  $\alpha_2$ -adrenergic receptor agonist, dexmedetomidine (DEX), increased tumor growth and metastasis. Neither isoproterenol (ISO), a  $\beta$ -AR agonist, nor phenylephrine, an  $\alpha_1$ -AR agonist, altered tumor growth or metastasis. Neither DMI- nor DEX-induced tumor growth was associated with increased angiogenesis. In DMI-treated mice, tumor VEGF, IL-6, and the prometastatic chemokines RANTES, M-CSF, and MIP-2 were reduced. Tumor collagen microstructure was examined using second harmonic generation (SHG), a nonabsorptive optical scattering process to highlight fibrillar collagen. In DMI- and DEX-treated mice, but not ISO-treated mice, tumor SHG was significantly altered without changing fibrillar collagen content, as detected by immunofluorescence. These results demonstrate that  $\alpha_2$ -AR activation can promote tumor progression in the absence of direct sympathetic input to breast tumor cells. The results also suggest that SNS activation may regulate tumor progression through alterations in the extracellular matrix, with outcome dependent on the combination of adrenergic receptor activated. These results underscore the complexities underlying SNS regulation of breast tumor pathogenesis, and suggest that the therapeutic use of adrenergic receptor blockers, tricyclic antidepressants, and adrenergic receptor agonists must be approached cautiously in patients with breast cancer. *Cancer Prev Res*; 6(12); 1262–72. ©2013 AACR.

### Introduction

In patients with cancer, chronic emotional stress or other negative psychological factors such as depression or lack of social support promote tumor growth and progression (1, 2). The sympathetic nervous system (SNS) is an important pathway by which stress can facilitate tumor growth (3–6). The SNS neurotransmitters norepinephrine and epinephrine activate  $\alpha$ - and  $\beta$ -adrenergic receptors (AR). In animal models using  $\beta$ -AR-expressing cancer cell lines, stressor exposure or  $\beta$ -AR stimulation increased tumor growth and/or metastasis by mechanisms such as increased

tumor angiogenesis and density of tumor associated macrophages (7, 8). SNS activation can also target  $\beta$ -AR-expressing host cells residing in the tumor or in metastatic sites to promote tumor growth and metastasis (6, 9). These studies provide compelling evidence that norepinephrine and AR-expressing tumor cells or host stromal cells modulate tumor pathogenesis.

Despite progress in understanding the molecular mechanisms underlying sympathetic regulation of tumor progression, several critical questions remain. First, the role for  $\alpha$ -AR has not been carefully examined despite the fact that in human breast cancer,  $\alpha$ -AR expression has been linked to poor prognosis (10). Second, variation in breast cancer cell line adrenergic receptor expression (11, 12) is recapitulated in human breast tumors that display heterogeneity in  $\alpha$ - and  $\beta$ -AR expression (10). The functional consequences of such heterogeneity have yet to be systematically explored. It is reasonable to assume that when breast cancer cells express no or low levels of adrenergic receptor, host stromal adrenergic receptor would be the direct targets of elevated norepinephrine. Stromal cells, including cells of the immune system, endothelial cells, and fibroblasts, express  $\alpha$ -AR and  $\beta$ -AR normally and in tumors (8, 13, 14). We propose that

**Authors' Affiliations:** Departments of <sup>1</sup>Pathology and <sup>2</sup>Biomedical Engineering; and <sup>3</sup>Neuroscience Graduate Program, School of Medicine and Dentistry, University of Rochester, Rochester, New York

**Note:** Supplementary data for this article are available at Cancer Prevention Research Online (<http://cancerprevres.aacrjournals.org>).

**Corresponding Author:** Kelley S. Madden, Department of Biomedical Engineering, University of Rochester Medical Center, Goergen Hall, RC Box 270168, Rochester, NY 14627. Phone: 585-273-5724; Fax: 585-276-2254; E-mail: Kelley\_Madden@urmc.rochester.edu

**doi:** 10.1158/1940-6207.CAPR-13-0079

©2013 American Association for Cancer Research.

SNS activation can promote tumor pathogenesis by acting on stromal cells to alter the tumor extracellular matrix.

To test this hypothesis, we have used multiphoton laser scanning microscopy and second harmonic generation (SHG) to visualize a component of the tumor stroma, fibrillar collagen. SHG is an endogenous optical signal produced when 2 excitation photons combine to produce one emission photon, "catalyzed" by a non-centrosymmetric structure, such as ordered collagen triple helices (15). Tumor collagen fiber microstructure, as revealed by SHG, is of great interest because several studies have suggested that it influences tumor progression, specifically tumor metastasis. It is important to note that not all collagen fibers produce detectable SHG (16), and that tumor cells can migrate toward blood vessels via SHG<sup>+</sup> fibers, locomoting along such fibers more efficiently than cells moving independently. Interestingly, the extent of SHG-associated tumor cell motility is correlated with metastatic ability (17, 18). In patients with breast cancer biopsies, we demonstrated shifts in SHG emission patterns associated with progression to more metastatic disease (19), and lymph node metastasis was associated with increased breast tumor SHG<sup>+</sup> collagen I density (20). Finally, SHG-based tumor-associated collagen signatures are prognostic factors for disease-free survival, independent of tumor grade, size, and hormonal receptor status (21). Thus, SHG imaging represents a novel imaging modality to assess the impact of SNS activation on tumor extracellular matrix and explore stromal pathways that may be activated by norepinephrine to influence tumor progression.

We demonstrate here that 4T1, a metastatic mammary adenocarcinoma (22), lacks functional  $\alpha$ - and  $\beta$ -AR, and is unable to respond to norepinephrine *in vitro*. Therefore, we propose 4T1 as an excellent model for investigating effects of SNS activation on tumors in the absence of direct sympathetic input to the tumor cells themselves. To explore the impact of elevated norepinephrine in the 4T1 tumor model, mice were treated with the norepinephrine reuptake inhibitor, desipramine (DMI), a drug used clinically as an antidepressant (23, 24). We demonstrate that chronic treatment with DMI increased orthotopic 4T1 tumor growth, whereas highly selective  $\alpha_2$ -AR activation by treatment with dexmedetomidine (DEX) increased both tumor growth and metastasis. DMI and DEX treatments were associated with altered SHG-emitting tumor collagen. These results provide evidence that activation of the SNS can promote tumor progression and metastasis through interactions with the tumor stroma, and can do so through activation of  $\alpha_2$ -AR.

## Materials and Methods

### Mice

Female BALB/cByJ mice (6–8 weeks of age; The Jackson Laboratories) were housed 3 to 4 per cage with food and water *ad libitum*, and used experimentally 2 weeks after arrival. All animal procedures were carried out in accordance with the National Institutes of Health Guide for the Care and Use of Laboratory Animals and were approved by

the University of Rochester Committee on Animal Resources. The University of Rochester Animal Resource is fully accredited by AAALAC International.

### Cell lines and tissue culture

4T1 (mammary adenocarcinoma; CRL-2539), MDA-MB-231 (MB-231; HTB-26), and human foreskin fibroblast-1 cells (HFF; SCRC-1041) were acquired from American Type Culture Collection (ATCC) within the last 2 years. ATCC authenticates cell lines using short tandem repeat analyses. Upon acquisition, cells were expanded for no more than 3 passages and frozen. All cell lines were used within 3 months of thawing. For passaging, 4T1 was grown in RPMI containing penicillin/streptomycin and 10% fetal calf serum. MB-231 and HFF were grown in Dulbecco's modified Eagle medium containing L-glutamine and supplemented with penicillin/streptomycin and 10% fetal calf serum. All media and media components were purchased from Gibco (Invitrogen Inc.). All cells were regularly tested for mycoplasma contamination.

*In vitro* culture of 4T1 cells to measure proliferation and cytokine production was described previously (11). Proliferation was assessed using CyQuant NF Proliferation Assay kit (Invitrogen) following the manufacturer's instructions. Fluorescence was detected with a 485 nm excitation filter and 530 nm emission filter using a multiwell plate reader (Biotek). For cytokines, cell-free supernatants were harvested after 72 hours in culture and stored at  $-80^{\circ}\text{C}$ .

### Drug treatment

Drug treatments commenced 2 days before tumor cell injection and continued for the duration of the experiment. For DMI treatment, continuous release pellets (Innovative Research of America) were implanted subcutaneously under ketamine/xylazine anesthesia (90/9 mg/kg). The adrenergic receptor agonists ISO (Sigma-Aldrich), phenylephrine (Sigma-Aldrich), and DEX (Pfizer) were dissolved in sterile saline. Mice were injected intraperitoneally (i.p.) daily for the duration of the experiment. ISO and phenylephrine doses were chosen based on ISO-induced increased tumor pathogenesis reported in other murine tumor models (7, 8) and on pilot toxicity studies. Two doses of DEX were tested: 10  $\mu\text{g}/\text{kg}$  elicited no apparent sedative effects and 25  $\mu\text{g}/\text{kg}$  elicited mild and transient anesthetic effects (slowed movements following injection that were no longer apparent 1 hour after injection). DMI, ISO, and phenylephrine treatment elicited early and transient decreases in body weight ( $\leq 10\%$ ) that recovered over time.

### Tumor implantation, growth, and tissue harvest

4T1 cells ( $1 \times 10^5$  in sterile saline) were injected into the third mammary fat pad (MFP) under ketamine/xylazine anesthesia. Tumors were measured with calipers every 2 to 3 days without knowledge of experimental group. Mice were sacrificed by pentobarbital overdose (200 mg/kg, i.p.) followed by cervical dislocation to harvest tumor, spleen, and lungs. Tumors and spleens were weighed and divided. For

catecholamine and cytokine analyses, tissue was immediately placed on dry ice and stored at  $-80^{\circ}\text{C}$ .

Tumor volume ( $V$ ) was calculated using the equation  $V = 1/2 \times \text{length} \times \text{width}^2$ . Tumor growth is presented either as the raw tumor volume over time or as normalized tumor growth. Normalized tumor growth was calculated by dividing an individual's tumor volume at a given time point by its volume at the earliest time point all tumors were detected (day 3 or 5 post-4T1).

### Norepinephrine/normetanephrine and cytokine analyses

For norepinephrine and normetanephrine, tissue was homogenized in 0.01 M HCl at 10% volume (mL) by tissue weight. Norepinephrine and normetanephrine were determined by ELISA (Rocky Mountain Diagnostics) following the manufacturer's instructions. For cytokines, tissue was homogenized in radioimmunoprecipitation assay buffer containing protease inhibitors (Pierce). Cytokines were measured using mouse-specific ELISAs (R&D Systems) following the manufacturer's instructions.

For multiple analyte analysis, a Milliplex mouse cytokine/chemokine magnetic bead panel kit (Millipore; catalogue #MCYTOMAG-70K) was used following the manufacturer's instructions. A Luminex 200 plate reader equipped with xPonent software (University of Rochester Flow Cytometry Core) was used to determine median fluorescence intensity for each analyte. The concentration of each analyte was calculated using the corresponding standard curve fit to a 5-parameter logistic equation.

For all ELISAs, absorption was measured at 450 nm using a multiwell plate reader (Synergy HT; Biotek Instruments Inc.). Curve fitting and sample concentration calculations were conducted with Gen5 software (Biotek). Concentrations were normalized to total protein in homogenates as determined with a BCA protein assay (Pierce).

### Immunohistochemistry, SHG, and image analysis

Tumors were fixed in 4% paraformaldehyde for 72 hours, followed by incubation in 10% sucrose and 30% sucrose for 24 hours each. Three adjacent tumor sections (20- $\mu\text{m}$ -thick) were collected every 100  $\mu\text{m}$ . Standard immunohistochemical techniques were used to detect blood vessels using rat-anti CD31<sup>+</sup> antibody (diluted 1:20; Abcam), proliferating cells using polyclonal rabbit-anti Ki67 (1:500; Abcam) or collagen I using polyclonal rabbit anti-collagen type I antibody (1:200; Abcam). Species-appropriate Alexa-Fluor-594-conjugated secondary antibodies (Invitrogen) were used to detect the primary antibodies. Fluorescein isothiocyanate (FITC)-conjugated anti-F4/80<sup>+</sup> antibody (Abcam) was used to detect F4/80<sup>+</sup> macrophages.

For immunofluorescent and SHG imaging of collagen, tumor sections were imaged using multiphoton microscopy. Five random fields of view per tumor section were imaged by a blinded observer using a 0.8 NA 20 $\times$  water immersion objective lens and electronic zoom at 1 $\times$ , one section per tumor. SHG and immunofluorescence emission was collected simultaneously under constant imaging

conditions in each sample, including excitation wavelength (810 nm), laser power (8 mW at the sample), and photomultiplier tube voltages. To detect immunofluorescence, fluorophore emission was collected using bandpass filters 520/40 (for FITC) and 635/30 (for Alexa-Fluor 594). SHG signal was separated from fluorescence by a 475 nm long-pass dichroic (Semrock) and detected through a bandpass 405/30 emission filter.

All images were analyzed by personnel blinded to group using custom algorithms in ImageJ (NIH Freeware). To quantify CD31 and Ki67 immunofluorescence, a threshold that excluded autofluorescence was determined in adjoining tissue sections stained with secondary antibody alone, and the percentage of pixels above threshold was calculated. Average blood vessel area was calculated and normalized to cell density based on 4',6-diamino-2-phenylindole nuclear staining. To quantify SHG and anti-collagen immunostaining, a common threshold was determined for all samples by determining background pixels averaged from 2 tissue-free images from each channel. The average background intensity was subtracted from all images, then common SHG and immunostained thresholds were applied to distinguish SHG or immunostained pixels from background pixels. Two calculations were used to represent SHG or immunohistochemical collagen signal: the percentage of pixels above threshold in each image and the average intensity of those pixels above threshold. The SHG and collagen immunostaining values from 5 regions of interest from each tumor section were averaged for each animal.

### Lung metastases

Lungs were fixed in 10% formalin and paraffin embedded. Five- $\mu\text{m}$ -thick sections were collected every 100  $\mu\text{m}$  through the entire lung. Tissue sections were stained using standard hematoxylin and eosin (H&E) techniques. Metastases were visualized using a  $\times 4$  objective lens and counted in each tissue section by a blinded observer.

### $\beta$ -AR Expression and Intracellular Cyclic AMP

A standard radioligand-binding assay was used to determine specific binding of  $^{125}\text{I}$ -cyanopindolol (NEN Radiochemicals) to whole cells to quantify  $\beta$ -AR expression, as described previously (11). The procedure to measure intracellular cAMP was described previously (11). Cyclic AMP content was measured by ELISA (R&D Systems) following the manufacturer's instructions.

### Statistical analyses

Statistical analyses were conducted with GraphPad PRISM software with  $P < 0.05$  considered statistically significant. When 2 groups were compared, an  $F$  test for variance was conducted to compare variance. If variance was similar, an unpaired two-tailed Student  $t$  test was used. If variance differed, group comparisons were conducted using the nonparametric Mann-Whitney  $U$  test. To compare more than 2 groups, one- or two-way ANOVA was used. When variance differed significantly between groups, the nonparametric Kruskal-Wallis test was used, with *post*

*hoc* analysis by Dunn's multiple comparison test. Tumor growth over time was analyzed using repeated measures two-way ANOVA. Significant interactions or main effects were analyzed by simple effects or by Holm-Sidak multiple comparison test.

## Results

### 4T1 tumor cells do not respond to norepinephrine *in vitro* or signal via adrenergic receptor

To determine if norepinephrine directly regulates 4T1 tumor cell functional responses, norepinephrine or selective adrenergic receptor agonists were incubated with 4T1 cells *in vitro*. Norepinephrine did not alter 4T1 proliferation (Fig. 1A) or VEGF production (Fig. 1B) under *in vitro* conditions that altered VEGF production and proliferation in MB-231

and other  $\beta$ -AR-expressing breast cancer cell lines (11). Furthermore, specific binding of the  $\beta$ -AR ligand  $^{125}$ I-cyanopindolol was readily detectable with MB-231 cells, but not 4T1 cells (Fig. 1C), and isoproterenol (ISO), a  $\beta$ -AR agonist, elevated intracellular cAMP in MB-231 cells but not in 4T1 cells (Fig. 1D). Together, these results demonstrate that 4T1 cells do not possess cell surface  $\beta$ -AR. In terms of  $\alpha$ -AR, the  $\alpha_1$ -agonist phenylephrine did not significantly alter 4T1 proliferation or VEGF production (Fig. 1E and F). The  $\alpha_2$ -agonist DEX had no effect except at the highest concentration tested (42  $\mu$ mol/L), where 4T1 proliferation was reduced and VEGF production was increased (Fig. 1G and H; Supplementary Fig. S1A and S1B). However, yohimbine, an  $\alpha_2$ -AR antagonist, did not block these DEX-induced effects (Supplementary Fig. S1A and S1B), and there was no evidence for  $\alpha_2$ -AR signaling by cAMP inhibition (Supplementary

**Figure 1.** 4T1 cells do not express functional adrenergic receptor. Norepinephrine (NE) does not alter 4T1 cell proliferation (A) or VEGF production (B). 4T1 cells were incubated with NE at the concentrations indicated. Results are expressed as mean  $\pm$  SD of triplicate wells from a representative experiment of 2 experimental repetitions. Statistical analyses: A, no main effects of NE, time, or NE  $\times$  time interaction; B, no main effects of NE or NE  $\times$  time interaction, main effect of time,  $P < 0.0001$ ; C,  $\beta$ -AR expression as measured by specific  $^{125}$ I-CYP ligand binding of 4T1 (stars) and the  $\beta$ -AR-expressing line MB-231 (diamonds). D,  $\beta$ -AR agonist ISO induced cAMP response in MB-231 compared with 4T1. E, F, 4T1 incubated with the  $\alpha_1$ -AR agonist phenylephrine (PE). Kruskal-Wallis test, no significant effects of PE. G, H, 4T1 incubated with the  $\alpha_2$ -AR agonist DEX. G, Kruskal-Wallis test, effect of DEX ( $P = 0.03$ , indicated by asterisk), with no significant differences versus 0 drug by Dunn's multiple comparisons test; H, Kruskal-Wallis test, DEX treatment,  $P = 0.053$  with no differences versus 0 drug by Dunn's multiple comparisons test.

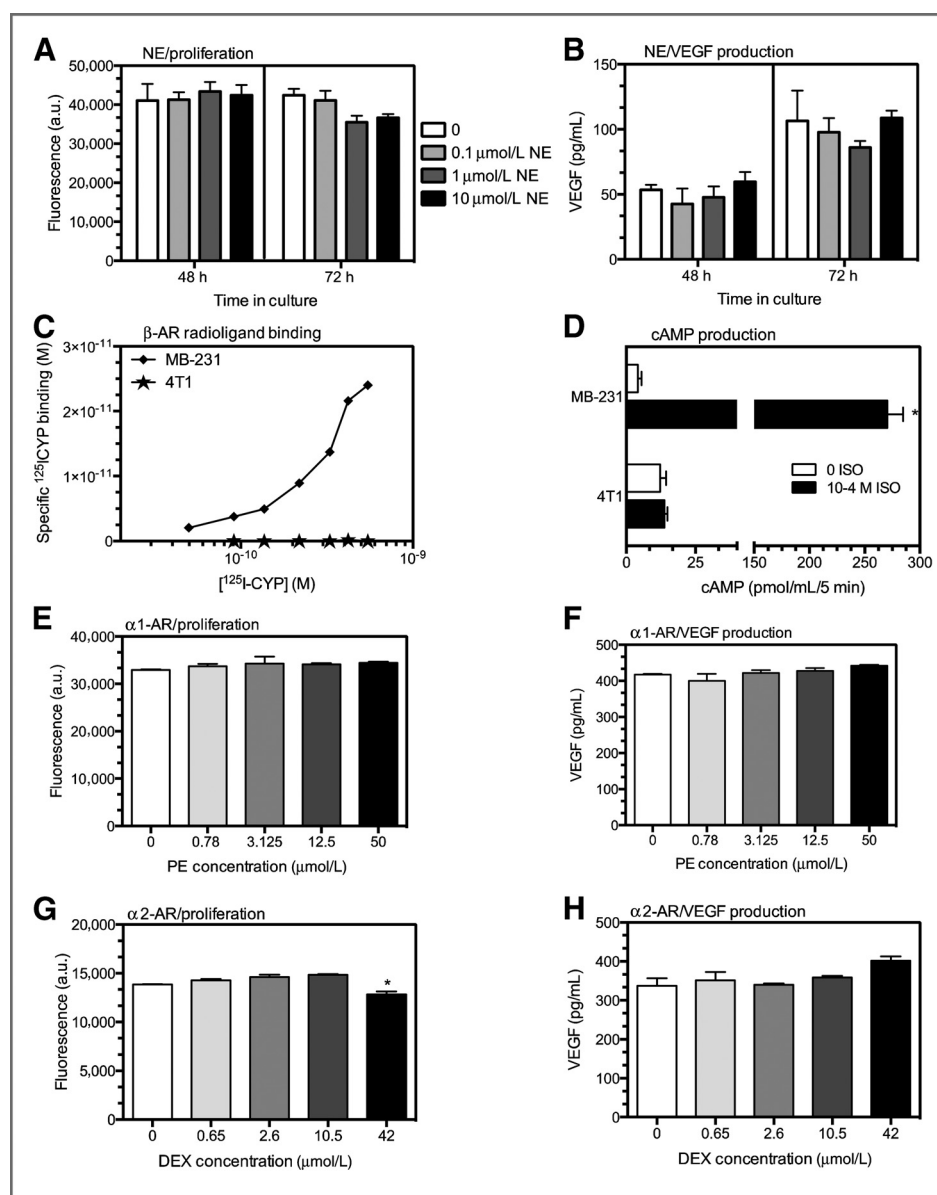


Fig. S1C; ref. 25), as demonstrated here in a human fibroblast line (Supplementary Fig. S1D). We conclude that 4T1 cells do not express functional  $\alpha_1$ -,  $\alpha_2$ -, or  $\beta$ -AR and therefore norepinephrine cannot directly affect 4T1 function. We next tested if elevated synaptic norepinephrine altered 4T1 tumor pathogenesis *in vivo*.

#### **DMI, a norepinephrine reuptake inhibitor, increases 4T1 tumor growth, but not metastasis**

DMI inhibits norepinephrine reuptake through the norepinephrine transporter and thereby increases synaptic norepinephrine (23, 24). To assess alterations in synaptic norepinephrine in the periphery, norepinephrine and its metabolite normetanephrine were measured in the densely innervated spleen. Norepinephrine concentration primarily represents norepinephrine synthesized and stored intraneuronally, but normetanephrine is produced by an extraneuronal enzyme (catechol-*O*-methyltransferase), and reflects norepinephrine released and metabolized in the synapse (26). In mice implanted subcutaneously with 21-day continuous release pellets containing DMI (10 mg) or placebo, DMI increased splenic norepinephrine 2-fold and normetanephrine 4-fold relative to placebo in association with reduced spleen mass 3 days after pellet implantation (Supplementary Fig. S2A–S2C). The increased normetanephrine is evidence of effective norepinephrine uptake blockade, and elevated normetanephrine (but not norepinephrine) was detected in the spleen up to 7 days after DMI implantation (data not shown). In comparison to daily intraperitoneal injection of DMI, subcutaneous pellets elicited greater magnitude and longer lasting elevation in splenic norepinephrine and normetanephrine (data not shown).

To assess tumor growth, mice were implanted with pellets containing DMI or placebo 2 days before 4T1 injection, a treatment regimen similar to the chronic pharmacological  $\beta$ -AR activation that elicited increased tumor growth/metastasis in  $\beta$ -AR-expressing tumor models (7–9). Using pellets containing 5, 7.5, or 10 mg DMI in pilot studies (data not shown), we determined the 10 mg dose increased tumor growth most effectively. DMI treatment (10 mg) increased tumor volume ( $\text{mm}^3$ ; Fig. 2A; see figure legends for statistical analyses) and growth rate (volume normalized; Fig. 2B), in association with significantly increased tumor weight by day 14 post-4T1 injection (Fig. 2C). Despite the increase in tumor growth, metastasis to the lungs was not altered in DMI-treated mice (Fig. 2D and E). DMI treatment significantly reduced tumor VEGF, a key proangiogenic cytokine (Fig. 2F), and transiently decreased tumor IL-6, a proinflammatory cytokine with proangiogenic activity (Fig. 2G); however, DMI treatment did not alter CD31<sup>+</sup> blood vessel density (Supplementary Fig. S3). Tumor norepinephrine was not altered by DMI treatment (Fig. 2H). A transient increase in tumor normetanephrine was detected at day 12 post-4T1 injection (Fig. 2I).

#### **$\alpha_2$ -AR activation increases breast tumor growth and metastasis**

To determine if selective activation of adrenergic receptor can increase tumor growth, mice were injected daily with 5

mg/kg ISO (nonselective  $\beta$ -AR agonist), 10 mg/kg phenylephrine ( $\alpha_1$ -AR), or 10 and 25  $\mu\text{g}/\text{kg}$  DEX ( $\alpha_2$ -AR) beginning 2 days before 4T1 injection and continuing until sacrifice. Neither ISO nor phenylephrine treatment altered normalized tumor growth, tumor weight, or lung metastases (Fig. 3A–D). Tumor VEGF and IL-6 did not differ between phenylephrine or ISO treatment and saline controls at sacrifice (Fig. 3E and F). Daily treatment with the highly selective  $\alpha_2$ -AR agonist DEX (10 and 25  $\mu\text{g}/\text{kg}$ ) increased the rate of tumor growth and the number of metastasis in the lung compared with saline controls (Fig. 3G and H). Immunohistochemistry using anti-Ki67 to detect proliferating cells revealed an increase in proliferating cells in the 10  $\mu\text{g}/\text{kg}$  DEX group compared with saline and 25  $\mu\text{g}/\text{kg}$  groups (Fig. 3I). DEX treatment did not alter tumor VEGF (Fig. 3J) or IL-6 (Fig. 3K) at sacrifice.

#### **Potential cytokine/chemokine mechanisms underlying DMI- and DEX-induced tumor pathogenesis**

To further probe the mechanisms underlying differences in DMI versus DEX-induced tumor progression, additional tumor cytokines and chemokines were measured by multiplex analysis. In DMI-treated mice, the proinflammatory cytokine TNF- $\alpha$  was nonsignificantly increased (Fig. 4A; Mann–Whitney,  $P = 0.07$ ). A similar trend was detected in mice treated with 10  $\mu\text{g}/\text{kg}$  DEX (Fig. 4B; ANOVA,  $P = 0.052$ ) but not in phenylephrine- or ISO-treated mice (data not shown). TNF- $\alpha$  added directly to 4T1 cells did not alter proliferation *in vitro* (Supplementary Fig. S4), indicating that elevated TNF- $\alpha$  cannot directly increase 4T1 tumor growth. Furthermore, neither DMI nor DEX treatment altered the proinflammatory cytokine IL-1 $\beta$ , the T-cell-associated cytokines IL-2 and IFN- $\gamma$ , or the anti-inflammatory cytokine IL-10 (data not shown). However, several tumor chemokines that promote tumor metastasis and regulate macrophage activity including RANTES (CCL-5), M-CSF (CSF-1), and MIP-2 (CCL-2) were decreased by DMI treatment (Fig. 4A), but not altered by DEX treatment (Fig. 4B). Neither DMI nor DEX treatment significantly altered the density of F4/80<sup>+</sup> tumor macrophages (Supplementary Fig. S5).

#### **DMI- and DEX-induced tumor growth is associated with altered SHG-producing tumor collagen**

Structural alterations in fibrillar collagen, uniquely visible via SHG imaging, are associated with tumor cell proliferation and motility (18, 27). Our laboratory has demonstrated that stromal TNF- $\alpha$  knockout, or depletion of macrophages, reduced tumor growth and metastasis and was associated with alterations in SHG (28). These findings, combined with the association between DMI- and DEX-induced tumor growth and trends toward increased tumor TNF- $\alpha$ , led us to explore a matrix-based mechanism underlying the increased tumor growth.

We analyzed collagen in 4T1 tumors from DMI-, DEX-, and ISO-treated mice using 2 methods: standard immunohistochemical analysis and SHG imaging. Figure 5A shows 2 representative images from a 4T1 tumor with SHG-producing collagen (in blue) and collagen type I

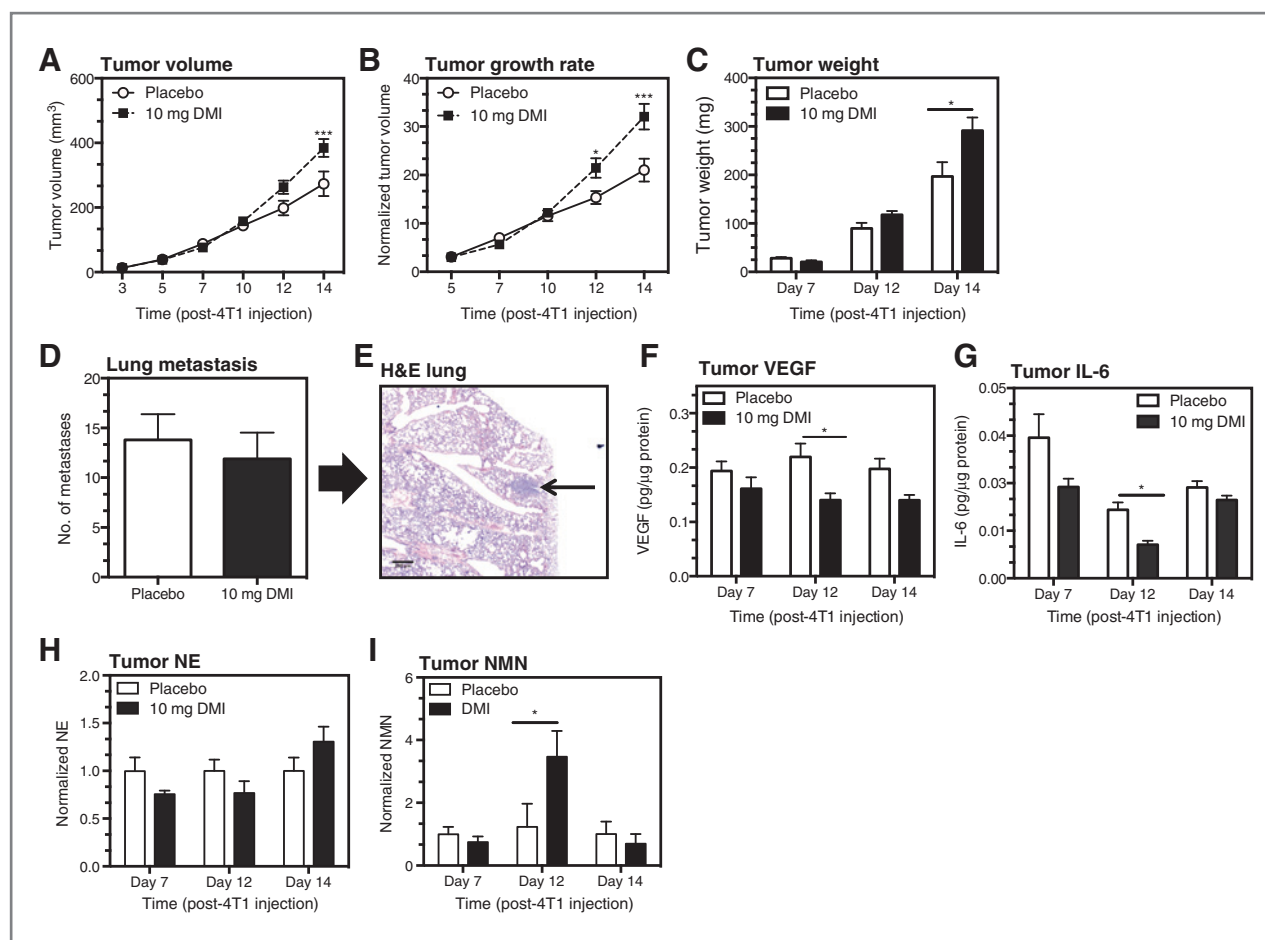


**Figure 2.** DMI treatment increased tumor growth but not metastasis. Mice were implanted with 10 mg DMI or placebo continuous release pellets 2 days before 4T1 inoculation. Tumor growth expressed as volume (A) or normalized (B) and as tumor weight (C). Lung metastasis (D) were measured 14 days post-4T1 injection. E, representative H&E-stained lung with metastatic lesion indicated by arrow.  $\times 4$  magnification; scale bar = 200  $\mu\text{m}$ . A, D, results represent 1 of 2 experimental replications at each time point. For (H) and (I) results from 2 experimental repetitions were normalized relative to the respective placebo controls. Results are expressed as mean  $\pm$  SEM,  $n = 6-7$  mice per group for day 7 and 12,  $n = 9-10$  per group day 14 post-4T1 injection. Statistical analyses: (A) main effect of DMI treatment,  $P = 0.047$ ; treatment  $\times$  time interaction,  $P < 0.0001$ ; main effect of time,  $P < 0.0001$ ; B, main effect of DMI treatment,  $P = 0.0005$ ; treatment  $\times$  time interaction,  $P = 0.0001$ , main effect of time,  $P < 0.0001$ ; C, tumor weight: main effect of DMI,  $P = 0.02$ ; DMI  $\times$  time interaction,  $P = 0.04$ , main effect of time,  $P < 0.0001$ ; D, lung metastasis: Student  $t$  test,  $P = 0.6$ ; F, VEGF: DMI treatment,  $P = 0.0006$ , no interaction or effect of time; G, IL-6: main effect of DMI treatment,  $P = 0.004$ , no DMI  $\times$  time interaction, main effect of time,  $P = 0.0001$ ; H, tumor normetanephrine (NMN): DMI  $\times$  time interaction,  $P = 0.02$ ). Asterisks indicate significant differences versus corresponding placebo control group by Holm-Sidak's multiple comparisons test ( $P < 0.05$ ).

detected by immunohistochemistry (in green) in the same section. Image analysis revealed that in 4T1 tumors from DMI-treated mice, the SHG-emitting pixel intensity was increased (Fig. 5B) without a change in the density of SHG-emitting collagen as determined by the number of SHG pixels above a common threshold (Fig. 5C). No change in total collagen was detected by anti-collagen I immunohistochemistry (Fig. 5D). However, DEX treatment did not alter the intensity of SHG pixels above threshold (Fig. 5E), but it increased the number of SHG pixels above threshold (Fig. 5F) with no change in total collagen (Fig. 5G). The  $\beta$ -agonist ISO produced no change in SHG intensity (Fig. 5H) and a nonsignificant increase in SHG pixel number (Fig. 5I,  $P = 0.07$ ). By immunohistochemistry, ISO also produced a nonsignificant reduction in total collagen pixel intensity (Fig. 5J,  $P = 0.15$ ). These alterations in SHG

indicate changes in tumor collagen microstructure with DMI, DEX, and ISO treatment, and each treatment uniquely correlates with augmentation of primary tumor growth (DMI), tumor growth and metastasis (DEX), or no alteration (ISO; summarized in Table 1).

## Discussion

Adrenergic receptor activation promotes tumor growth or metastasis in several animal models of cancer in which the tumor cells express functional adrenergic receptor (7, 8, 29). We demonstrate here that the mammary adenocarcinoma cell line 4T1 lacks  $\alpha$ -AR and  $\beta$ -AR expression and signaling capacity and is unable to directly respond to norepinephrine. To our knowledge, no studies have investigated the *in vivo* impact of sympathetic activation and norepinephrine

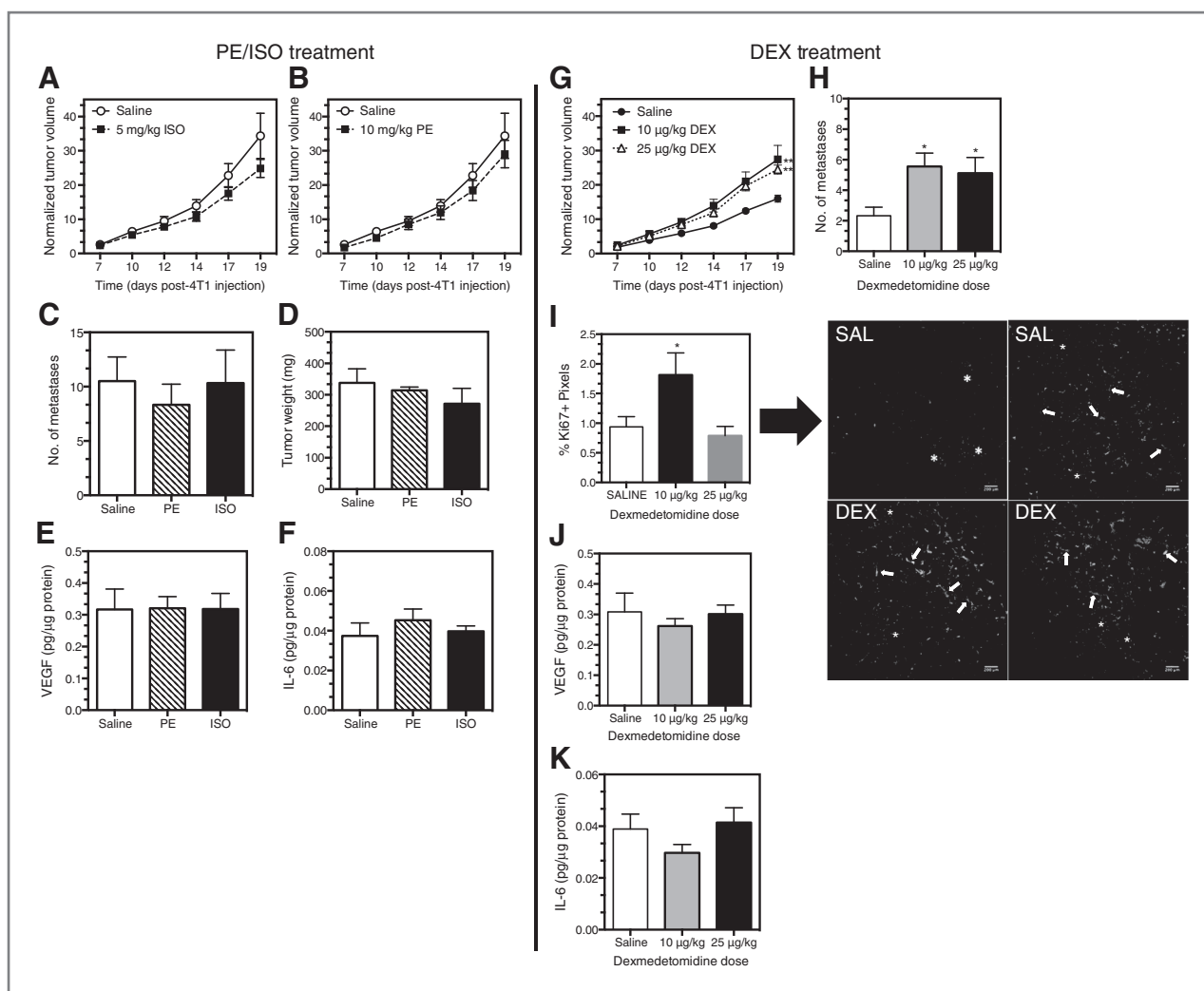


**Figure 3.** 4T1 tumor growth and metastasis in mice treated with ISO, PE, or DEX. Treatment was initiated 2 days before 4T1 injection and continued daily until sacrifice on day 19 post-4T1 injection. ISO and PE treatment were part of the same experiment and shared a saline control group, but for ease of comparison, the normalized tumor growth for ISO and PE are graphed separately in (A) and (B). A–F, PE and ISO treatment,  $n = 6$  per group. G–K, DEX treatment,  $n = 9$  per group. I, representative images of Ki67<sup>+</sup> proliferating cells in 2 tumors each from saline and DEX-treated (10 µg/kg) mice;  $\times 10$  magnification; scale bar = 200 µm. Asterisks and arrows indicate 2 morphologies apparent with Ki67 staining in 4T1 tumors. All results are expressed as mean  $\pm$  SEM. Statistical analyses: A, ISO, normalized tumor volume: no main effect of treatment ( $P = 0.14$ ) or interaction by time ( $P = 0.22$ ), main effect of time ( $P < 0.0001$ ); B, PE, normalized tumor volume: no treatment ( $P = 0.4$ ) or interaction ( $P = 0.4$ ), main effect of time ( $P < 0.0001$ ); C–F, PE or ISO versus saline, Student  $t$  test,  $P > 0.05$ . G, DEX, normalized tumor volume, main effect of treatment,  $P = 0.009$ ; interaction,  $P < 0.0001$ ; time,  $P < 0.0001$ ; \*\*Simple effects analysis of main effect,  $P < 0.0001$  versus saline; H, metastasis,  $P = 0.03$ ; \*Holm–Sidak analysis,  $P < 0.05$  versus saline; I, Ki67 analysis: Kruskal–Wallis,  $P = 0.04$ ; J, VEGF, Kruskal–Wallis,  $P = 0.6$ ; K, IL-6, Kruskal–Wallis,  $P = 0.3$ .

stimulation on tumor pathogenesis when the tumor cells cannot directly respond to norepinephrine. Doing so removes the influence of tumor adrenergic receptors and thus allows the investigation of adrenergic receptor stimulation of adrenergic receptor-expressing host stromal cells, effects that may be masked when tumor cells express functional adrenergic receptor. Under these conditions, we demonstrated that inhibition of norepinephrine reuptake to elevate synaptic norepinephrine promotes 4T1 tumor growth, and  $\alpha_2$ -AR activation can drive tumor growth and metastasis. The distinct alterations in SHG emission from tumor collagen accompanying elevated norepinephrine and adrenergic receptor stimulation suggests that SNS acti-

vation may modify the tumor extracellular matrix to regulate pathogenesis. Together, these results reveal novel pathways by which SNS activation can drive tumor growth and metastasis despite the inability of the tumor cells themselves to respond to norepinephrine.

#### A role for $\alpha_2$ -AR and host stromal cells in tumor growth and metastasis

The finding that DMI treatment elevated norepinephrine and increased 4T1 tumor growth is consistent with other reports demonstrating augmentation of tumor growth and/or metastasis associated with sympathetic innervation and  $\beta$ -AR-expressing tumor or stromal cells (6–8). However, our

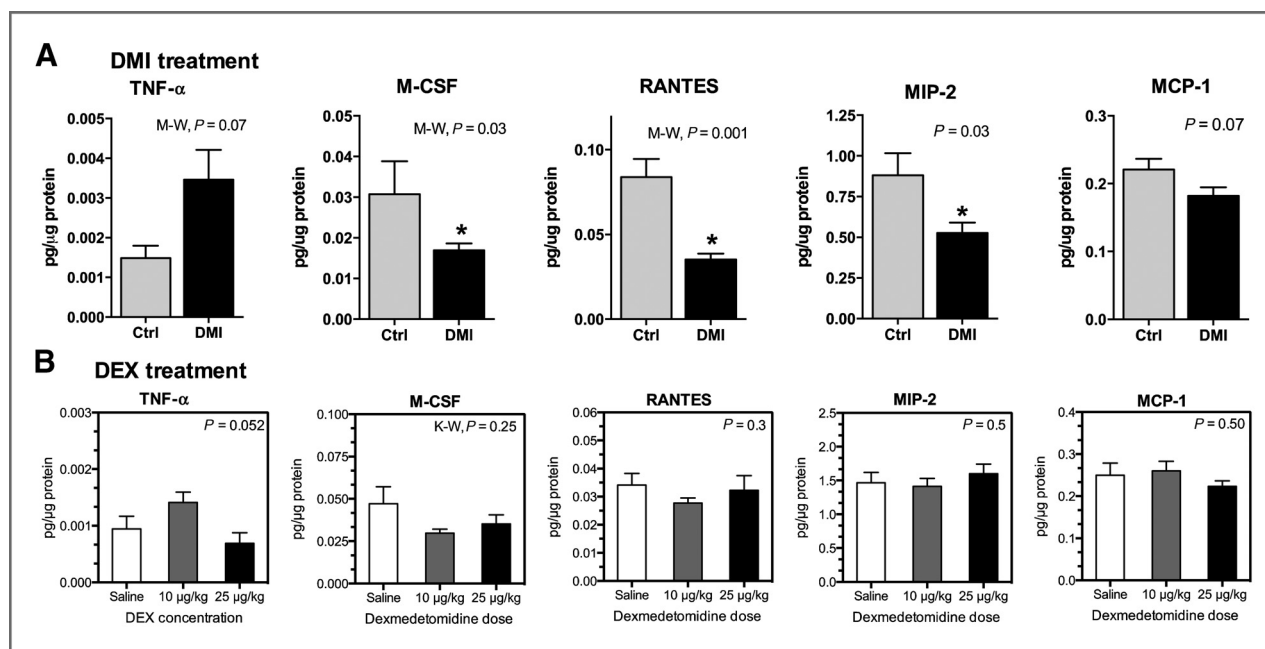


Figure 4. Multiplex analysis of tumor chemokines and cytokines in mice treated with (A) DMI or (B) DEX. DMI elicited reductions in chemokines that were not observed with DEX treatment. Results are expressed as mean  $\pm$  SEM,  $n = 7$  to 8 mice per group. A, Student  $t$  test or nonparametric Mann–Whitney (M–W)  $P$ -values are indicated for each chemokine/cytokine. B,  $P$ -values represent analysis by one-way ANOVA. \* indicates significant differences versus corresponding control group ( $P < 0.05$ ).

results differ in several important ways from these reports. We found no evidence that increased tumor growth was associated with  $\beta$ -AR activation or with increased angiogenesis or proangiogenic cytokines. Furthermore, in this adrenergic receptor-negative tumor model,  $\beta$ -AR activation with ISO did not increase lung metastasis or elevate M-CSF (also known as CSF-1; data not shown), as reported by Sloan and colleagues. We contend a  $\beta$ -AR-induced reduction in CSF-1 or other stromal-derived cytokines/chemokines may be obscured if tumor cytokine production (such as CSF-1) is increased by  $\beta$ -AR activation. In this scenario, whether or not the tumor cells can respond to  $\beta$ -AR stimulation may dictate directionally opposite tumor outcomes.

Our results are consistent with a small number of reports of increased proliferation by  $\alpha_2$ -AR-expressing breast tumor cell *in vitro* and increased tumor growth *in vivo* (13, 29, 30), but we have been unable to detect functional  $\alpha_2$ -AR in several breast cancer cell lines (data not shown). In fact, DEX at supra micromolar concentrations may act on imidazoline receptors (31) to reduce 4T1 cell proliferation and increase VEGF production *in vitro* (Fig. 1G and H). This concentration of DEX, orders of magnitude above the  $K_i$  for  $\alpha_2$ -AR (1.08 nmol/L; ref. 32), is unlikely to be achieved *in vivo* at the doses used here. Instead, we propose that DEX activation of host stromal  $\alpha_2$ -AR increased tumor growth and metastasis. Intriguingly, in human breast cancer, the  $\alpha_{2A}$ -AR gene was one of 26 tumor stroma genes that together predicted poor outcome (33). One question raised by our results is why DMI treatment—and increased synaptic norepinephrine—did not activate  $\alpha_2$ -AR to affect metastatic outcome along with increased tumor growth. One possi-

bility is that norepinephrine stimulation of  $\beta$ -AR or  $\alpha_1$ -AR pathways may oppose  $\alpha_2$ -AR signaling in the tumor or elsewhere in the periphery. This is supported by the observation that although DEX ligation of  $\alpha_2$ -AR did not affect VEGF, IL-6, RANTES, and other prometastatic cytokines, DMI-induced elevation of synaptic norepinephrine reduced them, presumably via adrenergic receptors other than  $\alpha_2$ , thus providing an antimetastatic counter to the prometastatic effects of  $\alpha_2$ -AR stimulation by elevated norepinephrine. One way to test this possibility is to selectively block adrenergic receptor in DMI-treated mice, but we found the combination of DMI and  $\beta$ -blocker treatment was associated with a high level of mortality; we therefore tested direct stimulation of  $\beta$ -AR and  $\alpha_1$ -AR. Although we did not detect significant alterations in 4T1 tumor growth and metastasis with ISO or phenylephrine treatment, in ISO-treated mice, a trend toward reduced tumor growth (Fig. 3A) and chemokine production was noted (data not shown), and we are further exploring  $\beta$ -AR activation in this tumor model.

We have yet to identify the stromal targets of norepinephrine and  $\alpha_2$ -AR stimulation or their location. DMI only transiently increased synaptic norepinephrine in the tumor, as indicated by the norepinephrine metabolite normetanephrine. It should be noted that at no time point post-DMI treatment was splenic or tumor norepinephrine or normetanephrine content reduced, indicative of sympathetic nerve depletion because of chronic elevation of norepinephrine. Splenic norepinephrine and normetanephrine were dramatically increased early after DMI implantation, an effect that subsided but was still apparent as the tumor developed (data not shown). The DMI-induced increase in

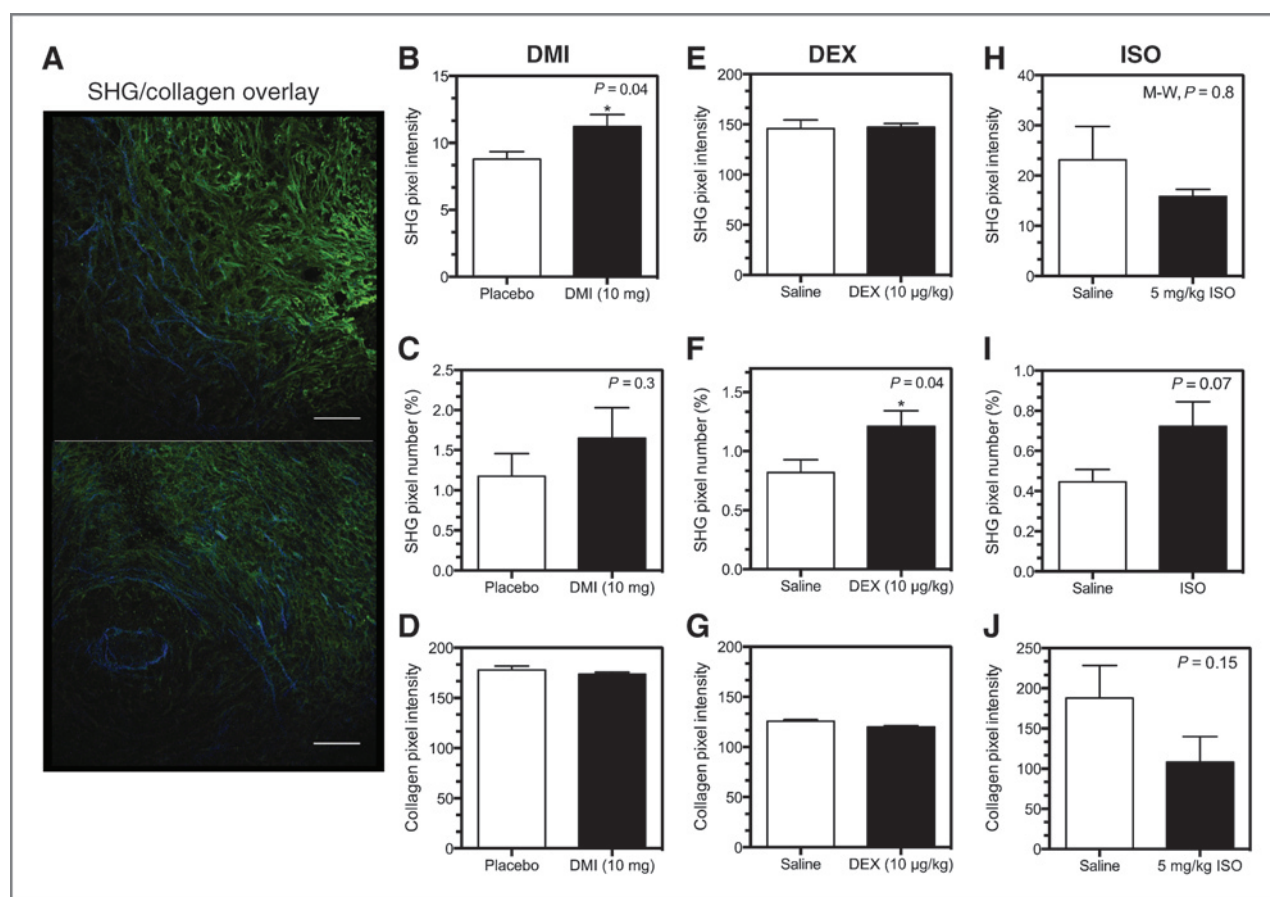


**Figure 5.** Tumor collagen structure is differentially altered by DMI, DEX, and ISO treatment. Tumor slices were stained for collagen by standard immunohistochemical techniques and imaged to detect immunofluorescent and SHG emission by multiphoton microscopy. Image analysis was conducted with Image J as described in materials and methods. A, 2 representative pseudo-colored images of SHG (blue) versus collagen type I (green) from a 4T1 tumor. Scale bars = 100 µm. B, E, H, SHG pixel intensity above threshold; C, F, I, percentage of SHG pixels above threshold; D, G, J, anticollagen immunohistochemical analysis. Results shown are mean  $\pm$  SEM,  $n = 8$  to 9 mice per group for both DMI and DEX experiments;  $n = 6$  per groups for ISO experiment. Asterisk indicates significant differences based on Student  $t$  test,  $P < 0.05$  versus placebo or saline by Student  $t$  test; M-W = Mann-Whitney nonparametric  $U$  test.

splenic norepinephrine points to the potential targeting of adrenergic receptor-expressing cells in extratumoral organs, such as spleen and bone marrow, that play a role in 4T1 pathogenesis (34). Similarly, DEX treatment may target  $\alpha_2$ -expressing cells within the tumor and the lung to promote metastasis. Furthermore, we cannot rule out these drugs acting at the level of the central nervous system. For example, the DEX-induced increase in tumor Ki67<sup>+</sup> proliferating cells (Fig. 3I) and TNF- $\alpha$  (Fig. 4B) at 10 µg/kg, but not 25 µg/kg, may indicate distinct mechanisms underlying DEX treatment

involving the mild sedation (central nervous system effects) observed with 25 µg/kg DEX. Nonetheless, our results demonstrate that the elevated tumor growth associated with DEX and DMI treatment is driven by changes apparent within the tumor, including the extracellular matrix.

#### **A novel mechanism for SNS regulation of tumor progression: collagen microstructure and SHG imaging**

Tumor stromal cells, including macrophages and fibroblasts, regulate tumor collagen structure. The detected SHG

**Table 1.** Summary of DMI, DEX, and ISO-induced tumor matrix alterations

Treatment (AR-selectivity)	Tumor growth	Metastasis	SHG <sup>+</sup> content (intensity)	SHG <sup>+</sup> fibers (% pixels)	Total collagen (IF)
DMI (mixed AR)	Increased	No change	Increased	No change	No change
DEX ( $\alpha_2$ )	Increased	Increased	No change	Increased	No change
ISO ( $\beta$ -AR)	No change	No change	No change	No change	Decreased

signal from a collagen fiber is sensitive to the amount of collagen (15), as well as the diameter of the fibrils that form fibers (35, 36), their spacing (36), and the order versus disorder in fibril packing (37). Here, we define a change in one or more of the latter 3 parameters (fibril diameter, fibril spacing, and order) as a change in collagen fiber "microstructure." Hence, the signal produced by SHG differs from immunofluorescent detection of collagen, which is sensitive to epitope concentration and reports primarily the amount of collagen in a given region of interest. The 2 readouts [SHG and immunofluorescence (IF)] from a given collagen fiber can be compared with gain insight into the extent of changes in fibril microstructure (primarily alters SHG) versus changes in collagen content (alters both SHG and IF; see refs. 28, 38, and 39).

As revealed by image analysis, tumor SHG-emitting collagen was increased by both DMI and DEX treatment in subtly different ways. In DMI-treated mice, tumor SHG pixel intensity above threshold increased without an increase in the percentage of pixels above threshold, representing a change in SHG<sup>+</sup> fiber microstructure (Fig. 5B and C). However, increased SHG emission from tumors from DEX-treated mice was because of an increase in the percentage of pixels above threshold without an increase in the intensity of those pixels above threshold (Fig. 5E and F), suggesting an increase in SHG<sup>+</sup> fiber content relative to control tumors. Neither of these types of increased SHG was associated with altered total collagen as measured by IF (Fig. 5D and G), indicative of an alteration in the structure of the tumor collagen and not collagen deposition. Interestingly, ISO elicited a trend toward decreased total collagen as measured by IF (Fig. 5I), and yielded no change in tumor growth or metastasis despite the trend toward increased SHG<sup>+</sup> fiber content (Fig. 5I). Based on the evidence that microstructural changes in tumor collagen, as detected by SHG, may drive tumor cell proliferation, local invasion, and metastasis (21, 40, 41), we contend that the treatment-dependent changes in SHG-emitting collagen shown here reflect a stromal-based mechanism by which adrenergic receptor activation may promote tumor progression. Studies are underway to understand the adrenergic receptor mechanisms that alter SHG<sup>+</sup> collagen microstructure and to demonstrate that such changes lead to DEX- or DMI-induced tumor progression. These results illustrate the potential power of using SHG imaging in the 4T1 model to distinguish overlapping and opposing effects of increased norepinephrine with sympathetic activation consistent with our proposal that norepinephrine elicits effects via mixed adrenergic receptor signaling that can oppose each other.

### Clinical implications

An important aspect of this work is that DMI and DEX are used clinically. A retrospective study examining the clinical use of antidepressants and breast cancer development found an association between DMI and increased breast cancer risk (42), consistent with the protumor growth effect shown here. DEX is used as a sedative to

treat cancer pain, adding urgency to delve further into the mechanisms underlying chronic DEX treatment and increased tumor growth and metastasis (43, 44). Finally, our results with DMI and elevated synaptic norepinephrine imply a balance between prometastatic effects of  $\alpha_2$ -AR and antimetastatic  $\beta$ -AR with increased norepinephrine release. If true, caution should be applied in the clinical adjuvant use of  $\beta$ -blockers, as proposed by others (3, 45).

In summary, our results strongly implicate  $\alpha_2$ -AR activation as a promoter of tumor pathogenesis in the absence of direct sympathetic input to the tumor cells. The results suggest a unique, matrix-based mechanism whereby norepinephrine can facilitate breast tumor growth through regulation of the tumor extracellular matrix, specifically collagen microstructure. Further investigation into this mechanism is critical in part because of the possibility of using SHG imaging to detect SNS-induced alterations in the tumor matrix as a marker of a more aggressive tumor phenotype. Our results suggest that norepinephrine can elicit directionally opposing effects within the tumor that must be carefully investigated to understand the impact of stress-induced SNS activation in a disease as molecularly heterogeneous as breast cancer.

### Disclosure of Potential Conflicts of Interest

No potential conflicts of interest were disclosed.

### Authors' Contributions

**Conception and design:** M.J. Szpunar, E.B. Brown, K.S. Madden

**Development of methodology:** M.J. Szpunar, E.B. Brown

**Acquisition of data (provided animals, acquired and managed patients, provided facilities, etc.):** M.J. Szpunar, K.A. Burke, R.P. Dawes, E.B. Brown, K.S. Madden

**Analysis and interpretation of data (e.g., statistical analysis, biostatistics, computational analysis):** M.J. Szpunar, K.A. Burke, R.P. Dawes, E.B. Brown, K.S. Madden

**Writing, review, and/or revision of the manuscript:** M.J. Szpunar, K.A. Burke, R.P. Dawes, E.B. Brown, K.S. Madden

**Administrative, technical, or material support (i.e., reporting or organizing data, constructing databases):** E.B. Brown

**Study supervision:** E.B. Brown, K.S. Madden

### Acknowledgments

The authors thank K. Liverpool, D. Byun, T. Bubel, G. Arcuri, T. Wolfgang, and P. Staska for their excellent technical assistance.

### Grant Support

M.J. Szpunar was supported by Department of Defense Predoctoral Training Award (W81XWH-10-1-0058); Medical Scientist Training Program (NIH T32 GM07356); National Center for Research Resources (TL1 RR024135). K.A. Burke was supported by Department of Defense Era of Hope Scholar Research Award (W81XWH-09-1-0405) to E.B. Brown. R.P. Dawes was supported by NIH Training Grant in Neuroscience. E.B. Brown was supported by Pew Scholar in the Biomedical Sciences Award; Department of Defense Era of Hope Scholar Research Award (W81XWH-09-1-0405); National Institutes of Health Director's New Innovator Award (1 DP2 OD006501-01). K.S. Madden was supported by Department of Defense IDEA Award (W81XWH-10-01-008), National Institutes of Health (1 R21 CA152777-01).

The costs of publication of this article were defrayed in part by the payment of page charges. This article must therefore be hereby marked *advertisement* in accordance with 18 U.S.C. Section 1734 solely to indicate this fact.

Received March 2, 2013; revised October 13, 2013; accepted October 15, 2013; published online December 5, 2013.

## References

- Reiche EM, Nunes SO, Morimoto HK. Stress, depression, the immune system, and cancer. *Lancet Oncol* 2004;5:617–25.
- Armaiz-Pena GN, Lutgendorf SK, Cole SW, Sood AK. Neuroendocrine modulation of cancer progression. *Brain Behav Immun* 2009;23:10–5.
- Cole SW, Sood AK. Molecular pathways:  $\beta$ -adrenergic signaling in cancer. *Clin Cancer Res* 2012;18:1201–6.
- Antoni MH, Lutgendorf SK, Cole SW, Dhabhar FS, Sephton SE, McDonald PG, et al. The influence of bio-behavioural factors on tumour biology: pathways and mechanisms. *Nat Rev Cancer* 2006;6:240–8.
- Lutgendorf SK, Sood AK. Biobehavioral factors and cancer progression: physiological pathways and mechanisms. *Psychosom Med* 2011;73:724–30.
- Magnon C, Hall SJ, Lin J, Xue X, Gerber L, Freedland SJ, et al. Autonomic nerve development contributes to prostate cancer progression. *Science* 2013;341:1236361.
- Thaker PH, Han LY, Kamat AA, Arevalo JM, Takahashi R, Lu C, et al. Chronic stress promotes tumor growth and angiogenesis in a mouse model of ovarian carcinoma. *Nat Med* 2006;12:939–44.
- Sloan EK, Priceman SJ, Cox BF, Yu S, Pimentel MA, Tangkanangnukul V, et al. The sympathetic nervous system induces a metastatic switch in primary breast cancer. *Cancer Res* 2010;70:7042–52.
- Campbell JP, Karolak MR, Ma Y, Perrien DS, Masood-Campbell SK, Penner NL, et al. Stimulation of host bone marrow stromal cells by sympathetic nerves promotes breast cancer bone metastasis in mice. *PLoS Biol* 2012;10:e1001363.
- Powe DG, Voss MJ, Habashy HO, Zanker KS, Green AR, Ellis IO, et al.  $\alpha$ - and  $\beta$ -adrenergic receptor (AR) protein expression is associated with poor clinical outcome in breast cancer: an immunohistochemical study. *Breast Cancer Res Treat* 2011;130:457–63.
- Madden KS, Szpunar MJ, Brown EB.  $\beta$ -Adrenergic receptors ( $\beta$ -AR) regulate VEGF and IL-6 production by divergent pathways in high  $\beta$ -AR-expressing breast cancer cell lines. *Breast Cancer Res Treat* 2011;130:747–58.
- Vandewalle B, Revillion F, Lefebvre J. Functional  $\beta$ -adrenergic receptors in breast cancer cells. *J Cancer Res Clin Oncol* 1990;116:303–6.
- Bruzzone A, Pinero CP, Rojas P, Romanato M, Gass H, Lanari C, et al.  $\alpha$ (2)-Adrenoceptors enhance cell proliferation and mammary tumor growth acting through both the stroma and the tumor cells. *Curr Cancer Drug Targets* 2011;11:763–74.
- Nance DM, Sanders VM. Autonomic innervation and regulation of the immune system (1987–2007). *Brain Behav Immun* 2007;21:736–45.
- Moreaux L, Sandre O, Charpak S, Blanchard-Desce M, Mertz J. Coherent scattering in multi-harmonic light microscopy. *Biophys J* 2001;80:1568–74.
- Sidani M, Wyckoff J, Xue C, Segall JE, Condeelis J. Probing the microenvironment of mammary tumors using multiphoton microscopy. *J Mammary Gland Biol Neoplasia* 2006;11:151–63.
- Wang W, Wyckoff JB, Frohlich VC, Oleynikov Y, Huttelmaier S, Zavadil J, et al. Single cell behavior in metastatic primary mammary tumors correlated with gene expression patterns revealed by molecular profiling. *Cancer Res* 2002;62:6278–88.
- Condeelis J, Segall JE. Intravital imaging of cell movement in tumours. *Nat Rev Cancer* 2003;3:921–30.
- Burke K, Tang P, Brown E. Second harmonic generation reveals matrix alterations during breast tumor progression. *J Biomed Opt* 2013;18:31106.
- Kakkad SM, Solaiyappan M, Argani P, Sukumar S, Jacobs LK, Leibfritz D, et al. Collagen I fiber density increases in lymph node positive breast cancers: pilot study. *J Biomed Opt* 2012;17:116017.
- Conklin MW, Eickhoff JC, Riching KM, Pehlke CA, Eliceiri KW, Provenzano PP, et al. Aligned collagen is a prognostic signature for survival in human breast carcinoma. *Am J Pathol* 2011;178:1221–32.
- Aslakson CJ, Miller FR. Selective events in the metastatic process defined by analysis of the sequential dissemination of subpopulations of a mouse mammary tumor. *Cancer Res* 1992;52:1399–405.
- Schildkraut JJ, Dodge GA, Logue MA. Effects of tricyclic antidepressants on the uptake and metabolism of intracisternally administered norepinephrine-H3 in rat brain. *J Psychiatr Res* 1969;7:29–34.
- Glowinski J, Axelrod J. Inhibition of uptake of tritiated-noradrenaline in the intact rat brain by imipramine and structurally related compounds. *Nature* 1964;204:1318–9.
- Marjamaki A, Ala-Uotila S, Luomala K, Perala M, Jansson C, Jalkanen M, et al. Stable expression of recombinant human  $\alpha$ 2-adrenoceptor subtypes in two mammalian cell lines: characterization with [3H]rauwolscine binding, inhibition of adenylate cyclase and RNase protection assay. *Biochim Biophys Acta* 1992;1134:169–77.
- Eisenhofer G, Kopin IJ, Goldstein DS. Catecholamine metabolism: a contemporary view with implications for physiology and medicine. *Pharmacol Rev* 2004;56:331–49.
- Egeblad M, Rasch MG, Weaver VM. Dynamic interplay between the collagen scaffold and tumor evolution. *Curr Opin Cell Biol* 2010;22:697–706.
- Burke RM, Madden KS, Perry SW, Zettel ML, Brown EB. Tumor-associated macrophages and stromal TNF- $\alpha$  regulate collagen structure in breast tumor models as visualized by second harmonic generation. *J Biomed Opt* 2013;18:86003.
- Bruzzone A, Pinero CP, Castillo LF, Sarappa MG, Rojas P, Lanari C, et al.  $\alpha$ 2-Adrenoceptor action on cell proliferation and mammary tumour growth in mice. *Br J Pharmacol* 2008;155:494–504.
- Vazquez SM, Mladovan AG, Perez C, Bruzzone A, Baldi A, Luthy IA. Human breast cell lines exhibit functional  $\alpha$ 2-adrenoceptors. *Cancer Chemother Pharmacol* 2006;58:50–61.
- Khan ZP, Ferguson CN, Jones RM.  $\alpha$ 2 and imidazoline receptor agonists. Their pharmacology and therapeutic role. *Anaesthesia* 1999;54:146–65.
- Piletz JE, Zhu H, Chikkala DN. Comparison of ligand binding affinities at human I1-imidazoline binding sites and the high affinity state of  $\alpha$ 2 adrenoceptor subtypes. *J Pharmacol Exp Ther* 1996;279:694–702.
- Finak G, Bertos N, Pepin F, Sadekova S, Souleimanova M, Zhao H, et al. Stromal gene expression predicts clinical outcome in breast cancer. *Nat Med* 2008;14:518–27.
- DuPre SA, Hunter KW Jr. Murine mammary carcinoma 4T1 induces a leukemoid reaction with splenomegaly: association with tumor-derived growth factors. *Exp Mol Pathol* 2007;82:12–24.
- Han X, Burke RM, Zettel ML, Tang P, Brown EB. Second harmonic properties of tumor collagen: determining the structural relationship between reactive stroma and healthy stroma. *Opt Express* 2008;16:1846–59.
- Williams RM, Zipfel WR, Webb WW. Interpreting second-harmonic generation images of collagen I fibrils. *Biophys J* 2005;88:1377–86.
- Lacomb R, Nadiarykh O, Townsend SS, Campagnola PJ. Phase matching considerations in second harmonic generation from tissues: effects on emission directionality, conversion efficiency and observed morphology. *Opt Commun* 2008;281:1823–32.
- Diop-Frimpong B, Chauhan VP, Krane S, Boucher Y, Jain RK. Losartan inhibits collagen I synthesis and improves the distribution and efficacy of nanotherapeutics in tumors. *Proc Natl Acad Sci U S A* 2011;108:2909–14.
- Ingman WV, Wyckoff J, Gouon-Evans V, Condeelis J, Pollard JW. Macrophages promote collagen fibrillogenesis around terminal end buds of the developing mammary gland. *Dev Dyn* 2006;235:3222–9.
- Provenzano PP, Eliceiri KW, Campbell JM, Inman DR, White JG, Keely PJ. Collagen reorganization at the tumor-stromal interface facilitates local invasion. *BMC Med* 2006;4:38.
- Provenzano PP, Inman DR, Eliceiri KW, Knittel JG, Yan L, Rueden CT, et al. Collagen density promotes mammary tumor initiation and progression. *BMC Med* 2008;6:11.
- Sharpe CR, Collet JP, Belzile E, Hanley JA, Boivin JF. The effects of tricyclic antidepressants on breast cancer risk. *Br J Cancer* 2002;86:92–7.
- Roberts SB, Wozencraft CP, Coyne PJ, Smith TJ. Dexmedetomidine as an adjuvant analgesic for intractable cancer pain. *J Palliat Med* 2011;14:371–3.
- Ugur F, Gulcu N, Boyaci A. Intrathecal infusion therapy with dexmedetomidine-supplemented morphine in cancer pain. *Acta Anaesthesiol Scand* 2007;51:388.
- Powe DG, Entschladen F. Targeted therapies: using  $\beta$ -blockers to inhibit breast cancer progression. *Nat Rev Clin Oncol* 2011;8:511–2.

RESEARCH ARTICLE

Open Access

# Fluoxetine modulates breast cancer metastasis to the brain in a murine model

Yuriy Shapovalov<sup>1,2</sup>, Martha Zettel<sup>1</sup>, Sara C Spielman<sup>1</sup>, Stacy A Amico-Ruvio<sup>1</sup>, Emily A Kelly<sup>1</sup>, Grayson O Sipe<sup>1</sup>, Ian M Dickerson<sup>1</sup>, Ania K Majewska<sup>1\*†</sup> and Edward B Brown<sup>2\*†</sup>

## Abstract

**Background:** Despite advances in the treatment of primary breast tumors, the outcome of metastatic breast cancer remains dismal. Brain metastases present a particularly difficult therapeutic target due to the “sanctuary” status of the brain, with resulting inability of most chemotherapeutic agents to effectively eliminate cancer cells in the brain parenchyma. A large number of breast cancer patients receive various neuroactive drugs to combat complications of systemic anti-tumor therapies and to treat concomitant diseases. One of the most prescribed groups of neuroactive medications is anti-depressants, in particular selective serotonin reuptake inhibitors (SSRIs). Since SSRIs have profound effects on the brain, it is possible that their use in breast cancer patients could affect the development of brain metastases. This would provide important insight into the mechanisms underlying brain metastasis. Surprisingly, this possibility has been poorly explored.

**Methods:** We studied the effect of fluoxetine, an SSRI, on the development of brain metastatic breast cancer using MDA-MB-231BR cells in a mouse model.

**Results:** The data demonstrate that fluoxetine treatment increases the number of brain metastases, an effect accompanied by elevated permeability of the blood–brain barrier, pro-inflammatory changes in the brain, and glial activation. This suggests a possible role of brain-resident immune cells and glia in promoting increased development of brain metastases.

**Conclusion:** Our results offer experimental evidence that neuroactive substances may influence the pathogenesis of brain metastatic disease. This provides a starting point for further investigations into possible mechanisms of interaction between various neuroactive drugs, tumor cells, and the brain microenvironment, which may lead to the discovery of compounds that inhibit metastasis to the brain.

**Keywords:** Breast cancer, Brain metastasis, Fluoxetine, Blood–brain barrier

## Background

Despite recent advances in the treatment of primary breast cancer tumors, the incidence of fatal metastatic events remains high. Brain metastasis represents a particularly challenging complication of breast cancer. It is estimated that 10-15% of breast cancer patients have symptomatic brain metastases [1,2] and as many as 30% of patients reveal brain metastases on autopsy [3,4]. The

brain provides a unique microenvironment for tumor growth. It is a particularly difficult therapeutic target due to the complexity of brain function as well as the reduced ability of therapeutic agents to cross the blood–brain barrier (BBB) [5]. In fact, many of the newest and most effective treatments for primary tumors are ineffective in treating breast tumor metastases in the brain [1,5]. It is becoming increasingly clear that prevention and treatment of metastatic brain tumors requires a better understanding of the mechanisms that determine complex interactions between this unique metastatic milieu and tumor cells [2].

In this study we explore the mechanisms that underlie brain metastases by investigating possible effects of

\* Correspondence: Ania\_Majewska@urmc.rochester.edu; Edward\_Brown@urmc.rochester.edu

†Equal contributors

<sup>1</sup>Department of Neurobiology and Anatomy, University of Rochester School of Medicine & Dentistry, 601 Elmwood Ave, Box 603, Rochester, NY 14642, USA

<sup>2</sup>Department of Biomedical Engineering, University of Rochester, Box 270168, Rochester, NY 14627, USA

antidepressant drug treatment on their development. We present evidence that a selective serotonin reuptake inhibitor (SSRI), fluoxetine, facilitates increased brain-specific formation of breast cancer metastases in a mouse model of the disease. This is accompanied by increased permeability of the BBB and elevated production of pro-inflammatory cytokines, indicating that fluoxetine treatment may promote the entry of cancer cells into the brain via changes in the function of the BBB. This provides important insight into the mechanisms governing breast tumor metastasis to the brain, and possible ways to manipulate those mechanisms in order to reduce brain metastases. This approach has additional clinical relevance because it has been well documented that up to 25% of women with breast cancer suffer from clinical depression, a much higher percentage compared to the incidence observed in the general population [6,7]. As a result, antidepressant drug use among breast cancer patients can be as high as 50% [8]. The SSRIs in particular have found widespread use in the clinical management of breast cancer-associated depression, hot flashes, and chemo brain [9,10]. Recently, however, there has been increasing concern about pharmacologic interactions between several SSRI antidepressants and anti-tumor medications used in breast cancer therapy [11,12]. Several studies indicate that simultaneous administration of these drugs may lead to decreased anti-tumor therapeutic effectiveness and increased risk of recurrent breast cancer or death, due to drug competition for binding sites at the relevant metabolic liver enzymes [13,14]. Even though these reports warrant further experimental validation that considers genetic factors, patient drug compliance, and population dynamics [15,16], there is no doubt that any clinical approach to the prevention and treatment of primary and metastatic breast cancer must take into account possible adverse effects of prescription drug use.

## Methods

### Cells

For intracardiac and tail-vein injections, we used the MDA-MB-231BR-GFP (231BR) human cell line that exhibits an ability to metastasize to the brain [17], a generous gift from Dr. P. Steeg. Cells were maintained in DMEM supplemented with 1% penicillin-streptomycin mixture. A YFP-expressing CNS-1 rat glioma cell line was used for intracranial injections, a generous gift from Dr. R. Mathews [18]. CNS-1 cells were grown in RPMI 1640 medium with 100 µg/ml of hygromycin B. All cell growth media were supplemented with 10% fetal bovine serum (FBS). Cells were regularly checked for mycoplasma contamination, with consistently negative test results.

### Fluoxetine administration and cell injection

All animal experimental protocols were approved by the University of Rochester Committee for Animal Research. Fluoxetine was added at 200 mg/L into drinking water supplied to adult female Nu/Nu mice (Charles River Laboratories) 21 days before either intracardiac or tail-vein injections, and continued during the 3-week survival period. For stereotactic injections into the brain parenchyma, animals were placed on dietary fluoxetine at 200 mg/L for 4 weeks before the cell injections; fluoxetine administration continued for 1 additional week, at which time brains were harvested. 231BR or CNS-1 cells were re-suspended in cold DPBS containing 0.5% FBS, and placed on ice prior to injection. *Intracardiac injections*: After anesthesia with Avertin, we injected  $10^5$  231BR cells into the left cardiac ventricle. Placement of the needle into the left ventricle was confirmed by the presence of pulsating arterial blood. *Tail vein injections*: Mice were placed into a mouse restrainer (Braintree Scientific) and injected with  $10^6$  231BR cells into a tail vein. At the end of each series of injections, cell viability was determined by Trypan Blue staining. Mice were weighed before and after experiments and checked for behavioral abnormalities every three days. No pathologic changes were detected in this study. *Intracranial injections*: Animals were anesthetized with isoflurane and placed into a stereotactic apparatus. A craniotomy was made, and  $10^4$  CNS-1 cells were introduced into the frontal cortex of Nu/Nu adult female mice.

### Fluoxetine and norfluoxetine quantification by liquid chromatography mass spectrometry (LC-MS/MS)

Mice were treated with 200 mg/L of fluoxetine in drinking water for 30 days. 100 µl of serum was collected at day 0 and every 10 days throughout the fluoxetine treatment. SRMs for fluoxetine and norfluoxetine were performed by direct infusion in the positive mode using 50% methanol with 0.1% formic acid. The parent ion m/z, fragment ion m/z, collision energy, and tube lens voltage for the two compounds were 296.1 m/z. 134.1 m/z, 5, 68 for fluoxetine; and 310.1 m/z, 44.3 m/z, 13, 66 for norfluoxetine. To extract the compounds from serum, 5 volumes of acetonitrile (ACN) were added to the serum (500 µl of ACN to 100 µl of serum), followed by vortexing for 2 min and centrifugation at 16,000 g for 5 min at 4°C. The supernatant was collected and dried down in a SpeedVac. The dried material was reconstituted in 100 µl of 50% methanol, and 10 µl was injected for the LC-MS/MS run. LC-MS/MS runs were performed at 40°C on a Thermo Quantum Access Max triple quadrupole mass spectrometer, with a Dionex Ultimate 3000 UPLC, configured with a 150 × 2.1 mm Accucore RP-MS column. The solvent system used 0.1% formic acid as solvent A and 100% methanol as solvent B, with a gradient elution run, beginning with 30%

B for 0.5 minutes, ramping to 95% B over 1.5 minutes, holding at 95% B for 1 minute, and returning to 30% B in 0.25 minutes, with a final 30% B equilibration step for 2 minutes. Raw data files were imported into LCQUAN software, including a standard curve spanning concentrations of 10 nM - 3.16  $\mu$ M, extracted from serum for fluoxetine and norfluoxetine. Area under the curve analysis was used to quantify the compounds in unknown samples.

Additional file 1: Figure S1A reveals that after 10 days of treatment, the mean concentration of fluoxetine reached 128 ng/ml, with the range of 55-243  $\pm$  16 ng/ml. After 20 and 30 days of fluoxetine administration, the mean fluoxetine levels were 160 and 178 ng/ml, with the range of 80-306  $\pm$  25 and 24-363  $\pm$  39 ng/ml, respectively. The mean norfluoxetine concentration at the 10-day time point was 282 ng/ml, with the range of 140-479  $\pm$  41 ng/ml, whereas at the 20 and 30 day interval, the mean norfluoxetine levels were 364 and 414 ng/ml, with the range of 74-532  $\pm$  41 and 153-579  $\pm$  46 ng/ml, respectively (Additional file 1: Figure S1B). The serum levels of fluoxetine were within the range reported previously for human serum samples [19]. However, norfluoxetine concentration reached  $\sim$  twofold higher levels than in human populations [19], probably due to the differences in metabolic transformation of the parent drug in mice versus humans.

#### Immunohistochemistry and image analysis

To quantify brain metastasis, mice injected intracardially with 231BR cells were perfused with 4% paraformaldehyde. The brains were serially sectioned in the coronal plane at 50  $\mu$ m. Sections were viewed on an AX70 Microscope (Olympus, Center Valley, PA) using an epifluorescence setup. Digital images were obtained using a MicroFire camera (Optronics, Muskogee, OK) and Image Pro software (Media Cybernetics, Bethesda, MD). Images were analyzed in ImageJ by a blinded observer. As reported previously in the literature [20], we classified visible metastases as "macrometastases" or "micrometastases" depending upon their size. Specifically, a cluster of cells that was greater than 100  $\mu$ m in greatest extent was counted as a single "macrometastasis" while any cells in a cluster smaller than 100  $\mu$ m in extent were defined as multiple "micrometastases" and counted individually. To quantify lung metastasis, lungs were perfused with 4% paraformaldehyde and embedded in paraffin. 5  $\mu$ m serial sections were cut through the lungs at 300  $\mu$ m intervals and stained with hematoxylin-eosin. The number of lung metastases was determined in 4–6 tissue sections per animal by a blinded investigator using an AX70 Microscope (Olympus, Center Valley, PA) in trans-illumination mode. To investigate brain-resident tumor growth, the brains of mice injected with CNS-1 tumors were serially sectioned

at 50  $\mu$ m. The sections were imaged by a blinded observer as described for 231BR cells above, and images were analyzed in ImageJ. Three measures were used to quantify CNS-1 tumor growth: the number of brain sections containing cells, the total number of tumor-containing pixels in the sections, and the maximum width that the cells spread perpendicular to the initial injection track. Imaging parameters and thresholds were kept constant between sections.

For immunohistochemistry (IHC), sections were washed in 0.1 M phosphate buffered saline (PBS), followed by incubation in 1% hydrogen peroxide to block endogenous peroxidase activity. Next, tissue was incubated in blocking solution containing 0.3% Triton-X and 5% normal donkey serum (NDS) in 0.1 M PBS. After an additional wash, the sections were incubated for 48 h in a humidified chamber at 4°C in primary antibody solution containing one of the following antibodies: rabbit anti-Iba-1 (1:500, Wako Pure Chemical Industries, Richmond, VA); mouse anti-IA/IE (1:200, BD Pharmingen, San Jose, CA); mouse anti-CD11b (1:200, AbD Serotec, Raleigh, NC); mouse anti-CD45 (1:300, AbD Serotec, Raleigh, NC); mouse anti-CD68 (1:800, Abcam, Cambridge, MA); rabbit anti-GFAP (1:1500, Abcam, Cambridge, MA); and Wisteria Floribunda Lectin (WFA) (1:500, Vector Laboratories). The sections were subsequently washed and incubated for 4 h at room temperature with either of the following secondary antibodies: Alexa Fluor 594 donkey anti-rabbit IgG (1:500) or Alexa Fluor 594 donkey anti-mouse IgG (1:500) (Molecular Probes, Carlsbad, CA). The sections were washed, mounted, and cover-slipped using ProLong Gold Antifade Reagent (Molecular Probes, Carlsbad, CA).

Sections were viewed on an AX70 Microscope (Olympus, Center Valley, PA) using an epifluorescence setup. Digital images were obtained using a MicroFire camera (Optronics, Muskogee, OK) and Image Pro software (Media Cybernetics, Bethesda, MD). Images were analyzed by a blinded observer using ImageJ. To determine the amount of glial staining in relation to distance from 231BR metastases, we created binary masks of tumors and glial staining. The tumor mask was then expanded iteratively by one pixel and the number of stained pixels within the region defined by the tumor mask was measured to produce the fraction of stained pixels as a function of distance from the edge of the tumor. All measurements were confined to the brain area in which the tumor resided to correct for differences in glial expression between brain areas. Tumors in control and fluoxetine groups were not statistically different in size for all stains. WFA antibody was used to visualize perineuronal nets in brain sections from animals that were injected with 231BR cells. To quantify WFA staining, background subtracted normalized average pixel intensity value was determined for various brain regions and compared between the control and fluoxetine groups.

### Thinned skull imaging

Chronic imaging of mouse visual cortex was performed using a thinned skull preparation as previously described [21], using GFP-M mice [22] that received 100 mg/L of fluoxetine in drinking water for 4 weeks. Briefly, a two-photon microscope with a Mai Tai laser (Spectra Physics) and a modified Olympus Fluoview 300 confocal unit was used. An Olympus LUMPlan fl/IR 20X/0.95NA was used to identify the binocular visual cortex based on cortical vasculature; an area containing brightly labeled neurons was chosen for imaging. 3D image stacks were obtained at high magnification to allow for dendritic spine reconstruction in layers 1 and 2 of the visual cortex. After the initial imaging session, the scalp was sutured and the animals were returned to the animal facility. The animals were re-anesthetized 4 days later and the same area was identified based on the blood vessel and dendritic patterns [21]. 3D image stacks of the same dendritic regions were again obtained at high magnification. The percentage of lost and new spines was determined relative to the total number of spines present in the initial imaging session using ImageJ.

### Proliferation and migration assay

For proliferation assays, 231BR cells were plated at 20,000 per well and incubated for 6 h to allow cells to adhere. The medium was replaced with DMEM containing fluoxetine at 1–5000 ng/ml. Cell numbers counted after 24, 48, and 72 h of incubation. Results are representative of two independent experiments. A migration assay was performed using the FluoroBlok 24-well insert system with 8.0  $\mu$ m pore size (BD Biosciences, Bedford, MA). 231BR cells were grown for 48 h in DMEM containing various fluoxetine concentrations, trypsinized, counted, and seeded in serum-free DMEM/fluoxetine mixture onto the apical side of the insert at 50,000 per well. DMEM/fluoxetine with 10% FBS was added as a chemoattractant to the basal chamber. Following overnight incubation at 37°C in 5% CO<sub>2</sub>, cells were stained with calcein AM and then read on a bottom reading fluorescent plate reader.

### Evan's Blue spectroscopy

Mice were injected via tail vein with 100  $\mu$ l/10 g body weight of 2% Evan's Blue in PBS. 1 hour after the injection, the animals were perfused with sterile isotonic saline, and the brains were removed and dried in a vacuum oven for 24 hours. Brain tissue was subsequently homogenized in a volume of PBS based on dry tissue weight, and then subjected to protein precipitation with trichloroacetic acid. The spectroscopic analysis of the supernatant was performed at 620 nm to determine Evan's Blue absorbance.

### Quantitative RT-PCR

Animals were perfused with PBS containing 2 IU/ml of heparin. RNA was isolated from the brain tissue using

TRIzol reagent, and 1  $\mu$ g of the purified RNA product was subsequently reverse transcribed using Superscript III reverse transcriptase kit (Invitrogen). PCR was performed using TaqMan® Gene Expression Assays from Applied Biosystems, and the results were normalized to the expression of G3PDH.

### Cytokine immunoassay

Mice were perfused with PBS. Brain tissue was homogenized in RIPA buffer containing protease inhibitors (Thermo Scientific). 25  $\mu$ l of protein extract was used in the subsequent immunoassay to determine cytokine expression. For the multiplex assay, a custom-made plate of mouse cytokines was used according to manufacturer's instructions (EMD Millipore). Data were acquired on a FLEXMAP 3D system and analyzed with MILLIPLEX Analyst (EMD Millipore). Cytokine expression was determined in duplicate and subsequently normalized to sample protein concentration.

### Statistical analysis

Means and standard errors of the mean are presented, and significance was established using either Student's *t*-test or analysis of variance (ANOVA). When ANOVA revealed statistical significance, multiple comparison *post hoc* analysis was performed to confirm differences between experimental groups.  $P < 0.05$  was considered statistically significant.

## Results

### Fluoxetine increases the ability of breast cancer cells to metastasize to the brain

To study the effects of fluoxetine on the ability of breast cancer cells to metastasize to the brain, we pretreated Nu/Nu mice with fluoxetine for three weeks prior to the intracardiac injection of 231BR breast cancer cells. Administration of fluoxetine in drinking water resulted in therapeutic concentrations in the serum as explain in the methods (Figure 1). Three weeks post-injection, metastases in fixed brain sections appeared either as isolated cells that could be readily distinguished and counted, which we term "micrometastases", or as large groups of interconnected cells which could not be accurately distinguished and hence were counted as a single "macrometastasis" by our blinded observer (Figure 1A). Animals that received fluoxetine demonstrated a 52% increase in the total number of brain metastases compared with control: fluoxetine ( $n = 11$ ),  $35.54 \pm 3.90$  vs. control ( $n = 12$ ),  $23.33 \pm 2.46$  tumors/section,  $p = 0.02$  (Figure 1B). This significant change in brain metastatic ability was largely due to increased incidence of micrometastases: fluoxetine,  $32.59 \pm 3.64$  vs. control,  $21.43 \pm 3.64$  tumors/section,  $p = 0.03$ , a 52% increase (Figure 1C). While not statistically significant, the same trend was evident for the number of

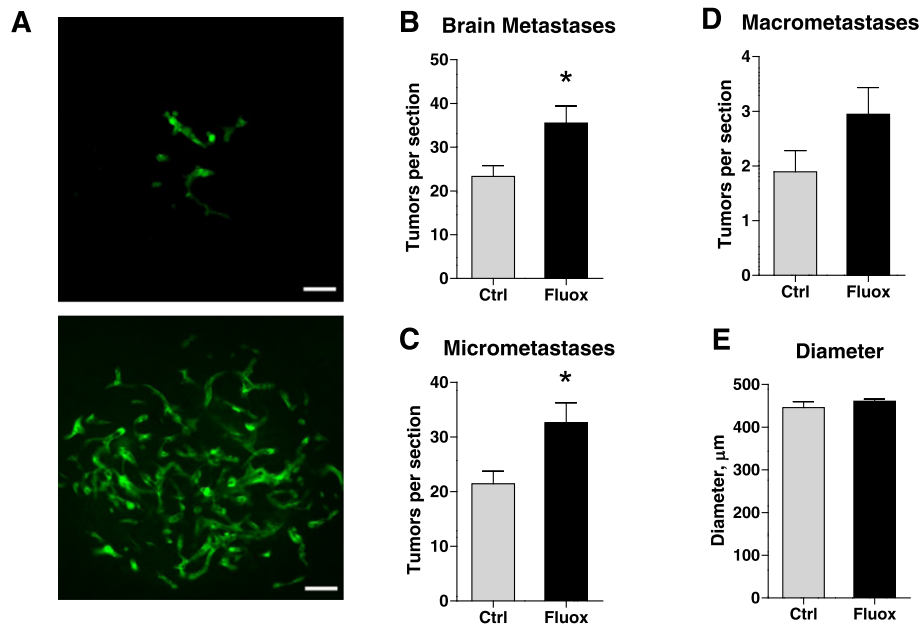


**Figure 1 Fluoxetine increases breast tumor metastasis to the brain.** Nu/Nu mice were treated with fluoxetine and injected with 231BR cells as described. **A**) Representative images of micrometastases (upper panel) and a macrometastasis (lower panel) in the brain of Nu/Nu mice 3 weeks after cell injection. Metastases were visualized in brain tissue by fluorescent microscopy. Note that the cells exhibited a tendency to localize perivascularly and form “sleeves” around blood vessels. Fluoxetine treatment increased the total number of metastases observed within the brain (**B**) as well as the number of brain micrometastases (**C**),  $p < 0.05$ ,  $t$ -test. **D**) While there was a trend towards an increase in the number of macrometastases, it did not reach statistical significance,  $p = 0.08$ ,  $t$ -test. **E**) The diameter of macrometastases did not differ between the fluoxetine and control group.  $n = 11-12$  per group. Scale bar: 50  $\mu\text{m}$ .

macrometastases, with a 56% increase in the fluoxetine group: fluoxetine,  $2.95 \pm 0.49$  vs. control,  $1.89 \pm 0.39$  tumors/section,  $p = 0.08$  (Figure 1D). The same outcomes have been observed in two independent experiments which have been pooled to produce the results described above.

Fluoxetine is a neuroactive substance suggesting that its effects may be brain-specific. In addition, 231BR cells have been selected for their preferential metastatic affinity to the brain. However, fluoxetine treatment may have altered metastatic targeting of 231BR cells and modified their potential to produce tumor growth elsewhere. To investigate this, we determined whether metastasis to another organ, the lung, was affected by fluoxetine treatment. Animals were treated as above and 231BR cells were then injected via the tail vein. Mouse lungs were removed after a 3 week survival period during which the animals continued to receive fluoxetine treatment. The tissue was fixed, paraffin embedded, serially sectioned, and stained with hematoxylin/eosin. The number of metastases in the lungs (Figure 2A) was determined using light microscopy. As shown in Figure 2B, fluoxetine treatment did not affect the ability of breast cancer cells to produce lung metastases, with  $1.06 \pm 0.22$  vs.  $0.93 \pm 0.10$  tumors/section in the fluoxetine and control groups, respectively,  $p = 0.31$ , suggesting that fluoxetine

affects the entry of cells *specifically* into the brain rather than causing a non-specific increase in the cancer cells' ability to survive within and/or extravasate from the vasculature.

#### Proliferative and migration capacity of 231BR cells is not affected by fluoxetine

While the lack of a fluoxetine effect on lung metastasis suggests a brain-specific mechanism, we wanted to further rule out the possibility that fluoxetine interacts directly with 231BR cells to increase their proliferation and/or migration. Therefore, we performed *in vitro* proliferation assays in the presence of 1, 10, 100, 1000 or 5000 ng/ml of fluoxetine and measured 231BR proliferative activity at 24, 48, and 72 hours. Fluoxetine did not increase 231BR proliferation *in vitro* (Figure 3A). Incubation with 5000 ng/ml of fluoxetine caused an *arrest* in cellular proliferation starting at 48 hours (Figure 3A), with higher fluoxetine doses - 20  $\mu\text{g/ml}$ , 100  $\mu\text{g/ml}$ , 500  $\mu\text{g/ml}$ , and 1000  $\mu\text{g/ml}$  - exhibiting a clear toxic effect on 231BR cells (Figure 3C). Additionally, incubation with various concentrations of fluoxetine did not increase migration of 231BR cells *in vitro* (Figure 3B). These assays demonstrate that fluoxetine does not increase proliferation or migration of 231BR cells, thereby supporting our hypothesis that fluoxetine specifically affects the brain microenvironment.

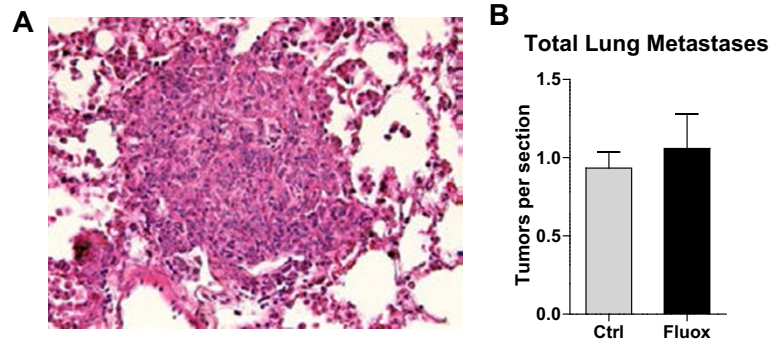


**Figure 2** Fluoxetine has no effect on breast tumor metastasis to the lungs. Nu/Nu mice were treated with fluoxetine and injected with 231BR cells as described. **A)** Representative image of H&E staining of lung tissue containing metastasis 3 weeks after cell injection. **B)** Fluoxetine treatment did not affect lung metastasis development,  $p = 0.31$ ,  $t$ -test.  $n = 5$  per group.

### Fluoxetine treatment does not affect dendritic spine turnover and perineuronal nets

Our results suggest that fluoxetine acts on the brain microenvironment to enhance its capacity to foster metastasis. Two mechanisms that may contribute to this effect are: an enhanced growth of the established tumors within the brain parenchyma, or an increased ability for metastatic cells to penetrate the BBB. To examine the

former possibility we examined the extracellular environment of the brain after fluoxetine treatment. Fluoxetine has been shown to modulate synaptic plasticity [23], a process that is dependent on remodeling of the brain extracellular matrix (ECM) [24]. ECM changes have the potential to influence breast tumor growth within the brain, since the invasion process is critically dependent upon the extracellular substrate [25]. To

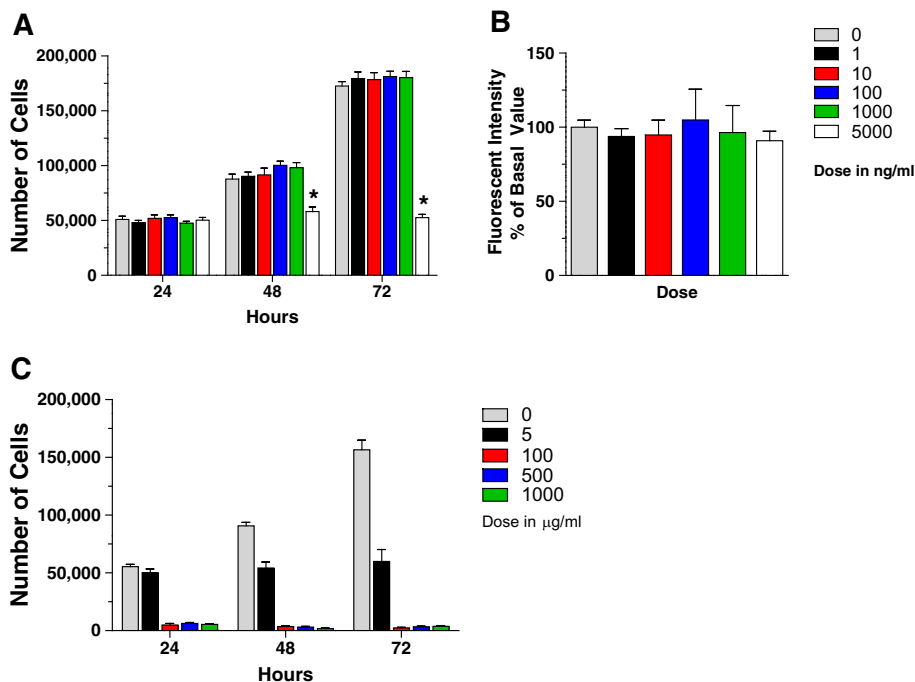
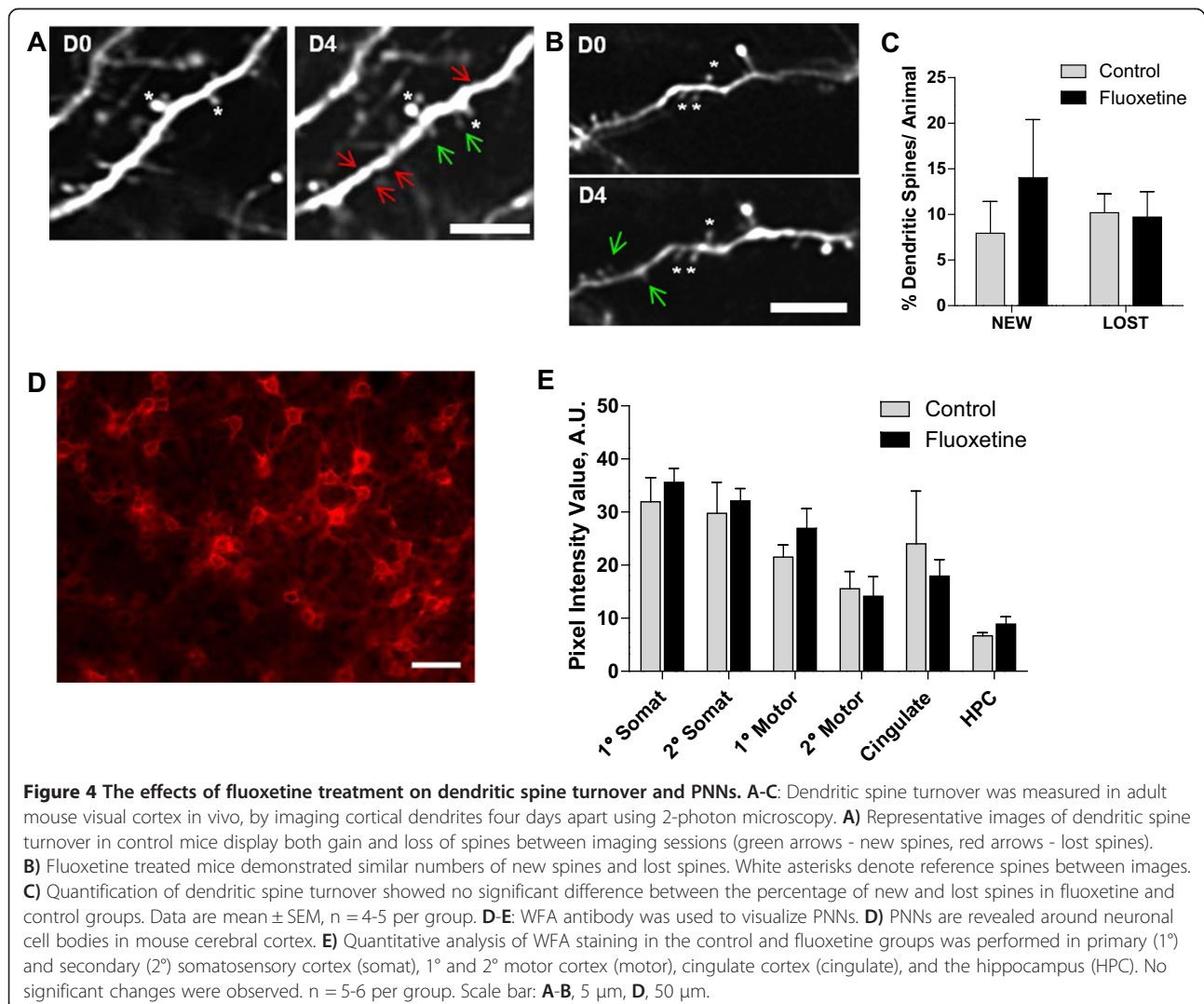


**Figure 3** The effect of fluoxetine on proliferation and migration of 231BR cells. **A)** Fluoxetine treatment did not affect 231BR proliferation in vitro at 24, 48, and 72 h of incubation, except at 5000 ng/ml, when the drug caused cell growth arrest,  $p < 0.001$ , 2-way ANOVA with Bonferroni post-hoc analysis.  $n = 6-8$ . **B)** Migratory ability of 231BR cells in vitro was not affected by fluoxetine treatment,  $p = 0.98$ , one-way ANOVA, with Dunnett's multiple comparison test.  $n = 8$ . **C)** At high doses, fluoxetine produces cytotoxic effect on 231BR breast cancer cells. Cell numbers were obtained after 24, 48, and 72 h of incubation with fluoxetine, as described. Whereas incubation with 5000 ng/ml (5 µg/ml) of fluoxetine caused an arrest in cellular proliferation starting at 48 hours, higher fluoxetine doses - 100 µg/ml, 500 µg/ml, and 1000 µg/ml - exhibited a clear toxic effect on 231BR cells.  $n = 4-7$ . Two independent experiments were conducted for each assay.

determine whether fluoxetine treatment altered the extracellular brain environment, we first assayed dendritic spine turnover *in vivo*, a process that is highly sensitive to brain ECM composition [26,27]. GFP-M mice [22] were treated with fluoxetine for 4 weeks. Dendritic spines, which are the postsynaptic structures of the majority of excitatory synapses in the central nervous system, were imaged *in vivo* through a thinned-skull window on two separate imaging sessions spaced four days apart. As expected, examination of dendritic spine turnover revealed that animals in both the control (Figure 4A) and fluoxetine (Figure 4B) group demonstrate dynamic gain and loss of spines. However, quantitative analysis showed no significant difference in the percentages of either new or lost spines between the experimental groups (Figure 4C), suggesting that fluoxetine does not enhance structural plasticity at cortical synapses.

We also evaluated the direct effect of fluoxetine treatment on ECM composition, in particular on perineuronal

nets (PNNs), a major component of the brain ECM that is rich in chondroitin sulfate proteoglycans [28]. PNNs have been implicated in modulating neuronal plasticity [29], and thus could be a prime target of fluoxetine action. Brain tissue of mice that received fluoxetine and were injected with 231BR cells was examined using a wisteria floribunda antibody (WFA) that recognizes PNNs (Figure 4D). The average fluorescent intensity of WFA staining was determined quantitatively across brain regions and compared between the control and fluoxetine groups. As shown in Figure 4E, WFA staining was highly variable throughout different brain regions, with primary and secondary somatosensory cortex exhibiting the highest level of PNN expression. Areas of primary and secondary motor cortex, as well as cingulate cortex, demonstrated somewhat lower WFA staining intensity, with hippocampus having the lowest expression of PNNs. However, a comparison within individual brain regions failed to reveal any difference between the control and



fluoxetine experimental groups (Figure 4E). These results suggest that the increase in brain metastatic ability of breast cancer cells elicited by fluoxetine treatment is not modulated via large-scale changes in ECM either at synaptic sites or in PNNs.

#### Effect of fluoxetine on tumor growth within the brain parenchyma

The lack of changes in dendritic spine dynamics and ECM structure suggests that fluoxetine may facilitate the entry of cancer cells into the brain rather than their subsequent growth within the brain parenchyma. This predicts that tumors growth is not altered by fluoxetine once cells are established within the brain. In support of this view, fluoxetine treatment did not affect the size of 231BR macro-metastases: the average diameter was  $1599 \pm 17$  a.u. in the fluoxetine group vs.  $1547 \pm 49$  a.u. in the control group,  $p = 0.19$  (Figure 1E). We hypothesized that if fluoxetine was changing the brain microenvironment to foster growth of established brain tumors, this should enhance the ability of any brain-resident tumors to grow within the brain. To test this, we performed stereotactic injections of a rat glioma cell line, CNS-1, into the frontal cortex of Nu/Nu mice, in order to examine whether fluoxetine would affect brain tumor development after introduction of malignant cells directly into the brain parenchyma. While intracranial injection of CNS-1 cells led to the development of brain tumors in mice (Figure 5A), 4 weeks of pre-surgical treatment with 200 mg/L of fluoxetine, followed by a 1 week survival period, did not affect brain tumor size when compared to the control group. Tumor spread, assayed by the number of sections containing CNS-1 cells, was comparable between the fluoxetine and control groups,  $47.56 \pm 3.24$  and  $49.8 \pm 5.98$ , respectively,  $p = 0.76$  (Figure 5B), as was the distance traveled by infiltrating tumor cells ( $771 \pm 51$   $\mu\text{m}$  in the fluoxetine group vs.  $751.4 \pm 92$   $\mu\text{m}$  in the control group,  $p = 0.86$ , Figure 5C). The overall tumor size (total image pixel count per tumor), which may reflect the ability of tumor cells to

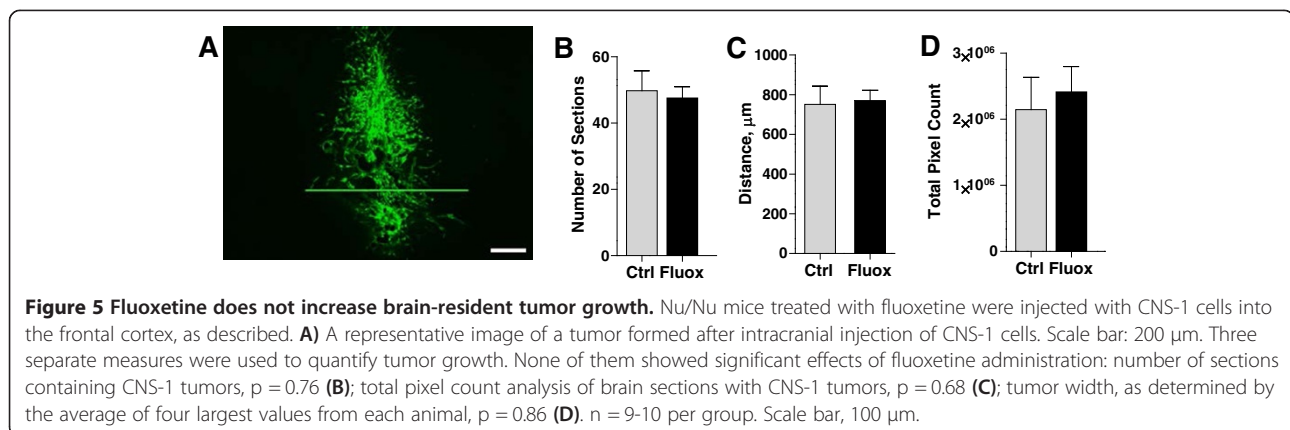
proliferate within the brain, was comparable between treated and untreated groups,  $2.148 \pm 0.49 \times 10^6$  vs.  $2.148 \pm 0.38 \times 10^6$ , respectively,  $p = 0.66$  (Figure 5D). These findings suggest that fluoxetine may impact the ability of breast cancer cells to enter the brain, without altering their ability to infiltrate and spread once they have established metastatic foci within the brain parenchyma.

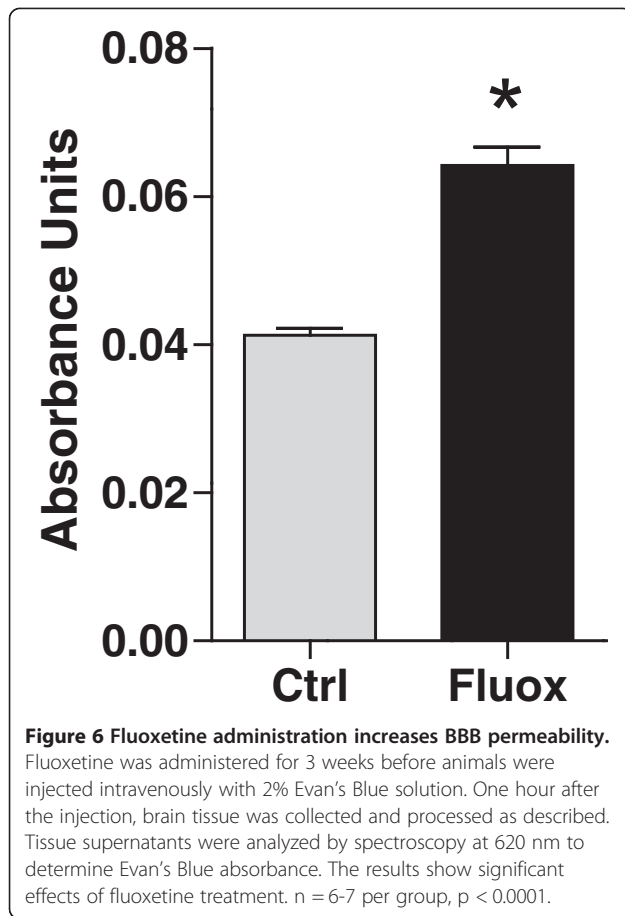
#### Effect of fluoxetine on blood-brain barrier permeability

A possible mechanism of increased brain metastatic breast cancer modulated by fluoxetine administration is a direct effect on BBB permeability. The BBB plays a critical role in the process of extravasation of cancer cells and determines their ability to seed the brain parenchyma [30,31]. After a 3-week treatment with fluoxetine, we analyzed Evan's Blue absorbance in brain extracts after tail vein injection of the dye to examine whether fluoxetine has any effect on BBB permeability. Brain extracts from animals that were treated with fluoxetine for 3 weeks demonstrate a statistically significant 54% increase in Evan's Blue absorbance compared to the control group,  $p < 0.0001$  (Figure 6). Thus, fluoxetine administration leads to changes in the BBB that promote increased permeability and may facilitate the increased entry of breast cancer cells into the brain.

#### Fluoxetine stimulates production of pro-inflammatory cytokines

A possible mechanism for changes in BBB permeability is production of cytokines that have been shown to modulate BBB function in models of injury, ischemia, and neurodegeneration [32,33]. To determine whether fluoxetine treatment leads to increased expression of pro-inflammatory markers, mice were treated with fluoxetine, and brain extracts were analyzed using real-time PCR and multiplex ELISA. PCR analysis revealed that fluoxetine administration induced mRNA expression of several pro-inflammatory cytokines such as TNF- $\alpha$ , IL-1 $\alpha$ , and IL-1 $\beta$  as well as an adhesion molecule ICAM-1, with levels





increasing 4.96-, 2.27-, 3.76-, and 4.44-fold, respectively,  $p < 0.05$  (Figure 7A). Transcription of two other pro-inflammatory molecules, IL-6 and MHC-II, was not significantly altered by fluoxetine treatment,  $p = 0.52$  and  $0.87$ , respectively. Protein analysis confirmed significantly elevated levels of TNF- $\alpha$ , IL-1 $\alpha$ , and IL-1 $\beta$ , and demonstrated high levels of other cytokines - MCP-1, MIP-2, and RANTES,  $p < 0.05$  (Figure 7B). The results of mRNA and protein expression assays demonstrate that fluoxetine can alter the inflammatory environment within the brain and stimulates cytokine production. This in turn may affect BBB permeability and lead to increased brain metastasis of circulating breast cancer cells.

#### Fluoxetine enhances glial activation in the vicinity of brain metastatic tumors

Microglia and astrocytes are two possible sources of pro-inflammatory markers that may affect the functioning of the BBB and thereby facilitate enhanced entry of tumor cells to the brain. To determine whether fluoxetine altered the activation pattern of glia around tumors, we stained brain sections with a number of antibodies specific for microglia and astrocytes (Figure 8). Both microglial and astrocytic markers were markedly elevated in proximity to

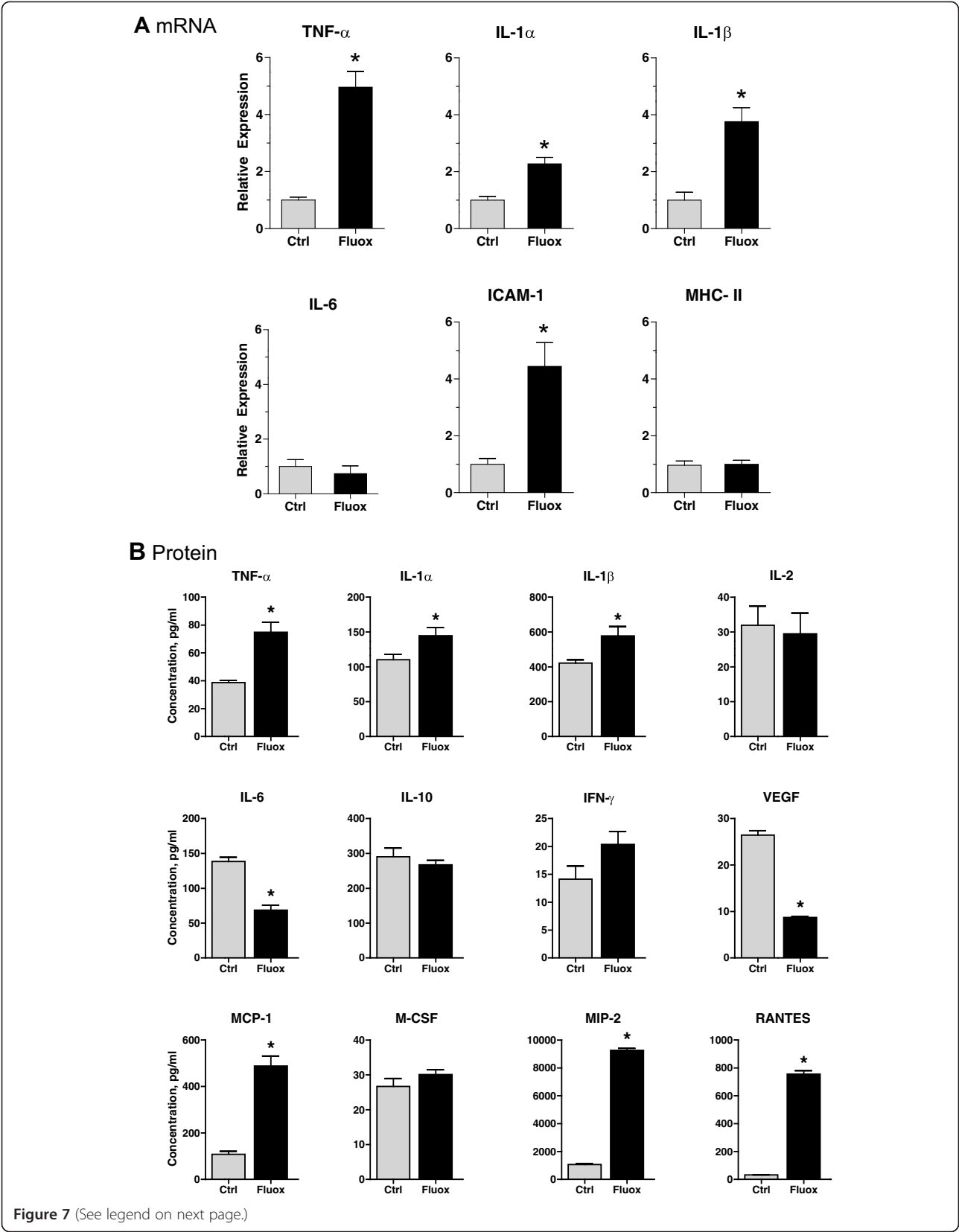
the tumor in control animals, indicating an inflammatory response around metastases. Interestingly, fluoxetine treatment elevated the expression of both microglial and astrocytic markers showing that fluoxetine altered inflammatory signaling in response to metastasis (Figure 9). Signal intensity for microglial markers IA-IE and CD68 was significantly higher in the fluoxetine group throughout the entire area we examined (up to 400  $\mu\text{m}$  distance from the tumor,  $p < 0.001$ ). Other microglia-specific antibodies, Iba-1 and CD45, exhibited higher expression levels closer to the tumor, following fluoxetine administration ( $p < 0.001$  and  $p < 0.01$ ), whereas CD11b levels were higher between 200 and 400  $\mu\text{m}$  away from the tumor ( $p < 0.01$ ). In addition, staining intensity for GFAP, an astrocytic marker, was significantly higher between 100–400  $\mu\text{m}$  in the fluoxetine treated animals compared to control,  $p < 0.01$  (Figure 9). In each case the tumors examined were not significantly different in size in control and fluoxetine groups (Figure 10).

#### Discussion

In this study we describe fluoxetine's ability to increase the number, but not the size, of metastases in a murine model of breast tumor metastasis to the brain. This increase is accompanied by changes in the BBB and the inflammatory environment of the brain, with no detectable changes in the properties of the brain ECM. These results provide several insights into the possible mechanisms by which fluoxetine alters brain metastasis, and hence possible avenues for future therapeutic manipulation of the metastatic outcome.

#### Fluoxetine and the brain ECM

Fluoxetine is thought to exert its anti-depressant effects by promoting brain plasticity, synaptogenesis and neurogenesis [23,34]. These processes are critically dependent on the brain ECM, as is tumor invasion [35], suggesting that fluoxetine could achieve its metastasis-altering effects in part by remodeling the extracellular milieu of the brain [36]. We examined this possibility by focusing on an ECM component, the PNN, which has been shown to play a critical role in modulating plastic changes in the brain. PNNs are established during brain development, as inhibitory and excitatory circuits mature and the brain becomes less plastic [37]. Both enzymatic removal of PNNs and fluoxetine treatment enhance plasticity in the adult [23,38]. However, we detected no significant change in PNNs in different brain areas after fluoxetine treatment, which suggests that the effects of fluoxetine on brain plasticity and metastasis are mediated through a different pathway. In agreement with this, synapse remodeling, a process that is highly sensitive to the extracellular environment [24,27], was also not affected by fluoxetine. Given the apparent lack of fluoxetine-induced ECM remodeling in our brain



(See figure on previous page.)

**Figure 7 Fluoxetine upregulates levels of pro-inflammatory cytokines.** **A)** To detect mRNA levels, brain tissue was collected after 3 weeks of fluoxetine treatment. mRNA was isolated, reverse transcribed, and subjected to real-time PCR analysis in order to determine expression levels of several pro-inflammatory markers. Experimental data were normalized to the expression of G3PDH, a housekeeping gene.  $n = 5$  per group,  $p < 0.05$ . **B)** For protein analysis, after 3 weeks of fluoxetine administration, a custom-made mouse cytokine/chemokine panel was used to determine protein concentration of several pro-inflammatory markers in brain extracts from control and treated animals. Analyte expression was normalized to protein concentration in individual samples.  $n = 6$  per group,  $p < 0.05$ .

metastasis model, it is not surprising that neither the size of breast tumor metastases established in the brain nor the size of resident glioma tumors appeared sensitive to fluoxetine treatment in our experiments. These results suggest that the effects of fluoxetine on the establishment of brain metastasis are not mediated via the brain ECM.

#### Fluoxetine treatment and glia

The pathogenesis of the vast majority of CNS diseases, including depression, is mediated, at least in part, by inflammatory processes. Although fluoxetine acts as a serotonin reuptake inhibitor, it also has strong effects on peripheral immune cells [39] and brain resident immune cells [40-42]. We observed fluoxetine-induced alterations in expression of several cytokines indicative of glial activation, and observed that fluoxetine enhanced glial activation in the vicinity of established brain metastases. This suggests that fluoxetine can alter inflammatory signaling in vivo, and that this alteration may be a mechanism by which fluoxetine elevates breast tumor metastasis to the brain in our murine model.

The contribution of microglia and astrocytes to the pathology of brain resident tumors has been well documented [43-45]. However, their involvement in metastatic events is less clear. Several studies have described activated glia associated with metastatic lesions in the brain parenchyma, suggesting an important role for these cells in metastatic growth within the brain [25,43]. While the immune function of these cells could contribute to defending the brain against cancer cell invasion, it is becoming clear that brain tumor cells can co-opt glia to promote tumor growth and invasion. Tumor cells and glia undergo a complex molecular cross talk that influences glial behavior and subsequent tumor progression [44,45]. Activated glia can produce multiple cytokines, chemokines, and enzymes that lead to increased tumor invasion, including IL-1 $\beta$  and TNF- $\alpha$  [46], markers that were up-regulated in this study. Surprisingly, the elevated levels of pro-inflammatory markers after fluoxetine treatment did not affect the growth of gliomas or breast tumor metastasis already established in the brain, despite the fact that many of these inflammatory molecules have been shown

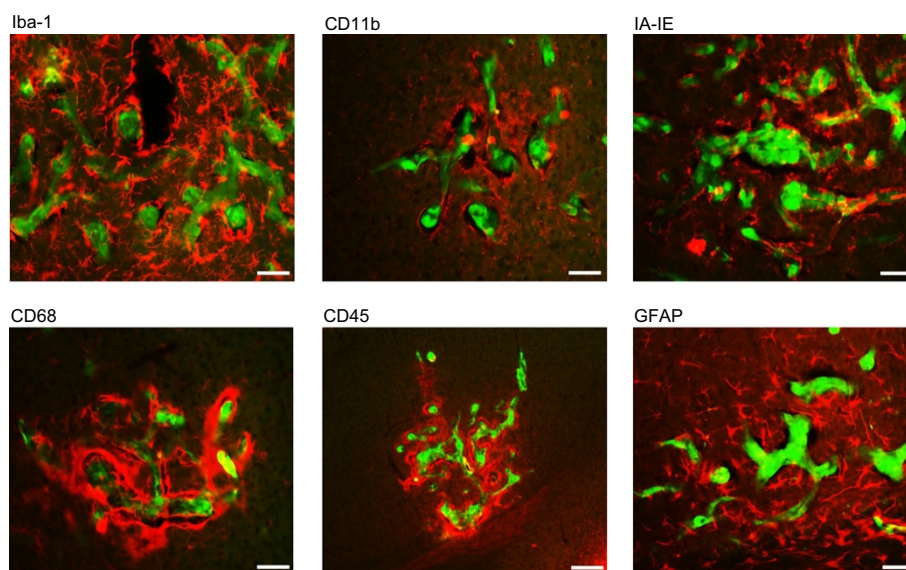
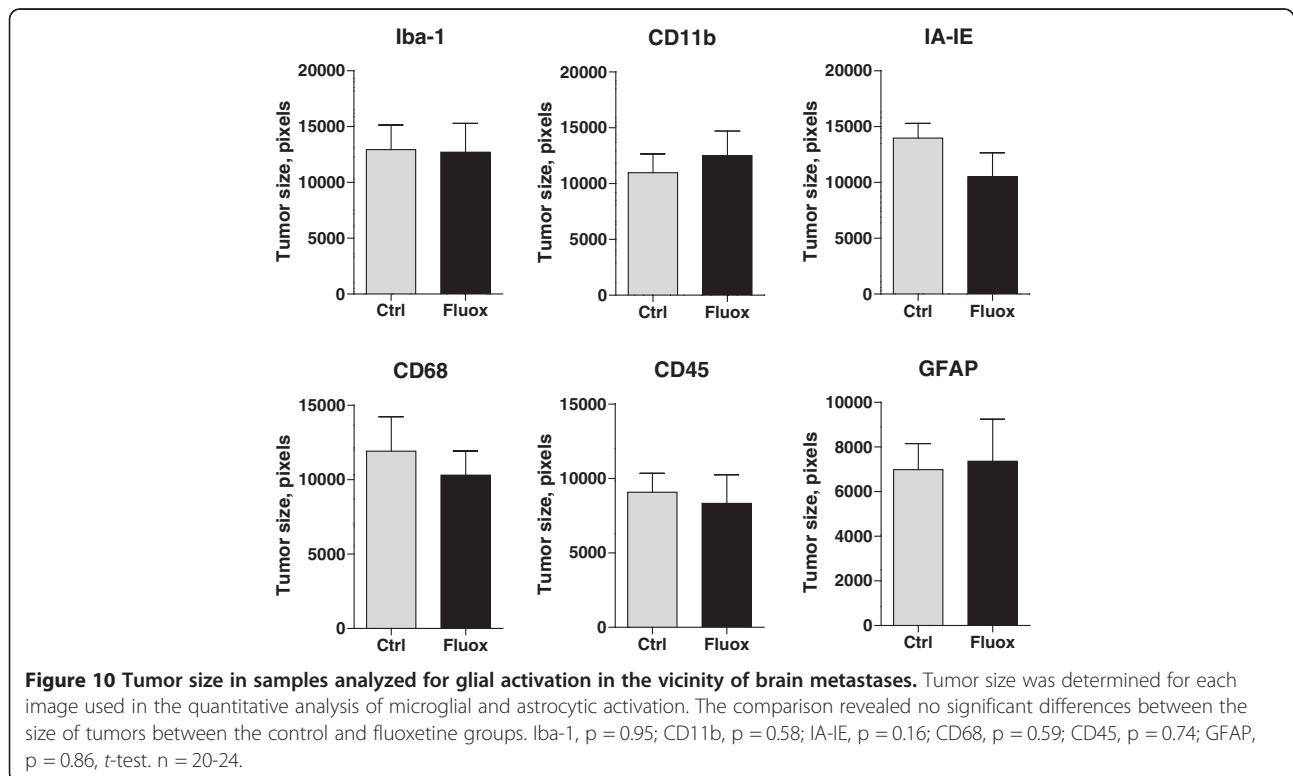
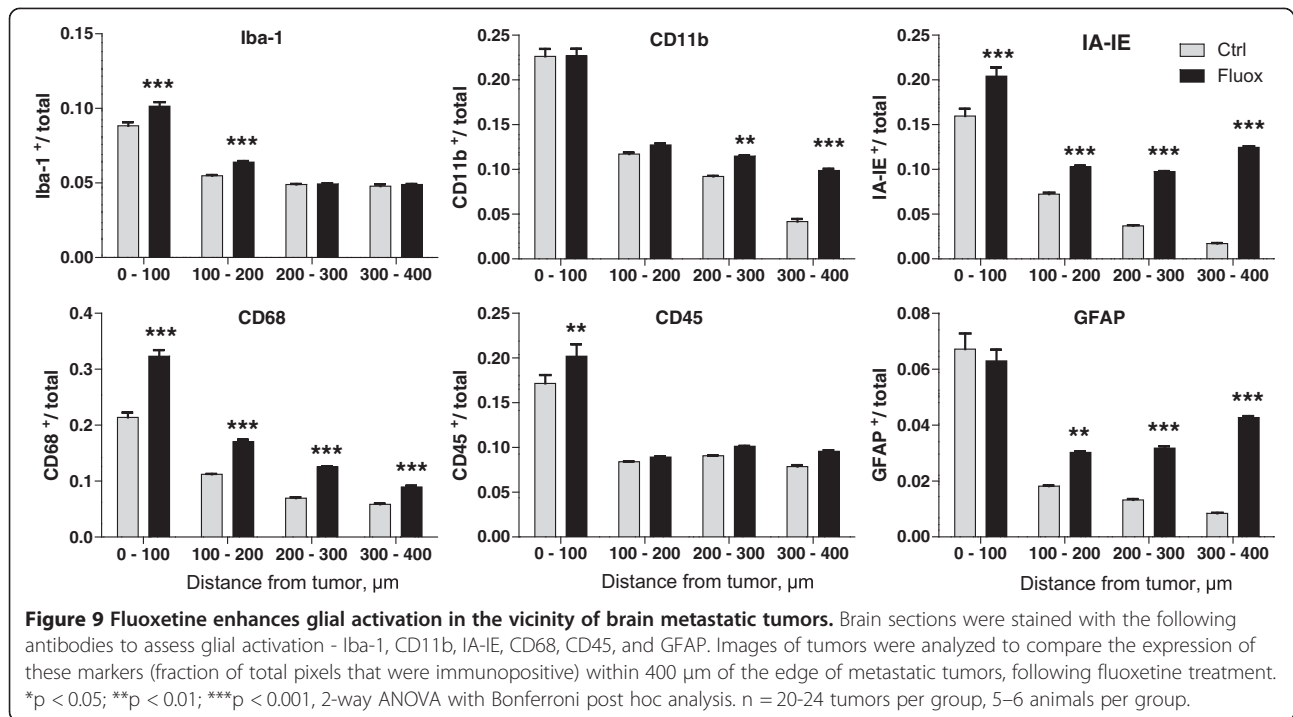


**Figure 8 Glial cells are activated in the vicinity of brain metastatic tumors.** Tissue sections from the control and fluoxetine groups were stained with antibodies against Iba-1, CD11b, IA-IE, CD68, CD45, and GFAP to determine the degree of microglial and astrocytic activation within 400  $\mu\text{m}$  of metastatic breast cancer cells.



to play a significant role in tumor survival and angiogenesis [47,48]. Possibly, the source or extent of fluoxetine-driven expression of these molecules is such as to change the entry of cells into the brain but not affect their subsequent growth.

It is interesting to note that in our study, chronic fluoxetine treatment *increased* inflammatory marker expression in the brain, while other studies examining peripheral and brain effects of fluoxetine have reported anti-inflammatory effects with *reduced* expression of markers such as TNF- $\alpha$  [40-42], although inflammatory effects of fluoxetine were also observed [41]. There are several possible reasons for this discrepancy. First, the majority of studies focus on the effects of fluoxetine within the context of pathological inflammation due to either LPS injection [40] or CNS disease [42]. Thus the effects on baseline inflammatory state have not been examined. Second, most studies examining inflammatory markers have focused on *in vitro* settings where cells behave differently than they do *in vivo* [41]. Our data suggest that fluoxetine, at neuroactive doses, can increase inflammatory signaling *in vivo* in the *absence of pathological changes in the brain* and this in turn may affect breast tumor metastasis.

#### Inflammation and BBB

Glial cells, and astrocytes in particular, are critical elements of the BBB and could influence tumor cell entry into the brain through its manipulation. Glia-derived cytokines and proteases have been implicated in promoting cancer cell navigation through the BBB [32,33,49]. Interestingly, brain-resident glia are frequently localized to the sites of cancer cell arrest in brain capillaries [25]. The intimate relationship between glia and tumor cells that have not yet entered the brain might imply a role for glia in shepherding tumor cells through the BBB. In addition, glial cells also produce MCP-1, MIP-2, and RANTES (all of which were increased after fluoxetine treatment) that could promote metastasis indirectly by stimulating infiltration into the brain of peripheral cells with pro-tumor activities such as myeloid-derived suppressor cells (MDSC), tumor-associated macrophages (TAM), and tumor-associated neutrophils (TAN). These cells may in turn contribute to the vicious circle of the pro-invasion phenotype created by fluoxetine administration, via additional secretion of IL-1 $\beta$ , TNF- $\alpha$ , and other cytokines. Moreover, in the process of infiltrating the brain parenchyma, MDSCs, TAMs, and TANs may create a "back door" whereby cancer cells in the immediate vicinity can accompany the infiltrating cells as they leave the capillaries.

#### Fluoxetine treatment and the BBB

A surprising result of fluoxetine administration is significantly increased BBB permeability even in the absence of

circulating tumor cells. These data suggest that fluoxetine may facilitate the entry of breast cancer cells into the brain by affecting the function of the BBB directly rather than enhancing the transport of tumor cells specifically. In other disease models such as CNS trauma, ischemia and neurodegeneration, a number of pro-inflammatory mediators are released by brain parenchymal cells, including endothelial cells and glia [50]. These mediators, including IL-1 $\beta$  and TNF- $\alpha$ , increase BBB permeability [32,49] via altered expression of tight-junction proteins as well as increased production of reactive oxygen species and metalloproteases [51]. Therefore, the increased expression of IL-1 $\beta$  and TNF- $\alpha$  that we observed after fluoxetine administration may directly lead to the impairment of BBB function and increased permeability of the barrier, thus precipitating increased brain metastasis.

Another important step in tumor cell extravasation is cell arrest within the blood vessels of the brain. Paracrine stimulation by pro-inflammatory molecules such as TNF- $\alpha$ , IL-1 $\beta$ , and MIP-2, leads to increased synthesis of chemokines and expression of cell adhesion molecules such as ICAM-1, E-selectin, and vascular cell adhesion molecule-1 (VCAM-1) by cerebrovascular endothelial cells [52], which may increase anchorage of tumor cells and eventually lead to facilitated cellular invasion from the circulation into the brain [53]. These same changes may directly or indirectly lead to increased ability of MDSCs, TAMs, and TANs to enter the brain and further influence tumor cell entry across the BBB. Additionally, inflammatory expression may influence the survival of tumor cells within the vasculature and thus enhance the probability of brain metastasis.

#### Conclusions

Our data provide the first experimental evidence that a neuroactive drug can promote increased entry of cancer cells into the brain parenchyma. The results of this study suggest a novel drug-induced, brain-specific mechanism whereby permeability of the BBB is altered by 1) the effect of fluoxetine on cellular components of the brain microenvironment to stimulate production of pro-inflammatory cytokines that can in turn modulate BBB function, 2) direct effect of fluoxetine on the components of the barrier, or 3) a combination of these two mechanisms. These findings suggest that neuroactive drugs used to treat depression and chemo brain in patients need to be carefully screened for unexpected effects on brain metastasis. In addition, they open new opportunities in the search for pharmacologic drugs that would inhibit brain metastasis by restricting permeability of the BBB or, conversely, would improve the delivery of therapeutic agents to the brain by opening up the BBB. Such drugs would have the advantage of targeting the brain rather than the heterogeneous and rapidly mutating tumor cell and could be used to limit brain-specific metastasis of many different primary tumor types.

## Additional file

**Additional file 1: Figure S1.** Fluoxetine reaches therapeutically relevant levels in mouse serum. Nu/Nu mice were treated with fluoxetine for 30 days as described. Mouse serum was collected at day 0 and every 10 days throughout the experiment. The concentration of fluoxetine and its major metabolite, norfluoxetine, was determined by LC-MS/MS. A) The mean fluoxetine concentration reaches 128 ng/ml after 10 days of treatment and remains at therapeutic levels at 30 days. B) The mean norfluoxetine level after 10 days is 282 ng/ml, and continues to increase.

## Competing interests

The authors declare that they have no competing interest.

## Authors' contributions

YS, EBB, and AKM designed research directions and protocols; YS, MZ, EAK, GOS, SAA-R, and IMD performed research protocols; YS, EAK, and AKM analyzed data; and YS, EBB, and AKM wrote the manuscript. All authors read and approved the final manuscript.

## Acknowledgments

Financial support was provided by the Department of Defense Breast Cancer Research Program (BCRP) awards W81XWH-09-1-0328, W81XWH-07-1-0626, and the American Institute for Cancer Research Award 09A151 to AKM and EBB; the Department of Defense BCRP award W81XWH-09-1-0405 and NIH Director's New Innovator Award 1DP2OD006501-01 to EBB. We gratefully acknowledge technical assistance and expertise of Dr. Yelena Tkachenko at the Department of Pediatrics; Dr. Fred Hagen and Kevin Welle at the University of Rochester Medical Center (URMC) Proteomics Core; Dr. John A. Olschowka, and Dr. M. Kerry O'Banion at the Department of Neurobiology and Anatomy; as well as the help with multiplex assays provided by Dr. Michael L. Moeller and Christine Walway-Benetti from EMD Millipore.

Received: 19 February 2014 Accepted: 6 August 2014

Published: 16 August 2014

## References

- Lin NU, Bellon JR, Winer EP: CNS metastases in breast cancer. *J Clin Oncol* 2004, **22**:3608–3617.
- Weil RJ, Palmieri DC, Bronder JL, Stark AM, Steeg PS: Breast cancer metastasis to the central nervous system. *Am J Pathol* 2005, **167**:913–920.
- Lee YT: Breast carcinoma: pattern of metastasis at autopsy. *J Surg Oncol* 1983, **23**:175–180.
- Cho SY, Choi HY: Causes of death and metastatic patterns in patients with mammary cancer. Ten-year autopsy study. *Am J Clin Pathol* 1980, **73**:232–234.
- Lockman PR, Mittapalli RK, Taskar KS, Rudraraju V, Gril B, Bohn KA, Adkins CE, Roberts A, Thorsheim HR, Gaasch JA, Huang S, Palmieri D, Steeg PS, Smith QR: Heterogeneous blood-tumor barrier permeability determines drug efficacy in experimental brain metastases of breast cancer. *Clin Cancer Res* 2010, **16**:5664–5678.
- Fann JR, Thomas-Rich AM, Katon WJ, Cowley D, Pepping M, McGregor BA, Gralow J: Major depression after breast cancer: a review of epidemiology and treatment. *Gen Hosp Psychiatry* 2008, **30**:112–126.
- Hegel MT, Moore CP, Collins ED, Kearing S, Gillock KL, Riggs RL, Clay KF, Ahles TA: Distress, psychiatric syndromes, and impairment of function in women with newly diagnosed breast cancer. *Cancer* 2006, **107**:2924–2931.
- Coyne JC, Palmer SC, Shapiro PJ, Thompson R, DeMichele A: Distress, psychiatric morbidity, and prescriptions for psychotropic medication in a breast cancer waiting room sample. *Gen Hosp Psychiatry* 2004, **26**:121–128.
- Loprinzi CL, Sloan JA, Perez EA, Quella SK, Stella PJ, Mailliard JA, Halyard MY, Pruthi S, Novotny PJ, Rumman TA: Phase III evaluation of fluoxetine for treatment of hot flashes. *J Clin Oncol* 2002, **20**:1578–1583.
- Stearns V, Beebe KL, Iyengar M, Dube E: Paroxetine controlled release in the treatment of menopausal hot flashes: a randomized controlled trial. *JAMA* 2003, **289**:2827–2834.
- Desmarais JE, Looper KJ: Interactions between tamoxifen and antidepressants via cytochrome P450 2D6. *J Clin Psychiatry* 2009, **70**:1688–1697.
- Henry NL, Stearns V, Flockhart DA, Hayes DF, Riba M: Drug interactions and pharmacogenomics in the treatment of breast cancer and depression. *Am J Psychiatry* 2008, **165**:1251–1255.
- Kelly CM, Juurlink DN, Gomes T, Duong-Hua M, Pritchard KI, Austin PC, Paszat LF: Selective serotonin reuptake inhibitors and breast cancer mortality in women receiving tamoxifen: a population based cohort study. *BMJ* 2010, **340**:c693.
- Andersohn F, Willich SN: Interaction of serotonin reuptake inhibitors with tamoxifen. *BMJ* 2010, **340**:c783.
- Cronin-Fenton D, Lash TL, Sorensen HT: Selective serotonin reuptake inhibitors and adjuvant tamoxifen therapy: risk of breast cancer recurrence and mortality. *Future Oncol* 2010, **6**:877–880.
- Jenkinson ML: SSRIs and tamoxifen. Why condemn fluoxetine? *BMJ* 2010, **340**:c1319.
- Yoneda T, Williams PJ, Hiraga T, Niewolna M, Nishimura R: A bone-seeking clone exhibits different biological properties from the MDA-MB-231 parental human breast cancer cells and a brain-seeking clone in vivo and in vitro. *J Bone Miner Res* 2001, **16**:1486–1495.
- Barth RF, Kaur B: Rat brain tumor models in experimental neuro-oncology: the C6, 9 L, T9, RG2, F98, BT4C, RT-2 and CNS-1 gliomas. *J Neurooncol* 2009, **94**:299–312.
- Urinovska R, Brozmanova H, Sistik P, Silhan P, Kacirova I, Lemr K, Grundmann M: Liquid chromatography-tandem mass spectrometry method for determination of five antidepressants and four atypical antipsychotics and their main metabolites in human serum. *J Chromatogr B Analyt Technol Biomed Life Sci* 2012, **907**:101–107.
- Palmieri D, Bronder JL, Herring JM, Yoneda T, Weil RJ, Stark AM, Kurek R, Vega-Valle E, Feigenbaum L, Halverson D, Vortmeyer AO, Steinberg SM, Aldape K, Steeg PS: Her-2 overexpression increases the metastatic outgrowth of breast cancer cells in the brain. *Cancer Res* 2007, **67**:4190–4198.
- Kelly EA, Majewska AK: Chronic imaging of mouse visual cortex using a thinned-skull preparation. *J Vis Exp* 2010.
- Feng G, Mellor RH, Bernstein M, Keller-Peck C, Nguyen QT, Wallace M, Nerbonne JM, Lichtman JW, Sanes JR: Imaging neuronal subsets in transgenic mice expressing multiple spectral variants of GFP. *Neuron* 2000, **28**:41–51.
- Maya Vetencourt JF, Sale A, Viegi A, Baroncelli L, De Pasquale R, O'Leary OF, Castren E, Maffei L: The antidepressant fluoxetine restores plasticity in the adult visual cortex. *Science* 2008, **320**:385–388.
- Berardi N, Pizzorusso T, Maffei L: Extracellular matrix and visual cortical plasticity: freeing the synapse. *Neuron* 2004, **44**:905–908.
- Lorger M, Felding-Habermann B: Capturing changes in the brain microenvironment during initial steps of breast cancer brain metastasis. *Am J Pathol* 2010, **176**:2958–2971.
- Frischknecht R, Gundelfinger ED: The Brain's extracellular matrix and its role in synaptic plasticity. *Adv Exp Med Biol* 2012, **970**:153–171.
- Oray S, Majewska A, Sur M: Dendritic spine dynamics are regulated by monocular deprivation and extracellular matrix degradation. *Neuron* 2004, **44**:1021–1030.
- Kwok JC, Dick G, Wang D, Fawcett JW: Extracellular matrix and perineuronal nets in CNS repair. *Dev Neurobiol* 2011, **71**:1073–1089.
- Wang D, Fawcett J: The perineuronal net and the control of CNS plasticity. *Cell Tissue Res* 2012, **349**:147–160.
- Deeken JF, Loscher W: The blood-brain barrier and cancer: transporters, treatment, and Trojan horses. *Clin Cancer Res* 2007, **13**:1663–1674.
- Gerstner ER, Fine RL: Increased permeability of the blood-brain barrier to chemotherapy in metastatic brain tumors: establishing a treatment paradigm. *J Clin Oncol* 2007, **25**:2306–2312.
- de Vries HE, Blom-Roosemalen MC, van Oosten M, de Boer AG, van Berkel TJ, Breimer DD, Kuiper J: The influence of cytokines on the integrity of the blood-brain barrier in vitro. *J Neuroimmunol* 1996, **64**:37–43.
- Abbott NJ: Inflammatory mediators and modulation of blood-brain barrier permeability. *Cell Mol Neurobiol* 2000, **20**:131–147.
- Wang JW, David DJ, Monckton JE, Battaglia F, Hen R: Chronic fluoxetine stimulates maturation and synaptic plasticity of adult-born hippocampal granule cells. *J Neurosci* 2008, **28**:1374–1384.
- Kim Y, Stolarska MA, Othmer HG: The role of the microenvironment in tumor growth and invasion. *Prog Biophys Mol Biol* 2011, **106**:353–379.
- Dityatev A, Schachner M: Extracellular matrix molecules and synaptic plasticity. *Nat Rev Neurosci* 2003, **4**:456–468.
- Hensch TK: Critical period plasticity in local cortical circuits. *Nat Rev Neurosci* 2005, **6**:877–888.

38. Pizzorusso T, Medini P, Berardi N, Chierzi S, Fawcett JW, Maffei L: **Reactivation of ocular dominance plasticity in the adult visual cortex.** *Science* 2002, **298**:1248–1251.
39. Roumestan C, Michel A, Bichon F, Portet K, Detoc M, Henriquet C, Jaffuel D, Mathieu M: **Anti-inflammatory properties of desipramine and fluoxetine.** *Respir Res* 2007, **8**:35.
40. Zhang F, Zhou H, Wilson BC, Shi JS, Hong JS, Gao HM: **Fluoxetine protects neurons against microglial activation-mediated neurotoxicity.** *Parkinsonism Relat Disord* 2012, **18**(Suppl 1):S213–S217.
41. Tynan RJ, Weidenhofer J, Hinwood M, Cairns MJ, Day TA, Walker FR: **A comparative examination of the anti-inflammatory effects of SSRI and SNRI antidepressants on LPS stimulated microglia.** *Brain Behav Immun* 2012, **26**:469–479.
42. Mostert JP, Admiraal-Behloul F, Hoogduin JM, Luyendijk J, Heersema DJ, van Buchem MA, De Keyser J: **Effects of fluoxetine on disease activity in relapsing multiple sclerosis: a double-blind, placebo-controlled, exploratory study.** *J Neurol Neurosurg Psychiatry* 2008, **79**:1027–1031.
43. Fitzgerald DP, Palmieri D, Hua E, Hargrave E, Herring JM, Qian Y, Vega-Valle E, Weil RJ, Stark AM, Vortmeyer AO, Steeg PS: **Reactive glia are recruited by highly proliferative brain metastases of breast cancer and promote tumor cell colonization.** *Clin Exp Metastasis* 2008, **25**:799–810.
44. Seike T, Fujita K, Yamakawa Y, Kido MA, Takiguchi S, Teramoto N, Iguchi H, Noda M: **Interaction between lung cancer cells and astrocytes via specific inflammatory cytokines in the microenvironment of brain metastasis.** *Clin Exp Metastasis* 2011, **28**:13–25.
45. Markovic DS, Vinnakota K, Chirasani S, Synowitz M, Raguet H, Stock K, Sliwa M, Lehmann S, Kalin R, van Rooijen N, Holmbeck K, Heppner FL, Kiwit J, Matyash V, Lehnardt S, Kaminska B, Glass R, Kettenmann H: **Gliomas induce and exploit microglial MT1-MMP expression for tumor expansion.** *Proc Natl Acad Sci U S A* 2009, **106**:12530–12535.
46. Hoelzinger DB, Demuth T, Berens ME: **Autocrine factors that sustain glioma invasion and paracrine biology in the brain microenvironment.** *J Natl Cancer Inst* 2007, **99**:1583–1593.
47. Ben-Baruch A: **The tumor-promoting flow of cells into, within and out of the tumor site: regulation by the inflammatory axis of TNFalpha and chemokines.** *Cancer Microenviron* 2011, **5**:151–164.
48. Sosnoski DM, Krishnan V, Kraemer WJ, Dunn-Lewis C, Mastro AM: **Changes in cytokines of the bone microenvironment during breast cancer metastasis.** *Int J Breast Cancer* 2012, **2012**:160265.
49. Abbott NJ: **Astrocyte-endothelial interactions and blood-brain barrier permeability.** *J Anat* 2002, **200**:629–638.
50. Bell RD, Zlokovic BV: **Neurovascular mechanisms and blood-brain barrier disorder in Alzheimer's disease.** *Acta Neuropathol* 2009, **118**:103–113.
51. Coisne C, Engelhardt B: **Tight junctions in brain barriers during central nervous system inflammation.** *Antioxid Redox Signal* 2011, **15**:1285–1303.
52. Stanimirovic DB, Wong J, Shapiro A, Durkin JP: **Increase in surface expression of ICAM-1, VCAM-1 and E-selectin in human cerebrovascular endothelial cells subjected to ischemia-like insults.** *Acta Neurochir Suppl* 1997, **70**:12–16.
53. Worthylake RA, Burridge K: **Leukocyte transendothelial migration: orchestrating the underlying molecular machinery.** *Curr Opin Cell Biol* 2001, **13**:569–577.

doi:10.1186/1471-2407-14-598

**Cite this article as:** Shapovalov et al.: Fluoxetine modulates breast cancer metastasis to the brain in a murine model. *BMC Cancer* 2014 **14**:598.

**Submit your next manuscript to BioMed Central and take full advantage of:**

- Convenient online submission
- Thorough peer review
- No space constraints or color figure charges
- Immediate publication on acceptance
- Inclusion in PubMed, CAS, Scopus and Google Scholar
- Research which is freely available for redistribution

Submit your manuscript at  
www.biomedcentral.com/submit



**Multiphoton fluorescence recovery after photobleaching in bounded systems**

Kelley D. Sullivan

*Department of Physics and Astronomy, University of Rochester, Rochester, New York 14627, USA*

Edward B. Brown\*

*Department of Biomedical Engineering, University of Rochester, Rochester, New York 14627, USA*

(Received 28 July 2010; revised manuscript received 17 January 2011; published 16 May 2011)

Multiphoton fluorescence recovery after photobleaching (MP-FRAP) is a laser microscopy technique used to measure diffusion coefficients of macromolecules in biological systems. The three-dimensional resolution and superior depth penetration within scattering samples offered by MP-FRAP make it an important tool for investigating both *in vitro* and *in vivo* systems. However, biological systems frequently confine diffusion within solid barriers, and to date the effect of such barriers on the measurement of absolute diffusion coefficients via MP-FRAP has not been studied. We have used Monte Carlo simulations of diffusion and MP-FRAP to understand the effect of barriers of varying geometries and positions relative to the two-photon focal volume. Furthermore, we supply ranges of barrier positions within which MP-FRAP can confidently be employed to measure accurate diffusion coefficients. Finally, we produce two new MP-FRAP models that can produce accurate diffusion coefficients in the presence of a single plane boundary or parallel infinite plane boundaries positioned parallel to the optical axis, up to the resolution limit of the multiphoton laser scanning microscope.

DOI: [10.1103/PhysRevE.83.051916](https://doi.org/10.1103/PhysRevE.83.051916)

PACS number(s): 87.64.kv, 66.10.C-, 87.64.mn, 87.64.Aa

**I. INTRODUCTION**

Multiphoton fluorescence recovery after photobleaching (MP-FRAP) is a laser microscopy technique typically employed to measure diffusion coefficients within biological systems [1]. MP-FRAP is performed by using a brief, high-intensity, laser flash to generate photobleaching within a region of interest in a fluorescent sample. The laser is then attenuated and the region of interest is monitored as still-fluorescent molecules from outside the region diffuse in to replace the outwardly diffusing bleached molecules. The resulting fluorescence *versus* time curve can be fitted to an analytical formula to produce the diffusion coefficient of the mobile fluorophore. In an MP-FRAP experiment, fluorescence and photobleaching are both generated via multiphoton excitation [1]. The intrinsic spatial confinement of multiphoton excitation results in a three-dimensionally (3D) resolved bleaching/monitoring volume [2] and allows the use of MP-FRAP to measure three-dimensionally resolved diffusion coefficients within intact samples. This intrinsic spatial confinement obviates the need for a confocal pinhole and allows MP-FRAP, as well as the multiphoton laser-scanning microscope upon which it is based, to probe living tissue down to depths of several hundred micrometers. In its original formulation [1] MP-FRAP was demonstrated with a parked bleaching and monitoring beam. Several variants of MP-FRAP have since been demonstrated with patterned photobleaching accomplished by interfering beams [3], beam scanning [4], and other methods. In this work we refer to the experiment performed in its classical parked beam configuration as MP-FRAP.

Other techniques employed to measure biological diffusion include (single-photon) fluorescence recovery after photobleaching (FRAP), FRAP with spatial Fourier analysis (SFA-FRAP), single particle tracking (SPT), and fluorescence

correlation spectroscopy (FCS). FRAP is the precursor to MP-FRAP and was developed in the 1970s [5–7] to probe transport parameters in biological systems. Due to the lack of spatial confinement of the one-photon excitation process, FRAP is applied to two-dimensional samples, defined as having an axial extent that is significantly smaller than the Rayleigh length of the focused bleach and monitor beam. High-resolution measurements with high numerical aperture (NA) lenses are therefore limited to thin samples ( $<1\ \mu\text{m}$ ). FRAP can be used on thicker samples by using cylindrical beams (i.e., a low NA lens) with longer Rayleigh lengths. This again provides a two-dimensional measurement of the diffusion coefficient, averaged over the axial extent of the sample. Finally, FRAP with a confocal pinhole can be used to achieve 3D resolved measurements [8], but rely on numerical analysis rather than analytical formulas. The use of spatial Fourier analysis allows SFA-FRAP [9] to probe diffusion in intact thick tissue, but the technique also has low spatial resolution ( $\sim 40\ \mu\text{m}$ ) and is limited to the depth penetration of epifluorescence microscopy ( $\sim 50\ \mu\text{m}$ ). SPT tracks individual molecules via high spatiotemporal imaging to determine their transport properties, with two-dimensional (2D) imaging techniques (i.e., epifluorescence) producing 2D resolved measurements of diffusion coefficients [10,11] and 3D imaging techniques producing 3D resolved measurements of diffusion coefficients. FCS comes in both one-photon [12] and two-photon [13,14] varieties and like MP-FRAP it can be used to measure diffusion with high, 3D, resolution. SPT and FCS rely on low fluorophore concentrations (with accompanying low signals), while MP-FRAP relies on high fluorophore concentrations (with accompanying large signals), making the techniques complementary, especially in the difficult optical environment of scattering tissue.

The effect of barriers to diffusion is an important and relevant topic regarding the study of both biological and nonbiological systems. MP-FRAP has been employed to

\*Edward.Brown@urmc.rochester.edu

measure absolute diffusion coefficients in the cytoplasm of cells [1,15], in cartilage [16], in optically fabricated gels [17], and in blood plasma [18]. In these cases, the volume surrounding the bleached spot was assumed to be “open,” with barriers to diffusion at infinity. However, many biological systems inherently confine measurements to regions within solid barriers to diffusion, such as cell walls and organelles. *In vivo* systems in particular offer few free volumes for diffusion measurements. Clearly, when the focal volume is positioned within a cell there is concern that the confined geometry will affect the measured diffusion coefficient. However, even when the bleach and monitor volume is positioned outside of individual cells, the tissue interstitium exhibits a complex structure that can interfere with free diffusion due to adjacent cellular structures. Determining the effects of these barriers, and the distances over which these effects become significant, is absolutely necessary for MP-FRAP to be performed accurately *in vivo*.

In the limit that these barriers become extremely close, their impact is relatively straightforward to model because they simply change the dimensionality of the system. For example, it has been shown that an MP-FRAP experiment in microvilli (an extremely narrow tube) can be modeled by one-dimensional diffusion [19,20]. However, there has been no analysis of MP-FRAP applied in systems with boundaries to diffusion positioned at intermediate distances, i.e., neither approaching zero nor at infinity, in order to determine their effects on the reported diffusion coefficient.

There have been several recent studies investigating the various effects caused by barriers to diffusion in relation to micro- and nanostructures [21,22], nuclear magnetic resonance [23], diffusion-convection processes [24,25], anomalous diffusion [26], and diffusion in channels [27]. However, the results of these studies are not presented in the context of experimental biological diffusion measurement techniques. In recognition of the prevalence of small volumes presented by many biological systems, work has been done to apply FCS [28–32], SPT [33,34], and FRAP [35] in systems where the focal volume is confined. While MP-FRAP has been applied to both living cells and *in vivo*, to date the effect of barriers on the measurement of absolute diffusion coefficients via MP-FRAP has been largely neglected (although in the development of one patterned photobleaching variant of MP-FRAP the effect of axial boundaries was considered [4]).

Barriers to diffusion are omnipresent *in vivo*, and their effects must be considered when attempting to perform accurate MP-FRAP. In this work we explore the effects of different barrier geometries on the diffusion coefficient reported by MP-FRAP, discuss the mechanism by which these barriers affect the reported diffusion coefficient, and determine the appropriate distances at which the effects of barriers can be neglected. To do this we simulate the diffusive spread of a distribution of bleached molecules in the presence of various barriers to diffusion via Monte Carlo simulation and then calculate the resultant (two-photon) fluorescence signal, producing an artificial fluorescence *versus* time curve. We then fit many such curves to the classical MP-FRAP equation, which assumes all barriers are at infinity, and explore how the presence of differing barriers produces errors in the reported diffusion coefficient. In the case of both a single

plane boundary and two parallel infinite plane boundaries oriented parallel to the optical axis, we introduce new models of MP-FRAP that explicitly account for the presence of one or more boundaries and explore how these new models improve the accuracy of the reported diffusion coefficients. This work is essential to the application of MP-FRAP *in vivo*.

## II. MONTE CARLO MODEL OF MP-FRAP

### A. Initial fluorophore distribution

The initial concentration distribution of unbleached fluorophore immediately after the photobleaching pulse, in the limit that the boundaries to diffusion are at infinity, is given by Brown *et al.* [1]:

$$c(x, y, z; t = 0) = c_o \exp \left[ - (1/b) q_b \delta_b \langle I_{bl}^b(x, y, z) \rangle \Delta t \right], \quad (1)$$

where  $c_o$  is the initial equilibrium concentration of fluorophore,  $b$  is the number of photons absorbed per photobleaching event,  $q_b$  is the quantum efficiency for  $b$ -photon photobleaching,  $\delta_b$  is the multiphoton fluorescence action cross-section of the fluorophore for the order of excitation required for photobleaching,  $\langle I_{bl}^b(x, y, z) \rangle$  is the time average of the bleach intensity raised to the  $b$ th power, and  $\Delta t$  is the duration of the bleaching pulse.

The bleach intensity can be approximated as a 3D Gaussian [1]:

$$\langle I_{bl}^b(x, y, z) \rangle = \langle I_{bl}^b(0, 0, 0) \rangle \exp \left[ - \frac{2b(x^2 + y^2)}{\omega_r^2} - \frac{2bz^2}{\omega_z^2} \right], \quad (2)$$

where  $\omega_r$  and  $\omega_z$  are the  $1/e^2$  radial and axial dimensions of the two-photon focal volume, respectively, and  $\langle I_{bl}^b(0, 0, 0) \rangle$  is the time average of the intensity at the two-photon focal volume center raised to the  $b$ th power.

For the purpose of simulation, it is more efficient and effective to follow the bleached fluorophores [36–38]. Substituting Eq. (2) into Eq. (1), setting  $b = 2$  for a two-photon bleaching process and  $c_o = 1$  in anticipation of populating nodes later to determine the amplitude, and noting that the bleach depth parameter is defined as  $\beta \equiv (1/b) q_b \delta_b \langle I_{bl}^b(0, 0, 0) \rangle \Delta t$ , we find the initial distribution of *bleached* fluorophore:

$$c_{bl}(x, y, z; t = 0) = 1 - \exp \left\{ -\beta \exp \left[ - \frac{4(x^2 + y^2)}{\omega_r^2} - \frac{4z^2}{\omega_z^2} \right] \right\}. \quad (3)$$

The bleach depth parameter was chosen to be  $\beta = 0.25$ , a value typical of experimental *in vivo* MP-FRAP recovery curves [1,18]. The axial and radial extents of the two-photon focal volume were defined as  $\omega_r \equiv 2.6\lambda / (2\pi \text{NA})$  and  $\omega_z \equiv 8.8n\lambda / [2\pi(\text{NA})^2]$ , respectively, where  $\lambda$  is the wavelength of the excitation laser,  $n$  is the index of refraction of the immersion medium, and NA is the numerical aperture of the lens [39]. Our simulations represent the NA extremes of typical water-immersion lenses ( $\lambda = 780$  nm,  $n = 1.33$ , NA = 0.5 or 1.2). Space was discretized into a regular lattice with spacing defined by the expected diffusion properties (see “Diffusion” below). One thousand bleached fluorophores were placed at lattice points using Eq. (3) as the probability distribution and with the caveat that no fluorophores were allowed outside any diffusive barriers introduced into the system. Multiple

occupancy on a single node was permitted, though rarely occurred.

It is important to note that the size of the bleaching distribution is not necessarily the same as that of the optical focal volume. As explained in Brown *et al.* [1], the shape of the photobleaching volume will depend upon the photochemical mechanism of photobleaching, the bleach depth parameter, and the characteristic radii of the optical point spread function (PSF). In order to explore a tractable parameter space, we are assuming the simple first-order model of photobleaching photochemistry described within Brown *et al.*, an experimentally relevant value for the bleach depth parameter of  $\beta = 0.25$ , and two values of microscope NA (and hence two values for each of the characteristic radii of the optical PSF) of 0.5 and 1.2. Due to the relatively small value of  $\beta$ , this produces a characteristic size for the bleaching volume that is within 3% of the size of the optical PSF; hence we plot the effects of barrier proximity as a function of distance from the center of the focal volume in units of  $\omega_r$  and  $\omega_z$ , the radial and axial  $e^{-2}$  extents of the PSF, respectively. To extrapolate these results to other photobleaching chemistries or greater bleach depths, one can calculate the characteristic radial and axial dimensions of that photobleaching distribution and treat those as  $\omega_r$  and  $\omega_z$  for comparison to our results.

### B. Diffusion

Diffusion was modeled as a random walk on a 3D lattice [37,38,40,41]. Lattice spacing was determined by the 3D diffusion equation,  $\langle r^2 \rangle = 6Dt$ , where the diffusion coefficient,  $D$ , was chosen *a priori* and the time step,  $t$ , was chosen to be approximately 1/1000 of the typical diffusive recovery time for a system with a diffusion coefficient  $D$  and with radial and axial focal volume widths  $\omega_r$  and  $\omega_z$ . For both the low and high NA cases,  $D$  was chosen as  $10 \mu\text{m}^2/\text{s}$ , approximately the experimental diffusion coefficient for 2000 kD fluorescein dextran [18]. The corresponding time steps were chosen as 3.12 and 0.376  $\mu\text{s}$ , respectively, and the lattice spacings were calculated to be 13.7 and 4.75 nm, respectively.

### C. Boundary conditions

Four boundary models were applied to the diffusing system: a single infinite plane boundary parallel and perpendicular to the optical axis, two parallel infinite plane boundaries parallel and perpendicular to the optical axis, a hollow infinite cylindrical boundary parallel and perpendicular to the optical axis, and a hollow spherical boundary. In the context of our simulations a barrier is considered infinite if a particle cannot cross the barrier at any time during the simulation. The parallel, cylindrical, and spherical boundaries were positioned symmetrically about the focal volume center, and the positions of all of the boundaries were defined as fractions of  $\omega_r$  or  $\omega_z$  relative to the focal volume center. All boundaries were assumed to be perfectly reflecting; i.e., any particle attempting to cross a boundary was returned to the node it was occupying when the step began. There were no bleached or unbleached molecules beyond the boundaries at  $t = 0$  or at any subsequent point.

### D. MP-FRAP

The fluorescence intensity generated by a weak monitoring beam that is held stationary in the sample and produces fluorescence through an  $m$ -photon process is given by

$$F(t) = \frac{\delta_m E}{m} \int \langle I_{mo}^m(x, y, z) \rangle c(x, y, z; t) dx dy dz, \quad (4)$$

where  $\delta_m$  is the multiphoton fluorescence action cross-section of the fluorophore for the order of excitation required to produce fluorescence,  $E$  is the collective efficiency of the detection system, and  $m$  is the number of photons absorbed per excitation event.

We can calculate the “missing fluorescence” that would be generated by the *bleached* fluorophores were they not bleached by re-expressing the integral as a sum of the monitor intensity [given by Eq. (2) with  $b \rightarrow m$ ] over all bleached fluorophore locations  $(x_i, y_i, z_i)$ . We can also let  $(1/m)E\delta_m \rightarrow 1$ , as it will be divided out when the fluorescence is normalized for fitting:

$$F_{bl}(t) = \sum_i \exp \left[ -\frac{2b(x_i^2 + y_i^2)}{\omega_r^2} - \frac{2bz_i^2}{\omega_z^2} \right]. \quad (5)$$

To obtain the normalized fluorescence of the *unbleached* molecules,  $F(t)/F_o$ , we first normalize the missing fluorescence of the bleached molecules by the prebleach fluorescence of all the fluorophores in the system,  $F_o$ , and then subtract from one:  $F(t)/F_o = 1 - F_{bl}(t)/F_o$ .  $F_o$  was determined by first setting  $t = 0$  and  $\beta = 0.25$  in Eq. (6), below, truncating the sum to the first ten terms, and solving for  $F(0)/F_o$ . This value was then substituted into  $F(0)/F_o = 1 - F_{bl}(0)/F_o$  to deduce  $F_o$  from  $F_{bl}(0)$ .

The natural variation of a Monte Carlo simulated random walk introduced a small amount of noise into the resulting  $F(t)$  recovery curves. On top of this, we added Poisson distributed noise to mimic the typical distribution of noise arising from photon counting experiments, and in an amount typical of *in vitro* MP-FRAP experiments [1,18]. Fluorescence recoveries were terminated when the change in the recovered fluorescence was less than 1% over a time equivalent to the half-time for complete recovery of a freely diffusing system with diffusion coefficient  $D$ .

Unless otherwise stated, all simulated  $F(t)$  curves were fit to the accepted diffusive recovery model [1] for a stationary bleaching and monitoring beam:

$$\frac{F(t)}{F_o} = \sum_{n=0}^{\infty} \frac{(-\beta)^n}{n!} \frac{1}{(1+n+2nt/\tau_D)} \frac{1}{(1+n+2nt/R\tau_D)^{1/2}}, \quad (6)$$

where  $\tau_D$  is the characteristic diffusion time and  $R$  is the square of the ratio of the axial and radial dimensions of the focal volume. The diffusion coefficient is given by  $D = \omega_r^2/8\tau_D$ .

## III. RESULTS AND DISCUSSION

### A. Single plane boundary

We begin our Monte Carlo investigation by introducing a single infinite plane reflective boundary parallel to the optical axis, at a range of distances measured in units of  $\omega_r$  relative to the focal volume center. This models diffusion measurements

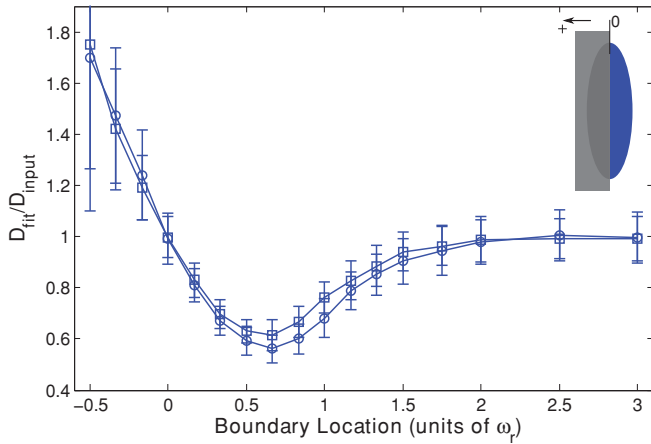


FIG. 1. (Color) Single boundary parallel to the optical axis at a range of positions, presented as fractions of  $\omega_r$  from the focal volume center, for both a high NA (squares) lens and a low NA (circles) lens. Negative position values indicate that the boundary has crossed the focal volume center (i.e., more than half the focal volume is hidden behind the boundary). Fluorescence recovery curves were generated via Monte Carlo simulation and fit to the standard MP-FRAP model [Eq. (6)]. Fit diffusion coefficients were normalized to the input diffusion coefficient; hence an accurate fit produces a ratio of one.

adjacent to cell walls [42–44]. We then generate an initial distribution of bleached molecules according to Eq. (1), with the caveat that no molecules are located beyond the boundary. Then we simulate the random diffusion of those molecules and produce an  $F(t)$  curve as described above. The resultant curve is fit to Eq. (6), the MP-FRAP formula that assumes all boundaries are at infinity. The fit diffusion coefficient is then divided by the true diffusion coefficient (defined *a priori* in setting up the diffusion random walk); hence errors due to the presence of a boundary are readily identified by a deviation of this ratio from one. Note that we ceased our simulations at a boundary location of  $-0.5\omega_r$  because at this point the average fluorescence from the focal volume in steady state is  $<10\%$  of the value of the unobstructed focal volume.

The resultant data are presented in Fig. 1 and show that MP-FRAP begins to yield diffusion coefficients significantly different from the input diffusion coefficient (defined hereafter as when the mean fit diffusion coefficient is more than 1 standard deviation (SD) different from the input diffusion coefficient) when the boundary passes a distance of  $1.3\omega_r$  from the focal volume center for a high NA lens and a distance of  $1.5\omega_r$  for a low NA lens. In each of these cases, the fit diffusion coefficient,  $D_{\text{fit}}$ , becomes significantly different from the input coefficient,  $D_{\text{input}}$ , before the boundary crosses the focal volume center ( $0\omega_r$ ), and the deviation is biphasic, with  $D_{\text{fit}}$  initially smaller than  $D_{\text{input}}$ , then becoming significantly larger than  $D_{\text{input}}$  as the boundary crosses the focal volume center. The erroneously low value of  $D_{\text{fit}}$  is most pronounced when the boundary is in the range of  $\sim 0\omega_r-1.5\omega_r$ , and we hypothesized that this occurs because the boundary hinders the complete escape of bleached molecules from the focal volume, forcing a selection of fluorophores to reside longer in the neighborhood of the focal volume, thereby lengthening the recovery time. We further hypothesized that as a growing

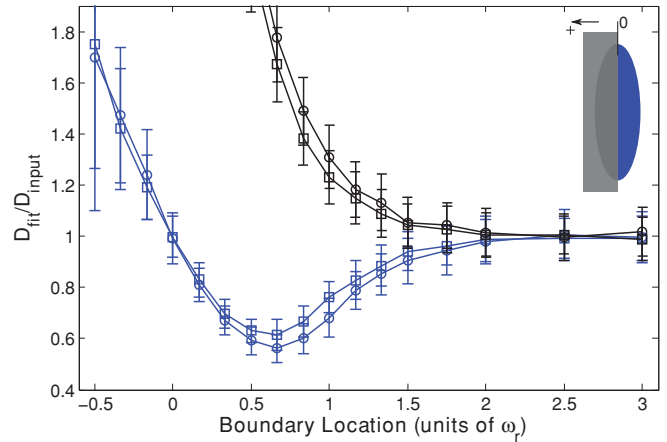


FIG. 2. (Color) Single “destructive” boundary (black) and “reflective” boundary (blue) parallel to the optical axis at a range of positions, presented as fractions of  $\omega_r$  from the focal volume center for a high NA (squares) lens and a low NA (circles) lens. Negative position values indicate that the boundary has crossed the focal volume center. Fluorescence recovery curves were generated via Monte Carlo simulation and fit to the standard MP-FRAP model. Fit diffusion coefficients were normalized to the input diffusion coefficient.

portion of the focal volume becomes “hidden” behind the boundary its characteristic radial size will become smaller than  $\omega_r$  and fitting of the resultant recovery curves to Eq. (6), which assumes that  $\omega_r$  is the relevant radial length scale, will produce the erroneously large values of  $D_{\text{fit}}$  that become apparent as the wall approaches  $-0.5\omega_r$ .

To test these hypotheses we first repeated the series of Monte Carlo simulations, now using a “destructive” boundary instead of a “reflective” one, such that each bleached molecule that attempted to cross the boundary was removed from the simulation. As shown in Fig. 2, removal of the reflected fluorophores eliminated the initially low values of  $D_{\text{fit}}$  but retained the later large values, suggesting that it is indeed reflection of bleached molecules off of the boundary and back into the focal volume that lengthens the recovery time and leads to the initial erroneously small values of  $D_{\text{fit}}$ . One may note that the curves describing the destructive case begin to upswing while those for the reflective case are still in their initial downturn. At this point in the reflective case the effect on recovery is dominated by the fluorophores reflecting back into the region of the focal center, and only as the boundary crosses the focal center does the effect on shortening  $\omega_r$  begin to overcome particle deflection and reverse the trend, eventually leading to too-large values of  $D_{\text{fit}}$ .

Next, to demonstrate the effect that changing the focal volume dimensions has on fluorescence recovery and fitting, we generated data assuming an unobstructed focal volume and free diffusion, but with  $\omega_r$  reduced to mimic the influence of the barriers reducing the focal volume as introduced in the simulations. We then fit the resulting fluorescence curves assuming a focal volume with the original  $\omega_r$ . As  $\omega_r$  was reduced to successively smaller values, the fit diffusion coefficient became increasingly large, beyond the value of  $D_{\text{input}}$  (data not shown). This reproduces the trend seen in

Fig. 2 and suggests that the erroneously large values of  $D_{\text{fit}}$  are indeed due solely to a reduction in the bleaching distribution and monitoring volume, and hence are an overestimate of their characteristic size during the fitting process.

Inspection of Fig. 1 also reveals that the low NA curve is more affected by the approach of the barrier than is the high NA curve, with more significantly low initial values for  $D_{\text{fit}}$ . We hypothesized that this is due to the different aspect ratios of the focal volumes ( $\omega_z/\omega_r = 3.75$  for the high NA case and  $\omega_z/\omega_r = 9$  for the low NA case). The fastest route for diffusive escape from an initial bleached distribution will be along the shortest dimension of the initial distribution, and the higher aspect ratio of the low NA focal volume means that the diffusive transport in the direction of the approaching barrier is a more significant contributor to fluorescence recovery for that objective lens than for a higher NA objective, resulting in a more significant effect of the barrier. To test this hypothesis we repeated the series of Monte Carlo simulations, but brought in a barrier to diffusion that was perpendicular to the optical axis. The fastest route for diffusive escape in this geometry is now parallel to the surface of the approaching barrier and thus unhindered by it, leading us to predict that the initially low values of  $D_{\text{fit}}$  should deviate from  $D_{\text{input}}$  far less than for the case of boundaries parallel to the optical axis. Furthermore, the low values of  $D_{\text{fit}}$  should now be *least* significant for the low NA case, as that has the highest aspect ratio. As shown in Fig. 3, the initially low values of  $D_{\text{fit}}$  for the boundary perpendicular to the optical axis do indeed deviate less from  $D_{\text{input}}$  and are now least significant for the low NA case, thus confirming our hypothesis. Figure 3 also reveals that MP-FRAP begins to yield diffusion coefficients significantly different from the input diffusion when a boundary perpendicular to the optical axis passes  $-0.3\omega_z$  for a high NA lens. For the low NA case,  $D_{\text{fit}}$  does not deviate significantly for any of the boundary locations assessed.

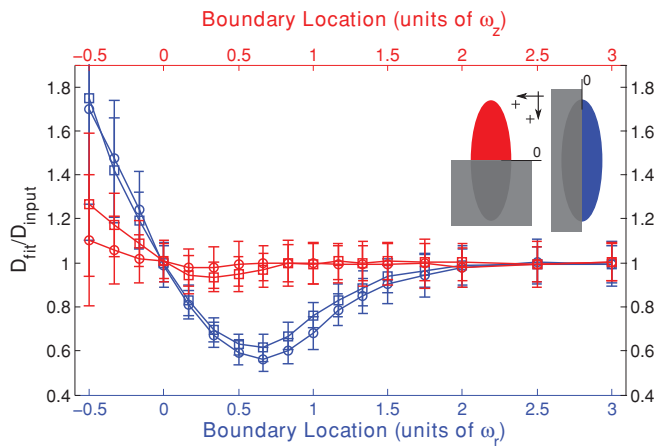


FIG. 3. (Color) Single boundary parallel (blue) and perpendicular (red) to the optical axis at a range of positions, presented as fractions of  $\omega_r$  or  $\omega_z$ , respectively, from the focal volume center for a high NA (squares) lens and a low NA (circles) lens. Negative position values indicate that the boundary has crossed the focal volume center. Fluorescence recovery curves were generated via Monte Carlo simulation and fit to the standard MP-FRAP model. Fit diffusion coefficients were normalized to the input diffusion coefficient.

To improve the accuracy of the reported diffusion coefficient for the case of a single barrier to diffusion, we have derived an alternative analytical model of the fluorescence recovery (see Appendix) that takes into account the presence of the barrier. For a barrier lying parallel to the optical axis, the new model is

$$\frac{F(t)}{F'_o} = \frac{1}{2} \frac{1}{\text{erfc}(-2u/\omega_r)} \sum_{n=0}^{\infty} \frac{(-\beta)^n}{n!} \frac{1}{[n + \mu_n(t)]} \frac{1}{[n + \nu_n(t)]^{1/2}} \times \left\{ \text{erfc} \left[ -2 \left[ 1 + n/\mu_n(t) \right]^{1/2} \frac{u}{\omega_r} \right] + \exp \left[ -\frac{16n}{n + \mu_n(t)} \left( \frac{u}{\omega_r} \right)^2 \right] \times \text{erfc} \left[ -2 \frac{[1 - n/\mu_n(t)]}{[1 + n/\mu_n(t)]^{1/2}} \frac{u}{\omega_r} \right] \right\}, \quad (7)$$

where  $\mu_n(t) = 1 + 2nt/\tau_D$ ,  $\nu_n(t) = 1 + 2nt/R\tau_D$ , and  $u$  is the  $x$  or  $y$  position of the bleached molecule distribution center relative to the boundary. For a barrier perpendicular to the optical axis, the form is the same but  $\mu_n \rightarrow \nu_n$  and  $\omega_r \rightarrow \omega_z$  in the exponential and complementary error functions.

When this new MP-FRAP “single boundary” model is used to fit simulated diffusion curves produced in the presence of a single barrier parallel to the optical axis at a known distance, the fit diffusion coefficients improve dramatically over a wide range of barrier distances (see Fig. 4). For the case of a barrier perpendicular to the optical axis,  $D_{\text{fit}}$  does not improve significantly over the already generally accurate results using the standard model (data not shown). Figure 4 shows that  $D_{\text{fit}}$  remains accurate until after the boundary has crossed the center of the focal volume ( $0\omega_r$ ), but becomes significantly different from  $D_{\text{input}}$  as a boundary parallel to the optical axis passes  $-0.15\omega_r$  from the focal volume center

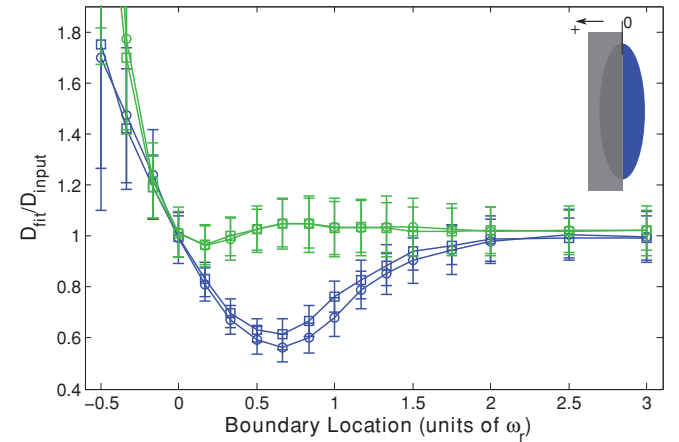


FIG. 4. (Color) Single boundary parallel to the optical axis at a range of positions, presented as fractions of  $\omega_r$  from the focal volume center for a high NA (squares) lens and a low NA (circles) lens. Negative position values indicate that the boundary has crossed the focal volume center. Fluorescence recovery curves were generated via Monte Carlo simulation and fit to the standard MP-FRAP model (blue) and the new MP-FRAP model (green) designed for use near a single barrier. Fit diffusion coefficients were normalized to the input diffusion coefficient.

for both a high NA lens and a low NA lens. If the position of the boundary is not known, we can allow  $u$  to be a free fitting parameter. However, doing so yields erroneous values for the diffusion coefficient for barrier positions  $< 1\omega_r$  (data not shown).

### B. Parallel plane boundaries

Two parallel infinite plane reflective boundaries mimic systems such as the regions between cell walls found in tumor and brain extracellular space [42–44]. To model this system we introduce parallel plane barriers symmetrically about the focal volume center, positioned parallel or perpendicular to the optical axis at a range of distances measured in units of  $\omega_r$  or  $\omega_z$  relative to the focal volume center. As before, the data are presented as  $D_{\text{fit}}/D_{\text{input}}$  as a function of boundary location. In each case, Fig. 5 shows that as the boundaries approach the focal volume, the fit diffusion coefficient begins to drop compared to the input diffusion coefficient.  $D_{\text{fit}}$  becomes significantly different from  $D_{\text{input}}$  as boundaries parallel to the optical axis pass  $1.5\omega_r$  from the focal volume center for a high NA lens and  $1.8\omega_r$  for a low NA lens. For boundaries perpendicular to the optical axis,  $D_{\text{fit}}$  becomes statistically significantly different from  $D_{\text{input}}$  as the boundaries pass  $0.5\omega_z$  from the focal center for a high NA lens. For the low NA case,  $D_{\text{fit}}$  does not deviate significantly for any of the boundary locations assessed.

As in the case of the single boundary, the effect on the diffusion coefficient is more significant for the case of two parallel plane boundaries running parallel to the optical axis. As demonstrated previously, this arises because boundaries parallel to the optical axis reduce the opportunity for diffusing

molecules to leave the focal volume via the shorter radial dimension, which predominantly determines the duration of recovery for a freely diffusing sample. This is also shown by the opposite behaviors of low and high NA lenses in the two geometries. When the boundaries are parallel to the optical axis, the low NA lens is the most affected because radial diffusion is more significant in this high aspect ratio focal volume. Conversely, when the boundaries are perpendicular to the optical axis, the low NA lens is the least affected, for the same reason. Unlike the single boundary case, however, as the boundaries significantly reduce the focal volume  $D_{\text{fit}}$  does not rise but levels off. The characteristic length of the focal volume is reduced in the direction normal to the plane surfaces, suggesting that the characteristic recovery time should become shorter, as in the single boundary case. However, as the distance between the planes approaches zero, diffusion is effectively confined to two dimensions, and this effect dominates.

By letting  $\omega_z \rightarrow \infty$  in Eq. (6) we obtain a two-dimensional form of the MP-FRAP model, which is valid in the limit of a 2D system perpendicular to the optical axis and identical to the original one-photon FRAP model [5]:

$$\frac{F(t)}{F_o} = \sum_{n=0}^{\infty} \frac{(-\beta)^n}{n!} \frac{1}{1 + n + 2nt/\tau_D}. \quad (8)$$

By generating data using this 2D formula and then fitting the data to the standard 3D model we find that in the limit of 2D diffusion the 3D model should yield a value of the diffusion coefficient that is  $0.84 \pm 0.04$  times the accepted value for a high NA lens and  $0.96 \pm 0.03$  times the accepted value for a low NA lens. These limits are plotted in Fig. 5 as the dashed lines and coincide with the values of the normalized diffusion coefficients at small values of  $\omega_z$  as determined by the Monte Carlo simulations of MP-FRAP. The asterisks (\*) mark data sets that, when refit with the 2D MP-FRAP model given by Eq. (8), recovered the input diffusion coefficient to within 1 SD.

To improve the accuracy of the reported diffusion coefficient for the case of parallel infinite plane barriers to diffusion, we have derived an alternative analytical model of the fluorescence recovery (see the Appendix) that takes into account the presence of the barriers. For barriers lying parallel to the optical axis, the new model is

$$\begin{aligned} \frac{F(t)}{F''_o} = & \frac{1}{3} \frac{1}{\text{erf}(2u/\omega_r)} \sum_{n=0}^{\infty} \frac{(-\beta)^n}{n!} \frac{1}{[n + \mu_n(t)]} \frac{1}{[n + \nu_n(t)]^{1/2}} \\ & \times \left\{ \text{erf} \left[ -2[1 + n/\mu_n(t)]^{1/2} \frac{u}{\omega_r} \right] \right. \\ & + \exp \left[ -\frac{16n}{n + \mu_n(t)} \left( \frac{u}{\omega_r} \right)^2 \right] \\ & \times \left( \text{erf} \left[ -2 \frac{[1 - n/\mu_n(t)]}{[1 + n/\mu_n(t)]^{1/2}} \frac{u}{\omega_r} \right] \right. \\ & \left. \left. + \text{erf} \left[ -2 \frac{[1 + 3n/\mu_n(t)]}{[1 + n/\mu_n(t)]^{1/2}} \frac{u}{\omega_r} \right] \right) \right\}. \quad (9) \end{aligned}$$

For barriers perpendicular to the optical axis, the form is the same but  $\mu_n \rightarrow \nu_n$  and  $\omega_r \rightarrow \omega_z$  in the exponential and error functions.

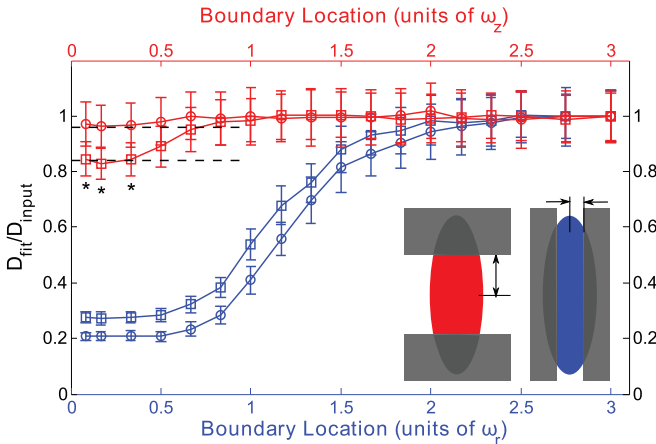


FIG. 5. (Color) Two parallel boundaries parallel (blue) or perpendicular (red) to the optical axis at a range of positions symmetric about the focal volume center and presented as fractions of  $\omega_r$  or  $\omega_z$  for a high NA (squares) lens and a low NA (circles) lens. Fluorescence recovery curves were generated through Monte Carlo simulation and fit to the standard MP-FRAP model. Fit diffusion coefficients were normalized to the input diffusion coefficient. Dashed lines mark the limit of 2D diffusion as indicated by generating data with the 2D MP-FRAP recovery equation and fitting it to the 3D MP-FRAP recovery equation. For data points marked with an asterisk (\*), the accurate diffusion coefficient was recovered when the data were fit with the 2D MP-FRAP model.

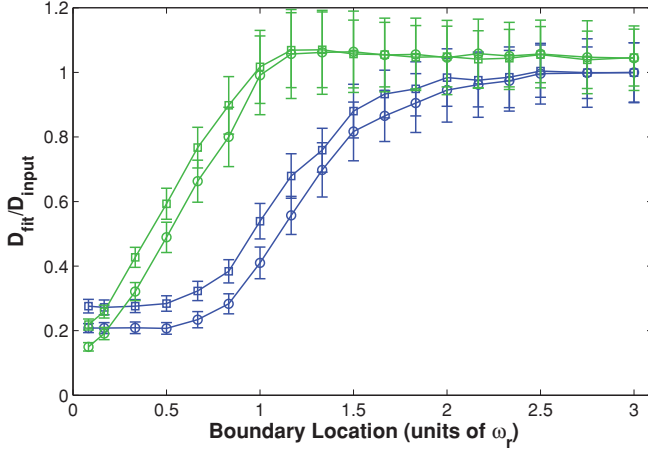


FIG. 6. (Color) Two parallel plane boundaries parallel to the optical axis at a range of positions, presented as fractions of  $\omega_r$  from the focal volume center for a high NA (squares) lens and a low NA (circles) lens. Fluorescence recovery curves were generated via Monte Carlo simulation and fit to the standard MP-FRAP model (blue) and the new MP-FRAP model (green) designed for use between two parallel plane barriers. Fit diffusion coefficients were normalized to the input diffusion coefficient.

When this new MP-FRAP “parallel boundary” model is used to fit simulated diffusion curves produced assuming the presence of two parallel plane barriers parallel to the optical axis at a known distance, the fit diffusion coefficients improve dramatically over a wide range of barrier distances (see Fig. 6). For the case of barriers perpendicular to the optical axis the values for  $D_{\text{fit}}$  do not improve significantly over the already widely accurate results using the standard model (data not shown). Figure 6 shows that  $D_{\text{fit}}$  becomes significantly different from  $D_{\text{input}}$  as boundaries parallel to the optical axis pass  $\omega_r$  from the focal volume center for both a high NA lens and a low NA lens. If the position of the boundary is not known, we can allow  $u$  to be a free fitting parameter. However, doing so yields poor fits for barrier positions  $< 1\omega_r$  (data not shown).

### C. Cylindrical boundary

An infinite hollow cylindrical boundary provides an excellent approximation for neuronal dendrites and axons, in which transport measurements are of interest in neurobiological research [45,46]. In our simulations, we introduce a cylindrical boundary both parallel and perpendicular to the optical axis, positioned symmetrically about the focal volume center with a range of radii measured in units of  $\omega_r$  and  $\omega_z$ . Again, the data are presented as  $D_{\text{fit}}/D_{\text{input}}$  as a function of boundary location. As with the case of the parallel plane boundaries, Fig. 7 shows that as the cylindrical boundary approaches the focal volume,  $D_{\text{fit}}$  begins to drop compared to  $D_{\text{input}}$ , and these effects occur at values of  $\omega_r$  for the case of a cylindrical boundary parallel to the optical axis larger than for corresponding values of  $\omega_z$  in the perpendicular case. Specifically,  $D_{\text{fit}}$  becomes significantly smaller than  $D_{\text{input}}$  as the radius of a cylinder parallel to the optical axis becomes smaller than  $1.8\omega_r$  for a high NA lens and  $2\omega_r$  for a low NA lens.  $D_{\text{fit}}$  becomes statistically significantly smaller than  $D_{\text{input}}$  as the radius of a cylinder perpendicular

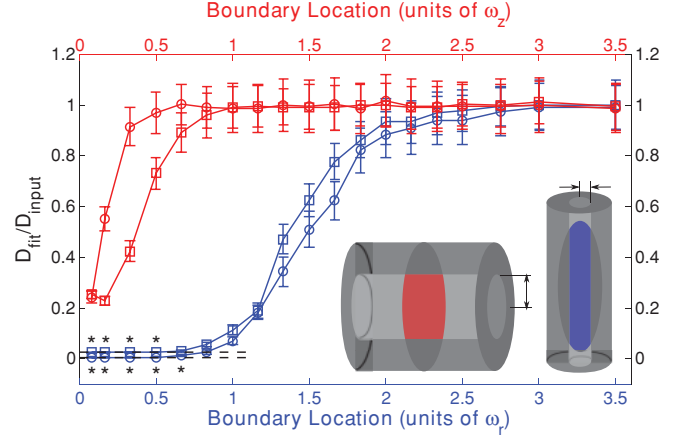


FIG. 7. (Color) Cylindrical boundary parallel (blue) and perpendicular (red) to the optical axis at a range of positions, symmetric about the focal volume center and presented as fractions of  $\omega_r$  or  $\omega_z$ , for a high NA (squares) lens and a low NA (circles) lens. Fluorescence recovery curves were generated through Monte Carlo simulation and fit to the standard MP-FRAP model. Fit diffusion coefficients were normalized to the input diffusion coefficient. Dashed lines mark the limit of 1D diffusion as indicated by generating data with the 1D MP-FRAP recovery equation and fitting it to the 3D MP-FRAP recovery equation. For data points marked with an asterisk (\*), the accurate diffusion coefficient was recovered when the data were fit with the 1D MP-FRAP model.

to the optical axis becomes smaller than  $0.7\omega_z$  for a high NA lens and  $0.3\omega_z$  for a low NA lens.

Similar to the parallel plane boundaries, we find that when the cylindrical boundary is sufficiently constricting the diffusion effectively becomes one dimensional (1D). Consequently, although the size of the available volume decreases  $D_{\text{fit}}$  does not increase above  $D_{\text{input}}$  after initially dropping significantly below  $D_{\text{input}}$ . In the limit of 1D diffusion, the MP-FRAP model can be altered to account for the dimensional change. By letting  $\omega_r \rightarrow \infty$  in Eq. (6) we obtain a 1D form of the MP-FRAP model for diffusion along the optical axis:

$$\frac{F(t)}{F_0} = \sum_{n=0}^{\infty} \frac{(-\beta)^n}{n!} \frac{1}{(1 + n + 2nt/R\tau_D)^{1/2}}. \quad (10)$$

By generating data using this 1D model and fitting it to the 3D model we find that in the limit of 1D diffusion the 3D model should yield a value of the diffusion coefficient that is  $0.026 \pm 0.001$  times the accepted value for a high NA lens and  $0.006 \pm 0.001$  times the accepted value for a low NA lens. These limits are plotted in Fig. 7 as the dashed lines and coincide with the values of the normalized diffusion coefficients at small values of  $\omega_r$  as determined by the Monte Carlo simulations of MP-FRAP. The asterisks (\*) mark data sets that, when refit with the 1D MP-FRAP model, recovered the input diffusion coefficient, within 1 SD.

### D. Spherical boundary

A hollow spherical boundary well approximates a cell body, cell nucleus, or dendritic spine [47–49]. We introduce the spherical boundary symmetrically about the focal volume center with a range of radii measured in units of  $\omega_r$ . The data

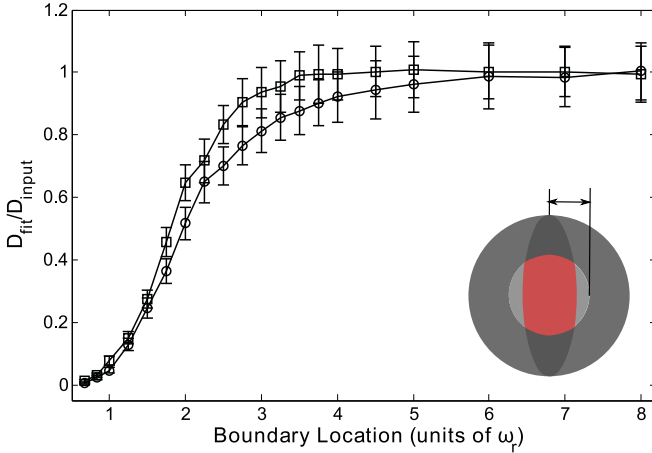


FIG. 8. (Color) Spherical boundary at a range of positions, symmetric about the focal volume center and presented as fractions of  $\omega_r$ , for a high NA (squares) lens and a low NA (circles) lens. Fluorescence recovery curves were generated through Monte Carlo simulation and fit to the standard MP-FRAP model. Fit diffusion coefficients were normalized to the input diffusion coefficient.

are presented as  $D_{\text{fit}}/D_{\text{input}}$  as a function of boundary location. Figure 8 shows that the fit diffusion coefficient drops rapidly relative to the input diffusion coefficient as the boundaries narrow in on the focal volume. Specifically,  $D_{\text{fit}}$  becomes significantly smaller than  $D_{\text{input}}$  as the radius of the sphere becomes smaller than  $2.75\omega_r$  for a high NA lens and  $3.75\omega_r$  for a low NA lens.

As the sphere becomes sufficiently small, many (and eventually all) of the bleached molecules will be unable to leave the focal volume. This suggests that the standard 3D MP-FRAP model [Eq. (6)], which assumes free diffusion of the entire fluorophore population, may be inappropriate to fit the recovery. The concept of an “immobile fraction” has been discussed previously [1,50] in the context of fluorophore populations attached to the extracellular matrix or cell cytoskeleton and involves an additional fitting parameter to account for the incomplete recovery caused by a subset of immobile fluorophores. We refit the data generated for free diffusion within a spherical boundary using standard 3D MP-FRAP with a fitting parameter for an immobile fraction, but did not achieve significantly more accurate values for the diffusion coefficient (data not shown). This arises because the

case of an immobile fluorophore population and our case of a trapped but mobile population are only superficially similar. In the case of an immobile fraction, a subset of fluorophores are permanently (relative to the duration of the experiment) fixed in space. The remaining fluorophores, however, are assumed to diffuse freely. In the case of fluorophores confined within a spherical boundary, however, while many fluorophores remain within the focal volume they are always free to move. As the bleached molecules spread from their initial center-heavy distribution to a more uniform distribution, the fluorescence of the sample changes. The shape of the recovery is subtly, yet significantly, different from the case of immobile fluorophores, and fitting with this added parameter does not significantly improve the resultant diffusion coefficient.

### E. Summary

Using Monte Carlo simulations, we have defined the range of applicability of MP-FRAP to measure diffusion in the presence of barriers of various geometries and positions relative to the focal volume center. Table I summarizes the results of our simulations. Using the standard MP-FRAP model, the onset of deviations in the fit diffusion coefficient is at a distance of  $1.3\omega_r$ – $1.5\omega_r$  for a single plane barrier parallel to the optical axis and  $\sim 0.3\omega_z$  for a barrier perpendicular to the optical axis. Using the new MP-FRAP single boundary model (Eq. (7)) for a barrier parallel to the optical axis, the initially low values of  $D_{\text{fit}}$  are avoided and the point of onset of significant deviations greatly improves to  $\sim 0.15\omega_r$ . For two parallel plane boundaries, the onset of deviations is at a distance of  $1.5\omega_r$ – $1.8\omega_r$  for barriers parallel to the optical axis and  $<0.1\omega_z$  to  $\sim 0.5\omega_z$  for barriers perpendicular to the optical axis. To improve the range of applicability for barriers parallel to the optical axis, the user could perform MP-FRAP analysis using the new two-boundary model [Eq. (9)], enabling accurate diffusion coefficients to be produced down to  $\omega_r$ . The onset of deviations within a hollow cylindrical boundary is at a radius of  $\sim 1.8\omega_r$ – $2\omega_r$  for a cylinder parallel to the optical axis and  $\sim 0.3\omega_z$ – $0.7\omega_z$  for a cylinder perpendicular to the optical axis. In each of these geometries, the high-aspect ratio of two-photon focal volumes leads to greater deviations when the boundaries are brought in parallel to the optical axis. For the sphere, the onset of deviations occurs at a radius of  $\sim 2.75\omega_r$ – $3.75\omega_r$  and is not improved by fitting with an immobile fraction term.

TABLE I. Summary of results of fitting fluorescence recovery curves in the presence of reflective boundaries to diffusion with the standard MP-FRAP diffusive-recovery model. Boundaries are located symmetrically about the focal volume center at positions measured in units of  $\omega_r$  or  $\omega_z$ . The boundary locations for a single parallel-plane boundary and two parallel-plane boundaries laying parallel to the optical axis within which the standard MP-FRAP model yields erroneous diffusion coefficients can be narrowed by using the new models presented in the text.

Boundary geometry	Orientation with respect to optical axis	Boundary limit with standard MP-FRAP	Boundary limit with new model
Single plane	parallel	$1.3\omega_r$ – $1.5\omega_r$	$\sim 0.15\omega_r$
	perpendicular	$\sim 0.3\omega_z$	
Parallel-plane	parallel	$1.5\omega_r$ – $1.8\omega_r$	$1\omega_r$
	perpendicular	$<0.1\omega_z$ – $\sim 0.5\omega_z$	
Cylinder	parallel	$1.8\omega_r$ – $2\omega_r$	
	perpendicular	$0.3\omega_z$ – $0.7\omega_z$	
Sphere		$2.75\omega_r$ – $3.75\omega_r$	

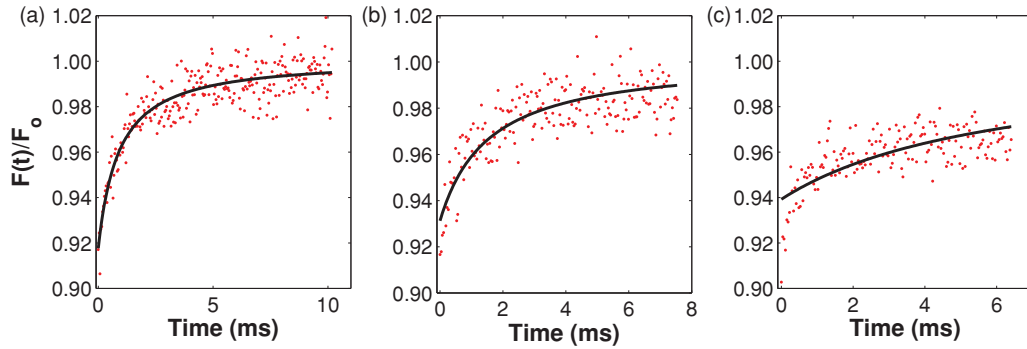


FIG. 9. (Color) Representative recovery curves and fits for the case of a cylindrical barrier of three different radii ( $3.5\omega_r$ ,  $1.5\omega_r$ , and  $1.0\omega_r$ , respectively), oriented parallel to the optical axis. In (a) the shape of the recovery curve matches that for free diffusion, and  $D_{\text{fit}}/D_{\text{input}} = 1.02$ . By direct comparison with (a) the recovery curve in (b) appears altered, but the shape is typical of MP-FRAP recovery curves and the fit looks good by eye. However,  $D_{\text{fit}}/D_{\text{input}} = 0.59$ ;  $D_{\text{fit}}$  is *not* accurate. In (c) the curve is significantly altered in shape and the fit both looks poor to the eye and yields an inaccurate diffusion coefficient,  $D_{\text{fit}}/D_{\text{input}} = 0.15$ .

For all geometries, the error in the fit diffusion coefficient as the boundary approaches the focal volume is initially presented as a deviation below the input diffusion coefficient. This is caused by a hindrance of the ability of bleached molecules to leave the environment of the focal volume as a result of reflection off of the boundary wall(s) and back into the focal volume. For the case of a single plane barrier to diffusion, after initially dipping below  $D_{\text{input}}$ ,  $D_{\text{fit}}$  begins to rise, eventually leading to deviations greater than  $D_{\text{input}}$ . This is caused by truncation of the bleach distribution and monitor volume as the focal volume crosses into the boundary wall. This same trend is not seen for the other geometries, however, even though our simulations bring the boundaries inside the focal volume, thus also truncating the bleach distribution and monitor volumes. Instead,  $D_{\text{fit}}$  levels off in all cases. For the parallel plane and cylindrical boundaries, this is because the confinement mimics the approach to a 2D (parallel plane) or 1D (cylindrical) system. When data at this limit for barriers parallel to the optical axis are refit with the corresponding 1D or 2D MP-FRAP models,  $D_{\text{fit}}$  returns the same value as  $D_{\text{input}}$ . For the case of the spherically confining boundary,  $D_{\text{fit}}$  continues to get smaller as the boundaries move inward.

Given the significant errors evident in the fit diffusion coefficient when the various boundaries closely confine the focal volume, it is reasonable to expect that the corresponding recovery curves would be significantly altered compared to their unbounded counterparts and that the fits may be obviously poor by simple inspection. In the case of a single plane barrier or two parallel-plane barriers, while the recovery curves do lengthen as the boundaries are brought in (hence the drop in  $D_{\text{fit}}$ ), they retain the classic recovery curve shape and fits to recovery curves for *all* boundary locations assessed look good by inspection (data not shown). It is not until a cylindrical barrier is brought in to narrowly confine the focal volume that any obvious error is detected. Figure 9 shows representative data sets and fits for recovery curves generated within cylindrical boundaries of three different radii. To simulate the data shown in Fig. 9(a) the cylinder radius was  $3.5\omega_r$ . In this case the boundary was far enough away to achieve a result consistent with free diffusion, and  $D_{\text{fit}}/D_{\text{input}} = 1.02$ . To generate the data in Fig. 9(b) the

cylinder radius was  $1.5\omega_r$ . Although by direct comparison with Fig. 9(a) the recovery curve does appear altered, the shape is typical of MP-FRAP recovery curves and the fit looks good by eye. However, in agreement with Fig. 7,  $D_{\text{fit}}/D_{\text{input}} = 0.59$ ; the fit diffusion coefficient is *not* accurate. Finally, to produce the data in Fig. 9(c) the cylinder radius was  $1.0\omega_r$ , very nearly at the limit of 1D diffusion. In this case the curve is further altered and the fit now looks poor to the eye. Again in agreement with Fig. 7,  $D_{\text{fit}}/D_{\text{input}} = 0.15$ . Clearly, the experimental researcher cannot rely on inspection of recovery curves and fits to indicate an error in the measurement, except in the extreme case of a narrowly constrained cylinder. Instead, she or he should follow the guidelines described here.

Most MP-FRAP experiments are performed using a multiphoton laser scanning microscopy (MPLSM) platform, with a radial and axial resolution of imaging of  $\sim\omega_r$  and  $\sim\omega_z$ , respectively [51], although improved resolution can be achieved with deconvolution techniques [52]. Furthermore, MP-FRAP relies on large fluorophore concentrations, typically high enough to allow *in vivo* imaging of the diffusing fluorophore population. Based upon our results, the user can therefore image the spatial distribution of fluorophores and avoid MP-FRAP analysis using the standard model [Eq. (6)] when the boundaries move within the locations presented in the third column of Table I. In the cases of planar barriers and a cylindrical barrier, all oriented perpendicular to the optical axis, one cannot take advantage of the full range of safe barrier distances because the resolution limit of the microscope ( $\sim 1\omega_z$ ) prevents us from accurately determining our position relative to the barrier with accuracy less than the resolution limit. In those cases, MP-FRAP should only be performed when the barrier is at a resolvable distance from the focal volume center (typically  $\geq 1\omega_z$ ) to ensure that unsafe regions are not interrogated. In the case of a single barrier or two parallel-plane barriers lying parallel to the optical axis, the range of safe barrier distances has been extended by the new models [Eqs. (7) and (9)] down to or below the resolution limit.

In some experiments, the diffusing population may be concentrated enough to use for MP-FRAP but too dilute to allow imaging of the diffusive barriers. In this case, a second fluorophore could be employed to highlight the boundaries

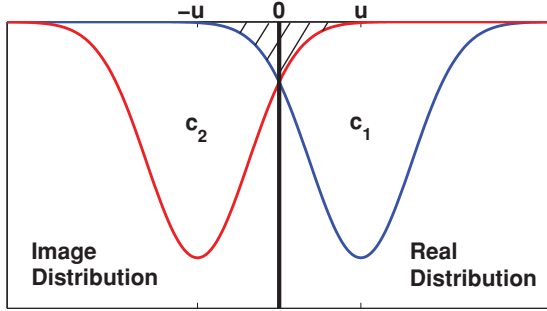


FIG. 10. (Color) Placement of real and “image” bleached molecule concentration distributions for the case of a single infinite plane boundary. The overlap of the image distribution in the region of the real distribution as the two distributions spread ( $t > 0$ ) mimics the behavior of diffusing molecules that bounce off the barrier and back into the focal volume. At  $t = 0$ , there will be overcounting of bleached molecules when the two distributions are close to the barrier. This error will remain small until the image distribution peak approaches the barrier.

within and between which the measurement will be taken, for example, by labeling the cell walls or by introducing a second diffusible fluorophore into the region of tissue interstitium under study. By using an appropriately chosen color for the second population, the spectral overlap in fluorescence is minimized and the effects on the MP-FRAP results will be negligible.

Our results provide assurance to the experimental researcher that if she or he can successfully image the region of interest of the intended measurement, then MP-FRAP can now be relied upon to yield an accurate measurement of the absolute diffusion coefficient within the constrained space. This opens up a wide range of *in vivo* systems within which MP-FRAP can now be confidently applied.

#### IV. CONCLUSION

In this paper, we have used Monte Carlo simulations to model multiphoton fluorescence recovery after photo-bleaching in the presence of reflecting boundaries of various geometries and sizes. Our results show that MP-FRAP can produce erroneous values of the diffusion coefficient even when the boundaries are significantly larger than the focal volume. The size limit at which the boundaries begin affecting the MP-FRAP measurement varies with the geometry of the boundary, with the two extremes being a single plane perpendicular to the optical axis ( $D_{\text{fit}}$  becomes erroneous at  $\sim -0.3\omega_z$ ) and a sphere ( $D_{\text{fit}}$  becomes erroneous at  $3.75\omega_r$ ). The significance of the error is a function of the aspect ratio of the focal volume (i.e., the NA) and the orientation of the barriers, with barriers to diffusion in the radial direction having the greatest effect. Using our guidelines, a researcher can first image a sample using two-photon fluorescence and then measure and locate a region with the appropriate dimensions to allow an accurate measurement of the diffusion coefficient using the appropriate model. For both a single barrier and paired barriers parallel to the optical axis, we present a new model of MP-FRAP that can be used to produce accurate diffusion coefficients for boundary distances much closer than

is possible with the standard MP-FRAP model. Measurements of diffusion via MP-FRAP can now be completed with confidence in an array of *in vivo* systems previously believed to be inaccessible.

#### ACKNOWLEDGMENTS

The authors would like to thank Matthew C. Sullivan for several useful conversations. This work was supported by the Department of Defense Era of Hope Scholar Research Award Program (No. W81XWH-09-1-0405), the NIH Directors New Innovator Award Program (No. 1DP2OD006501-01), and the Pew Scholars Program in the Biomedical Sciences (Edward Brown).

#### APPENDIX

The time-dependent concentration distribution of unbleached fluorophore following the bleach pulse is given by Brown *et al.* [1]. When written in Cartesian coordinates for a concentration distribution centered at the origin, the expression is

$$c(x, y, z; t) = c_o \sum_{n=0}^{\infty} \frac{(-\beta)^n}{n!} \frac{1}{\mu_n(t) v_n(t)^{1/2}} \times \exp\left[-\frac{2bn}{\omega_r^2} \frac{x^2}{\mu_n(t)}\right] \exp\left[-\frac{2bn}{\omega_r^2} \frac{y^2}{\mu_n(t)}\right] \times \exp\left[-\frac{2bn}{\omega_z^2} \frac{z^2}{v_n(t)}\right], \quad (\text{A1})$$

where

$$\mu_n(t) = 1 + 8bnDt/\omega_r^2, \quad (\text{A2})$$

$$v_n(t) = 1 + 8bnDt/\omega_z^2. \quad (\text{A3})$$

For the case of a single infinite plane boundary at the origin we can develop an approximate analytical model by replacing the barrier with the real distribution and an “image” distribution placed symmetrically about the origin at positions  $u$  and  $-u$ , which represent the distance of the real distribution from the barrier (see Fig. 10). In the region to the right of the origin, this closely models the behavior of the system: as the distributions spread due to diffusion, the overlap of the image distribution with the real distribution mimics the behavior of those fluorophores that bounce off the barrier and back into the space to the right of the barrier. With this approximation, there is some overcounting of the initial fluorophore population (hatched region in Fig. 10) when the two distributions are oriented close to the barrier. This “extra” distribution of bleached molecules will evolve over time, producing an error in the fluorescence as a function of time, and hence in the diffusion coefficient,  $D$ . However, this error remains small until the peak of the image distribution approaches the origin. As the two distributions perfectly overlap the error in  $D$  disappears and then grows again as the distribution centers continue past one another.

The combined concentration distribution, assuming a barrier parallel to the optical axis in the  $x$  dimension, is given by

$$c'(x, y, z; t) = (1/2)[c_1(x - u, y, z; t) + c_2(x + u, y, z; t)], \quad (\text{A4})$$

where  $c_1$  and  $c_2$  are produced by introducing a coordinate shift into Eq. (A1), and the  $1/2$  accounts for the fact that we have introduced an image distribution that doubles the true concentration of fluorophore.

The fluorescence recovery is monitored by a low-intensity laser beam centered on the real concentration distribution and is given by

$$F'(t) = \frac{\delta_m E}{2m} \int \langle I_{mo}^m(x-u, y, z) \rangle c'(x, y, z; t) dx dy dz, \quad (\text{A5})$$

where  $\delta_m$  is the multiphoton fluorescence action cross-section,  $E$  is the collection efficiency of the system,  $m$  is the number of photons required to produce fluorescence from a single fluorophore, and  $\langle I_{mo}^m(x-u, y, z) \rangle$  is the time-average of the bleach intensity raised to the  $m$ th power, given by

$$\langle I_{mo}^m(x-u, y, z) \rangle = \langle I_{mo}^m(0, 0, 0) \rangle e^{-(2m/\omega_r^2)(x-u)^2} \times e^{-(2m/\omega_r^2)y^2} e^{-(2m/\omega_z^2)z^2}. \quad (\text{A6})$$

It is important to note that while for the standard model derivation the integral in  $F(t)$  is taken over all space, in the presence of a single barrier the integral along the dimension interrupted by the barrier (in this case  $x$ ) is taken only from  $0 \rightarrow \infty$ .

When Eqs. (A4) and (A6) are substituted into Eq. (A5) and the integral is performed, the simplified expression for the fluorescence recovery, letting  $m = b = 2$ , is

$$\begin{aligned} \frac{F'(t)}{F'_o} &= \frac{1}{2} \frac{1}{\text{erfc}(-2u/\omega_r)} \sum_{n=0}^{\infty} \frac{(-\beta)^n}{n!} \frac{1}{[n + \mu_n(t)]} \frac{1}{[n + \nu_n(t)]^{1/2}} \\ &\times \left\{ \text{erfc} \left[ -2 \left[ 1 + n/\mu_n(t) \right]^{1/2} \frac{u}{\omega_r} \right] \right. \\ &+ \exp \left[ -\frac{16n}{n + \mu_n(t)} \left( \frac{u}{\omega_r} \right)^2 \right] \\ &\left. \times \text{erfc} \left[ -2 \frac{[1 - n/\mu_n(t)]}{[1 + n/\mu_n(t)]^{1/2}} \frac{u}{\omega_r} \right] \right\}, \quad (\text{A7}) \end{aligned}$$

where  $F'_o$  is the equilibrium value of the fluorescence before the photobleaching pulse. We can compare Eq. (A7) with the standard MP-FRAP model [Eq. (6)] to gain some insight into the new form. As noted earlier, the  $1/2$  arises from our introduction of the image distribution. The first complementary error function comes from the calculation of  $F'_o$ , which is evaluated over the limits  $0 \rightarrow \infty$ . The first part of the summation, appearing on the first line, is the standard MP-FRAP equation. Finally, the contribution to the fluorescence recovery is shared between the real concentration distribution, represented by the second complementary error function, and the image concentration distribution, represented by the exponential  $\times$  complementary error function term. In the limit  $u \rightarrow \infty$ ,

$$\frac{F'(t)}{F'_o} = \frac{1}{2} + \frac{1}{2} \sum_{n=0}^{\infty} \frac{(-\beta)^n}{n!} \frac{1}{[n + \mu_n(t)]} \frac{1}{[n + \nu_n(t)]^{1/2}}. \quad (\text{A8})$$

With the image distribution center pushed to negative infinity, the distribution of unbleached molecules in the region of the focal volume (at positive infinity) is at equilibrium and contributes a constant  $1/2$  to the normalized fluorescence.

Meanwhile, the real distribution center translates to infinity with the focal volume and produces a fluorescence recovery with the same form as a standard fluorescence recovery. At full recovery ( $t \rightarrow \infty$ ),  $F'(t)/F'_o = 1$ , as expected.

This derivation can be repeated for a wall perpendicular to the optical axis by introducing the appropriate coordinate shifts in  $z$ , rather than  $x$  or  $y$ . The result has the same form as Eq. (A7), but with  $\omega_r \rightarrow \omega_z$  and  $\mu_n(t) \rightarrow \nu_n(t)$  in the exponential and complementary error functions.

Following similar logic leading to the derivation of the "single boundary" MP-FRAP model, we can also produce an approximate analytical model for use in the presence of two parallel infinite-plane boundaries. In this case, we place the real concentration distribution at the origin and model two boundaries placed symmetrically about the distribution center (at  $u$  and  $-u$ ) with an image distribution on the opposite side of each barrier (at  $-2u$  and  $2u$ ). The concentration distribution for this configuration has three parts,  $c''(x, y, z; t) = (1/3)[c_1(x - 2u, y, z; t) + c_2(x, y, z; t) + c_3(x + 2u, y, z; t)]$ , and the integration to determine the fluorescence is limited to  $-u \rightarrow u$  along the dimension in which the barriers appear. The resulting normalized fluorescence recovery, for boundaries parallel to the optical axis, is given by

$$\begin{aligned} \frac{F''(t)}{F''_o} &= \frac{1}{3} \frac{1}{\text{erf}(2u/\omega_r)} \sum_{n=0}^{\infty} \frac{(-\beta)^n}{n!} \frac{1}{[n + \mu_n(t)]} \frac{1}{[n + \nu_n(t)]^{1/2}} \\ &\times \left\{ \text{erf} \left[ -2 \left[ 1 + n/\mu_n(t) \right]^{1/2} \frac{u}{\omega_r} \right] \right. \\ &+ \exp \left[ -\frac{16n}{n + \mu_n(t)} \left( \frac{u}{\omega_r} \right)^2 \right] \\ &\times \left( \text{erf} \left[ -2 \frac{[1 - n/\mu_n(t)]}{[1 + n/\mu_n(t)]^{1/2}} \frac{u}{\omega_r} \right] \right. \\ &\left. \left. + \text{erf} \left[ -2 \frac{[1 + 3n/\mu_n(t)]}{[1 + n/\mu_n(t)]^{1/2}} \frac{u}{\omega_r} \right] \right) \right\}. \quad (\text{A9}) \end{aligned}$$

Similar to the single boundary formula, the  $1/3$  arises from the introduction of the two image distributions. The first error function comes from the calculation of  $F''_o$ , which is evaluated from  $-u \rightarrow u$ . The standard MP-FRAP model appears again and is weighted by contributions from the real distribution, represented by the second error function, and the image distributions, represented by the two exponential  $\times$  error function terms. In the limit  $u \rightarrow \infty$ ,

$$\frac{F''(t)}{F''_o} = \frac{2}{3} + \frac{1}{3} \sum_{n=0}^{\infty} \frac{(-\beta)^n}{n!} \frac{1}{[n + \mu_n(t)]} \frac{1}{[n + \nu_n(t)]^{1/2}}. \quad (\text{A10})$$

Here, the image distributions contribute a constant  $1/3$  each to the normalized fluorescence, while the real distribution recovers as would a standard MP-FRAP curve. At full recovery ( $t \rightarrow \infty$ ),  $F''(t)/F''_o = 1$ , as expected.

As with the one-boundary model, this derivation can be repeated for walls perpendicular to the optical axis by introducing the appropriate coordinate shifts in  $z$ , rather than  $x$  or  $y$ . The result has the same form as Eq. (A9), but with  $\omega_r \rightarrow \omega_z$  and  $\mu_n(t) \rightarrow \nu_n(t)$  in the exponential and error functions.

- [1] E. B. Brown, E. S. Wu, W. Zipfel, and W. W. Webb, *Biophys. J.* **77**, 2837 (1999).
- [2] W. Denk, J. H. Strickler, and W. W. Webb, *Science* **248**, 73 (1990).
- [3] S. K. Davis and C. J. Bardeen, *Rev. Sci. Instrum.* **73**, 2128 (2002).
- [4] D. Mazza, K. Braeckmans, F. Cella, I. Testa, D. Vercauteren, J. Demeester, S. S. De Smedt, and A. Diaspro, *Biophys. J.* **95**, 3457 (2008).
- [5] D. Axelrod, D. E. Koppel, J. Schlessinger, E. Elson, and W. W. Webb, *Biophys. J.* **16**, 1055 (1976).
- [6] M. Edidin, M. Zagzansky, and T. Lardner, *Science* **191**, 466 (1976).
- [7] D. E. Koppel, D. Axelrod, J. Schlessinger, E. L. Elson, and W. W. Webb, *Biophys. J.* **16**, 1315 (1976).
- [8] U. Kubitschek, P. Wedekind, and R. Peters, *J. Microsc.* **192**, 126 (1998).
- [9] D. A. Berk, F. Yuan, M. Leunig, and R. K. Jain, *Biophys. J.* **65**, 2428 (1993).
- [10] H. Geerts, M. D. Brabander, R. Nuydens, S. Geuens, M. Moeremans, J. D. Mey, and P. Hollenbeck, *Biophys. J.* **52**, 775 (1987).
- [11] H. Qian, M. P. Sheetz, and E. L. Elson, *Biophys. J.* **60**, 910 (1991).
- [12] D. Magde, E. L. Elson, and W. W. Webb, *Biopolymers* **13**, 29 (1974).
- [13] K. M. Berland, P. T. C. So, and E. Gratton, *Biophys. J.* **68**, 694 (1995).
- [14] J. Mertz, C. Xu, and W. W. Webb, *Opt. Lett.* **20**, 2532 (1995).
- [15] W. Watanabe, S. Matsunaga, T. Higashi, K. Fukui, and K. Itoh, *J. Biomed. Opt.* **13**, 031213 (2008).
- [16] R. M. Williams, W. R. Zipfel, M. L. Tinsley, and C. E. Farnum, *Biophys. J.* **93**, 1039 (2007).
- [17] S. Basu, V. Rodionov, M. Terasaki, and P. J. Campagnola, *Opt. Lett.* **30**, 159 (2005).
- [18] K. D. Sullivan, W. H. Sipprell III, E. B. Brown Jr., and E. B. Brown III, *Biophys. J.* **96**, 5082 (2009).
- [19] S. Coscoy, F. Waharte, A. Gautreau, M. Martin, D. Louvard, P. Mangeat, M. Arpin, and F. Amblard, *Proc. Natl. Acad. Sci. USA* **99**, 12813 (2002).
- [20] F. Waharte, C. M. Brown, S. Coscoy, E. Coudrier, and F. Amblard, *Biophys. J.* **88**, 1467 (2005).
- [21] D. S. Grebenkov, *Phys. Rev. E* **76**, 041139 (2007).
- [22] P. S. Burada, P. Hänggi, F. Marchesoni, G. Schmid, and P. Talkner, *Chem. Phys. Chem.* **10**, 45 (2009).
- [23] A. F. Fröhlich, S. N. Jespersen, L. Ostergaard, and V. G. Kiselev, *J. Magn. Reson.* **194**, 128 (2008).
- [24] N. Krepyshcheva, L. Di Pietro, and M. C. Neel, *Phys. Rev. E* **73**, 021104 (2006).
- [25] P. Szymczak and A. J. C. Ladd, *Phys. Rev. E* **68**, 036704 (2003).
- [26] V. I. Yudson and P. Reineker, *Phys. Rev. E* **64**, 031108 (2001).
- [27] C. Ribrault, A. Triller, and K. Sekimoto, *Phys. Rev. E* **75**, 021112 (2007).
- [28] A. Gennerich and D. Schild, *Biophys. J.* **79**, 3294 (2000).
- [29] A. Gennerich and D. Schild, *Biophys. J.* **83**, 510 (2002).
- [30] M. Foquet, J. Kurlach, W. R. Zipfel, W. W. Webb, and H. G. Craighead, *Anal. Chem.* **76**, 1618 (2004).
- [31] E. Etienne, P.-F. Lenne, J. N. Sturgis, and H. Rigneault, *Appl. Opt.* **45**, 4497 (2006).
- [32] I. von der Hocht and J. Enderlein, *Exp. Mol. Pathol.* **82**, 142 (2007).
- [33] M. J. Saxton, *Biophys. J.* **69**, 389 (1995).
- [34] S. M. Görisch, M. Wachsmuth, C. Ittrich, C. P. Bacher, K. Rippe, and P. Lichter, *Proc. Natl. Acad. Sci. USA* **101**, 13221 (2004).
- [35] I. F. Sbalzarini, A. Mezzacasa, A. Helenius, and P. Koumoutsakos, *Biophys. J.* **89**, 1482 (2005).
- [36] D. M. Soumpasis, *Biophys. J.* **41**, 95 (1983).
- [37] F. P. Coelho, W. L. Vaz, and E. Melo, *Biophys. J.* **72**, 1501 (1997).
- [38] M. J. Saxton, *Biophys. J.* **81**, 2226 (2001).
- [39] E. Brown and W. Webb, in *Caged Compounds*, edited by Gerard Marriott, *Methods in Enzymology* Vol. 291 (Academic Press, San Diego, 1998), pp. 356–380.
- [40] P. K. Tsourkas, M. L. Longo, and S. Raychaudhuri, *Biophys. J.* **95**, 1118 (2008).
- [41] S. Wieser, M. Axmann, and G. J. Schütz, *Biophys. J.* **95**, 5988 (2008).
- [42] G. Alexandrakis, E. B. Brown, R. T. Tong, T. D. McKee, R. B. Campbell, Y. Boucher, and R. K. Jain, *Nat. Med.* **10**, 203 (2004).
- [43] D. K. Binder, M. C. Papadopoulos, P. M. Haggie, and A. S. Verkman, *J. Neurosci.* **24**, 8049 (2004).
- [44] M. C. Papadopoulos, J. K. Kim, and A. S. Verkman, *Biophys. J.* **89**, 3660 (2005).
- [45] M. Gabso, E. Neher, and M. E. Spira, *Neuron* **18**, 473 (1997).
- [46] H. Schmidt, O. Arendt, E. B. Brown, B. Schwaller, and J. Eilers, *J. Neurochem.* **100**, 727 (2007).
- [47] K. Svoboda, D. W. Tank, and W. Denk, *Science* **272**, 716 (1996).
- [48] A. Majewska, E. Brown, J. Ross, and R. Yuste, *J. Neurosci.* **20**, 1722 (2000).
- [49] K. Holthoff, D. Tsay, and R. Yuste, *Neuron* **33**, 425 (2002).
- [50] T. J. Feder, I. Brust-Mascher, J. P. Slattery, B. Baird, and W. W. Webb, *Biophys. J.* **70**, 2767 (1996).
- [51] W. R. Zipfel, R. M. Williams, and W. W. Webb, *Nat. Biotechnol.* **21**, 1369 (2003).
- [52] M. Crivaro, H. Enjieu-Kadji, R. Hatanaka, S. Nakauchi, J. Bosch, J. Judin, J. Riera, and R. Kawashima, *J. Microsc.* (2010), doi: 10.1111/j.1365-2818.2010.03473.x



Published in final edited form as:

*Biotechnol Bioeng.* 2013 May ; 110(5): 1476–1486. doi:10.1002/bit.24799.

## Engineering Superficial Zone Features in Tissue Engineered Cartilage

Tony Chen<sup>1,2</sup>, Matthew J. Hilton<sup>2</sup>, Edward B. Brown<sup>1</sup>, Michael J. Zuscik<sup>2</sup>, and Hani A. Awad<sup>1,2</sup>

<sup>1</sup>Department of Biomedical Engineering, University of Rochester, Rochester, NY

<sup>2</sup>The Center for Musculoskeletal Research, University of Rochester Medical Center, Rochester, NY

### Abstract

A major challenge in cartilage tissue engineering is the need to recreate the native tissue's anisotropic extracellular matrix structure. This anisotropy has important mechanical and biological consequences and could be crucial for integrative repair. Here we report that hydrodynamic conditions that mimic the motion-induced flow fields in between the articular surfaces in the synovial joint induce the formation of a distinct superficial layer in tissue engineered cartilage hydrogels, with enhanced production of cartilage matrix proteoglycan and type II collagen. Moreover, the flow stimulation at the surface induces the production of the surface zone protein Proteoglycan 4 (aka PRG4 or lubricin). Analysis of second harmonic generation signature of collagen in this superficial layer reveals a highly aligned fibrillar matrix that resembles the alignment pattern in native tissue's surface zone, suggesting that mimicking synovial fluid flow at the cartilage surface in hydrodynamic bioreactors could be key to creating engineered cartilage with superficial zone features.

### Keywords

Tissue Engineering; Bioreactors; Cartilage; Chondrocyte; Interstitial flow; Shear Stress; Two Photon Microscopy

## INTRODUCTION

Articular cartilage, the soft tissue that lines the ends of articulating bones in diarthrodial joints, has unique composition and structure features that enable it to facilitate nearly frictionless motion, while supporting loads that exceed the body weight, many times over, for millions of cycles throughout life. The remarkable resilience of articular cartilage is attributed to its biphasic composition and anisotropic extracellular matrix (ECM) structure (Mow and Wang 1999), which give rise to spatially heterogeneous *in vivo* biomechanics and differentially affect the metabolism of the chondrocytes – a paradigm known as mechanobiology (Wong and Carter 2003). When injured, articular cartilage lacks the intrinsic repair capacity of vascularized tissues such as bone, and even with the current surgical repair options, it generally heals with an inferior fibrocartilage scar tissue. This outcome feeds a cycle of injury-degeneration that leads to accelerated osteoarthritis (OA) later in life due to altered joint mechanics (Guilak et al. 2001). OA is the most prevalent

---

**Corresponding Author** Hani A. Awad, PhD Department of Biomedical Engineering The Center for Musculoskeletal Research University of Rochester Medical Center– Box 665 601 Elmwood Avenue, Rochester, NY 14642 (585) 273-5268 (V) | (585) 276-2177 (F) hani\_awad@urmc.rochester.edu.

disease in the US, equal in numbers to the next top 4 disorders combined (heart, pulmonary, mental health and diabetic conditions) (CDC 2009), which is projected to affect >67M people in the US by 2020 (Hootman and Helmick 2006). Given that there are no treatment strategies for OA that can rejuvenate the articular cartilage, regenerative medicine approaches such as tissue engineering offer important strategies to repair focal cartilage defects and preempt OA.

Cartilage tissue engineering typically involves seeding a scaffold or hydrogel with chondrocytes or stem cells and cultivating the resulting construct in bioreactors. Some bioreactors are designed to enhance interstitial nutrient transport through direct perfusion (Sittinger et al. 1994) or enhanced mixing (Vunjak-Novakovic et al. 1999). Other bioreactors are designed to mimic *in vivo* biomechanics to stimulate the constructs using compressive deformations (Buschmann et al. 1995; Mauck et al. 2000) or sliding articular motion (Wimmer et al. 2004). While these bioreactors typically yield constructs with enhanced ECM composition and improved biomechanical properties over time, they generally do not regenerate the zonal anisotropy in the collagen framework that characterizes native cartilage. Failure to restore the structural anisotropy of collagen in engineered cartilage has been cited as a contributing factor to the oft-reported failure of integrative repair (Khan et al. 2008).

Articular cartilage has been classically described as a stratified tissue with three successive “zones” based on ECM structural and compositional features (Figure 1) (Jeffery et al. 1991; Mow and Wang 1999). Of particular interest to this investigation, the densely-packed collagen fibers in the *surface zone* of cartilage are oriented parallel to the articular surface in a prestressed state (Clark 1990; Mow and Lai 1974), effectively forming a permeability barrier to regulate fluid efflux and the tissue's swelling behavior under loading, providing the tissue with the resilience to resist tensile and shear stresses during articular motion, and contributing to the production of the surface zone protein Proteoglycan 4 (PRG4), which facilitates the nearly frictionless articular motion (Klein et al. 2006). The significance of the dynamic interactions between the synovial fluid (SF) and the surface zone of cartilage during sliding articulation has long been recognized in squeeze film joint lubrication (Hou et al. 1989) and in hydrodynamic instabilities that could lead to chondrodegeneration (Mow et al. 1974). However, the metabolic effects of these interactions and their implications for cartilage tissue engineering have to date been understated.

During articular motion, the sliding of the mating cartilages and the pressure gradients they induce within the joint compartment drive SF flow over the surfaces of cartilage (McCarty et al. 2011). The solutions for the simplified problems of Poiseuille and Couette viscous flow over a biphasic cartilage layer, which represent simplified approximations of the kinematic conditions in the articulating joint, have been formulated by applying the appropriate pseudo-slip and kinematic boundary conditions at the SF-cartilage interface, and predict the induction of interstitial flow within a thin boundary region in the surface layer of cartilage (Hou et al. 1989). These interstitial flow fields likely affect collagen metabolism and alignment, as has been observed in fibroblast-seeded collagen matrices (Ng et al. 2005), and cultured chondrocytes in perfusion and parallel plate bioreactors (Gemmiti and Guldberg 2009; Pazzano et al. 2000).

We have recently experimentally quantified the interstitial flow fields in a boundary layer near the surface of engineered cartilage hydrogel under Poiseuille flow (Chen et al. 2012), which simulates SF-cartilage interactions during articulation. These flow fields are mostly unidirectional, parallel to the surface of hydrogel. We also observed that in addition to the hydrodynamic effects, this interstitial flow enhances convective mass transport in this boundary layer, and ECM production near the surface (Chen et al. 2012). Therefore, we

hypothesized that the induced interstitial flow boundary region has important mechanobiologic implications for engineering the anisotropy of the surface zone in tissue-engineered cartilage.

To test our hypothesis, we designed a modular multi-chamber bioreactor system to cultivate chondrocyte-seeded agarose (hereafter tissue engineered cartilage or TEC) hydrogels in a stirred-tank bioreactor under simulated Couette flow conditions (Fig. 2). The hydrodynamic flow conditions were generated by periodic rotation of the multi-chamber system holding the TEC hydrogels within the culture media in the stirred tank. Since it has been reported that hypoxia enhances chondrogenesis (Wang et al. 2005), the TEC hydrogels were cultured in 5% oxygen conditions either under surface flow conditions in the bioreactor or under control no flow conditions in a hypoxia chamber for 14 days. The TEC hydrogels were then evaluated using histology, immunohistochemistry (IHC), in situ hybridization (ISH), proteoglycan (PG) biochemistry, and collagen organization using 2-photon second harmonic generation (SHG).

## METHODS

### Bioreactor Design and Operation

A modular multi-chamber bioreactor system was custom designed to hold 4 TEC hydrogels and cultivate them in a stirred tank under simulated flow conditions (Fig 2). The multi-chamber bioreactor features 4 compartments with rectangular wells into which the TEC hydrogels are cast, and 4 channels over the TEC hydrogel wells. The assembled bioreactor compartments with the TEC hydrogels are mounted onto the agitator shaft of a Bioflo 110® stirred tank bioreactor (New Brunswick Scientific, Edison, NJ). Chondrocyte-seeded TEC hydrogels were cultivated in the stirred tank for 2 weeks in hypoxic conditions (5% O<sub>2</sub>) under simulated flow conditions generated by motorized rotation of the modular bioreactor/agitator assembly in culture media. This results in hydrodynamic conditions in the flow channels that simulate Couette flow.

### TEC Hydrogel Preparation and Cultivation

All reagents were purchased from Invitrogen (Carlsbad, CA) unless otherwise noted. Chondrocytes were aseptically isolated from the elbow joints of pigs within 24 hours after slaughter as previously described (Chen et al. 2012). Briefly, cartilage bits from the joint were minced and enzymatically digested using pronase (CalBioChem, San Diego CA) for 1.5 hours followed by type-2 collagenase (Worthington Biochemical, Lakewood NJ) for 16 hours. The digested tissue suspension was then strained through a 40µm cell strainer and the retrieved cells were suspended in complete media (DMEM/F-12, 10% FBS, 1% P/S) supplemented with 10 ng/mL rhTGF-β1 (R&D Systems, Minneapolis MN) and mixed with molten (~40 °C) type VII agarose (Sigma-Aldrich) solution in PBS to create a 40×10<sup>6</sup> cells/mL in 2% agarose solution. The chondrocyte/agarose solution was cast in the rectangular wells of the 4 sliding bioreactor compartments and allowed to polymerize at room temperature for 20 minutes to form the TEC hydrogel, after which it was anchored posteriorly by a cell-free agarose layer. The modular compartments of the system were then assembled and mounted on the agitator shaft of the Bioflo 110® stirred tank. These TEC hydrogels were cultured in complete media supplemented with ascorbic acid and maintained at 37 °C, 5% O<sub>2</sub> and 7.4 pH. To simulate Couette flow at the surface of the TEC hydrogels, the bioreactor system mounted on the agitator shaft was rotated periodically in a half-square wave (0–25 rpm, 1 minute on followed by 1 minute off) for 40 minutes, followed by steady rotational speed of 25 rpm for the remainder of the day. Due to the non-circular geometry of the bioreactor compartments, computational fluid dynamics (CFD) simulation predicted that the start of rotation from rest effectively results in oscillatory shear stress (~2 Hz) on the

surface of the TEC hydrogel, which was dampened as the rotation reached steady state within 1 minute (data not shown). Therefore, this regimen was used to simulate periods of loading and unloading during a moderate (*e.g.* walking at 1 to 2 Hz) activity, which has been shown in the literature to provide anabolic mechanical signals to chondrocytes in tissue engineered constructs (Mauck et al. 2000). Based on the dimensions of the bioreactor, this regimen effectively induced a range of nominal shear stresses of 0–0.12 Pa at the surface of the TEC hydrogel. This rotational regimen was repeated daily for 14 days. Alternatively, control TEC hydrogels in identical bioreactor wells were placed in a hypoxia chamber (Billups-Rothensberg, Del Mar, CA) maintained at 5% O<sub>2</sub>, 5% CO<sub>2</sub>, and 37 °C, and cultured for 14 days without simulated flow. After the 14 day culture period, the hydrogels were retrieved and cylindrical disks were sampled and either placed in 10% Neutral Buffered Formalin (NBF) for histology, ISH, and IHC processing, or frozen for biochemical analysis.

### Histology and Immunohistochemistry

Samples were fixed in 10% NBF at room temperature for 24 hours. Samples were then removed from the NBF and dehydrated under vacuum through graded alcohol steps (30, 50, 70, 80, 95 and 100% ethanol) for one hour each, followed by two fifteen minute washes in Xylenes (Sigma-Aldrich, St. Louis MO). Samples were then infiltrated with 2 changes of paraffin at 60 °C for 2 hours each under vacuum before embedding. After samples were embedded in paraffin, 5 µm sections were cut and stained with Toluidine Blue and Picrosirius Red, or processed for immunohistochemistry. Briefly, sections were quenched of endogenous peroxidases using DAKO Dual Enzyme Block (DAKO, Glostrup Denmark). Antigen retrieval was performed using 4 mg/mL pepsin in 0.01 N HCl at 37 °C for 30 minutes. Sections were then blocked for an hour with 2% solution of Normal Rabbit Serum (Vector Laboratories, Burlingame CA) followed by a 1:100 dilution of mouse anti-Collagen II (II-II6B3; Developmental Studies Hybridoma Bank, Iowa City, IA) or a mouse monoclonal anti-Collagen I (Cat #: ab90395; Abcam, Cambridge MA), in Normal Rabbit Serum. Biotinylated horse anti-mouse secondary antibody (Vector Laboratories) was then added for 30 minutes followed by addition of Pierce High Sensitivity Streptavidin-HRP (Thermo Fisher Scientific Inc, Rockford IL) for 20 minutes. Romulin AEC (Invitrogen) was used to detect the labeled antigens. Lubricin immunofluorescence (green) staining was performed using a goat polyclonal antibody (Cat #: sc-50078; Santa Cruz Biotechnology, Inc., Santa Cruz CA). A FITC-conjugated anti-goat secondary was added for 30 minutes and then counterstained with DAPI (blue) for cell nuclei.

### In Situ Hybridization

ISH assays were generally performed as previously described (Hilton et al. 2005), using <sup>35</sup>S-labeled riboprobes. Briefly, tissue sections were de-paraffinized in xylene, rehydrated through an alcohol gradient, postfixed in 4% paraformaldehyde, and rinsed in PBS. Sections were then treated with 10 µg/ml Proteinase K, 0.2 M HCl, and 0.1 M triethanolamine with acetic anhydride for 10 min each followed by PBS rinses. Sections were dehydrated in 100% alcohol and hybridized overnight with the appropriate antisense riboprobe at 55 °C. Riboprobes were generated from cDNA clones for *Agc1* and *Col2a1* available from Open Biosystems, Inc. Unbound riboprobes were removed from the tissue sections using a series of 2X and 0.2X SSC washes and dehydrated in alcohol before exposing the slides to Kodak NTB radiographic emulsion. Finally, the slides were developed using Kodak developer and fixer, counterstained with 0.5% Toluidine Blue, and imaged in both bright-field and dark-field using an Axioskop 40 microscope (Zeiss), a SPOT RT3 digital camera, and compatible software. Composite bright-field/dark-field images were constructed using Adobe Photoshop.

## Biochemical Analysis

Samples were digested using 0.5 Units/mL of papain (Sigma-Aldrich) with 2 mM L-cysteine (Sigma-Aldrich) and 2 mM ethylenediaminetetraacetic acid (EDTA; Sigma-Aldrich) for 16 hours. The dissolved specimens were stored frozen at  $-80^{\circ}\text{C}$  until assayed using 1,9-dimethylmethylene blue (DMMB) and Quant-iT™ PicoGreen assays for sulfated-glycosaminoglycan (s-GAG) and double-stranded DNA content, respectively, as previously described (Awad et al. 2004).

## Second Harmonic Generation (SHG) Two-Photon Microscopy

Five microns thick paraffin histological sections were baked, deparaffinized in xylene and rehydrated through graded alcohols. The sections were then dehydrated and coverslipped. The sections were imaged using two-photon microscopy as previously described (Brown et al. 2003) at 810 nm excitation wavelength with a 20x/0.95NA objective and images were captured using identical imaging settings (laser power, photomultiplier tube voltage, etc.).

## Fiber Alignment Algorithm

Alignment of collagen fibers was determined using a custom written Matlab (The Mathworks Inc, Natick MA) program based on a previously established algorithm (Chaudhuri et al. 1987). Regions of interest in the superficial layers of native porcine cartilage and TEC hydrogels ( $512 \times 512$  pixel) polarized light microscopy or SHG images were cropped. The cropped image was padded with the mean grayscale value of the image. A modified Blackman-Harris window was used to soften the edges of the padded image. The 2-D Fast Fourier Transform (FFT) of the processed images was applied. A cosine sector filter was used to isolate  $15^{\circ}$  bands of the FFT. The pixel intensity of the  $15^{\circ}$  band was then summed as a representation of the collagen fiber frequency within this orientation band, and the cosine sector process was repeated up to  $180^{\circ}$  in  $15^{\circ}$  increments or bands. A rose plot histogram of collagen fiber orientation was constructed and normalized to the angle band with the maximum frequency.

## RESULTS

### Hydrodynamic Bioreactor Culture Induces Heterogeneous Collagen ECM

We examined the effects of the hydrodynamic bioreactor stimulation on collagen metabolism and organization. *Col2a1* mRNA expression, assessed by ISH, was spatially uniform throughout the control TEC hydrogels (Fig. 3a), whereas the expression in the bioreactor-cultivated constructs was significantly increased at the surface (Fig. 3b). Consistent with these observations, IHC staining for type II collagen demonstrated the formation of a fibrous superficial layer in the bioreactor-cultivated constructs (Fig. 3d). These distinct features were lacking in the controls, in which no evidence of a mature, fibrous ECM formation could be observed (Fig. 3c). We also examined the distribution of type I collagen in our constructs. IHC staining against type I collagen was mostly negative in the ECM, except for faint and punctate intracellular staining, regardless of whether the constructs were grown in control conditions or in the bioreactor (Fig. 3e and f).

The degree of collagen alignment was then assessed by imaging the constructs using multiphoton laser-scanning microscopy (MPLSM) and analyzing the SHG phenomenon, which is caused primarily by collagen in connective tissues and tumors (Han et al. 2008b). SHG is sensitive to the structural characteristics of the collagen fibers, including their thickness and alignment. In control constructs, SHG indicates that fibrillar collagen is primarily found in a pericellular halo in the region typically described as the pericellular matrix (PCM) around the chondrocytes (Fig. 3g). In addition to the SHG signal in the PCM, the bioreactor-cultivated TEC hydrogels also showed a unique, robust SHG signal and a

higher order organization in the dense superficial layer stimulated by flow (Fig. 2*h*) that was not observed in control constructs. The distribution of collagen fiber orientations in the superficial layer of the TEC hydrogels were determined in MATLAB using a Fast-Fourier Transform (FFT)-based algorithm, and plotted as rose plot histograms. Wherein the control TEC hydrogels showed no preferred orientation or parallelism (Fig. 3*i*), the bioreactor-cultivated TEC hydrogels showed a higher degree of parallelism with preferred orientations within  $0\pm 30$  degrees bands (Fig. 3*j*), with remarkable qualitative resemblance to the orientation distribution and parallelism in the superficial zone of native cartilage tissue (Fig. 3*k*).

### Hydrodynamic Bioreactor Culture Induces Heterogeneous Proteoglycan Production

Since PG represents the second major constituent of the solid ECM in cartilage, we also assessed the expression of aggrecan and the content and spatial distribution of sulfated glycosaminoglycans (GAG). Quantitatively, the GAG content in the bioreactor-cultivated hydrogels was significantly increased ( $p < 0.05$ ) compared to the control hydrogels (Fig. 4*a*). As demonstrated by ISH, aggrecan (*Agc1*) mRNA was uniformly expressed by the chondrocytes throughout the depth of the TEC hydrogels cultured under control conditions (Fig. 4*b*). In contrast, the bioreactor-cultivated TEC hydrogels showed increased expression of *Agc* in the surface layer (Fig. 4*c*). Consistent with these observations, PG accumulation in the ECM of the control TEC hydrogels was diffuse but uniformly distributed, with more intense accumulation in the PCM region, as indicated by Toluidine Blue staining (Fig. 4*d*). In addition to these features, the bioreactor-cultivated TEC hydrogels exhibited a unique structurally mature superficial layer with dense accumulation of PGs (Fig. 4*e*) that was lacking in control constructs. Whereas the cells throughout the control TEC hydrogels had rounded morphology (Fig. 4*d*) as typically observed in these hydrogels (Mauck et al. 2000), the cells in the superficial layer in the bioreactor-cultivated TEC hydrogels were more flattened and aligned (Fig. 4*e*), resembling superficial zone chondrocytes in native articular cartilage (Klein et al. 2006).

### Hydrodynamic Bioreactor Culture Induces Surface Zone Protein PRG4

Since proteoglycan 4 (PRG4) is a component of synovial fluid secreted by superficial zone chondrocytes and synoviocytes, and contributes to lubricating the mating cartilage surfaces in the joint (Jones et al. 2009), we performed IHC probing for PRG4 synthesis in our TEC hydrogels. Consistent with published observations on the role of surface shear in stimulating *Prg4* gene expression (Wimmer et al. 2004), we found a significant upregulation of PRG4 in our bioreactor-cultivated TEC hydrogels (Fig. 4*g*), compared to control constructs (Fig. 4*f*).

## DISCUSSION

Several bioreactor systems have been developed to optimize growth of tissue engineered cartilage subject to hydrodynamic conditions, including bioreactors utilizing continuous perfusion of the culture medium (Bujia et al. 1995; Neves et al. 2002; Raimondi et al. 2006; Sittinger et al. 1994), hydrodynamic shear and continuous mixing in spinner flasks (Bueno et al. 2009; Gooch et al. 2001; Vunjak-Novakovic et al. 1999), and concentric rotating cylinders (Saini and Wick 2003; Williams et al. 2002). In addition, dynamic compressive deformations that mimic in vivo joint loads in tissue engineering bioreactors (Buschmann et al. 1995; Mauck et al. 2000) have been shown to stimulate the biosynthetic activity of chondrocytes or stem cells and improve the biochemical composition and biomechanical properties of TEC constructs (e.g. agarose hydrogels) over time (Hung et al. 2004). In the latter, the observed enhancement in PG biosynthetic activity on the periphery of the constructs in unconfined compressive loading has been correlated with increased interstitial fluid flow, rather than hydrostatic pressure or compressive strains in these peripheral

regions, suggesting an important mechanotransduction role for interstitial fluid flow (Buschmann et al. 1995; Buschmann et al. 1999). Despite improvements in the growth characteristics of engineered cartilage constructs, these bioreactor systems typically have not yielded engineered tissue with stratified structural organization or mechanical properties similar to native cartilage. As such, the provision of a physiologically relevant hydrodynamic environment and the associated interstitial flow fields might be required for stimulating distinct compositional and structural features in the superficial region of engineered cartilage.

The hydrodynamic bioreactor system we used in this study was designed to simulate aspects of SF-cartilage interfacial fluid flow during *in vivo* joint articulation. Squeeze or thin-film lubrication is a primary mode of lubrication that facilitates the nearly frictionless articulation of cartilage in synovial joints. In this mode of lubrication, which involves cartilage-SF-cartilage relative motion (Hou et al. 1992), SF cannot instantaneously be squeezed out from the gap as the bearing surfaces approach each other. A pressure is therefore built up as a result of the viscous resistance generated by SF as it is being slowly squeezed from the gap. The pressure field in the fluid film can support large loads for short periods of 1 or 2 seconds before the film is depleted. With articular motion, pressure gradients force SF flow in the thin film between the articulating cartilage layers. This tribology problem of flow of SF over a biphasic cartilage layer has been described by Hou and Mow (1989) (Hou et al. 1989) and approximated to the classical problems of Poiseuille and Couette flow over a hydrated porous solid (Beavers and Joseph 1967). Inspired by this approximation, we have previously conceptualized a bioreactor chamber in which Poiseuille flow can be introduced to stimulate TEC hydrogels (Chen et al. 2012). We demonstrated through direct experimental measurements that this hydrodynamic stimulation induces interstitial fluid flow gradients within a boundary region near the TEC hydrogel surface. We also observed that PG and type II collagen synthesis is enhanced in that superficial region in association with enhanced convective mass transport (Chen et al. 2012). However, while these results were promising, the TEC hydrogels lacked many features of native articular cartilage. Thus, we undertook to evaluate the effects of hydrodynamic stimulation in the rotating bioreactor system on the evolution of surface zone features in TEC hydrogels. The bioreactor-cultivated hydrogels were subjected to simulated surface flow conditions generating nominal shear stress range of 0–0.12 Pa at the surface of the TEC hydrogel, which was selected based on previous reports (Gemmiti and Guldborg 2009) demonstrating anabolic effects in engineered cartilage under surface flow stimulation in this range of shear stress. While not directly measured in our current system, we believe that the simulated Couette flow in the rotating bioreactor induces interstitial flow and convective transport fields in the TEC hydrogels similar to those measured experimentally (Chen et al. 2012), which could explain the experimentally observed heterogeneity in composition of the ECM, qualitatively manifested by increased gene expression and ECM accumulation of PG and type II collagen, respectively, in the superficial layer. Future studies should attempt to quantify the PG and type II collagen accumulation in the superficial layer and correlate their levels with surface shear stress and convective transport changes. However, it was noted that *Col2a1* expression was suppressed in the region immediately beneath the newly formed superficial layer. The mechanism of this suppression is not clear but one explanation might be that the *de novo* accumulated ECM in the superficial layer might create a transport barrier that was not predicted in our experimental or computational analysis of the day 0 TEC hydrogels (Chen et al. 2012). Modulating the hydrodynamic conditions at the surface to account for permeability and transport barrier changes might be necessary to overcome this limitation. This warrants further examination in future studies.

Previous reports examining the growth of TEC constructs in concentric wall (Saini and Wick 2003) and wavy wall (Bueno et al. 2005) mixed bioreactors have demonstrated the

formation of a fibrous type I collagen capsule on the periphery of engineered cartilage disks. However, our control and bioreactor culture conditions resulted in constructs that were mostly devoid of type I collagen. Indeed, the gene expression and IHC staining data suggest that the fibrillar ECM in the superficial region of our bioreactor-cultivated TEC hydrogels is predominantly comprised of type II collagen, the phenotypic collagen in healthy, native articular cartilage. Furthermore, the enhanced collagen alignment of this distinct superficial layer bears qualitative resemblance to the surface zone of articular cartilage. While we cannot definitively explain the differences in these results, one possibility might be related to the high oxygen (hyperoxia or 21% O<sub>2</sub>) concentration used in these previous studies. Since it has been reported that hypoxia enhances chondrogenesis (Markway et al. 2010; Wang et al. 2005), our TEC hydrogels were cultured in 5% O<sub>2</sub> conditions either under surface flow conditions in the bioreactor or under control no flow conditions in a hypoxia chamber. Indeed, previous studies demonstrate that hypoxia and hypoxia-inducible factor 1- $\alpha$  (HIF-1 $\alpha$ ) not only enhance gene expression of type II collagen and aggrecan, but also downregulate the gene expression of types I and III collagen (Duval et al. 2009). Interestingly, oxygen transport through tissue-engineered cartilage in a parallel plate (Poiseuille) flow bioreactor has been modeled, and while demonstrating higher tissue oxygenation with bioreactor flow compared to controls, the model also suggested that the flow induces a time- and depth-dependent gradients in oxygen concentration in the engineered cartilage (Pierre et al. 2008). By extrapolating these model results to our system, one can assume that the surface region of our TEC hydrogels was maintained at the hypoxic 5% O<sub>2</sub> concentration, whereas the deeper regions might be at significantly more hypoxic conditions (<<5%), although this has yet to be mathematically or experimentally determined. The hydrodynamic conditions at the surface of the TEC hydrogels could also differentially affect the ECM at the surface of the TEC constructs. For example, it has been demonstrated through computational fluid dynamics (CFD) modeling that turbulent eddies at the surfaces of TEC disk in concentric wall bioreactors create high shear stress states that could contribute to the formation of the observed fibrous capsule (Williams et al. 2002). Future work will attempt to use CFD and multiphysics models to map the interstitial flow fields and quantify the hydrodynamic (shear stress) and transport effects in our experimental bioreactor. Furthermore, it is possible that the biomaterial used in engineered cartilage constructs could modulate the ECM produced by the cells. Indeed, while previous studies utilizing poly-lactic acid (PLA) or poly-glycolic acid (PGA) scaffolds reported the formation of a fibrous type I collagen capsule, we didn't observe this phenomenon in our agarose TEC hydrogels. It is tempting to hypothesize that the acidic environment resulting from the degradation of the PLA and PGA scaffolds might have contributed to the formation of the collagenous capsule. While it has been reported that collagen synthesis and cell viability of chondrocytes in agarose hydrogels is not pH-dependent within a pH range of 7.3 to 6.6 (Wu et al. 2007), it is still possible that lower, more acidic pH microenvironments might be detrimental to collagen synthesis or perhaps more catalytic to the activity of MMP3, a cartilage acid metalloprotease (Wilhelm et al. 1993), which could affect the collagen ECM indirectly.

Our results also suggest that hydrodynamic stimulation of the TEC hydrogels enhanced PG synthesis, and induced a gradient in the PG distribution within the newly formed ECM. Interestingly, the dense accumulation of PGs in the superficial layer of the TEC hydrogel appears to be at odds with PG distribution within native adult tissue (Fig. 1a), in which the PGs are most abundant in the middle zone and least abundant in the surface zone (Ratcliffe et al. 1984). This is likely due to the lack of compressive and shears forces in our system, since it has been suggested that regions of cartilage that experience intermittent compressive *and* shear stresses in the joint are characterized by a highly parallel collagen network and relatively low proteoglycan content as a consequence of the loading pattern (Hytinen et al. 2009). It has also been shown that the combination of sliding (shear) and compressive

motion upregulates PRG4, which is a multidomain glycoprotein (also known as lubricin) product of the *Prg4* gene (Jones et al. 2009), in chondrocyte-seeded engineered scaffolds (Wimmer et al. 2004). Consistent with published observations on the role of surface shear in stimulating *Prg4* gene expression (Wimmer et al. 2004), we found a significant increase of PRG4 in our bioreactor-cultivated TEC hydrogels (Fig. 4g), compared to control constructs (Fig. 4f). This observation has important ramifications for engineering cartilage constructs with lubricious properties (Blewis et al. 2010). Surprisingly, the hydrodynamic stimulation-induced secretion of PRG4 was not restricted to the superficial layer, but was observed deeper within the TEC hydrogels. It is possible that paracrine signals from the superficial chondrocytes subjected to hydrodynamic stimulation might become available to deeper chondrocytes along transport gradients. This possibility remains to be verified. However, it is important to note that while PRG4 in native tissue is thought to be produced by the phenotypically distinct surface chondrocytes, it has been shown that chondrocytes harvested from middle/deep regions of cartilage secrete PRG4 in monolayer or in alginate hydrogels, albeit at significantly reduced levels compared to surface zone chondrocytes (Klein et al. 2006).

One limitation of this study is that we did not evaluate the effects of the hydrodynamic culture conditions, and the resulting heterogeneity in the collagen ECM on the biomechanical properties of the TEC hydrogels. It has been shown that similar hydrodynamic stimulation regimen in parallel plate bioreactors results in significant enhancements in the tensile properties of engineered cartilage (Gemmiti and Guldberg 2006; Gemmiti and Guldberg 2009). However, it has also been long understood that collagen interacts with other ECM molecules including PG and thus plays multiple roles in determining the shear and swelling properties of articular cartilage (Mow and Wang 1999), as well as the compressive biomechanical properties. Future studies will examine the effects of bioreactor cultivation on the biomechanical properties of the TEC hydrogels.

One of the major limitations of the current work is that the bioreactor-cultivated TEC hydrogels lacked other important features of articular cartilage, including the characteristic middle and deep zone architecture. This suggests that the biomimetic surface flow in our bioreactor is not sufficient to recapitulate the stratified zonal architecture of the native tissue. Other methods of creating stratified tissue have been reported, including exploiting the differential behavior of zonal chondrocytes to create anatomically-shaped, scaffold-free constructs with stratified layers for cartilage engineering applications (Han et al. 2008a), and the use of pre-aligned, mesenchymal stem cell-seeded electrospun fibers (Wise et al. 2009). These studies suggest that predisposing cells to a preferred alignment and morphology, perhaps even by a mechanical stimulus such as interstitial fluid flow, may provide necessary cues to create differential tissue alignment and anisotropy. We believe that our approach, perhaps in combination with other loading regimens and/or prealigned scaffold fabrication techniques, could lead to transformative advances in cartilage tissue engineering and merits future studies of efficacy in cartilage repair *in vivo*.

## CONCLUSIONS

In conclusion, the hydrodynamic bioreactor culture that we have described enables the formation of TEC hydrogels with surface zone features. The *in vitro* results show that hydrodynamic stimulation of the surface of the TEC constructs with fluid flow enhances the metabolism of type II collagen and proteoglycans, including aggrecan and PRG4, and induces a distinct superficial layer with enhanced collagen alignment. This study emphasizes the importance of mimicking the flow conditions at SF-cartilage interface in providing appropriate mechanical signals and nutritious gradients to induce surface zone features in

engineered cartilage hydrogels. These results represent an exciting first step towards the creation of stratified engineered cartilage constructs.

## Acknowledgments

The Authors have no conflict of interest to report. The Authors would like to thank Ryan Tierney and Anat Kohn for their excellent technical assistance with histology and ISH, respectively. The Authors would like to acknowledge funding from grants from Whitaker Foundation, the Empire State Stem Cell Board (NYSTEM N08G-019 for HA), the DoD BCRP (W81XWH-09-1-0405 for EB) and the NIH (R01 AR056696 for HA, DP2 OD006501 for EB, R01 AR057022 for MH, and P30 AR061307 for HA and MH).

## REFERENCES

- Awad HA, Wickham MQ, Leddy HA, Gimble JM, Guilak F. Chondrogenic differentiation of adipose-derived adult stem cells in agarose, alginate, and gelatin scaffolds. *Biomaterials*. 2004; 25(16): 3211–22. [PubMed: 14980416]
- Beavers GS, Joseph DD. Boundary Conditions at a Naturally Permeable Wall. *J Fluid Mech*. 1967; 30:197–207.
- Blewis ME, Lao BJ, Jadin KD, McCarty WJ, Bugbee WD, Firestein GS, Sah RL. Semi-permeable membrane retention of synovial fluid lubricants hyaluronan and proteoglycan 4 for a biomimetic bioreactor. *Biotechnology and bioengineering*. 2010; 106(1):149–60. [PubMed: 20014439]
- Brown E, McKee T, diTomaso E, Pluen A, Seed B, Boucher Y, Jain RK. Dynamic imaging of collagen and its modulation in tumors in vivo using second-harmonic generation. *Nature medicine*. 2003; 9(6):796–800.
- Bueno EM, Bilgen B, Barabino GA. Wavy-walled bioreactor supports increased cell proliferation and matrix deposition in engineered cartilage constructs. *Tissue engineering*. 2005; 11(11–12):1699–709. [PubMed: 16411815]
- Bueno EM, Bilgen B, Barabino GA. Hydrodynamic parameters modulate biochemical, histological, and mechanical properties of engineered cartilage. *Tissue engineering*. 2009; Part A 15(4):773–85. [PubMed: 18803479]
- Bujia J, Sittinger M, Minuth WW, Hammer C, Burmester G, Kastenbauer E. Engineering of cartilage tissue using bioresorbable polymer fleeces and perfusion culture. *Acta Otolaryngol*. 1995; 115(2): 307–10. [PubMed: 7610828]
- Buschmann MD, Gluzband YA, Grodzinsky AJ, Hunziker EB. Mechanical compression modulates matrix biosynthesis in chondrocyte/agarose culture. *Journal of Cell Science*. 1995; 108(Pt 4):1497–508. [PubMed: 7615670]
- Buschmann MD, Kim YJ, Wong M, Frank E, Hunziker EB, Grodzinsky AJ. Stimulation of aggrecan synthesis in cartilage explants by cyclic loading is localized to regions of high interstitial fluid flow. *Archives of Biochemistry & Biophysics*. 1999; 366(1):1–7. [PubMed: 10334856]
- CDC. Prevalence and most common causes of disability among adults--United States 2005. *MMWR Morb Mortal Wkly Rep*. 2009; 58:421–426. [PubMed: 19407734]
- Chaudhuri S, Nguyen H, Rangayyan RM, Walsh S, Frank CB. A Fourier domain directional filtering method for analysis of collagen alignment in ligaments. *IEEE transactions on biomedical engineering*. 1987; 34(7):509–18. [PubMed: 3610201]
- Chen T, Buckley M, Cohen I, Bonassar L, Awad HA. Insights into interstitial flow, shear stress, and mass transport effects on ECM heterogeneity in bioreactor-cultivated engineered cartilage hydrogels. *Biomechanics and modeling in mechanobiology*. 2012; 11(5):689–702. [PubMed: 21853351]
- Clark JM. The organisation of collagen fibrils in the superficial zones of articular cartilage. *Journal of anatomy*. 1990; 171:117–30. [PubMed: 2081698]
- Duval E, Leclercq S, Elissalde JM, Demoor M, Galera P, Boumediene K. Hypoxia-inducible factor 1alpha inhibits the fibroblast-like markers type I and type III collagen during hypoxia-induced chondrocyte redifferentiation: hypoxia not only induces type II collagen and aggrecan, but it also inhibits type I and type III collagen in the hypoxia-inducible factor 1alpha-dependent

- redifferentiation of chondrocytes. *Arthritis and rheumatism*. 2009; 60(10):3038–48. [PubMed: 19790048]
- Gemmiti CV, Guldberg RE. Fluid flow increases type II collagen deposition and tensile mechanical properties in bioreactor-grown tissue-engineered cartilage. *Tissue Eng*. 2006; 12(3):469–79. [PubMed: 16579680]
- Gemmiti CV, Guldberg RE. Shear stress magnitude and duration modulates matrix composition and tensile mechanical properties in engineered cartilaginous tissue. *Biotechnol Bioeng*. 2009; 104(4): 809–20. [PubMed: 19591192]
- Gooch KJ, Blunk T, Courter DL, Sieminski AL, Bursac PM, Vunjak-Novakovic G, Freed LE. IGF-I and mechanical environment interact to modulate engineered cartilage development. *Biochem Biophys Res Commun*. 2001; 286(5):909–15. [PubMed: 11527385]
- Guilak F, Butler DL, Goldstein SA. Functional tissue engineering: the role of biomechanics in articular cartilage repair. *Clin Orthop Relat Res*. 2001; (391 Suppl):S295–305. [PubMed: 11603713]
- Han EH, Bae WC, Hsieh-Bonassera ND, Wong VW, Schumacher BL, Gortz S, Masuda K, Bugbee WD, Sah RL. Shaped, stratified, scaffold-free grafts for articular cartilage defects. *Clinical orthopaedics and related research*. 2008a; 466(8):1912–20. [PubMed: 18506565]
- Han X, Burke RM, Zettel ML, Tang P, Brown EB. Second harmonic properties of tumor collagen: determining the structural relationship between reactive stroma and healthy stroma. *Optics express*. 2008b; 16(3):1846–59. [PubMed: 18542263]
- Hilton MJ, Gutierrez L, Martinez DA, Wells DE. EXT1 regulates chondrocyte proliferation and differentiation during endochondral bone development. *Bone*. 2005; 36(3):379–86. [PubMed: 15777636]
- Hootman JM, Helmick CG. Projections of US prevalence of arthritis and associated activity limitations. *Arthritis and rheumatism*. 2006; 54(1):226–9. [PubMed: 16385518]
- Hou JS, Holmes MH, Lai WM, Mow VC. Boundary conditions at the cartilage-synovial fluid interface for joint lubrication and theoretical verifications. *J Biomech Eng*. 1989; 111(1):78–87. [PubMed: 2747237]
- Hou JS, Mow VC, Lai WM, Holmes MH. An analysis of the squeeze-film lubrication mechanism for articular cartilage. *J Biomech*. 1992; 25(3):247–59. [PubMed: 1564060]
- Hung CT, Mauck RL, Wang CC, Lima EG, Ateshian GA. A paradigm for functional tissue engineering of articular cartilage via applied physiologic deformational loading. *Ann Biomed Eng*. 2004; 32(1):35–49. [PubMed: 14964720]
- Hyttinen MM, Holopainen J, van Weeren PR, Firth EC, Helminen HJ, Brama PA. Changes in collagen fibril network organization and proteoglycan distribution in equine articular cartilage during maturation and growth. *Journal of anatomy*. 2009; 215(5):584–91. [PubMed: 19732210]
- Jeffery AK, Blunn GW, Archer CW, Bentley G. Three-dimensional collagen architecture in bovine articular cartilage. *The Journal of bone and joint surgery. British volume*. 1991; 73(5):795–801.
- Jones AR, Chen S, Chai DH, Stevens AL, Gleghorn JP, Bonassar LJ, Grodzinsky AJ, Flannery CR. Modulation of lubricin biosynthesis and tissue surface properties following cartilage mechanical injury. *Arthritis and rheumatism*. 2009; 60(1):133–42. [PubMed: 19116897]
- Khan IM, Gilbert SJ, Singhrao SK, Duance VC, Archer CW. Cartilage integration: evaluation of the reasons for failure of integration during cartilage repair. A review. *European cells & materials*. 2008; 16:26–39. [PubMed: 18770504]
- Klein TJ, Schumacher BL, Blewis ME, Schmidt TA, Voegtline MS, Thonar EJ, Masuda K, Sah RL. Tailoring secretion of proteoglycan 4 (PRG4) in tissue-engineered cartilage. *Tissue engineering*. 2006; 12(6):1429–39. [PubMed: 16846341]
- Markway BD, Tan GK, Brooke G, Hudson JE, Cooper-White JJ, Doran MR. Enhanced chondrogenic differentiation of human bone marrow-derived mesenchymal stem cells in low oxygen environment micropellet cultures. *Cell transplantation*. 2010; 19(1):29–42. [PubMed: 19878627]
- Mauck RL, Soltz MA, Wang CC, Wong DD, Chao PH, Valhmu WB, Hung CT, Ateshian GA. Functional tissue engineering of articular cartilage through dynamic loading of chondrocyte-seeded agarose gels. *J Biomech Eng*. 2000; 122(3):252–60. [PubMed: 10923293]
- McCarty WJ, Masuda K, Sah RL. Fluid movement and joint capsule strains due to flexion in rabbit knees. *Journal of biomechanics*. 2011

- Mow VC, Lai WM. Some surface characteristics of articular cartilage. I. A scanning electron microscopy study and a theoretical model for the dynamic interaction of synovial fluid and articular cartilage. *J Biomech.* 1974; 7(5):449–56. [PubMed: 4443358]
- Mow VC, Lai WM, Eisenfeld J, Redler I. Some surface characteristics of articular cartilage. II. On the stability of articular surface and a possible biomechanical factor in etiology of chondrodegeneration. *J Biomech.* 1974; 7(5):457–68. [PubMed: 4443359]
- Mow VC, Wang CC. Some bioengineering considerations for tissue engineering of articular cartilage. *Clinical Orthopaedics & Related Research.* 1999; (367 Suppl):S204–23. [PubMed: 10546648]
- Neves AA, Medcalf N, Brindle KM. Tissue engineering of meniscal cartilage using perfusion culture. *Ann N Y Acad Sci.* 2002; 961:352–5. [PubMed: 12081938]
- Ng CP, Hinz B, Swartz MA. Interstitial fluid flow induces myofibroblast differentiation and collagen alignment in vitro. *Journal of cell science.* 2005; 118(Pt 20):4731–9. [PubMed: 16188933]
- Pazzano D, Mercier KA, Moran JM, Fong SS, DiBiasio DD, Rulfs JX, Kohles SS, Bonassar LJ. Comparison of chondrogenesis in static and perfused bioreactor culture. *Biotechnol Prog.* 2000; 16(5):893–6. [PubMed: 11027186]
- Pierre J, Gemmiti CV, Kolambkar YM, Oddou C, Guldborg RE. Theoretical analysis of engineered cartilage oxygenation: influence of construct thickness and media flow rate. *Biomech Model Mechanobiol.* 2008; 7(6):497–510. [PubMed: 17999099]
- Raimondi MT, Moretti M, Cioffi M, Giordano C, Boschetti F, Lagana K, Pietrabissa R. The effect of hydrodynamic shear on 3D engineered chondrocyte systems subject to direct perfusion. *Biorheology.* 2006; 43(3–4):215–22. [PubMed: 16912395]
- Ratcliffe A, Fryer PR, Hardingham TE. The distribution of aggregating proteoglycans in articular cartilage: comparison of quantitative immunoelectron microscopy with radioimmunoassay and biochemical analysis. *The journal of histochemistry and cytochemistry : official journal of the Histochemistry Society.* 1984; 32(2):193–201. [PubMed: 6363519]
- Saini S, Wick TM. Concentric cylinder bioreactor for production of tissue engineered cartilage: effect of seeding density and hydrodynamic loading on construct development. *Biotechnol Prog.* 2003; 19(2):510–21. [PubMed: 12675595]
- Sittinger M, Bujia J, Minuth WW, Hammer C, Burmester GR. Engineering of cartilage tissue using bioresorbable polymer carriers in perfusion culture. *Biomaterials.* 1994; 15(6):451–6. [PubMed: 8080936]
- Vunjak-Novakovic G, Martin I, Obradovic B, Treppo S, Grodzinsky AJ, Langer R, Freed LE. Bioreactor cultivation conditions modulate the composition and mechanical properties of tissue-engineered cartilage. *J Orthop Res.* 1999; 17(1):130–8. [PubMed: 10073657]
- Wang DW, Fermor B, Gimble JM, Awad HA, Guilak F. Influence of oxygen on the proliferation and metabolism of adipose derived adult stem cells. *J Cell Physiol.* 2005; 204(1):184–91. [PubMed: 15754341]
- Wilhelm SM, Shao ZH, Housley TJ, Seperack PK, Baumann AP, Gunja-Smith Z, Woessner JF Jr. Matrix metalloproteinase-3 (stromelysin-1). Identification as the cartilage acid metalloprotease and effect of pH on catalytic properties and calcium affinity. *The Journal of biological chemistry.* 1993; 268(29):21906–13. [PubMed: 8408046]
- Williams KA, Saini S, Wick TM. Computational fluid dynamics modeling of steady-state momentum and mass transport in a bioreactor for cartilage tissue engineering. *Biotechnol Prog.* 2002; 18(5): 951–63. [PubMed: 12363345]
- Wimmer MA, Grad S, Kaup T, Hanni M, Schneider E, Gogolewski S, Alini M. Tribology approach to the engineering and study of articular cartilage. *Tissue Eng.* 2004; 10(9–10):1436–45. [PubMed: 15588403]
- Wise JK, Yarin AL, Megaridis CM, Cho M. Chondrogenic differentiation of human mesenchymal stem cells on oriented nanofibrous scaffolds: engineering the superficial zone of articular cartilage. *Tissue engineering.* 2009; Part A 15(4):913–21. [PubMed: 18767972]
- Wong M, Carter DR. Articular cartilage functional histomorphology and mechanobiology: a research perspective. *Bone.* 2003; 33(1):1–13. [PubMed: 12919695]

Wu MH, Urban JP, Cui ZF, Cui Z, Xu X. Effect of extracellular pH on matrix synthesis by chondrocytes in 3D agarose gel. *Biotechnology progress*. 2007; 23(2):430–4. [PubMed: 17286385]

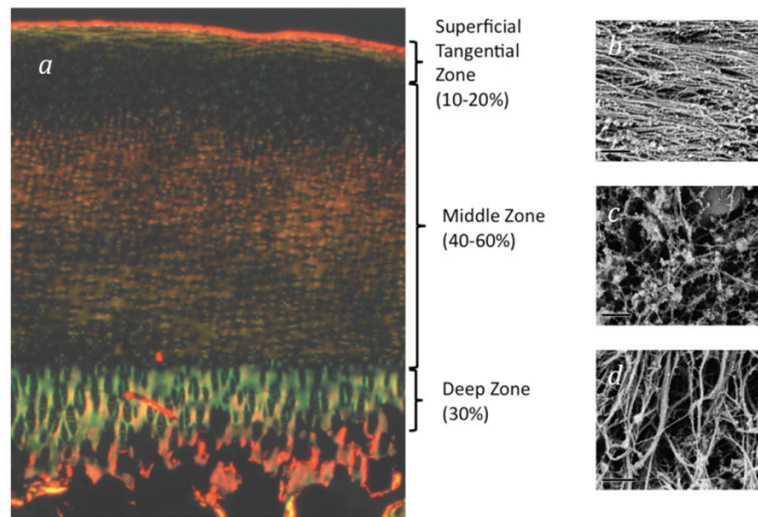


**Figure 1. Zonal Anisotropy of Articular Cartilage**

(a) Safranin O/Fast Green stained articular cartilage micrograph depicting the spatial distribution of proteoglycan (red) and non-proteoglycan (green) ECM through the chondral depth. (b) Polarized light microscopy image of articular cartilage depicting the depth-dependent anisotropy in the collagen fiber alignment. Light enhanced regions denote the presence of aligned structures while dark regions denote randomly aligned fibers. The anisotropy is verified with scanning electron microscopy (SEM) imaging of regions of interest spanning the 3 classical zones of cartilage. (c) The superficial tangential zone has collagen fibers aligned parallel to the cartilage surface. (d) The middle zone has randomly aligned fibers. (e) The deep zone has vertically aligned fibers. (SEM Scale bars represent 1  $\mu\text{m}$ .)

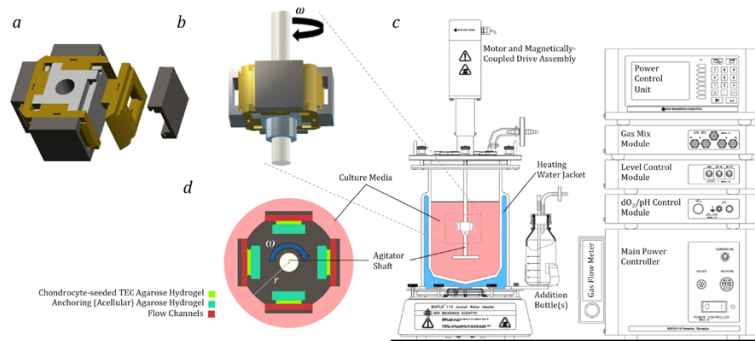


### Figure 2. Bioreactor Design

A modular bioreactor was custom designed to hold 4 tissue engineered cartilage (TEC) hydrogels and cultivate them in a stirred tank under simulated flow conditions. (a) A partially exploded view of the modular bioreactor consisting of a base block (light grey), 4 sliding compartments (gold) with rectangular wells into which the TEC hydrogels are cast, and 4 lids (dark grey) that form channels over the TEC hydrogel compartments. (b) The modular compartments of the system were then assembled and mounted on the agitator shaft of the Bioflo 110® stirred tank. (c) Schematic representation of the Bioflo 110® stirred tank bioreactor (New Brunswick Scientific, Edison, NJ) consisting of a water-jacketed culture vessel with stackable control units and various probes and tubing (not shown) to regulate temperature, pH, dissolved gas(s) concentration, and the rotational speed of the agitator. (d) TEC hydrogels were cultured in complete media supplemented with ascorbic acid and maintained at 37°C, 5% O<sub>2</sub> and 7.4 pH for 14 days, and were subjected to simulated surface flow conditions generated by periodic rotation in the stirred tank filled with culture media in a half-square wave (0–25 rpm at 0.004 Hz) for 40 minutes, followed by steady rotational speed of 25 rpm for the remainder of the day, which resulted in a nominal shear stress of 0.12 Pa at the surface of the TEC hydrogel.

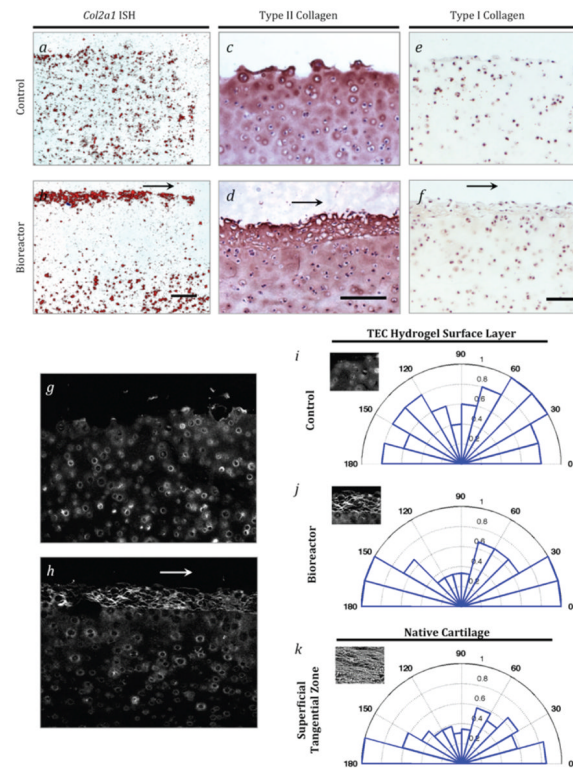


**Figure 3. Effects of the bioreactor cultivation on collagen transcription, synthesis, and alignment in the chondrocyte-seeded TEC hydrogel after 14 days in culture**

Spatial localization of type II collagen mRNA is visualized using *in situ* hybridization (ISH) for *Col2a1* in (a) control and (b) bioreactor-cultivated TEC hydrogels. Type II collagen accumulation and distribution in (c) control and (d) bioreactor-cultivated TEC hydrogels is visualized with immunohistochemistry (IHC). Type I collagen IHC staining in (e) control and (f) bioreactor-cultivated TEC hydrogels. Arrows in b, d, and f indicate the flow direction. Scale bars in a–f represent 250 microns. Two-photon microscopy imaging of second harmonic generation (SHG) of fibrillar collagen in the (g) control and (h) bioreactor-cultivated TEC hydrogels. Note the strong SHG signal depicting improved alignment in the hydrodynamically-stimulated superficial layer in bioreactor-cultivated TEC hydrogels, which is absent in controls. Note also the localization of the SHG signal to the pericellular matrix around the chondrocytes throughout the controls and in the deeper regions of bioreactor-cultivated TEC hydrogels. Fiber orientations in the superficial region of the hydrogels were determined in MATLAB using a Fast Fourier Transform-based algorithm, and binned in 15° intervals and plotted as normalized frequency histograms (rose plots) for (i) control and (j) bioreactor-cultivated hydrogels, as well as for (k) the superficial zone of articular cartilage. Note that the collagen fibers are predominately aligned along the direction of fluid flow in the hydrodynamically-stimulated surface regions of the TEC hydrogels (j), which bears striking resemblance to the native superficial zone alignment pattern (k).

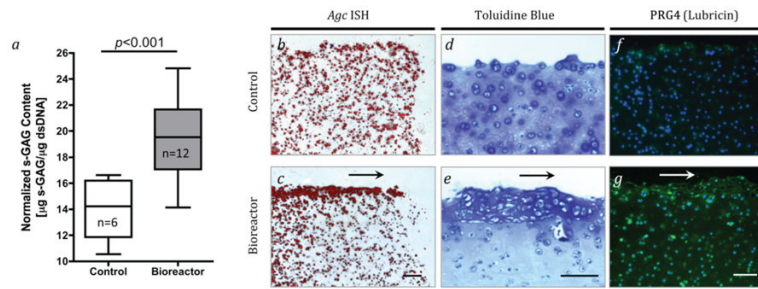


**Figure 4. Effects of the bioreactor cultivation on PGs expression, synthesis, and accumulation in the chondrocyte-seeded TEC hydrogel after 14 days in culture**

(a) The proteoglycan content in control and bioreactor-cultivated TEC hydrogels were quantified biochemically using the DMMB assay. Data presented as box plots showing the mean, quartiles, and range of the PG content normalized by DNA content. Note that the origin of the vertical axis starts at  $10 \mu\text{g s-GAG}/\mu\text{g dsDNA}$ . Asterisk indicates significant differences as determined by an unpaired t-test ( $\alpha < 0.05$ ). Spatial localization of aggrecan mRNA is visualized using *in situ* hybridization (ISH) for *Agc1* in (b) control and (c) bioreactor-cultivated TEC hydrogels. Proteoglycan accumulation and distribution is visualized using Toluidine blue stained histological sections of (d) control and (e) bioreactor-cultivated TEC hydrogels. Representative immunofluorescence staining for PG4 (green fluorescence) at the surface of (f) control and (g) bioreactor-cultivated hydrogels counter stained with DAPI (blue) for cell nuclei. Scale bars in b–g represent 250 microns. Arrows in c, e, and g indicate the flow direction.

# Restricted diffusion of calretinin in cerebellar granule cell dendrites implies $\text{Ca}^{2+}$ -dependent interactions via its EF-hand 5 domain

Oliver Arendt<sup>1</sup>, Beat Schwaller<sup>2</sup>, Edward B. Brown<sup>3</sup>, Jens Eilers<sup>1</sup> and Hartmut Schmidt<sup>1</sup>

<sup>1</sup>Carl-Ludwig Institute for Physiology, Medical Faculty, University of Leipzig, 04103 Leipzig, Germany

<sup>2</sup>Unit of Anatomy, Department of Medicine, University Fribourg, 1700 Fribourg, Switzerland

<sup>3</sup>School of Medicine and Dentistry, Department of Biomedical Engineering, University of Rochester, Rochester, NY, USA

## Key points

- The dynamics of the second messenger  $\text{Ca}^{2+}$  are tightly controlled by  $\text{Ca}^{2+}$ -binding proteins (CaBPs).
- The diffusional mobility of a given CaBP, such as calretinin (CR), defines how it affects the range-of-action of  $\text{Ca}^{2+}$  but, if unexpectedly low, may also indicate that the CaBP acts as a  $\text{Ca}^{2+}$  sensor, undergoing specific protein interactions.
- Here we quantified the diffusional mobility of CR in dendrites of cerebellar granule cells using microscopic methods.
- We find that CR diffuses unexpectedly slow, that its mobility is further reduced when  $\text{Ca}^{2+}$  levels are elevated and that a distinct region of CR interacts with specific targets in a  $\text{Ca}^{2+}$ -dependent manner.
- Our findings indicate a new 'sensor' role for CR, which may allow for  $\text{Ca}^{2+}$ -dependent feedback control of neuronal excitability.

**Abstract**  $\text{Ca}^{2+}$ -binding proteins (CaBPs) are important regulators of neuronal  $\text{Ca}^{2+}$  signalling, acting either as buffers that shape  $\text{Ca}^{2+}$  transients and  $\text{Ca}^{2+}$  diffusion and/or as  $\text{Ca}^{2+}$  sensors. The diffusional mobility represents a crucial functional parameter of CaBPs, describing their range-of-action and possible interactions with binding partners. Calretinin (CR) is a CaBP widely expressed in the nervous system with strong expression in cerebellar granule cells. It is involved in regulating excitability and synaptic transmission of granule cells, and its absence leads to impaired motor control. We quantified the diffusional mobility of dye-labelled CR in mouse granule cells using two-photon fluorescence recovery after photobleaching. We found that movement of macromolecules in granule cell dendrites was not well described by free Brownian diffusion and that CR diffused unexpectedly slow compared to fluorescein dextrans of comparable size. During bursts of action potentials, which were associated with dendritic  $\text{Ca}^{2+}$  transients, the mobility of CR was further reduced. Diffusion was significantly accelerated by a peptide embracing EF-hand 5 of CR. Our results suggest long-lasting,  $\text{Ca}^{2+}$ -dependent interactions of CR with large and/or immobile binding partners. These interactions render CR a poorly mobile  $\text{Ca}^{2+}$  buffer and point towards a  $\text{Ca}^{2+}$  sensor function of CR.

(Received 8 April 2013; accepted after revision 28 May 2013; first published online 3 June 2013)

**Corresponding author** H. Schmidt: Carl-Ludwig-Institute for Physiology, Medical Faculty, University Leipzig Liebigstr. 27, 04103 Leipzig, Germany. Email: hartmut.schmidt@medizin.uni-leipzig.de

**Abbreviations** CaBP, Ca<sup>2+</sup>-binding protein; CR, calretinin; CR\*, dye-labelled calretinin; FD, fluorescein-labelled dextran; FRAP, fluorescence recovery after photobleaching;  $\gamma$ , transport coefficient; IQR, interquartile range; PMTs, photomultiplier tubes.

## Introduction

The precise functional roles of most members of the large and diverse group of Ca<sup>2+</sup>-binding proteins (CaBPs) are still poorly understood. While the distinct Ca<sup>2+</sup>-binding kinetics of the different CaBPs are evidently of central importance for their function, other properties also need to be considered to give meaning to the cell type-specific expression of CaBPs, of which some differ little in their Ca<sup>2+</sup>-binding behaviour. Diffusional mobility, interaction with binding partners and possible sensor functions are such properties that define the range of action (Allbritton *et al.* 1992) and mode of action (Schwaller, 2009) of CaBPs.

Calretinin (CR) is an EF-hand CaBP closely related to calbindin-D28k and calmodulin with well-characterized Ca<sup>2+</sup>-binding kinetics (Faas *et al.* 2007). It is widely expressed in the nervous system, including the Calyx of Held (Felmy & Schneggenburger, 2004) and cerebellar granule cells (Rogers, 1989; Schwaller *et al.* 2002). Its absence increases release probability at granule cell terminals (Schmidt *et al.* 2013) and alters excitability of granule cells (Gall *et al.* 2003), which at the behavioural level leads to impaired motor co-ordination (Schiffmann *et al.* 1999). Despite its functional importance and abundant expression, little is known about the mobility and possible interactions of CR within neurons. Some reports point towards immobilization at membranes (Winsky & Kúznicki, 1995; Hack *et al.* 2000) while others suggest that CR acts as a Ca<sup>2+</sup> sensor (Kúznicki *et al.* 1995*a,b*) that binds to Ca<sub>v</sub>2.1 channels (Christel *et al.* 2012) and other targets (Marilley & Schwaller, 2000).

Mobility and binding of proteins of interest can be quantified with fluorescence recovery after photobleaching (FRAP) (Axelrod *et al.* 1976), allowing for measurements in spines (Svoboda *et al.* 1996; Star *et al.* 2002; Schmidt *et al.* 2003*a*, 2005, 2007*b*), small dendrites (this study), axons (Schmidt *et al.* 2007*a*), somata (Brown *et al.* 1999) and membranes (Feder *et al.* 1996), i.e. in situations where equations for 1D, 2D and 3D diffusion apply. However, more complex situations such as bounded systems (Sullivan & Brown, 2011) or anomalous subdiffusion (Brown *et al.* 1999) can also be quantified with adapted diffusion equations. Interactions with cellular targets become evident by prolonged recovery times, especially if the targets are large or immobile and if the interaction has slow off rates (Schmidt *et al.* 2005). Finally, binding sites can be identified by quantifying the effects of synthetic peptides that resemble putative binding domains (Schmidt *et al.* 2005).

Here we employed FRAP to study the mobility of CR in dendrites of cerebellar granule cells. We found that molecular movement is better described by anomalous subdiffusion than normal diffusion and that CR showed a strongly reduced mobility when compared to inert tracers. Increasing the intracellular Ca<sup>2+</sup> concentration ([Ca<sup>2+</sup>]<sub>i</sub>) significantly reduced the mobility further, while a peptide consisting of 35 amino acids, containing the sequence of EF-hand 5 of CR, significantly increased the mobility of CR. Our data indicate that CR acts as poorly mobile buffer and possibly as a Ca<sup>2+</sup> sensor in granule cells.

## Methods

### Ethical approval

All experiments were carried out in accordance with institutional guidelines for animal experiments, and were approved by the state directorate of Saxony, Germany.

### Slice preparation and solutions

Acute cerebellar brain slices were prepared from 21–24-day-old mice of either sex that were killed by decapitation under isoflurane (Curamed, Karlsruhe, Germany) anaesthesia. The vermis was isolated and mounted in a chamber filled with cooled (0–2°C) artificial cerebrospinal fluid. Parasagittal slices (200  $\mu$ m thick) were cut using a vibratome (HM 650 V; Microm, Walldorf, Germany) and kept in artificial cerebrospinal fluid at 35°C for 40 min before they were transferred to the recording chamber. Experiments were performed at room temperature. Artificial cerebrospinal fluid contained (in mM): 125 NaCl, 2.5 KCl, 1.25 NaH<sub>2</sub>PO<sub>4</sub>, 26 NaHCO<sub>3</sub>, 1 MgCl<sub>2</sub>, 2 CaCl<sub>2</sub> and 20 glucose, gassed with 95% O<sub>2</sub> and 5% CO<sub>2</sub> (pH 7.3–7.4 at 20–22°C). Unless stated otherwise, all chemicals were from Sigma-Aldrich, Seelze, Germany. For FRAP experiments, the pipette solution was composed of (in mM): 150 potassium gluconate, 10 NaCl, 3 magnesium ATP, 0.3 sodium GTP, 10 HEPES, 0.08 dye-labelled CR (CR\*) or 0.5 fluorescein-labelled dextran (FD; 10 or 40 kDa) and 50  $\mu$ M EGTA dissolved in bidistilled water (Sigma-Aldrich, Seelze, Germany).

We set the concentration of CR to 80  $\mu$ M because the buffer capacity of granule cells has been estimated to be ~60 (Brenowitz & Regehr, 2007) and CR is their major

endogenous buffer (Schiffmann *et al.* 1999). Depending on assumptions about concentrations of unknown buffers and the  $\text{Ca}^{2+}$  affinity of CR (Faas *et al.* 2007), the CR concentration will be 40–80  $\mu\text{M}$  (Schmidt *et al.* 2013), a concentration range we expect to be reached after 20 min equilibration time with a pipette solution containing 80  $\mu\text{M}$  CR.

For  $\text{Ca}^{2+}$  imaging, the pipette solution contained 50  $\mu\text{M}$  of the  $\text{Ca}^{2+}$ -indicator dye Oregon Green BAPTA-1 (OGB-1; Molecular Probes, Eugene, OR, USA) and 50  $\mu\text{M}$  of the  $\text{Ca}^{2+}$ -insensitive dye Atto 637 (Atto-Tec, Siegen, Germany) instead of  $\text{CR}^*$  or FD/EGTA. The pH was adjusted to 7.3 with KOH.

### Labelled calretinin and gel electrophoresis

Purified human recombinant CR (266 of 271 amino acids (98%) identical to mouse CR) expressed in *Escherichia coli* was labelled with Alexa-488 (Molecular Probes) as described previously (Schmidt *et al.* 2003a). Labelling conditions (pH 9.0) were selected to preferentially label the  $\alpha$ -amino group of CR, while  $\epsilon$ -amino groups were not labelled significantly. The labelled protein was purified on a size exclusion column (20  $\times$  0.8 cm, gel volume 10 ml) containing Bio-Gel P-6 (medium, fractionation range 1–6 kDa; Bio-Rad, Hercules, CA, USA) to remove unbound dye. 0.3–1 ml labelling reaction mixture was applied to the column and eluted with buffer [50 mM  $(\text{NH}_4)\text{HCO}_3$ , 0.1 mM  $\text{CaCl}_2$ , pH 8.3]. The molecular Alexa/CR ratio was 2.6–4.5. The purity of the protein was tested by gel electrophoresis of dye-labelled and native CR (250  $\mu\text{g}$  each), using a 15% SDS-polyacrylamide gel.

To test for unbound dye in FD solutions, FDs were dissolved in purified water (500  $\mu\text{M}$ ) and separated on a 2.5% agarose gel, prepared and run in standard Tris-acetate EDTA buffer solution for 1 h at 50 V. In addition, mixtures of FDs and fluorescein were run on the same gel.

### Cell loading and electrophysiology

Patch pipettes were pulled from borosilicate glass (Hilgenberg, Malsfeld, Germany) with a PC-10 puller (Narishige, Tokyo, Japan) to resistances of 10–11 M $\Omega$ . Whole-cell patch clamp recordings were obtained with an Axopatch 200A amplifier (Axon Instruments Inc., Union City, CA, USA), a LIH 1600 AD/DA converter and Patch Master 2.2 software (HEKA, Lambrecht, Germany). Seal formation was slightly prolonged by  $\text{CR}^*$  or FDs. The resting membrane potential was held constant by injecting up to  $-50$  pA holding current in the current clamp mode. The cells were equilibrated with the dye-containing pipette

solution for at least 20 min before FRAP or  $\text{Ca}^{2+}$  imaging experiments.

### Fluorescence recovery after photobleaching recordings

Two-photon FRAP experiments were performed as described previously (Schmidt *et al.* 2003a) on granule cell dendrites between 20 and 50 min after the whole cell configuration had been established. Briefly, a custom modified Fluoview 300 laser-scanning microscope (LSM; Olympus, Hamburg, Germany) equipped with a mode-locked Ti:sapphire laser (Tsunami; Spectra Physics, Darmstadt, Germany) set to a centre wavelength of 765 nm was used. The laser light was intensity modulated with a Pockels cell (model 350-80 LA-BR; Conoptics, Danbury, CT, USA; controlled via the AD/DA converter and Patch Master software) and focused on the specimen by a 60 $\times$ /0.9 NA water immersion objective (Olympus). The fluorescence and laser intensity were recorded simultaneously using the internal photomultiplier tubes (PMTs) of the LSM, and sampled in the point mode (sampling frequency 500 kHz, 1 ms binning).

The baseline fluorescence and the fluorescence recovery were measured at laser intensities of 3–8 mW (measured at the exit of the objective). For bleaching, a 1 ms long, high-intensity laser pulse (20–40 mW) was applied. The specimen and system background were recorded by focusing the laser beam on unstained tissue next to the granule cell dendrite and by completely blocking the laser beam, respectively, using the same intensity protocol as during the FRAP recordings.

Aqueous FRAP recordings of 3, 10, 40 and 70 kDa FD or  $\text{CR}^*$  (50  $\mu\text{M}$  each), were performed in a droplet of intracellular solution, using photon counting instrumentation. The LSM was custom-modified so that two external, photon counting capable PMTs could be attached to the system. The first, red-sensitive PMT (PMC 100-1; Becker & Hickl, Berlin, Germany) was placed close to the scanning mirrors of the LSM and, by detecting scattered laser light, was used to record the excitation intensity. The second, red-insensitive PMT (PMC 100-0; Becker & Hickl) collected the fluorescence signal after it was diverted out of the LSM by a mirror placed into the emission pathway. The PMT signals were recorded using a time-correlated single photon counting board (TimeHarp; PicoQuant, Berlin, Germany) and SymPhoTime 4.2 software (PicoQuant). For each aqueous FRAP experiment, 2500 individual measurements, repeated at 20 Hz, were averaged. The duration of the bleach pulse was reduced to 10  $\mu\text{s}$ , to prevent significant diffusion during bleaching (Brown *et al.* 1999). Baseline fluorescence was recorded for 1 ms and the recovery for 20 ms. In recording the fluorescence and system background, the intracellular solution was

replaced by water or the laser beam was blocked, respectively.

### Peptides

In indicated experiments 80  $\mu\text{M}$  of a synthetic peptide ('EF5-peptide') or a scrambled control peptide were co-dialysed with 40  $\mu\text{M}$  CR\* via the somatic patch pipette.

EF5-peptide EFNAIFTFYDKDGSYIDENELDALK  
 DLYEKNKK  
 Scrambled peptide EDNFKLDNLKDYAKELFIAGYLYG  
 EEKFIKTSDDN

The EF5-peptide, assumed to represent the putative binding domain of CR, contained the entire EF-hand domain 5 (the  $\text{Ca}^{2+}$ -chelating loop is marked in bold) and part of the linker EF5 to EF6 (underlined). This 35 amino acid stretch is highly conserved, i.e. 100% identical between rat and mouse. Ninety-four per cent (33 of 35 residues) are identical in the human CR sequence.

### Analysis of fluorescence recovery after photobleaching data

FRAP data were analysed with custom written routines in Igor Pro (Wavemetrics, Lake Oswego, OR, USA). The raw fluorescence data were corrected for the specimen background, the laser intensity data for the system background. To correct for non-linear switching artefacts of the Pockels cell, the fluorescence was subsequently divided by the square of the laser intensity (Brown *et al.* 1999) and, thereafter, normalized to the baseline fluorescence ( $F/F_0$ ). Data were only accepted for analysis if the initial bleaching during the baseline period was less than 15%.

The first second of the fluorescence recovery in dendrites ( $F(t)$ ) was fitted with a one-dimensional diffusion equation (Schmidt *et al.* 2007a) of the form:

$$F(t) = F_{\infty} \sum_{n=0}^{\infty} \frac{(-\beta)^n}{n!} \frac{1}{\left(1 + n + \frac{16Dt}{\omega_r^2}\right)^{1/2}} \quad (1)$$

where  $D$  is the diffusion coefficient,  $F_{\infty}$  is the postbleach fluorescence after recovery,  $\beta$  is the bleach depth parameter and  $\omega_r$  is the radial  $e^{-2}$  radius of the two-photon excitation volume. For our system,  $\omega_r$  has dimensions of  $\sim 0.53 \mu\text{m}$  in tissue and  $\sim 0.57 \mu\text{m}$  in water (Schmidt *et al.* 2007a). A fit for anomalous subdiffusion was implemented by replacing terms of  $Dt$  by  $D_{(t)} \cdot t$ , then by  $\Gamma \cdot t^{\alpha}$  and finally by  $(\gamma t)^{\alpha}$  (Feder *et al.* 1996; Brown *et al.* 1999), where  $\gamma$  is a mobility coefficient and  $\alpha \leq 1$  is the anomalous sub-

diffusion exponent. This yielded the following equation:

$$F(t) = F_{\infty} \sum_{n=0}^{\infty} \frac{(-\beta)^n}{n!} \frac{1}{\left(1 + n + \frac{16(\gamma t)^{\alpha} n}{\omega_r^2}\right)^{1/2}} \quad (2)$$

The first 20 ms of the aqueous recovery were described with the free 3D diffusion equation given in Brown *et al.* (1999):

$$F(t) = F_{\infty} \sum_{n=0}^{\infty} \frac{m^{3/2}(-\beta)^n}{n!(m + bn + (bnmt/\tau_D))} \times \frac{1}{(m + bn + (bnmt/R\tau_D))^{1/2}} \quad (3)$$

with the characteristic radial diffusion time  $t_D = \omega_r^2/8D$ , and the ratio of the beam dimensions  $R = \omega_z^2/\omega_r^2$ , where  $\omega_z \sim 1.8 \mu\text{m}$  (Schmidt *et al.* 2007a) is the axial  $e^{-2}$  radius of the two-photon excitation volume. The parameters  $m$  and  $b$  represent the number of photons absorbed per molecule in a fluorescence and bleaching event, respectively. Assuming two-photon excitation, we used  $m = b = 2$  and ignored possible higher-order processes. During fitting, the series were truncated after the sixth partial sum. The reliability of all fits was judged by inspection of the residuals (i.e. data – fit).

### Ca<sup>2+</sup> imaging

Ca<sup>2+</sup> signals were recorded at 67 Hz, using 50  $\mu\text{M}$  of the fluorescent Ca<sup>2+</sup> indicator dye OGB-1. As OGB-1 is dim at resting Ca<sup>2+</sup> levels, 50  $\mu\text{M}$  of the Ca<sup>2+</sup> insensitive red fluorescent dye Atto 637 was used in addition. Both dyes were excited at  $\sim 810 \text{ nm}$ . The fluorescence signals were split by a 570 nm dichroic mirror. The red fluorescence was filtered with a 645–685 nm bandpass, the green signal with a 510–550 nm bandpass filter (AHF, Tübingen, Germany). In both channels, a 700 nm short-pass filter was used for blocking residual excitation light.

Analysis of Ca<sup>2+</sup> signals was done using Igor Pro. Changes in intracellular free Ca<sup>2+</sup> were expressed as background subtracted relative increases in OGB-1 fluorescence ( $\Delta F/F_0$ ).  $\Delta F/F_0$  traces were subsequently smoothed using a five-point sliding average algorithm.

### Numerical simulations

Numerical simulations were performed according to previously published principles and with previous parameters (see Schmidt *et al.* 2003b, 2007b, 2013 and references therein). The kinetics of dendritic Ca<sup>2+</sup> dynamics were described by numerically solving coupled sets of differential equations in a single compartment model using NDSolve of Mathematica 9 (Wolfram Research,

Oxfordshire, UK). The model covered  $\text{Ca}^{2+}$  influx, a surface-based clearance mechanism ( $K_M$   $3 \mu\text{M}$ ), binding and diffusion of  $\text{Ca}^{2+}$ , ATP ( $370 \mu\text{M}$ ,  $k_{\text{on}}$   $500 \mu\text{M}^{-1} \text{s}^{-1}$ ,  $k_{\text{off}}$   $100,000 \text{s}^{-1}$ ), CR ( $80 \mu\text{M}$ ,  $k_{\text{on, tense}}$   $1.8 \mu\text{M}^{-1} \text{s}^{-1}$ ,  $k_{\text{on, relaxed}}$   $310 \mu\text{M}^{-1} \text{s}^{-1}$ ,  $k_{\text{on, v}}$   $7.3 \mu\text{M}^{-1} \text{s}^{-1}$ ,  $k_{\text{off, tense}}$   $53 \text{s}^{-1}$ ,  $k_{\text{off, relaxed}}$   $20 \text{s}^{-1}$ ,  $k_{\text{off, v}}$   $252 \text{s}^{-1}$ ) and, during model adjustment, OGB-1 ( $40 \mu\text{M}$ , i.e. 80% of the pipette concentration,  $k_{\text{on}}$   $430 \mu\text{M}^{-1} \text{s}^{-1}$ ,  $k_{\text{off}}$   $140 \text{s}^{-1}$ ).  $\text{Ca}^{2+}$  binding was simulated by second order kinetics, except for binding sites I–IV of CR, for which cooperativity was implemented. The extrusion mechanism was balanced by a  $\text{Ca}^{2+}$  leak to generate a resting  $[\text{Ca}^{2+}]_i$  of  $45 \text{nM}$ ;  $[\text{Mg}^{2+}]_i$  was set to  $590 \mu\text{M}$ . The model was adjusted to the measured fluorescence transients using an influx train (Gaussian width  $600 \mu\text{s}$ ,  $96 \text{Hz}$  average frequency with 6% adaptation factor for the interspike interval). The amplitude of the  $\text{Ca}^{2+}$  influx and pump velocity were the only variables. During adjustment, a 35% whole cell wash-out reduction for endogenous CR was used. For simulating FRAP recordings, OGB-1 and wash-out correction were removed from the simulation and the fractional  $\text{Ca}^{2+}$  occupancy of CR was calculated.

### Statistics

Unless denoted otherwise average data are given as median and interquartile range (IQR). For comparing groups of non-normally distributed data the Mann–Whitney–Wilcoxon rank sum test (comparison of two groups) or the Kruskal–Wallis ANOVA on ranks (comparison of more than two groups) was used.

### Results

The aim of the present study was to analyse the mobility of the endogenous CaBP, CR, in its native neuronal environment using two-photon FRAP (Brown *et al.* 1999; Schmidt *et al.* 2003a). For this purpose we chose cerebellar granule cells, which constitute the major fraction of brain neurons (Braitenberg & Atwood, 1958) and are known to strongly express CR (Rogers, 1989; Arai *et al.* 1991; Resibois & Rogers, 1992). To our knowledge this is the first study of FRAP experiments in granule cells. Thus, in a first set of experiments we established the experimental and theoretical framework of FRAP in dendrites of granule cells using FD. Subsequently, the mobility of CR\* was quantified under resting conditions, during neuronal activity and during interference with possible binding partners.

### Anomalous subdiffusion of fluorescein dextrans in granule cell dendrites

Granule cells were dialysed with a pipette solution containing either 10 kDa or 40 kDa FDs in the whole

cell patch clamp configuration. Within minutes, the morphology of the cells (soma, initial axon segment and dendrites) could be resolved under two-photon excitation (Fig. 1A). Granule cells had three to five dendrites of  $6\text{--}24 \mu\text{m}$  length, which terminated in the typical glomerular structure. The single ascending axons

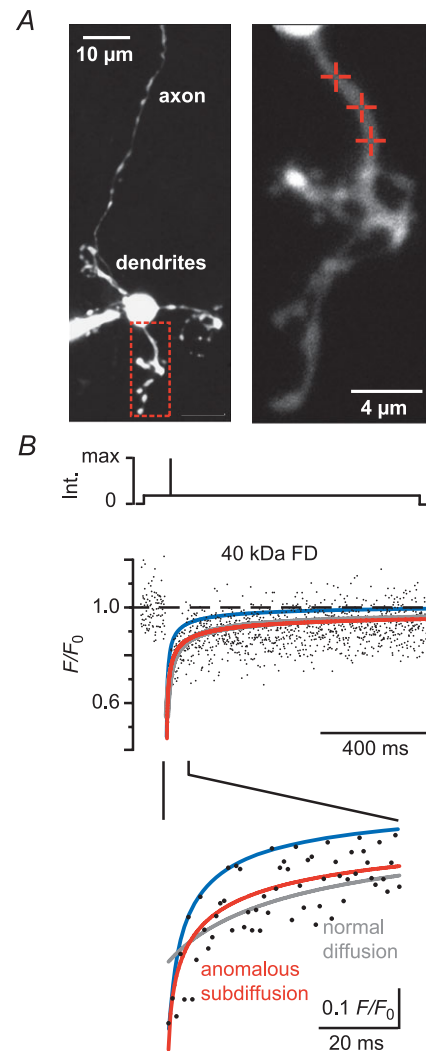


**Figure 1. Anomalous subdiffusion in granule cell dendrites**

A, left: contrast-enhanced two-photon image (z-stack) of a granule cell filled with a 40 kDa FD ( $500 \mu\text{M}$ ) via a somatic patch pipette. The red box outlines the dendritic region shown magnified on the right. Cross-hairs denote the positions on which fluorescence recovery after photobleaching recordings (shown in B) were performed. B, top: scheme of the laser intensity protocol. Middle: dendritic fluorescence recovery after photobleaching time course. The dots represent the average of three normalized recordings ( $F/F_0$ ) from the spots denoted in A. The lines represent fits to the fluorescence recovery assuming free diffusion (grey line, eqn 1 in Methods) or anomalous subdiffusion (red line, eqn 2). The blue line shows the calculated recovery for free diffusion using the previously published diffusion coefficient of 40 kDa FD (Schmidt *et al.* 2007a). The lower panel shows the initial recovery expanded in time. Note that the subdiffusion model yields the best fit to the recovery. FD, fluorescein dextrans; Int., laser intensity.

originating from the somata or a dendrite were rather dim due to their small diameter. To measure the mobility of FDs, the low-power laser beam was directed to single points of interest on the dendrites. The soma, together with the patch pipette, represents a large reservoir of unbleached molecules that may accelerate fluorescence recovery. To minimize this effect, FRAP spots were at distances of at least  $4 \mu\text{m}$  from their somatic point of origin ( $9 \pm 4 \mu\text{m}$ , means  $\pm$  SD,  $n = 65$  cells). For photo-bleaching a brief (1 ms), high-intensity laser pulse was applied to irreversibly bleach the fluorophores within the focal volume. The fluorescence was subsequently monitored again at low laser intensity and the recovery of the fluorescence, which reflects diffusion of unbleached FD molecules from neighbouring regions into the focal volume, was recorded (Fig. 1B).

A model of free Brownian motion [eqn (1), cf. Schmidt *et al.* 2007a] fitted the late recovery phase well. It failed, however, to capture the initial recovery (Fig. 1B, grey line). Moreover, the obtained  $D$  values were surprisingly small. Median values were  $2 \mu\text{m}^2 \text{s}^{-1}$  (IQR  $0.3\text{--}6.0 \mu\text{m}^2 \text{s}^{-1}$ ) for 10 kDa FDs ( $n = 69$  recordings from 24 cells) and  $1.5 \mu\text{m}^2 \text{s}^{-1}$  ( $0.6\text{--}4.0 \mu\text{m}^2 \text{s}^{-1}$ ) for 40 kDa FDs ( $n = 69$  recordings from 23 cells). These values are approximately five times smaller than those reported for FDs in axons of Purkinje cells (Schmidt *et al.* 2007a). The previously published  $D$  values would lead to significantly faster recoveries (blue line in 1B) than the one determined in this study. Incorporating an immobile fraction (IF) into the diffusion model (cf. Schmidt *et al.* 2005) improved the fit (not shown) and yielded  $D$  values compatible with the literature. The requirement for an IF, however, is not in line with the assumption that FDs are inert markers with respect to their intracellular mobility (Luby-Phelps *et al.* 1985, 1995; Reits & Neefjes, 2001; Schmidt *et al.* 2005; Sprague & McNally, 2005).

We tested for the possibility that the rapid initial recovery was due to the presence of free dye in the FDs containing solutions. Using gel electrophoresis of these solutions we found only a single band for each FD that was clearly separated from a free dye band tested in a separate column (data not shown), indicating that dye contamination is not responsible for the initial rapid recovery phase. A further possibility is that radial diffusion contributed to recovery, a phenomenon known to affect fluorescence recovery in bounded systems (Sullivan & Brown, 2011). However, the radial ( $\omega_r$ ) and axial ( $\omega_z$ ) radii of the bleach spot at the  $e^{-2}$  intensity were  $0.53$  and  $1.95 \mu\text{m}$ , respectively in our system (Schmidt *et al.* 2007a). Both values are larger than the radii of the dendrites estimated from fluorescence images ( $\leq 0.5 \mu\text{m}$ ) or reported in the literature (Eccles *et al.* 1967; Ito, 1984). The size of the focal volume is thus larger than or equal to the radial dendritic dimension, and FRAP data are unlikely to be distorted by radial diffusion.

The described discrepancies between model and data (early recovery phase) and between published and estimated  $D$  values (late recovery) are resolved if molecular movements are described by anomalous subdiffusion (Feder *et al.* 1996; Brown *et al.* 1999). Anomalous subdiffusion is a process in which free diffusion of inert molecules is hindered by the cell's geometry (Ölveczky & Verkman, 1998; Sbalzarini *et al.* 2005; Santamaria *et al.* 2006), molecular crowding or transient trapping (Bouchaud & Georges, 1990; Saxton, 1996; Weiss *et al.* 2004). In many cases, however, the physical mechanisms inducing anomalous subdiffusion remain ill-defined. Therefore, the model below gives just an *ad hoc* fit with no direct information about the diffusion-hindering processes in the compartment under study. In subdiffusion models, the mean square displacement of the diffusing particle is no longer proportional to time, but obeys a power law in time and the diffusion coefficient  $D$  becomes a function of time (Feder *et al.* 1996), i.e.:

$$\langle X^2 \rangle \propto D(t) \cdot t = \Gamma \cdot t^\alpha = (\gamma t)^\alpha \quad (4)$$

where  $\alpha \leq 1$  is the anomalous subdiffusion exponent and  $\Gamma$  is a transport coefficient (Feder *et al.* 1996; Brown *et al.* 1999).

Anomalous subdiffusion models have previously been shown to improve fits to FRAP data obtained in biological systems and to eliminate the requirement of an IF (Feder *et al.* 1996; Brown *et al.* 1999; Klafter & Sokoov, 2005). Mathematically, anomalous subdiffusion was implemented by replacing terms of  $Dt$  in eqn (1) by  $(\gamma t)^\alpha$ . The effective diffusion coefficient at any time  $t$  (e.g.  $D_{10\text{ms}}$ ) is then equal to  $\gamma^\alpha t^{\alpha-1}$  (Brown *et al.* 1999). This results in a 1D anomalous subdiffusion equation (eqn (2)), which substantially improved the accuracy of the fit during the initial phase of the recovery (Fig. 1B, red trace, lower panel) and eliminated the requirement of an IF.

The values of  $\gamma$  are not in units of  $\mu\text{m}^2 \text{s}^{-1}$  and can only be compared directly between groups if  $\alpha$  values are identical. To allow comparing fitting results with different  $\alpha$  values, the time-dependent diffusion coefficient  $D_{(t)}$  at  $t = 10$  ms after bleaching was calculated. We found a median  $D_{10\text{ms}}$  of  $12 \mu\text{m}^2 \text{s}^{-1}$  (IQR  $8\text{--}18 \mu\text{m}^2 \text{s}^{-1}$ ) for 10 kDa FD ( $n = 69$  from 24 cells) and of  $10 \mu\text{m}^2 \text{s}^{-1}$  ( $7\text{--}14 \mu\text{m}^2 \text{s}^{-1}$ ) for 40 kDa FD ( $n = 69$  from 23 cells). While the data showed a substantial variability, most likely due to the signal-to-noise ratio of FRAP recordings in thin dendritic structures, the  $D_{10\text{ms}}$  values of the dextrans were significantly different from each other ( $P < 0.05$ ). The median anomaly exponent  $\alpha$  was not significantly different for 10 and 40 kDa FDs  $0.64$  ( $0.47\text{--}0.89$ ) and  $0.68$  ( $0.60\text{--}0.87$ ), respectively,  $P > 0.1$ ]. These results point towards a size dependency of  $D_{(t)}$  (larger molecules diffuse more slowly), while  $\alpha$  is independent of molecular weights between 10 kDa and 40 kDa and, thus, may reflect cellular

hindrances (Saxton & Jacobson, 1997; Santamaria *et al.* 2006). Taken together, the molecular movement of inert traces in granule cell dendrites is not well described by free diffusion, while a model of 1D anomalous subdiffusion improved data description.

### Dye-labelled calretinin diffusion in granule cell dendrites

Having established a basic framework for diffusion in granule cells, we continued with FRAP experiments on dendrites loaded with a pipette solution that contained  $80 \mu\text{M}$  CR\* (Fig. 2A). The cells equilibrated with CR\* on timescales similar to the dextrans, i.e. cellular structures were clearly resolvable after  $\sim 15$  min loading time, indicating that CR\* had access to all cellular compartments. For FRAP recordings of CR\*, similar laser intensity protocols as for the FDs were used. Subsequently, data were quantified using the anomalous subdiffusion model (Fig. 2B). On average, the fits yielded an  $\alpha$ -value of 0.68 (IQR 0.52–0.95,  $n = 63$  from 18 cells) for CR\*, a value not different from the  $\alpha$ -values for the FDs ( $P > 0.7$ ; Fig. 2E). Thus, in addition to its independence of the molecular weight,  $\alpha$  is also independent of the nature of the diffusing particle, which is in accordance with the notion of  $\alpha$  as a structural parameter. By contrast, the median time-dependent diffusion coefficient at  $t = 10$  ms was remarkably low, being only  $3.2$  (IQR 1.6–5.9)  $\mu\text{m}^2 \text{s}^{-1}$  (Fig. 2C and E). This value is significantly smaller than  $D_{10\text{ms}}$  of 10 kDa FD ( $P < 0.001$ ) and even of 40 kDa FD ( $P < 0.001$ ), which has a higher molecular weight than CR\* ( $\sim 31.5$  kDa).

### Validation of dye-labelled calretinin fluorescence recovery after photobleaching

To exclude the possibility that the observed reduction in  $D_{10\text{ms}}$  of CR\* in comparison to the FDs is due to the labelling procedure or to agglomeration of the protein, CR\* purity was tested by SDS-gel electrophoresis (Fig. 3A) and by single-photon time-correlated FRAP recordings in a cuvette (Fig. 3B).

The gel electrophoresis resulted in clear, single bands for CR and CR\*, showing that in each case only one diffusing species was present and that the staining increased the mass of the protein only slightly and as expected. For time-correlated FRAP recordings, FDs of various sizes or CR\* ( $50 \mu\text{M}$  each) were dissolved in the intracellular solution and were measured independently (Fig. 3B). In cuvettes, the fluorescence recovery curves of FDs as well as of CR\* were well described by a 3D free Brownian diffusion model (Brown *et al.* 1999). The diffusional mobility of the molecules decreased with increasing molecular weight (Fig. 3C). The means  $\pm$  s.e.m. values for 3 kDa, 10 kDa,

40 kDa and 70 kDa were  $250 \pm 6$ ,  $141 \pm 1$ ,  $71 \pm 1$  and  $40 \pm 1 \mu\text{m}^2 \text{s}^{-1}$ , respectively. The logarithms of these data were well fitted by a straight line with a slope of  $-0.55$  when plotted against logarithms of their molecular weights (Fig. 3C), which is consistent with previous reports on aqueous diffusion of FDs (Arrio-Dupont *et al.* 1996). For CR\* the aqueous  $D$  was determined as  $120 \pm 1 \mu\text{m}^2 \text{s}^{-1}$  (means  $\pm$  s.e.m.). When introduced into the above log-log plot, this value falls close to the fitting line, with a deviation towards faster diffusion. The latter may be explained by differences between the tertiary structure of FDs and of CR\* but is in absolute contrast to the slowed cytoplasmic diffusion of CR\* in granule cell dendrites. Thus, these data indicate that the reduced dendritic CR\* mobility is neither due to impurities of CR\* nor to the labelling procedure or to other technical aspects.

### Dependence of dye-labelled calretinin diffusion on granule cell activity

The above data suggest that CR undergoes a specific, yet unidentified interaction in dendrites, i.e. CR could have characteristics of a  $\text{Ca}^{2+}$  sensor. For a  $\text{Ca}^{2+}$  sensor, such an interaction should depend on the intracellular  $\text{Ca}^{2+}$  concentration ( $[\text{Ca}^{2+}]_i$ ). To test for this sensor hypothesis, we analysed whether CR\* diffusion would be affected by an elevated  $[\text{Ca}^{2+}]_i$ .

Granule cells were loaded via a somatic patch pipette with  $50 \mu\text{M}$  of the  $\text{Ca}^{2+}$  indicator dye Oregon Green BAPTA-1 (OGB-1) and, as OGB-1 is dim at resting  $\text{Ca}^{2+}$  levels, additionally with  $50 \mu\text{M}$  of the red fluorescent,  $\text{Ca}^{2+}$  insensitive dye Atto-637. Collecting fluorescence from both dyes allowed resolving the cell morphology despite the low indicator concentration (Fig. 4A). Trains of action potentials were evoked by somatic step depolarization (Fig. 4B, upper panel) and resulted in an average firing frequency of  $96 \pm 20$  Hz (means  $\pm$  SD,  $n = 16$  cells). During action potential firing, the dendritic fluorescence increased (Fig. 4B, lower panel) and reached a plateau value of  $42 \pm 7\%$   $\Delta F/F_0$  within  $\sim 0.3$  s (means  $\pm$  s.e.m.,  $n = 6$  cells). This demonstrates that somatic APs are associated with a dendritic  $\text{Ca}^{2+}$  influx in granule cells, with amplitude and time course being consistent with previous reports from granule cells (Gall *et al.* 2005) as well as from pyramidal neurons (Helmchen *et al.* 1996). We performed numerical simulations (see Methods for details), to back-calculate the  $\text{Ca}^{2+}$  transient in the absence of OGB-1 and to estimate the corresponding fraction of  $\text{Ca}^{2+}$ -bound CR during the train. This simulation indicated that saturation of CR by  $\text{Ca}^{2+}$  increased from 4.7% under resting conditions to 11.7% during the plateau of the  $\text{Ca}^{2+}$  transient (Fig. 4C).

Next, CR\* FRAP recordings were performed during granule cell activation identical to the above but without

the dyes necessary for  $\text{Ca}^{2+}$  imaging (Fig. 4D). The bleach pulse was applied at a time when a stable elevation in  $[\text{Ca}^{2+}]_i$  and  $\text{Ca}^{2+}$ -saturated CR could be expected based on the imaging experiments and the simulation. Fitting the corresponding fluorescence recovery with the 1D anomalous subdiffusion model yielded a median  $D_{10\text{ms}}$  of 2.2 (IQR 1.2–4.0)  $\mu\text{m}^2\text{s}^{-1}$  ( $n = 56$  from 10 cells), a value significantly smaller than under resting conditions (Fig. 4E;  $P < 0.05$ ). In contrast, no change in the  $\alpha$ -value was observed ( $\alpha = 0.66$ , IQR 0.56–0.83, not shown). Control experiments performed with 10 kDa FD showed no effect of stimulation on either  $D_{10\text{ms}}$  (14.4  $\mu\text{m}^2\text{s}^{-1}$ , IQR 9.8–24.6  $\mu\text{m}^2\text{s}^{-1}$ ;  $n = 36$  from 9 cells) or  $\alpha$  (0.68, IQR 0.60–0.89), indicating that the calcium-dependent decrease in mobility is specific to CR (Fig. 4E).

### Identification of the binding site of calretinin

FRAP allows testing for specific binding sites by co-dialysing peptides that block the putative binding site and, thereby, accelerate the mobility of the protein (Schmidt *et al.* 2005). We reasoned that CR's EF-hand 5 could represent a likely candidate region for interaction with other proteins. As no structural data are currently available for CR, we compared the structures of the related hexa-EF-hand CaBPs, calbindin D-28k (Kojetin *et al.* 2006) and secretagogin (Bitto *et al.* 2009). In both proteins, EF-hand domains 1–4 form relatively compact structures insulated from EF-hand 5 by the non-functional EF-hand 6. EF-hand 5, which is highly conserved between mice, rats and humans (94% identity at the amino acid level), has a rather low  $\text{Ca}^{2+}$  affinity of  $\sim 36 \mu\text{M}$

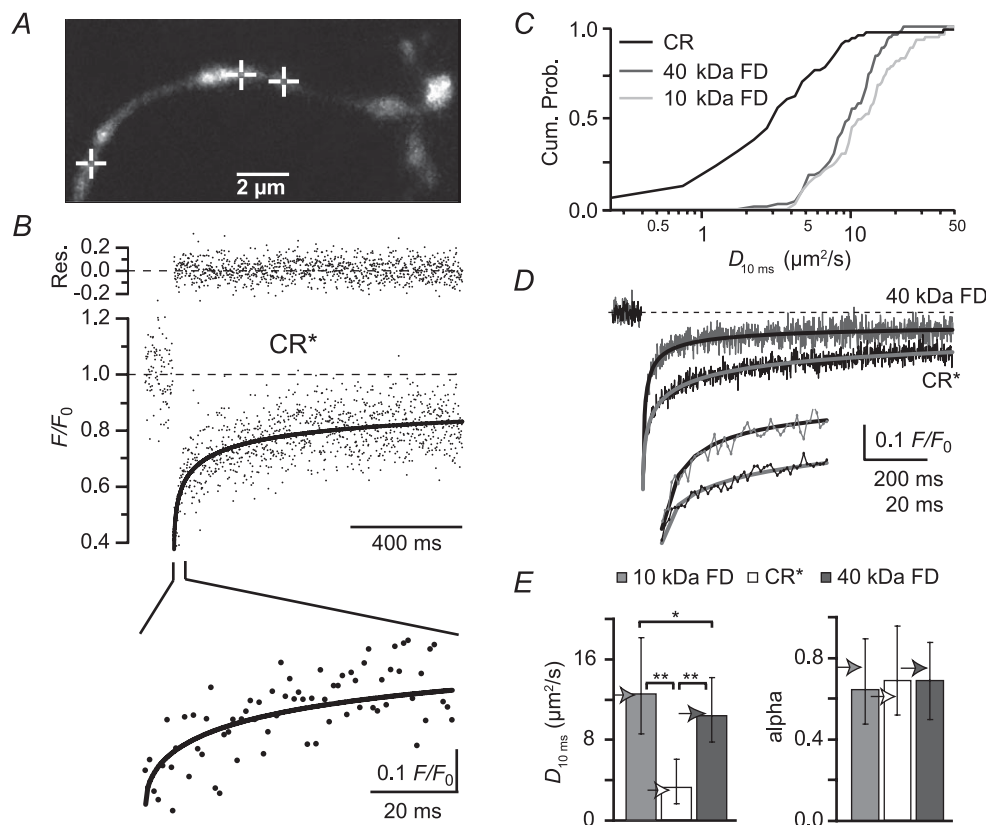


**Figure 2. Reduced mobility of CR in granule cells**

A, granule cell dendrite loaded with  $80 \mu\text{M}$  of CR\* via a somatic patch pipette. The cross-hairs mark the spots at which FRAP experiments were performed. B, average of three FRAP recordings from the points indicated in A. The black line represents a fit by the subdiffusion equation. In the top line, the residuals (measured values – fit values) are shown. The lower panel shows the initial recovery expanded in time. C, cumulative probability histograms of time-dependent  $D$  values at 10 ms ( $D_{10\text{ms}}$ ). D, grand averages of FRAP recordings from different cells but with similar bleach depth (45–55%) obtained with 40 kDa FD (grey,  $n = 31$  from 10 cells) and CR\* (black,  $n = 25$  from six cells), fitted with the anomalous subdiffusion equation (continuous lines). The lower panel shows the initial recoveries expanded in time. E, values of  $D_{10\text{ms}}$  and anomalous subdiffusion coefficients (alpha) for 10 and 40 kDa FD and CR\*, as indicated ( $n = 69$  FRAP measurements from 24 cells for 10 kDa FD,  $n = 69$  from 23 cells for 40 kDa FD, and  $n = 63$  from 18 cells for CR\*). The arrowheads indicate the values obtained by fitting the grand averages for 40 kDa FD and CR\* (as in D) and for 10 kDa FD ( $n = 39$  from 10 cells). Note that the molecular weight of CR\* is  $\sim 31.5$  kDa. \* $P < 0.05$ , \*\* $P < 0.001$ . CR, calretinin; CR\*, dye-labelled CR; FD, fluorescein dextrans; FRAP, fluorescence recovery after photobleaching.

(Faas *et al.* 2007) to  $\sim 500 \mu\text{M}$  (Schwaller *et al.* 1997), and is freely accessible to the aqueous environment, rendering it a likely interaction site. We synthesized a peptide embracing mouse EF-hand 5 and a small part of the 5/6 linker region (Fig. 4C). When co-dialysed with CR\* into granule cells, FRAP recordings revealed a significantly increased mobility of CR with  $D_{10\text{ms}}$  of  $7.7 \mu\text{m}^2 \text{s}^{-1}$  (IQR  $4.1\text{--}12.4 \mu\text{m}^2 \text{s}^{-1}$ ;  $n = 92$  from 17 cells) without affecting  $\alpha$  ( $0.59$ , IQR  $0.42\text{--}0.84$ ) (Fig. 4F). This was a specific effect of the EF-hand 5 peptide as a scrambled peptide (Fig. 4G) did not affect CR's mobility ( $D_{10\text{ms}} = 2.3 \mu\text{m}^2 \text{s}^{-1}$  (IQR  $1.4\text{--}5.0 \mu\text{m}^2 \text{s}^{-1}$ ;  $\alpha = 0.69$ , IQR  $0.55\text{--}0.96$ ;  $n = 76$  from seven cells).

## Discussion

Using two-photon FRAP we analysed the mobility of CR in granule cell dendrites. We found that anomalous subdiffusion better describes the movement of macromolecules (inert tracers and CR) than free diffusion and that the movement of CR, the main  $\text{Ca}^{2+}$  buffer expressed in granule cells, is further hindered by specific interactions with yet unidentified binding partners. The interaction is most likely mediated by the EF-hand 5 region of CR and enhanced by  $\text{Ca}^{2+}$  binding of EF-hands 1–4, indicating that CR acts as a  $\text{Ca}^{2+}$  sensor in granule cells.

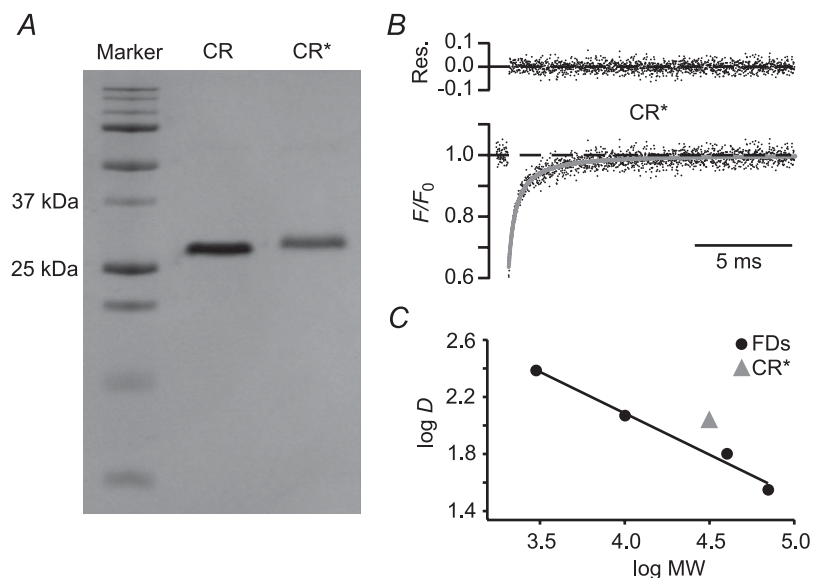
Despite an increasing amount of observations of anomalous subdiffusion (Klafter & Sokoov, 2005), its physical importance is not well understood and distinct mechanisms may underlay this phenomenon. Anomalous subdiffusion has been shown to occur when diffusing molecules are temporarily trapped. Trapping can be due to molecular interactions (Feder *et al.* 1996; Saxton, 1996, 2001; Luby-Phelps, 2000) or to morphological constraints (Santamaria *et al.* 2006, 2011), which delay diffusion in a

time-dependent manner (cf. eqn (4)). The trapping has to operate on a timescale similar to diffusion to induce subdiffusion. Substantially longer-lasting interactions induce fixed offsets in the FRAP curves (Schmidt *et al.* 2005), while shorter-lasting interactions lead to slowed but otherwise normal diffusion (Sprague & McNally, 2005). However, it is often difficult to distinguish between the various diffusion regimes, in particular since IF and the subdiffusion coefficient  $\alpha$  can have a dependency on each other (Feder *et al.* 1996). The use of inert tracer dyes, therefore, is of crucial importance to clarify the diffusion regime applicable for the solute of interest (Sprague & McNally, 2005).

The prevalence and the significance of anomalous diffusion are only slowly emerging (Klafter & Sokoov, 2005). For diffusion over longer stretches of spiny dendrites of Purkinje cells, spines act as molecular traps and cause diffusion to become anomalous (Santamaria *et al.* 2006, 2011). In the same cell type, diffusion of inert tracer dyes can be described by normal diffusion when analysed in smooth dendrites (Santamaria *et al.* 2006), in axons (Schmidt *et al.* 2007a), or between single spines and their parent dendrite (Schmidt *et al.* 2003a, 2005). Within the cytosol of Purkinje cells, therefore, normal diffusion prevails, arguing against other than morphological constraints to hinder diffusion in Purkinje cells (Santamaria *et al.* 2011). On the other hand, diffusion of green fluorescent protein in somata of rat basophilic leucemia (RBL) cells is anomalous (Brown *et al.* 1999) while diffusion of dextrans and parvalbumin is normal in somata of Purkinje cells (Schmidt *et al.* 2007a), indicating molecule- and/or cell type-specific differences in diffusional mobility. To the best of our knowledge, our dextran data (Fig. 1) represent the first example of anomalous subdiffusion

### Figure 3. CR\* diffusion *in vitro*

A, SDS-gel of native and CR\* (CR and CR\*, respectively). MW markers are shown in the left lane: 10, 15, 20, 25, 37, 50, 75, 100, 150 and 250 kDa from bottom to top. B, aqueous fluorescence recovery after photobleaching time course of CR\* dissolved in pipette solution in a cuvette (average of 2500 individual recordings) and a fit to a three-dimensional, normal diffusion equation (grey line; top: residuals). C, logarithms of the mean aqueous  $D$  values of CR\*, 3 kDa, 10 kDa, 40 kDa and 70 kDa FD plotted against the logarithms of their MW. Four experiments each. S.E.M. values are smaller than the markers. Linear regression to the dextran data yielded a slope of  $-0.55$ . CR, calretinin; CR\*, dye-labelled CR; FD, fluorescein dextrans; MW, molecular weight; Res., residuals.



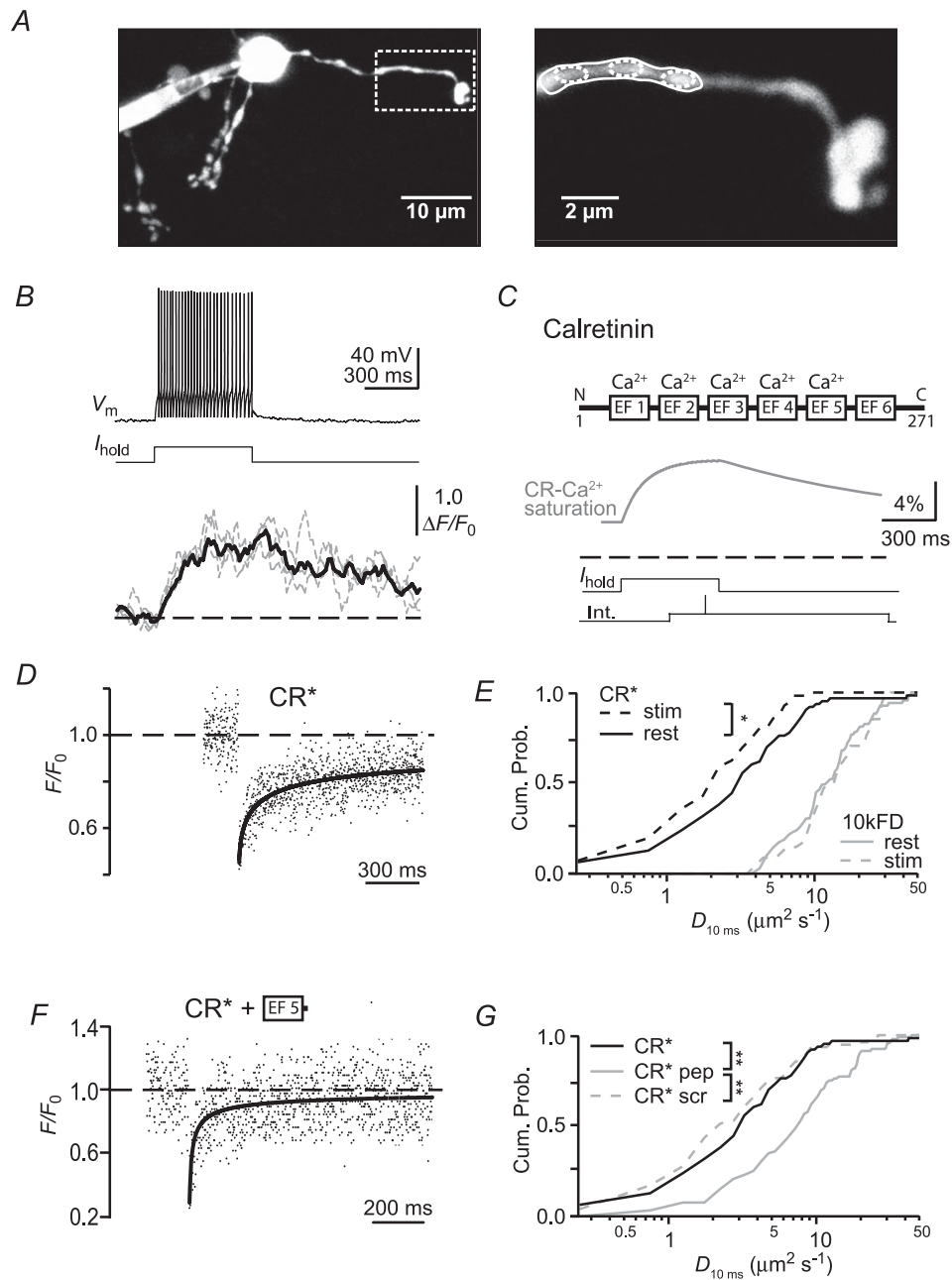


#### Figure 4. Decreased mobility of CR\* during neuronal activity

**A**, left: a granule cell loaded with  $50 \mu\text{M}$  OGB-1 and  $50 \mu\text{M}$  Atto-637 via a somatic patch pipette. The box delineates the dendritic region (shown magnified on the right) from which the fluorescence signals in **B** were recorded. The corresponding regions of interest are denoted by solid and dashed ellipses. **B**, top: voltage response ( $V_m$ ) to a somatic current injection ( $I_{\text{hold}}$ ) of the granule cell shown in **A**. Bottom: associated relative fluorescence increases of OGB-1 ( $\Delta F/F_0$ ) recorded from the dendritic regions indicated by the small dashed (grey traces) and large solid ellipses (black trace) in **A**. **C**, scheme of CR (upper panel) with the EF-hands of which five bind  $\text{Ca}^{2+}$  (Schwaller *et al.* 1997). The N- and C-terminals as well as the numbering of the amino acids are indicated. The lower panel shows a numerical simulation of CR's  $\text{Ca}^{2+}$  saturation during the average action potential train in the absence of indicator dye. The dashed line indicates 0% saturation. The resting saturation is 4.7%. The two bottom traces illustrate the experimental approach for FRAP recordings during action potential firing. **D**, FRAP time course of CR\* during repetitive firing (average of six recordings). The continuous line represents a fit of the recovery to the subdiffusion equation. **E**, cumulative probability graph of  $D_{10\text{ms}}$  values under control conditions ('CR\* rest', '10 kDa FD rest'; data from Fig. 2C) and during action potential firing ('CR\* stim';  $n = 56$  recordings from 10 cells;

occurring in aspiny dendrites. Data from aspiny dendrites of neocortical interneurons (Goldberg *et al.* 2003) and cerebellar stellate cells (Soler-Llavina & Sabatini, 2006) make it unlikely that morphological constraints delay diffusion. In consequence, transient trapping by interactions with large and/or immobile molecules could be responsible for anomalous diffusion (Saxton, 1996). For an inert tracer such as FD as well as for proteins, electrostatic interactions may represent a probable explanation. Further experimentation, however, will be required to identify the factors inducing anomalous diffusion in dendrites and somata.

CR diffused unexpectedly slowly in granule cells, especially when compared to dextrans of similar molecular weight (Fig. 2C and E). Typically, proteins diffuse faster than dextrans (Fig. 3C), most likely due to their different tertiary structure (Arrio-Dupont *et al.* 1996). In Purkinje cells, for example, the observed diffusion coefficient for parvalbumin is  $\sim 1.4$  times larger than that expected for a dextran of comparable size (Schmidt *et al.* 2003a). We attribute CR's low mobility to an interaction with yet unidentified intracellular binding partners.

Depending on the endogenous concentration of CR ( $[CR]_{\text{endo}}$ ), we may have over- or underestimated the retardation of CRs mobility. If  $[CR]_{\text{endo}}$  would be substantially higher than our estimate of  $80 \mu\text{M}$ , saturation of binding partners may occur in unperturbed cells, leading to a higher average mobility. If, on the other hand,  $[CR]_{\text{endo}}$  would be substantially lower (and if binding partners are already substantially saturated at  $80 \mu\text{M}$ ), we may have underestimated CR's mobility. However, given the quantitative data on the endogenous  $\text{Ca}^{2+}$ -binding capacity of granule cells (Brenowitz & Regehr, 2007), for which CR is the only endogenous  $\text{Ca}^{2+}$  buffer expressed at a relevant concentration (Schiffmann *et al.* 1999), and given the  $\text{Ca}^{2+}$ -binding kinetics of CR (Faas *et al.* 2007), we consider  $80 \mu\text{M}$  to represent the most likely value, or at least an upper limit of  $[CR]_{\text{endo}}$ . In line with this assumption, we could recently show that this CR concentration maximizes the overlap between simulations and  $\text{Ca}^{2+}$  imaging data as well as electrophysiological recordings from wild-type and CR-deficient mice (Schmidt *et al.* 2013).

Irrespective of the stoichiometry, the binding partners must be of considerable size and/or they must be immobilized to explain the substantial immobilization they exert on CR. Interestingly, CR has been shown to be associated with membranes (Winsky & Kúznicki, 1995;

Hack *et al.* 2000) and to regulate voltage-gated  $\text{Ca}^{2+}$  channels (Christel *et al.* 2012). However, the expected dendritic channel density is too low to convey a substantial retardation of  $\mu\text{M}$  amounts of CR, therefore additional targets need to be considered, such as interactions with cytoskeletal or cytoskeletal-associated elements (Marilley & Schwaller, 2000).

Independent of the identity of the target, we suggest EF-hand 5 as the likely interaction site of CR (Fig. 4F and G). EF-hand 5 has a rather low  $\text{Ca}^{2+}$  affinity ( $\sim 36 \mu\text{M}$ , Faas *et al.* 2007), rendering it important for buffering  $\text{Ca}^{2+}$  close to the mouth of open  $\text{Ca}^{2+}$  channels (Schmidt *et al.* 2013) but poorly suited to affect the low-amplitude  $\text{Ca}^{2+}$  dynamics occurring within dendrites and somata.

Characteristic for a  $\text{Ca}^{2+}$  sensor are conformational changes upon  $\text{Ca}^{2+}$  binding, which enable interaction with binding partners (da Silva & Reinach, 1991; Ikura, 1996). Such conformational changes were found for rat and for human CR upon  $\text{Ca}^{2+}$  binding *in vitro* (Kúznicki *et al.* 1995a,b; Schwaller *et al.* 1997). Furthermore, Winsky and Kúznicki (1995) demonstrated a  $\text{Ca}^{2+}$ -dependent interaction of CR with a brain membrane fraction *in vitro* and Hack *et al.* (2000) showed for chick auditory brainstem neurons that CR gets concentrated beneath the plasma membrane during postnatal development. Our data suggest that EF-hand 5 acquired an additional function as an interacting site. As CR's mobility is reduced by submicromolar  $\text{Ca}^{2+}$  and as EF-hand 6 is non-functional (Schwaller *et al.* 1997),  $\text{Ca}^{2+}$  binding by EF-hands 1–4 (Faas *et al.* 2007) is proposed to allosterically affect the EF-hand 5 region.

It cannot be excluded that the labelling procedure affected the spatial structure of CR and, therefore, its molecular interactions, because this possibility is an inherent and at present unavoidable problem of any labelling procedure. Yet, because of the small size of the fluorescent label and because our procedure led to a preferential labelling of the  $\alpha$ -amino group, which is at the opposite site of the proposed interaction site, we consider it unlikely that the labelling strongly affected CR's tertiary structure and, thereby, induced the specific binding via EF-hand 5.

In other  $\text{Ca}^{2+}$  sensor proteins of the EF-hand family, e.g. the neuronal  $\text{Ca}^{2+}$  sensor subfamily,  $\text{Ca}^{2+}$ -dependent immobilization is caused by the 'myristoyl switch', where a myristoyl group attached to an amino acid in the N-terminal region is inserted in the plasma membrane

\* $P < 0.05$  and '10 kDa FD\* stim';  $n = 36$  recordings from nine cells). *F*, FRAP time course of CR\* in the presence of peptide resembling EF-hand 5 of CR, the putative interaction site. The continuous line represents a fit of the recovery to the subdiffusion equation. Note the accelerated recovery compared to Fig. 2B. *G*, cumulative probability histograms of  $D_{10\text{ms}}$  values under control conditions (CR\*; as in 2C) or in the presence of peptide representing EF-hand 5 of CR ('pep';  $n = 92$  recordings from 17 cells) or a scrambled peptide ('scr';  $n = 76/7$ ). \*\* $P < 0.001$ . CR, calretinin; CR\*, dye-labelled CR; FD, fluorescein dextrans.

caused by a  $\text{Ca}^{2+}$ -dependent conformational change of the protein (Spilker & Braunewell, 2003; Burgoyne, 2004). We hypothesize that the low-affinity EF-hand 5 represents another way of transiently immobilizing a CaBP (CR) to specific targets. Thus, in light of our findings CR, initially considered as a conventional mobile  $\text{Ca}^{2+}$  buffer, has to be viewed as an immobilizable neuronal  $\text{Ca}^{2+}$  sensor. Whether the effects of immobilized CR are linked to its  $\text{Ca}^{2+}$ -binding properties or to modulation of CR targets remains to be determined. Identifying CR's specific binding partners, possibly also differing in various CR-expressing subpopulations will be of importance in understanding the physiological significance behind CR's cell type-specific expression in the CNS.

## References

- Allbritton NL, Meyer T & Stryer L (1992). Range of messenger action of calcium ion and inositol 1,4,5-trisphosphate. *Science* **258**, 1812–1815.
- Arai R, Winsky L, Arai M & Jacobowitz DM (1991). Immunohistochemical localization of calretinin in the rat hindbrain. *J Comp Neurol* **310**, 21–44.
- Arrio-Dupont M, Cribier S, Foucault G, Devaux PF & d'Albis A (1996). Diffusion of fluorescently labeled macromolecules in cultured muscle cells. *Biophys J* **70**, 2327–2332.
- Axelrod D, Koppel DE, Schlessinger J, Elson E & Webb WW (1976). Mobility measurement by analysis of fluorescence photobleaching recovery kinetics. *Biophys J* **16**, 1055–1069.
- Bitto E, Bingman CA, Bittova L, Frederick RO, Fox BG & Phillips GN (2009). X-ray structure of Danio rerio secretagoin: A hexa-EF-hand calcium sensor. *Proteins* **76**, 477–483.
- Bouchaud JP & Georges A (1990). Anomalous diffusion in disordered media – statistical mechanisms, models and physical applications. *Phys Rep* **195**, 127–293.
- Braitenberg V & Atwood RP (1958). Morphological observations on the cerebellar cortex. *J Comp Neurol* **109**, 1–33.
- Brenowitz SD & Regehr WG (2007). Reliability and heterogeneity of calcium signaling at single presynaptic boutons of cerebellar granule cells. *J Neurosci* **27**, 7888–7898.
- Brown EB, Wu ES, Zipfel W & Webb WW (1999). Measurement of molecular diffusion in solution by multiphoton fluorescence photobleaching recovery. *Biophys J* **77**, 2837–2849.
- Burgoyne RD (2004). The neuronal calcium-sensor proteins. *Biochim Biophys Acta* **1742**, 59–68.
- Christel CJ, Schaefer R, Wang S, Henzi T, Kreiner L, Grabs D, Schwaller B & Lee A (2012). Calretinin regulates  $\text{Ca}^{2+}$ -dependent inactivation and facilitation of  $\text{Ca}_v2.1$   $\text{Ca}^{2+}$  channels through a direct interaction with the  $\alpha_12.1$  subunit. *J Biol Chem* **287**, 39766–39775.
- da Silva AC & Reinach FC (1991). Calcium binding induces conformational changes in muscle regulatory proteins. *Trends Biochem Sci* **16**, 53–57.
- Eccles JC, Ito M & Szentagothai J (1967). *The cerebellum as a neuronal machine*. Springer, Berlin.
- Faas GC, Schwaller B, Vergara JL & Mody I (2007). Resolving the fast kinetics of cooperative binding:  $\text{Ca}^{2+}$  buffering by calretinin. *PLoS Biol* **5**, e311.
- Feder TJ, Brust-Mascher I, Slattery JP, Baird B & Webb WW (1996). Constrained diffusion or immobile fraction on cell surfaces: a new interpretation. *Biophys J* **70**, 2767–2773.
- Felmy F & Schneggenburger R (2004). Developmental expression of the  $\text{Ca}^{2+}$ -binding proteins calretinin and parvalbumin at the calyx of held of rats and mice. *Eur J Neurosci* **20**, 1473–1482.
- Gall D, Roussel C, Susa I, D'Angelo E, Rossi P, Bearzatto B, Galas MC, Blum D, Schurmans S & Schiffmann SN (2003). Altered neuronal excitability in cerebellar granule cells of mice lacking calretinin. *J Neurosci* **23**, 9320–9327.
- Gall D, Prestori F, Sola E, D'Errico A, Roussel C, Forti L, Rossi P & D'Angelo E (2005). Intracellular calcium regulation by burst discharge determines bidirectional long-term synaptic plasticity at the cerebellum input stage. *J Neurosci* **25**, 4813–4822.
- Goldberg JH, Tamas G, Aronov D & Yuste R (2003). Calcium microdomains in aspiny dendrites. *Neuron* **40**, 807–821.
- Hack NJ, Wride MC, Charters KM, Kater SB & Parks TN (2000). Developmental changes in the subcellular localization of calretinin. *J Neurosci* **20**, RC67(61–65).
- Helmchen F, Imoto K & Sakmann B (1996).  $\text{Ca}^{2+}$  buffering and action potential-evoked  $\text{Ca}^{2+}$  signaling in dendrites of pyramidal neurons. *Biophys J* **70**, 1069–1081.
- Ikura M (1996). Calcium binding and conformational response in EF-hand proteins. *Trends Biochem Sci* **21**, 14–17.
- Ito M (1984). *The cerebellum and neuronal control*. Raven Press, New York.
- Klafter J & Sokoov I (2005). Anomalous diffusion spreads its wing. *Physics World* **August**, 29–32.
- Kojetin DJ, Venters RA, Kordys DR, Thompson RJ, Kumar R & Cavanagh J (2006). Structure, binding interface and hydrophobic transitions of  $\text{Ca}^{2+}$ -loaded calbindin-D28K. *Nat Struct Mol Biol* **13**, 641–647.
- Kúznicki J, Strauss KI & Jacobowitz DM (1995a). Conformational changes and calcium binding by calretinin and its recombinant fragments containing different sets of EF hand motifs. *Biochemistry* **34**, 15389–15394.
- Kúznicki J, Wang TL, Martin BM, Winsky L & Jacobowitz DM (1995b). Localization of  $\text{Ca}^{2+}$ -dependent conformational changes of calretinin by limited tryptic proteolysis. *Biochem J* **308**, 607–612.
- Luby-Phelps K (2000). Cytoarchitecture and physical properties of cytoplasm: volume, viscosity, diffusion, intracellular surface area. *Int Rev Cytol* **192**, 189–221.
- Luby-Phelps K, Lanni F & Taylor DL (1985). Behavior of a fluorescent analogue of calmodulin in living 3T3 cells. *J Cell Biol* **101**, 1245–1256.
- Luby-Phelps K, Hori M, Phelps JM & Won D (1995).  $\text{Ca}^{2+}$ -regulated dynamic compartmentalization of calmodulin in living smooth muscle cells. *J Biol Chem* **270**, 21532–21538.
- Marilley D & Schwaller B (2000). Association between the calcium-binding protein calretinin and cytoskeletal components in the human colon adenocarcinoma cell line WiDr. *Exp Cell Res* **259**, 12–22.

- Ölveczky BP & Verkman AS (1998). Monte Carlo analysis of obstructed diffusion in three dimensions: application to molecular diffusion in organelles. *Biophys J* **74**, 2722–2730.
- Reits EA & Neefjes JJ (2001). From fixed to FRAP: measuring protein mobility and activity in living cells. *Nat Cell Biol* **3**, E145–147.
- Resibois A & Rogers JH (1992). Calretinin in rat brain: an immunohistochemical study. *Neuroscience* **46**, 101–134.
- Rogers JH (1989). Immunoreactivity for calretinin and other calcium-binding proteins in cerebellum. *Neuroscience* **31**, 711–721.
- Santamaria F, Wils S, De Schutter E & Augustine GJ (2006). Anomalous diffusion in Purkinje cell dendrites caused by spines. *Neuron* **52**, 635–648.
- Santamaria F, Wils S, De Schutter E & Augustine GJ (2011). The diffusional properties of dendrites depend on the density of dendritic spines. *Eur J Neurosci* **34**, 561–568.
- Saxton MJ (1996). Anomalous diffusion due to binding: a Monte Carlo study. *Biophys J* **70**, 1250–1262.
- Saxton MJ (2001). Anomalous subdiffusion in fluorescence photobleaching recovery: a Monte Carlo study. *Biophys J* **81**, 2226–2240.
- Saxton MJ & Jacobson K (1997). Single-particle tracking: applications to membrane dynamics. *Annu Rev Biophys Biomol Struct* **26**, 373–399.
- Sbalzarini IF, Mezzacasa A, Helenius A & Koumoutsakos P (2005). Effects of organelle shape on fluorescence recovery after photobleaching. *Biophys J* **89**, 1482–1492.
- Schiffmann SN, Cheron G, Lohof A, D'Alcantara P, Meyer M, Parmentier M & Schurmans S (1999). Impaired motor coordination and Purkinje cell excitability in mice lacking calretinin. *Proc Natl Acad Sci U S A* **96**, 5257–5262.
- Schmidt H, Brown EB, Schwaller B & Eilers J (2003a). Diffusional mobility of parvalbumin in spiny dendrites of cerebellar Purkinje neurons quantified by fluorescence recovery after photobleaching. *Biophys J* **84**, 2599–2608.
- Schmidt H, Stiefel K, Racay P, Schwaller B & Eilers J (2003b). Mutational analysis of dendritic Ca<sup>2+</sup> kinetics in rodent Purkinje cells: role of parvalbumin and calbindin D28k. *J Physiol* **551**, 13–32.
- Schmidt H, Schwaller B & Eilers J (2005). Calbindin D28k targets *myo*-inositol monophosphatase in spines and dendrites of cerebellar Purkinje neurons. *Proc Natl Acad Sci U S A* **102**, 5850–5855.
- Schmidt H, Arendt O, Brown EB, Schwaller B & Eilers J (2007a). Parvalbumin is freely mobile in axons, somata and nuclei of cerebellar Purkinje neurons. *J Neurochem* **100**, 737–735.
- Schmidt H, Kunerth S, Wilms C, Strotmann R & Eilers J (2007b). Spino-dendritic crosstalk in rodent Purkinje neurons mediated by endogenous Ca<sup>2+</sup>-binding proteins. *J Physiol* **581**, 619–629.
- Schmidt H, Brachtendorf S, Arendt O, Hallermann S, Ishiyama S, Bornschein G, Gall D, Schiffmann SN, Heckmann M & Eilers J (2013). Nanodomain coupling at an excitatory cortical synapse. *Curr Biol* **23**, 244–249.
- Schwaller B (2009). The continuing disappearance of 'pure' Ca<sup>2+</sup> buffers. *Cell Mol Life Sci* **66**, 275–300.
- Schwaller B, Durussel I, Jermann D, Herrmann B & Cox JA (1997). Comparison of the Ca<sup>2+</sup>-binding properties of human recombinant calretinin-22k and calretinin. *J Biol Chem* **272**, 29663–29671.
- Schwaller B, Meyer M & Schiffmann S (2002). 'New' functions for 'old' proteins: the role of the calcium-binding proteins calbindin D-28k, calretinin and parvalbumin, in cerebellar physiology. Studies with knockout mice. *Cerebellum* **1**, 241–258.
- Soler-Llavina GJ & Sabatini BL (2006). Synapse-specific plasticity and compartmentalized signaling in cerebellar stellate cells. *Nat Neurosci* **9**, 798–806.
- Spilker C & Braunewell KH (2003). Calcium-myristoyl switch, subcellular localization, and calcium dependent translocation of the neuronal calcium sensor protein VILIP-3, and comparison with VILIP-1 in hippocampal neurons. *Mol Cell Neurosci* **24**, 766–778.
- Sprague BL & McNally JG (2005). FRAP analysis of binding: proper and fitting. *Trends Cell Biol* **15**, 84–91.
- Star EN, Kwiatkowski DJ & Murthy VN (2002). Rapid turnover of actin in dendritic spines and its regulation by activity. *Nat Neurosci* **5**, 239–246.
- Sullivan K & Brown E (2011). Multiphoton fluorescence recovery after photobleaching in bounded systems. *Phys Rev E Stat Nonlin Soft Matter Phys* **83**, 051916.
- Svoboda K, Tank DW & Denk W (1996). Direct measurement of coupling between dendritic spines and shafts. *Science* **272**, 716–719.
- Weiss M, Elsner M, Kartberg F & Nilsson T (2004). Anomalous subdiffusion is a measure for cytoplasmic crowding in living cells. *Biophys J* **87**, 3518–3524.
- Winsky L & Kúznicki J (1995). Distribution of calretinin, calbindin D28k, and parvalbumin in subcellular fractions of rat cerebellum: effects of calcium. *J Neurochem* **65**, 381–388.

## Additional information

### Competing interests

None.

### Author contributions

Conception and design of the experiments: H.S. and J.E.; collection, analysis and interpretation of data: O.A., B.S., E.B.B., H.S. and J.E.; drafting and revising the manuscript: O.A., B.S., E.B.B., H.S. and J.E. All authors approved the final version of the manuscript.

### Funding

This work was supported by grants to J.E. and H.S. (DFG, EI 342/4), to E.B. (NIH 1DP2OD00650-01 and DoD BCRP W81XWH-09-1-0405) and to B.S. (SFN no. 130680).

### Acknowledgements

We thank Gudrun Bethge for technical assistance.



# HHS Public Access

Author manuscript

*J Bone Miner Res.* Author manuscript; available in PMC 2015 October 24.

Published in final edited form as:

*J Bone Miner Res.* 2015 July ; 30(7): 1217–1230. doi:10.1002/jbmr.2460.

## Spatiotemporal Analyses of Osteogenesis and Angiogenesis via Intravital Imaging in Cranial Bone Defect Repair

Chunlan Huang<sup>1</sup>, Vincent P. Ness<sup>1</sup>, Xiaochuan Yang<sup>1</sup>, Hongli Chen<sup>1</sup>, Jiebo Luo<sup>3</sup>, Edward B Brown<sup>2</sup>, and Xinping Zhang<sup>1</sup>

<sup>1</sup>Center for Musculoskeletal Research, University of Rochester, School of Medicine and Dentistry, Rochester, NY 14642, USA

<sup>2</sup>Department of Biomedical Engineering, University of Rochester, Rochester, NY14642, USA

<sup>3</sup>Department of Computer Science, University of Rochester, Rochester, NY14642, USA

### Abstract

Osteogenesis and angiogenesis are two integrated components in bone repair and regeneration. A deeper understanding of osteogenesis and angiogenesis has been hampered by technical difficulties of analyzing bone and neovasculature simultaneously in spatiotemporal scales and in three-dimensional formats. To overcome these barriers, a cranial defect window chamber model was established that enabled high-resolution, longitudinal, and real-time tracking of angiogenesis and bone defect healing via Multiphoton Laser Scanning Microscopy (MPLSM). By simultaneously probing new bone matrix via second harmonic generation (SHG), neovascular networks via intravenous perfusion of fluorophore, and osteoblast differentiation via 2.3kb collagen type I promoter driven GFP (Col2.3GFP), we examined the morphogenetic sequence of cranial bone defect healing and further established the spatiotemporal analyses of osteogenesis and angiogenesis coupling in repair and regeneration. We demonstrated that bone defect closure was initiated in the residual bone around the edge of the defect. The expansion and migration of osteoprogenitors into the bone defect occurred during the first 3 weeks of healing, coupled with vigorous microvessel angiogenesis at the leading edge of the defect. Subsequent bone repair was marked by matrix deposition and active vascular network remodeling within new bone. Implantation of bone marrow stromal cells (BMSCs) isolated from Col2.3GFP mice further showed that donor-dependent bone formation occurred rapidly within the first 3 weeks of implantation, in concert with early angiogenesis. The subsequent bone wound closure was largely host-dependent, associated with localized modest induction of angiogenesis. The establishment of a live imaging platform via cranial window provides a unique tool to understand osteogenesis and angiogenesis in repair and regeneration, enabling further elucidation of the spatiotemporal regulatory mechanisms of osteoprogenitor cell interactions with host bone healing microenvironment.

---

Corresponding author contact information: Dr. Xinping Zhang, The Center for Musculoskeletal Research, University of Rochester Medical Center, 601 Elmwood Avenue, Rochester, NY 14642, USA, [Xinping\\_Zhang@URMC.rochester.edu](mailto:Xinping_Zhang@URMC.rochester.edu).

**AUTHOR CONTRIBUTION:** Conceived and designed the experiments: XPZ. Performed the surgery: CH XCY HC. Performed imaging and image analyses: XPZ VN JL EB. Wrote the paper and/or contributed to writing: XPZ EB JL.

## Keywords

osteogenesis; angiogenesis; intravital imaging; BMSC; cranial defect repair

---

## INTRODUCTION

Bone defect healing is a dynamic progenitor cell-driven tissue morphogenetic process that requires coordinated osteogenesis and angiogenesis at the site of repair (1,2). The coordination between osteogenesis and angiogenesis is thought to be achieved by the complex interplay of auto- and paracrine factors produced by osteoblasts, endothelial cells and their precursors (3,4). While the essential role of osteogenesis and angiogenesis in bone defect repair has been established, the molecular and cellular interplay between bone forming and vessel forming cells has yet to be fully elucidated. Furthermore, due to the lack of an animal model that permits real-time, longitudinal, and high resolution analyses of osteogenesis and angiogenesis, our understanding of the spatiotemporal regulation of osteogenesis and angiogenesis during defect repair remains extremely limited. Since bone defect repair is a dynamic process controlled at multiple spatial and temporal scales, establishing the capability to analyze osteoprogenitor cell dynamics and their interaction with neovasculature is crucial for advancing our understanding of bone defect repair and for further optimizing material-based approaches to orchestrating spatiotemporal delivery of single or multiple cues capable of instructing both host and donor cells for improved bone defect reconstruction (5).

Multiphoton laser scanning microscopy (MPLSM) has emerged as a superior *in vivo* imaging modality for analyses of thick tissues in living animals (6,7). The key advantages of MPLSM include confocal-like imaging quality, reduced photo-damage, and enhanced imaging depth. Multiphoton microscopy further permits morphological and functional analyses of neovasculature with benefits of high spatiotemporal resolution, minimal invasiveness and 3D capability (8–11). In addition to imaging nonlinear fluorescence excitation, multiphoton microscopy can also be used for imaging bone matrix through second harmonic generation (SHG) (12,13). The unique capability of this technology that allows simultaneous visualization of cells, ECM, as well as the surrounding vascular networks, offers a superior imaging modality for dynamic, real-time and simultaneous analyses of osteogenesis and angiogenesis in bone tissue repair and regeneration.

The goal of our current study was to establish a MPLSM-based live imaging platform for real-time, non-destructive, and high resolution analyses of osteogenesis and angiogenesis in bone defect repair and regeneration. Utilizing a cranial defect window chamber model and an osteogenic-specific promoter-driven GFP reporter mouse model (Col2.3GFP), we demonstrated for the first time the spatiotemporal analysis of defect healing and osteogenesis and angiogenesis coupling at the site of cranial bone defect repair and regeneration. Our study highlighted the coordinated interactions between osteogenic and angiogenic compartments during repair and regeneration, further validating the use of MPLSM combined with the cranial defect window chamber model as a unique and novel tool for understanding bone defect repair and for delineating the molecular and cellular

interactions of the osteogenesis and angiogenesis coupling in bone defect repair and reconstruction.

## MATERIALS AND METHODS

### Animals and reagents

Col2.3GFP transgenic mice were purchased from the Jackson Laboratory (Bar Harbor, Maine). NestinGFP mice were kindly provided by Dr. Grigori N. Enikolopov at Cold Spring Harbor Laboratories (14,15). Immunocompromised mice (bg-nu/nu-xid) were purchased from Harlan Sprague Dawley Inc. All surgical interventions were approved by the Institutional Animal Care and Use Committee at the University of Rochester.

### Cranial defect window chamber model

The cranial window chamber model in mice has been previously reported for analyses of brain cell function and tumor-associated neovascularization (16,17). The model was further modified to meet the need for long-term tracking of defect healing via intravital imaging. Briefly, the surgical mouse was anesthetized with a mixture of Ketamine and Xylazine and placed on a stereotaxic frame (Stoelting Co. Wood Dale, IL) for microsurgery. To create a window chamber, a custom-made 0.5 mm-thick spacer made of poly (aryl-ether-ether-ketone) (PEEK) was glued onto skull using cyanoacrylate glue (Loctite, Cat #45404). The defect region was carefully exposed through a circular 6 mm (diameter) opening at the center of the spacer. A full thickness defect was created in the parietal bone of mouse calvarium using a tungsten vanadium inverted cone bur (Armstrong Tool & Supply Company, Livonia, Michigan) attached to a high-speed micro-drill (Stoelting Co. Wood Dale, IL). A circular cover-glass slip was gently lowered to cover the open-skull region and glued onto the top of the spacer. The wound was sealed to the edge of the optical window with a thin layer of dental cement (Stryker, Cat#0700-6-437, surgical grade). The custom-made spacer was used to position the animal head onto a platform for subsequent MPLSM imaging. A schematic illustrating the cranial defect window chamber model in mice is shown in Supplemental Fig. S1A&B. Once established, the mouse with a window chamber can survive over a 6-month period with no visible signs of distress.

The size of the defect was controlled using a 0.9 mm or 1.8 mm size Busch inverted cone bur (Armstrong Tool & Supply Company, Livonia, MI) which generates a 1 mm or 2 mm full thickness defect, respectively, in the parietal bone. The healing dynamics of 1 mm or 2 mm-sized defects was examined by MPLSM and microCT over a 3 month period. Although both defects failed to completely heal in the window chamber over a 3 month period (supplemental Fig. S2), 1 mm defects induced a more robust healing response at the leading edge of the defect, and therefore were used in the MPLSM analyses for osteogenesis and angiogenesis.

### Multiphoton-Laser-Scanning Microscopy (MPLSM)

An Olympus FV1000-AOM multiphoton imaging system (Olympus), equipped with a Titanium:Sapphire laser (Spectra-Physics), a C-Apochromat 10X/0.45 (Zeiss), and a 25X/1.05 (Olympus) water immersion objective, was used for live imaging of the cranial defect

healing. Images were acquired at 512×512 pixels, 0.2 μs pixel dwell with the laser tuned to 780nm. The fluorescence of GFP and second harmonic signals (SHG) was collected with a 517/23-nm and a 390/20-nm bandpass filters (Semrock, Rochester, NY), respectively. To visualize the blood vessel network, Q-tracker 655 nanocrystals (Invitrogen, Grand Island, NY) were injected intravenously via a femoral vein into mouse circulation according to the instruction from the manufacturer (Invitrogen). Far red fluorescence from nanocrystals was detected using a far red bandpass emission filter (Semrock), 655/40 nm). Using the 10x water immersion objective lens (Zeiss), a 1.3×1.3 mm multichannel z-series stack with 5μm steps was obtained. The z-series stack allowed 3D reconstruction of the defect up to a depth of 300μm (supplemental Video 1&2). The defects were imaged at the indicated time points post-surgery until euthanized. The multichannel 2D slice viewing and 3D reconstruction of defect were conducted using Amira software developed by Visualization Sciences Group (VSG, Burlington MA).

### Quantification of SHG propagation and Col2.3GFP cell dynamics in cranial defect repair

To characterize collagen matrix propagation and Col2.3GFP (+) cell dynamics, the defect was imaged over a period of 9 weeks by MPLSM. To ensure accuracy of the analyses, all imaging parameters, including laser power, PMT voltages and compensation were maintained constant throughout the entire experiment. Based on the SHG microscopy, which provided the contour of the defect region, a region of interest (ROI) was established in the time-series images, referencing back to the circular defect region at the day 1 following surgery. To quantify SHG propagation within an ROI, a global thresholding method was used to quantify the total number of SHG (+) voxels above an appropriate threshold in time-series images. The percentage volume of SHG occupying the total volume of the defect was used to depict the propagation of collagen bone matrix within the defect. Similarly, the volume of GFP (+) cells occupying the defect regions within defined ROI was obtained by quantifying the total number of green fluorescent voxels above an appropriate threshold across the time-series images. SHG signal from bone matrix could be easily distinguished from soft tissue by its distinct morphology and its association with Col2.3GFP cells during healing. A schematic illustrating the measurements of SHG and GFP (+) cells can be found in Supplemental Fig. S3. All measurements were performed using a combination of Image J and Amira.

To examine the extent of bone defect healing, the area of the defect was measured in ImageJ by tracing the circular defect region in the 2D images obtained from MPLSM. Since we are using a Busch inverted cone bur to create the defect, the shape of the defect is circular or nearly circular. Based on mathematical calculations, the radius of a circle can be

approximated using the area of the circular region, i.e.,  $r = \sqrt{\text{Area}/\pi}$ . The mean of the cell advancing distance from the edges of the bone was determined by calculating the difference of the outer radius (corresponding to the original edge of the defect) and the inner radius (corresponding to the leading edge of the expanding cells). The original radius of the defect at day 1 was calculated as  $r_0 = \sqrt{A_0/\pi}$ , where  $A_0$  is the area of the defect at day 1. The area of the defect region that was not occupied by the cells at each indicated time point was

used to approximately calculate the radius of the inner circle as:  $r_{\text{inner}} = \sqrt{(A_{\text{inner}}/\pi)}$ , where  $A_{\text{inner}}$  is the area of the void in the defect. The advancing distance of osteoblasts at the indicated time points is then given by  $r_0 - r_{\text{inner}}$ . The difference was further normalized by the radius of the original defect and plotted as a function of time.

### **Quantitative and histomorphometric analyses of neovascularization at the site of cranial bone defect repair**

A method for quantitative analyses of blood vessels was illustrated in supplemental Fig. S4 and supplemental video 3. Briefly, blood vessels (red channel) and SHG (white channel) were imaged simultaneously. The entire defect as illustrated by SHG and the surrounding vascular network (supplemental Fig. S4A) was reconstructed in 3D format using a multichannel z-series stack. To analyze the vascular network (supplemental Fig. S4B), a region of interest (ROI) was created to include all the vessels associated with the SHG signals produced by bone matrix. This vascular network was then isolated using Amira Segmentation Editor to obtain the final segmented vascular image (Fig. S4C), which was subjected to a series of morphometric analyses: vascular volume (Vasc. Vol.), total volume (T. Vol.), and vascular volume fraction (Vol. Fract.) (i.e., the ratio of Vasc. Vol. over T. Vol.). Using Amira's AutoSkeleton module, which implements a distance-ordered homotopic thinning operation, the segmented 3D vascular network was further skeletonized to generate a line-based network that was topologically equivalent to the original network (supplemental Fig. S4D) (18,19). The skeleton was superimposed on the original image to assess the relative accuracy of this method (supplemental Fig. S2E). The final skeletonized vessel network was obtained by manually retracing of the skeletons using Amira's Filamental Editor to remove false segments. Based on the skeletonized network, the number of vascular segments (NV), total vessel length (T. Length), and vessel length fraction (L.Fract.) (i.e., ratio of vessel length to total volume) were read from the Amira software. The average vessel thickness (Avg. Vess. Th.) and the associated vessel thickness distribution (Fig. S4F&G) were further calculated using an ImageJ plugin developed by Robert Dougherty (20). The complete process for quantification of vascularity was illustrated in Supplemental Video 3.

To detail the dynamic changes of osteogenesis and angiogenesis coupling at the site of repair and to ensure clear visualization of microvessels at the site of defect, clusters of Col2.3GFP osteoblasts were tracked in time series at a higher magnification over a period of 9 weeks. Quantitative and histomorphometric analyses of neovasculature as described above were performed simultaneously with volumetric quantification of Col2.3GFP cells and SHG. Analyses were performed in 5 regions from a group of 4 mice, covering a field of view of  $0.75 \times 0.75 \times 0.15 \text{mm}^3$  for each region.

### **CD31 Immunohistochemical staining of vascular network in cranial defect**

Mouse was perfused with 4% paraformaldehyde at week 2 following surgery. The cranial defect region of the mouse skull was harvested. The sample was treated with 3% bovine albumin in PBS containing 0.3% Triton X-100, followed by staining with CD31 antibody conjugated with Phycoerythrin (PE) (BD Pharmingen, Cat# BD 553373) or  $\alpha$ SMA antibody

conjugated with Cy3 (Sigma. Cat# C6198, clone 1A4). The samples were imaged via MPLSM as described above. The multichannel images obtained were analyzed using Amira and Image J. Calvarial defect samples were cryo-sectioned and stained with CD31 or  $\alpha$ SMA antibodies. Tissue sections (5 $\mu$ m thick) were imaged and photographed under a fluorescent microscope (Zeiss Axio Imager, Zeiss) using 40x lens.

### Isolation, seeding and implantation of bone marrow stromal cells (BMSCs)

Bone marrow cells were isolated from 2-month-old Col2.3GFP transgenic mice as previously described with slight modification (21). Briefly, bone marrow cells were flushed from marrow cavity by slowly injecting  $\alpha$ -MEM at one end of the bone using a sterile 21-gauge needle. The marrow suspension was dispersed gently by pipetting several times to obtain a single cell suspension. The cell suspension was further filtered through a 70 $\mu$ m cell strainer (Falcon) to remove debris. The collected cell suspension was gently overlaid onto Hitopaque1083 (Sigma) and centrifuged at 1100g for 20mins. Mononuclear cells were collected from the interphase and plated on six-well plates at a density of  $2 \times 10^6$ /cm<sup>2</sup> and cultured in  $\alpha$ -MEM containing 15% FBS (HyClone Laboratories) for 48 hours. The medium was removed by the end of 48 hours and the culture was washed to remove all non-adherent cells. Adherent cells were further cultured in fresh MEM with 15% FBS for additional 10 days. The adherent bone marrow stromal cells (BMSCs) were released from the culture plate at day 10 using trypsin and EDTA. The recovered BMSCs were mixed with naturalized collagen solution (3mg/ml, BioMatrix) and congealed at 37°C for 30 mins (22). A 2 mm<sup>3</sup> gel containing about  $2 \times 10^5$  cells was punched out and subsequently implanted into a 2 mm defect.

### Longitudinal live microCT scanning

Mice were sedated with isoflurane and restrained in a custom-made chamber containing isoflurane. The mouse skull was scanned by a Scanco Viva CT40 system (Scanco Medical) at a voxel size of 17.5  $\mu$ m. Imaging was performed on the same groups of mice repeated over three months. From the 2D images generated, the defect was reconstructed in 3D and analyzed using Amira software combined with Image J. The rate of the defect healing was evaluated by calculating the area of the defect closure over a period of 3 months.

### Statistical analyses

Data are expressed as the mean  $\pm$  SEM. Comparison was made among time-series data sets obtained from a group of 4 mice. Statistical significance was determined using repeated measures one-way ANOVA and a Tukey's posthoc test in GraphPad (GraphPad Prism, San Diego, CA). A p value <0.05 was considered statistically significant. Multivariate correlation analyses were performed in Excel and GraphPad. The Pearson correlation coefficients (R) between groups were analyzed in GraphPad to obtain a p value and an F value. A p value <0.05 following Bonferroni correction was considered statistically significant.

## RESULTS

### Real-time imaging of bone defect repair via MPLSM in the cranial defect window chamber model

A defect was created in the parietal bone of a 2.3kb collagen type 1 promoter-driven GFP transgenic mouse (Col2.3GFP), which permitted the tracking of osteoblast differentiation at the repair site (23). The superior optical sectioning capability of MPLSM enabled simultaneous visualization of GFP (+) cells (Green channel), SHG (+) collagen matrix (white channel), and neovasculature (red channel) at 2D and 3D dimensions (Supplemental Fig. S1E–G and Supplemental videos 1&2). Reconstruction of the images from live microCT scanning (Supplemental Fig. S1D) and MPLSM/SHG microscopy (Supplemental Fig. S1E) illustrated the remarkable agreement between these two approaches, which combine the high depth penetration of microCT scanning with the molecular and cellular specificity of MPLSM.

To perform longitudinal analyses, the entire defect was surveyed and reconstructed to illustrate bone (white), vessels (red), and osteoblasts (green) separately or in combination at the indicated time points (Fig. 1). As shown, the nascent blood vessels were found at week 1, extending outward to the rim of the defect (Fig. 1A2). The newly formed vessels were often irregular and disorganized. Mature vessels were visualized after week 2, radially distributed around the bone defect (Fig. 1A3). Angiogenesis at the defect region persisted during the first 6 weeks and subsided at week 9 (Fig. 1A4–6). GFP and SHG signal at the site of repair were assessed (Fig. 1, panel B). Col2.3 GFP (+) cells were first identified in the residual bone around the edge of the defect during week 1 (Fig. 1B2, arrows). More GFP (+) osteoblasts appeared at week 2 around the rim of the defect (Fig. 1B3). These GFP (+) osteoblasts expanded in size and volume, further advancing into the defect in week 3 and onward. The propagation of SHG (+) signals within the defect was evident at week 3 and progressively increased over time (Fig. 1B4–5). Quantitative analyses showed that GFP (+) osteoblast volume increased at week 2, peaked between 3–6 weeks and decreased at week 9 (Fig. 1C, n=4). The SHG signal within the defect continued to increase over a 9-week period, with significant propagation detected between week 3 and 9 (Fig. 1D). A greater percentage of defect closure at the center region was observed in the first 3–4 weeks of healing as indicated by the percent rate of defect closure (Fig. 1E). Measurement of the osteoblast advancing distance towards the center of the defect indicated that osteoblast progenitors expanded into the defect at a faster pace during the first 3 weeks of healing (Fig. 1F). The average advancing distance of GFP (+) cells at the leading edge of the defect was calculated as ~6 $\mu$ m/day during the first three weeks and ~2 $\mu$ m/day during the last 4–9 weeks (n=4). A similar faster rate of defect closure within the first 4 weeks of healing was further confirmed by live microCT scans (supplemental Fig. S2A). Collectively, these data indicate that effective bone wound closure depends on osteoblastic activity initiated at the leading edge of the bone defect during early stages of healing.

## Real-time tracking of the clusters of Col2.3GFP (+) osteoblasts and the coupled angiogenesis at the site of defect repair

To examine the dynamics and coupling of osteogenesis and angiogenesis during repair, clusters of Col2.3GFP (+) cells identified at the edge of the bone defect were tracked at a higher magnification over a period of 9 weeks (Fig. 2, panel A to E). As shown, at week 1, GFP (+) clusters were found in the residual bone at the edge of the bony defect (Fig. 2, panel A, and Fig. 2F1 as indicated by arrows). These clusters of GFP (+) cells were found to be in close proximity of the invading blood vessels (Fig. 2F2, arrows). At week 2, the same clusters of Col2.3 GFP (+) cells expanded into the defect site, surrounded by numerous newly formed microvessels at the leading edge of the bone defect (Fig. 2, panel B). Weak SHG signals were detected among these cells (Fig. 2B3), indicating that they were less mature osteoblasts. At a higher magnification, micro-capillary vessels were found intertwined within these expanded Col2.3 GFP (+) cell clusters (Fig. 2G1&2 yellow arrows). A few GFP (+) cells were found extending along blood vessels in bone matrix (Fig. 2G1&2, blue arrow). At week 3, the same groups of cells expanded into the wound and increased in size and volume (Fig. 2, panel C). These cells produced a significant amount of bone matrix as indicated by the induction of high contrast SHG signals (Fig. 2C3). At a deeper level, microvessels were found embedded within new bone matrix (Fig. 2C4–6). The larger vessels inside bone matrix were surrounded by Col2.3 GFP (+) cells (high magnification Fig. 2H1&2, blue arrows). Careful examination showed that GFP (+) osteoblasts were situated along the edges of the bony channels, suggesting the active modeling of the bony channel by osteoblasts to support vascular ingrowth in bone tissue. By week 6, angiogenesis subsided as evidenced by the reduction of microvessels at the site of the defect repair (Fig. 2, panel D). Within the new bone matrix, enlarged sinusoidal blood vessels were formed (Fig. 2D4–6 and Fig. 2I1&2, yellow arrows). Continued tracking of the defect at week 9 showed a significant reduction of Col2.3GFP (+) cells at the site of healing, along with regression of vessels within and around bone matrix (Fig. 2, panel E). More mature bone matrix was built along the edge of bony defect as indicated by high contrast SHG signals. Remodeled blood vessels could be found intertwined within bone marrow spaces (Fig. 2J1&2, arrows).

Another time-series of images obtained at a different repair site further highlighted the key changes in neovasculature during repair (Fig. 3, panel A to E). Notably, the micro-capillary vessels were found intertwined within the expanding osteoblast clusters at the leading edge of the bone defect throughout weeks 2 and 3 (Fig. 3A1–3 and B1–3, circled region). Measurements of these vessels showed an average diameter of  $7.35 \pm 3.2 \mu\text{m}$  ( $n=50$ ). The quantity of these microvessels at the leading edge of the defect dwindled as the osteoblastogenesis subsided at a later stage of healing (Fig. 3C3–E3, circled regions), indicating a critical role of these microvessels for expansion and migration of the osteoblasts into the center of the defect wound. In addition to the changes in microvessels, active modeling and remodeling of blood vessel network within new bone matrix were noted (Fig. 3C3&D3&E3, arrows). The appearance of the large and irregular sinusoidal vessels in the bony tissue was evident at a later stage of healing and coincided with active remodeling of bone matrix and formation of bone marrow space.

To characterize the dynamic changes of osteogenesis and angiogenesis coupling during defect healing, quantitative histomorphometric analyses of GFP (+) cells, SHG and neovascularization were performed at the active bone repair sites using time-series images obtained at a higher magnification. Osteoblast volume increased at week 2, peaked at week 3 and decreased at week 9 (Fig. 4A). SHG progressively increased over a period of 9 weeks indicating the propagation and deposition of new bone matrix (Fig. 4B). Localized angiogenesis was characterized and quantified using a series of measurements. *T. Length* and *L. Fract.* were increased at week 1, preceding the induction of osteoblastogenesis. The two parameters peaked during weeks 2 and 3, coinciding with the peak of osteoblastogenesis, and further reduced at week 6, preceding the decline of osteogenesis at week 9 (Fig. 4C and D, n=4). Compared to *T.Length* and *L.Fract.*, other measurements namely *Vasc. Vol.* and *Avg. Vess. Th.* showed a similar trend of induction but exhibited a significant variability among samples (Fig. 4E, F and G). In the vessel thickness distribution analyses, similar trend of changes were observed, with vessels less than 10µm exhibiting a better correlation with osteoblast volume during healing (Fig. 4H).

Multivariate correlation analyses were performed using time-series data obtained from histomorphometric imaging analyses to determine the correlation among SHG volume, Col2.3 GFP (+) cell volume, and vascularity. SHG was found to be correlated with neither GFP volume nor vascularity (Supplemental Table 1.). In contrast, Col2.3GFP (+) cell volume demonstrated statistically significant correlations with a number of vascular measurements, including *T. Length*, *L.Fract.*, *Avg. Vess. Th.*, *Vasc. Vol.* and *Vol. Fract.* (Table 1). Among them, *T. Length Fract.* showed the strongest correlation with GFP (+) cell volume ( $R=0.69$ ,  $p=0.0016$ ), and *Vasc. Vol.* and *Vol. Fract.* showed the weakest ( $R=0.52$ ,  $p=0.02$ ). If three parameters were combined, e.g., *Vasc. Vol.*, *T. Length* and *Avg. Vess. Th.* in a multivariate regression analysis, an improved correlation coefficient ( $R$ ) reached to 0.82, with a  $R^2$  of 0.62 ( $p<0.001$ ), demonstrating a significant correlation of vascularity with Col2.3GFP (+) cells at the regions of active repair. In vessel distribution analyses, we found that vessels less than 10 µm showed a better correlation with osteoblast volume than vessels greater than 10 µm ( $R=0.60$ ,  $p=0.02$ ), again suggesting that microvessel angiogenesis is critical for osteoblast-dependent repair.

To further characterize the regenerative microvasculature at the leading edge of the cranial defect, a nestin-GFP transgenic mouse model, which has been shown to mark nascent vessels in collagen-mediated angiogenesis and in skin wound healing (24,25), was utilized. In un-injured mice, nestin-GFP (+) cells could be occasionally identified in bone marrow space adjacent to a blood vessel in parietal bone. In the suture, a large number of nestin-GFP (+) cells could be found associated with blood vessels (data not shown). Following cranial defect surgery, nestin-GFP (+) cells were identified at the repair site at week 1, attaching to the irregularly shaped nascent blood vessels at the surface of the bone wound (Fig. 5A). For a duration of week 2 and onward, a large number of nestin-GFP (+) blood vessels were found at the surface of bone wound, primarily located in soft tissue (Fig. 5B). Only a very small number of nestin-GFP (+) cells were identified at the leading edge of the bone defect (Fig. 5C), indicating that the microvasculature at the bone repair site was mostly nestin-GFP negative. To establish the identity of nestin-GFP (+) cells associated with blood vessels,

immunofluorescent stainings on intact calvaria sample harvested from the defect site were performed. As shown, nestin-GFP (+) vessels co-localized with CD31 (+) vessels primarily in soft tissue on the surface of the bone wound (Fig. 5D). Microvessels at the leading edge of the bone defect were largely negative for nestin (Fig. 5E). Both endothelial and pericytic location of nestin-GFP (+) cells were observed in MPLSM imaging (Fig. 5F). Higher magnification MPLSM images depicted nestin-GFP (+) cells as typical endothelial lining cells along CD31 (+) vessels (Fig. 5G–I, arrows). Nestin-GFP (+) cells also stained positive for  $\alpha$ SMA (Fig. 5K–M, arrow). Further immunohistochemical stainings of CD31 and  $\alpha$ SMA using histologic sections prepared from calvaria samples confirm the co-localization of nestin-GFP (+) cells with CD31 (+) endothelial cells (Fig. 5J, arrow) and  $\alpha$ SMA(+) pericytes (Fig. 5N, arrow), demonstrating that nestin marks both endothelial cells and pericytes on blood vessels. To further establish the expression of nestin in nascent forming vessels, we performed tubular formation assay using stromal vascular fraction of adipose tissue from nestin-GFP mice (26). Extensive nestin (+) tubular networks were identified in the culture, co-localizing with CD31 (supplemental Fig. S7).

### Real-time tracking of donor BMSC-mediated bone defect repair and reconstruction

The establishment of a chronic window chamber model further enables us to track donor progenitor cell-mediated bone regeneration at the defect site. To track donor cell differentiation and bone formation in real-time and longitudinal fashion, bone marrow stromal cells (BMSCs) derived from Col2.3 GFP mice were implanted into the site of a cranial defect. Prior to implantation, all BMSCs were GFP (–). Upon differentiation, osteogenic cells including osteoblasts and early osteocytes in forming osteoid become GFP (+), facilitating tracking of osteogenic differentiation and bone forming activity *in vivo* (23,27). As illustrated, progressive new bone formation within the defect region was detected by live longitudinal microCT scans over a period of 14 weeks (Fig. 6, panel A). A similar time course of defect healing was depicted by 3D reconstruction of MPLSM images obtained from the same defect (Fig. 6, panel B). The analyses of the MPLSM time-series showed that clusters of Col2.3GFP (+) BMSCs appeared at day 10 post-implantation, surrounded by nascent blood vessels (Fig. 6B1). Col2.3 GFP (+) cells were quickly replaced with bone tissue between days 14–20 as indicated by live microCT scanning (Fig. 6A2) and MPLSM imaging (Fig. 6B2). A significant number of GFP (+) cells were found embedded in new bone matrix indicating direct donor cell-dependent new bone formation during the early stages of healing (Fig. 6C2). Continued monitoring of the defect over the next 11 weeks showed progressive bone wound closure (Fig. 6B3–B6&C3–C6). Based on the presence of the donor GFP (+) cells in the time-series images, it was evident that late stage bone formation and bone wound closure were largely dependent on the host (Fig. 6C3–6 and D3–6). Although scattered donor GFP (+) bone nodules (yellow arrows in Fig. 6C3&C4) were found within the defect, tracking of these isolated bone nodules showed that the GFP (+) donor osteoblasts slightly expanded in volume and were eventually embedded within host bone at a later stage. While host-dependent bone formation primarily arose from the edge of the defect, scattered GFP (–) bone nodules (host origin) could be identified within the center region of the defect. Examination of the neovascularization at the defect site showed that induction of overall vascularity coincided with early osteogenesis (Fig. 6. Panel D). Blood vessels remodeled and regressed as the bone matrix built up and became more

mature. Only modest induction of vascularity was shown at the localized region, corresponding to the enhanced host bone formation at weeks 9 and 14 (Fig. 6D5&D6, white boxed region).

Donor-dependent bone formation and the associated neovascularization were further illustrated at a higher magnification over time (Fig. 6, panel E&F). At day 10, nascent vessels were found invading the differentiated GFP (+) osteoblastic donor cells (Fig. 6E1). These cells quickly laid down bone matrix between days 10 and 20 as indicated by SHG (Fig. 6E2). Microvessels were found closely encircled around GFP (+) cells within new bone at days 20–30 following implantation (Fig. 6E2–3 and F2–3). These blood vessels were subsequently remodeled and regressed as more bone matrix was built, leading to the formation of vascular channels and bone marrow spaces (Fig. 6E4–6& F4–6). Interestingly, we found that some donor GFP (+) cells persisted in newly formed bone, particularly in areas where marrow cavity and sinusoidal vessels were formed at a later stage (Fig. 6F2–6). Histology of the same sample harvested at week 14 illustrated the donor-derived bone in the calvaria defect (supplemental Fig. S8).

## DISCUSSION

To gain a better understanding of the spatiotemporal regulation of osteogenesis and angiogenesis in defect repair, we established a cranial defect window chamber model in mice that allows high-resolution, longitudinal, and real-time analyses of bone defect healing and osteogenesis and angiogenesis coupling via Multiphoton Laser Scanning Microscopy (MPLSM). Using this novel intravital imaging approach, we demonstrate for the first time the longitudinal and spatiotemporal analyses of osteogenesis and angiogenesis in cranial bone defect repair and regeneration. Our study provides basis for understanding molecular and cellular interactions of bone and vessel forming cells in cranial bone defect repair and regeneration, further offering a unique *in vivo* real-time imaging tool to track the fate of the progenitor cells and their interactions with host healing microenvironment.

Bone defect repair is a dynamic tissue morphogenetic process orchestrated by progenitor cells, chemokines and growth factors produced at the site of repair. Despite the fact that the cranial bone defect model is being used as the first stage of *in vivo* study for bone regeneration and bone tissue engineering, the dynamic morphogenetic process of cranial bone defect healing has been poorly described. The spatiotemporal regulation of osteogenesis and angiogenesis in defect repair remains superficially understood. By simultaneously tracking SHG, Col2.3GFP (+) osteoblasts, and neovascularization in a windowed cranial defect model via MPLSM, we established the morphogenetic sequence and spatiotemporal coordination of osteogenesis and angiogenesis in cranial bone defect healing. Our study showed that at the early stage of healing, the expansion of the Col2.3GFP (+) osteoblasts coupled with vigorous angiogenesis and characteristic formation of micro-capillary vessels at the leading edge of the defect. The significance of the coupling with micro-capillary vessels is further corroborated by multivariate correlation analyses which demonstrated a strong correlation of osteoblast volume with vascular parameters, particularly the blood vessel length and vessels less than 10 $\mu$ m in diameters at the site of repair. In concomitance with the early small vessel angiogenesis, the rate of the defect

healing, as measured by the advancing distance of GFP (+) osteoblasts into the defect, was 3 times faster in the first 3 weeks than the last 6 weeks. These data collectively suggest that localized small vessel angiogenesis at the early stage of repair is critical for the expansion of osteoblasts and the induction of bone formation. Hence, prolonging this early osteogenic and angiogenic phase could be beneficial for enhancing defect closure.

In contrast to the early stage, the late stage bone defect healing was characterized by slow expansion of osteoblasts at the leading edge and active vascular network remodeling within the newly formed bone matrix. Vascular remodeling and regression are integral components of angiogenesis in tissue repair (28). The proper remodeling and pruning of neovasculature are critical for establishing bone homeostasis, developing sinusoids and restoring bone marrow in repair (29–31). How this remodeling process is regulated in repair and how it is affected by bone healing microenvironment in defect repair remain poorly understood. Further detailed studies using available fluorescent transgenic reporter mouse models will facilitate mapping of the spatiotemporal cues of the “morphogenetic field” of cranial defect repair, offering new insights for development of material-based approaches to orchestrating controlled delivery of growth factors and chemokines for repair and reconstruction.

The origin and sources of osteoblast precursors remains as one of the key interests in skeletal repair and regeneration. While periosteal progenitor cells have been recognized as a major source (32,33), studies have reported the contribution of skeletal progenitors from bone marrow, dura, as well as perivascular cells in cranial repair and regeneration (34–37). A 2.3kb collagen type I promoter driven GFP transgenic mouse model (Col2.3GFP) was used in our current study. It is reported that Col2.3GFP labels mature osteoblasts and osteocytes in forming bone (23,38). However, in our experiments, we found that Col2.3GFP also labeled early osteoprogenitors that had the capacity to migrate and expand into the wound healing site. Careful tracking of these cells showed that the osteoprogenitors originated from the residual bone at the rim of the bone defect (Fig. 1 and 2). The unique location of these cells suggests a potential contribution of osteoblasts from the living cells dwelling inside the bone tissue. It is known that skeletal progenitors can be directly isolated from the crushed bone chips (39), and several studies show that osteocytes can undergo dedifferentiation and migrate out of lacunae to form osteoblasts *in vitro* (40,41). Further lineage tracing experiments in cranial windowed defects will assist in establishing the key sources of the osteoblasts in cranial defect repair.

Perivascular cells, often referred to as pericytes, have been shown as a source of skeletal stem/progenitor cells (31,42,43). The unique pericytic location of osteoblastic cells in repair tissue has been described by Maes et al. who suggest that osteoblast precursors (OSX +ve cells) enter the cartilage and bone along with blood vessels to form new trabecular bone during endochondral bone formation (44). A similar close location of osteoblasts with blood vessel was observed in our current study in both un-injured (supplemental Fig. S5C, arrows) and injured bone (Fig. 2G&H2). Careful analyses showed that the majority of the GFP (+) osteoblasts along blood vessels were situated along the surface of bony channels, suggesting a mechanism that involves the induction of osteoblasts along vessel paths to facilitate dynamic vascular ingrowth and remodeling within the newly formed bone.

In attempt to further characterize the neovascularization in repair, we examined the distribution of nestin-GFP (+) cells in repair tissue. Nestin (+) perivascular cells have been shown to constitute hematopoietic stem cell niches in bone marrow and further participate in bone remodeling and homeostasis (14). Nestin-GFP has also been associated with nascent vessels in collagen-induced angiogenesis and in skin wounds (25). Using nestin-GFP transgenic mice in cranial defect model, we found that nestin-GFP expressions were primarily associated with blood vessels in inflammatory soft tissues at the surface of the defect. In contrast, the regenerative micro-vasculature at the leading edge of bone defect was mostly negative for nestin-GFP (Figure 5). Further immunofluorescent staining established the localization of nestin-GFP (+) cells as CD31 (+) endothelial cells and  $\alpha$ SMA (+) perivascular cells on blood vessels. These data confirm the heterogeneity of the nestin-promoter driven GFP cells on blood vessels (42,45) and further demonstrates the preferential distribution and localization of nestin-GFP (+) vessels in repair.

While BMSCs have been used in repair and reconstruction of bone tissue in animal models and in human trials, the mechanisms by which BMSCs participate in bone defect repair are not completely understood (46–48). The establishment of an intravital bone healing platform provides a unique tool to track BMSC differentiation and further investigate the role of BMSC in repair and reconstruction. Using this novel imaging approach combined with longitudinal microCT scanning in the cranial defect window chamber model, we obtained a sequence of images illustrating BMSC-mediated bone regeneration *in vivo* (Figure 6). Our analyses on these images showed that 1) donor BMSCs underwent differentiation in concert with early angiogenesis; 2) donor BMSC-dependent regeneration occurred rapidly within the first 3 weeks of implantation, with significant numbers of Col2.3GFP (+) BMSCs incorporated into bone; 3) active vascular remodeling occurred in donor-derived bone tissue with potential participation of donor derived Col2.3GFP (+) osteoblasts; 4) late stage bone repair and defect closure occurred at a slower rate and were mostly host dependent; 5) the persistent late stage bone healing was associated with localized modest induction of angiogenesis and active remodeling of blood vessels. These observations collectively support a mechanism of coordinated and joint contribution of both the donor and host bone forming cells in bone defect repair. Since only modest and localized angiogenesis was observed during late stage bone defect healing, the persistent bone formation in these regions could be attributed to the unique capabilities of BMSCs to produce a wide array of trophic factors that stimulate host osteogenesis and modulate local inflammatory and immune responses in repair (47,49–51). The anti-inflammatory and anti-fibrotic actions of BMSCs have been extensively reported in cardiac and skin injury models (52–54).

Current analyses of osteogenesis and angiogenesis in bone defect repair largely rely on histology, which is destructive and challenging in providing a three-dimensional perspective of the repair tissue. A micro CT-based approach has been successfully used in quantitative analyses of osteogenesis and angiogenesis in bone tissue repair and regeneration (55–57). However, micro CT-based analysis does not permit longitudinal analyses of the neovasculature and has limitations when imaging small vessels less than 20 $\mu$ m in diameter (58,59). Other methodologies such as Optical Coherence Tomography (OCT) (60), Doppler (61,62) and Magnetic Resonance Imaging (MRI) can provide functional assessment of blood

vessels but lack the resolution to correlate the neovascularization with cellular differentiation during bone tissue repair and reconstruction. MPLSM, due to its high 3D spatiotemporal resolution and deep tissue penetration, is ideal for real-time tracking of clusters of progenitor cells and their complex residing vascular microenvironment *in vivo*. This unique capability offers distinctive advantages over MicroCT and histology for simultaneous and dynamic analyses of osteogenesis and angiogenesis coupling in real-time and 3D format. In conjunction with fluorescent transgenic mouse models and cell/vessel labeling technologies, MPLSM could provide a valuable tool for analyses of cell-cell, cell-vessel, and cell-matrix interactions in dynamic biological processes, such as bone defect repair and bone tissue engineering (4,12,34,63,64).

As every other available technology that has pros and cons, MPLSM also has a number of limitations when imaging bone tissue in living animals. These include: 1) the surgical challenge in establishing a clean window for repeated imaging; 2) the limitation in maximum penetration in bone tissue (250–300  $\mu\text{m}$ ); 3) the potential tissue response from repeated imaging; and 4) the reliance on technical innovations in fluorochrome and cell labeling system to probe biological system. However, despite these disadvantages, MPLSM remains the top choice for *in vivo* imaging of thick and complex tissue. Technology development will continue to push the boundaries of multiphoton-based imaging technology to provide a better and more suitable platform for obtaining comprehensive pictures of biological systems at high macroscopic resolutions (65).

In summary, by establishing a MPLSM-based intravital imaging modality in a cranial defect window chamber model, we examined the morphogenetic process of cranial bone defect healing and further established the spatiotemporal analyses of osteogenesis and angiogenesis coupling in repair and regeneration. Our study provides the basis for real-time tracking of progenitor cell fate and understanding of the molecular and cellular interactions of bone and vessel forming cells in bone defect repair. The establishment of an intravital imaging modality further facilitates elucidation of spatiotemporal regulatory mechanisms of osteoprogenitor cell interactions with the host bone healing microenvironment, aiding in development of novel material-based approaches aimed at modulating progenitor cell behavior and engineering bone healing microenvironment for enhanced bone defect repair. With the increasing need for design of smart biomaterials for controlled delivery of growth factors, a deeper understanding of the spatiotemporal cues of osteogenesis and angiogenesis, as well as vascular remodeling and regression will facilitate the development of novel material-based therapeutics for improving defect repair and reconstruction.

## Supplementary Material

Refer to Web version on PubMed Central for supplementary material.

## Acknowledgments

We thank Michael Thullen for microCT scanning and related imaging analyses. This study is supported by grants from the Musculoskeletal Transplant Foundation, NYSTEM N08G-495 and N09G346, Department of Defense (W81XWH-09-1-0405) and the National Institutes of Health (R21 DE021513, RC1 AR058435, DP2 OD006501, AR R01 AR048681, P50 AR054041, and P30AR061307).

## References

1. Carano RA, Filvaroff EH. Angiogenesis and bone repair. *Drug Discov Today*. 2003; 8(21):980–9. [PubMed: 14643161]
2. Hankenson KD, Dishowitz M, Gray C, Schenker M. Angiogenesis in bone regeneration. *Injury*. 2011; 42(6):556–61. [PubMed: 21489534]
3. Riddle RC, Khatri R, Schipani E, Clemens TL. Role of hypoxia-inducible factor-1alpha in angiogenic-osteogenic coupling. *J Mol Med (Berl)*. 2009; 87(6):583–90. [PubMed: 19415227]
4. Ramasamy SK, Kusumbe AP, Wang L, Adams RH. Endothelial Notch activity promotes angiogenesis and osteogenesis in bone. *Nature*. 2014; 507(7492):376–80. [PubMed: 24647000]
5. Guldberg RE. Spatiotemporal delivery strategies for promoting musculoskeletal tissue regeneration. *J Bone Miner Res*. 2009; 24(9):1507–11. [PubMed: 19653806]
6. Niesner RA, Hauser AE. Recent advances in dynamic intravital multi-photon microscopy. *Cytometry A*. 2011; 79(10):789–98. [PubMed: 21905212]
7. Kikuta J, Ishii M. Recent advances in intravital imaging of dynamic biological systems. *J Pharmacol Sci*. 2012; 119(3):193–7. [PubMed: 22786560]
8. Fukumura D, Jain RK. Imaging angiogenesis and the microenvironment. *APMIS*. 2008; 116(7–8):695–715. [PubMed: 18834413]
9. McDonald DM, Choyke PL. Imaging of angiogenesis: from microscope to clinic. *Nat Med*. 2003; 9(6):713–25. [PubMed: 12778170]
10. Lecoq J, Parpaleix A, Roussakis E, Ducros M, Goulam Houssen Y, Vinogradov SA, Charpak S. Simultaneous two-photon imaging of oxygen and blood flow in deep cerebral vessels. *Nat Med*. 2011; 17(7):893–8. [PubMed: 21642977]
11. Parpaleix A, Goulam Houssen Y, Charpak S. Imaging local neuronal activity by monitoring PO(2) transients in capillaries. *Nat Med*. 2013; 19(2):241–6. [PubMed: 23314058]
12. Ambekar R, Chittenden M, Jasiuk I, Toussaint KC Jr. Quantitative second-harmonic generation microscopy for imaging porcine cortical bone: comparison to SEM and its potential to investigate age-related changes. *Bone*. 2012; 50(3):643–50. [PubMed: 22155019]
13. Brown E, McKee T, diTomaso E, Pluen A, Seed B, Boucher Y, Jain RK. Dynamic imaging of collagen and its modulation in tumors in vivo using second-harmonic generation. *Nat Med*. 2003; 9(6):796–800. [PubMed: 12754503]
14. Mendez-Ferrer S, Michurina TV, Ferraro F, Mazloom AR, Macarthur BD, Lira SA, Scadden DT, Ma'ayan A, Enikolopov GN, Frenette PS. Mesenchymal and haematopoietic stem cells form a unique bone marrow niche. *Nature*. 2010; 466(7308):829–34. [PubMed: 20703299]
15. Mignone JL, Kukekov V, Chiang AS, Steindler D, Enikolopov G. Neural stem and progenitor cells in nestin-GFP transgenic mice. *J Comp Neurol*. 2004; 469(3):311–24. [PubMed: 14730584]
16. Holtmaat A, Bonhoeffer T, Chow DK, Chuckowree J, De Paola V, Hofer SB, Hubener M, Keck T, Knott G, Lee WC, Mostany R, Mrcic-Flogel TD, Nedivi E, Portera-Cailliau C, Svoboda K, Trachtenberg JT, Wilbrecht L. Long-term, high-resolution imaging in the mouse neocortex through a chronic cranial window. *Nat Protoc*. 2009; 4(8):1128–44. [PubMed: 19617885]
17. Madden KS, Zettel ML, Majewska AK, Brown EB. Brain tumor imaging: live imaging of glioma by two-photon microscopy. *Cold Spring Harb Protoc*. 2013; (3)
18. Cassot F, Lauwers F, Fouard C, Prohaska S, Lauwers-Cances V. A novel three-dimensional computer-assisted method for a quantitative study of microvascular networks of the human cerebral cortex. *Microcirculation*. 2006; 13(1):1–18. [PubMed: 16393942]
19. Pudney C. Distance-Ordered Homotopic Thinning: A Skeletonization Algorithm for 3D Digital Images. *Computer Vision and Image Understanding*. 1998; 72(3):404–413.
20. Dougherty, R.; Kunzelmann, KH. Computing Local Thickness of 3D Structures with ImageJ. *Microscopy & Microanalysis Meeting*; Ft. Lauderdale, Florida. 2007.
21. Zhang X, Schwarz EM, Young DA, Puzas JE, Rosier RN, O'Keefe RJ. Cyclooxygenase-2 regulates mesenchymal cell differentiation into the osteoblast lineage and is critically involved in bone repair. *J Clin Invest*. 2002; 109(11):1405–15. [PubMed: 12045254]

22. Farhat YM, Al-Maliki AA, Chen T, Juneja SC, Schwarz EM, O'Keefe RJ, Awad HA. Gene expression analysis of the pleiotropic effects of TGF-beta1 in an in vitro model of flexor tendon healing. *PLoS One*. 2012; 7(12):e51411. [PubMed: 23251524]
23. Kalajzic I, Kalajzic Z, Kaliterna M, Gronowicz G, Clark SH, Lichtler AC, Rowe D. Use of type I collagen green fluorescent protein transgenes to identify subpopulations of cells at different stages of the osteoblast lineage. *J Bone Miner Res*. 2002; 17(1):15–25. [PubMed: 11771662]
24. Callegari A, Bollini S, Iop L, Chiavegato A, Torregrossa G, Pozzobon M, Gerosa G, De Coppi P, Elvassore N, Sartore S. Neovascularization induced by porous collagen scaffold implanted on intact and cryoinjured rat hearts. *Biomaterials*. 2007; 28(36):5449–61. [PubMed: 17905428]
25. Amoh Y, Li L, Yang M, Moossa AR, Katsuoaka K, Penman S, Hoffman RM. Nascent blood vessels in the skin arise from nestin-expressing hair-follicle cells. *Proc Natl Acad Sci U S A*. 2004; 101(36):13291–5. [PubMed: 15331785]
26. Koh YJ, Koh BI, Kim H, Joo HJ, Jin HK, Jeon J, Choi C, Lee DH, Chung JH, Cho CH, Park WS, Ryu JK, Suh JK, Koh GY. Stromal vascular fraction from adipose tissue forms profound vascular network through the dynamic reassembly of blood endothelial cells. *Arterioscler Thromb Vasc Biol*. 2011; 31(5):1141–50. [PubMed: 21393582]
27. Paic F, Igwe JC, Nori R, Kronenberg MS, Franceschetti T, Harrington P, Kuo L, Shin DG, Rowe DW, Harris SE, Kalajzic I. Identification of differentially expressed genes between osteoblasts and osteocytes. *Bone*. 2009; 45(4):682–92. [PubMed: 19539797]
28. Wietecha MS, Cerny WL, DiPietro LA. Mechanisms of vessel regression: toward an understanding of the resolution of angiogenesis. *Curr Top Microbiol Immunol*. 2013; 367:3–32. [PubMed: 23224648]
29. Lo Celso C, Fleming HE, Wu JW, Zhao CX, Miake-Lye S, Fujisaki J, Cote D, Rowe DW, Lin CP, Scadden DT. Live-animal tracking of individual haematopoietic stem/progenitor cells in their niche. *Nature*. 2009; 457(7225):92–6. [PubMed: 19052546]
30. Morrison SJ, Scadden DT. The bone marrow niche for haematopoietic stem cells. *Nature*. 2014; 505(7483):327–34. [PubMed: 24429631]
31. Sacchetti B, Funari A, Michienzi S, Di Cesare S, Piersanti S, Saggio I, Tagliafico E, Ferrari S, Robey PG, Riminucci M, Bianco P. Self-renewing osteoprogenitors in bone marrow sinusoids can organize a hematopoietic microenvironment. *Cell*. 2007; 131(2):324–36. [PubMed: 17956733]
32. Ozerdem OR, Anlatıcı R, Bahar T, Kayaselcuk F, Barutcu O, Tuncer I, Sen O. Roles of periosteum, dura, and adjacent bone on healing of cranial osteonecrosis. *J Craniofac Surg*. 2003; 14(3):371–9. discussion 380–2. [PubMed: 12826809]
33. Uddstromer L. The osteogenic capacity of tubular and membranous bone periosteum. A qualitative and quantitative experimental study in growing rabbits. *Scand J Plast Reconstr Surg*. 1978; 12(3):195–205. [PubMed: 368969]
34. Park D, Spencer JA, Koh BI, Kobayashi T, Fujisaki J, Clemens TL, Lin CP, Kronenberg HM, Scadden DT. Endogenous bone marrow MSCs are dynamic, fate-restricted participants in bone maintenance and regeneration. *Cell Stem Cell*. 2012; 10(3):259–72. [PubMed: 22385654]
35. Levi B, Nelson ER, Li S, James AW, Hyun JS, Montoro DT, Lee M, Glotzbach JP, Commons GW, Longaker MT. Dura mater stimulates human adipose-derived stromal cells to undergo bone formation in mouse calvarial defects. *Stem Cells*. 2011; 29(8):1241–55. [PubMed: 21656608]
36. Feng J, Mantesso A, De Bari C, Nishiyama A, Sharpe PT. Dual origin of mesenchymal stem cells contributing to organ growth and repair. *Proc Natl Acad Sci U S A*. 2011; 108(16):6503–8. [PubMed: 21464310]
37. Gosain AK, Santoro TD, Song LS, Capel CC, Sudhakar PV, Matloub HS. Osteogenesis in calvarial defects: contribution of the dura, the pericranium, and the surrounding bone in adult versus infant animals. *Plast Reconstr Surg*. 2003; 112(2):515–27. [PubMed: 12900610]
38. Kalajzic Z, Liu P, Kalajzic I, Du Z, Braut A, Mina M, Canalis E, Rowe DW. Directing the expression of a green fluorescent protein transgene in differentiated osteoblasts: comparison between rat type I collagen and rat osteocalcin promoters. *Bone*. 2002; 31(6):654–60. [PubMed: 12531558]
39. Short B, Wagey R. Isolation and culture of mesenchymal stem cells from mouse compact bone. *Methods Mol Biol*. 2013; 946:335–47. [PubMed: 23179842]

40. Robey PG, Termine JD. Human bone cells in vitro. *Calcif Tissue Int.* 1985; 37(5):453–60. [PubMed: 2998572]
41. Torreggiani E, Matthews BG, Pejda S, Matic I, Horowitz MC, Grecevic D, Kalajzic I. Preosteocytes/osteocytes have the potential to dedifferentiate becoming a source of osteoblasts. *PLoS One.* 2013; 8(9):e75204. [PubMed: 24040401]
42. Zhou BO, Yue R, Murphy MM, Peyer JG, Morrison SJ. Leptin-receptor-expressing mesenchymal stromal cells represent the main source of bone formed by adult bone marrow. *Cell Stem Cell.* 2014; 15(2):154–68. [PubMed: 24953181]
43. Becerra J, Santos-Ruiz L, Andrades JA, Mari-Beffa M. The stem cell niche should be a key issue for cell therapy in regenerative medicine. *Stem Cell Rev.* 2011; 7(2):248–55. [PubMed: 21052872]
44. Maes C, Kobayashi T, Selig MK, Torrekens S, Roth SI, Mackem S, Carmeliet G, Kronenberg HM. Osteoblast precursors, but not mature osteoblasts, move into developing and fractured bones along with invading blood vessels. *Dev Cell.* 2010; 19(2):329–44. [PubMed: 20708594]
45. Ono N, Ono W, Mizoguchi T, Nagasawa T, Frenette PS, Kronenberg HM. Vasculature-associated cells expressing nestin in developing bones encompass early cells in the osteoblast and endothelial lineage. *Dev Cell.* 2014; 29(3):330–9. [PubMed: 24823376]
46. Bianco P, Cao X, Frenette PS, Mao JJ, Robey PG, Simmons PJ, Wang CY. The meaning, the sense and the significance: translating the science of mesenchymal stem cells into medicine. *Nat Med.* 2013; 19(1):35–42. [PubMed: 23296015]
47. Phinney DG, Prockop DJ. Concise review: mesenchymal stem/multipotent stromal cells: the state of transdifferentiation and modes of tissue repair--current views. *Stem Cells.* 2007; 25(11):2896–902. [PubMed: 17901396]
48. Gamie Z, Tran GT, Vyzas G, Korres N, Heliotis M, Mantalaris A, Tsiridis E. Stem cells combined with bone graft substitutes in skeletal tissue engineering. *Expert Opin Biol Ther.* 2012; 12(6):713–29. [PubMed: 22500826]
49. Caplan AI, Dennis JE. Mesenchymal stem cells as trophic mediators. *Journal of Cellular Biochemistry.* 2006; 98(5):1076–1084. [PubMed: 16619257]
50. Caplan AI. Adult mesenchymal stem cells for tissue engineering versus regenerative medicine. *J Cell Physiol.* 2007; 213(2):341–7. [PubMed: 17620285]
51. Liu Y, Wang L, Kikuri T, Akiyama K, Chen C, Xu X, Yang R, Chen W, Wang S, Shi S. Mesenchymal stem cell-based tissue regeneration is governed by recipient T lymphocytes via IFN-gamma and TNF-alpha. *Nat Med.* 2011; 17(12):1594–601. [PubMed: 22101767]
52. Ortiz LA, Dutreil M, Fattman C, Pandey AC, Torres G, Go K, Phinney DG. Interleukin 1 receptor antagonist mediates the antiinflammatory and antifibrotic effect of mesenchymal stem cells during lung injury. *Proc Natl Acad Sci U S A.* 2007; 104(26):11002–7. [PubMed: 17569781]
53. Qi Y, Jiang D, Sindrilaru A, Stegemann A, Schatz S, Treiber N, Rojewski M, Schrezenmeier H, Vander Beken S, Wlaschek M, Bohm M, Seitz A, Scholz N, Durselen L, Brinckmann J, Ignatius A, Scharffetter-Kochanek K. TSG-6 released from intradermally injected mesenchymal stem cells accelerates wound healing and reduces tissue fibrosis in murine full-thickness skin wounds. *J Invest Dermatol.* 2014; 134(2):526–37. [PubMed: 23921952]
54. Lee RH, Pulin AA, Seo MJ, Kota DJ, Ylostalo J, Larson BL, Semprun-Prieto L, Delafontaine P, Prockop DJ. Intravenous hMSCs improve myocardial infarction in mice because cells embolized in lung are activated to secrete the anti-inflammatory protein TSG-6. *Cell Stem Cell.* 2009; 5(1):54–63. [PubMed: 19570514]
55. Duvall CL, Robert Taylor W, Weiss D, Guldberg RE. Quantitative microcomputed tomography analysis of collateral vessel development after ischemic injury. *Am J Physiol Heart Circ Physiol.* 2004; 287(1):H302–10. [PubMed: 15016633]
56. Duvall CL, Taylor WR, Weiss D, Wojtowicz AM, Guldberg RE. Impaired angiogenesis, early callus formation, and late stage remodeling in fracture healing of osteopontin-deficient mice. *J Bone Miner Res.* 2007; 22(2):286–97. [PubMed: 17087627]
57. Zhang X, Xie C, Lin AS, Ito H, Awad H, Lieberman JR, Rubery PT, Schwarz EM, O'Keefe RJ, Guldberg RE. Periosteal progenitor cell fate in segmental cortical bone graft transplantations: implications for functional tissue engineering. *J Bone Miner Res.* 2005; 20(12):2124–37. [PubMed: 16294266]

58. Vasquez SX, Gao F, Su F, Grijalva V, Pope J, Martin B, Stinstra J, Masner M, Shah N, Weinstein DM, Farias-Eisner R, Reddy ST. Optimization of microCT imaging and blood vessel diameter quantitation of preclinical specimen vasculature with radiopaque polymer injection medium. *PLoS One*. 2011; 6(4):e19099. [PubMed: 21533123]
59. Marxen M, Thornton MM, Chiarot CB, Klement G, Koprivnikar J, Sled JG, Henkelman RM. MicroCT scanner performance and considerations for vascular specimen imaging. *Med Phys*. 2004; 31(2):305–13. [PubMed: 15000616]
60. Hu S, Wang LV. Photoacoustic imaging and characterization of the microvasculature. *J Biomed Opt*. 2010; 15(1):011101. [PubMed: 20210427]
61. ElMaraghy AW, Schemitsch EH, Richards RR. Femoral and cruciate blood flow after retrograde femoral reaming: a canine study using laser Doppler flowmetry. *J Orthop Trauma*. 1998; 12(4): 253–8. [PubMed: 9619460]
62. Hinsley DE, Hobbs CM, Watkins PE. The role of laser Doppler flowmetry in assessing the viability of bone fragments in an open fracture. *Injury*. 2002; 33(5):435–8. [PubMed: 12095725]
63. Kusumbe AP, Ramasamy SK, Adams RH. Coupling of angiogenesis and osteogenesis by a specific vessel subtype in bone. *Nature*. 2014; 507(7492):323–8. [PubMed: 24646994]
64. Villa MM, Wang L, Huang J, Rowe DW, Wei M. Visualizing osteogenesis in vivo within a cell-scaffold construct for bone tissue engineering using two-photon microscopy. *Tissue Eng Part C Methods*. 2013; 19(11):839–49. [PubMed: 23641794]
65. Hoover EE, Squier JA. Advances in multiphoton microscopy technology. *Nat Photonics*. 2013; 7(2):93–101. [PubMed: 24307915]

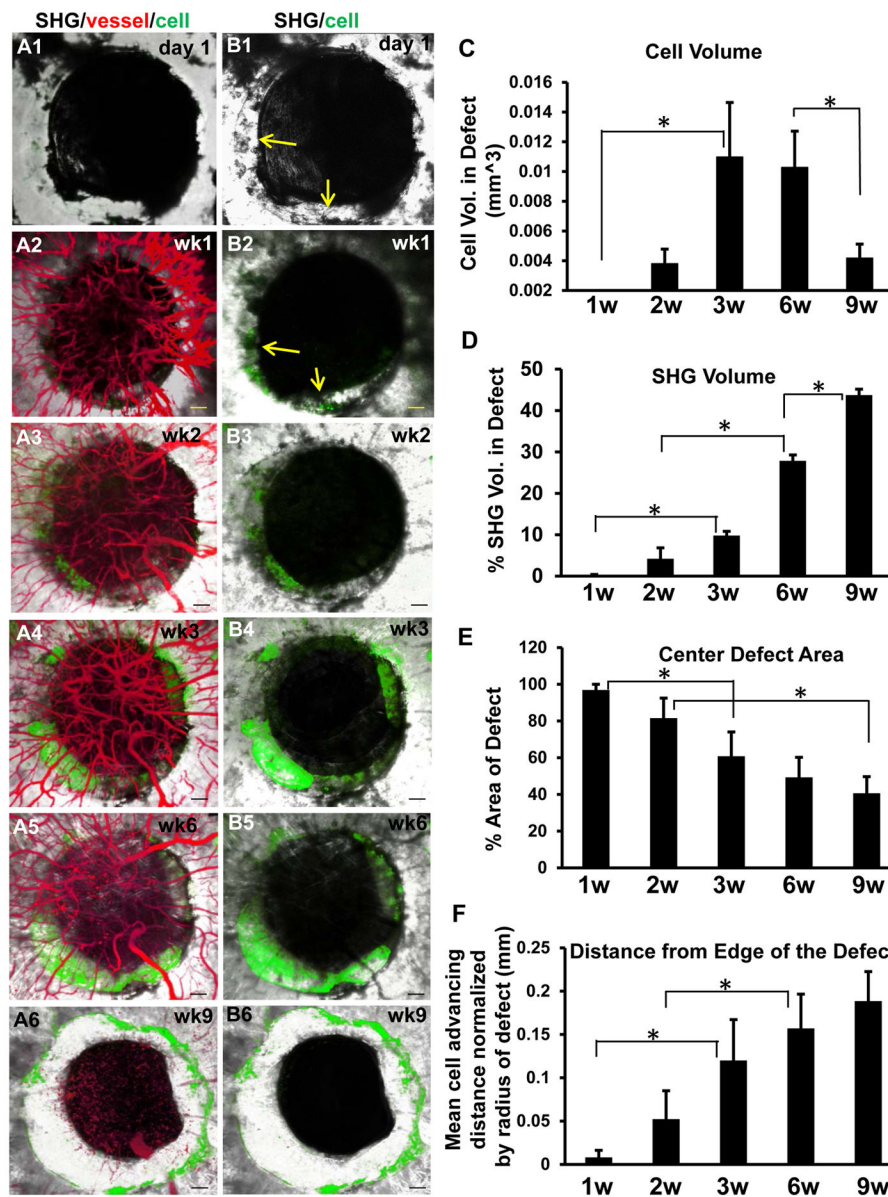


**Figure 1. Longitudinal analyses of cranial defect healing via MPLSM in Col2.3GFP mice**  
 A 1 mm cranial defect healing was tracked over a period of 9 weeks using MPLSM. Progressive defect healing and neovascularization are illustrated in a time-series images reconstructed by Col2.3GFP(+) osteoblasts (green), SHG (+) bone matrix (white) and blood vessels (red) in combination as indicated (panel A and B). Volumetric analyses of GFP (+) osteoblasts (C) and SHG (D) over a 9 week period within the defect region are shown. Using the area and radius of the defect on day 1 as a reference, the % area of the defect in the center region (E), and the cell advancing distance relative to the radius of the original defect (F) were further calculated. Data are expressed as the mean  $\pm$  SEM (n=4). \* indicates significant difference ( $p < 0.05$ ). Scale bar = 100 $\mu$ m.

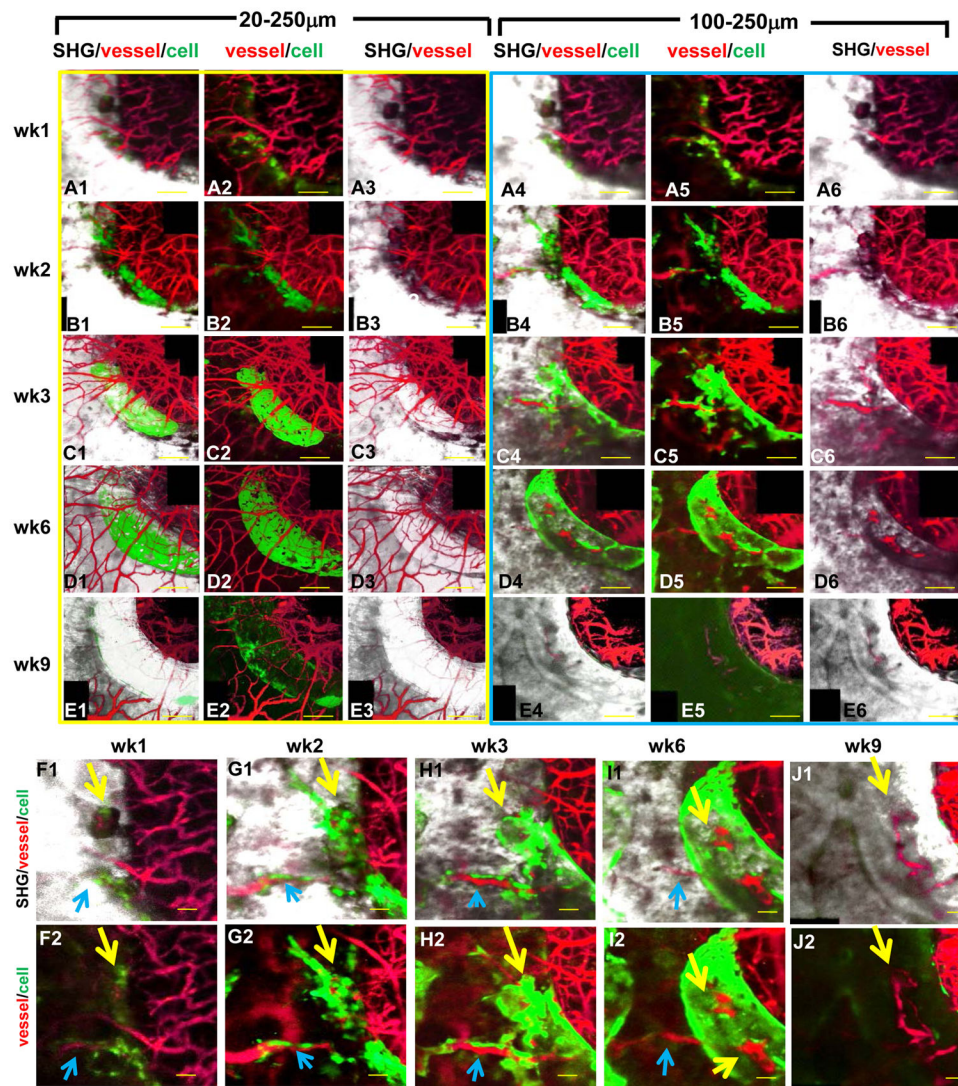


**Figure 2. Real-time tracking of the clusters of Col2.3GFP (+) osteoblasts and the coupled angiogenesis at the site of defect repair**

Clusters of GFP (+) osteoblasts at the edge of bone defect were tracked via MPLSM at a high magnification at week 1 (A1–6), 2 (B1–6), 3 (C1–6), 6 (D1–6) and 9 (E1–6). The region of interest was reconstructed and shown at a depth of 20–250µm (panel 1–3) and 100–250µm (panel 4–6). The cluster of Col2.3GFP (+) cells (indicated by yellow arrows) and the associated vessels were further zoomed-in to illustrate the spatial interaction of clusters of GFP (+) cells and neovasculature at week 1 (G1–2), 2 (H1–2), 3 (I1–2), 6 (J1–2) and 9 (K1–2). Osteoblasts were identified along microvessels or closely associated with vasculature at week 2 and 3 (G1&2, H1&2, blue arrows). Scale bar =100µm in B–F, 40µm in G–K.

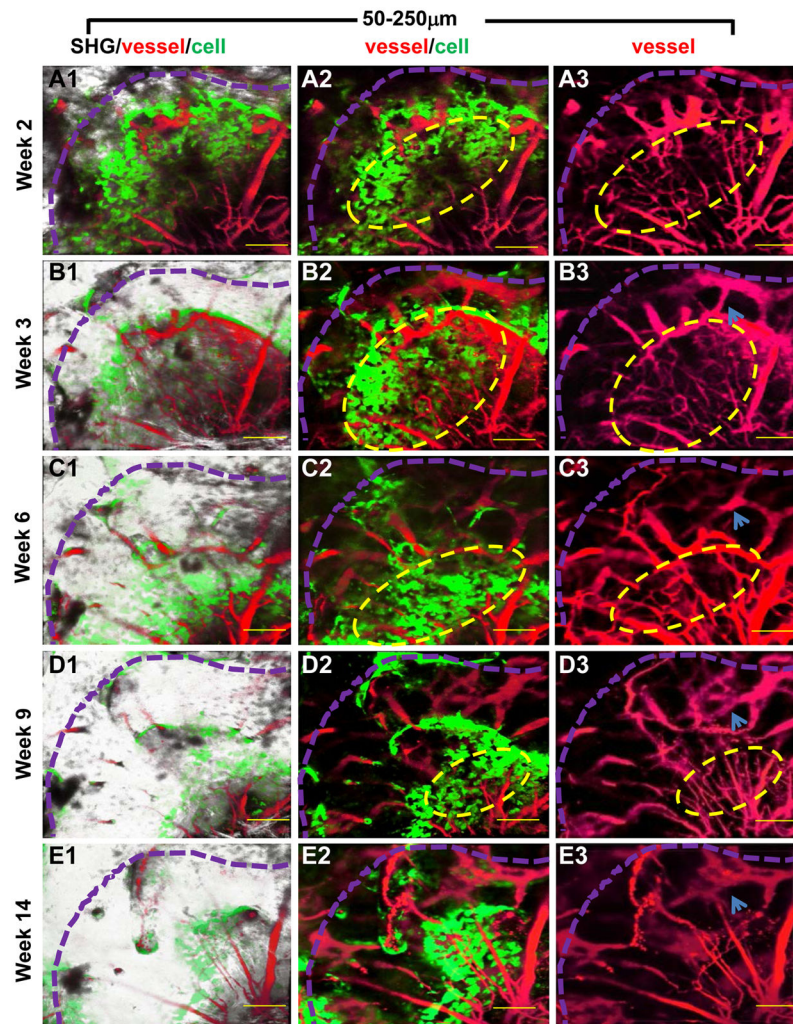


**Figure 3. Real-time tracking of angiogenesis and vascular modeling in cranial defect repair**  
Dynamics of defect healing and neovascularization was shown in time-series images reconstructed by Col2.3GFP (+) osteoblasts (green), blood vessels (red) and SHG (+) bone matrix (white) at a depth of 50–250 $\mu$ m (A1–3, B1–3, C1–3, D1–3 and E1–3) at week 2, 3, 6, 9 and 14. The purple dash lines marks the defect at day 1 in all images. The combined images of SHG, GFP, and vessels demonstrate the progressive new bone formation at the leading edge of the defect (panel A1, B1, C1, D1 and E1). Images of GFP and blood vessels combined (panel A2, B2, C2, D2 and E2), and images of blood vessels alone at the same site (panel A3, B3, C3, D3, E3) are shown to illustrate the spatial interaction of osteoblasts and blood vessels over time. The association of osteoblasts with micro-capillary vessel is indicated by yellow circles. The formation and remodeling of vascular channels within newly formed bone are indicated by blue arrows in B3–D3. Scale bar =125 $\mu$ m.

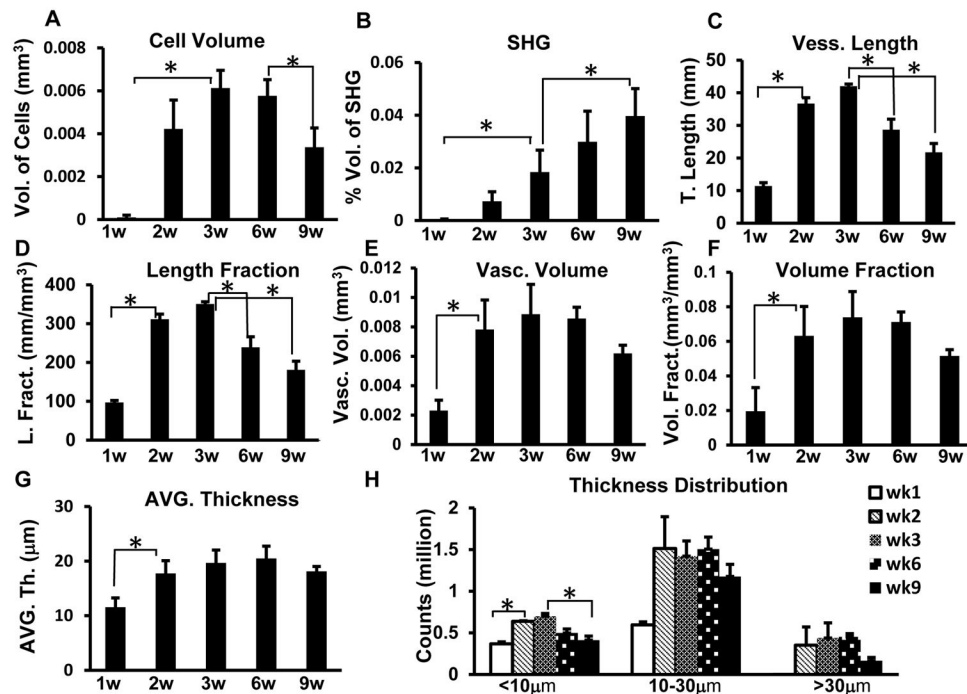


**Fig. 4. Quantitative and histomorphometric analyses of GFP (+) cells, SHG, and neovasculture during defect healing**

Quantitative and histomorphometric analyses of SHG, GFP and vascularity were performed as described. Osteoblast volume peaked at week 3 and 6, decreased at week 9 (A) whereas SHG progressively accumulated up to 9 weeks (B). Blood vessel length (C), length fraction (D), vascular volume (E) and volume fraction (F) increased at week 1 and peaked at week 3, coupled with osteoblast expansion and differentiation. Average vessel thickness (G) and thickness distribution (H) at the site of the defect repair are shown. Data are expressed as the mean + SEM. \* indicates significant difference ( $p < 0.05$ ).  $n = 4$ .

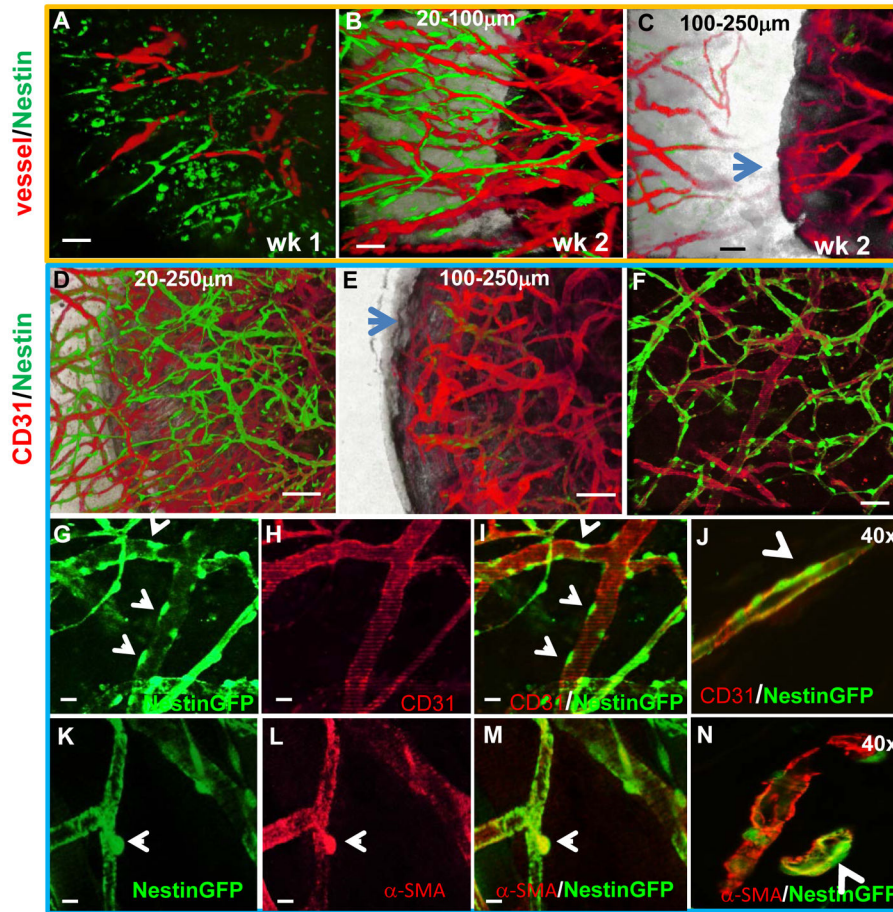


**Fig. 5. Distribution of nestin-GFP (+) cells at the cranial defect site**

A windowed defect was created in nestin-GFP transgenic mouse. The reconstructed live MIPSM images at week 1 and 2 show nestin-GFP (+) cells associated with nascent blood vessels at week 1 (A) and 2 (B) in soft tissue on top of bone. Microvasculature at the leading edge of the defect was largely negative for nestin-GFP (C). CD31 immunofluorescent staining of intact calvaria samples demonstrated that nestin-GFP (+) cells were primarily associated with blood vessel at the surface of bone wound (D). Only a few nestin-GFP (+) cells were identified on vessels leading into the bone tissue (F). Higher magnification 3D reconstruction of MIPSM image depicts CD31 (+) nestin-GFP (+) vessels at the defect site (F). Nestin GFP (+) cells demonstrated typical morphology of endothelial lining cells (G) and were co-localized with CD31 (H: CD31 only, I: nestinGFP overlaying with CD31). Immunofluorescent staining of CD31 using histologic section confirmed the co-localization of nestin-GFP (+) cells with CD31 (+) endothelial cells (J). Immunofluorescent staining of  $\alpha$ SMA showed co-localization of nestin-GFP (+) cells with  $\alpha$ SMA (+) pericytes (K: nestinGFP only; L:  $\alpha$ SMA(+) vessel only; M: nestinGFP overlaying with  $\alpha$ SMA; arrow indicate  $\alpha$ SMA+ perivascular cells). Immunofluorescent staining of CD31 using histologic section confirmed the co-localization of nestin-GFP (+) cells with  $\alpha$ SMA (N).

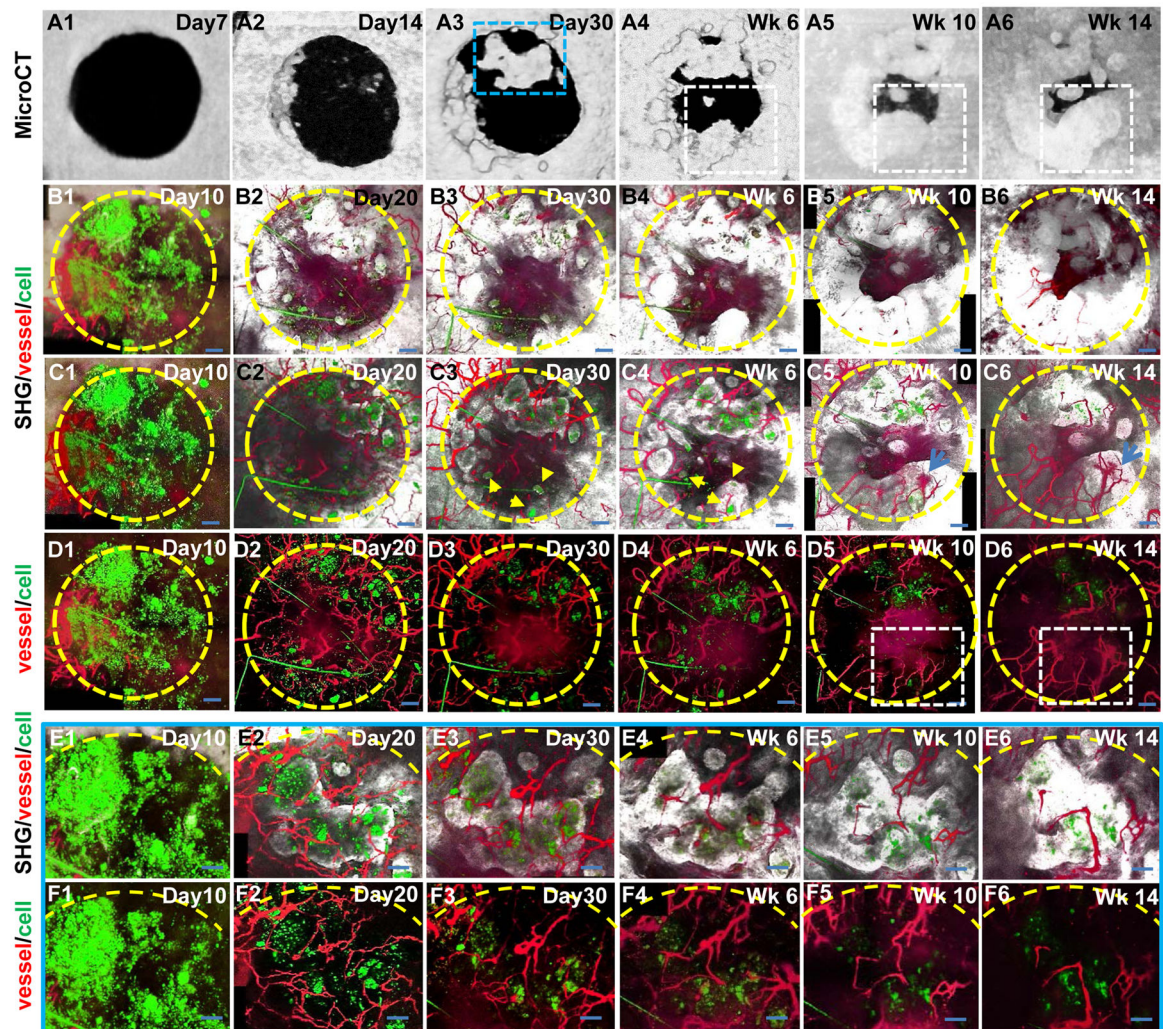


**Fig. 6. Live tracking of donor BMSCs and neovascularization during cranial defect repair and regeneration**

Donor BMSCs isolated from Col2.3GFP mice were implanted into a cranial defect window chamber created in an immunocompromised mouse. The entire defect was scanned and reconstructed at the indicated time points by microCT (panel A) and MPLSM (panel B&C&D), with yellow circle indicating the defect region. The 3D time-series images of the defect (panel B) were reconstructed by Col2.3GFP(+) osteoblasts (green), SHG (+) bone matrix (white) and blood vessel (red) to show progressive defect healing over a period of 14 weeks. The same time-series 3D images reconstructed by GFP (green) and blood vessels (red) were superimposed with a 2D image of SHG to show the distribution and incorporation of donor GFP (+) cells into bone matrix (panel C). The same time series 3D images reconstructed by GFP (green) and blood vessels (red) (panel D) illustrate the spatial interaction of GFP (+) cells with neovasculature during the entire process of repair. Blue boxed region in A3 corresponds to the region undergoing donor-dependent bone formation. White boxed region in A4–6 and D5–6 corresponds to the region primarily undergoing host-dependent bone formation. Arrows in C3 and C4 indicates donor derived bone nodules.

Arrows in C5 and C6 indicate the formation of bone marrow space and remodeling of sinusoidal vessels in new bone. Blue boxed region in A3 is further zoomed-in to illustrate the dynamic progression of donor dependent bone formation (panel E) and spatial interaction of donor cells with neovasculature (panel F). Scale bar =200  $\mu\text{m}$  in panel B, C and D. Scale bar=100 $\mu\text{m}$  in panel E and F.

**Table 1**

Pearson's Correlation Coefficient (R) for histomorphometric analyses of neovasculature

	Vasc. Vol. Fract.	AVG. Vess. Th.	T. Vess. Length Fract.	Vessel <10mm	Vessel 10-30mm	Vessel >30mm
<b>Cell Vol.</b>	0.52 (p=0.026) (F=6.032)	0.65 (p=0.0037) (F=11.53)	0.69 (p=0.0016) (F=14.28)	0.60 (p=0.02) (F=7.14)	0.47 (p=0.05) (F=4.785)	0.48 (p=0.05) (F=4.529)

The table lists Pearson's Correlation Coefficient (R) for histomorphometric analyses of vascularity and osteoblastogenesis as determined by Col2.3GFP (+) cell volume. The p and F values of the indicated coefficient are listed in parenthesis. A p value <0.05 is considered statistically significant.

RESEARCH

Open Access



# Second harmonic generation microscopy reveals altered collagen microstructure in usual interstitial pneumonia versus healthy lung

Robert Matthew Kottmann<sup>1\*†</sup>, Jesse Sharp<sup>2†</sup>, Kristina Owens<sup>1</sup>, Peter Salzman<sup>3</sup>, Guang-Qian Xiao<sup>4</sup>, Richard P. Phipps<sup>5</sup>, Patricia J. Sime<sup>1</sup>, Edward B. Brown<sup>2</sup> and Seth W. Perry<sup>2\*</sup>

## Abstract

**Background:** It is not understood why some pulmonary fibroses such as cryptogenic organizing pneumonia (COP) respond well to treatment, while others like usual interstitial pneumonia (UIP) do not. Increased understanding of the structure and function of the matrix in this area is critical to improving our understanding of the biology of these diseases and developing novel therapies. The objectives herein are to provide new insights into the underlying collagen- and matrix-related biological mechanisms driving COP versus UIP.

**Methods:** Two-photon second harmonic generation (SHG) and excitation fluorescence microscopies were used to interrogate and quantify differences between intrinsic fibrillar collagen and elastin matrix signals in healthy, COP, and UIP lung.

**Results:** Collagen microstructure was different in UIP versus healthy lung, but not in COP versus healthy, as indicated by the ratio of forward-to-backward propagating SHG signal ( $F_{\text{SHG}}/B_{\text{SHG}}$ ). This collagen microstructure as assessed by  $F_{\text{SHG}}/B_{\text{SHG}}$  was also different in areas with preserved alveolar architecture adjacent to UIP fibroblastic foci or honeycomb areas versus healthy lung. Fibrosis was evidenced by increased col1 and col3 content in COP and UIP versus healthy, with highest col1:col3 ratio in UIP. Evidence of elastin breakdown (i.e. reduced mature elastin fiber content), and increased collagen:mature elastin ratios, were seen in COP and UIP versus healthy.

**Conclusions:** Fibrillar collagen's subresolution structure (i.e. "microstructure") is altered in UIP versus COP and healthy lung, which may provide novel insights into the biological reasons why unlike COP, UIP is resistant to therapies, and demonstrates the ability of SHG microscopy to potentially distinguish treatable versus intractable pulmonary fibroses.

**Keywords:** Second harmonic generation, SHG, Fibrosis, Collagen, Matrix, Lung, Pulmonary, Two photon, Fluorescence, Microscopy, Usual interstitial pneumonia, Idiopathic pulmonary fibrosis, Cryptogenic organizing pneumonia

## Background

Pulmonary fibrosis results from accumulation of fibroblasts, scar-forming myofibroblasts, and extracellular matrix proteins including collagen, often leading to irreversible loss of lung function. It can be caused by various factors including toxins, radiation exposure, autoimmune

disorders, and infection. Idiopathic Pulmonary Fibrosis (IPF) is a severe form of fibrotic lung disease that can progress to respiratory failure and has a prognosis worse than lung cancer. There are currently few effective therapies. Usual interstitial pneumonia (UIP) is the histopathology underlying IPF and is characterized by heterogeneity of disease and accumulation of fibroblast foci and collagen with an emphasis on collagen type I (col1) over type III (col3) [1, 2], and abnormalities in other matrix molecules including elastin [3]. IPF is one of many diseases associated with significant collagen and other matrix protein

\* Correspondence: Matt\_Kottmann@URMC.Rochester.edu; Seth\_Perry@urmc.rochester.edu

†Equal contributors

<sup>1</sup>Department of Medicine, University of Rochester, Rochester, NY, USA

<sup>2</sup>Department of Biomedical Engineering, University of Rochester, Rochester, NY, USA  
Full list of author information is available at the end of the article

accumulation. It is the most common of the idiopathic interstitial pneumonias, is increasing in prevalence, and it is a progressive disease that causes significant morbidity and mortality. The median duration of survival from the time of diagnosis is only 2.9 years [4, 5]. There are currently few effective FDA approved treatments for IPF (for review and overview of current and targeted therapies for IPF, please see: [6–10]), making research into IPF pathogenesis critical.

Cryptogenic organizing pneumonia (COP) is another common fibrotic lung disease. It is also characterized by accumulation of matrix components resulting in organized areas of granulation tissue in the lung. Components of this pathologic matrix accumulation in COP also include col1 and col3 (with an emphasis on col3 over col1, in contrast to UIP), fibronectin, and proteoglycans [1, 11]. In contrast to UIP, the granulation tissue found in COP accumulates in the airspaces and small airways rather than in the interstitial spaces and importantly, COP is a treatable disease with most cases responding to corticosteroids. Although the matrix components of UIP and COP have some similarities, it is unknown why the excess matrix in COP can be reabsorbed or cleared after treatment with corticosteroids while the matrix in UIP is resistant to treatment and resolution [1].

A growing body of literature supports the roles of matrix organization and structure as important effectors of fibrotic lung disease. Extracellular matrix (ECM) components have important mechanobiological properties including the abilities to activate pro-fibrotic cytokines; regulate cell trafficking; and modulate cell activation, proliferation, survival and differentiation [12, 13]. The organization and structure of the ECM, including collagen, also helps regulate availability of and interactions with a large variety of cell-matrix binding sites critical for controlling lung function. These findings further reinforce the notion that in biology, structure is a key determinant of function. Indeed, other data suggests that ECM stiffness regulates key cellular activities that may contribute to IPF [14], as well as endogenous lung function [15]. Hence, there is heightened interest in the content and structure of the matrix, and how abnormal content and structure may impact lung pathophysiology. For these reasons, we hypothesized that differences in ECM structure, and collagen microstructure in particular, underlie the different natural histories, prognoses, and responses to treatment of UIP and COP.

To explore this question, we used Second Harmonic Generation (SHG) Microscopy (SHGM) to compare the matrix of UIP and COP to that of healthy lung tissue. SHGM is a variant of two photon (2P) microscopy that can detect the fibrillar collagens (FCs) without exogenous labels. The fibril-forming collagens include collagen types 1–3, 5, 11, 24, and 27 [16], and at least several of these FCs such as types I, III, and V are key players in lung fibroses including

usual interstitial pneumonia (UIP) and cryptogenic organizing pneumonia (COP) [1–3, 11]. SHGM can be used to interrogate changes in collagen's macrostructural properties (e.g. collagen fiber density, arrangement, and organization), as well as collagen's subresolution microstructural properties (e.g. the diameter, order versus disorder, and/or packing density of collagen fibrils within larger collagen fibers) [17–22]. These microstructural features of individual collagen fibers, as they can influence SHG directionality from that fiber (i.e.  $F_{SHG}/B_{SHG}$ , defined below), are herein collectively referred to as collagen "microstructure". In this aspect, SHGM is unique in its ability to interrogate subresolution structure of FCs (e.g. col1 and col3) in intact and potentially live samples without exogenous labels, abilities which also make SHGM an attractive potential clinical and investigational diagnostic tool. Thus this technique can utilize intrinsic properties of matrix components to characterize the content and organization of the ECM in these fibrotic lung diseases.

Using SHGM, herein we describe important differences in matrix content and organization in UIP/IPF and COP compared to healthy lung tissue. Specifically, we found differences in collagen's subresolution structural properties in UIP compared to COP and healthy lung as assessed by SHGM and the  $F_{SHG}/B_{SHG}$  ratio. Importantly, even adjacent normal UIP tissue exhibited these differences in collagen microstructure compared to healthy lung, thus introducing the compelling possibilities that altered collagen microstructure might lead to or correlate with fibrosis in the relatively intractable disease UIP, but not in the more treatable COP. We also report different col1:col3 ratios in UIP versus COP and healthy lung tissue, which is important especially in the context of our  $F_{SHG}/B_{SHG}$  data, because others have reported that altered col1:col3 ratios can drive (or perhaps be driven by) changes in FC microstructure such as fibril diameter [23–25], which is one aspect of collagen microstructure interrogated by the  $F_{SHG}/B_{SHG}$  ratio [17–22]. Finally, we show both UIP and COP have differences in mature elastin fiber content, and elastin:collagen ratio, suggesting that both fibrotic disease have identifying physiological differences in matrix structure suggestive of lung disease, but only the less tractable disease, UIP, exhibits differences in underlying collagen microstructure. These results are important because they provide new insights into the potential biological and biostructural underpinnings of refractory versus "treatable" lung fibroses, with an emphasis on subresolution collagen microstructure, and demonstrate SHGM's potential as a powerful new tool for aiding in the diagnosis and treatment of lung fibrosis.

## Methods

### Patient populations and source of tissue

Formalin-fixed paraffin embedded human lung tissue sections were obtained from the University of Rochester

Department of Pathology using an RSRB approved protocol, by database search for resected lung tissue from mixed-sex patients with pathologically confirmed diagnoses of either UIP or COP. Additional UIP lung tissue was obtained from the NIH sponsored Lung Tissue Research Consortium. All UIP and COP biopsy specimens contained established, moderate to severe fibrosis by Pathologist diagnosis. Healthy lung tissue specimens were obtained from non-smoker subjects who had a lung biopsy for a lesion that was confirmed either benign or not primary lung cancer, from regions adjacent to the lesions that did not contain any portion of the lesion.

### Histology and immunohistochemistry

Immunohistochemistry (IHC) for col1 and col3 was performed as previously described [19] and excerpted in part herein (with modifications). Briefly, formalin fixed paraffin embedded (FFPE) lung biopsies obtained as above were sectioned at 15  $\mu$ m, then static-mounted on positively charged slides. For IHC, sections were deparaffinized with xylene and graded ethanols, followed by 30 minutes microwaving (65 °C) in sodium citrate solution for antigen retrieval, 2  $\times$  5 min in sterile PBS, then blocked for one hour (10 % goat serum, 0.5 % BSA, 0.2 % Triton-X, 0.3 M glycine in PBS). Primary antibodies for Collagen I (#C2456, Sigma-Aldrich, St. Louis, MO; 1:1000) and/or Collagen III (#ab7778, Abcam, Cambridge, UK; 1:200) diluted in blocking buffer, were then applied for 2 h at room temperature in a humidified chamber, followed by 3  $\times$  5 min PBS wash, then one hour of Alexa Fluor 594-conjugated goat anti-rabbit (for Col3) or goat anti-mouse (for Col1) IgG secondary antibodies (1:500 in 2 % goat serum, 0.25 % BSA; Invitrogen, Carlsbad, CA). Optimal antibody dilutions and incubation times were pre-determined empirically. Following staining for col1 and/or col3, lung sections were washed 3  $\times$  5 min in PBS and mounted in ProLong Gold Antifade reagent (without DAPI; Invitrogen, Carlsbad, CA), then allowed to dry before imaging. Imaging and quantification of these tissues labeled for col1 and col3 was then performed as described in “Col1/Col3 ratio imaging” below. Hematoxylin-eosin (H&E) staining was performed by standard methods as previously described [19].

### Two photon and SHG microscopy

#### *F<sub>SHG</sub>/B<sub>SHG</sub> Imaging*

Formalin fixed paraffin embedded human lung tissue sections for healthy, UIP and COP were obtained and prepared on slides as described above then imaged (unstained, unless otherwise described) for forward ( $F_{SHG}$ ) and backward ( $B_{SHG}$ ) SHG signals as previously described [19, 26, 27] and as excerpted in part herein, with modifications. We [26] and others [28] have demonstrated that reliable  $F_{SHG}/B_{SHG}$  data is obtained from paraffin embedded human biopsy tissues. Double-blinded samples were

imaged using a custom built multiphoton microscope, with a Mai Tai titanium:sapphire laser (Newport/Spectra Physics, Santa Clara, CA) providing two-photon (2P) excitation (100 fs pulses at 80 MHz and 810 nm) which was circularly polarized by passing the beam through a Berek compensator (Model 5540, New Focus, Irvine, CA) before the scanner. Beam scanning and image acquisition were performed with a custom-modified Fluoview FV300 confocal scanner interfaced with a BX61WI upright microscope (Olympus, Center Valley, PA), with an Olympus XLUMPLFL20xW water immersion lens (20 $\times$ , 0.95 N.A.) collecting the epi-directed backscattered SHG ( $B_{SHG}$ ) and an Olympus 0.9 N.A. optical condenser simultaneously collecting the forward-scattered SHG ( $F_{SHG}$ ) using HQ405/30 m-2P emission filters (Chroma, Rockingham, VT) and HC125-02 photomultiplier tubes (PMTs) (Hamamatsu Corporation, Hamamatsu, Japan) for both  $F_{SHG}$  and  $B_{SHG}$ . Excitation light (810 nm) was separated from emission signals by a short pass dichroic mirror (Chroma 670 DCSX) on the backwards ( $B_{SHG}$ ) side, and a 565 nm long pass dichroic mirror (565 DCSX, Chroma) on the forward ( $F_{SHG}$ ) side. Thus  $F_{SHG}$  and  $B_{SHG}$  were simultaneously captured in two distinct channels on every scan. The resulting two-channel ( $F_{SHG}$  and  $B_{SHG}$ ) images were 680 microns across. Laser power was monitored and kept constant throughout each experiment and across experimental repetitions, as were PMT voltage, gain, and offset. Because the goal was to compare relative differences in  $F_{SHG}/B_{SHG}$  between the experimental conditions, and all experimental conditions to be compared were imaged during each imaging session, further calibration of the PMTs (e.g. to a reference standard) was not required.

Using these methods, we obtained z-stacks (3  $\mu$ m steps over the entire tissue thickness) for  $F_{SHG}$  and  $B_{SHG}$  in two channels simultaneously, from 3-6 sections, ~5 random collagen-containing regions of interest (ROIs) (images)/section, and 15–30 ROIs total per patient, for N = 5, 5, and 10 Healthy, COP, and UIP patients respectively. All data was plotted as N = number of patients per group. For each channel ( $F_{SHG}$  and  $B_{SHG}$ ), the image stack was maximum intensity projected (which effectively “autofocuses” each Z-stack into comparable single images), then image analysis was performed with ImageJ as previously described [19, 26, 27]. Briefly, background was defined by the average pixel counts of an equivalent laser-excited maximum intensity projected image stack taken from an area of the slide with no tissue, and subtracted from the raw  $F_{SHG}$  or  $B_{SHG}$  maximum intensity projected image stacks. These background subtracted  $F_{SHG}$  and  $B_{SHG}$  images were divided to create an  $F_{SHG}/B_{SHG}$  ratio image. To calculate  $F_{SHG}/B_{SHG}$ , a common threshold was applied to all  $F_{SHG}/B_{SHG}$  ratio images to distinguish fibrillar collagen pixels from background pixels, and subthreshold background (i.e. non collagen

fiber) pixels were excluded from analysis by binary masking. This average  $F_{\text{SHG}}/B_{\text{SHG}}$  value from each image was averaged across all images per patient, to yield a single representative  $F_{\text{SHG}}/B_{\text{SHG}}$  value for each patient, which were then expressed as mean  $F_{\text{SHG}}/B_{\text{SHG}} \pm \text{SEM}$  for the Healthy, COP, and UIP patient populations.

#### **Col1/Col3 ratio imaging**

The same patient sets or subsets as described above for  $F_{\text{SHG}}/B_{\text{SHG}}$  imaging were immunofluorescently (IF) labeled for Col1 and Col3 as described in “Histology and Immunohistochemistry” above. Following this labeling with anti-Col1 and anti-Col3 antibodies, two photon imaging was performed as described for  $F_{\text{SHG}}/B_{\text{SHG}}$ , except now two-photon excited fluorescence (TPEF) for immunofluorescently labeled Col1 or Col3 was captured in the backwards (epidirected) channel only, with the IF signal captured with a HQ635/30 m-2P emission filter (Chroma) and HC125-01 Hamamatsu PMT. Z-stacks from each ROI were obtained, intensity projected, and background subtracted for all sections and ROIs per patient as described for  $F_{\text{SHG}}/B_{\text{SHG}}$  above. Fluorescent intensities from the resultant images were quantified with ImageJ and then expressed as mean anti-Col1 or anti-Col3 IF pixel intensity  $\pm \text{SEM}$  per patient, as described above and previously [19]. Col1:Col3 ratio was quantified in the same fashion, then dividing the mean Col1/Col3 signals for each patient.

#### **Collagen/elastin ratio imaging**

The same patient sets or subsets were imaged and quantified for total FC content (i.e. total  $F_{\text{SHG}} + B_{\text{SHG}}$  signals) and intrinsic autofluorescence (AF) from mature lung elastin (captured at 515–555 nm), as follows. Imaging was performed exactly as for  $F_{\text{SHG}}/B_{\text{SHG}}$ . Immediately after each simultaneous  $F_{\text{SHG}}$  and  $B_{\text{SHG}}$  stacks was taken, the backward channel filter was replaced with a 535/40 emission filter (Chroma) and a replicate stack taken, to capture intrinsic autofluorescence (AF) from mature lung elastin in exactly the same ROIs from which collagen SHG was obtained. Elastin AF,  $F_{\text{SHG}}$ , and  $B_{\text{SHG}}$  images were processed as described above. This mean Elastin AF signal per patient  $\pm \text{SEM}$  was quantified and expressed both by itself and relative to the total FC signal (i.e. total SHG signal, or  $F_{\text{SHG}} + B_{\text{SHG}}$ ).

#### **Statistical analyses**

All data are expressed as patient means  $\pm \text{SEM}$ . A one way ANOVA with Dunnett’s post-hoc tests correcting for multiple comparisons were used to establish statistical significance using “R” (<http://www.R-project.org>) and GraphPad Prism (<http://www.graphpad.com>) software. Results were considered significant if  $p < 0.05$ .

## **Results**

### **Fibrillar collagen microstructure in the ECM is different in UIP, but not COP, versus healthy lung**

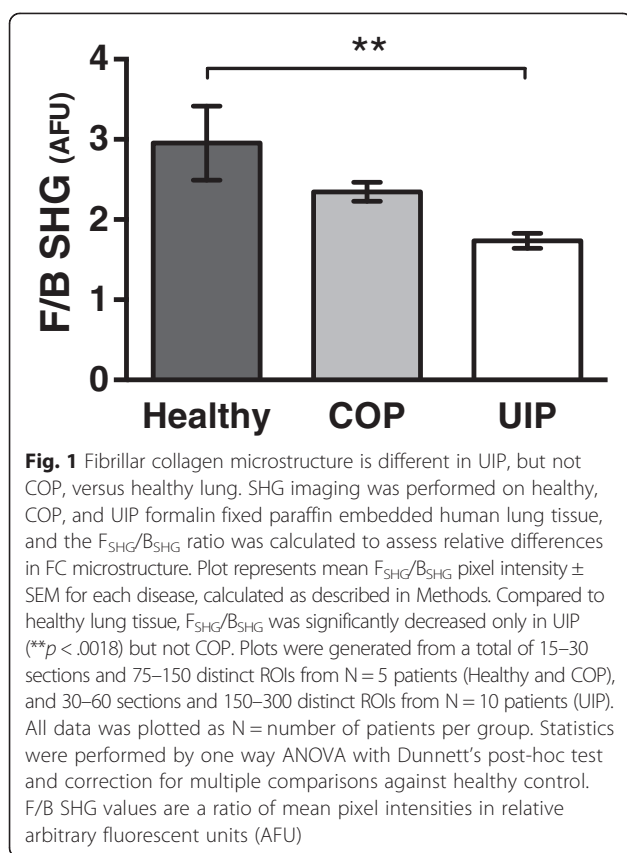
SHG in general is sensitive to changes in collagen microstructure including regularity or ordering of collagen fibrils within larger collagen fibers; fibril compaction; and fibril diameter, tilt angle, or pitch angle [17–22, 29–34]. SHG is emitted both forwards and backwards (i.e. epidirected) from the SHG-generating scatterers in the focal volume, and the  $F_{\text{SHG}}/B_{\text{SHG}}$  ratio in particular is primarily sensitive to the spatial extent of SHG-generating scatterers along the optical axis, i.e. the effective diameter or packing arrangement/density/order versus disorder of collagen fibrils within the SHG focal volume [18–22, 26]. Therefore, to determine if a relatively intractable lung fibrosis such as UIP has a different underlying FC microstructure in the ECM versus a treatable lung fibrosis such as COP, or versus healthy lung, we used SHGM to interrogate the mean  $F_{\text{SHG}}/B_{\text{SHG}}$  ratio in the ECM of UIP, COP, and healthy lung tissues. Intriguingly, we found this  $F_{\text{SHG}}/B_{\text{SHG}}$  ratio was significantly decreased UIP versus healthy lung, but unchanged in COP versus healthy lung (Fig. 1). Figure 2 illustrates the results quantified in Fig. 1 with representative  $F_{\text{SHG}}$ ,  $B_{\text{SHG}}$ , and  $F_{\text{SHG}}/B_{\text{SHG}}$  images from each condition. Although corresponding clinical data such as symptoms or pulmonary function testing was not available, all patients with UIP and COP had moderate to severe pathology on the biopsy specimens. Importantly, the lack of significant variability in the  $F_{\text{SHG}}/B_{\text{SHG}}$  ratio between patients in each disease group and between healthy controls suggests there is a disease specific phenotype. Additional studies will be necessary to determine whether there is a difference in the  $F_{\text{SHG}}/B_{\text{SHG}}$  ratio seen in UIP on the basis of disease severity.

Figure 3 shows representative H&E staining (2A-C) matched to the same fields of view (FOVs) for  $F_{\text{SHG}}$  (2D-F) for healthy, COP, and UIP respectively, and illustrates that the SHG signal (white pixels, 2D-F) quantified from these lung tissues arises as expected chiefly from small airways (yellow arrows) and parenchymal alveolar space in healthy lung (2A/D), and from fibrotic collagen deposition (blue arrows) in COP (2B/E) and UIP (2C/F).

Together these results show that FC microstructure is altered in UIP but not in COP versus healthy lung.

### **Lung tissue with preserved alveolar architecture adjacent to UIP fibroblastic foci or honeycomb areas has different fibrillar collagen microstructure versus healthy lung**

Next, we wondered whether lung tissue with preserved alveolar architecture adjacent to UIP fibroblastic foci or honeycomb areas also had different FC microstructure versus healthy lung as measured by  $F_{\text{SHG}}/B_{\text{SHG}}$ , which might suggest the possibility of underlying collagen structural deficits that could predict or predispose development



of UIP. Indeed, fibroblastic foci, honeycomb areas, and surrounding normal appearing lung tissue in UIP all had similar  $F_{SHG}/B_{SHG}$  ratios, which were all different versus the  $F_{SHG}/B_{SHG}$  of healthy lung tissue (Fig. 4). These results provide an exciting, previously unreported “first glance” into the biologic underpinnings of UIP as relates to FC microstructure, and suggest the possibility that pre-existing alterations in FC microstructure even in “normal” lung tissue may foreshadow or precipitate development of UIP.

#### Col1, Col3, and Col1/Col3 ratio differences in UIP versus COP and healthy lung

Col1 and col3 are implicated in the pathology of UIP and COP, and as fibrotic diseases, col1 and col3 levels in UIP and COP are anticipated to be higher compared to healthy lung. Moreover, previous reports have suggested that col1 is the primary collagen deposited in UIP, whereas col3 assumes this role in COP [1]. Importantly, relative col1 and col3 expression levels can interact to regulate aspects of collagen microstructure such as collagen fibril or fiber diameter [23–25]. Conversely, by altering availability of fibroblast (or other effector cell type) binding sites on collagen fibrils, changes in collagen's subresolution fibril microstructure may regulate relative collagen expression levels. Therefore, we wished to determine how changes in  $F_{SHG}/B_{SHG}$  ratio (Fig. 1),

indicative of altered collagen microstructure in lung ECM, correspond with changes in col1/col3 deposition in UIP, COP, and healthy lung.

We found higher col1 levels in both UIP and COP compared to healthy lung, with UIP showing the highest col1 levels versus COP and healthy (Fig. 5a). Both UIP and COP had similarly elevated col3 levels versus healthy lung (Fig. 5b). Overall, this resulted in relative col1:col3 ratios that were significantly elevated in UIP versus healthy controls, but not in COP versus healthy controls (Fig. 5c). Fig. 5d-f illustrate higher Col3 levels in COP (4E) and UIP (4F) versus healthy (4D), as shown in 4B. Together, these results demonstrate the expected evidence of fibrosis in both UIP and COP compared to healthy lung controls, and confirm previous observations of higher relative col1:col3 deposition in UIP, versus more abundant col3 over col1 deposition in COP [1].

These Col1:Col3 ratio findings are also interesting in the context of the  $F_{SHG}/B_{SHG}$  differences demonstrated in Fig. 1, because altered Col1:Col3 ratios are reported to regulate collagen fibril diameter and/or structure (i.e. FC microstructure) [23–25], and accordingly UIP shows a difference in both col1:col3 ratio (Fig. 5c) and  $F_{SHG}/B_{SHG}$  (i.e. FC microstructure) (Fig. 1) versus healthy lung, whereas COP shows neither a difference in col1:col3 ratio nor  $F_{SHG}/B_{SHG}$  versus healthy lung. Overall, these results suggest a possible relationship between FC microstructure differences and altered col1:col3 ratios in intractable UIP fibrosis, but not in the more treatment responsive COP fibrosis.

#### Elastin and elastin:collagen ratios differ in UIP and COP versus healthy lung

In parallel with SHGM imaging, intrinsic tissue autofluorescence representing principally mature lung elastin can be captured simultaneously with SHG [35], to provide additional insights into how ECM structure and organization may differ in UIP versus COP. Elastin is another lung ECM component that interacts closely with collagen to regulate lung function [36–39] and is frequently dysregulated in fibrotic lung diseases [40, 41]. Elastin's intrinsic autofluorescence captured by two-photon excitation fluorescence (TPEF) microscopy arises from the pyridoxine-based pyridolamine cross-links [35, 42] found only in mature elastin fibers [43], thus making TPEF of elastin a useful indicator for the mature elastin fiber content of lung tissue. Therefore, we captured this signal for the same healthy, UIP, and COP specimens, then quantified and expressed it both by itself and relative to the total FC signal (i.e. total SHG signal, or  $F_{SHG} + B_{SHG}$ ), to see whether there were other underlying differences in ECM structure or organization that we could identify and quantify by SHGM and two-

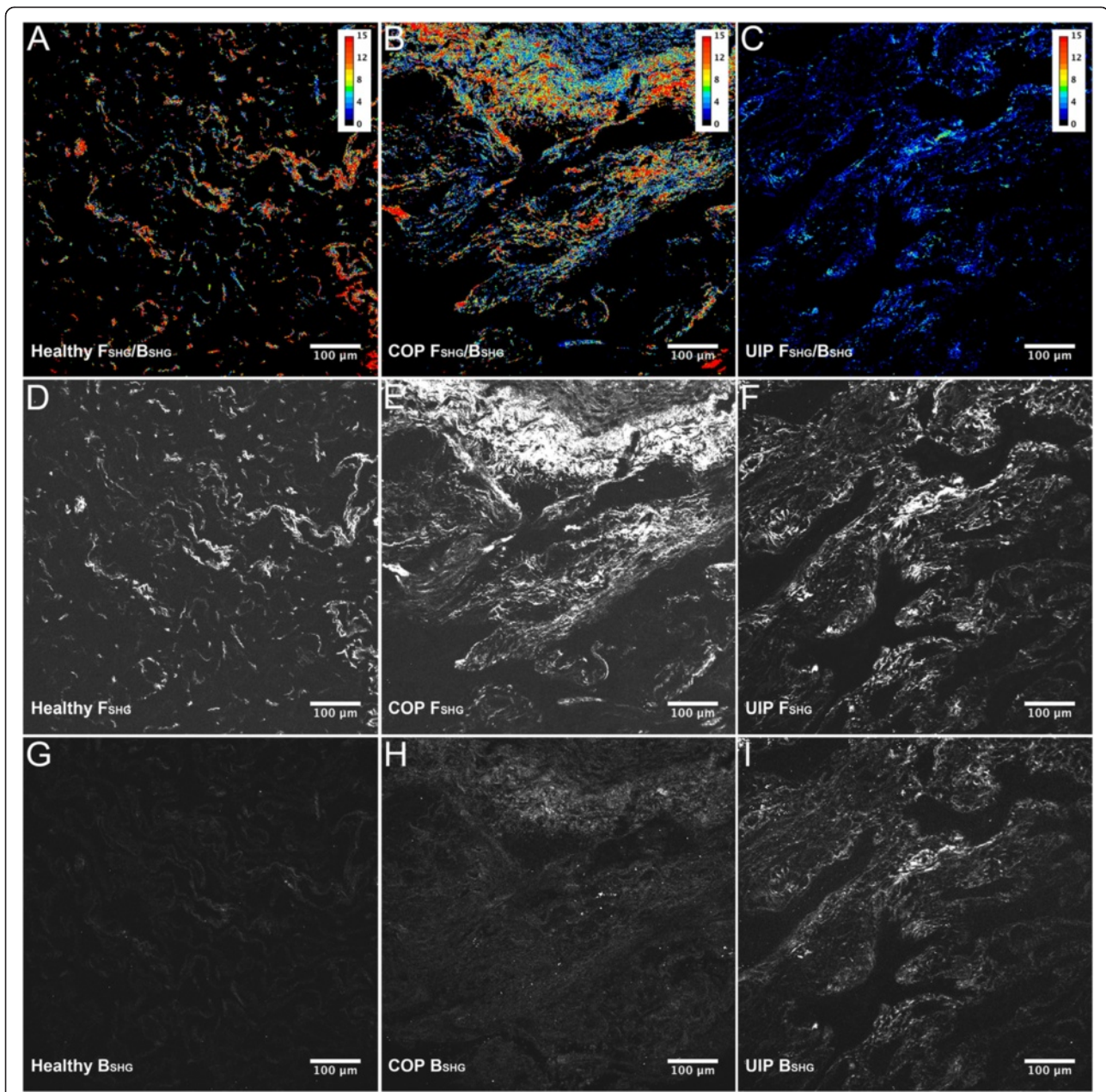
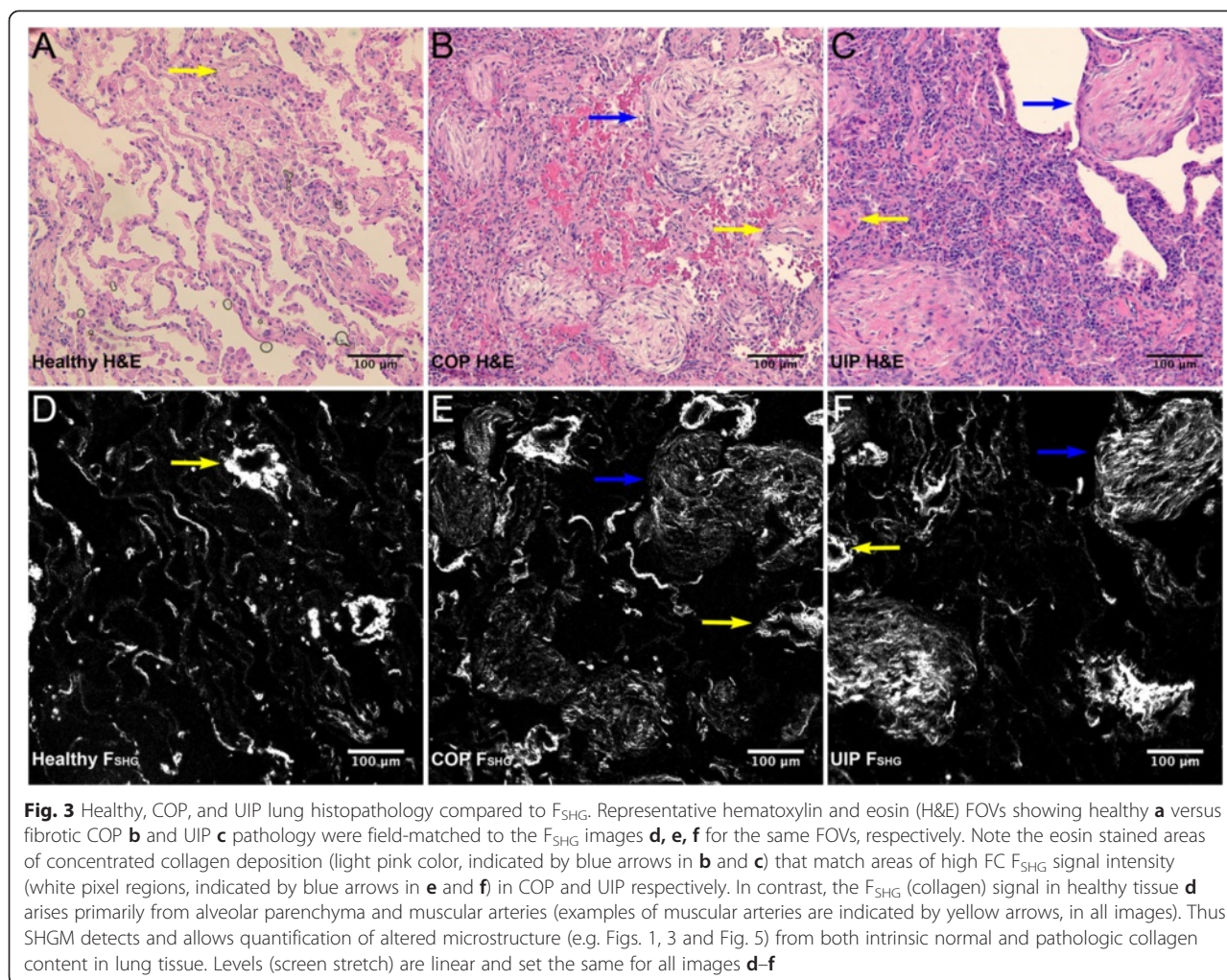


**Fig. 2** Illustration of  $F_{SHG}$ ,  $B_{SHG}$ , and  $F_{SHG}/B_{SHG}$  imaging as seen in Fig. 1. SHG imaging was performed on healthy, COP, and UIP formalin fixed paraffin embedded human lung tissue, and  $F_{SHG}$ ,  $B_{SHG}$ , and  $F_{SHG}/B_{SHG}$  ratio images obtained, as described for Fig. 1. Panels **a-c**, showing look-up-table (LUT) "heatmaps" applied to the  $F_{SHG}/B_{SHG}$  ratio pixel values for representative  $F_{SHG}/B_{SHG}$  images, illustrate that Healthy lung tissues have the lowest collagen content (as expected) but higher  $F_{SHG}/B_{SHG}$  ratios compared to COP and UIP which evidence fibrosis and lower average  $F_{SHG}/B_{SHG}$  ratios as quantified in Fig. 1. Panels **d-f** and **g-i** respectively show the corresponding  $F_{SHG}$  and  $B_{SHG}$  images for each condition, with Healthy tissue again showing the lowest collagen content and highest  $F_{SHG}$  signal intensity relative to  $B_{SHG}$  signal intensity (i.e. the highest  $F_{SHG}/B_{SHG}$  ratio), whereas COP has high fibrosis and slightly higher  $B_{SHG}$  relative to  $F_{SHG}$  signals (intermediate  $F_{SHG}/B_{SHG}$  ratio), and UIP also has evident fibrosis and the least differential between the  $F_{SHG}$  and  $B_{SHG}$  signal intensities (i.e. the lowest  $F_{SHG}/B_{SHG}$  ratio). Levels (screen stretch) are linear and set the same for images **a-c** and **d-i**

photon excitation fluorescence (TPEF) microscopy. Using this methodology, total mature elastin signal was similarly decreased in both UIP and COP compared to healthy lung tissue (Fig. 6a), and FC:mature elastin ratios (Fig. 6b) were similarly increased in UIP and COP compared to healthy. However, in neither of these parameters was UIP different

from COP. Panels 5C-D illustrate the lower FC:mature elastin ratio seen in healthy versus UIP respectively.

These data demonstrate that compared to healthy lung, both fibrotic lung diseases (UIP and COP) are characterized by significant gross physiologic disruptions in ECM structure and organization that can be quantified with non-



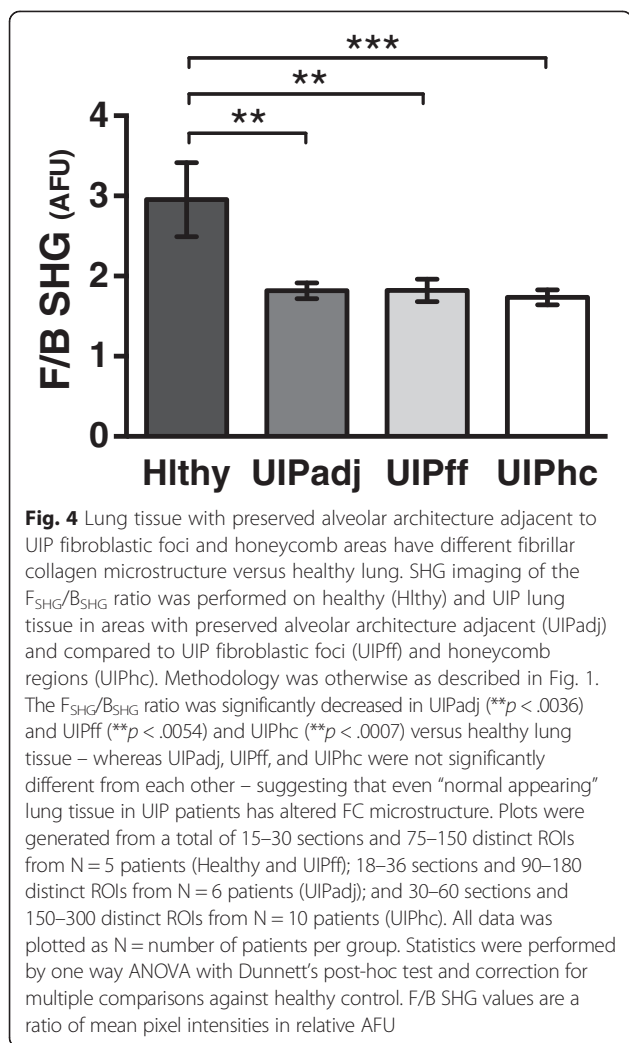
invasive and non-tissue destructive combined SHG and TPEF microscopy. Yet only the more intractable UIP fibrosis shows evidence of disrupted FC microstructure as interrogated by  $F_{SHG}/B_{SHG}$ , thus highlighting the compelling possibility that together these techniques may help make clinical distinctions between intractable and treatable lung fibroses.

## Discussion

Pulmonary fibrosis is characterized by accumulation of ECM proteins in lung tissue. The mechanisms leading to pathologic (or non pathologic) accumulation and organization of matrix proteins remain poorly understood. Although we have some insight into the composition, structure and/or organization of the matrix, many properties of the matrix remain uninvestigated. Numerous matrix proteins likely contribute to organ dysfunction in pulmonary fibrosis, however, we are only beginning to understand how homeostasis and organization of these proteins impact cellular function.

Collagen, produced and organized mainly by fibroblasts and scar-forming myofibroblasts, is one of the most abundantly studied matrix proteins. At least twenty-eight different collagen subtypes have been described to date. All collagen species contain three alpha peptide sequences forming a triple helix. Collagen type is determined by the type(s) of alpha peptides and post translational modifications, hydroxylation, and/or glycosylation. Further modification of collagen structure occurs after release into the extracellular space. Here, crosslinking and joining of the helices occur to form collagen fibrils and larger collagen fibers, and fibrosis (aberrant excess deposition of collagen) may occur.

Due to their ability to provide information on the intrinsic content and structure of collagen and other endogenous ECM proteins without exogenous labels or tissue destroying procedures (see description of SHGM and TPEF in Background and Results, respectively), there has been increasing interest in using SHGM and TPEF to provide insights into the matrix structure of healthy and diseased lung, both for fibrotic as well as



non-fibrotic lung diseases [28, 36, 44–48] (and for lung cancers, not discussed herein). One group reported that combined TPEF and SHG identified “characteristic features of fibroblastic foci in human Idiopathic Pulmonary Fibrosis samples” [47], whereas another report used  $F_{SHG}$  and  $B_{SHG}$  signals to differentiate Col1 from Col3 in lung tissue from patients with chronic obstructive pulmonary disease (COPD) [48]. Also in COPD, Tjin et al. found the  $F_{SHG}/B_{SHG}$  ratio was different in COPD versus non-diseased lung tissue [28]. However, reports demonstrating a diagnostic capability of quantifiable SHGM and TPEF parameters to discriminate between different clinical lung fibroses, or perhaps more importantly to provide insights into the underlying etiology or structure-function origins of lung disease, are still scarce.

In this report, we extend these works by using SHGM and TPEF imaging to identify key differences in the ECM of UIP compared to COP and healthy control lung tissue. UIP and COP were chosen because they are both

characterized by increases in matrix proteins, particularly FCs, yet they have contrasting natural histories, responses to corticosteroids, and prognoses. The reasons why UIP is progressive and difficult to treat are not clear. One possible explanation is that there may be a fundamental difference in collagen’s content, structure, and/or organization in the UIP ECM that renders collagen more structurally more resistant to degradation in UIP versus COP. We tested this hypothesis using SHGM, a microscopy approach that is sensitive to the intrinsic FC organization and microstructure within the matrix, to confirm whether FC in UIP has different microstructural properties versus COP or healthy lung.

Using this approach, we have demonstrated that FC microstructure in the ECM of UIP is significantly different from FC microstructure in either COP or healthy control lung tissue, as evidenced by the  $F_{SHG}/B_{SHG}$  ratio. Changes in this  $F_{SHG}/B_{SHG}$  ratio suggest that there is a significant difference in the density, structure, and/or organization of FC in UIP compared to COP and healthy lung tissue, particularly with regard to the effective diameter or packing arrangement/density of collagen fibrils in the ECM [18–22, 26]. These results are compelling because while previous studies (discussed above) have elegantly demonstrated the utility of SHGM for investigating lung fibroses, or have shown expression changes in several collagen subtypes in fibrotic lung diseases, to our knowledge this is the first report of abnormalities in ECM and FC microstructure in UIP as being quantifiable and differentiable from other lung fibroses (and from healthy) by SHGM, specifically  $F_{SHG}/B_{SHG}$ . Still more compelling is the fact that only the intractable fibrosis (UIP) demonstrated significant differences in FC microstructure versus healthy lung, whereas the treatable fibrosis (COP) did not, thus providing compelling and to our knowledge seminal evidence that alterations in collagen’s fundamental underlying structure may contribute to whether or not pulmonary fibroses are treatment responsive. These results provide previously unavailable insights into the biological underpinnings of treatment-resistant pulmonary fibrosis, and also highlight the potential of SHGM as a novel clinical diagnostic and investigational tool for distinguishing between intractable and treatable lung fibroses.

We also found that lung tissue with preserved alveolar architecture adjacent to UIP fibroblastic lesions and honeycomb areas all have different FC microstructure (i.e.  $F_{SHG}/B_{SHG}$ ) versus healthy lung. Moreover, there was no difference in  $F_{SHG}/B_{SHG}$  between UIP fibroblastic foci, honeycomb areas, and adjacent areas with preserved alveolar architecture (Fig. 4). Together these results suggest the possibility that pre-existing alterations in FC structure even in “normal” lung tissue may foreshadow or precipitate (or at minimum, associate with)

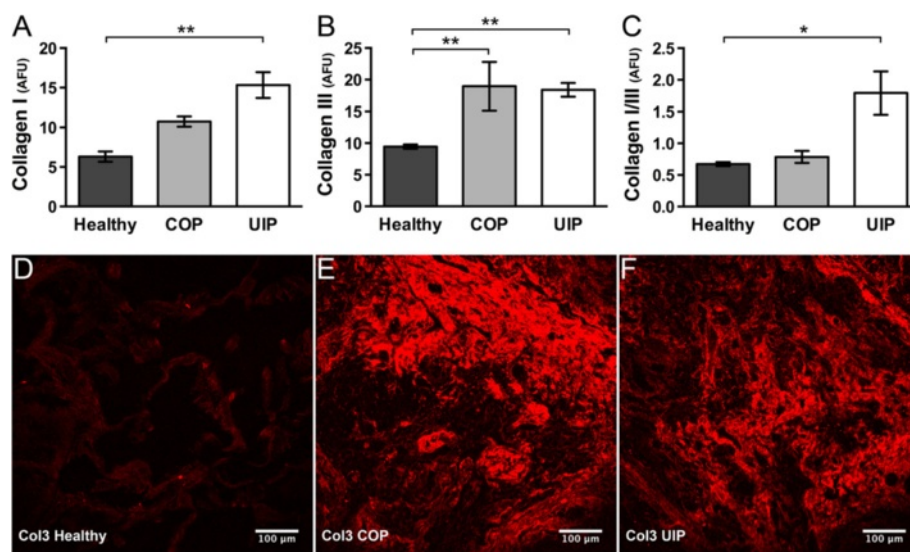


**Fig. 5** Increased Col1 and Col3 deposition, and Col1:Col3 ratio differences, in UIP or COP versus healthy lung. **a** Compared to healthy, Col1 deposition was significantly increased in UIP (\*\* $p < .0033$ ) and trended toward an increase in COP ( $p = .13$ ). **b** Col3 deposition was about equally increased in both COP (\*\* $p < .009$ ) and UIP (\*\* $p < .004$ ) versus healthy. Overall, this led to **c** The Col1:Col3 ratio being effectively equivalent in COP versus healthy, but significantly increased in UIP versus healthy (\* $p < .015$ ). Plots were generated from  $\geq 9$ -18 sections and  $\geq 45$ -90 distinct ROIs from  $N \geq 3$  patients per condition. All data was plotted as  $N =$  number of patients per group. Statistics were performed by one way ANOVA with Dunnett's post-hoc test and correction for multiple comparisons against healthy control. Values for Collagen I and III represent mean immunofluorescence pixel intensities in relative AFU (Panels **a**, **b**), or a ratio thereof (Panel **c**). In panels **d-f**, for illustrative purposes, the originally grayscale Col3 immunofluorescence is shown with "Red" LUT applied in ImageJ for Healthy, COP, and UIP respectively, with levels (screen stretch) linear and set the same for all images. Note the round Masson's bodies characteristic of COP (in **e**), whereas **f** represents an area of widespread late-stage fibrosis in UIP

development of UIP. In other words, underlying collagen structural deficits – perhaps present in pre-UIP tissue well before the onset of UIP – might be a biomarker that predicts or predisposes development of future UIP.

As expected, both col1 and col3 were elevated in UIP and COP versus healthy lung, with col1 deposition being predominant to col3 in UIP, and vice-versa in COP, as has been previously reported [1]. These results are significant in the context of our other results reported herein because it is known that changes in FC ratios, particularly col1:col3 ratios, plays a significant role in regulating collagen fibril diameter [23–25] (one component of collagen microstructure). Similarly, by regulating the availability of fibroblast (or other effector cell type) binding sites on collagen fibrils, changes in collagen's subresolution fibril microstructure could in turn control relative levels of FC expression. In other words, different col1:col3 ratios may in turn drive or be driven by altered collagen microstructure in UIP. Together with the earlier data, these results demonstrate that the ECM of UIP not only contains more collagen (particularly more col1) than the ECM of COP and/or healthy lung tissue, but also that there are significant differences in the subresolution microstructure of these collagen fibrils (i.e. fibril diameter, density, and/or organization, as interrogated by  $F_{SHG}/B_{SHG}$ ) in UIP versus COP and healthy, independent

of the absolute amount of collagen deposition in each disease.

Finally, we demonstrated that mature elastin content in both UIP and COP is reduced compared to healthy controls (Fig. 6). Elastin's intrinsic autofluorescence originates from pyridoxine-based pyridolamine cross-links [35, 42] found primarily in mature elastin fibers [43], therefore TPEF of endogenous lung elastin preferentially identifies mature elastin fibers in lung tissue. These results are consistent with the concept that breakdown of mature elastin fibers in the lung, and their "replacement" with often excess deposition of immature elastin fibers and elastin precursors, is believed to contribute to reduced lung function in a variety of pulmonary diseases [49]. In other words, increased elastosis (i.e. breakdown of mature elastin fibers), as has been demonstrated for both UIP and COP [50], most likely leads to a compensatory increase in elastin production in an (ultimately unsuccessful) effort to restore the mature elastin fibers which have been lost.

Hence our results here together with these previous studies all support the concept of increased elastin turnover (i.e. synthesis and "deposition" of "immature" elastin components) consequent to breakdown and loss of mature elastin fibers in UIP and COP, with resultant deficits in pulmonary function. Indeed Enomoto et al. show

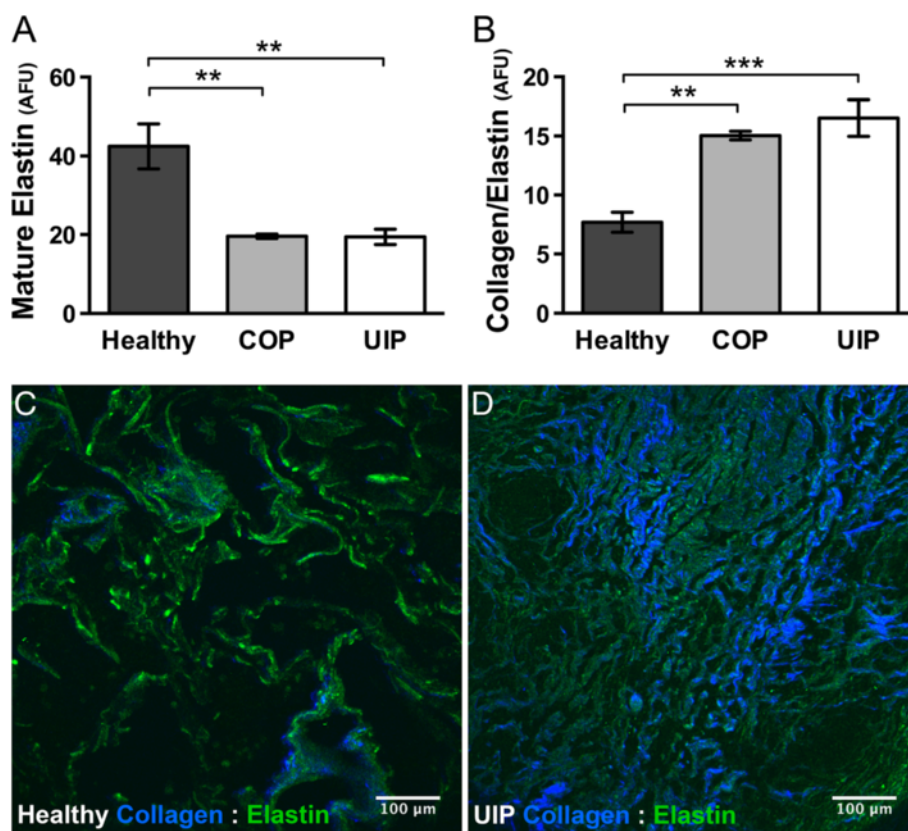


**Fig. 6** Elastin content and Collagen:Elastin ratio differ in UIP and COP versus healthy lung. **a** Mature elastin fiber content was similarly decreased in both COP ( $*p < .007$ ) and UIP ( $*p < .004$ ) versus healthy lung tissue, and **b** The total fibrillar collagen/mature elastin ratio was similarly increased in both COP ( $**p < .004$ ) and UIP ( $***p < .0008$ ) compared to healthy. Plots represent mean pixel intensity  $\pm$  SEM for these elastin autofluorescence (Panel **a**) and ( $F_{\text{SHG}} + B_{\text{SHG}}$ /Elastin autofluorescence) (Panel **b**) signals captured as described in Methods, in relative AFU. Plots were generated from a total of 12–24 sections and 60–120 distinct ROIs from  $N = 4$  patients (Healthy and UIP), and 9–18 sections and 45–90 distinct ROIs from  $N = 3$  patients (COP). All data was plotted as  $N =$  number of patients per group. Statistics were performed by one way ANOVA with Dunnett's post-hoc test and correction for multiple comparisons against healthy control. Representative merged images **c** and **d** illustrate this lower total FC SHG (blue):mature elastin (green) ratio as seen in **c** healthy compared to **d** UIP. (Compare total amount and intensity of the blue summed  $F_{\text{SHG}} + B_{\text{SHG}}$  collagen SHG signal, relative to the green mature elastin signal, in the healthy **c** versus UIP **d** panels respectively). Panel **d** represents an area of widespread late-stage fibrosis in UIP. For illustrative purposes, the originally grayscale SHG and elastin fluorescence signals are shown with "Blue" and "Green" LUTs applied in ImageJ respectively, with levels (screen stretch) linear and set the same for all channels in all images

a significant increase in very fragmented appearing elastin (i.e. likely to be fragmented mature elastin fibers and/or deposition of immature elastin precursors; see Fig. 1 in [51]) associated with a decline in lung function in IPF [51]. Others have also reported apparently increased elastin production, for example increased elastin gene expression and protein expression [52], as well as increased enzymatic breakdown of mature elastin in COPD and IPF [50], in these and other [53] pulmonary fibroses. Finally Eurlings et al. recently reported increased collagen and decreased elastin in aveolar and small airway walls of chronic obstructive pulmonary disease (COPD) [54], another disease with fibrotic pathology, similar to what we demonstrate herein for COP and UIP (Fig. 3 and Fig. 5).

Taken together with our findings on different FC microstructure in UIP but not COP versus healthy lung, these observations on elastin content are especially compelling because they demonstrate that compared to healthy lung, both fibroses (UIP and COP) have significant identifying physiologic disruptions in ECM structure and organization that are quantifiable with non-invasive and non-tissue destructive combined SHG and TPEF microscopy. Yet only the more intractable UIP fibrosis has disrupted FC microstructure identifiable by  $F_{\text{SHG}}/B_{\text{SHG}}$ , and thus together these techniques may represent novel clinical diagnostic tools for distinguishing between intractable and treatable lung fibroses. The continual pre-clinical advancement of SHG and TPEF endoscopic technology makes the prospect of such a

diagnostic tool for distinguishing between intractable and treatable lung fibroses all the more compelling [17, 55].

While both UIP and COP are fibrotic diseases, UIP is a fatal disease affecting the alveolar walls and subpleural areas, while COP is a treatable disease affecting the alveolar spaces and bronchiolar lumen. Thus while both have fibrosis, their topography and natural history are distinct, and therefore any inter-disease comparative study of this nature cannot completely exclude the possibility that some measured differences might be attributable at least in part to temporal or anatomical/topographical differences in the lung tissues examined between the patient groups. Moreover, incorporating additional corresponding clinical data such as symptoms or pulmonary function testing (unavailable for these current patient sets) will allow us to strengthen our findings and interpretations in future studies. Nonetheless the possibility that non-invasive and non-tissue destructive combined SHG and TPEF microscopy, utilized either *ex vivo* or perhaps ultimately *in vivo*, may be able to distinguish and/or predict onset or outcome of tractable versus fatal lung fibroses remains compelling.

In summary, using SHG and TPEF microscopy, herein we identify several previously unreported key differences between UIP, COP and healthy lung tissue. The collagen microstructure differences we observed in UIP ECM provide novel insights as to why this pathology may be resistant to many therapies. For example, an ECM and/or collagen fibrils that are more densely packed, more ordered or disordered, and/or more cross-linked may be more resistant to homeostatic turnover and exhibit differences in matrix stiffness that are key to modifying cellular activity of resident cells and activation of pro-fibrogenic cytokines such as transforming growth factor beta (TGF- $\beta$ ). Identifying all the microstructural changes present in UIP and/or the mechanisms that regulate them will be a critical part of our future research. These ongoing studies will seek to determine more specifically exactly what features of collagen's microstructure (e.g. fibril diameter, fibril density, and/or hetero- or homotypic fibril composition or organization) are different in UIP versus COP and healthy lung, and identify molecular targets that may effect these changes in collagen's underlying microstructure. Although further studies are required to ascertain whether or not the altered FC microstructure as we demonstrate here is an underlying cause of (rather than just associated with) differences in natural history, treatment responsiveness, and/or prognosis between UIP and COP, at minimum these results introduce the intriguing possibility of using SHG microscopy as a novel clinical biomarker that may help predict treatment responsiveness of idiopathic fibrotic lung disease.

## Conclusions

To date it is unknown why some lung fibroses respond well to therapies, yet others remain relatively intractable. Herein, we report differences in collagen's subresolution structure or organization (i.e. "microstructure") and airway matrix structure in usual interstitial pneumonia versus cryptogenic organizing pneumonia and healthy lung, as identified by quantifiable nonlinear SHG and TPEF microscopy parameters. These findings may offer key insights into the biologic underpinnings of refractory versus treatable pulmonary fibroses, and highlight the potential of second harmonic generation microscopy as a novel diagnostic tool for distinguishing between these clinical scenarios.

## Competing interests

The authors declare that they have no competing interests.

## Author's contributions

R M K; study design and manuscript author; J S; SHG imaging, data acquisition and analysis; K O; data acquisition; P S; statistical data analysis; G Q X; data acquisition, study design; R P P; manuscript review and revision, study design; P J S; manuscript review and revision, study design; E B B; manuscript review and revision, study design; S W P; SHG study design, data analysis, manuscript author. All authors read and approved the final manuscript.

## Acknowledgements

The authors thank Drs. Mark G. Jones and Kelley S. Madden for helpful discussions; Mr. Wade C. Narrow for assistance with acquiring samples; and the reviewers for their helpful suggestions on this manuscript. Grants and funding support provided by: University of Rochester Buswell Medicine Fellowship and Empire Clinical Research Investigator Program Career Development Award (RMK); NIH HL-075432, NIH HL-66988, The Chandler and Solimano Fund, and the Pulmonary Fibrosis Foundation (PJS); NIH T32 HL066988 and NIEHS P30ES01247 (RPP); DoD BCRP Era of Hope Scholar Research Award W81XWH-09-1-0405 and NIH Director's New Innovator Award 1DP2 OD006501-01 (EBB); and NIH R21DA030256 (SWP). The project described in this publication was supported by the University of Rochester CTSA award number KL2 RR024136 from the National Center for Research Resources and the National Center for Advancing Translational Sciences of the National Institutes of Health. The content is solely the responsibility of the authors and does not necessarily represent the official views of the National Institutes of Health. This paper is subject to the NIH Public Access Policy.

## Author details

<sup>1</sup>Department of Medicine, University of Rochester, Rochester, NY, USA.

<sup>2</sup>Department of Biomedical Engineering, University of Rochester, Rochester, NY, USA.

<sup>3</sup>Department of Biostatistics and Computational Biology, University of Rochester, Rochester, NY, USA.

<sup>4</sup>Department of Pathology and Laboratory Medicine, University of Rochester, Rochester, NY, USA.

<sup>5</sup>Department of Environmental Medicine, University of Rochester, Rochester, NY, USA.

Received: 12 June 2014 Accepted: 13 May 2015

Published online: 27 May 2015

## References

1. Cordier JF. Cryptogenic organising pneumonia. *Eur Respir J*. 2006;28:422–46.
2. Parra ER, Teodoro WR, Velosa AP, de Oliveira CC, Yoshinari NH, Capelozzi VL. Interstitial and vascular type V collagen morphologic disorganization in usual interstitial pneumonia. *J Histochem Cytochem*. 2006;54:1315–25.
3. Parra ER, Kairalla RA, de Carvalho CR, Capelozzi VL. Abnormal deposition of collagen/elastic vascular fibres and prognostic significance in idiopathic interstitial pneumonias. *Thorax*. 2007;62:428–37.

4. Nadrous HF, Ryu JH, Douglas WW, Decker PA, Olson EJ. Impact of angiotensin-converting enzyme inhibitors and statins on survival in idiopathic pulmonary fibrosis. *Chest*. 2004;126:438–46.
5. Kim HJ, Perlman D, Tomic R: Natural history of idiopathic pulmonary fibrosis. *Respir Med*. 2015. epub.
6. Cowvey JR, Mancl EE. Recent evidence for pharmacological treatment of idiopathic pulmonary fibrosis. *Ann Pharmacother*. 2014;48(12):1611–9.
7. Cottin V, Maher T. Long-term clinical and real-world experience with pirfenidone in the treatment of idiopathic pulmonary fibrosis. *Eur Respir Rev*. 2015;24:58–64.
8. Spagnolo P, Sverzellati N, Rossi G, Cavazza A, Tzouveleakis A, Crestani B, et al. Idiopathic pulmonary fibrosis: An update. *Ann Med*. 2015;47:15–27.
9. Kim ES, Keating GM. Pirfenidone: a review of its use in idiopathic pulmonary fibrosis. *Drugs*. 2015;75:219–30.
10. Staitieh BS, Renzoni EA, Veeraghavan S. Pharmacologic therapies for idiopathic pulmonary fibrosis, past and future. *Ann Med*. 2015;47:1–6.
11. Cottin V, Cordier JF. Cryptogenic organizing pneumonia. *Semin Respir Crit Care Med*. 2012;33:462–75.
12. Tschumperlin DJ, Boudreault F, Liu F. Recent advances and new opportunities in lung mechanobiology. *J Biomech*. 2010;43:99–107.
13. Tschumperlin DJ, Liu F, Tager AM. Biomechanical regulation of mesenchymal cell function. *Curr Opin Rheumatol*. 2013;25:92–100.
14. Marinkovic A, Liu F, Tschumperlin DJ. Matrices of physiologic stiffness potentially inactivate idiopathic pulmonary fibrosis fibroblasts. *Am J Respir Cell Mol Biol*. 2013;48:422–30.
15. Suki B, Stamenovic D, Hubmayr R. Lung parenchymal mechanics. *Compr Physiol*. 2011;1:1317–51.
16. Shoulders MD, Raines RT. Collagen structure and stability. *Annu Rev Biochem*. 2009;78:929–58.
17. Perry SW, Burke RM, Brown EB. Two-photon and second harmonic microscopy in clinical and translational cancer research. *Ann Biomed Eng*. 2012;40:277–91.
18. Perry SW, Han X, Brown EB. Second Harmonic Generation in Tumors: Scattering and Polarization. In: Pavone FS, Campagnola PJ, editors. *Second Harmonic Generation Imaging*. Volume In Press. London, UK: Taylor and Francis; 2012.
19. Perry SW, Schueckler JM, Burke K, Arcuri GL, Brown EB. Stromal matrix metalloproteinase-13 knockout alters Collagen I structure at the tumor-host interface and increases lung metastasis of C57BL/6 syngeneic E0771 mammary tumor cells. *BMC Cancer*. 2013;13:411.
20. Han X, Burke RM, Zettel ML, Tang P, Brown EB. Second harmonic properties of tumor collagen: determining the structural relationship between reactive stroma and healthy stroma. *Opt Express*. 2008;16:1846–59.
21. Lacombe R, Nadiarnykh O, Townsend SS, Campagnola PJ. Phase Matching considerations in Second Harmonic Generation from tissues: Effects on emission directionality, conversion efficiency and observed morphology. *Opt Commun*. 2008;281:1823–32.
22. Mertz J, Moreaux L. Second harmonic generation by focused excitation of inhomogeneously distributed scatterers. *Optics Communications*. 2001;196:325–30.
23. Cameron GJ, Alberts IL, Laing JH, Wess TJ. Structure of type I and type III heterotypic collagen fibrils: an X-ray diffraction study. *J Struct Biol*. 2002;137:15–22.
24. Fleischmajer R, Perlsh JS, Burgeson RE, Shaikh-Bahai F, Timpl R. Type I and type III collagen interactions during fibrillogenesis. *Ann N Y Acad Sci*. 1990;580:161–75.
25. Romanic AM, Adachi E, Kadler KE, Hojima Y, Prockop DJ. Copolymerization of pNcollagen III and collagen I. pNcollagen III decreases the rate of incorporation of collagen I into fibrils, the amount of collagen I incorporated, and the diameter of the fibrils formed. *J Biol Chem*. 1991;266:12703–9.
26. Burke K, Tang P, Brown E. Second harmonic generation reveals matrix alterations during breast tumor progression. *J Biomed Opt*. 2013;18:31106.
27. Burke KA, Dawes RP, Cheema MK, Van Hove A, Benoit DS, Perry SW, et al. Second-harmonic generation scattering directionality predicts tumor cell motility in collagen gels. *J Biomed Opt*. 2015;20:051024.
28. Tjin G, Xu P, Kable SH, Kable EP, Burgess JK. Quantification of collagen I in airway tissues using second harmonic generation. *J Biomed Opt*. 2014;19:36005.
29. Brown E, McKee T, DiTomaso E, Pluen A, Seed B, Boucher Y, et al. Dynamic imaging of collagen and its modulation in tumors in vivo using second-harmonic generation. *Nat Med*. 2003;9:796–800.
30. Brown EB, Campbell RB, Tsuzuki Y, Xu L, Carmeliet P, Fukumura D, et al. In vivo measurement of gene expression, angiogenesis and physiological function in tumors using multiphoton laser scanning microscopy. *Nat Med*. 2001;7:864–8.
31. Odin C, Guilbert T, Alkilani A, Boryskina OP, Fleury V, Le Grand Y. Collagen and myosin characterization by orientation field second harmonic microscopy. *Opt Express*. 2008;16:16151–65.
32. Plotnikov SV, Millard AC, Campagnola PJ, Mohler WA. Characterization of the myosin-based source for second-harmonic generation from muscle sarcomeres. *Biophys J*. 2006;90:693–703.
33. Su PJ, Chen WL, Chen YF, Dong CY. Determination of collagen nanostructure from second-order susceptibility tensor analysis. *Biophys J*. 2011;100:2053–62.
34. Tiaho F, Recher G, Rouede D. Estimation of helical angles of myosin and collagen by second harmonic generation imaging microscopy. *Opt Express*. 2007;15:12286–95.
35. Zipfel WR, Williams RM, Christie R, Nikitin AY, Hyman BT, Webb WW. Live tissue intrinsic emission microscopy using multiphoton-excited native fluorescence and second harmonic generation. *Proc Natl Acad Sci U S A*. 2003;100:7075–80.
36. Abraham T, Hirota JA, Wadsworth S, Knight DA. Minimally invasive multiphoton and harmonic generation imaging of extracellular matrix structures in lung airway and related diseases. *Pulm Pharmacol Ther*. 2011;24:487–96.
37. Faffe DS, Zin WA. Lung parenchymal mechanics in health and disease. *Physiol Rev*. 2009;89:759–75.
38. Mijailovich SM, Stamenovic D, Fredberg JJ. Toward a kinetic theory of connective tissue micromechanics. *J Appl Physiol*. 1993;74:665–81.
39. Yuan H, Ingenito EP, Suki B. Dynamic properties of lung parenchyma: mechanical contributions of fiber network and interstitial cells. *J Appl Physiol*. 1997;83:1420–31. discussion 1418–1429.
40. Blaauboer ME, Boeijen FR, Emson CL, Turner SM, Zandieh-Doulabi B, Hane-maaijer R, et al. Extracellular matrix proteins: A positive feedback loop in lung fibrosis? *Matrix Biol*. 2013;34:170–8.
41. Pierce RA, Mariani TJ, Senior RM. Elastin in lung development and disease. *Ciba Found Symp*. 1995;192:199–212. discussion 212–194.
42. Deyl Z, Macek K, Adam M, Vancikova O. Studies on the chemical nature of elastin fluorescence. *Biochim Biophys Acta*. 1980;625:248–54.
43. Luisetti M, Ma S, Iadarola P, Stone PJ, Viglio S, Casado B, et al. Desmosine as a biomarker of elastin degradation in COPD: current status and future directions. *Eur Respir J*. 2008;32:1146–57.
44. Abraham T, Hogg J. Extracellular matrix remodeling of lung alveolar walls in three dimensional space identified using second harmonic generation and multiphoton excitation fluorescence. *J Struct Biol*. 2010;171:189–96.
45. Abraham T, Wadsworth S, Carthy JM, Pechkovsky DV, McManus B. Minimally invasive imaging method based on second harmonic generation and multiphoton excitation fluorescence in translational respiratory research. *Respirology*. 2011;16:22–33.
46. Dong CY, Campagnola PJ. Optical diagnostics of tissue pathology by multiphoton microscopy. *Expert Opin Med Diagn*. 2010;4:519–29.
47. Pena AM, Fabre A, Debarre D, Marchal-Somme J, Crestani B, Martin JL, et al. Three-dimensional investigation and scoring of extracellular matrix remodeling during lung fibrosis using multiphoton microscopy. *Microsc Res Tech*. 2007;70:162–70.
48. Suzuki M, Kayra D, Elliott WM, Hogg JC, Abraham T. Second harmonic generation microscopy differentiates collagen type I and type III in diseased lung tissues. In: Konig K, editor. *PROCEEDINGS OF SPIE VOLUME 8226, Multiphoton Microscopy in the Biomedical Sciences XII: 82263F-82269*. Bellingham WA: Society of Photo-Optical Instrumentation Engineers (SPIE).
49. Souza AB, Santos FB, Negri EM, Zin WA, Rocco PRM. Lung tissue remodeling in the acute respiratory distress syndrome. *J de Pneumol*. 2003;29:235–45.
50. Skjot-Arkil H, Clausen RE, Nguyen QH, Wang Y, Zheng Q, Martinez FJ, et al. Measurement of MMP-9 and -12 degraded elastin (ELM) provides unique information on lung tissue degradation. *BMC Pulm Med*. 2012;12:34.
51. Enomoto N, Suda T, Kono M, Kaida Y, Hashimoto D, Fujisawa T, et al. Amount of elastic fibers predicts prognosis of idiopathic pulmonary fibrosis. *Respir Med*. 2013;107:1608–16.
52. Hoff CR, Perkins DR, Davidson JM. Elastin gene expression is upregulated during pulmonary fibrosis. *Connect Tissue Res*. 1999;40:145–53.
53. Stone PJ, Konstan MW, Berger M, Dorkin HL, Franzblau C, Snider GL. Elastin and collagen degradation products in urine of patients with cystic fibrosis. *Am J Respir Crit Care Med*. 1995;152:157–62.

54. Eurlings IM, Dentener MA, Cleutjens JP, Peutz CJ, Rohde GG, Wouters EF, et al. Similar matrix alterations in alveolar and small airway walls of COPD patients. *BMC Pulm Med*. 2014;14:90.
55. Peyrot DA, Lefort C, Steffenhagen M, Mansuryan T, Ducourthial G, Abi-Haidar D, et al. Development of a nonlinear fiber-optic spectrometer for human lung tissue exploration. *Biomed Opt Express*. 2012;3:840–53.

**Submit your next manuscript to BioMed Central  
and take full advantage of:**

- Convenient online submission
- Thorough peer review
- No space constraints or color figure charges
- Immediate publication on acceptance
- Inclusion in PubMed, CAS, Scopus and Google Scholar
- Research which is freely available for redistribution

Submit your manuscript at  
[www.biomedcentral.com/submit](http://www.biomedcentral.com/submit)





Published in final edited form as:

*Ann Biomed Eng.* 2012 February ; 40(2): 277–291. doi:10.1007/s10439-012-0512-9.

## Two-Photon and Second Harmonic Microscopy in Clinical and Translational Cancer Research

SETH W. PERRY<sup>1,2</sup>, RYAN M. BURKE<sup>1</sup>, and EDWARD B. BROWN<sup>1</sup>

<sup>1</sup>Department of Biomedical Engineering, University of Rochester, Goergen Hall Box 270168, Rochester, NY 14627, USA

<sup>2</sup>Department of Neurology, University of Rochester School of Medicine and Dentistry, 601 Elmwood Avenue, Rochester, NY 14642, USA

### Abstract

Application of two-photon microscopy (TPM) to translational and clinical cancer research has burgeoned over the last several years, as several avenues of pre-clinical research have come to fruition. In this review, we focus on two forms of TPM—two-photon excitation fluorescence microscopy, and second harmonic generation microscopy—as they have been used for investigating cancer pathology in *ex vivo* and *in vivo* human tissue. We begin with discussion of two-photon theory and instrumentation particularly as applicable to cancer research, followed by an overview of some of the relevant cancer research literature in areas that include two-photon imaging of human tissue biopsies, human skin *in vivo*, and the rapidly developing technology of two-photon microendoscopy. We believe these and other evolving two-photon methodologies will continue to help translate cancer research from the bench to the bedside, and ultimately bring minimally invasive methods for cancer diagnosis and treatment to therapeutic reality.

### Keywords

Two-photon microscopy; Cancer; Second harmonic generation; Collagen; SHG; Endoscopy

## INTRODUCTION

Over the last 20 years, two-photon microscopy (TPM) has enjoyed explosive growth in its application to biomedical research. One of many areas in which two-photon (2P) microscopy has proven its utility is that of cancer research. In pre-clinical (i.e., laboratory models), translational, and clinical research, TPM has afforded a range of insights into cancer biology in areas related to tumor stroma and microenvironment; metastasis; angiogenesis; tumor metabolism, physiology and gene expression; and drug delivery and gene therapy. As is absolutely prerequisite to advance scientific knowledge to successful diagnosis and treatment of disease in humans, many of these studies have utilized TPM methods in pre-clinical cell and animal laboratory models, as that is where much of medicine begins. Much of this pre-clinical work has been elegantly reviewed in detail elsewhere, often focused on particular areas of cancer research, or on particular 2P methodologies (and of course, including relevant clinical studies as available and topically

appropriate). For example, Provenzano *et al.*<sup>91</sup> capably discuss a range of research studies that have utilized multiphoton microscopy and fluorescence lifetime imaging microscopy (FLIM) to further our understanding of the tumor microenvironment and metastatic mechanisms. Several other excellent articles focus in whole or in part on reviewing intravital two-photon imaging investigations of tumor angiogenesis<sup>36,71,107</sup> and metastasis.<sup>4,19,54,63</sup> Other colleagues have discussed application of intravital TPM to studies of stromal cell dynamics and interactions in the tumor microenvironment,<sup>38,70</sup> and to understanding the mechanisms and contributions of immune cells and the immune response to tumor pathology.<sup>121</sup>

To complement and extend these many capable works, we will begin with an overview of technologies, then will focus on implementation of two-photon optical microscopy primarily as applied to human biological materials—that is, either biopsied tissue (both fixed and fresh), or *in vivo* imaging—over a wide range of cancer types. A few pre-clinical studies will be mentioned when they relate closely to the clinical and translational studies surveyed. In closing, we will briefly highlight applications of TPM to human tissues in areas other than cancer. In this fashion, we hope to provide a broad overview of the demonstrated potential of two-photon optical microscopy instruments and methodologies as diagnostic and prognostic tools for human disease.

## TWO-PHOTON MICROSCOPY THEORY AND INSTRUMENTATION FOR CANCER RESEARCH

As a principle of quantum mechanics, two-photon excitation was initially theorized by Maria Goppert-Mayer,<sup>39</sup> then first demonstrated in laser-excited crystals 30 years later,<sup>53</sup> and first applied to living biological specimens as TPM—thus triggering TPM's explosive growth in biological research—another 30 years after that.<sup>25</sup> As applied to biology, TPM utilizes customized, semi-customized, or turn-key commercial laser-scanning type microscopes, where the typical visible laser light sources [e.g., for confocal microscopy (CM)] have been replaced by pulsed, high-intensity near-infrared (IR) (usually ~680–1100 nm) lasers. Notably, the advent of commercially available turn-key tunable, mode-locked Titanium:Sapphire near-IR (~680–1080 nm) lasers with femto- to pico-second pulse widths greatly facilitated the widespread introduction of commercially available 2P microscopes, which in turn has enabled the expansion of multi-photon microscopy techniques to broader realms of biomedical research. Please see Zipfel *et al.*<sup>125</sup> and Rocheleau and Piston<sup>98</sup> for further technical background on TPM as a tool for biological research.

### Two-Photon Excitation Fluorescence (TPEF) vs. Second Harmonic Generation (SHG) Microscopy

In the most common TPM technique, sometimes referred to as TPEF microscopy, an exogenous or endogenous fluorescent molecule is excited by the near-IR laser, and the resultant fluorescent signal is recorded by photomultiplier tubes (PMTs), thus providing a means of optically monitoring physiologic and biochemical events within the cells or other biologic tissue. In addition to the two-photon excitation of a fluorophore and subsequent monitoring of the fluorescent emission signal (i.e., TPEF), TPM can be also be utilized to take advantage of other physical and optical properties of two-photon interactions with tissue. For example, another TPM technique increasingly applied to cancer research is SHG microscopy. SHG, like TPEF, also depends on two photons interacting simultaneously with a target. Unlike TPEF, however, in which two photons are absorbed by the target to produce a single photon of fluorescent emission (with some energy loss), with SHG there is no *absorption* of photons by the target. Rather SHG involves *scattering* of photons and no energy loss, whereby two photons interacting simultaneously with a non-centrosymmetric

target combine to produce a new photon with exactly twice the energy (thus twice the frequency, and half the wavelength) of the interacting photons<sup>10,81,83,95</sup> (Fig. 1). Hence, 2P irradiation of an SHG generating target at 810 nm will emit SHG photons at 405 nm.

These differences between TPEF and SHG notwithstanding, here it is also important to note that because of the *similarities* between TPEF and SHG, both of which involve laser-induced two-photon interactions with the imaged subject matter, the majority of TPM hardware and technical considerations discussed below apply equally to TPEF and SHG microscopy, with the fundamental difference being that spectrally distinct emission filters are used to capture the disparate SHG and TPEF signals. Therefore, for clarity herein, we will use “TPEF” to refer specifically to TPEF microscopy, “SHG” to refer specifically to SHG microscopy, and “TPM” to refer generically to TPM features which are mutually applicable to both distinct methodologies. In addition, while TPEF microscopy can utilize either exogenous or endogenous (intrinsic) fluorescent molecules, herein we will primarily discuss TPEF signals arising from the numerous intrinsic fluorophores found in biologic tissue.

### Instrument and Image Acquisition Considerations for Clinical and Translational Cancer Research

As laser scanning microscopy techniques, the laser/substrate interactions and emission capture (of TPEF and/or SHG signals) in TPM typically occur one pixel at time, by raster-scanning the laser focal point over the designated XY specimen area within the microscopic field of view. As such, typically configured TPM generally achieves <1 frame/second. However there are numerous reports of video rate (30 frames/second) and super-video rate (usually by multi-focal approaches,<sup>1,5,6,34,55,72,104</sup>) TPM enabled by hardware customization to improve scanning speeds, and many of these methods could conceivably be applied to clinical and translational cancer research. Video-rate or better TPM may ultimately prove useful for imaging human cancer tissue physiology in real-time, and/or for high throughput imaging of archival tissue specimens.

The pulsed, near-IR laser is in fact integral to application of TPM in living biological tissues. In conventional one-photon fluorescence excitation, a single-photon excitation of a fluorophore results in the emission of a single lower energy photon of longer wavelength (i.e., the Stokes shift). Two-photon excitation theory holds that when irradiance is of sufficient intensity (MW-GW/cm<sup>2</sup>),<sup>60</sup> two photons interacting simultaneously or nearly simultaneously ( $\sim 10^{-16}$  s)<sup>25</sup> with a fluorophore will produce a single photon of fluorescence, equivalent to if that fluorophore had been excited by *one* photon of twice the energy (i.e., half the wavelength) of each of the two exciting photons. Thus to achieve 2P fluorescence excitation, longer near-IR (i.e., double wavelength) lasers substitute for the shorter visible spectrum lasers or light sources typically used for one-photon excitation fluorescence microscopy (e.g., confocal and widefield fluorescence microscopy). To obtain the high light intensities required to achieve 2P fluorescence excitation, near-IR lasers typically produce very brief pulses (usually  $\sim 150$  femtoseconds or less) at high Hz, which creates sufficient *peak* (instantaneous) energy to produce 2P excitation, while keeping *average* energy low enough to minimize specimen damage.<sup>110</sup> In this fashion, these rapid, ultra-brief high power pulses, together with focusing of the laser through the objective lens, ensure that photons are sufficiently “crowded” in space and time to enable 2P interactions to occur.<sup>98</sup> This means that in TPM, laser excitation of fluorescence is confined exclusively to the microscope objective’s focal volume, because only here is there sufficient photon density to cause significant 2P excited fluorescence. Thus unlike other fluorescence approaches (e.g., confocal, widefield), 2P excitation light does not cause significant “stray” fluorescence as it passes through tissue above or below the focal plane, thus greatly reducing photobleaching and photodamage in the specimen and eliminating the need for a confocal pinhole, enabling

imaging deeper into tissue.<sup>98,125</sup> Moreover in tissue, near-IR scatters less than shorter wavelengths (facilitating deeper penetration), and are less damaging than shorter wavelengths. All these features make TPM ideally suited for live biologic imaging. Still important to note however, is that while these aspects of TPM greatly reduce the potential for “out of plane” photodamage and phototoxicity compared to one-photon microscopy approaches (e.g., CM), they cannot eliminate “in plane” photodamage, because in order to generate TPEF signal photons “in plane,” one must by necessity generate photobleaching. This “in plane” photobleaching is mitigated by the lack of confocal pinhole and the accompanying increased sensitivity, resulting in fewer signal photons (and photobleaching events) generated per detected photon, relative to confocal imaging. Thus particularly when considering any TPM approach for *in vivo* and clinical imaging, due attention must be given to both the peak and total energy exposures of the specimens, so as to minimize potential tissue damage and phototoxicity related imaging artifacts.

Many excellent references discuss TPM theory and instrumentation in further detail.<sup>5,6,25,60,87,98,110,125</sup> Herein we will focus principally on the application of TPM to clinical and translational cancer research, referring to our colleagues’ works for additional background.

## MONITORING INTRINSIC BIOLOGIC SIGNALS BY TPM

The fluorophores excited and monitored in TPDM can be either exogenously applied—e.g., fluorescent dyes, fluorescent reporter proteins such as green fluorescent protein (GFP), or fluorescently labeled antibodies—or they can be fluorescent molecules endogenous to the tissue. In pre-clinical *in vitro* and *in vivo* research models, such exogenous fluorophores are commonly used to investigate molecular events by TPM. In clinical and translational cancer research, although exogenous fluorescent molecules can be employed—for example, staining of archival tissue by fluorescently labeled antibodies, or administration of tracer dye molecules for *in vivo* imaging—frequently investigators are seeking to track endogenous fluorescent signals by TPM to gain information about extra/ intracellular processes and interactions in normal vs. disease states. Therein lies one of the strengths of TPM: the ability to investigate intrinsic biologic activity *in vivo* in real time, with near-IR excitation, without the need for additional extrinsic marker molecules that may be toxic or otherwise interfere with normal metabolic activity. For investigations of cancer biology, particularly as applies to *ex vivo* and *in vivo* imaging of human tissue as is our focus herein, this ability to monitor intrinsic metabolism becomes particularly appealing, with the idea that these signals may ultimately yield diagnostic or prognostic clues about cancer. Therefore, and because usage of exogenous fluorophores in pre-clinical cancer research models has been well covered elsewhere (see references in “Introduction” section above), herein we will focus our discussion principally on endogenous fluorescent markers and other optical phenomena that can be monitored by TPM in the context of clinical and translational cancer research.

### Endogenous Fluorophores

Biological tissues contain many molecules endogenous to normal cellular biochemistry that also happen to be fluorescent, and this fluorescence can therefore be exploited by researchers to provide a window into cellular activity. Some of the endogenous fluorescent molecules found in tissues, and that have been fluorescently imaged, include: the mitochondrial matrix proteins nicotinamide adenine dinucleotide (NADH), flavin adenine dinucleotide (FAD), and lipoamide dehydrogenase; the structural proteins elastin, keratin, and collagen; and the pigments lipofuscin, melanin, and porphyrins (these and other intrinsic fluorophores are thoroughly reviewed in Wang *et al.*<sup>110</sup> and Zipfel *et al.*<sup>124</sup>). The fluorescence of these molecules often arises from smaller fluorophores that comprise their structure, such as the UV-emitting amino acids tryptophan, tyrosine, and phenylalanine, and

the 350–600 nm emitting vitamins or vitamin derivatives such as retinol (form of vitamin A), riboflavin (vitamin B2), niacin (vitamin B3) and pyridoxine (vitamin B6), folic acid (vitamin B9), and cholecalciferol (vitamin D3).<sup>124</sup> A majority of intracellular fluorescence arises from NADH, flavins, retinol, tryptophan, and indoleamine derivatives of tryptophan such as serotonin and melatonin, whereas most extracellular fluorescence arises from the structural proteins elastin and collagen.<sup>124</sup> TPEM of NADH and FAD, and both TPEM and SHG microscopy (see next section) of collagen, have arguably been the most investigated intrinsic fluorophores in cancer research. (NADH and FAD have also been heavily investigated in cancer by 1P microscopy approaches, although below we focus our discussions primarily on 2P investigations of these intrinsic fluorophores in cancer research.) As fluorophores, any of these molecules can be excited by either 1P or 2P excitation. However, the benefits of 2P over 1P microscopy for tissue imaging described above, and because the 1P excitation spectra for most of these compounds falls in the tissue-damaging ultraviolet (UV) range, makes 2P excitation ideal for imaging these molecules in living tissue.

In addition to capturing the intensity or emission spectra of these intrinsic biologic fluorophores, the *fluorescence lifetime*, which is sensitive to binding states, molecular interferences, and other aspects of the molecular environment,<sup>3,16,67,91,109,120</sup> can be measured using FLIM. Thus, TPM FLIM data can provide important information about the local biochemical milieu that may aid in distinguishing benign from pathologic cancer features, and as such FLIM is being increasingly employed as a tool in TPM cancer research. A number of elegant discussions and detailed demonstrations of FLIM's utility in cancer research have been presented,<sup>21,91,94</sup> including for human skin imaging,<sup>97</sup> and thus we won't cover this topic in great detail here. However, below we do discuss some FLIM findings as they otherwise fall under our topical criteria, i.e., studies of cancer pathology in *ex vivo* and *in vivo* human tissue.

## Second Harmonic Generation

As described above and in Fig. 1, SHG is another two-photon interaction whereby rather than producing a fluorescence excitation, two photons instead interact simultaneously with a non-centrosymmetric target to produce a new photon with exactly twice the energy (i.e., twice the frequency, and half the wavelength) of the interacting photons.<sup>10,81,83,95</sup> Hence this emitted SHG signal can be generated and monitored using TPM equipment, and is frequently collected in parallel with a TPEF signal, thus providing another means by which TPM can capture biochemical information from intrinsic biologic molecules.

Both TPEF and SHG are often referred to as “nonlinear” optical processes, because the intensity of their emission signals (i.e., the rate at which 2P interactions occur) is proportional to the square of the irradiating intensity. In other words, doubling the irradiating intensity produces four times the emission signal (TPEF or SHG). Contrast this with 1P excitation, in which the fluorescence emission scales linearly with the excitation intensity. Because SHG and TPEF are nonlinear processes, they are *similar* in that they are spatially confined and hence highly useful for 3D imaging and can be performed simultaneously with TPM. They are *different* because SHG is coherent, and hence the amount, direction, and polarization of SHG emission is strongly influenced not just by the scatterers' concentration, but also by their spacing, order vs. disorder, and orientation (Fig. 2). Thus, SHG provides a window into molecular structure not readily available with TPEF alone. Please see Campagnola and Loew,<sup>10</sup> Nadiarnykh *et al.*,<sup>82</sup> Han and Brown,<sup>43</sup> Han *et al.*,<sup>44</sup> and Campagnola<sup>9</sup> for detailed overviews of these concepts.

In the context of cancer and this review, collagen, of which there are many forms, is a highly ordered non-centrosymmetric extracellular matrix (ECM) protein that generates a strong

SHG signal (Fig. 3), and a significantly weaker TPEF signal. In purified gel form, the strength of collagen's SHG and TPEF signals vary with the irradiating wavelength, with 800 nm irradiation producing the strongest SHG (400 nm) and a weak TPEF (~450–600 nm emission, with peak at ~525 nm), whereas 730 nm irradiation produces the strongest collagen TPEF (same emission spectra) and a relatively weaker (but still potent) SHG signal (365 nm) compared to 800 nm irradiation.<sup>126</sup> Collagen was first identified as an SHG-generating component of biological tissue in studies from two groups 20–30 years ago.<sup>30,100</sup> However only with the serious emergence of TPM in biological research did capturing of the SHG signal from collagen and biological tissues become more readily accessible.<sup>8,11,12,22,41,56,106,124,126</sup> Several early pre-clinical studies utilized TPM to image SHG and collagen in *ex vivo* or *in vivo* tumor tissue,<sup>8,42,112</sup> and since then TPM SHG has become a widely employed tool for probing cancer biology, since probing collagen's molecular organization may provide important insights into cancer pathogenesis.

Precisely how and what features of collagen molecular organization affect SHG are topics of significant ongoing investigation, and beyond the scope of this review. Suffice to say for the moment that SHG is enhanced by non-random (and not anti-parallel<sup>33,103</sup>) molecular organization (which promotes constructive enhancement of the vectorial SHG signal, rather than destructive interference), and by ordering on the scale of the irradiating wavelength.<sup>10,81,82,103</sup> Polarization of the SHG signal, and the forward to backward (F/B) ratio of the emitted SHG, can also provide information about the orientation of individual SHG scatterers, and the length scale over which ordering occurs, respectively.<sup>43,44,82,116</sup> Readers can refer to those cited references for technical detail, but for the purposes of this discussion, the key points are that collagen's concentration, spacing, order vs. disorder, and orientation will influence the amount, direction, and polarization of its SHG emission (Fig. 2).

## UTILIZATION OF TPM IN CLINICAL AND TRANSLATIONAL CANCER RESEARCH

In this section, we seek to provide a useful summary of some of the findings enabled by TPM on human clinical tissue in cancer research. With quite a few papers meeting these criteria published in the last few years, we will particularly strive to cover some of this more recent work. Our discussion will be organized going “up the ladder” of clinical and translational research with human specimens, from *ex vivo* biopsied tissue (organized by imaging target, e.g., SHG, NADH, *etc.*), to real-time imaging in human subjects. Included in this latter section will be discussion of some evolving TPM technologies for human imaging—e.g., subsurface TPM endoscopy. Finally we will briefly discuss future directions for TPM imaging of human disease.

### TPM in Human Biopsied Tissue

Most often, the endpoint goal of biomedical research is to translate and evolve findings from pre-clinical laboratory research to treatments for human disease. As part of this process, many pre-clinical research investigations ultimately lead to studies of *ex vivo* or *in vivo* human tissue, and ideally to clinical drug or therapy trials as findings warrant. That we are able to discuss applications of TPM in the clinical and translational research findings relayed here is a testament to the wealth of excellent pre-clinical research that has made these studies possible.

### Quantitative SHG of Collagen

Many of the pre-clinical cancer studies utilizing TPM have been aimed at understanding the role of collagen and other intrinsic molecular markers in breast cancer (reviewed in

Provenzano *et al.*<sup>91</sup> and Provenzano *et al.*<sup>92</sup>). It is theorized that organization or reorganization of collagen, a key component of the ECM, may play roles in tumor genesis, progression, and/or metastasis.<sup>8,44,47,90,101,118</sup> As discussed above, differences in collagen organization, in turn, may be realized as measurable differences in SHG characteristics (Fig. 4). Significant pre-clinical research helped lead to a recent extensive analysis of collagen SHG in biopsied human breast carcinoma tissue. In an analysis of microarrayed tumor tissue cores from 196 breast cancer patients, Conklin *et al.*<sup>20</sup> found that an increased presence of collagen fibers aligned perpendicularly to the tumor boundary (as determined by SHG signal) was associated with decreased survival. Moreover, inclusion of SHG intensity data (to provide some measure of the amount and/or ordering of collagen fibers), rather than just visual assessment of the “directionality” of the SHG signal relative to the tumor interface, slightly increased the significance of this effect.<sup>20</sup> In pre-clinical work in a mouse model of breast cancer, this same group had previously termed this kind of collagen arrangement (i.e., oriented perpendicularly to the tumor boundary) a “tumor-associated collagen signature-3” (TACS-3), whereas TACS-2 indicated straight “taut” fibers often parallel to the tumor boundary, and TACS-1 reflected the presence of dense collagen near small tumors.<sup>90</sup> Because tumor cells preferentially migrate along aligned collagen fibers,<sup>93,113</sup> it is hypothesized that progression in collagen organization sequentially through the TACS-1–3 stages may underlie the transition to tumor metastasis.<sup>20,90</sup> Together these findings help solidify a clinically relevant role for collagen and SHG as biomarkers with prognostic value for predicting breast cancer outcome.

Other work has provided detailed quantitative analyses of differences in SHG properties between normal and cancerous human ovarian biopsy tissue. In this report, Nadiarnykh *et al.*<sup>82</sup> found that compared to normal tissue, malignant ovarian tissue was characterized by denser and more ordered collagen, as determined by qualitative analyses of collagen SHG patterns, and by quantitative analyses of SHG intensity (higher in cancer), and of the scattering properties of the SHG signal (higher in cancer). The SHG F/B ratio was found to be lower in the malignant tissues, again consistent with denser and more regularly packed fibrils that would more efficiently backscatter the SHG.<sup>82</sup> This work provides useful quantitative methods and guidelines for using SHG to distinguish healthy from cancerous tissue. Another study displayed similar differences in collagen morphology and structure in ovarian vs. normal tissue, which they quantified as an increased SHG pixel uniformity in the cancer tissue, reflecting a transition from discrete, randomly oriented linear fibrils to a wavy, more uniformly organized collagen network in the normal vs. cancer tissue, respectively.<sup>58</sup>

Studies have used SHG to differentiate cancerous from normal tissue for other cancer types as well. To control or normalize for artifacts unrelated to experimental effects, many of these studies have expressed the SHG signal as a ratio, relative to some defined or undefined tissue autofluorescence signal acquired at the same excitation wavelength. For example, in a pilot study, by defining their multiphoton autofluorescence (MAF) to SHG index (MAFSI) as  $MAF-SHG/MAF+SHG$ , Wang *et al.*<sup>111</sup> found lower SHG (i.e., MAFSI closer to “1”) in lung adenocarcinoma (LAC) and squamous cell carcinoma (SCC) compared to pair-matched normal lung tissue from the same patient. Likewise, by performing multiple analyses of SHG and TPEF pixels in their TPM images, Zhuo *et al.*<sup>122</sup> found several significant differences in normal vs. neoplastic human esophageal stroma. In brief, compared to normal esophageal stroma, neoplastic stroma displayed: 1. A less defined, more diffuse collagen fibril structure (as determined by how rapidly neighboring SHG pixels “fall off” in value); 2. Loss of collagen (i.e., reduced SHG pixel area); 3. Reduced spacing between elastin fibers; 4. Increased elastin area, and 5. Reduced ratio of collagen to elastin (i.e., SHG/TPEF) signals.<sup>122</sup> In these studies, the TPEF signal at 850 nm excitation was attributed to elastin (TPEF from collagen is negligible at 850 nm<sup>126</sup>), and could be seen from 450 to 625+ nm with a peak at ~510 nm.<sup>122</sup> A similar recent study by many of the same authors also found

reduced collagen area (i.e., ratio of SHG pixels to total pixels) in cancerous compared to normal gastric tissues.<sup>17</sup> Fortunately, although collagen and elastin have some overlap of their TPEF excitation and emission spectra, they can be most readily distinguished because only collagen will produce SHG.<sup>15,17,122,124</sup>

### Optical Biopsies

Other studies have been more qualitatively focused on achieving “optical biopsies,” endeavoring to characterize and map intrinsic fluorescent optical signals for correlation of tissue architecture and pathology with “gold standard” hematoxylin-eosin (H&E) stained histopathology slides. If successful, TPM may eventually provide a more rapid, real time substitute for traditional histopathological processing and analyses. In *ex vivo* intact human gastrointestinal mucosa, using TPM of intrinsic fluorescent signals alone, Rogart *et al.*<sup>99</sup> found they could discern a level of structural detail similar to that found in H&E slides, and that TPM was superior to CM for these purposes. Similar conclusions were drawn in comparative analysis of TPM-imaged and H&E stained normal and cancerous human ovarian biopsy tissue, and this study went on to also identify several parameters uniquely discernible by TPM (e.g., collagen SHG changes, and red-shifted cellular intrinsic fluorescence) by which they could distinguish normal from cancerous tissue *in vivo* in a pre-clinical mouse model of ovarian cancer.<sup>115</sup>

In another study of gastric tissues, Yan *et al.*<sup>119</sup> found they could distinguish cancer from control gastric tissue with simple qualitative comparisons of observed TPM SHG and TPEF features, which also correlated well with common identifying characteristics on the equivalent stained histopathology slides. Similar observations were made using TPM of intrinsic signals alone to distinguish between normal, nodular goiter, and papillary cancerous thyroid tissues.<sup>50</sup> In a similar but somewhat more detailed study, Tewari *et al.*<sup>105</sup> used intrinsic TPM optical signals gathered at 780 nm excitation and 3 emission bands—355–425 nm (SHG), 420–530 nm (short wave autofluorescence that captured mostly elastin, NADH, and FAD in these tissues), and 530–650 (long wave autofluorescence, theorized to capture lipofuscin signal)—to positively identify all key prostatic and periprostatic anatomical structures, and distinguish between normal, benign hyperplastic, and cancerous prostate glands. Finally, in non-human tissue, a similar detailed approach identified normal and cancer pathology in mouse lung tissue using intrinsic TPM signals.<sup>86</sup> Pre-clinical animal optical biopsy work has also identified oral cancer as an area which may ultimately benefit from *in vivo* TPM diagnostics in the clinic.<sup>37,114</sup> With the continued development of TPM endoscopy, these findings are particularly significant, as they harbingers the possibility of real-time *in vivo* TPM diagnostics of cancer.

### NADH and Metabolic Analyses

Several intrinsic intracellular fluorophores can provide information about cells’ metabolism and oxidative reduction capacity. Since tumor growth is an energyheavy process, this metabolic information may in turn prove useful for distinguishing cancerous vs. normal tissue. NADH and FADH<sub>2</sub> (reduced FAD, i.e., flavin adenine dinucleotide hydroquinone) are two reducing agents (electron donors) instrumental in mitochondrial production of ATP by oxidative phosphorylation within the electron transport chain. Because NADH and FADH<sub>2</sub> are both produced and utilized (i.e., oxidized) during the process of cellular respiration, relative concentrations of the oxidized and reduced forms can provide an overall measure of cellular metabolism. NADH is only fluorescent in its reduced form (NADH), whereas FADH<sub>2</sub> is fluorescent mainly in its oxidized FAD<sup>+</sup> form, and these fluorescent forms can be imaged by TPM.<sup>89,124</sup> Thus utilizing these captured signals ratiometrically, often referred to as the “Redox ratio” (i.e., reduction oxidation ratio), can provide a measure of cellular metabolism. This Redox ratio has been expressed in many forms, but when

expressed as  $[FAD^+]/[NADH]$ , a decrease in this ratio typically corresponds to an increase in overall cellular metabolism.<sup>13,102</sup> Because these techniques measure metabolic status, live *ex vivo* tissue is usually used for real-time physiological assessment, although useful NADH and FAD TPM measurements can apparently also be obtained from fixed tissue.<sup>21</sup>

In fresh human bladder biopsies imaged within 1 h of extraction, Cicchi *et al.*<sup>18</sup> found a decrease in both the Redox ratio (expressed as  $FAD-NADH/FAD^+ NADH$ ) and the fluorescence lifetimes of NADH and FAD, in cancerous compared to healthy bladder mucosa. The authors were also able to differentiate cancerous vs. normal tissue by an index of SHG (445 nm) and TPEF (475–620 nm) signals, expressed as  $SHG-TPEF/SHG+TPEF$ , with this index being lower in carcinoma *in situ* bladder tissue. In contrast, in fresh ovarian tissue biopsies, Kirkpatrick *et al.*<sup>58</sup> found their redox ratio  $FAD/FAD+NAD(P)H$  was lower in normal “low risk” tissue, trended higher in normal “high risk” tissue, and was significantly *higher* in cancerous ovarian biopsies. Since *lower* redox ratio has commonly been associated with cancerous tissue (e.g., the reports above) and with higher aerobic metabolism,<sup>13,102</sup> the authors reasonably theorized that their cancerous specimens: 1. May have been substrate limited (thus limiting their aerobic metabolism), and/or 2. May have been glycolytic, which can increase the cellular concentration of reduced nicotinamide adenine dinucleotide phosphate (NADPH) relative to NADH, which may in turn cause a higher redox ratio in the tumor tissue.<sup>58</sup> (NADH and NADPH serve different cellular roles and are optically indistinguishable. Therefore the term “NAD(P)H” is sometimes used to indicate that both forms will be included in the optical signal. Usually the mitochondrial NADH signal will dominate, but under conditions that significantly increase NADPH relative to NADH, the redox ratio and results may be affected accordingly.<sup>49,89,124</sup>) Finally, in fresh colonic biopsy tissues, the redox ratio (as  $NADH/FAD$ ) was higher in pre-cancer and cancer tissues than in normal tissues.<sup>123</sup>

### Intrinsic Signals and Tissue Processing Considerations

Some evidence suggests that (often harsh) tissue post-processing procedures (with or without freezing, fixation, *etc.*) may significantly affect how intrinsic fluorescent signals respond under TPM. The studies above have obtained SHG signals from fresh (live tissue), fresh frozen, and formalin fixed biopsy tissue, and we have obtained SHG signal from both unstained and H&E stained paraffin embedded human archival breast cancer tissue (data not shown), indicating that SHG signals can be obtained from tissue subject to a range of processing techniques. On the other hand, in collagen gels we have observed qualitative differences in the collagen SHG signal in paraformaldehyde fixed vs. unfixed gels (data not shown), and others have observed that SHG signal may be diminished or absent under some fixation and histological processing/staining conditions.<sup>90</sup> These effects might result from tissue dehydration and shrinkage, from fixation-induced protein cross-linking which could vary with fixative type, from stains interfering with the SHG signal, or from other yet unknown sources.<sup>77,82</sup> Along similar lines, in normal human lung that had been frozen and thawed, one group observed strong SHG and auto-fluorescence from fibrous connective tissue (presumably collagen) around alveolar septae at 780 nm excitation.<sup>111</sup> Another group using fresh mouse lung found a similar pattern at 860 nm excitation, but not at 780 nm.<sup>86</sup> These findings suggest that either species differences or tissue processing differences (e.g., fresh vs. frozen) may result in spectral shifting, deterioration, or physical rearrangement of some intrinsic signals. On the other hand, in their working mouse models Conklin *et al.*<sup>21</sup> found that compared to unfixed live specimens, fixation, paraffin embedding, and other slide processing did not significantly impact the fluorescence properties of—nor their ability to obtain useful information from—NADH and FAD measurements. As a whole, it is evident that work is still needed in this area to further clarify whether and how fixation and different

histological processing affects TPM SHG and intrinsic fluorophore signals, and if so, what the implications are for how we compare and contrast SHG cancer studies in clinical tissue.

### TPM in Human Subjects

In many cases, the goal of exploratory work in biopsies is to ultimately translate those findings toward development of *in vivo* cancer diagnostic tools. Accordingly, feasibility studies have been performed and work is ongoing for TPM cancer detection in two main areas: 1. *in vivo* TPM imaging of human skin, and 2. *in vivo* TPM endoscopy of deeper tissue areas. Each will be discussed in turn. It is relevant to note that *confocal* (one-photon) human *in vivo* skin and endoscopy imaging, and technology commercialization (e.g., Lucid's Vivascope and Mauna Kea Technology's Cellvizio or Pentax/Optiscan's ISC-1000 units, respectively), has generally run ahead of two-photon based development of similar technologies, and some comparisons of confocal vs. TPM approaches for clinical *in vivo* imaging have been presented.<sup>52,57,59,73,78</sup> While discussion of these *confocal* technologies is beyond this review, at minimum they help demonstrate that clinical devices using 2P laser excitation should be achievable, especially with continued development of miniaturized lenses and 2P compatible delivery fibers.<sup>32,35</sup>

### *in vivo* TPM Imaging of Human Skin

Normal and diseased human skin has been subject to extensive analysis by TPM, both *ex vivo* and *in vivo*, for the purposes of identifying optical biopsy characteristics that might lead to less-invasive discrimination between normal and diseased tissues.<sup>7,15,29,45,59,62,108</sup> Moreover, studies by several groups that have examined *ex vivo* human skin biopsies demonstrate that TPM approaches can histopathologically characterize and discriminate normal vs. cancerous skin tissues (reviewed in Tsai *et al.*,<sup>108</sup> Lin *et al.*,<sup>68</sup> and Paoli *et al.*<sup>84</sup>). To avoid redundancy, we briefly highlight a few recent studies demonstrating TPM's potential for identifying skin cancer *in vivo*, as well as an emerging TPM method for skin cancer diagnosis.

Dimitrow *et al.*<sup>27</sup> used TPM of intrinsic TPEF to examine the pigmented skin cancer melanoma in 83 patients, both *ex vivo* and *in vivo*. A six-axes diagnostic matrix was constructed to distinguish between nevi (clinically benign, sharply circumscribed, chronic, usually pigmented lesions of the skin) and melanoma, with the following four features being most indicative of melanoma: 1. Overall chaotic epidermal structure; 2. Presence of dendritic cells; 3. Presence of pleomorphic cells; and 4. Poorly defined keratinocyte cell borders. Performing logistic regression analysis showed that using these criteria allowed for 85% accuracy (i.e., correct classification of the lesion) *in vivo*, and 97% accuracy *ex vivo*. This matrix also achieved an *in vivo* diagnostic sensitivity of 75%, and an *in vivo* specificity of 80%. Moreover and importantly, other elegant studies have demonstrated the potential of TPM FLIM to differentiate healthy from cancerous skin tissues.<sup>23,26</sup>

Other recent exciting developments in cancer TPM imaging have used a multiphoton technique sometimes broadly referred to as "pump-probe imaging." Briefly, rather than irradiate the sample with a single near-IR pulsed laser wavelength as is done in standard TPEF and SHG TPM approaches, pump-probe imaging irradiates the sample with two different near-IR wavelengths—the pump and probe pulses respectively—which are spatially colocalized but temporally offset (by ~femtosecond delays) at the sample. The target molecules are first excited by the pump laser, after which absorption of the subsequent probe laser will depend on excited state absorption, stimulated emission, and ground state depletion effects, which in turn will vary with the pump-probe wavelengths and pump-probe delay as they interact with the molecular characteristics of the targets.<sup>88,117</sup> Therefore varying the pump and probe wavelengths and the interpulse times between the pump and

probe beams, and monitoring the response signals, allows researchers to gather much more detailed molecular signatures than is available from standard TPEF techniques. Using such techniques, researchers have been able optically distinguish eumelanin from pheomelanin, despite their otherwise very similar linear near-IR absorptive properties.<sup>88</sup> Going further, the same group then microscopically differentiated and measured eumelanin and pheomelanin content in *ex vivo* human skin biopsies, and found that the ratio of eumelanin to pheomelanin could, along with other diagnostic criteria, help distinguish between melanoma, dysplastic nevi, and benign nevi.<sup>75</sup> These studies, also demonstrated *in vivo* in a mouse model,<sup>76</sup> offer exciting evidence that such pump-probe techniques, perhaps with the continued discovery of additional pump-probe molecular signatures in cancer tissue, may ultimately offer highly accurate *in vivo* diagnostics for skin cancer.

### **in vivo Two-Photon Microendoscopy**

In addition to *in vivo* skin imaging, another clinical TPM approach generating significant attention for cancer diagnostics is focused on developing technologies for intracavitary or intracorporeal two-photon microendoscopy (TPME). The “penetration depth” of normal TPM imaging is technically restricted to, at best, within ~1 mm of the imaged surface. Therefore for TPM cancer imaging of areas besides skin, microendoscopic approaches are required. Generally speaking, two photon microendoscopic approaches can be grouped into two broad categories: 1. Those using rigid, needle-like lenses, for imaging nearer the body surface (with keyhole incisions, for example), and 2. Those using these or similar lenses attached to a flexible fiberoptic probe, thus potentially enabling much deeper intracavity imaging, in traditional “endoscopic” fashion. Ideally such tools—through either surgical or non-surgical intracavitary access— might eliminate the need for more invasive or surgical biopsy-based approaches to cancer detection. Moreover, such approaches may eventually lead further to targeted microsurgical or ablation approaches based on non-linear optical microscopy.<sup>40</sup>

Toward these goals, considerable effort has been devoted to developing and improving TPME technologies. Yet contrary to the relative abundance of human *in vivo* work with 1P confocal microendoscopy, there have been relatively few human TPME studies, and fewer still pertaining specifically to cancer. Presumably this is because TPME technology is more nascent, partly because confocal microendoscopy technologies are not directly transferable due to TPME’s requirement for fiberoptics in which 2P pulses are not degraded.<sup>52</sup> However the advent of photonic crystal fibers and pre-chirped multicore fibers have advanced the technology in this regard, and miniaturization of imaging lenses (e.g., gradient index (GRIN) lenses) and scanning systems have further facilitated development fiber-based TPME systems toward clinical use.<sup>32,35,52,57,61,64,66,78</sup> In fact, there have been numerous demonstrations of fiber-based TPME of intact living tissue (e.g., Rivera *et al.*<sup>96</sup>, and references discussed therein), indicating that the fiber-based limitations for TPME may have been largely overcome. These advances, combined with the fact that fiber based *confocal* microendoscopy is now a relatively routine clinical procedure,<sup>85</sup> suggest that further refinement of prototype fiber-based TPME devices and navigating the important regulatory and safety considerations are the most likely next steps for advancing such “flexible fiber-type” TPME devices to clinical trial.

Human *in vivo* demonstrations of TPME have to our knowledge thus far used rigid needle-like endoscopic GRIN lenses to image SHG in muscle sarcomeres right below the skin surface,<sup>69</sup> and to image ulcerative skin wounds.<sup>61</sup> Cancer related pre-clinical *in vivo* animal work has also used fiber-based TPME to identify pre-cancerous goblet cells in mouse intestine,<sup>2</sup> and other work has explored imaging *in vivo* and *ex vivo* tissue with newly available “stick” objective lenses, which suffer from less spherical aberration than GRIN lenses, and have the potential to image laparoscopically up to centimeters below the body

surface.<sup>99,115</sup> Finally, in two slightly different but exciting TPME applications for cancer diagnostics and treatment, non-linear near-IR based laser microsurgery enables selective ablation of gold nanorod targeted cells,<sup>40,48</sup> and TPME flow cytometry methods may eventually enable *in vivo* identification of circulating tumor cells.<sup>14,46</sup> With these and similar ongoing studies, and with continued miniaturization and “fiberization” of TPME technology as discussed above, intracorporeal and intracavitary demonstrations of TPME specifically for human cancer should soon follow.

### Clinical and Pre-Clinical TPM Instrumentation

Several commercialized TPM devices further demonstrate the potential for TPM skin imaging in the clinic, including JenLab’s DermaInspect and MPTFlex clinically oriented MPM imagers (Jenlab GmbH, Saarbrücken, Germany). Many of the above skin studies were performed with these or very similar instruments. Based on the published reports above, these units scan at ~.05–1 frames/second dependent on the scan area and pixel resolution (and see data presented on Jenlab’s website), which is typical for standard TPM scanning configurations, and precludes realtime imaging at video rates which ultimately may be useful for cancer diagnostics *in vivo*, especially for monitoring physiologic activity. However, faster commercial confocal units (e.g., Lucid Vivascope, 9 frames/sat ~1K 9 1 K), and demonstrations of several TPM instruments that can achieve video-rate image acquisition *in vivo* (for some frame sizes),<sup>57,65</sup> suggest that improved acquisition speed should be within reach of evolving clinical TPM technologies.

To our knowledge a flexible fiber TPM clinical microendoscope has not yet seen commercialization. However, in an intriguing potential pre-commercial development, Lelek *et al.*<sup>66</sup> have performed “proof of concept” imaging of fluorescently labeled human colon crypt cells (apparently *ex vivo*), using a commercial CellVizio confocal microendoscope adapted to TPME by addition of a Ti:Sapphire laser and multicore fiber with pulse precompensation. The authors suggest that this TPME design confers ultimately higher frame rates compared to single core fiber based TPME systems.<sup>66</sup> Thus, it is feasible that commercial development of a flexible fiber based TPME may occur within the relatively near future.

### Safety Considerations

Two-photon microscopy of human skin can cause thermal mechanical damage at the epidermal-dermal junction, which is believed to result from linear (one photon) absorption of the near-IR irradiation by melanin, and can be at least partially mitigated by engineering controls to reduce the pulse repetition rate at the sample (thus lowering average power while maintaining peak power).<sup>74</sup> On the one hand, based on some estimates,<sup>31</sup> the laser powers and scan rates as described in most of the *in vivo/ex vivo* skin studies discussed above are not likely to incur more damage than one might get from natural UV exposure. On the other hand, the subject’s total exposure to and potential for damage from near-IR irradiation will likely depend on many factors including average and peak laser powers used during a session; total duration of exposure as influenced by scan rates and total number of XY planes or sections taken; and perhaps frequency or repetition of exposures to the same skin area over months or years. Therefore, further investigation and standardization of these criteria as they impact potential tissue damage will be important as clinical development and commercialization of new devices moves forward, so that appropriate risk assessments can be made regarding clinical safety. As discussed above, *in vivo* instruments that can maximize image acquisition speeds while minimizing total irradiation power (i.e., maximizing sensitivity) may help mitigate some of these concerns, while also being best able to minimize motion artifacts and capture physiology in real-time. Dela Cruz *et al.*<sup>24</sup> present an informed discussion of many of these issues, and demonstrate that in at least

some tissue types, images of suitable S/N and quality can be obtained at non-mutagenic laser doses. Thus while more work in these areas is needed, at present it appears that TPM technologies for clinical imaging will likely have risk profiles no worse than (and perhaps better than) many current clinical imaging modalities (X-ray, CT scan, etc.).

## FUTURE DIRECTIONS

Many other investigations underway apply TPM to human imaging and diseases beyond cancer, including other skin diseases, eye imaging, vascular and cardiovascular imaging, brain imaging, drug delivery, tissue engineering, fibrosis of liver or other organs, muscle disease, and other organ diseases for which TPM may provide diagnostic value.<sup>9,28,59,60,110</sup> Other TPM-related advanced techniques are being developed which include coherent anti-Stokes Raman scattering (CARS) imaging,<sup>35,79,80</sup> and development of SHG-generating exogenous dyes and nanoprobe for *in vivo* imaging of cellular events.<sup>83,95</sup> These and other developing TPM applications, together with the ongoing progress in human *in vivo* TPM cancer imaging discussed herein, will advance our ability to non-invasively diagnose and treat cancer as we progress into the coming decades.

## Acknowledgments

The authors thank the reviewers for their helpful suggestions on this manuscript, and sincerely apologize to all colleagues whose work we could not cite in this review due to space constraints. This work was supported by National Institute of Health grants R21DA030256 to SWP, and 1DP2OD006501-01 to EBB, and Department of Defense grant W81XWH-091-0405 to EBB. This paper is subject to the NIH Public Access Policy.

## REFERENCES

- Bahlmann K, So PT, Kirber M, Reich R, Kosicki B, McGonagle W, Bellve K. Multifocal multiphoton microscopy (MMM) at a frame rate beyond 600 Hz. *Opt. Express*. 2007; 15:10991–10998. [PubMed: 19547456]
- Bao H, Boussioutas A, Reynolds J, Russell S, Gu M. Imaging of goblet cells as a marker for intestinal metaplasia of the stomach by one-photon and two-photon fluorescence endomicroscopy. *J. Biomed. Opt.* 2009; 14:064031. [PubMed: 20059269]
- Bastiaens PI, Squire A. Fluorescence lifetime imaging microscopy: spatial resolution of biochemical processes in the cell. *Trends Cell Biol.* 1999; 9:48–52. [PubMed: 10087617]
- Beerling E, Ritsma L, Vrisekoop N, Derksen PW, van Rheenen J. Intravital microscopy: new insights into metastasis of tumors. *J. Cell Sci.* 2011; 124:299–310. [PubMed: 21242309]
- Bewersdorf J, Egnér A, Hell SW. Multifocal Multi-Photon Microscopy. In: Pawley, JB., editor. *Handbook of Biological Confocal Microscopy*. Springer; New York: 2006. p. 550-560.
- Bewersdorf J, Pick R, Hell SW. Multifocal multiphoton microscopy. *Opt. Lett.* 1998; 23:655–657. [PubMed: 18087301]
- Breunig HG, Studier H, König K. Multiphoton excitation characteristics of cellular fluorophores of human skin *in vivo*. *Opt. Express*. 2010; 18:7857–7871. [PubMed: 20588627]
- Brown E, McKee T, diTomaso E, Pluen A, Seed B, Boucher Y, Jain RK. Dynamic imaging of collagen and its modulation in tumors *in vivo* using second-harmonic generation. *Nat. Med.* 2003; 9:796–800. [PubMed: 12754503]
- Campagnola P. Second harmonic generation imaging microscopy: applications to diseases diagnostics. *Anal. Chem.* 2011; 83:3224–3231. [PubMed: 21446646]
- Campagnola PJ, Loew LM. Second-harmonic imaging microscopy for visualizing biomolecular arrays in cells, tissues and organisms. *Nat. Biotechnol.* 2003; 21:1356–1360. [PubMed: 14595363]
- Campagnola PJ, Millard AC, Terasaki M, Hoppe PE, Malone CJ, Mohler WA. Three-dimensional high-resolution second-harmonic generation imaging of endogenous structural proteins in biological tissues. *Biophys. J.* 2002; 82:493–508. [PubMed: 11751336]

12. Campagnola PJ, Wei MD, Lewis A, Loew LM. High-resolution nonlinear optical imaging of live cells by second harmonic generation. *Biophys. J.* 1999; 77:3341–3349. [PubMed: 10585956]
13. Chance B, Schoener B, Oshino R, Itshak F, Nakase Y. Oxidation–reduction ratio studies of mitochondria in freeze-trapped samples. NADH and flavoprotein fluorescence signals. *J. Biol. Chem.* 1979; 254:4764–4771. [PubMed: 220260]
14. Chang YC, Ye JY, Thomas TP, Cao Z, Kotlyar A, Tkaczyk ER, Baker JR Jr, Norris TB. Fiberoptic multiphoton flow cytometry in whole blood and in vivo. *J. Biomed. Opt.* 2010; 15:047004. [PubMed: 20799835]
15. Chen J, Lee A, Zhao J, Wang H, Lui H, McLean DI, Zeng H. Spectroscopic characterization and microscopic imaging of extracted and in situ cutaneous collagen and elastic tissue components under two-photon excitation. *Skin. Res. Technol.* 2009; 15:418–426. [PubMed: 19832952]
16. Chen Y, Periasamy A. Characterization of two-photon excitation fluorescence lifetime imaging microscopy for protein localization. *Microsc. Res. Tech.* 2004; 63:72–80. [PubMed: 14677136]
17. Chen J, Zhuo S, Chen G, Yan J, Yang H, Liu N, Zheng L, Jiang X, Xie S. Establishing diagnostic features for identifying the mucosa and submucosa of normal and cancerous gastric tissues by multiphoton microscopy. *Gastrointest. Endosc.* 2011; 73:802–807. [PubMed: 21457819]
18. Cicchi R, Crisci A, Cosci A, Nesi G, Kapsokalyvas D, Giancane S, Carini M, Pavone FS. Time- and spectral-resolved two-photon imaging of healthy bladder mucosa and carcinoma in situ. *Opt. Express.* 2010; 18:3840–3849. [PubMed: 20389394]
19. Condeelis J, Segall JE. Intravital imaging of cell movement in tumours. *Nat. Rev. Cancer.* 2003; 3:921–930. [PubMed: 14737122]
20. Conklin MW, Eickhoff JC, Riching KM, Pehlke CA, Eliceiri KW, Provenzano PP, Friedl A, Keely PJ. Aligned collagen is a prognostic signature for survival in human breast carcinoma. *Am. J. Pathol.* 2011; 178:1221–1232. [PubMed: 21356373]
21. Conklin MW, Provenzano PP, Eliceiri KW, Sullivan R, Keely PJ. Fluorescence lifetime imaging of endogenous fluorophores in histopathology sections reveals differences between normal and tumor epithelium in carcinoma in situ of the breast. *Cell Biochem. Biophys.* 2009; 53:145–157. [PubMed: 19259625]
22. Cox G, Kable E, Jones A, Fraser I, Manconi F, Gorrell MD. 3-dimensional imaging of collagen using second harmonic generation. *J. Struct. Biol.* 2003; 141:53–62. [PubMed: 12576020]
23. De Giorgi V, Massi D, Sestini S, Cicchi R, Pavone FS, Lotti T. Combined non-linear laser imaging (two-photon excitation fluorescence microscopy, fluorescence lifetime imaging microscopy, multispectral multiphoton microscopy) in cutaneous tumours: first experiences. *J. Eur. Acad. Dermatol. Venereol. (JEADV).* 2009; 23:314–316.
24. Dela Cruz JM, McMullen JD, Williams RM, Zipfel WR. Feasibility of using multiphoton excited tissue autofluorescence for in vivo human histopathology. *Biomed. Opt. Express.* 2010; 1:1320–1330. [PubMed: 21258552]
25. Denk W, Strickler JH, Webb WW. Two-photon laser scanning fluorescence microscopy. *Science.* 1990; 248:73–76. [PubMed: 2321027]
26. Dimitrow E, Riemann I, Ehlers A, Koehler MJ, Norgauer J, Elsner P, Konig K, Kaatz M. Spectral fluorescence lifetime detection and selective melanin imaging by multiphoton laser tomography for melanoma diagnosis. *Exp. Dermatol.* 2009; 18:509–515. [PubMed: 19243426]
27. Dimitrow E, Ziemer M, Koehler MJ, Norgauer J, Konig K, Elsner P, Kaatz M. Sensitivity and specificity of multiphoton laser tomography for in vivo and ex vivo diagnosis of malignant melanoma. *J. Invest. Dermatol.* 2009; 129:1752–1758. [PubMed: 19177136]
28. Dong CY, Campagnola PJ. Optical diagnostics of tissue pathology by multiphoton microscopy. *Expert Opin. Med. Diag.* 2010; 4:519–529.
29. Ericson MB, Simonsson C, Guldbbrand S, Ljungblad C, Paoli J, Smedh M. Two-photon laser-scanning fluorescence microscopy applied for studies of human skin. *J. Biophotonics.* 2008; 1:320–330. [PubMed: 19343655]
30. Fine S, Hansen WP. Optical second harmonic generation in biological systems. *Appl. Opt.* 1971; 10:2350–2353. [PubMed: 20111328]

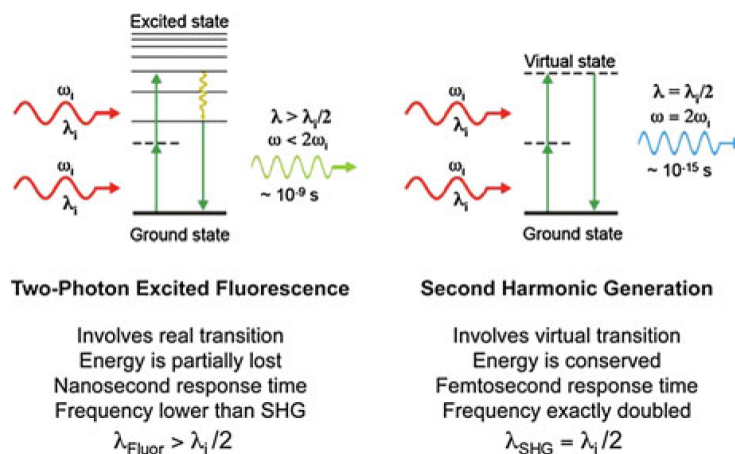
31. Fischer F, Volkmer B, Puschmann S, Greinert R, Breitbart W, Kiefer J, Wepf R. Risk estimation of skin damage due to ultrashort pulsed, focused near-infrared laser irradiation at 800 nm. *J. Biomed. Opt.* 2008; 13:041320. [PubMed: 19021328]
32. Flusberg BA, Cocker ED, Piyawattanametha W, Jung JC, Cheung EL, Schnitzer MJ. Fiber-optic fluorescence imaging. *Nat. Methods.* 2005; 2:941–950. [PubMed: 16299479]
33. Freund I, Deutsch M. Macroscopic polarity of connective tissue is due to discrete polar structures. *Biopolymers.* 1986; 25:601–606. [PubMed: 3708106]
34. Fricke M, Nielsen T. Two-dimensional imaging without scanning by multifocal multiphoton microscopy. *Appl. Opt.* 2005; 44:2984–2988. [PubMed: 15929287]
35. Fu L, Gu M. Fibre-optic nonlinear optical microscopy and endoscopy. *J. Microsc.* 2007; 226:195–206. [PubMed: 17535259]
36. Fukumura D, Duda DG, Munn LL, Jain RK. Tumor microvasculature and microenvironment: novel insights through intravital imaging in pre-clinical models. *Microcirculation.* 2010; 17:206–225. [PubMed: 20374484]
37. Ammer, A. Gatesman; Hayes, KE.; Martin, KH.; Zhang, L.; Spirou, GA.; Weed, SA. Multi-photon imaging of tumor cell invasion in an orthotopic mouse model of oral squamous cell carcinoma. *J. Vis. Exp.* 2011; 53:e2941.
38. Ghajar CM, Bissell MJ. Extracellular matrix control of mammary gland morphogenesis and tumorigenesis: insights from imaging. *Histochem. Cell Biol.* 2008; 130:1105–1118. [PubMed: 19009245]
39. Goppert-Meyer M. Uber Elementarakte mit zwei Quantensprungen. Göttinger Dissertation. *Ann. Phys.* 1931; 9:273–294.
40. Gu M, Bao HC, Li JL. Cancer-cell microsurgery using nonlinear optical endomicroscopy. *J. Biomed. Opt.* 2010; 15:050502. [PubMed: 21054074]
41. Guo Y, Ho PP, Tirkskliunas A, Liu F, Alfano RR. Optical harmonic generation from animal tissues by the use of picosecond and femtosecond laser pulses. *Appl. Opt.* 1996; 35:6810–6813. [PubMed: 21151266]
42. Guo Y, Savage HE, Liu F, Schantz SP, Ho PP, Alfano RR. Subsurface tumor progression investigated by noninvasive optical second harmonic tomography. *Proc. Natl Acad. Sci. USA.* 1999; 96:10854–10856. [PubMed: 10485915]
43. Han X, Brown E. Measurement of the ratio of forward-propagating to back-propagating second harmonic signal using a single objective. *Opt. Express.* 2010; 18:10538–10550. [PubMed: 20588906]
44. Han X, Burke RM, Zettel ML, Tang P, Brown EB. Second harmonic properties of tumor collagen: determining the structural relationship between reactive stroma and healthy stroma. *Opt. Express.* 2008; 16:1846–1859. [PubMed: 18542263]
45. Hanson KM, Bardeen CJ. Application of non-linear optical microscopy for imaging skin. *Photochem. Photobiol.* 2009; 85:33–44. [PubMed: 19161396]
46. He W, Wang H, Hartmann LC, Cheng JX, Low PS. In vivo quantitation of rare circulating tumor cells by multiphoton intravital flow cytometry. *Proc. Natl Acad. Sci. USA.* 2007; 104:11760–11765. [PubMed: 17601776]
47. Hompland T, Erikson A, Lindgren M, Lindmo T, de Lange Davies C. Second-harmonic generation in collagen as a potential cancer diagnostic parameter. *J. Biomed. Opt.* 2008; 13:054050. [PubMed: 19021430]
48. Huang X, El-Sayed IH, Qian W, El-Sayed MA. Cancer cell imaging and photothermal therapy in the near-infrared region by using gold nanorods. *J. Am. Chem. Soc.* 2006; 128:2115–2120. [PubMed: 16464114]
49. Huang S, Heikal AA, Webb WW. Two-photon fluorescence spectroscopy and microscopy of NAD(P)H and flavoprotein. *Biophys. J.* 2002; 82:2811–2825. [PubMed: 11964266]
50. Huang Z, Li Z, Chen R, Lin J, Li Y, Li C. In vitro imaging of thyroid tissues using two-photon excited fluorescence and second harmonic generation. *Photomed. Laser Surg.* 2010; 28(Suppl 1):S129–S133. [PubMed: 20649422]

51. Ingman WV, Wyckoff J, Gouon-Evans V, Condeelis J, Pollard JW. Macrophages promote collagen fibrillogenesis around terminal end buds of the developing mammary gland. *Dev. Dyn.* 2006; 235:3222–3229. [PubMed: 17029292]
52. Jung JC, Schnitzer MJ. Multiphoton endoscopy. *Opt. Lett.* 2003; 28:902–904. [PubMed: 12816240]
53. Kaiser W, Garret C. Two-photon excitation in CaF<sub>2</sub>: Eu<sup>2+</sup>. *Phys. Rev. Lett.* 1961; 7:229–231.
54. Kedrin D, Wyckoff J, Sahai E, Condeelis J, Segall JE. Imaging tumor cell movement in vivo. *Curr. Protoc. Cell Biol.* 2007 Chapter 19:Unit 19.17.
55. Kim KH, Buehler C, Bahlmann K, Ragan T, Lee WC, Nedivi E, Heffer EL, Fantini S, So PT. Multifocal multiphoton microscopy based on multianode photomultiplier tubes. *Opt. Express.* 2007; 15:11658–11678. [PubMed: 19547526]
56. Kim BM, Eichler J, Reiser KM, Rubenchik AM, Da Silva LB. Collagen structure and nonlinear susceptibility: effects of heat, glycation, and enzymatic cleavage on second harmonic signal intensity. *Lasers Surg. Med.* 2000; 27:329–335. [PubMed: 11074509]
57. Kim P, Puoris'haag M, Cote D, Lin CP, Yun SH. In vivo confocal and multiphoton microendoscopy. *J. Biomed. Opt.* 2008; 13:010501. [PubMed: 18315346]
58. Kirkpatrick ND, Brewer MA, Utzinger U. Endogenous optical biomarkers of ovarian cancer evaluated with multiphoton microscopy. *Cancer Epidemiol. Biomarkers Prev.* 2007; 16:2048–2057. [PubMed: 17932352]
59. Koehler MJ, Speicher M, Lange-Asschenfeldt S, Stockfleth E, Metz S, Elsner P, Kaatz M, Konig K. Clinical application of multiphoton tomography in combination with confocal laser scanning microscopy for in vivo evaluation of skin diseases. *Exp. Dermatol.* 2011; 20:589–594. [PubMed: 21539618]
60. Konig K. Multiphoton microscopy in life sciences. *J. Microsc.* 2000; 200:83–104. [PubMed: 11106949]
61. Konig, K.; Buckle, R.; Weinigel, M.; Elsner, P.; Kaatz, M. Clinical multiphoton tomography and clinical two-photon microendoscopy. In: Periasamy, A.; So, PT., editors. *Multiphoton Microscopy in the Biomedical Sciences IX*, Proceedings of the SPIE; New York: Oxford University Press; 2009. p. 7183191-7183199.
62. Konig K, Speicher M, Buckle R, Reckfort J, McKenzie G, Welzel J, Koehler MJ, Elsner P, Kaatz M. Clinical optical coherence tomography combined with multiphoton tomography of patients with skin diseases. *J. Biophotonics.* 2009; 2:389–397. [PubMed: 19598177]
63. Le Devedec SE, van Roosmalen W, Pont C, Lalai R, de Bont H, van de Water B. Two-photon intravital multicolour imaging to study metastatic behaviour of cancer cells in vivo. *Methods Mol. Biol.* 2011; 769:331–349. [PubMed: 21748686]
64. Le Harzic R, Riemann I, Weinigel M, Konig K, Messerschmidt B. Rigid and high-numerical-aperture two-photon fluorescence endoscope. *Appl. Opt.* 2009; 48:3396–3400. [PubMed: 19543347]
65. Lee AMD, Wang H, Yu Y, Tang S, Zhao J, Lui H, McLean DI, Zeng H. In vivo video rate multiphoton microscopy imaging of human skin. *Opt. Lett.* 2011; 36:2865–2867. [PubMed: 21808340]
66. Lelek M, Suran E, Louradour F, Barthelemy A, Viellerobe B, Lacombe F. Coherent femtosecond pulse shaping for the optimization of a non-linear micro-endoscope. *Opt. Express.* 2007; 15:10154–10162. [PubMed: 19547364]
67. Lin HJ, Herman P, Lakowicz JR. Fluorescence lifetime-resolved pH imaging of living cells. *Cytometry A: J. Int. Soc. Anal. Cytol.* 2003; 52:77–89.
68. Lin SJ, Jee SH, Dong CY. Multiphoton microscopy: a new paradigm in dermatological imaging. *Eur. J. Dermatol.* 2007; 17:361–366. [PubMed: 17673377]
69. Llewellyn ME, Barretto RP, Delp SL, Schnitzer MJ. Minimally invasive high-speed imaging of sarcomere contractile dynamics in mice and humans. *Nature.* 2008; 454:784–788. [PubMed: 18600262]
70. Lohela M, Werb Z. Intravital imaging of stromal cell dynamics in tumors. *Curr. Opin. Genet. Dev.* 2010; 20:72–78. [PubMed: 19942428]
71. Lunt SJ, Gray C, Reyes-Aldasoro CC, Matcher SJ, Tozer GM. Application of intravital microscopy in studies of tumor microcirculation. *J. Biomed. Opt.* 2010; 15:011113. [PubMed: 20210439]

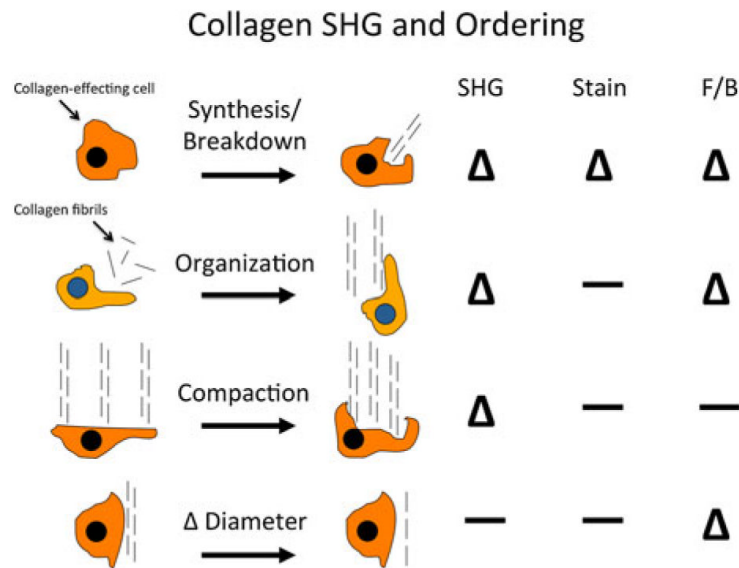
72. Martini J, Andresen V, Anselmetti D. Scattering suppression and confocal detection in multifocal multi-photon microscopy. *J. Biomed. Opt.* 2007; 12:034010. [PubMed: 17614718]
73. Masters B, So P. Confocal microscopy and multi-photon excitation microscopy of human skin in vivo. *Opt. Express.* 2001; 8:2–10. [PubMed: 19417779]
74. Masters BR, So PT, Buehler C, Barry N, Sutin JD, Mantulin WW, Gratton E. Mitigating thermal mechanical damage potential during two-photon dermal imaging. *J. Biomed. Opt.* 2004; 9:1265–1270. [PubMed: 15568947]
75. Matthews TE, Piletic IR, Selim MA, Simpson MJ, Warren WS. Pump-probe imaging differentiates melanoma from melanocytic nevi. *Sci. Transl. Med.* 2011; 3:71–72.
76. Matthews TE, Wilson JW, Degan S, Simpson MJ, Jin JY, Zhang JY, Warren WS. In vivo and ex vivo epi-mode pump-probe imaging of melanin and microvasculature. *Biomed Opt. Express.* 2011; 2:1576–1583. [PubMed: 21698020]
77. Meek KM. The use of glutaraldehyde and tannic acid to preserve reconstituted collagen for electron microscopy. *Histochemistry.* 1981; 73:115–120. [PubMed: 6797991]
78. Meier R, Kromer K, Stepp H, Sroka R. A comparison of confocal and two-photon microendoscopy. *IFMBE Proc.* 2009; 25(6):177–178.
79. Meyer T, Bergner N, Bielecki C, Krafft C, Akimov D, Romeike BF, Reichart R, Kalff R, Dietzek B, Popp J. Nonlinear microscopy, infrared, and Raman microspectroscopy for brain tumor analysis. *J. Biomed. Opt.* 2011; 16:021113. [PubMed: 21361676]
80. Min W, Freudiger CW, Lu S, Xie XS. Coherent nonlinear optical imaging: beyond fluorescence microscopy. *Annu. Rev. Phys. Chem.* 2011; 62:507–530. [PubMed: 21453061]
81. Mohler W, Millard AC, Campagnola PJ. Second harmonic generation imaging of endogenous structural proteins. *Methods.* 2003; 29:97–109. [PubMed: 12543075]
82. Nadiarykh O, LaComb RB, Brewer MA, Campagnola PJ. Alterations of the extracellular matrix in ovarian cancer studied by Second Harmonic Generation imaging microscopy. *BMC Cancer.* 2010; 10:94. [PubMed: 20222963]
83. Pantazis P, Maloney J, Wu D, Fraser SE. Second harmonic generating (SHG) nanoprobe for in vivo imaging. *Proc. Natl Acad. Sci. USA.* 2010; 107:14535–14540. [PubMed: 20668245]
84. Paoli J, Smedh M, Ericson MB. Multiphoton laser scanning microscopy—a novel diagnostic method for superficial skin cancers. *Semin. Cutan. Med. Surg.* 2009; 28:190–195. [PubMed: 19782943]
85. Paull PE, Hyatt BJ, Wassef W, Fischer AH. Confocal laser endomicroscopy: a primer for pathologists. *Arch. Pathol. Lab. Med.* 2011; 135:1343–1348. [PubMed: 21970490]
86. Pavlova I, Hume KR, Yazinski SA, Peters RM, Weiss RS, Webb WW. Multiphoton microscopy as a diagnostic imaging modality for lung cancer. *Proc. Soc. Photo Opt. Instrum. Eng.* 2010; 7569:756918. [PubMed: 20445820]
87. Pawley, JB., editor. *Handbook of Biological Confocal Microscopy.* Springer; New York: 2006. p. 1016
88. Piletic IR, Matthews TE, Warren WS. Probing near-infrared photorelaxation pathways in eumelanins and pheomelanins. *J. Phys. Chem. A.* 2010; 114:11483–11491. [PubMed: 20882951]
89. Piston DW, Masters BR, Webb WW. Three-dimensionally resolved NAD(P)H cellular metabolic redox imaging of the in situ cornea with two-photon excitation laser scanning microscopy. *J. Microsc.* 1995; 178:20–27. [PubMed: 7745599]
90. Provenzano PP, Eliceiri KW, Campbell JM, Inman DR, White JG, Keely PJ. Collagen reorganization at the tumor-stromal interface facilitates local invasion. *BMC Med.* 2006; 4:38. [PubMed: 17190588]
91. Provenzano PP, Eliceiri KW, Keely PJ. Multiphoton microscopy and fluorescence lifetime imaging microscopy (FLIM) to monitor metastasis and the tumor microenvironment. *Clin. Exp. Metastasis.* 2009; 26:357–370. [PubMed: 18766302]
92. Provenzano PP, Eliceiri KW, Yan L, Ada-Nguema A, Conklin MW, Inman DR, Keely PJ. Nonlinear optical imaging of cellular processes in breast cancer. *Microsc. Microanal.* 2008; 14:532–548. [PubMed: 18986607]

93. Provenzano PP, Inman DR, Eliceiri KW, Trier SM, Keely PJ. Contact guidance mediated three-dimensional cell migration is regulated by Rho/ROCK-dependent matrix reorganization. *Biophys. J.* 2008; 95:5374–5384. [PubMed: 18775961]
94. Provenzano PP, Rueden CT, Trier SM, Yan L, Ponik SM, Inman DR, Keely PJ, Eliceiri KW. Nonlinear optical imaging and spectral-lifetime computational analysis of endogenous and exogenous fluorophores in breast cancer. *J. Biomed. Opt.* 2008; 13:031220. [PubMed: 18601544]
95. Reeve JE, Anderson HL, Clays K. Dyes for biological second harmonic generation imaging. *Phys. Chem. Chem. Phys.* 2010; 12:13484–13498. [PubMed: 20820473]
96. Rivera DR, Brown CM, Ouzounov DG, Pavlova I, Kobat D, Webb WW, Xu C. Compact and flexible raster scanning multiphoton endoscope capable of imaging unstained tissue. *Proc. Natl Acad. Sci. USA.* 2011; 108:17598–17603. [PubMed: 22006303]
97. Roberts MS, Dancik Y, Prow TW, Thorling CA, Lin LL, Grice JE, Robertson TA, Konig K, Becker W. Non-invasive imaging of skin physiology and percutaneous penetration using fluorescence spectral and lifetime imaging with multiphoton and confocal microscopy. *Eur. J. Pharm. Biopharm.* 2011; 77:469–488. [PubMed: 21256962]
98. Rocheleau JV, Piston DW. Two-photon excitation microscopy for the study of living cells and tissues. *Curr. Protoc. Cell Biol.* 2003 Chapter 4:Unit 4.11.
99. Rogart JN, Nagata J, Loeser CS, Roorda RD, Aslanian H, Robert ME, Zipfel WR, Nathanson MH. Multiphoton imaging can be used for microscopic examination of intact human gastrointestinal mucosa ex vivo. *Clin. Gastroenterol. Hepatol.* 2008; 6:95–101. [PubMed: 18065276]
100. Roth S, Freund I. Second harmonic generation in collagen. *J. Chem. Phys.* 1979; 70:1637.
101. Schedin P, Keely PJ. Mammary gland ECM remodeling, stiffness, and mechanosignaling in normal development and tumor progression. *Cold Spring Harb. Perspect. Biol.* 2011; 3:a003228. [PubMed: 20980442]
102. Skala MC, Riching KM, Gendron-Fitzpatrick A, Eickhoff J, Eliceiri KW, White JG, Ramanujam N. In vivo multiphoton microscopy of NADH and FAD redox states, fluorescence lifetimes, and cellular morphology in precancerous epithelia. *Proc. Natl Acad. Sci. USA.* 2007; 104:19494–19499. [PubMed: 18042710]
103. Stoller P, Celliers PM, Reiser KM, Rubenchik AM. Quantitative second-harmonic generation microscopy in collagen. *Appl. Opt.* 2003; 42:5209–5219. [PubMed: 12962402]
104. Straub M, Lodemann P, Holroyd P, Jahn R, Hell SW. Live cell imaging by multifocal multiphoton microscopy. *Eur. J. Cell Biol.* 2000; 79:726–734. [PubMed: 11089921]
105. Tewari AK, Shevchuk MM, Sterling J, Grover S, Herman M, Yadav R, Mudalair K, Srivastava A, Rubin MA, Zipfel WR, Maxfield FR, Xu C, Webb WW, Mukherjee S. Multiphoton microscopy for structure identification in human prostate and periprostatic tissue: implications in prostate cancer surgery. *BJU Int.* 2011; 108(9):1421–1429. [PubMed: 21443651]
106. Theodossiou T, Rapti GS, Hovhannisyan V, Georgiou E, Politopoulos K, Yova D. Thermally induced irreversible conformational changes in collagen probed by optical second harmonic generation and laser-induced fluorescence. *Lasers Med. Sci.* 2002; 17:34–41. [PubMed: 11845366]
107. Tozer GM, Ameer-Beg SM, Baker J, Barber PR, Hill SA, Hodgkiss RJ, Locke R, Prise VE, Wilson I, Vojnovic B. Intravital imaging of tumour vascular networks using multi-photon fluorescence microscopy. *Adv. Drug Deliv. Rev.* 2005; 57:135–152. [PubMed: 15518926]
108. Tsai TH, Jee SH, Dong CY, Lin SJ. Multiphoton microscopy in dermatological imaging. *J. Dermatol. Sci.* 2009; 56:1–8. [PubMed: 19699614]
109. van Munster EB, Gadella TW. Fluorescence lifetime imaging microscopy (FLIM). *Adv. Biochem. Eng. Biotechnol.* 2005; 95:143–175. [PubMed: 16080268]
110. Wang BG, Konig K, Halhuber KJ. Two-photon microscopy of deep intravital tissues and its merits in clinical research. *J. Microsc.* 2010; 238:1–20. [PubMed: 20384833]
111. Wang CC, Li FC, Wu RJ, Hovhannisyan VA, Lin WC, Lin SJ, So PT, Dong CY. Differentiation of normal and cancerous lung tissues by multiphoton imaging. *J. Biomed. Opt.* 2009; 14:044034. [PubMed: 19725745]
112. Wang W, Wyckoff JB, Frohlich VC, Oleynikov Y, Huttelmaier S, Zavadij J, Cermak L, Bottinger EP, Singer RH, White JG, Segall JE, Condeelis JS. Single cell behavior in metastatic primary

- mammary tumors correlated with gene expression patterns revealed by molecular profiling. *Cancer Res.* 2002; 62:6278–6288. [PubMed: 12414658]
113. Wang W, Wyckoff JB, Goswami S, Wang Y, Sidani M, Segall JE, Condeelis JS. Coordinated regulation of pathways for enhanced cell motility and chemotaxis is conserved in rat and mouse mammary tumors. *Cancer Res.* 2007; 67:3505–3511. [PubMed: 17440055]
  114. Wilder-Smith P, Krasieva T, Jung WG, Zhang J, Chen Z, Osann K, Tromberg B. Noninvasive imaging of oral premalignancy and malignancy. *J. Biomed. Opt.* 2005; 10:051601. [PubMed: 16292949]
  115. Williams RM, Flesken-Nikitin A, Ellenson LH, Connolly DC, Hamilton TC, Nikitin AY, Zipfel WR. Strategies for high-resolution imaging of epithelial ovarian cancer by laparoscopic nonlinear microscopy. *Transl. Oncol.* 2010; 3:181–194. [PubMed: 20563260]
  116. Williams RM, Zipfel WR, Webb WW. Interpreting second-harmonic generation images of collagen I fibrils. *Biophys. J.* 2005; 88:1377–1386. [PubMed: 15533922]
  117. Wilson, JW.; Matthews, TE.; Degan, S.; Zhang, JY.; Simpson, MJ.; Warren, WS. CLEO:2011—laser applications to photonic applications, OSA Technical Digest (CD). Optical Society of America; 2011. Pump-probe melanoma imaging: applications to high-resolution and in vivo microscopy. paper PDPB5, 2011
  118. Wolf K, Alexander S, Schacht V, Coussens LM, von Andrian UH, van Rheenen J, Deryugina E, Friedl P. Collagen-based cell migration models in vitro and in vivo. *Semin. Cell Dev. Biol.* 2009; 20:931–941. [PubMed: 19682592]
  119. Yan J, Chen G, Chen J, Liu N, Zhuo S, Yu H, Ying M. A pilot study of using multiphoton microscopy to diagnose gastric cancer. *Surg. Endosc.* 2011; 25:1425–1430. [PubMed: 21046158]
  120. Yan L, Rueden CT, White JG, Eliceiri KW. Applications of combined spectral lifetime microscopy for biology. *Biotechniques.* 2006; 41:249, 251, 253. [PubMed: 16989084]
  121. Zal T, Chodaczek G. Intravital imaging of anti-tumor immune response and the tumor microenvironment. *Semin. Immunopathol.* 2010; 32:305–317. [PubMed: 20652252]
  122. Zhuo S, Chen J, Xie S, Hong Z, Jiang X. Extracting diagnostic stromal organization features based on intrinsic two-photon excited fluorescence and second-harmonic generation signals. *J. Biomed. Opt.* 2009; 14:020503. [PubMed: 19405709]
  123. Zhuo S, Yan J, Chen G, Chen J, Liu Y, Lu J, Zhu X, Jiang X, Xie S. Label-free monitoring of colonic cancer progression using multiphoton microscopy. *Biomed. Opt. Express.* 2011; 2:615–619. [PubMed: 21412466]
  124. Zipfel WR, Williams RM, Christie R, Nikitin AY, Hyman BT, Webb WW. Live tissue intrinsic emission microscopy using multiphoton-excited native fluorescence and second harmonic generation. *Proc. Natl Acad. Sci. USA.* 2003; 100:7075–7080. [PubMed: 12756303]
  125. Zipfel WR, Williams RM, Webb WW. Non-linear magic: multiphoton microscopy in the biosciences. *Nat. Biotechnol.* 2003; 21:1369–1377. [PubMed: 14595365]
  126. Zoumi A, Yeh A, Tromberg BJ. Imaging cells and extracellular matrix in vivo by using second-harmonic generation and two-photon excited fluorescence. *Proc. Natl Acad. Sci. USA.* 2002; 99:11014–11019. [PubMed: 12177437]



**FIGURE 1.** Non-linear TPEF and SHG compared. Shown are the Perrin–Jablonski fluorescence diagram for TPEF (left), and the energy-level diagram for SHG (right). In TPEF, two photons of incident frequency  $\omega_i$  and wavelength  $\lambda_i$  (in red) are simultaneously absorbed by a fluorophore, to produce a single photon (in green) whose wavelength is greater than one-half the irradiating wavelength  $\lambda_i$  (i.e., with some net energy loss). In SHG, two photons of frequency  $\omega_i$  and wavelength  $\lambda_i$  (in red) interacting simultaneously with a non-centrosymmetric target, combine to form a single photon (in blue) whose wavelength is exactly half that of the incident wavelength  $\lambda_i$  (i.e., no net energy loss). Hence, 2P irradiation of an SHG generating target at 810 nm will emit SHG photons at 405 nm, whereas TPEF emission might occur at ~500 nm for the same target excited at 810 nm. Diagram is reproduced and modified with kind permission from Pantazis *et al.*,<sup>83</sup> with acknowledgment to National Academy of Sciences, USA.

**FIGURE 2.**

Second harmonic generation is a coherent process. Because SHG is a coherent process, in this cartoon we illustrate how at least four aspects of collagen's homeostasis may influence collagen's raw TPM SHG signal, an antibody Stain for quantifying collagen levels, and the ratio of forward-scattered to backward-scattered SHG (F/B) for collagen. SHG is sensitive to the regular ordering of scatterers, so conversion of disordered collagen triple helices into ordered fibrils, or de novo synthesis/breakdown of ordered fibrils can alter the detected SHG. Compaction of fibrils can also alter the detected SHG by changing the spacing of fibrils and hence altering interference properties. Lastly, the diameter of ordered fibrils dictates the F/B ratio for collagen SHG.<sup>44</sup> Readers should appreciate that this overview, simplified for pictorial presentation and clarity, does not reflect all possible signal changes. For example, organization or compaction changes could alter antibody stain intensity, depending on how antibody binding epitopes get rearranged.

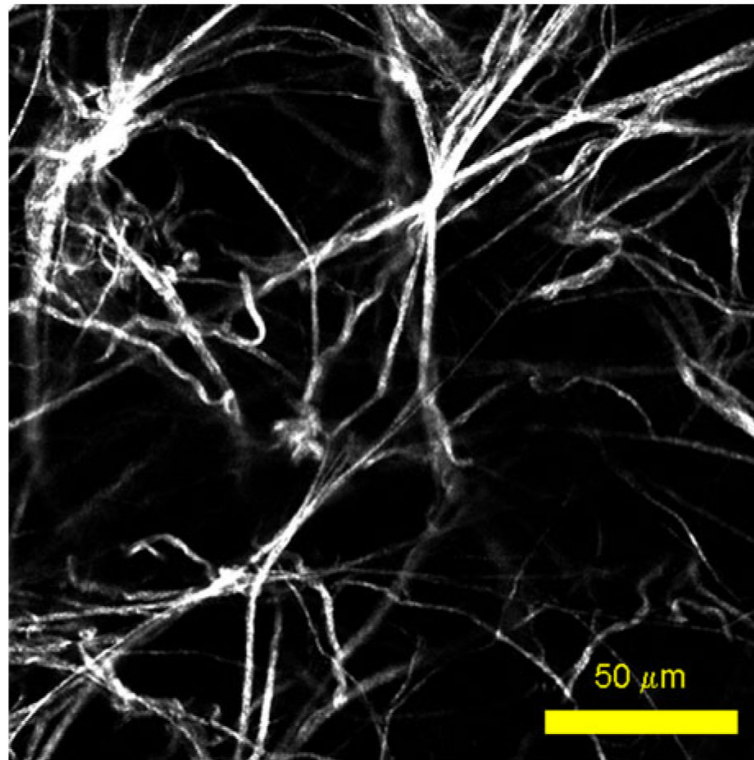


**FIGURE 3.** Tumor collagen produces strong SHG. Collagen in an *ex vivo* E0771 mammary tumor produces a strong SHG signal in response to near-IR two-photon irradiation, showing the fibrous structure characteristic of highly ordered collagen fibers. All work was approved by and performed in accordance with the guidelines of the Institutional Animal Care and Use Committee (IACUC).

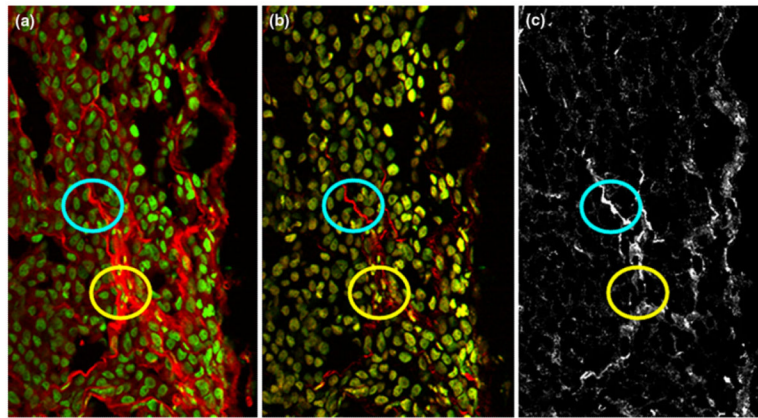


**FIGURE 4.**

Quantifying tumor collagen SHG. (a) Collagen in an *ex vivo* E0771 mammary tumor can be immunohistochemically (IHC) labeled and quantified with an anti-collagen antibody (pseudocolored red). (b) Collagen produces a strong SHG signal (pseudocolored red) (same field as in (a)). (c) Dividing the SHG (b) image signal by the IHC (a) image signal (SHG/IHC) provides a new “ratiometric” image (c) which indicates levels of SHG relative to total collagen on a pixel-by-pixel basis. Hence circled regions indicate where this ratio is clearly different (i.e., high or low pixel values), suggesting differences in relative collagen organization in these regions. Increased SHG signal relative to immunolabeling may represent a conversion of disordered triple helices to ordered fibrils, or compaction of fibrils.<sup>51</sup> An increase in both signals may represent *de novo* synthesis of ordered triple helices. Green signal is a nuclear counterstain. All work was approved by and performed in accordance with the guidelines of the IACUC. Diagram is modified from Brown *et al.*,<sup>8</sup> with permission, and acknowledgment to Nature Publishing Group.

**Appendix 1.** List of personnel receiving pay from the research effort:

Ed Brown Kelley Madden Avraham Salzman Khawarl Liverpool Kelley Sullivan Javier Lapeira Edith Lord Ping Tang Dan Byun Martha Zettel Ryan Burke Kelly Kyker-Snowman Kathryn Fitzgerald Kattie Litts	Sarah Sushchik Katie Cooley Seth Perry Jill Kulla Giuseppe Arcuri Erin Keegan Peter O'Connell Jill Schueckler Jesse Sharp Petr Stastka Zhou Xu Ryan Dawes Mehar Cheema
---	--